Deep Inelastic Exclusive ρ^0 Production using 485 GeV Muons

A thesis presented

by

Michael Henry Schmitt

to

The Department of Physics

in partial fulfillment of the requirements
for the degree of
Doctor of Philosophy
in the subject of
Physics
Harvard University
Cambridge, Massachusetts

October, 1991

Abstract

Neutral vector mesons share the quantum numbers as the photon, consequently, they are produced copiously in diffractive interactions of photons. The lightest of these, the ρ^0 meson, have been studied in the absorption of high energy virtual photons on hydrogen and deuterium. The mass spectrum, decay distribution, and momentum transfer to the target nucleon has been studied as a function of the kinematic variables. The interference of the two-pion resonance and continuum is constant as a function of the virtual photon mass, Q^2. The ρ^0 polarization changes from purely transverse at low Q^2 to predominantly longitudinal at high Q^2. The azimuthal decay distribution conforms to the expected form, including terms for transverse-transverse and transverse-longitudinal interference. The diffractive slope parameter declines only slightly with Q^2, indicating that for Q^2 up to approximately 4 GeV^2, production of exclusive ρ^0 mesons is a diffractive process.

Acknowledgements

This thesis is dedicated to my parents,

Judith and Gunther Schmitt.

Von Sonn' und Welten weiß ich nichts zu sagen,
Ich sehe nur, wie sich die Menschen plagen.
Der kleine Gott der Welt bleibt stets von gleichem Schlag,
Und ist so wunderlich als wie am ersten Tag.
Ein wenig besser würd' er leben,
Hättst du ihm nicht den Schein des Himmelslichts gegeben;
Er nennt's Vernunft und braucht's allein,
Nur tierischer als jedes Tier zu sein.
Er scheint mir, mit Verlaub von Euer Gnaden,
Wie eine der langbeinigen Zikaden,
Die immer fliegt und fliegend springt,
Und gleich im Gras ihr altes Liedchen singt;
Und läg er nur noch immer in dem Grase!
In jeden Quark begräbt er seine Nase.

Mephistopheles, to God, in the Prologue to Goethe's *Faust.*

Contents

5 Software   169

List of Figures

List of Tables

Chapter 1

Introduction

Quantum mechanics allows an interaction Hamiltonian to connect a photon (real or virtual) with systems of particles, as long as all quantum numbers respected by that Hamiltonian are preserved. Energy and momentum conservation may be violated for short times or distances consistent with the Heisenberg Uncertainty Principle. Denoting the "bare" photon by $|\gamma_B\rangle$, and the set of systems which share its quantum numbers by $|\gamma_H\rangle$, one can write [BSYP]

$$|\gamma\rangle \equiv \sqrt{Z_3}|\gamma_B\rangle + \sqrt{\alpha}|\gamma_H\rangle, \tag{1.1}$$

with

$$\sqrt{\alpha}|\gamma_H\rangle = \sum_n \frac{|n\rangle\langle n|H'|\gamma_B\rangle}{\nu - E_n}.$$

The component $\langle n|H'|\gamma_B\rangle$ lasts for a time $\Delta t \sim 1/\Delta E$, with $\Delta E = \nu - E_n$.

The "system" $|n\rangle$ may be a pair of fermions, a pair of scalars, or even a single vector particle. An external perturbation can intercept the photon when it has fluctuated into the system $|n\rangle$, thereby allowing an observation of it. Common examples include electron pair production, continuum production of pion pairs, and exclusive neutral vector meson photoproduction.

The similarity of the cross section for the exclusive photoproduction of ρ^0 mesons with elastic hadron interactions lead to the photon-hadron analogy, which says that the photon interacts as a hadron, rather than as a simple electromagnetic probe. Equation 1.1 is the starting point of the argument; an atomic nucleus interfering with the expansion of $|\gamma_H\rangle$ dominates any electromagnetic interaction with $|\gamma_B\rangle$. A thorough theoretical treatment leads to simple relations between the electromagnetic current operator, and the neutral vector meson operators [BSYP].

These relations allow predictions for the interactions of real and virtual photons, and are referred to as the "Vector Meson Dominance Model," (VDM).

The Vector Meson Dominance Model is known to describe the electroproduction of neutral vector mesons at small Q^2 and small t. Aside from a propagator term, the cross section for the process $\gamma^* N \to \rho^0 N$ is nearly independent of Q^2 and ν:

$$\sigma_\rho(Q^2) = \sigma_\rho(0) \left(\frac{M_\rho^2}{M_\rho^2 + Q^2}\right)^2 \left(1 + \epsilon\xi^2 \frac{Q^2}{M_\rho^2}\right) \exp(bt)$$

The assumption that the process is diffractive is made explicit with the exponential dependence on t. This factor is based on an analogy with elastic πp, Kp, and pp scattering, in which the cross section falls exponentially with t. Typical values for the slope parameter b range near 8 GeV^{-2}.

The helicity of the photon is transferred to the outgoing ρ^0, a phenomena known as "s-channel helicity conservation," – SCHC for short. To the extent that SCHC holds, the helicity of the ρ^0 can be predicted using QED to calculate the spin density of the virtual photon. Observation of the angular distributions of the decay pions gives a determination of the actual helicity state of the ρ^0, so that a test of SCHC is possible.

None of the standard gauge bosons mediate the elastic scattering of hadrons; the pomeron, which by definition carries the quantum numbers of the vacuum, is postulated to described the process.

For Q^2 less than about 1 GeV^2, all of the predictions of the VDM are upheld[1] The t distribution is peaked sharply with an exponential falloff parameter b near 7. The cross section varies with Q^2 as indicated above; the parameter ξ^2, which scales the ratio of longitudinal to transverse cross sections, is found to be small, $\xi^2 \approx 0.3$, and is nearly independent of Q^2. The pion decay distributions show little evidence for a violation of SCHC.

For higher Q^2, however, it appears that VDM does not describe the data well. It appears that the "soft hadronic properties" of the photon at low Q^2, which are the crux of the VDM, give way to more "pointlike" behavior. An analysis done by the EMC shows that the t slope parameter, b, falls to a value of only 2–3 GeV^{-2} for $Q^2 = 5 - 10$ GeV^2 [Aub85]. Furthermore, the ρ^0s are longitudinally polarized at high Q^2, while the cross section falls more rapidly with Q^2 than predicted by the

---

[1]See, for example, [Eck73, Joo76, Dak73, Fra77, Pap79, Dix79, Sha82]. Photoproduction results may be studied in [ABBHHM, Ast82].

formula above, even after setting $\xi^2 = 0$. If $\xi^2 = 0$, then only transversely polarized photons are absorbed, and with the observation of dominantly longitudinally polarized ρ^0s, SCHC is violated. The EMC conclude that at high Q^2, exclusive ρ^0 production is a hard scattering process that is poorly described by the VDM.

The EMC results on exclusive ρ^0 production have stimulated some new theoretical calculations of the process. Extensions of QCD into the non-perturbative regime can be tested using exclusive and elastic processes. In particular, models of the pomeron as a set of two colinear, nonperturbative gluons have enjoyed some measure of success in describing new data on elastic hadron scattering.[2] The EMC results prompted new calculations of the process. Theorists have suggested that the EMC results may be wrong, and await results from other lepton-scattering experiments [Cud90, Lan91].

The EMC data were taken exclusively at high Q^2, and most of the other experiments at low Q^2. No single experiment has observed the transition from diffractive behavior to hard scattering by a "point-like" photon. The E665 data taken during 1987–88 cover a wide range of Q^2 at high W. The transition from the kinematic regime near photoproduction ($Q^2 \approx 0.1$ GeV^2) to to the perturbative regime ($Q^2 \approx 4$ GeV^2) can be studied with one data set, with reasonable statistics (roughly 1000 events). An analysis of these data, with the goal of checking the EMC results, is presented in this thesis.

---

[2]The gluonic content of the pomeron has become a fashionable topic, in fact. There are several predictions for unusual jet structure at HERA, due to "photon-pomeron fusion!"

Chapter 2

Theory

2.1 Theory

The theoretical treatments of exclusive ρ^0 production are as extensive and varied as the experimental investigations. It is not possible to describe all theoretical questions and models here, rather, only a brief introduction is provided.

2.2 Kinematics

It is useful to think of the process $\mu N \rightarrow \mu' N' V^0$ in two steps: the muon provides a "source" of virtual photons, which subsequently interact with the target, producing a single neutral meson. It is the second stage ($\gamma^* N \rightarrow N' V^0$) which is interesting; for the purposes of physics discussion the muon simply provides a beam of virtual photons. Measurement of the muon trajectory determines the four-momentum of the virtual photon, as well as the probability that it is longitudinally polarized.

If l and l' are the measured four-momenta of the incident and scattered muons, then $q = l - l'$ is the four-momentum of the emitted virtual photon. Since q is a Lorentz vector, $Q^2 = -q^2$ is a Lorentz scalar, and as such is a useful quantity in this analysis. The energy component of q is called $\nu = E - E'$; it is the energy of the virtual photon as measured in a particular frame (such as the lab frame). Often the combination $q \cdot P$ appears, where P is the 4-momentum of the target, with rest mass M. In the lab frame, $q \cdot P = M\nu$.

Unfortunately, the recoiling target nucleon is not measured in E665. (It would be difficult to measure such slowly moving protons; $|\vec{P}| \sim 0.5$ GeV, typically.) The target is assumed to be at rest before the interaction, which determines P. Energy-momentum conservation gives

$$q + P = v + P',$$

where v is the four-momentum of the outgoing muon. The kinematics of the interaction can be described by two Lorentz invariant quantities, if the rest masses of P and v are given ($M' = M$ by assumption). Perhaps the most useful are the Mandelstam variables s and t, given by

$$
\begin{aligned}
t &= (P - P')^2 = (q - v)^2 \\
s &= (q + P)^2 = M^2 + 2M\nu + q^2 = W^2.
\end{aligned}
$$

t is the momentum transfer squared $\gamma^* - N$, and s is the center-of-mass energy squared, again $\gamma^* - N$.

(It is important to keep in mind that the muon in a sense has been removed from these definitions. In other contexts one would write

$$
\begin{aligned}
\hat{t} &= (l - l')^2 = q^2 \neq t \\
\hat{s} &= (l + P)^2 = M^2 + m_\mu^2 + 2ME \neq s.
\end{aligned}
$$

Although we may consider $\gamma^* N \to V^0 N'$ as a kind of elastic scattering process, we do not have $W^2 = M^2$, because $W^2 \neq (P')^2$; rather, W^2 is large due to the production of the high energy exclusive neutral meson.)

The fact that exclusive ρ^0 production is diffractive means that the cross section decreases rapidly with the momentum transfer to the target, t. Given the large $W = \sqrt{s}$ in these data, the target recoil energy is negligible, and in the lab, the energy of the ρ^0 and of the virtual photon are very nearly equal. This feature is distinctive, and is an important selection criterion in the analysis, as discussed in the analysis chapter.

The smallness of the momentum transfer from the photon to the target makes it nearly impossible to observe the recoiling system: $-\langle t \rangle \approx 0.15$ GeV^2, so the proton momentum is less than a few hundred MeV. These protons will not exit the target region, and cannot be detected in the forward spectrometer. Strong cuts on the energy of the ρ^0 and ν are used to reduce the number of events in which the target breaks up.[1]

---

[1] Newer data taken with a vertex drift chamber may allow explicit cuts on the recoiling target, in future analyses.

The ρ^0 meson decays very rapidly; it is a *resonance*, not a stable particle. It decays almost always into two charged pions. The momentum of these pions can be measured in the spectrometer, and used to infer the energy and momentum of the resonance. The identity of the observed tracks must be assumed, so that the energy of each may be calculated from its momentum. Labelling the positive track "1," and the negative track "2,"

$$\begin{aligned}
E_1 &= \sqrt{P_1^2 + m_\pi^2} \qquad E_2 = \sqrt{P_2^2 + m_\pi^2} \\
\vec{v} &\equiv \vec{P}_1 + \vec{P}_2 \\
M_v &= (E_1 - E_2)^2 - (\vec{P}_1 - \vec{P}_2)^2 \qquad \text{so} \\
E_v &= \sqrt{v^2 + M_v^2}.
\end{aligned}$$

This is the starting point of the calculations in this analysis.

2.3 Polarization

2.3.1 Virtual Photon

A virtual photon is a spin–1 "particle," and can exist in four helicity states, corresponding to the vector components ($J = 1, m = +1, 0, -1$) and the scalar component ($J = 0, m = 0$). The photon spin state is described by a tensor constructed from the electromagnetic current operator:

$$L_{\mu\nu} = \sum_{\text{leptonspins}} \lambda_{\mu\nu}$$

with

$$\lambda_{\mu\nu} = m^2 \langle l_2 | j_\mu^{\text{el}} | l_1 \rangle \langle l_1 | j^{\text{el}\ \nu\dagger} | l_2 \rangle.$$

Current conservation $q_\mu j^{\text{el}\ \mu} = 0$ constrains the tensor $L_{\mu\nu}$, and allows elimination of one degree of freedom. Traditionally, the scalar and longitudinal components are combined.

The matrix element for a process $\mu N \to \mu' N' V$ is given by

$$M = \frac{e^2}{m^2} \lambda_{\mu\nu} t^{\mu\nu},$$

where $t^{\mu\nu}$ is a hadronic tensor (similar to $\lambda_{\mu\nu}$), which depends on the hadronic electromagnetic current, J_μ^{el}.

6

The photon spin density tensor $\lambda_{\mu\nu}$ depends on the lepton vertex only: $\lambda_{\mu\nu} = \lambda_{\mu\nu}(Q^2, \nu)$. As Q^2 and ν are varied, the density varies, and the photon becomes more or less longitudinally polarized. A single parameter, ϵ, describes the degree of longitudinal polarization of the virtual photon: $\epsilon \rightarrow 0$ for transverse photons, and $\epsilon \rightarrow 1$ for longitudinal photons.

The parameter ϵ describes the probability that the virtual photon is polarized longitudinally, not the rate of absorption as a function of polarization. The latter depends on the matrix element for the reactions, which depends on the hadronic current. ϵ merely parametrized the availability of longitudinal photons.

It is customary to write the cross section as the sum of a cross section for the absorption of transverse photons, and for the absorption of longitudinal photons:

$$\sigma = \sigma_T + \epsilon\sigma_L = \sigma_T(1 + \epsilon R),$$

where R is the ratio of longitudinal to transverse cross sections.

2.3.2 Vector Meson

The final state meson is massive, so it can be found in any state of angular momentum consistent with $J = 1$:

$$\Psi = A_{-1}Y^1_{-1}(\theta, \phi) + A_0 Y^1_0(\theta, \phi) + A_{+1}Y^1_{+1}(\theta, \phi),$$

where the $Y^l_m(\theta, \phi)$ are the spherical harmonics. (The polar angle is θ, and the azimuthal, ϕ.) The coefficients A_m depend on the axis of quantization. In this analysis, the direction of the outgoing ρ^0 in the hadronic center-of-mass frame is used. This choice is called the "helicity frame," and is just one choice of several others. Experiments have shown that the helicity of the ρ^0 is sharpest in this frame, and that the other suggested frames appear to have little significance.

The decay distributions of the ρ^0 reflect its polarization because the hadronic interaction responsible for the decay respects parity. The decay distribution is therefore proportional to $|\Psi|^2$. If the ρ^0 is pure transverse, $m = \pm 1$, and writing $|A_{-1}| = |A_{+1}|e^{i\sigma}$, the decay distribution will be

$$W(\theta, \phi)_T = 2|A_1|^2[\sin^2\theta + \cos\sigma\sin^2\theta\cos 2\phi].$$

If the ρ^0 is pure longitudinal, then

$$W(\theta, \phi)_L = |A_0|^2\cos^2\theta.$$

In general, the ρ^0 state function will contain both transverse and longitudinal components, so that interference terms between these components will arise. This leads to a term in the decay distribution which is proportional to $\cos\phi$. A relatively straight forward treatment [GJ64] gives the expression

$$W(\theta, \phi) \propto \rho_{11} \sin^2\theta + (1 - 2\rho_{11})\cos^2\theta - \rho_{1-1}\sin^2\theta \cos 2\phi - \sqrt{2}\mathrm{Re}\rho_{10}\sin 2\theta \cos\phi.$$

In this expression, $\rho_{mm'}$ is the spin density matrix for the vector meson. This matrix has unit trace, so the scalar term is $\rho_{00} = 1 - \rho_{11} - \rho_{-1-1} = 1 - 2\rho_{11}$.

A more detailed treatment [SW73] gives an expression in terms of the photon polarization parameter ϵ, and the ratio of longitudinal and transverse cross sections R:

$$\begin{aligned}
W(\theta, \phi) &= \frac{1}{1 + \epsilon R}\frac{3}{8\pi}[(1 + \epsilon\cos 2\phi)\sin^2\theta + 2\epsilon R\cos^2\theta \\
&\quad - \sqrt{2\epsilon(1 + \epsilon)R}\cos\delta\sin 2\theta \cos\phi].
\end{aligned} \tag{2.1}$$

This expression was derived assuming SCHC, and natural parity exchange.

SCHC allows a connection between the ratio of cross sections $R = \sigma_L/\sigma_T$ and the ρ^0 polarization :

$$R = \frac{1}{\epsilon}\frac{r}{1 - r},$$

where r is the longitudinal polarization of the ρ^0.

If the distribution in equation 2.1 is integrated over the azimuthal angle ϕ, then a simple form is obtained:

$$W(\theta) = \frac{1}{1 + \epsilon R}\frac{3}{4}[\sin^2\theta + 2(\epsilon R)\cos^2\theta].$$

If either $\epsilon = 0$ or $R = 0$, then $W \propto \sin^2\theta$, and the ρ^0 polarization is pure transverse. This is the case in the production of exclusive ρ^0s by real photons, and by virtual photons of small Q^2. If (ϵR) is larger than one, such as might be the case at large Q^2, then W will resemble $\cos^2\theta$.

If the distribution is integrated over $\cos\theta$, then another simple form results:

$$W(\phi) = \frac{2}{3}(1 + \epsilon R)\left[1 + \frac{\epsilon}{1 + \epsilon R}\cos^2\phi\right].$$

This expression has a non-trivial dependence on ϕ, as long as ϵ and R are finite.

8

The term in equation 2.1 representing the interference between the longitudinal and transverse components can be isolated by integrating over the polar angle, with a weight factor $\cos\theta$:

$$W(\phi)|_{\cos\theta} = -\frac{1}{15}\sqrt{2\epsilon R(1+\epsilon)}\cos\delta\,\cos\phi.$$

Experiments have found that the interference is "maximal," so that $\cos\delta = 1$.

2.4 Diffractive Scattering

It is shown in many textbooks that solutions to Schrödinger's equation

$$(p^2 + V)\psi = E\psi \qquad \text{equivalently} \qquad (\nabla^2 + k^2)\psi = 2m\psi$$

can be written in the form

$$\psi = \psi_{\text{inc}} + \psi_s \qquad \psi_s = f(\theta,\phi)\frac{e^{ikr}}{r},$$

where the scattering amplitude $f(\theta,\phi)$ satisfies an integral equation

$$f(\theta,\phi) = -\frac{m}{2\pi}\int d^3r'\,\exp(-i\vec{k}\cdot\vec{r})\,V(\vec{r}')\psi(\vec{r}').$$

Under the first Born approximation this becomes

$$f(\theta,\phi) = -\frac{m}{2\pi}\int d^3r'\,\exp(-i\vec{q}\cdot\vec{r})\,V(\vec{r}'),$$

that is, the Fourier transform of the potential with respect to the momentum transfer, $\vec{q} = \vec{k}_0 - \vec{k}$. If $V(\vec{r}) = V(r)$, then $f = f(\theta)$.

For small sharp-edged scattering centers, $f(\theta)$ will be peaked at small θ, and will show functional structure which reflects the physical structure of the scatterer. For example, a black sphere of radius R_0 gives

$$f(\theta) = ikR_0^2\frac{J_1(kR_0\theta)}{kR_0\theta}.$$

Writing $t = -|\vec{q}|^2$,

$$-\frac{d\sigma}{dt} = \pi R_0^4\frac{J_1(\sqrt{|t|R_0^2})}{|t|R_0^2}.$$

Note

$$-\left(\frac{d\sigma}{dt}\right)_{t=0} = \frac{\pi}{4}R_0^4,$$

independent of $|\vec{k}|$.

If the scatterer has a gaussian profile,

$$\Gamma(r) = \Gamma_0 \exp\left[-\left(\frac{r}{R_0}\right)^2\right],$$

then the scattering amplitude will be

$$f(\theta) = \frac{i}{2}k\Gamma_0 R_0^2 \exp\left[-\left(\frac{k\theta R_0}{2}\right)^2\right],$$

leading to

$$-\frac{d\sigma}{dt} = \frac{\pi}{4}\Gamma_0^2 R_0^4 \exp(-b|t|) \qquad \text{where} \qquad b = \frac{1}{2}R_0^2.$$

It is in this sense that the slope of the t distribution is related to the size of the scatterer. If the proton is represented by a gaussian with $R_0 \approx 0.8$ fm, then $b \approx 8$ GeV^{-2}.

Although this picture is heuristic, is can be used to relate the exponential slope parameter for the t distribution in elastic scattering to the elastic form factors, which are well-measured. Taking $R_0 \approx \sqrt{2b}$, a value of $b = 2$ GeV^{-2}, such as suggested by the EMC results, gives $R_0 \approx 0.4$ fm, which seems too small. This value suggests that a smaller piece of the proton is taking part in the interactions, and that the reaction is no longer elastic; that the proton is not interacting as a whole.

2.5 Vector Dominance Model

This section provides only a very brief exposition of the vector dominance model. A much more detailed account can be found in [BSYP].

The Vector Meson Dominance Model (VDM) is based on a photon-hadron analogy rooted in the observation that the photoproduction of exclusive neutral vector mesons (such as the ρ^0, ϕ, and ω) closely resembles elastic hadron-hadron scattering (such as πp scattering). The interaction of a physical photon with a nucleon or nucleus is fundamentally different than its interaction with an electron.

The photon state function contains a significant hadronic component which can interact with hadronic targets hadronically; only the bare photon interacts with charged leptons.

The hadronic component of the photon arises from the coupling of the photon to the charged partons which compose the hadrons. Some systems of two (or more) quarks are neutral, have zero baryon number, one unit of angular momentum, have negative parity and negative charge conjugation – in short, have the same quantum numbers as the photon. According to quantum mechanics, the photon will fluctuate into these virtual quark systems for brief periods of time consistent with limits set by the uncertainty principle. For example, it may fluctuate into the particular system

$$\Psi = \frac{1}{2}\left[\left[-u\overline{u} + d\overline{d}\right]\right],$$

which represents the constituents of a ρ^0 meson. The energy violation is $\delta E \equiv \nu - E_\rho$, which is allowed for a brief time

$$\Delta t \sim \frac{1}{\Delta E} \approx \frac{Q^2 + M_\rho^2}{2\nu},$$

when M_ρ is the meson mass, and the photon energy is large $\nu \gg \sqrt{Q^2 + M_\rho^2}$. In fact the hadronic content of the photon can be discussed in terms of a perturbation series expansion in $1/\Delta E_n$, where several vector meson states are considered. There must be an interaction Hamiltonian to connect the photon to states; since angular momentum is conserved in electromagnetic and hadronic interactions, couplings of a single photon to scalar mesons (such as the π^0), for example, are suppressed.

The vector meson dominance model begins with an expression of the wave function of the photon (either real or virtual) as a sum of the bare photon and hadronic components. It is the bare component which mediates elastic μe scattering, for example, while the hadronic component is responsible for the phenomenon of nuclear shadowing. Since the hadronic interactions are much stronger than the electromagnetic interactions, the absorption of photons by nucleons is dominated by the interactions of its virtual hadronic components, which is to say that the photon behaves like a neutral vector meson. Glaring evidence for this surprising result is the magnitude of the cross section for the photoproduction of exclusive ρ^0s on hydrogen: it is about 10 μb, close to the cross section for the elastic scattering of pions by nucleons. Furthermore, the momentum spectrum of the target indicates that the process is diffractive, with the differential cross section $d\sigma/dt$ bearing a remarkable resemblance to that observed in elastic pion-nucleon scattering. The distributions suggest that incoming ρ^0 mesons are scattering elastically from the target nucleon, before decaying into two pions. Speaking heuristically, the photon is imagined to fluctuate into a virtual ρ^0, which scatters elastically from the target,

just as a real pion or kaon would, and in the process acquires the necessary energy or momentum to put it on the mass shell, before decaying into two pions.

In this sense the fluctuation of the photon into and out of a virtual ρ^0 state is interrupted by the nucleon; which is to say that the virtual hadronic components of the photon are perturbed by the nucleon so as to collapse its wavefunction in one of the specific terms. This interaction is mediated by a quasi-particle which carries the quantum numbers of the vacuum: the pomeron.

The pomeron originated in studies of the hierarchies of hadrons. A generalization of the partial wave expansion of elastic scattering amplitudes led to a system of calculations called Regge Theory. Bound state hadrons were found to correspond to poles in the partial wave expansion, when the angular momentum eigenvalues were generalized to be complex and continuous, rather than simply real and discrete. A categorization of known hadrons along Regge "trajectories" emerged, where each trajectory ("family" might have been a better word) was characterized by a common value for the angular momentum and parity. The series was connected by a contour parametrized by center-of-mass energy. The vacuum trajectory attained special significance in calculations of elastic scattering; the pomeron was invented within the context of these calculations.

The pomeron attained an identity and relevance beyond the scope of the theory of the scattering matrix, as limits on elastic form factors were derived in the high energy limit $\nu \to \infty$. In fact, early discussions of these limits led to the study of light-cone expansions, which culminated in the prediction of the scaling of the inelastic form factors by Bjorken.[2] The success of the quark-parton model in describing those and many other phenomena caused people to forget Regge theory and the pomeron. Recently, however, there is renewed interest in the pomeron, as theorists attempt to explain the rich data already collected on elastic and exclusive processes, using QCD.

The perhaps naive treatment of photon interactions in terms of old-fashioned perturbation theory was put on firmer theoretical ground. The electromagnetic current operator of the photon and of the ρ^0 were related based on the universality of electromagnetic form factors, leading to

$$e\langle n|j_\mu^{\text{em } I=1}|m\rangle = \frac{e}{f_\rho}\frac{M_\rho^2}{Q^2 + M_\rho^2}\ e\langle n|J_\mu^\rho|m\rangle,$$

where f_ρ parameterizes the coupling strength. The expression on the right hand side is related to the ρ^0 field operator; generalizing to the other neutral vector

---

[2]The relevant light-cone variable is ω, which turns out to be the inverse of x_{Bj}.

mesons the result was

$$j_\mu^{\text{em}} = \frac{M_\rho^2}{f_\rho}\rho_\mu^0 + \frac{M_\omega^2}{f_\omega}\omega_\mu + \frac{M_\phi^2}{f_\phi}\phi_\mu.$$

Later, one could consider including the heavier mesons, the J/ψ and the Υ, but it is assumed that the hadronic component of the photon is dominated by the lighter mesons, especially the ρ^0.

The main result of the equation of photon currents and vector meson operators is an ansatz for the cross section:

$$\sigma_\gamma = \sum_V \frac{e^2}{f_V^2}\left(\frac{M_V^2}{M_V^2 + Q^2}\right)^2\left(1 + \epsilon\xi_V^2\frac{Q^2}{M_V^2}\right)\sigma_V,$$

where the sum is over vector meson states V. Typically one neglects all of the meson states except the ρ^0; certainly this is the case when the final state is specified. The ratio of longitudinal to transverse cross sections is assumed to be proportional to Q^2:

$$R = \xi^2\frac{Q^2}{M^2}.$$

An additional assumption often ascribed to VDM is that helicity is conserved in the s-channel, which means that the helicity of the outgoing ρ^0, when measured in the helicity frame, correlates with the helicity of the incoming photon. All experiments with real photons and with photons at low Q^2 have found little or no violation of s-channel helicity conservation (SCHC).

2.6 QCD

The Vector Dominance Model was very popular during the 1960s and early 1970s, due to its success at relating photon and hadron interactions. The observation at SLAC of the scaling of inelastic cross sections with Bjorken's variable

$$x_{\text{Bj}} = \frac{1}{\omega} = \frac{1}{2}\frac{-q\cdot q}{q\cdot P} = \left(\frac{Q^2}{2M\nu}\right)_{\text{lab}}$$

started the development of Feynman's parton picture. The partons soon were identified with Gell-Mann's "quarks," which are charged, point-like objects symbolizing a fundamental SU(2) symmetry of the known hadron spectrum. Experimentally it was found that the nucleon contained neutral partons as well, these were identified with the vector "gluons" which mediated the strong force between quarks.

The complete theory of strong interactions is based on a Lagrangian built from non-commuting fields; at present it is generally believed to be the correct theory of the strong force – of the interaction between quarks and gluons. This theory is called "Quantum Chromo-Dynamics" (QCD), evoking analogies with quantum electro-dynamics (QED).[3]

Since QCD is so successful, it is reasonable to try to apply it to the production of exclusive vector meson states. First some relatively elementary aspects of the theory are mooted; later, some discussion of new ideas on the non-perturbative regime of this theory is given.

2.6.1 Quark Constituents

Quarks were invented to help organize the multitude of baryons and mesons known to exist in the 1960s. They are point-like fermions, like leptons, but they have fractional electric charge, and color charge. Hadrons are bound states of two or three quarks: baryons are composed of three quarks, and mesons of a quark–antiquark pair.[4] The properties of hadrons follow directly from the quantum numbers of the quarks; the theory is pleasing because only a handful of quarks are needed to account for the full spectrum of mesons and baryons. The rules for combining constituent quarks to form hadrons are given by the symmetry groups to which the quarks are said to belong [Clo79, chapters 3&4]. For example, the up (u) and down (d) quarks are arranged in an isospin doublet, in effect an echo of the proton-neutron isospin doublet. The nuclear force was observed to be independent of electric charge, so the Hamiltonian for nuclear interactions must be invariant under rotations in isospin space. It possesses an SU(2) symmetry for isospin, and the proton and neutron fit into the fundamental representation of isospin SU(2). The strong force possesses a symmetry with respect to u and d quarks, so they are placed in a fundamental representation of SU(2), for the Hamiltonian (or Lagrangian) of the strong interactions. Baryons and mesons fit into the representations which follow from the combination of quarks; in the case of baryons, group

---

[3]The most significant difference between the QED and the QCD Lagrangians is that the components of the photon field commute, while those of the gluon field do not, with several important consequences. This is discussed later in this chapter.

[4]This remark refers to the "constituent" quarks, i.e., those which account for the quantum numbers of the given hadron. According to perturbative QCD, however, such constituents do not exist. Instead, we are confronted with an uncountable number of quarks "inside" a hadron, depending on the given Lorentz frame. One speaks of "valence" quarks, which are a shadow of the constituent quarks, and the "sea" of quarks generated from the gluons which keep the valence quarks bound together inside the hadron. The precise relation between constituent quarks and the fleeting infinitude of QCD quarks is unclear.

I_3	isovector ($I = 1$)	isoscalar ($I = 0$)
+1	$\rho^+ = (u\bar{d})$	-
0	$\rho^0 = \frac{1}{\sqrt{2}}(-u\bar{u} + d\bar{d})$	$\omega = \frac{1}{\sqrt{2}}(u\bar{u} + d\bar{d})$
-1	$\rho^- = (d\bar{u})$	-

Table 2.1: Isospin Vector Meson Wavefunctions

theory gives

$$2 \times 2 \times 2 = 2 + 2 + 4,$$

where one doublet contains the neutron and the proton, another the N*, and the quadruplet contains the four Δ particles. In the case of scalar mesons,

$$2 \times \bar{2} = 1 + 3,$$

where the singlet refers to the pseudoscalar η^0, and the triplet is the ubiquitous π^+, π^0, π^- triplet. Vector mesons follow from a different combination of quark and anti-quarks, in which the spins are aligned: the singlet representation corresponds to the ω, and the triplet, to the ρ^+, ρ^0, ρ^- mesons.

The rough correspondence of masses within a representation is an indication that the SU(2) symmetry is preserved approximately in the complete Hamiltonian.[5]

The up and down quarks are merely the lightest of the five or six quarks that exist. The next heaviest quark is the strange quark. A strong-interaction Hamiltonian incorporating the three flavors of quark ("up," "down," and "strange") should exhibit an SU(3) symmetry. In this case the $[1 + 3]_V$ representations are imbedded in a larger set:

$$3 \times \bar{3} = 8 + 1.$$

The octet contains four K^* mesons (higher mass cousins of the $K^+, K^-, K^0, \overline{K^0}$ states), each of nonzero strangeness. The other four states have zero strangeness, and include the ω and three ρ states filling the SU(2) representations built from the up-down isospin representation. The singlet state is new: the ϕ vector meson is composed of a strange–anti-strange quark pair, and has therefore zero strangeness.

The ρ^+, ρ^0, ρ^- form a vector (triplet) in isospin space; they have $I = 1$. The SU(2)-flavor (isospin) wave functions are composed from the up-quark down-quark doublet: $2 \times \bar{2} = 3 + 1$, where the triplet has $I = 1$ and the singlet, $I = 0$. The explicit wavefunctions are given in table 2.1.

The ρ mesons are vector particles; they have $J = 1$ in addition to $I = 1$. They are relatively light, suggesting that the quark pair is in an s-state; the angular

---

[5]The complete Hamiltonian contains terms for electromagnetic and weak interactions which breaks the symmetry otherwise respected by the term for strong interactions.

momentum must be $L = 0$. Consequently the spins of the quarks are aligned, and with $S = 1$, the spin wave function is symmetric (it's part of a spin triplet).

The ρ^0 has negative parity, so the total wave function must be antisymmetric. With a symmetric spin wavefunction, the SU(2)-flavor wave function must be antisymmetric with respect to the interchange of the two quarks:

$$\rho^0 = \frac{1}{2}[(-u\bar{u} + d\bar{d}) - (-\bar{u}u + \bar{d}d)].$$

In the context of SU(2), the ω vector meson is a singlet in isospin space; it corresponds to the antisymmetric flavor combination

$$\omega = \frac{1}{\sqrt{2}}(u\bar{u} + d\bar{d}) = \frac{1}{2}[(u\bar{u} + d\bar{d}) - (u\bar{u} + d\bar{d})].$$

Since its quark content is similar to that of the ρ^0, it is natural that the two neutral mesons have nearly the same mass.

When SU(2) is extended to SU(3) in order to accommodate strangeness, additional isoscalar combinations appear. In particular, it is natural to expect $(s\bar{s})$ to appear in combination with $(u\bar{u} + d\bar{d})$, which has $I = 0$, rather than $(-u\bar{u} + d\bar{d})$, which has $I = 1$. Group theory gives the decomposition $3 \times \bar{3} = 8 + 1$, so the obvious candidate for the singlet state is

$$|SU(3), SU(2)\rangle = |1, 1\rangle = \frac{1}{\sqrt{3}}(u\bar{u} + d\bar{d} + s\bar{s}).$$

The isovector $(-u\bar{u} + d\bar{d})$ should contain no strangeness, so

$$|8, 3\rangle = \frac{1}{\sqrt{2}}(-u\bar{u} + d\bar{d});$$

the ρ^0 remains as it was. The third orthogonal state is

$$|8, 1\rangle = \frac{1}{\sqrt{6}}(-u\bar{u} + d\bar{d} - 2s\bar{s}).$$

The set of flavor states $|1, 1\rangle$, $|8, 3\rangle$, and $|8, 1\rangle$ occurs for both the pseudoscalar and the vector mesons. Label the latter states as

$$\omega_1 \equiv |1, 1\rangle, \qquad \omega_8 \equiv |8, 1\rangle, \qquad \rho^0 \equiv |8, 3\rangle.$$

It turns out that the *mass* eigenstates are mixtures of the flavor states ω_1 and ω_8, according to

$$\omega = \frac{\sqrt{2}}{\sqrt{3}}\omega_1 + \frac{1}{\sqrt{3}}\omega_8 = \frac{1}{\sqrt{2}}(u\bar{u} + d\bar{d})$$

$$\phi = \frac{1}{\sqrt{3}}\omega_1 - \frac{\sqrt{2}}{\sqrt{3}}\omega_8 = (s\bar{s}).$$

meson	mass (MeV)	width (MeV)	wave function	decay
ρ^0	770	153	$\frac{1}{\sqrt{2}}(-u\bar{u} + d\bar{d})$	$\pi^+\pi^- \sim 100\%$
ω	783	8.5	$\frac{1}{\sqrt{2}}(u\bar{u} + d\bar{d})$	$\pi^+\pi^-\pi^0$ 89.3% $\pi^0\gamma$ 8.0% $\pi^+\pi^-$ 1.7%
ϕ	1020	4.41	$(s\bar{s})$	K^+K^- 49.5% $K_L^0 K_S^0$ 34.4% $\rho^0\pi$ 12.9%
ψ	3097	0.068	$(c\bar{c})$	e^+e^- 6.9% $\mu^+\mu^-$ 6.9% hadrons 86.2%
Υ	9460	0.052	$(b\bar{b})$	$\tau^+\tau^-$ 3.0% e^+e^- 2.5% $\mu^+\mu^-$ 2.6%

Table 2.2: Summary of neutral vector mesons. Data taken from Particle Data Booklet [PDG].

The mixing is said to be "ideal" since the ϕ consists only of strange quarks, and the ω, of no strange quarks.

The ϕ decays mostly into two kaons (BR = 84.9%); the branching ratio for three pions is only BR = 12.9%, even though it is favored kinematically. This fact together with the Zweig rule supports the theory that the ϕ has pure strange constituents.

It is interesting that the quadruplet $(\rho^+, \rho^0, \rho^-), \omega$ is preserved when SU(2) is extended to SU(3). The main result is that a new, yet distinct, neutral vector meson, the $\phi = (s\bar{s})$, is created. When SU(3) is extended to SU(4), another singlet state is created: $\psi = (c\bar{c})$, which contains no up, down, or strange quark constituents. The neutral vector mesons and some of their properties are summarized in table 2.2.

2.6.2 Photon - quark pair Coupling

The neutral vector mesons are of interest, since they share quantum numbers with the photon: zero electric charge, zero strangeness, and the third component of isospin is zero, too. In view of the symmetries underlying the organization of states, one expects similarities in the properties of these mesons, especially with regard to their coupling to photons. Experiments at e^+e^- annihilation machines

were able to show how the production of neutral vector mesons proceeded through a time-like virtual photon.

Virtual photons with $q^2 = (l^+ + l^-)^2 > 0$ are produced when electrons and positrons annihilate. Since photons have $J^{PC} = 1^{--}$, direct production of neutral vector mesons is possible. The corresponding Feynman diagram is shown in figure 2.1. This amplitude is closely related to part of the amplitude in the leptoproduction of exclusive ρ^0 states, depicted in figure 2.2. In particular, the coupling of the time-like photon ("s"-channel) photons in e^+e^- annihilation to the ρ^0 should be the same as the coupling of the space-like photon ("t"-channel) in lepton scattering.
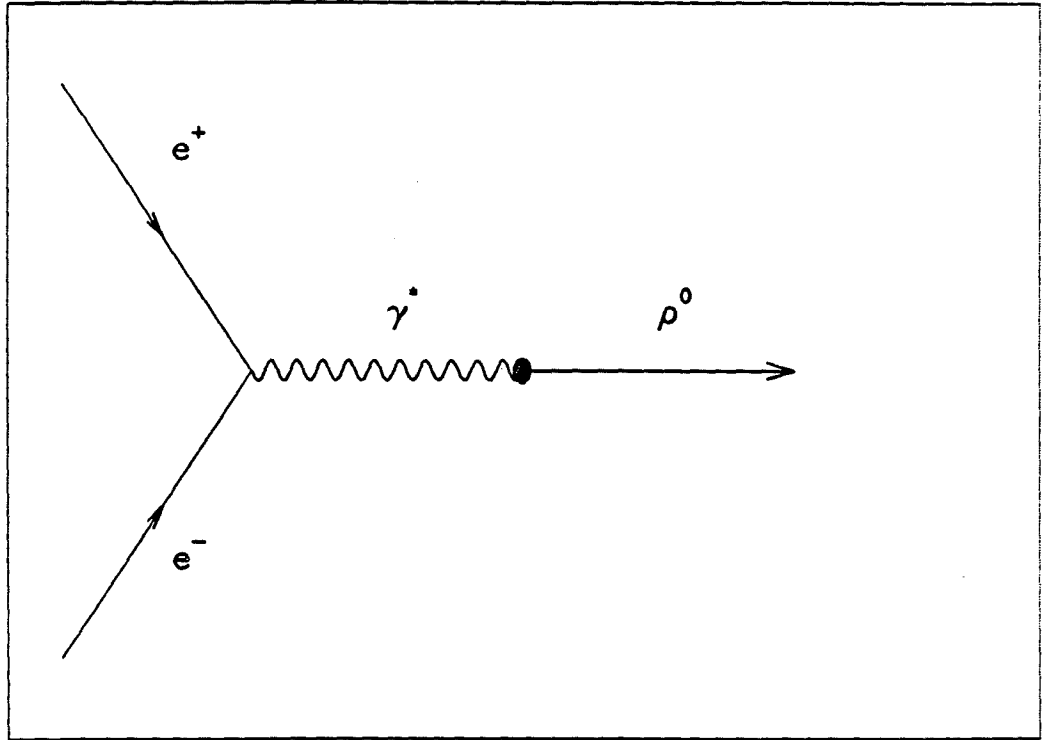
Figure 2.1: Feynman diagram for the production of ρ^0s in e^+e^- annihilation.

Within QCD, the coupling of the photon to the vector meson is expected to depend on the charge of the quark constituents

$$\langle q\bar{q}|H_I|\gamma^*\rangle = M \propto e_q f_\rho,$$

in which case

$$M_\rho^0 \propto \frac{1}{\sqrt{2}}\left[-\left(\frac{2}{3}\right)+\left(-\frac{1}{3}\right)\right] = -\frac{1}{\sqrt{2}}$$
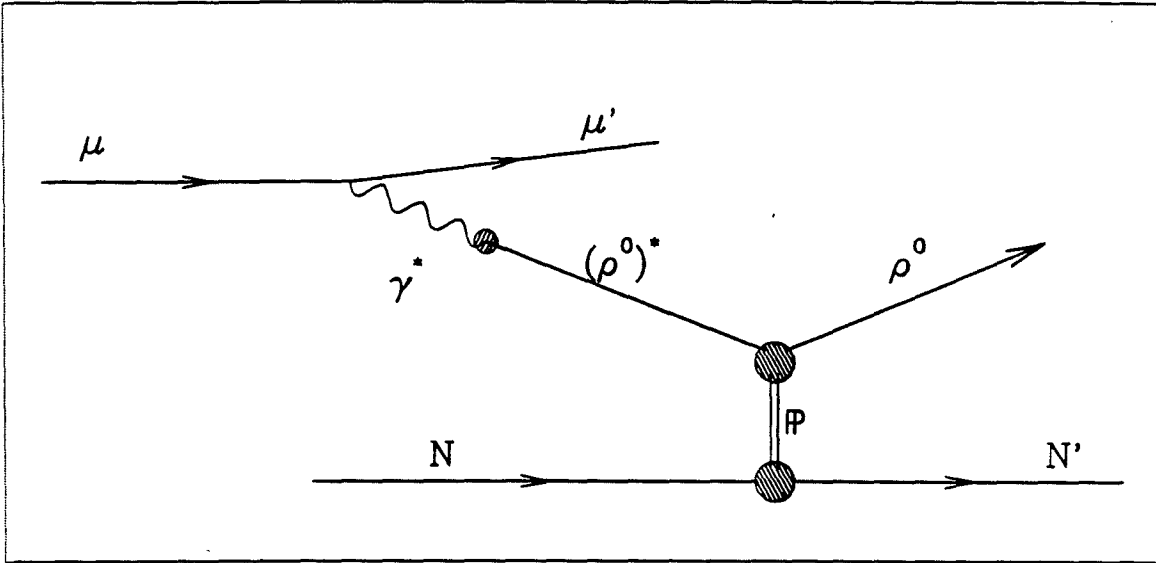
Figure 2.2: Feynman diagram for the production of ρ^0s in μ scattering.

$$M_\omega \propto \frac{1}{\sqrt{2}}\left[\left(\frac{2}{3}\right)+\left(-\frac{1}{3}\right)\right] = \frac{1}{3\sqrt{2}}$$

$$M_\phi \propto -\frac{1}{3}$$

$$M_\psi \propto \frac{2}{3}$$

$$M_\Upsilon \propto -\frac{1}{3}.$$

The e^+e^- production cross section is proportional to

$$|M_\rho^0|^2 \propto \frac{1}{2}$$

$$|M_\omega|^2 \propto \frac{1}{18}$$

$$|M_\phi|^2 \propto \frac{1}{9}$$

$$|M_\psi|^2 \propto \frac{4}{9}$$

$$|M_\Upsilon|^2 \propto \frac{1}{9},$$

so the relative photon-meson coupling should go as

$$\rho^0 : \omega : \phi : \psi : \Upsilon = 1 : \frac{1}{9} : \frac{2}{9} : \frac{8}{9} : \frac{2}{9}.$$

In fact, e^+e^- annihilation experiments have found that $\Gamma(e^+e^-) = \text{constants} \times e_q^2$.

2.7 Gluon Condensates

In this section a cursory exposition of some current ideas on gluon condensates is given.

2.7.1 Problems with Perturbative QCD

We believe the Lagrangian to contain the physics of fundamental interactions. The equations of motion yield field equations which describe the interactions of the particles they represent. In practice one simplifies the field equations by assuming the interaction term to be weak. This allows a treatment based on perturbation theory, culminating in the Feynman rules for the theory.

The Feynman rules for free fields have been applied successfully to many problems involving hard scattering (high momentum transfers). For example, the scaling violations observed in deep inelastic lepton scattering are well-described by applying the Altarelli-Parisi equations to the free fields and (bare) vertices of QCD.

Despite this success, fundamental difficulties in the use of perturbation series have been recognized for a long time (if often promptly forgotten or ignored). In the case of QCD the perturbation of expansion in powers of the coupling constant is questionable. Such a series does not converge rapidly at small momentum transfers. There is also a problem of infrared divergences, more acute than in electroweak theory.

The problem is that as a technique, perturbation series is well-known and in other circumstances (such as QED or electro-weak processes) highly successful. QCD poses special problems because of its fundamental non-Abelian character.

Any Yang-Mills theory entails a Lagrangian of the form

$$\mathcal{L}_{\text{YM}} = \bar{\psi}(i\not{D} - m)\psi - \frac{1}{2}\, Tr\, F_{\mu\nu}F^{\mu\nu}$$

where

$$\not{D} = \partial_\mu + iqA_\mu$$

$$F_{\mu\nu} = \frac{1}{iq}[D_\nu, D_\mu] = \partial_\nu A_\mu - \partial_\mu A_\nu + iq[A_\nu, A_\mu].$$

If the theory is Abelian, then $[A_\nu, A_\mu] = 0$, but for QCD the fundamental gauge fields do not commute, and so $[A_\nu, A_\mu] \neq 0$. These additional terms correspond to the gluon interacting with other gluons, as shown in figure 2.3. The fact that
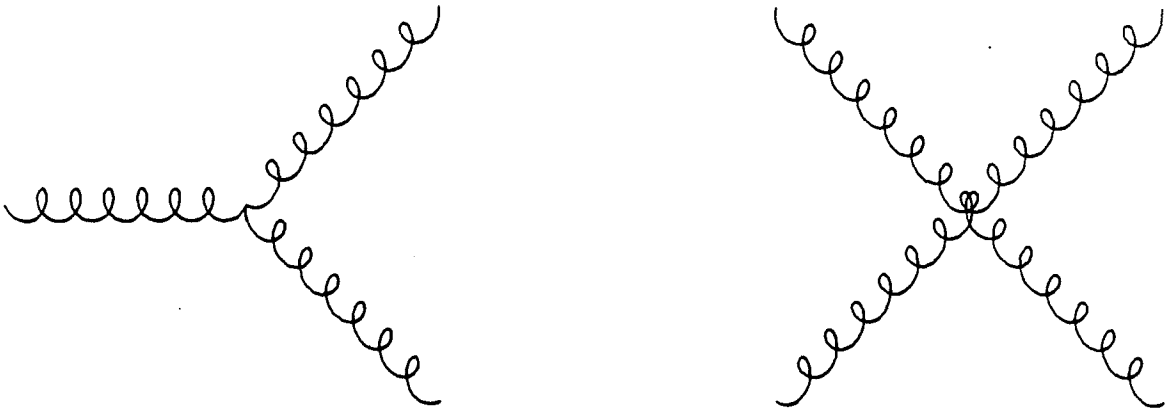
Figure 2.3: gluon self-interactions

gluons self-interact is intimately related to the fact that gluons and quarks are bound necessarily inside color singlet states. The gluon self-interaction modifies the physical gluon propagator through the graphs shown in figure 2.4. These are the vacuum fluctuations of the gluon [Qui83, p.223]. The quark bubble in figure 2.4a has the same effect on the gluon propagator as it does on the photon propagator – it causes the effective coupling to increase at short distances. The gluon bubbles in figure 2.4b, however, cause the effective coupling to *decrease*. The relative strength of these two effects depends on the number of quark flavors. With $N_f = 6$, the gluons dominate, and the effective QCD coupling decreases with distance. This phenomenon is termed "asymptotic freedom," and provides a vital distinction between QED and QCD. Note that is comes about because QCD is a non-Abelian theory.

Quigg illustrates nicely the peculiar properties of the QCD vacuum by modelling it heuristically by a "perfect" or "very effective" dia-electric medium. The

a)

b)
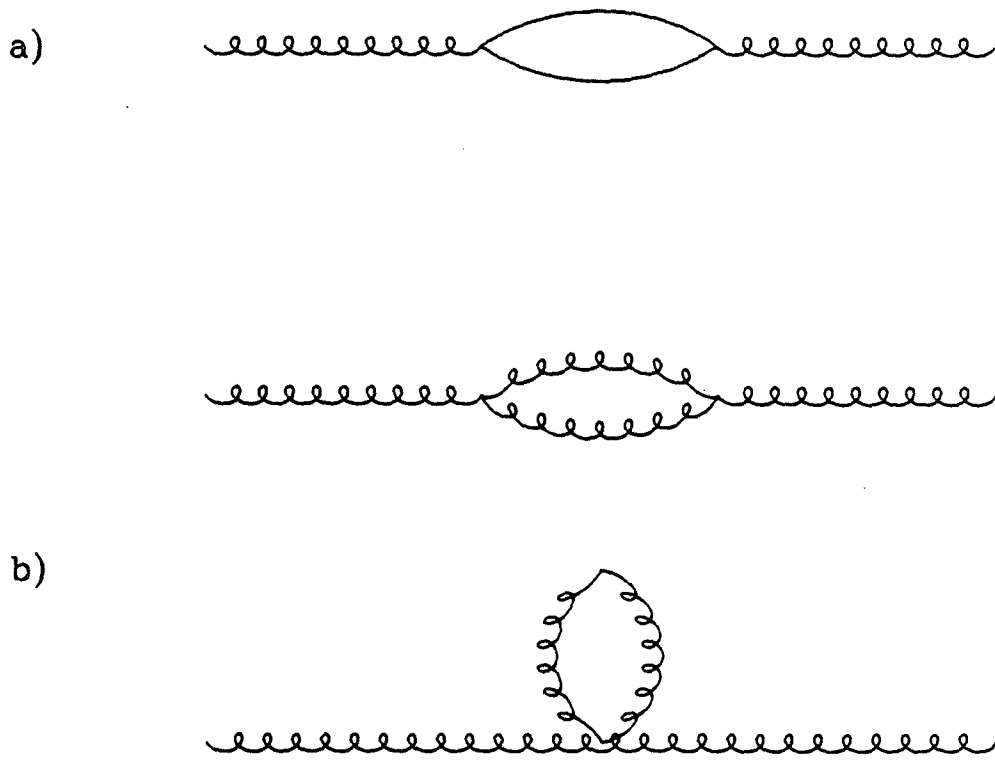
Figure 2.4: vacuum corrections to the gluon propagator

argument starts with the expression for the coupling constant g:

$$g^2(r) = \frac{g^2(r_0)}{\epsilon(r)}$$

where r and r_0 are distance scales, and $\epsilon(r)$ is now to be thought of as a dielectric "constant" (which nevertheless varies with the parameter r). It satisfies $\epsilon r_0 = 1$. Explicitly one would write

$$\frac{1}{\epsilon(r)} = 1 + \frac{1}{2\pi} \frac{g^2(r_0)}{4\pi} \left(11 - \frac{2}{3}N_f\right) \ln\left(\frac{r}{r_0}\right) + O(g^4).$$

In electrodynamics one has $\epsilon_{\text{vacuum}} = 1$ and $\epsilon_{\text{medium}} > 1$, which is acceptable intuitively because $\vec{D} = \vec{E} + \vec{P}$, and $\vec{P} \parallel \vec{E}$, so $\epsilon = |\vec{D}|/|\vec{E}| > 1$.

In the case of QCD one imagines $\epsilon_{\text{medium}} = 0$ or $\epsilon_{\text{medium}} \ll 1$, considering the static limit $t = q^2 \to 0$ or $r \to \infty$. If a test color charge is placed inside the medium, then a spherical bubble forms around the charge. The charge on the inner surface of this bubble is the *same* color as the test charge, because $\epsilon < 1$. (This is in contrast to electrodynamics.) The radius of the bubble is finite for $0 < \epsilon \ll 1$ and can be estimated by calculating the energy contained by the chromo-electric

fields in the hole and in the medium. It turns out that

$$R \propto \left(\frac{1}{\epsilon}\right)^{1/4}$$

$$W \cong \frac{4}{3}\left(\frac{Q^2}{2\epsilon}\right)^{3/4}(4\pi v)^{1/4}$$

where Q is the charge, R is the radius of the bubble, W is the energy of the system, and v is an unimportant positive constant. In the limit $\epsilon \to 0$ the radius becomes infinite, the energy W becomes infinite, which is meant to illustrate the impossibility of an isolated colored object.

Next Quigg suggests putting a test dipole in the medium. Since, however, the field lines fall off more rapidly (a pure dipole has no monopole moment), the radius of the bubble remains finite even when $\epsilon = 0$, as does the total energy of the system. This might illustrate quark confinement.

At the end of this section of his book Quigg poses a couple of interesting questions:

- What form does the vacuum of sourceless QCD take if it may be regarded as a perfect, or very effective, dia-electric medium?

- Is the QCD vacuum unstable against the formation of domains containing dipole pairs in the electrostatic model, corresponding to color-singlet, spin-singlet configurations?

2.7.2   The Non-Perturbative Vacuum

Theorists have shown that the vacuum energy density is in fact lowered by the existence of a constant "chromomagnetic" field $\vec{B}_c$ [Nac85]. This means that a perturbative vacuum should spontaneously develop such a vacuum field. Of course this does not happen because such a field would break Lorentz invariance. Nonetheless, one can consider an approximation to this lowest energy state in which the vacuum consists of a set of small, short-lived "domains" in which the chromomagnetic field assumes a random orientation. Averaged over long distances and times the vacuum has no net orientation $\hat{B}_c$; the size and lifetime of these fluctuating domains would be given by the fundamental constants of the strong interactions: Λ_{QCD} (≈ 1.5 fm $\approx 0.5 \times 10^{-23}$ s).[6] Neglecting the quark masses Λ_{QCD} is the only

---

[6]Nachtmann takes this picture as a working hypothesis – he is careful not to advocate any fundamental truth to this picture.

dimensionful parameter in QCD, so it must determine the mean chromoelectric $\langle|\vec{E}_c|\rangle$ and chromomagnetic $\langle|\vec{B}_c|\rangle$ fields.

The chromo-electro-magnetic fields $\vec{E}_c$ and $\vec{B}_c$ are by definition the analogs of the electric and magnetic fields of QED, which are derivable from the photon field tensor $F_{\mu\nu}$:

$$F_{\mu\nu} = \partial_\nu A_\mu - \partial_\mu A_\nu \qquad A_\mu = \text{photon field}$$

$$(\vec{E}_c)_i = F_{0i} \qquad (\vec{B}_c)_i = \epsilon_{ijk}F_{jk}$$

This means that the expectation value of the QCD fields $\vec{E}_c$, $\vec{B}_c$ are related to the contracted *gluon* field tensor $G_{\mu\nu}$:

$$\langle 0| : G_{\mu\nu}(x)G^{\mu\nu}(x) : |0\rangle \equiv M_c^4$$

where

$$G_{\mu\nu} = \partial_\nu B_\mu - \partial_\mu B_\nu + ig[B_\nu, B_\mu]$$
$$B_\mu = \text{gluon field,}$$
$$g = \text{coupling constant, and}$$
$$M_c = \text{is a new parameter.}$$

If the expectation values $\langle\vec{E}_c\rangle$ and $\langle\vec{B}_c\rangle$ are nonzero, then M_c is nonzero. In standard perturbative QCD, however, it is assumed that $M_c = 0$. Comparisons to experiment lead to estimates $M_c \approx 0.7 - 1.2$ GeV.

As an interesting aside Nachtman [Nac85] agrees that if correct QCD must create a massive proton from nearly massless quarks and strictly massless gluons.[7] The difficulty is that the only constant in the QCD lagrangian (aside from quark masses which we neglect here) is the bare coupling g, which is dimensionless. A dimensionful quantity can be introduced through a trick of "dimensional transmutation," as follows: Introduce a normalization scale M, which has the dimensions of mass. The results of a valid calculation cannot depend on M, so we have the renormalization group equation relating g and M:

$$\left(M\frac{\partial}{\partial M} + \beta(g)\frac{\partial}{\partial g}\right)m_p(M, g) = 0.$$

The running coupling constant is a function of the renormalization mass, according to the Callan-Symnazik equation:

$$\beta(g) = M\frac{dg}{dM} \cong -\frac{b}{16\pi^2}g^3 + O(g^5)$$

---

[7]Equivalently, it must explain or "predict" the observed value for Λ_{QCD}.

where the β function has been expanded in a power series in g. Note that the sign of the constant b determines the asymptotic behavior of the theory (i.e., whether it is confining or not). These two equations have a solution

$$m_p(M, g) = M \exp \left\{ - \int^{g(M)} \frac{dg'}{\beta(g')} \right\} \times \text{ constant.}$$

Taking $\alpha_s(M) \equiv g^2(M)/4\pi$, one can write

$$m_p(M) \cong M \exp \left\{ \frac{-2\pi}{b\alpha_s(M)} \right\}.$$

The point is that the coupling constant g changes if we change M in such a way that the proton mass m_p remains constant. In particular, hadron masses should be proportional to $\exp(-c/\alpha_s)$, with c a positive constant. The consequence that $m_{\text{hadron}} \propto \exp(-c/\alpha_s(Q^2))$, is really just a higher-twist result:

$$\exp \left(\frac{-c}{\alpha_s(Q^2)} \right) \cong \exp \left(\frac{-cb}{4\pi} \ln \frac{Q^2}{\Lambda^2} \right) = \left[\frac{Q^2}{\Lambda^2} \right]^{-\frac{cb}{4\pi}}.$$

In short, non-perturbative physics (such as the origin of hadron masses, or small-t scattering) seems to require treatment of high twist terms.

In particular, the gluon and quark propagators in non-perturbative regimes will require modification:

$$D_{\text{pert}}(Q^2) = 3 \sum e_q^2 \left\{ 1 + \frac{\alpha_s(0)}{\pi} + \cdots \right\} \tag{2.2}$$

$$D_{\text{full}}(Q^2) = 3 \sum e_q^2 \left\{ 1 + \frac{\alpha_s(0)}{\pi} + \cdots \right\} + O \left\{ \exp \left(\frac{-c}{\alpha_s(Q^2)} \right) \right\} \tag{2.3}$$

In other words,

$$D_{\text{full}}(Q^2) = D_{\text{pert}}(Q^2) + \left(\frac{1}{Q^2} \right)^2 C_{\text{pert}}(Q^2) \langle 0|G^2(x)|0 \rangle + \cdots$$

where the extra term corresponds to diagrams like that shown in figure 2.5. It is a basic and fundamental assumption these theorists make that all non-perturbative aspects of QCD enter through *universal* expectation values of operators such as

$$\langle 0|G^2(x)|0 \rangle \qquad \langle 0|(G^2(x))^2|0 \rangle \qquad \langle 0|\bar{q}(x)q(x)|0 \rangle.$$
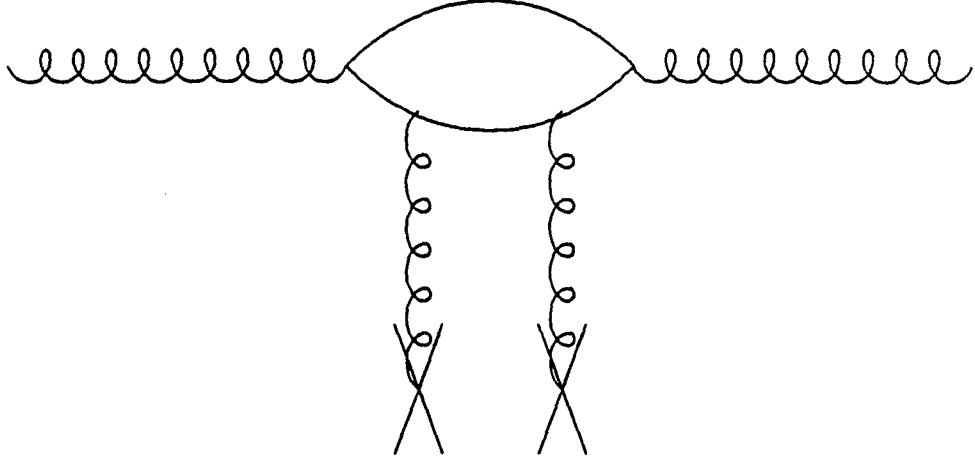
Figure 2.5: non-perturbative vacuum corrections to the gluon propagator

2.7.3 More Details about the Gluon Propagator

To illustrate their considerations of non-perturbative aspects of the gluon propagator, Landshoff and Nachtmann present a toy Abelian theory [LN87]. In the following Lagrangian, ϕ is the analog of the gluon field, and ψ of the quark field.

$$
\begin{aligned}
\mathcal{L} &= \mathcal{L}_{\text{free}} + \mathcal{L}' \\
\mathcal{L}_{\text{free}} &= \frac{1}{2}\left[(\partial_\mu\phi)(\partial^\mu\phi) - m_1^2\phi^2\right] - V(\phi)\frac{1}{2}\left[(\partial_\mu\psi)(\partial^\mu\psi) - m_2^2\psi^2\right] \\
\mathcal{L}' &= \lambda\phi^2\psi.
\end{aligned}
$$

As usual $\mathcal{L}'$ is considered a perturbation, and the S-matrix is

$$
\langle\text{out}|S|\text{in}\rangle = \langle\text{out}|\left\{1 + i\int dx_1\mathcal{L}'(x_1) + \frac{i^2}{2}\int dx_1 dx_2 T[\mathcal{L}'(x_1)\mathcal{L}'(x_2)] + \cdots\right\}|\text{in}\rangle
$$

which leads to consideration of an operator product expansion

$$
\begin{aligned}
\langle 0|T[\phi(x)\phi(0)]|0\rangle &= \sum_{n,J} c_n^J(x^2)\langle 0|\mathcal{O}_n^J(0)|0\rangle \\
&= c_0(x^2)\langle 0|1|0\rangle + c_2^{J=0}(x^2)\langle 0| : \phi^2(x) : |0\rangle + \cdots
\end{aligned}
$$

in which the ϕ-condensate $\langle 0| : \phi^2(x) : |0\rangle$ appears. It is explicitly a high-twist term in the expansion.

Landshoff and Nachtmann suggest that the condensate terms can be summed to give the expression

$$
\langle 0|T[\phi(x)\phi(0)]|0\rangle = \frac{1}{i}\Delta_{\text{p}}(x^2) + \frac{1}{i}\Delta_{\text{np}}(x^2)
$$

26

with the standard perturbative propagator

$$\frac{1}{i}\Delta_p(x^2) = c_0(x^2)$$

and a new, non-perturbative piece

$$\frac{1}{i}\Delta_{np}(x^2) = \langle 0| : \phi(x)\phi(0) : |0\rangle.$$

The important conclusion is that the scattering amplitude to all orders in the coupling λ is given by the ordinary Feynman diagrams using only those vertices given by the interaction term $\mathcal{L}'$, and with the full ϕ-propagator given by $\Delta_p + \Delta_{np}$ wherever there is a ϕ line.

Despite difficulties with the non-Abelian qualities of the true gluon field, Landshoff and Nachtmann hope that QCD behaves schematically in the same way as this toy theory. They go on to write the full gluon propagator as the sum of perturbative and non-perturbative pieces.

2.7.4 The QCD-Pomeron

As has been pointed out long ago, the pomeron behaves like a $C = +1$ isoscalar photon. A system of two gluons can have these same quantum numbers. Standard QCD calculations attempting to insert two parallel gluon lines where there is a pomeron line fail because of new infrared divergences absent when only one gluon is exchanged. Landshoff and Nachtmann perform the same calculation using their non-perturbative gluon propagators to bring the divergences under control [LN87]. This model of the pomeron (as consisting of two non-perturbative gluons) is called the "QCD pomeron."

First Landshoff and Nachtmann recall the result

$$\langle 0| : g^2 G^a_{\mu\nu}(0)G^{\mu\nu a}(0) : |0\rangle = M_c^4 > 0$$

and generalize it to

$$\langle 0| : g^2 G^a_{\mu\nu}(x)G^{\mu\nu a}(0) : |0\rangle = M_c^4 f(x/a)$$

where $f(x/a)$ is some function with $f(0) = 1$. The new parameter a is called the "gluon correlation length," and is related to the size of the vacuum fluctuation domains discussed above.

27

Based on their toy theory they write for the QCD gluon propagator

$$\langle 0|T[G_\mu(x)G_\nu(0)]|0\rangle = ig_{\mu\nu}\Delta_p(x^2) + ig_{\mu\nu}\Delta_{np}(x^2)$$

where the perturbative piece

$$ig_{\mu\nu}\Delta_p(x^2) = \langle 0, \text{pert}|T[G_\mu(x)G_\nu(0)]|0, \text{pert}\rangle$$

dominates at small $x^2 \to 0$, and the non-perturbative piece

$$ig_{\mu\nu}\Delta_{np}(x^2) = \langle 0| : G_\mu(x)G_\nu(0) : |0\rangle$$

is assumed to dominate at larger x^2.

A standard representation of the propagator in momentum space leads to the limiting behavior:

$$\begin{aligned}
M_c^4 &\equiv \langle 0| : g^2 G_{\mu\nu}(x)G^{\mu\nu}(x) : |0\rangle \\
&= -g^2 \int \frac{d^4k}{(2\pi)^4} 6k^2 D_{np}(-k^2)
\end{aligned}$$

where $D_{np}(-k^2)$ is the Fourier transform of $\Delta_{np}(x^2)$:

$$\begin{aligned}
\langle 0| : G_{\mu\nu}(x)G^{\mu\nu}(y) : |0\rangle &= ig_{\mu\nu}\Delta_{np}\left((x-y)^2\right) \\
&= -ig_{\mu\nu} \int \frac{d^4k}{(2\pi)^4} e^{-ik(x-y)} 6k^2 D_{np}(k^2).
\end{aligned}$$

Since M_c^4 is finite, $D_{np}(-k^2)$ must fall faster than $(k^2)^{-3}$ as $k^2 \to \infty$, which is equivalent to $x^2 \to 0$. (Of course, $D_p(-k^2)$ goes as $1/k^2$ for $k^2 \to \infty$.)

On the other hand, physical, on-shell gluons do not propagate freely through large distance (in contrast to photons), so the gluon propagator should not have a pole at $k^2 = 0$. It should be less singular than $1/k^2$ for $k^2 \to 0$ ($x^2 \to \infty$), and Landshoff and Nachtmann assert it must be finite at $k^2 = 0$. Schematically we have the situation shown in figure 2.6. Note that this is equivalent to decreeing there should be no infrared divergences for a physical propagator.

They say that the gluon correlation function (the non-perturbative propagator) plays a crucial role, and parametrize it according to

$$g^2 D_{np}(k^2) = -\frac{1}{6}M_c^4 a^6 F(a^2 k^2)$$

where $F(z)$ is a dimensionless function (almost the Fourier transform of $f(x^2)$), and a is the gluon correlation length in the vacuum.
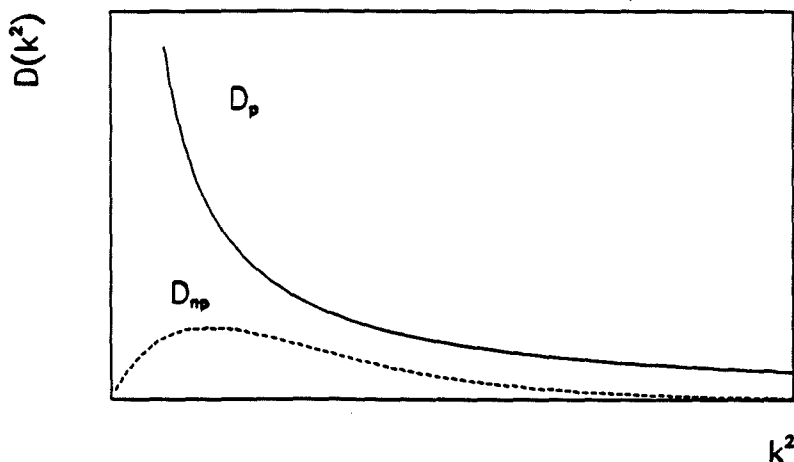
Figure 2.6: Schematic behavior of the gluon propagator

It is the non-perturbative propagator which determines the role of gluons in soft, long-distance phenomena. If small-t elastic scattering is mediated by pomerons, and if the pomeron consists of a pair of gluons, then those gluons must behave according to the non-perturbative propagator.

A slightly heuristic argument motivates a pomeron coupling to the quarks according to

$$A \propto 2s\gamma_\mu \otimes \gamma^\mu$$

which they say is the coupling of a $C = +1$ isoscalar photon. It is this coupling which predicts that s-channel helicity conservation should hold, even at high energy. This argument depends critically on the rapid fall-off of the non-perturbative gluon propagator at large k^2. Their statement is that the characteristics of pomeron exchange follow from the finite value of the gluon condensate M_c^4, at least in their toy Abelian theory. Hopefully the same consequences are obtainable for QCD!

The gluon correlation length a is a fundamental parameter in the theory. By considering the elastic scattering of hadrons they show that pomeron-like behavior is obtained in the exchange of two non-perturbative gluons if

$$a \ll R$$

where R is the radius of a light hadron. This is a very important assumption. In the toy theory a is a free parameter, and the condition $a \ll R$ is justified only a posteriori by the equivalence of the two gluons to a phenomenological pomeron, known to describe elastic scattering well. (It was invented for that purpose.)

In QCD the length a of course should not be a free parameter; the gluon-gluon and the gluon-quark vertices are related according to the Lagrangian. Neglecting

the quark masses there is only one fundamental measure in QCD, and the ration a/R should be calculable from this quantity.

It is important to note that R for heavy hadrons can be much smaller than R_{proton}. Comparisons with experiments lead to values $R \cong 0.15$ fm, which is comparable to the radius of a charmed or bottom hadron. In this case the non-perturbative gluons inside the pomeron can couple to different quarks inside one of the hadrons, and the character of the exchange is no longer that of a pomeron.

In other words, there may be some *effective* flavor dependence in the pomeron coupling, even though the gluon couplings are favor blind: the correlation length a is fixed, but the spatial separation of partons in a hadron (reflected in R) will depend on the parton masses.

It is worth repeating the discussion of hadron-hadron elastic scattering [DL84].

The phenomenological pomeron (i.e., with no prejudice about its QCD origins) gives for pp elastic scattering

$$\frac{d\sigma}{dt} = \frac{1}{4\pi} \left[3\beta F_1(t)\right]^4 s^{2\alpha_P(t)-2}$$

where β is the coupling strength of the pomeron to a quark, and $F_1(t)$ is the proton form factor. This expression is valid when single pomeron exchange dominates. The pomeron trajectory is

$$\alpha_{I\!P}(t) = 1.08 + 0.25t.$$

Using this expression the data imply $\beta^2 = 3.21 \text{GeV}^{-2}$, when double pomeron exchange is included the value goes up slightly to 3.43GeV^{-2}.

In similar ways the cross section for proton-deuteron elastic scattering is

$$\frac{d\sigma}{dt} = \frac{1}{4\pi} \left[3\beta F_1(t)\right]^2 \left[6\beta A(t)\right]^2 s^{2\alpha_P(t)-2}$$

and for πp elastic scattering

$$\frac{d\sigma}{dt} = \frac{1}{4\pi} \left[3\beta F_1(t)\right]^2 \left[2\beta F_\pi(t)\right]^2 s^{2\alpha_P(t)-2}.$$

Using a simple expression

$$F_\pi(t) = \frac{1}{1 - t/0.71}$$

they get very good agreement with data.

The exclusive ρ^0 cross section would be simply

$$\frac{d\sigma}{dt} = \frac{1}{4\pi} [3\beta F_1(t)]^2 [2\beta F_\rho(t)]^2 s^{2\alpha_P(t)-2}.$$

2.7.5 Exclusive ρ^0s

When EMC published its results on exclusive ρ^0 production, Donnachie and Land-shoff responded promptly. [DL87] They seized the opportunity to test the coupling of the pomeron to off-shell quarks. They state that the coupling decreases, but need to include a new phenomenological term μ_0 which controls this decrease. Based on the EMC data they find $\mu_0 \approx 1.2$ GeV.

They assume that the quark-quark coupling when mediated by pomeron exchange is given by

$$A \propto \beta_0^2 \gamma_\mu \cdot \gamma^\mu s^{2\alpha-2}$$

which they apply to the diagram in figure 2.7. In the case the virtual photon is
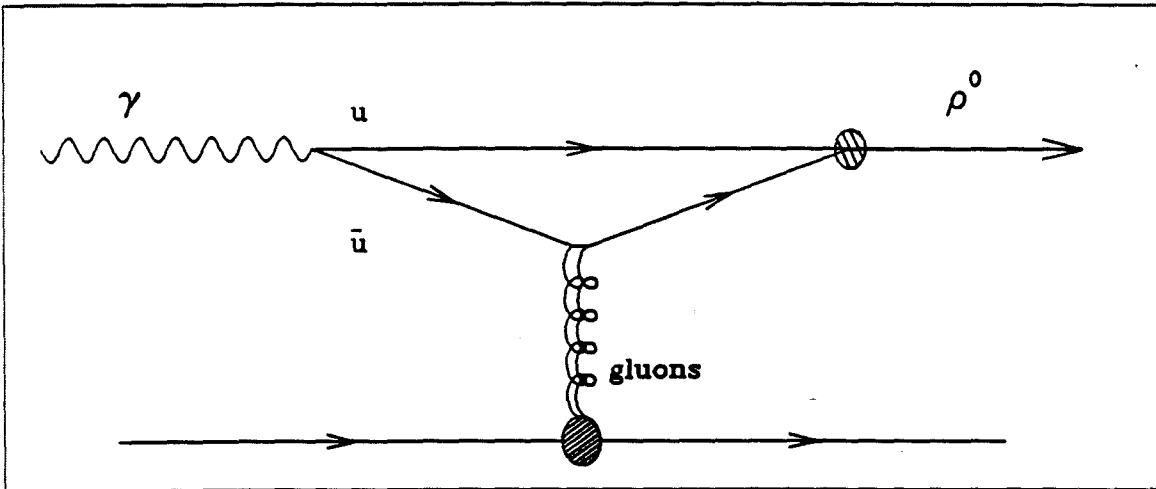
Figure 2.7: phenomenological quark-model pomeron-mediated exclusive ρ Feynman diagram

far off mass shell, the virtual quark indicated by the arrow is also far off mass shell, and the coupling between the quark and the pomeron is altered. This gives a handle on the parameter μ_0. The $\rho^0 - q\bar{q}$ vertex is handled nonrelativistically, and is normalized using the decay constant f_ρ for the process $\rho^0 \rightarrow e^+e^-$. The proton form factor $F_1(t)$ enters as described above. Their calculated cross section agrees well with EMC data at high Q^2.

The assumed coupling $\gamma_\mu \otimes \gamma^\mu$ leads to the prediction that as Q^2 increases, the production of longitudinal ρ^0s becomes more important in the EMC data. Further, disposing of the claim by EMC that the observed dominance of longitudinal ρ^0s at high Q^2 comes from transverse photons, they find that "a longitudinal ρ almost always arises from a longitudinal photon." [DL87, p.405]

They also disagree with the claim that the differential cross section

$$\frac{d\sigma}{dt} \propto \exp(-b|t|)$$

with $b \cong 1 - 2 \text{ GeV}^{-2}$, because it is inconsistent with the inclusion of elastic form factors for all the hadrons. They feel that the low value of b is due to contamination from inelastic events, which actually might be similar to diffractive dissociation.

A more detailed discussion was published recently [Cud90]. An approximation to the non-perturbative gluon propagator is used to show how the phenomenological constant μ_0 enters into the cross section.

Chapter 3

Hardware

3.1 The Muon Beam

The Fermilab muon beam used by E665 is unique: it has a mean energy of about
480 GeV, good collimation (the ratio of the halo to beam is less than 20%), high
purity (hadron and electron contamination is about (10^{-6}) [Car91]), a narrow
momentum bite (r.m.s. is 60 GeV), and a high degree of longitudinal polarization
($\lambda \approx -0.8$, for the 1987-88 500 GeV tune). This beam is also the first *dedicated*
muon beam at Fermilab.

Muons are produced by collecting the products of pion decay. The pions are
obtained by colliding protons from the Energy Doubler on a beryllium target. A
small fraction of the debris consists of high momentum, forward, charged pions,
which are selected magnetically, and channelled into a decay pipe. The pions which
do not decay there are absorbed in a beam dump, while the muons are collimated
and transported to the experimental hall.

The new muon line ("NM") was designed with two physics objectives in mind:
1) structure functions and hadronization, and 2) electroweak neutral and charged
currents. The first goal(s) benefits most from high luminosity, and is not concerned
much with beam polarization. The second goal, which was not pursued by E665,
requires a well-defined, variable polarization. It was found that no single beam
design could optimize both beam intensity and beam polarization [MM86]. Instead,
the muon beam was designed to operate in either of two modes, for which the optics
of the beam line differ.

3.1.1 Producing Muons from Protons

Hydrogen ions from a 200 MeV linac are supplied to an 8 GeV booster, which passes the protons to the main ring (MR). The peak excitation of the main ring before 1982 was 400 GeV. In 1982, a second accelerator made from superconducting magnets (the first of its kind) was built in the same tunnel as the MR [Edw85]. This new machine accelerated the protons to an energy of 800 GeV (hence the name "Energy Doubler"). The protons and antiprotons are circulated in the same ring; they are used by colliding beam experiment CDF. (See figure 3.1.) Simultaneous running of the energy doubler (ED) in a colliding beam and in fixed target mode is not possible.

Protons are extracted from the ED and distributed to the three fixed target beam lines during a spill of twenty-three second duration. One spill occurs every minute (approximately). In the main ring, the protons are bunched within a spill into a periodic "bucket" structure. The spacing of the buckets (18 ns) is determined by the design of the accelerating rf cavities, which resonate at 53 MHz. The length of the bucket is determined by the accelerating wave form. A reference signal (called the "RF" because it is tied to the ac fields in the rf cavities) is provided as an aid in triggering. E665 locked the phase of this signal to the actual passage of muons through the detector, determined by the quadruple coincidence of four small scintillator counters placed in the beam behind the apparatus.

The production of muons proceeds through three stages (see figure 3.2). First, 800 GeV protons are extracted from the energy doubler and focussed onto a beryllium target. Second, a beam of 600 GeV positive pions is isolated from the debris and noninteracting protons, and channelled into a decay pipe. Finally, decay muons are selected according to their momentum, and transported to the E665 beam spectrometer. The energy and trajectory of each beam muon is measured using four stations of MWPCs (the PBTs) and a dipole magnet (NMRE). The time of passage of the muon is signalled by a seven-fold coincidence of scintillator hodoscopes (SBTs).

3.1.2 Performance

During the period June, 1987 through February, 1988 the Energy Doubler provided 1.2×10^{12} muons to E665. Given a muon yield of 5.3×10^{-6} (typical), this corresponds to a total of 2×10^{17} protons (about 10% of the total number of protons). Typical intensities were 2×10^{12} protons/spill, or 5×10^5 muons/sec. The live time
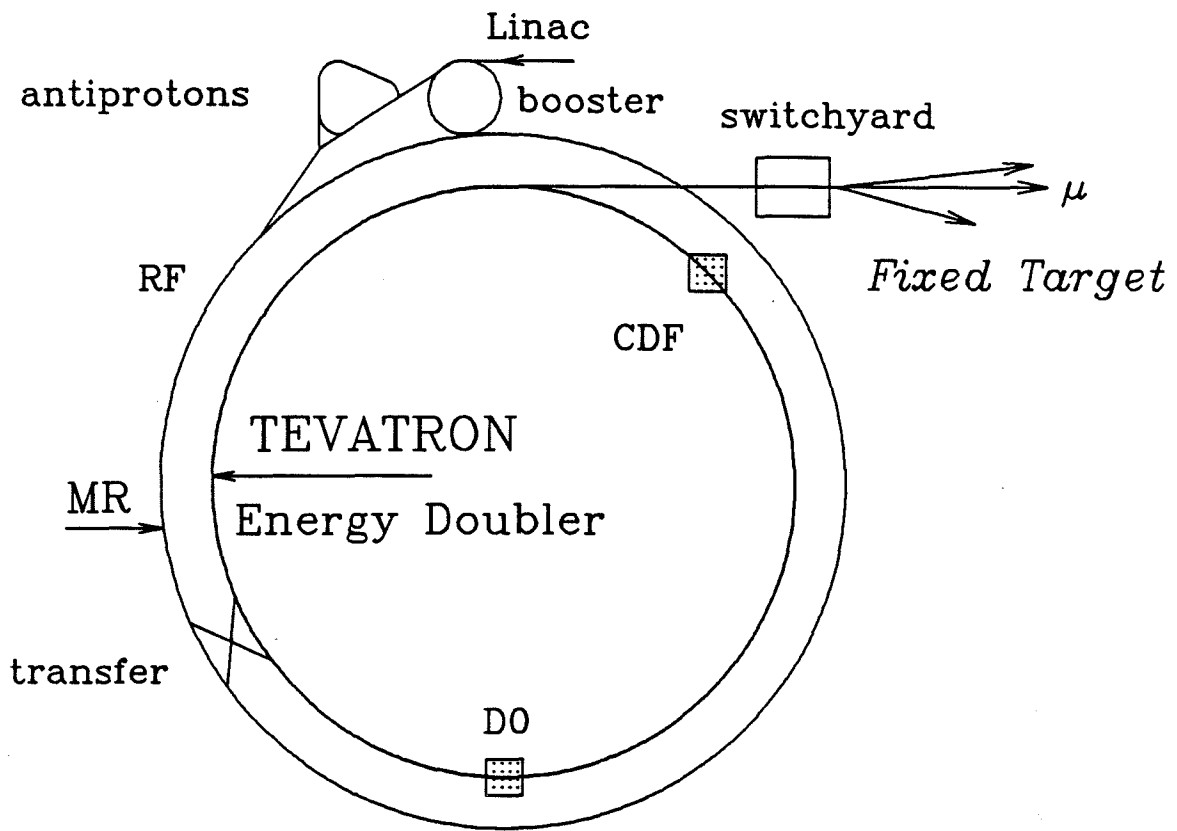
Figure 3.1: The 800 GeV TEVATRON at Fermilab. (after Edwards [Edw85])
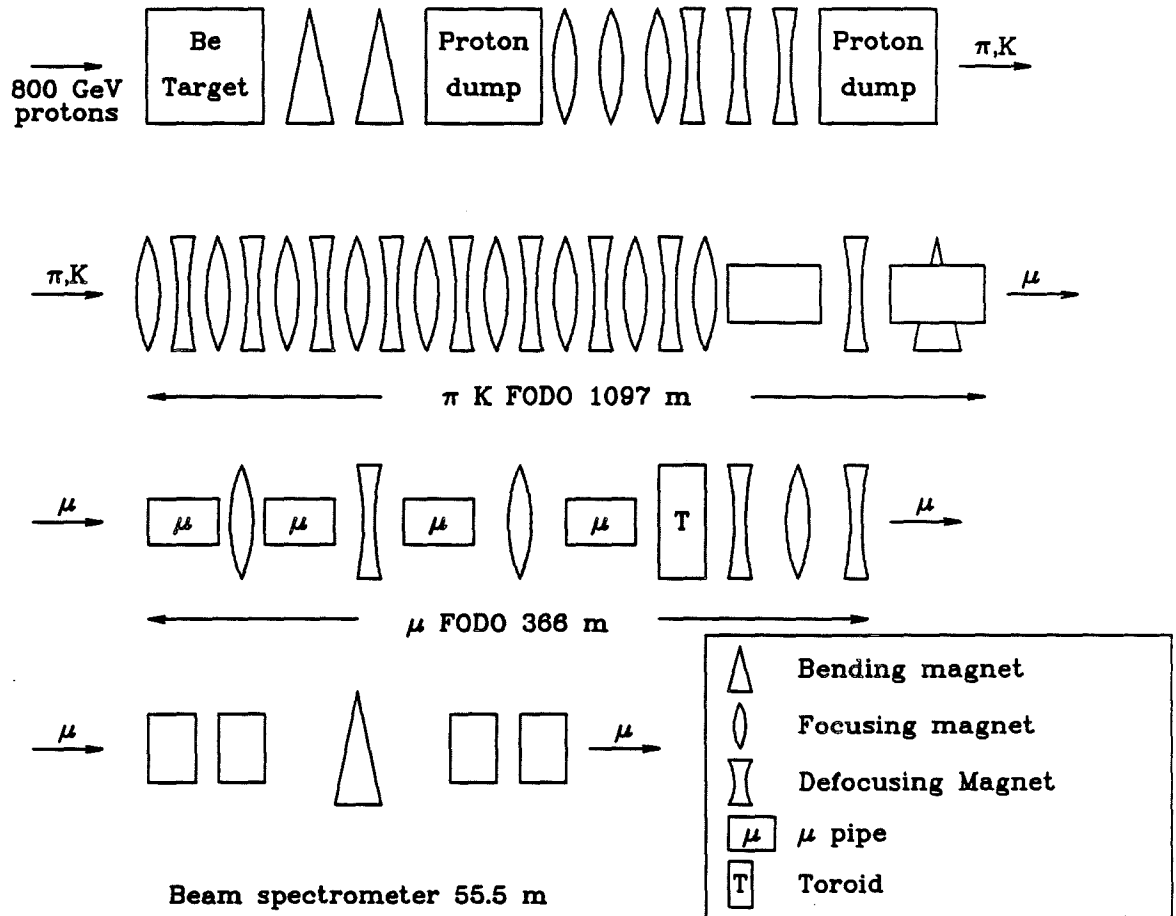
Figure 3.2: Schematic diagram of the NM (muon) beam line.

of the experiment was 80%.

3.1.3 Polarization

The muon polarization is important because it influences the spin density matrix of the virtual photon. (The helicity of the final state vector mesons is expected to correlate with the photon polarization.)

The muon polarization distribution depends on the kinematics and dynamics of the weak decay $\pi^+ \to \mu^+ \nu$. The pion is a scalar particle; in its rest frame there is no preferred direction for the decay axis (as defined by the muon momentum vector). Weak interactions, however, are not chirally invariant (they violate parity), and the W and Z bosons couple to left-handed leptons only. Consequently, the polarization of the muon measured with respect to some arbitrary axis is a function of the angle between the decay axis and the quantization axis. In the lab frame, the longitudinal polarization (defined with respect to the pion momentum vector) is given by :

$$\lambda = \frac{E_{dk} \cos \theta_{\text{dk}} + P_{dk}}{E_{dk} + P_{dk} \cos \theta_{\text{dk}}}$$

where E_{dk} and $P_{dk} = \sqrt{E_{dk}^2 - m_\mu^2}$ are the energy and momentum of the muon in the pion rest frame, and θ_{dk} is the polar angle of the decay axis with respect to the pion momentum vector [Mor88]. Since the muon lab energy is $E_\mu = (E_\pi/m_\pi)(E_{dk} + P_{dk} \cos \theta_{\text{dk}})$, (where E_π is the pion lab energy and $\beta \approx 1$), the muon polarization is related directly to the muon lab energy. Defining $z = E_\mu/E_\pi$,

$$\lambda = \left(\frac{m_\pi^2 + m_\mu^2}{m_\pi^2 - m_\mu^2}\right) - \left(\frac{2m_\mu^2}{m_\pi^2 - m_\mu^2}\right) \frac{1}{z} = 3.69 - \frac{2.69}{z}$$

So, $\lambda(z = 1) = 1$ and $\lambda(z = m_\mu^2/m_\pi^2 = 0.57) = -1$. (See figure 3.3.) Setting z determines λ, since m_π and m_μ are fixed, well-measured constants. The sharpness of λ depends simply on the sharpness of z, which depends on the muon and pion energies. The energy of each muon is measured to a precision of 0.5% at 500 GeV, but the pion energy is known only through the the optics. The better constrained E_π is, the sharper λ is determined. Unfortunately, E_π can be constrained only by a more selective beam optic, which means that sharpness on $\langle\lambda\rangle$ comes at the cost of luminosity.

The mean energy of muons when the beam line was set in the "high intensity" mode was estimated to be only 330 GeV, according to Monte Carlo calculations. The corresponding yield of muons per proton was 3.5×10^{-5}. The instantaneous

37
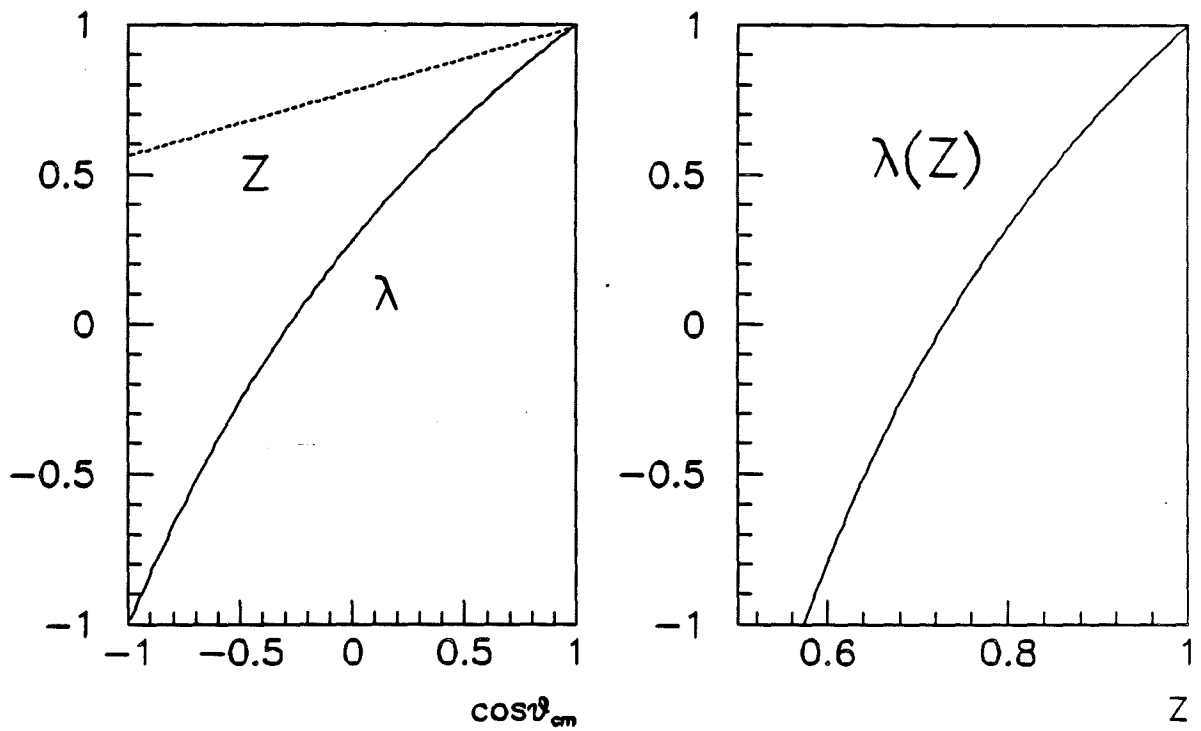
Figure 3.3: Variation of $z = E_\mu/E_\pi$ and mean polarization λ with the decay angle $\cos\theta_{dk}$, and the mean beam polarization λ versus z.

rate in the apparatus would be 10^7 μ/s (for a proton intensity of 6×10^{12} per spill), which is far too high for effective streamer chamber operation. The decision was taken to reduce the intensity of muons not by reducing the intensity of protons, and not by using the sharp-polarization mode (which reduces the number of pions), but by selecting only the very high energy muons for transport to the experimental hall. This "high-energy, high-intensity" mode provided up to 3.5×10^7 muons per spill, with a mean energy of 480 GeV. There is a slight difference in mean polarization for the lower energy half of the muon and the upper.

3.2 Detector Technology

In this section a simple explanation of some basic detector principles is given.

3.2.1 Wire Chambers

Wire chambers are the most common of all devices used in high energy physics experiments. They quantize the space through which charged particles travel. They measure the position, but not the energy or particle type.

The operation of wire chambers depends on the fact that charged particles ionize any material through which they pass. The ions produced in the gas volume of a chamber are collected on "sense" wires; they are caused to drift through the gaps between wires by a potential difference applied between the sense wires (anodes), and nearby cathode planes. (The cathode can be made of metal foil, or planes of wires.) The accelerating field is strong enough that the electrons freed as a result of ionization themselves ionize gas molecules; near the anode wire an avalanche occurs which provides the initial current pulse ultimately logged to tape as evidence of the passage of a charged particle. The multiplication of the initial ionization charge through the avalanche process is called the "gas gain," and it reaches values as high as 5×10^4.

Ordinary multi-wire proportional[1] chambers (MWPC) are inherently digital devices – they report only the presence of a hit on a wire. Drift chambers are digitized analog devices. They measure the time it takes the electrons from the initial ionization to drift to the sense wire. The resolution of proportional chambers is improved by placing the sense wires as close together as possible. The practical limit is 1 mm, which gives an rms position error of $1/\sqrt{12} = 0.29$ mm, for a single plane. The resolution of drift chambers is improved by increasing the clock rate of the TDCs which measure the drift time and by using gases in which the electrons drift more slowly; the resolution can be made as low as 35 μm.

E665 installed several MWPC devices, and two sets of large drift chambers, for the 1987-88 run. For the 1990 run, special drift chambers were built and installed in the vertex magnet.

---

[1]The word "proportional" refers to the fact that the signal size is proportional to the amount of ionization produced by the charged particle, in contrast to streamer or Geiger tubes.

3.2.2 Scintillator Hodoscopes

Ionization is a simple incoherent process. A small fraction of the energy lost by a charged particle as it passes through matter appears in the form of scintillation light. Photons in the blue range are emitted by molecules, usually organic. These photons penetrate the scintillating material much farther than the infrared photons produced in ordinary ionization, and can be detected easily using photomultiplier tubes. The "scintillator counter" is simply a slab of scintillator material attached to a photomultiplier tube. A scintillator hodoscope is an array of such counters configured to give information on the position of particles as they cause scintillation.

Scintillator hodoscopes can be compared to proportional wire chambers. They are inherently digital: they report only that a charged particle has passed through the scintillating material, not where.[2] Compared to MWPCs, however, they are fast. The scintillation takes place within a couple of nanoseconds in good scintillator material, and the amplification of the signal by the PM tube is fast. The signal passes through the scintillator at the speed of light in that material (e.g., 20 cm/ns), to be compared with electron drift velocities of e.g. 50 μm/ns. This means there is little variation in the time needed to produce a clean signal. The efficiency is usually very high. So hodoscopes are good for trigger purposes; in E665 this is their primary purpose. Particularly fine devices have such good timing characteristics, that they allow a differentiation of particle species by the time-of-flight method.

3.2.3 Multiple Scattering

As the charged and neutral particles produced in the muon-nucleon interaction fly through the apparatus, they interact with the air and the matter from which the detectors are made. These interactions produce the signals used to reconstruct trajectories, but at the same time they cause deflections and energy loss. If the measurement is to be meaningful, then the modified trajectory must resemble closely the original, unmeasured trajectory. The ultimate level on the sharpness of measurement is given by $\hbar c \approx 0.2$ GeV fm. A measurement of the momentum of a 10 GeV particle to 10 MeV would be far better than achieved in E665, yet this corresponds to a (transverse) localization of the particle to 20 fm – many orders

---

[2]Sometimes a photomultiplier tube is placed at both ends of a long piece of scintillator, in which case comparison of the pulse heights gives an indication of where along the hodoscope the particle passed.

of magnitude smaller than the radius of innermost atomic orbitals.

The smearing of a track as it passes through the apparatus is a classical process, and stochastic. The particle stumbles from one elastic scatter to the next. Its trajectory at point $\vec{x}$ is the sum of the initial velocity vector $\vec{v}_i$ at $\vec{x}_i$ and all the multiple scatters it suffered along the path from $\vec{x}_i$ to $\vec{x}$. The mean free path is given by the total cross section for elastic scattering: $l =$ etc. etc. On this scale the magnetic fields of the analyzing magnets are virtually constant. Since the matter through which the particle passes is unpolarized, the scatters on average are cylindrically symmetric around the current particle direction, and hence around its initial direction. Thus the average trajectory is the same as the ideal trajectory, except for energy loss.

The exact distribution of angular deviations is not easy to calculate. In the limit of very many scatters, a gaussian approximation is made which represents the central peak in the distribution, but which underestimates the tails from single scatters. According to this approximation, the rms polar angle of deflection about the initial particle direction is (PDG)

$$\theta_{\text{polar}}^{\text{rms}} = \sqrt{2}\,\theta_0,$$

where θ_0 is the rms of the polar angle of deflection projected onto a plane, and can be estimated from the formula

$$\theta_0 = z\,\frac{0.0141\text{ GeV}}{\beta P}\,\sqrt{X}\,\left(1 + \frac{1}{9}\log_{10} X\right),$$

where z is the charge of the incoming particle, P is its momentum, βc its velocity, and X is the length of matter through which it passes, measured along its initial direction, in radiation lengths. For all particles measured in the forward spectrometer, β is very close to one, and $z = 1$. The logarithmic term is negligible unless X is larger than one, so

$$\theta_{\text{polar}}^{\text{rms}}\,P \approx 0.02\sqrt{X}$$

(P in GeV, θ in radians, and X in radiation lengths). Notice that at this level of approximation, the rms angular deflection through two different, contiguous materials equals that from one material of the same length, when measured in units of the radiation length:

$$\theta_{\text{tot}} = \sqrt{\theta_1^2 + \theta_2^2} = \frac{\text{constant}}{P}\,\sqrt{X_1 + X_2}.$$

A charged particle passing through a dipole field is deflected through some angle θ_{bend}, according to

$$\theta_{\text{bend}} = \frac{P_{\text{T}}^{\text{magnet}}}{P},$$

where $P_{\text{T}}^{\text{magnet}}$ is a constant proportional to the strength of the magnetic field and the length of the path of the particle through the magnet. (It is usually expressed in GeV.) This angle will be blurred by multiple scattering; the fractional error will be

$$\frac{\theta_0}{\theta_{\text{bend}}} = \frac{0.0141 \text{ GeV } \sqrt{X}}{P_{\text{T}}^{\text{magnet}}}.$$

The thickness of the air and chambers in the forward spectrometer is roughly 0.3 radiation lengths, so

$$\frac{\sigma_P^{\text{MS}}}{P} = \frac{\theta_0}{\theta_{\text{bend}}} \approx \frac{0.024 \text{ GeV}}{P_{\text{T}}^{\text{magnet}}}.$$

The spectrometer was designed to give a momentum resolution of 1–2% at $P = 500$ GeV, so the magnet must be sufficiently strong and long that $P_{\text{T}}^{\text{magnet}} \sim 2$ GeV. In fact, the p_{T}-kick for the large analyzing magnet (CCM) is $P_{\text{T}}^{\text{CCM}} = 1.965$ GeV. The contribution of multiple scattering to track resolution is taken into account in the track fitting program.

The contribution of multiple scattering for tracks passing through the target is not negligible. It is 10–30 μr for a 500 GeV muon, but increases as $1/P$ to become as large as ~ 1 mr for a low-momentum pion produced in the target. These errors are included in the reconstruction of vertices.

3.2.4   Photon Conversions

The conversion of photons into electron pairs is related to the multiple scattering of electrons, as discussed in the calorimeter chapter. The length for converting photons is proportional to the radiation length:

$$X_\gamma = \frac{9}{7} X.$$

Taking the photon conversion probability to be exponential in x/X_γ, the fraction of photons converting in the forward spectrometer is about 32% — 11% if one ignores the RICH. For small thicknesses, the conversion probability is x/X_γ. An estimate of the probability of photons from π^0 decay converting in the target is based on the half-length of the target, giving 8% for hydrogen, 11% for deuterium, and 47% for xenon.

3.2.5 Target Reinteractions

Leptons passing through the apparatus will interact with matter only though electromagnetic processes, but hadrons can in addition interact through nuclear forces. If a pion interacts hadronically with the nucleus of an atom, the result is not simply a deviation of the pion though a small angle. Instead several particles may be produced. The pion is effectively lost at that point. Clearly this is damaging to event reconstruction. Fortunately, the probability of nuclear interactions is relatively low, because the nuclear force is short-ranged, and nuclei are small. Based on the nuclear interaction length, the probability that a primary pion interacts in the target varies from 3–17%. The probability that it interacts in the forward spectrometer is less than 5%.

3.3   Detector Description

A fine description of the E665 apparatus has been published already [Ada90]; additional details can be found in various theses [Michael, Ryan, Salvarani, Ecker, Jansen, Bhatti, Aïd]. This chapter is not an attempt to duplicate their work, rather, only those elements which played an important role in event reconstruction and in this physics analysis are discussed. The electromagnetic calorimeter is described in its own chapter.

The physics interest lies in the primary interactions of virtual photons with target protons and neutrons. These interactions occur at subatomic scales, and obviously cannot be observed directly. They must be reconstructed from the end products of the interactions – the charged and neutral debris observed in the apparatus. The ability to reconstruct the primary interactions depends on the design and the quality of the detectors assembled.

E665 is a generalized experiment, meant to study both the distribution of scattered muons (which allows measurement of differential cross sections), and the distribution of primary and secondary hadrons (which allows the study of quark and gluon fragmentation). This double goal led to a large aperture spectrometer system, and thin targets. The general strategy followed that of EMC – in fact, many of the detectors used in E665 were taken from EMC, and modified slightly.

There are three spectrometers in E665:

- Individual beam muon trajectories are measured in the beam spectrometer. A simple dipole magnet in enclosure NMR bends the incoming muons toward the east; this magnet is called NMRE.

- The forward-going particles, including the scattered muon, are detected in the forward spectrometer. The large Chicago Cyclotron Magnet ("CCM") is the anchor of the forward spectrometer.

- The slower charged particles in the forward hemisphere are detected in the wide-angle detector system. Charged particles in the backward event hemisphere are measured using the streamer chamber, with links to the wide angle tracks. The center point of the vertex spectrometer is the CERN Vertex Magnet ("CVM") inside which the streamer chamber and the target were installed.

In addition, neutral energy in the form of photons is measured in the electromag-

netic calorimeter.

These three spectrometers (beam, forward, and vertex) are discussed in more detail below, after certain basics are defined.

3.3.1 Coordinate Systems

The CCM is the center of the experiment not only in terms of event reconstruction (and mass!), it was the primary fundament ("monument") for surveys. In fact, the New Muon Lab itself was built around the CCM, which first was mounted on bedrock. It perhaps is appropriate, then, that the global coordinate system be defined with respect to the the Chicago Cyclotron Magnet: the axis of the magnet defines the Z-axis, and the X-axis is defined by the beam direction. In other words, $\hat{Z}$ points up, $\hat{X}$ points from south to north, and $\hat{Y} = \hat{Z} \times \hat{X}$ points from east to west. The point $(X, Y, Z) = (0, 0, 0)$ nominally is at the center of the CCM.

Local coordinates systems are defined for every detector. A wire plane, for example, is a one-dimensional detector which can report on the coordinate of a track along an axis perpendicular to the wires. This coordinate is designated θ, and its orthogonal partner is ω, which runs parallel to the wires. Most chambers and hodoscope planes are perpendicular to the X-axis, so the local coordinate pair (θ, ω) is related to the global coordinate pair (Y, Z) through a rotation. (The coordinate triplet (ω, θ, X) is right-handed, just like (Y, Z, X).) Consider the ideal wire which passes through $(Y, Z) = (0, 0)$, with a finite slope so that $Z = Y \tan A$. (Remember that Z is vertical, and Y is horizontal.) Then $\theta = Z \cos A - Y \sin A$, and the rotation is simply

$$\begin{pmatrix} \omega \\ \theta \end{pmatrix} = \begin{pmatrix} \cos A & \sin A \\ -\sin A & \cos A \end{pmatrix} \begin{pmatrix} Y \\ Z \end{pmatrix}.$$

E665 uses the angle $\alpha = A + \pi$, so in practice one calculates

$$\omega = -Y \cos \alpha - Z \sin \alpha,$$
$$\theta = Y \sin \alpha - Z \cos \alpha.$$

These coordinates are illustrated in figure 3.4. When one speaks of a Y plane, one refers to the coordinate measured (i.e., $\theta = Y$), so the wires in a Y plane are vertical.

Although wire spacings are on the order of millimeters, E665 measures all lengths in meters. (The experiment after all is 95 m long.) Energy and momentum are measured in GeV, and the magnetic fields, in kilogauss.

46
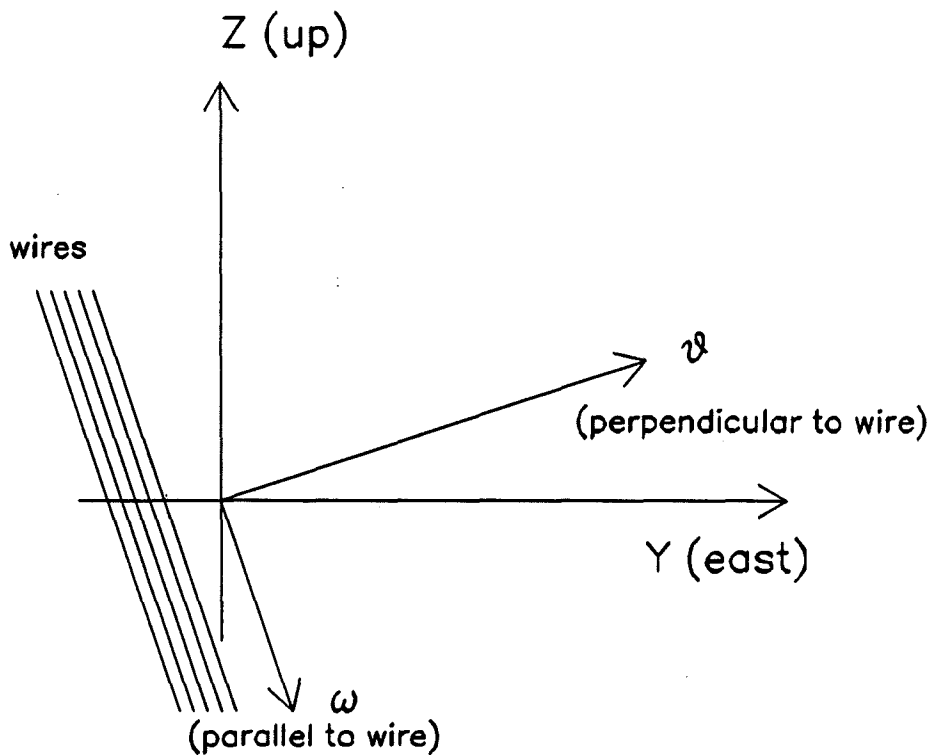
Figure 3.4: Definition of local plane coordinates θ and ω.

A scale drawing of the apparatus from a bird's eye view is given in figure 3.6. A glossary of detector names is given in table 3.1, and a list of key parameters for wire chambers and hodoscopes is given in table 3.2.

3.3.2 Beam Spectrometer

The beam spectrometer is particularly simple: there is a small aperture dipole magnet to bend the incoming muons, and small proportional chambers to determine the muon trajectory on both sides of the magnet. (See figure 3.5 for an illustration.)

The main challenge in the beam spectrometer is accuracy. All kinematic quantities depend on the beam energy, so it makes sense to reduce the measurement error as much as possible. This is accomplished by employing precise proportional chambers ("PBTs") spaced far apart. E665 installed sets of standard Fermilab "Fenker" chamber packets, at four distinct "beam-tagging stations," two on each side of NMRE [Fen83, Mon84]. The wire spacing is 1 mm, and the active area (approximately 0.12×0.12 m^2) covers the useful beam. At each station there are
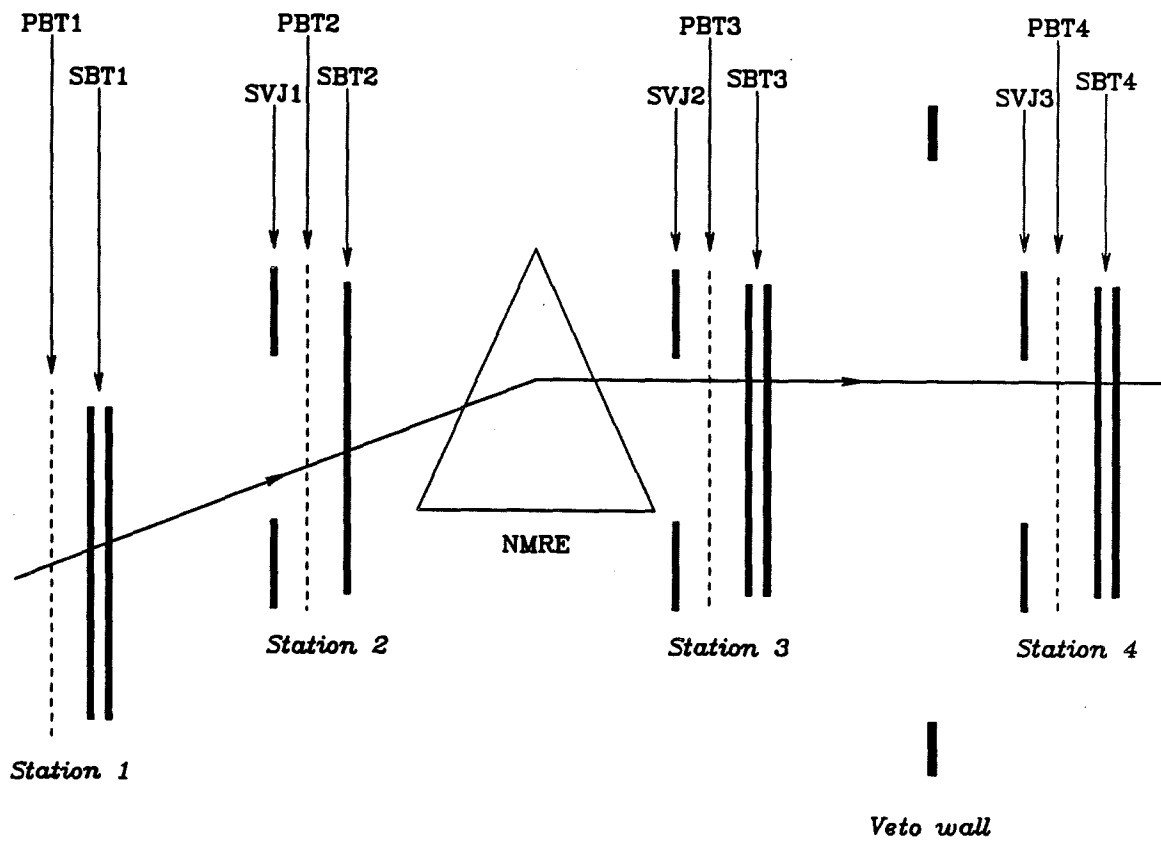
Figure 3.5: The E665 beam spectrometer.
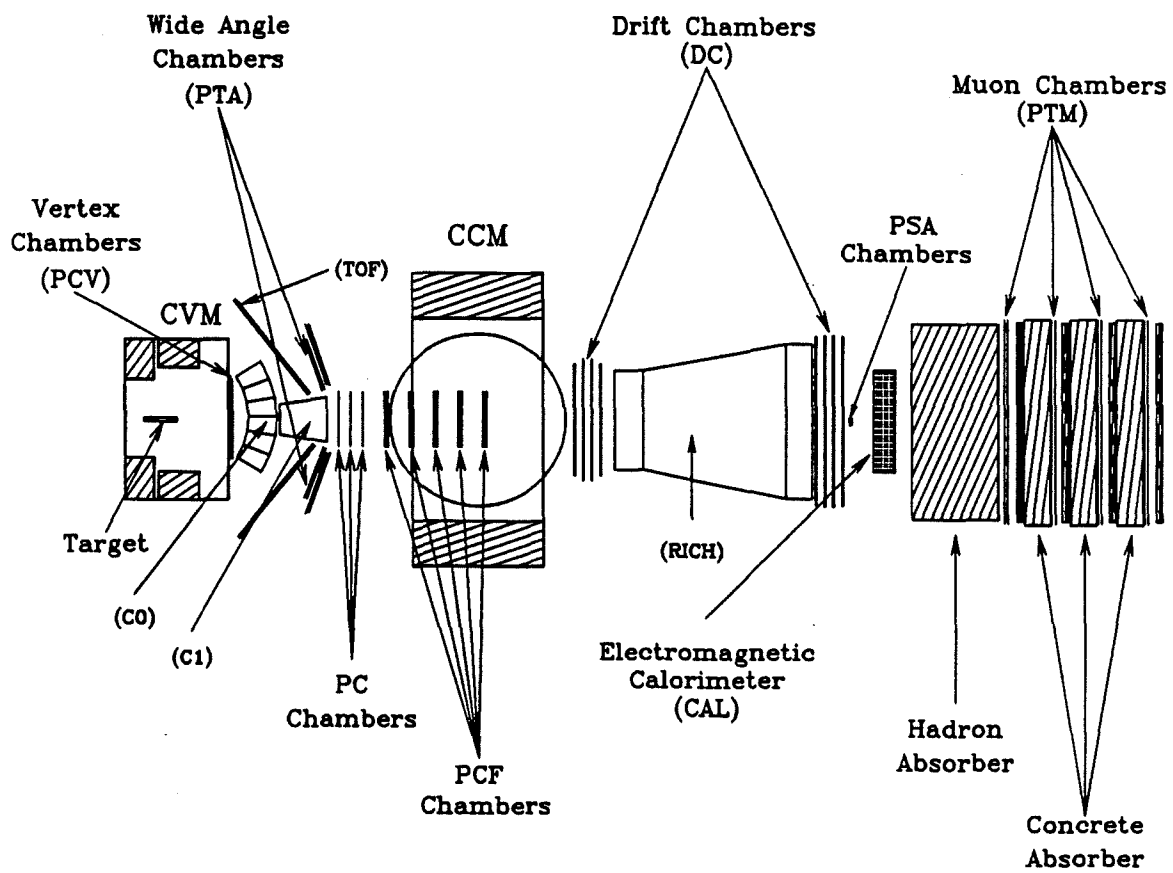
Figure 3.6: The E665 detector, viewed from above.

detector	location	purpose
PBT	beam spectrometer	MWPC for beam tracks
SBT	beam spectrometer	hodoscopes for beam tracks
PCN	forward spect'r, before CCM	MWPC for forward tracks
PCF	forward spect'r, inside CCM	MWPC for forward tracks
DCA	forward spect'r, after CCM	large DC for forward tracks
DCB	forward spect'r, after RICH	large DC for forward tracks
PSA	forward spect'r, after RICH	small MWPC for forward tracks
PTM	muon detector	MWPC for muon tracks
SMS	muon detector	small hodoscopes for muon tracks
SPM	muon detector	large hodoscopes for muon tracks
PCV	vertex spect'r, after CVM	MWPC for slow and forward tracks
PTA	vertex spect'r, large angles	MWPC for slow tracks
TOF	vertex spect'r, large angles	scintillators for slow tracks
SC	vertex spect'r, inside CVM	photographs of very slow tracks
C0	vertex spectrometer	threshold Cherenkov, wide angles
C1	vertex spectrometer	threshold Cherenkov, medium angles
RICH	forward spectrometer	Ring-Imaging Cherenkov, fast hadrons
CAL	forward spectrometer	electromagnetic shower detection

Table 3.1: Brief Glossary of Detector Names

proportional and drift chambers			
detector	pitch (mm)	aperture ($V \times H$ m^2)	orientation
PBT	1	0.12×0.12	$2Y, 2Z, U, V$
PCV	2	1×2.8	Y, U_1, U_2, V_1, V_2, Y
PCN	3	2×2	$3 \times (Y, Z, V, U)$
PCF	2	1×2	$5 \times (U, V, Z)$
DCA	50	2×4	$2Z, 2U, 2V, 2Z$
DCB	50	2×6	$2Z, 2U, 2V, 2Z$
PSA	1	0.12×0.12	$Z_1, Y_1, Z_2, Y_2, U_1, V_1, U_1, V_2$
PTM	12.7	3.6×7.2	$4 \times (Y, Z)$
PTA	12.7	2×2	$2 \times (Y, Z, U, V)$

scintillator hodoscopes			
detector	width (mm)	aperture ($V \times H$ m^2)	orientation
SBT	6	0.17×0.17	$(Y, Z), Y, 2 \times (Y, Z)$
SMS	13	0.2×0.2	$4 \times (Y, Z)$
SPM	500	3×7.5	$4 \times Y$
SVJ	~ 10	$\sim 0.1 \times 0.1$	U, V, U
SVW	500	3×7.5	Y

Table 3.2: Basic parameters for wire chambers and hodoscopes in E665.

two planes of Y wires, two Z, one U plane ($\alpha = 2\pi/3$), and one V ($\alpha = \pi/3$). These twenty-four planes provide a high degree of redundancy, so tracks can be reconstructed reliably, even when there are multiple beams.

Scintillator hodoscopes ("SBTs") are installed alongside the proportional tubes. There are four planes of vertical fingers, and three of horizontal fingers. The width of the individual fingers is gradated so that the flux of muons through each counter is about the same. Those in the center are 6.4 mm wide, and those at the edge are 24 mm wide. These counters provide quick, well-defined signals for triggering purposes, and are used offline to test the timing of reconstructed beam tracks.[3] The offline correlation of the SBT and PBT hits proved vital to the analysis.[4]

The beam is accompanied by a significant "halo" of muons.[5] The physical halo is not insignificant. Roughly ten percent of the muons entering the hall are halo. They can cause false triggers, so a large veto wall was erected upstream of the target to tag these muons [Mon86]. In addition, smaller veto counters ("veto jaws") are installed near the SBTs to define the boundary between beam and non-beam – i.e., halo. By definition, beam muons produce signals in all seven SBT planes, and no signal in beam veto counters. A subset of the non-beam muons explicitly triggers the apparatus using the signals from the beam veto counters, and the large scintillators behind the hadron absorber (described below). These designated halo tracks are used for calibration and alignment.

3.3.3   Forward Spectrometer

The forward spectrometer is considerably more complicated than the beam spectrometer. (See figure 3.6.) Its center is the superconducting Chicago Cyclotron Magnet (CCM), bracketted by a motley collection of wire chambers. The forward spectrometer determines the momentum of all tracks passing through the large CCM aperture, including the scattered muon. The range of momenta covered ranges from about 8 GeV to the beam energy (in the lab Lorentz frame), and is set by the width of the chambers in the CCM, and the strength of the CCM and vertex magnet fields.[6]

---

[3]The PBTs often contain remnants of a beam track from an earlier bucket. The scintillator generally latch only those signals which correspond to the beam particle which caused the event.

[4]In fact, the seven-fold SBT coincidence was accurate to one bucket due to a fortuitous mis-timing of the discriminated signals [Ada89].

[5]The halo around electron or hadron beams can be eliminated by physical collimators. This is not possible for muons, due to their very weak interaction with matter.

[6]This point is discussed in greater detail in the analysis chapter.

As in the beam spectrometer, chambers are placed on either side of the CCM to measure straight lines portions of tracks: the PCN chambers are on the upstream side, and the large-aperture drift chambers are installed on the downstream side.[7]

The PCN chambers are standard proportional chambers, installed and maintained by MPI [Man85a]. There are three sets of four planes. In each set there is a Y plane, Z plane, V plane with $\alpha \approx \pi/3$, and a U plane with $\alpha \approx 2\pi/3$. The wire spacing is 3 mm. A special three-piece graphite cathode was designed to limit the effects of beam loading at the center of the chambers. Distinct boundaries between a central disk of radius 3 cm, an annulus of outer radius 6 cm, and the rest of the plane can be seen in maps of the chamber efficiency. These effects are simulated in the Monte Carlo [RSB90].

The drift chambers (DCs) were custom-designed for E665 by Tom Kirk; they were built and are maintained by Fermilab. The construction is fairly elaborate [MKW85]. There are two sets, of different sizes: the DCA chambers hang from the downstream side of the CCM, and have an aperture of 2×4 m^2. The DCBs hang in front of the calorimeter, and have an aperture of 2×6 m^2. In each set there are eight planes: two Z followed by two U, then two V, and finally two Z again. The U and V planes are nearly vertical: the angle with respect to the Z-axis is slightly less than 0.1 radians. Pairs of similar planes are offset by a half-cell, so that they can help resolve hit ambiguities [Mel86]. The drift cells are two inches (5 cm) wide, and the drift velocity is approximately 4 cm/μs. The resolution was about 400 μm [Mel88a].[8]

Each DC Z plane is split into an east and a west half. The sense wires were glued to a nonconducting vertical strip after stringing, and then cut. The isolation of the two halves reduces the potential inefficiency of these horizontal wires due to limited two-track resolution.[9] They are read out separately, so at the level of offline decoding there are 24 planes total. The vertical strip produces a significant dead region in the drift chambers; this has been modelled in Monte Carlo simulations [Sch90e]. The readout uses special electronic circuits called "Mutes" [Kir78].

The projection of many straight line segments from the PCN and DCs into the CCM is a basic step in offline event reconstruction, and is supported by the information from the "PCF" proportional chambers. These chambers were built by the Nanometrics company, and are maintained by the University of Washing-

---

[7]The beam flows from upstream to downstream, like water in a river. (One can also say that is flows from south to north.) The beam spectrometer is upstream of the forward spectrometer.

[8]Recently, better calibration has brought the resolution down to the design value of 250 μm [Mel89a, Mel91b].

[9]The double-hit resolution was designed to be 100 ns, or 5 mm – 10% of a cell.

ton [Bha86]. The wire spacing is 2 mm, and the total aperture is 2×1 m^2. This size is close to the maximum that can be fit inside the CCM, and it is a determining factor in the range of momenta that can be reconstructed in the forward spectrometer. There are five groups of three chambers, installed at regular intervals from the upstream edge of the CCM to just past its center. Each triplet contains a plane of Z, U, and V wires, which allows construction of a spacepoint in each triplet. This capability proved essential in recouping losses due to inefficiencies in the PCN. The U and V wires run ± 15 deg (0.26 radians) to the vertical. Certain insensitive "support wires" were installed to ensure regular wire spacing. These wires produced significant dead regions which were measured and simulated in the Monte Carlo [RSB90].

The drift chambers cannot withstand the full flux of the unscattered beam[10]. The central portion of the wires in the center of each plane is deadened ("protected" might be a better word) by short lengths of plastic tubing. These dead regions have been measured, and simulated in the Monte Carlo [Sch90e]. The small-angle scattered muons and high energy hadrons passing into these dead regions are detected by small proportional wire chambers called the PSAs.[11] The PSAs are the same Fenker chambers used in the beam spectrometer [Ada86]. They have 1 mm wire spacing, and are 128 mm wide. There are two packages in the PSA: one containing two planes of Y wires and two of Z wires, and another like the first but rotated 45 degrees to give U and V wires. This high degree of redundancy made finding spacepoints in these chambers highly efficient, even during the periods when one of the planes was completely dead. The PSAs were built and are maintained by UIC.

An extra set of of proportional chambers called PCV was installed by MPI at the downstream opening of the CERN Vertex Magnet (CVM) [Man85b]. There are six planes with odd orientations: there are two Y planes, two different U, and two different V planes ($\alpha = \pm 45, \pm 18$ deg). The wire spacing is 2 mm. Although proposed as a part of the vertex spectrometer, fast tracks detected in the forward spectrometer also produce hits in PCV, which can help define trajectories. Using them in the early stages of event reconstruction turned out to be a mixed blessing, however. They are in the fringe fields of the CVM, and are two far away from PCN to resolve hits belonging to close-by tracks effectively. If the correct hits are chosen, then the track resolution is greatly enhanced.[12] If the wrong hits are chosen, then the otherwise correct track sometimes cannot be fit, and might not point back

---

[10]At most only one muon in 10^5 is deflected outside of the beam phase space.

[11]The PSAs cover the dead region of the downstream DCs ("DCB"). For the 1990 run, additional chambers (PSC) were installed to cover the dead region of the upstream drift chambers.

[12]For this reason, the anomalous PCV hit multiplicity was an issue in this analysis, as described in the Analysis chapter.

to the primary vertex.[13] These chambers shared the three-piece resistive cathode design used for the PCN; the central cathodes for the last two planes failed, leading to a significant loss of hits for forward tracks. This inefficiency is simulated in the Monte Carlo [RSB90].

3.3.4 Vertex Spectrometer

The third magnet in E665 is called the CERN Vertex Magnet (CVM). It was the main analyzing magnet in EMC. The target was housed in this magnet during 1987-88, so that slow hadrons were distributed to the wings on either side of the CCM. A set of proportional chambers (PTA) was installed by MIT to cover the tracks passing through the time-of-flight counters (TOF). Tracks were reconstructed by joining short lines in PCV to spacepoints in the PTAs. The momentum of these tracks could be determined only after the vertex was found: tracing a ray from the primary vertex through the PCV and PTA hits constrained the momentum enough to allow $\pi/K/p$ separation in the TOF [Erdmann, Siegert]. These "wide-angle" tracks were not used in this analysis.

Very slow particles cannot escape the CVM, but could be measured in the streamer chamber (SC).[14] This complex device was a veteran detector from EMC. Volker Eckart from MPI installed it in E665 [Eck85]. It took photographic exposures of light from streamers created from the ionization trail of charged particles. The dead time of the streamer chamber was much longer than other devices, and the photographs were costly and time-consuming to analyze, so only some events from the electronic detectors were photographed in the streamer chamber. A special multiplicity-based trigger using hits in PCN was developed for this purpose. The films have been processed at MPI, Fermilab, and Cracow.[15]

3.3.5 Muon System

Identification of the scattered muon is essential to any analysis. The distinguishing characteristic of muons is that they are charged but interact very weakly with matter. A 5 GeV muon will penetrate 3 m of steel, which otherwise will absorb

---

[13]Complex procedures in track fitting called "Super Rescue" and "PCV Hunt" were devised to ameliorate this situation, as described in the software chapter.

[14]The "escape momentum" varied from 0.8 to 2 GeV, depending on the vertex position.

[15]The streamer chamber was replaced in 1990 by a specially-designed drift chamber system, which can provide tracking on every event.

any hadron or electron. In E665 the electrons are absorbed in the electromagnetic calorimeter, and most hadrons are absorbed in a huge block of steel. The "hadron absorber" is 3 m thick, which corresponds to 170 radiation lengths, and 18 interaction lengths. The flux of hadrons through the absorber is negligible.[16]

Muons can be identified easily by the tracks they produce in detectors downstream of the hadron absorber. As in the case of the beam tagging system, both proportional chambers and scintillators are used. There are four identical stations, separated by concrete absorbers. Each contains four planes of proportional wire chambers ("PTM"), two Y planes and two Z. The wires are mounted in aluminum extrusions, and are one inch (2.54 cm) apart. Planes of the same orientation are offset by half a cell width.

Each PTM plane is deadened in the center, to protect the chamber from the flux of the unscattered beam. These dead regions are covered adequately by the SMS hodoscopes. These scintillator counters are narrow (13 mm), and are used in reconstructing the muon track. They are also used in the triggers, as described in a later section.

Large scintillator counters ("SPM") were used to tag muons scattered through large angles.

3.3.6 Electromagnetic Calorimeter

A gas-sampling electromagnetic calorimeter, built in a cooperative effort by Harvard and the University of Maryland, measures the energy of photons and electrons. It is discussed in detail in another chapter.

3.3.7 Particle Identification

E665 was designed with a serious intention to identify hadrons in forward fragmentation. The detectors installed for this purpose can be grouped into a vertex group, and a forward group.

The vertex group consists of the time-of-flight hodoscopes, and two threshold Cherenkov counters. A time-of-flight system (TOF) was mounted at large angles

---

[16]The hadron absorber is in fact the remains of the Rochester cyclotron.

to the beam, and can separate πs, Ks, and ps up to 2 GeV. These particles come mostly from the the backward hemisphere, and have been the subject of a two complete analyses [Erdmann, Siegert]. The Cherenkov counters, C0 and C1, are traditional threshold counters imported from EMC. They are useful for $\pi/K/p$ separation up to 20 GeV. However, data from these counters has not been analyzed.

The forward group is highlighted by the RICH detector. It is the most interesting of the particle ID detectors in E665, and was meant to identify hadrons from low momenta all the way to above 100 GeV. Unfortunately, due to fatal problems in hardware and software, no useful information is available from this detector.

The calorimeter is a particle ID detector in the sense that it can separate electrons from pions (or other minimum-ionizing particles). The performance of the calorimeter in this sense is discussed in detail in another chapter.

Determination of the event kinematics depends entirely on reconstruction of the beam and the scattered muon track. Of the several forward tracks that may be reconstructed, one is identified by matching it to a track behind the hadron absorber. This track is constructed from hits in the PTMs and SMS counters, and may be tagged by the SPMs. In this sense the hadron absorber together with PTMs, SMS, and SPM counters constitute a muon identification detector.

Clearly muon identification was essential to this analysis. The calorimeter also played an important role in separating hadrons and electrons. However, the other particle ID detectors were not used in the work of this thesis, and will not be discussed further.

parameter	hydrogen	deuterium	xenon
Z, A	1,1	1,2	43,131
length (m)	1.15	1.15	1.13
thickness (g/cm^2)	8.14	18.6	9.64
radiation lengths	0.133	0.152	1.137
interaction lengths	0.16	0.34	0.06
θ_{MS}^{rms} (μr)	10	11	30

Table 3.3: Basic target parameters.

3.4 Targets

E665 employed three targets during the 1987-88 run. Light targets were used in order to continue investigations EMC had undertook on structure functions and hadronization. A heavy (high atomic number) target also was used, because many collaborators were interested in the shadowing of virtual photons, and in the effects on the time development of hadrons of neighboring nucleons.

The targets necessarily were mounted inside the streamer chamber. As a consequence, they could not be switched frequently. In fact, E665 took data on one target for several weeks before switching to the next.

First, data were taken on a liquid deuterium target, after which a pressurized gaseous xenon target was used. Finally, liquid hydrogen was used as a target. The basic target parameters are listed in table 3.3. The "thickness" of each target is roughly the same, making it easy to achieve equal luminosity on each target. The target lengths as measured in radiation lengths were small to keep multiple scattering of hadrons and conversion of photons from π^0 decay to a minimum. The length of the targets measured in interaction lengths varies, with the deuterium target being the longest.

(A fair amount of data were taken on deuterium and xenon using a 100 GeV muon beam. None of these data were analyzed.)

3.5 Triggering

A deep-inelastic interaction is characterized by the large p_T imparted to the beam particle. Intuitively, this can be associated with a small impact parameter; it seems natural that violent collisions take place when the impact parameter is small, and that large impact parameters characterize nonviolent interactions, such as elastic or diffractive scattering. Thus, deep inelastic scatters have a much flatter distribution in the scattering angle than elastic scattering, or most other electromagnetic processes, such as μe scattering, bremsstrahlung, or low-Q^2 resonance scattering. This makes triggering straight-forward in principle: trigger the experiment when the beam muon is scattered at large angles. This is the essence of both muon triggers in E665.

How does one trigger on scattering angles? If there were no magnets, then the technique would be obvious: trigger the experiment whenever a muon emerged at an angle from the phase space of the beam. The coordinates of its impact point at a "trigger" plane downstream of the target would be proportional to $\sin\theta$, where θ is the polar scattering angle. If the scattered muon passes through a dipole magnet, however, then the dependence of the impact point on the scattering angle is smeared, at least in the plane perpendicular to the magnetic field. The magnet bends the scattered muon in this plane, but the amount of bending depends on the energy of the scattered muon. Consequently the flux of muons at a given point in the trigger plane represents a class of scattered muons occupying a range in θ and E' – it is no longer sharp in θ. In fact, since the angular deflection of a particle in a magnetic field is inversely proportional to its momentum, it is plausible that

$$Y_{\text{impact}} \approx D\theta + \frac{c_1}{E'} \quad \text{and} \quad Z_{\text{impact}} \approx D\theta,$$

where c_1 is a constant proportional to the strength of the magnet, and the distance from the target to the trigger plane. This smearing can be rectified, however, in a simple way. At a trivial level, all that is needed is another term to counter c_1/E'. In other words, another magnet with opposite sign field and a large enough "kick" can compensate the horizontal displacement induced by the first magnet:

$$Y_{\text{impact}} \approx D\theta + \frac{c_1}{E'} + \frac{c_2}{E'} = D\theta$$

if $c_2 = -c_1$. This constraint on c_1 and c_2 is known as the "focussing condition," and since c_1 and c_2 are independent of E', it holds regardless of the beam energy or the energy loss, ν. Note that since c_1 and c_2 depend on the position of the trigger plane, the focussing condition implicitly is valid only at that plane. Also, given a placement of the two magnets, the focussing condition sets only the relative $\int B \cdot dl$, not the absolute. In the 1987-88 run, the target was *inside* the vertex

magnet, causing a subtle but important violation of the focussing condition called the "target length effect." An explanation of this effect, and a more detailed calculation of the E665 optics is given in the analysis chapter.

There were two main physics triggers in 1987-88, both of which depended on the optics to place the scattered muon at a point outside the unscattered beam, at the trigger plane. The essential difference between them was the minimum angle at which they triggered, though in terms of electronics they were completely independent.[17] The large angle trigger, called LAT, simply demanded that a muon be detected outside a (large) veto region behind the hadron absorber. The small angle trigger, called SAT, demanded that no signal appear in a (small) veto region, also behind the steel. Data from both of these triggers were used in this analysis, so they are discussed in more detail below.

3.5.1 Large-Angle Trigger (LAT)

The large-angle trigger (LAT) could not be completed as originally designed, due to problems with building the custom-made electronics. The experiment took data with a rough equivalent installed at the beginning of the run. The main components were a beam logic signal provided by the SBT (small beam hodoscopes), a veto signal from the SMS (small muon hodoscopes), and a positive scattered muon signal from the SPM (large muon scintillators).

Beam tracks must be reconstructed in order to be useful; this means they must pass through all four beam tagging stations. This requirement was imposed at the trigger level by demanding a seven-fold coincidence from the SBTs, giving the basic beam signal:

$$B = SBT1Y \cdot SBT1Z \cdot SBT2Y \cdot SBT3Y \cdot SBT3Z \cdot SBT4Y \cdot SBT4Z.$$

The beam phase space was constrained further using the veto counters SVJ (veto jaws) and the halo reduced by the SVW (veto wall). The sum of all signals from these counters is called the "beam veto"

$$V = SVJ1 + SVJ2 + SVJ3 + SVW,$$

and the beam for the LAT was simply

$$LATBEAM = B \cdot \bar{V}.$$

---

[17] The fact that they were independent made it possible to determine the efficiency of one by playing it off against the other.

The SMS counters were placed so that most of the unscattered beam passed through them. This made them appropriate as a signal against unscattered beam. The sum of all signals from SMS counters in planes one and four constituted the muon veto signal:

$$MV = SMS1Y + SMS1Z + SMS4Y + SMS4Z.$$

This signal was not enough to reject all unscattered beams, so a signal from a genuine scattered muon was required, also. The SPM planes were constructed with a hole in the center, covered by the SMS counters. The size of this hole (approximately 0.2×0.2 m^2) determined the minimum scattering angle at which the LAT would fire: roughly the threshold is at $\theta = 3$ mr. They were bisected at horizontal plane, with a small overlap between the upper and lower halves. A three-out-of-four majority coincidence was formed for the upper half and lower half, separately, and the two signals summed:

$$S = [SPM1, SPM2, SPM3, SPM4]_{3/4}^{upper} + [SPM1, SPM2, SPM3, SPM4]_{3/4}^{lower}.$$

The scattered muon signal was simply

$$LATSCATTER = S \cdot \overline{MV}.$$

The overlap of the upper and lower halves was enough to avoid a significant acceptance problem[18], but the timing of the lower half was wrong, leading to a horrendous loss of efficiency. This loss, called the "up-down asymmetry," was studied in great detail; see [Aïd].

Good timing was required in order to reconstruct tracks well, achieved using a timing signal derived from the Tevatron RF. A "system busy" (SB) was used to block triggers when the data aquisition system was busy. The complete LAT logical definition was

$$LAT = LATBEAM \cdot LATSCATTER \cdot RF \cdot \overline{SB}.$$

The LAT was entirely scintillator-based. In fact this trigger was meant as a mere first-level, preliminary decision in the complete large-angle trigger. A second stage was planned which would have used signals from the PTMs (proportional muon tubes) to determine whether a valid scattered muon trajectory actually existed behind the absorber. (Although this second-level trigger was not operated during the 1987-88 run, it was installed for the 1990 run.)

---

[18]There is a very small loss of muons which start e.g. in the upper half, firing SPM1(u) and SPM2(u), but are scattered downward in the absorber between planes 2 and 3, and thus firing SPM3(d) and SPM4(d).

3.5.2 Small-Angle Trigger (SAT)

The small-angle trigger is considerably more complicated than the LAT. It is designed to trigger at very small scattering angles, in order to obtain inelastic data extending down below $x_{Bj} = 10^{-4}$, for the purpose of measuring the nuclear shadowing of cross sections.

Muons scattered through only 1 mr remain within the average phase space of the unscattered beam. The only solution is to reduce the phase space of the beam. This was accomplished in two domains: in the transverse extent of the beam, and in time. The SBTs allowed a maximum of beam to strike the target. The beam was peaked at the center of the counters, however, so that if the beam passing through the edges were rejected, the beam phase space would be tighter, without losing too much flux. The beam was broad only when integrated over time; the intensity was low so that it is sensible to talk about individual beam trajectories. Within a more restrictive beam definition, the impact point at the trigger plane of each beam particle could be estimated, based on the signals of individual SBT counters. The absence of a signal in the SMS counters at the predicted position meant that the beam had scattered. The minimum scattering angle for this trigger was set by the size of the SMS veto spot, which for 1987-88 was approximately 5 cm horizontal by 20 cm vertical. The trigger acceptance at $\theta = 1$ mr was about 50%.

Conceptually, the SAT was a refined extension of the LAT, but in terms of implementation, it was considerably more sophisticated.[19] A precise beam definition was required in order to predict the impact point of the unscattered muon. Monte Carlo studies revealed the combinations of fired SBT counters corresponding to the desired beam phase space. The combinations included three Y planes (SBT2Y, SBT3Y, SBT4Y) and three Z planes (SBT1Z, SBT3Z, SBT4Z). These planes are designated planes A, B, and C. Two three-dimensional matrices were defined, with each dimension corresponding to one of the planes A, B, or C. The number of elements in each dimension corresponded to the number of counters in the plane. The allowed combinations were designated with a logical "yes," and the forbidden combinations with a "no." The two beam trigger matrices, BY and BZ, were loaded into fast random-access memories. In any bucket, the pattern of fired and silent hodoscopes in each of the A, B, C planes acted as an address to look-up the validity of the trajectory in the RAMs. The beam was required to produce a "yes" in both BY and BZ.

The beam trigger matrix technique is susceptible to multiple beams in a bucket,

---

[19]This brief description is based on [Magill]. See also [Jaf89].

and to noise in the SBTs. To reduce these effects, a "clean beam" requirement was devised. First, the simple sum of all SBT counters was formed. It was timed relatively forward and backward, to allow a veto of any possible beam trajectories immediately before or immediately after the current one. Second, hits in the outside edges of the SBTs in the current bucket were used as veto, in order to reject odd coincidences of beam and halo, and to help reduce a problem with a "warm" SBT counter in station four. In essence the outer counters in the SBT planes were used by the SAT the way the LAT used the veto jaws. The signal $CLEAN$ was the sum of signals from adjacent buckets, and signals from the outer SBT counters. The SAT beam definition was

$$SATBEAM = BY \cdot BZ \cdot \overline{CLEAN}.$$

This definition accepted about 12% of the beam accepted by the LAT. More refined Monte Carlo studies and improvements to the definition of $CLEAN$ allowed an increase of this fraction to 70% for the 1990 run.

The definition of an unscattered beam was based on signals from two SBT stations, and signals from SMS planes 1 and 2. The same matrix technique was used: VY for Y and VZ for Z. The A planes were SBT3Y and SBT1Z, the B planes were SBT4Y and SBT4Z, and the C planes were formed from the logical sum of signals from SMS stations 1 and 2: [SMS1Y+SMS2Y] and [SMS1Z+SMS2Z]. The A and B planes are required to belong to valid BY and BZ combinations. The veto spot was chosen to be five SMS counters wide. Due to technical problems, only VY was used, so the SAT veto spot consisted of five vertical counters:

$$SATSCATTER = \overline{VY}.$$

Note that there is no positive muon requirement. This meant that there were significant backgrounds from hadrons and electrons in the beam, but these were easily removed in offline analysis. The acceptance of the SAT at large energy transfers (high y_{Bj}) is better than that of the LAT.

(A positive muon signal from the SMS counters was used for diagnostic purposes. It was not used in the trigger itself. Two two-dimensional matrices were defined (MY and MZ) using the signals from SMS1Y, SMS2Y, SMS1Z, and SMS2Z.)

The SAT used the same RF signal for timing as the LAT, and also the same system busy. The full SAT definition was

$$SAT = SATBEAM \cdot SATSCATTER \cdot RF \cdot \overline{SB}.$$

3.5.3 Monitoring Triggers

A number of non-physics events were logged to tape along with the LAT and SAT events. These included random samples of the beams defined by the LAT and SAT, and of the halo. The halo trigger required the coincidence of a signal in the beam veto counters (both jaws and wall), and a 3/4 majority coincidence in the SPMs. The random LAT beam ("RBEAM"), random SAT beam ("RSAT"), and halo triggers were heavily prescaled using custom-built modules. Data from these three triggers have been essential in several studies of the data.

A third physics trigger was defined using the energy deposited in the electromagnetic calorimeter. It was called "FCAL," and was tuned and timed for the hydrogen data only. The energy detected by the anode wires was summed, except for those in the center, which were swamped by high-energy Bremsstrahlung photons. The effective signal in each quadrant was derived from the sums, and a coincidence between opposite quadrants required. The LATBEAM signal was used to time the FCAL trigger. This trigger was too biased to be used directly for physics analysis, but since it required no scattered muon, it was useful for checking the LAT and SAT.

3.6   Normalization

The event yield is related to the cross section through the luminosity:

$$\frac{dN}{dx} = L \, \frac{d\sigma}{dx},$$

for any variable x. The luminosity L depends on the target thickness, and on the flux of muons. The term "normalization" pertains to determining the number of muons used to produced the given yield of events. There were three methods for determining the beam flux.

1. ("Event Scalers") Use Camac scalers to count the number of beam signals, and record this number with every event.

2. ("Spill Scalers") Use scalers to sum the number of beam signals for a spill, and write this information to tape between spills.

3. ("Random Beam") Select randomly a subset of the beam triggers and write them to tape. If the fraction of events recorded is known, then the beam flux

is obtained simply by counting the number of these events per interesting event.

This redundancy turned out not to be superfluous; there were problems with event scalers which were solved through comparison with the spill scalers and number of random beams. The random beam sample also was particularly useful in understanding the structure of the beam. For example, a fraction (roughly 10%) of the events contained two beam tracks, one of which was the remnant from an earlier bucket. It was better to reject these events as the old beam could confuse pattern recognition. A determination of the fraction of the luminosity lost is straight-forward using the random beam sample. Similarly, the number of true beams that failed to be reconstructed was easily checked using the random beam sample.

Since the random beam sample was not correlated with any trigger, it could be used to check biases in the triggers with respect to the beam. For example, a common false trigger consisted of an old beam signal and an in-time halo; the beam trigger was present but the muon veto was not, and the halo provided the necessary positive muon signal to trigger the experiment. The incidence of an accidental trigger could be checked by looking at the random beam sample.

The event scalers were faulty, but detailed studies identified the problems and fixes were devised [Bha88]. The rescued event scaler information was combined with the hardware clock time to give various measures of the beam and time across a variety of intervals [Sch88b]. For example, the beam since the last LAT event, or since the last SAT event, or since the last event of any type, was available for every event. As events were dropped, certain beam items were updated, so that at any time the total number of beam muons from a run could be calculated by summing over the beam recorded with the events from that run.

The number of beams from any (non-empty) spill is easily obtained, allowing a check against the spill scalers. It was found that the LAT beams agreed perfectly [Bha88], but there were some problems with the SAT beams. These eventually were tracked down to a logic module which intermittently produced a long gate, and to reflections in the cable bringing the rf strobe to the SAT logic [Magill, pp.81–84]. After these problems were handled, agreement between the event scalers and the random beam normalization was excellent.

Chapter 4

Calorimeter

4.1 The Electromagnetic Calorimeter

4.1.1 Introduction

The E665 electromagnetic calorimeter was built mainly for detecting the photons from π^0 decay. Monte Carlo studies had shown that the inclusion of "neutral energy" in jet axis determination helped considerably [Pip81, Michael]. Additional important uses for the calorimeter have been found, including

1. detection of high energy photons in Bremsstrahlung events, allowing an *empirical* check on radiative corrections calculations [Mag90a, Magill], and a separation of deep-inelastic and electromagnetic events [Jaf90, Sch89d],

2. reconstruction of π^0s in deep-inelastic scattering [Ramberg].

3. electron tagging in μe scatters,

4. electron-hadron separation,

5. offline event filter independent of the scattered muon to check muon reconstruction [Sch89b],

6. additional uses may include J/ψ identification through its decay into e^+e^-.

Note that the E665 calorimeter is useless for measuring the energy of charged hadrons or muons. Hadron-induced showers are fundamentally different than photon-induced or electron-induced showers, and require a different calorimeter design for measurement. Hadron calorimetry will not be discussed in this thesis. The energy of muons, due to their weak interaction with matter (which is due to their relatively heavy mass – they don't radiate) cannot be measured accurately with calorimetry (same as neutrinos).

In this chapter, the principles of electromagnetic cascades are presented, followed by a description of the E665 calorimeter, its operation, and its performance.

4.1.2   Principles of Operation

General Concepts

Photons can be detected only through calorimetry because they leave no tracks (traces of ionization) to be detected in wire chambers. To date the only practical method of measuring the energy of a photon is to absorb it in a mass of material. The photon starts an electromagnetic cascade ("shower") consisting of electrons, positrons, and photons (with other particles like muons only at negligible levels). The electrons and positrons ionize the material, and this ionization is detected in one way or another (e.g., light in scintillating material, light in dense crystals, ions in gas or even liquid), as depicted schematically in figure 4.1.

The construction and qualities of a calorimeter are determined by the characteristics of electromagnetic showers, which in turn depend on the interactions of electrons and photons in matter. Both the high energy (several GeV to several hundred GeV) and the low energy (several MeV) domains are important. The physicist wants to measure the energy of multi-GeV photons and electrons, but it is the ionization produced by multi-MeV electrons which provides the signal.

Electron Interactions in Matter

Matter consists of highly charged heavy particles (nuclei) surrounded by electrons, which are light and singly charged. A free electron passing through matter can

- ionize atoms, giving a small amount of energy to the atomic electrons it frees,
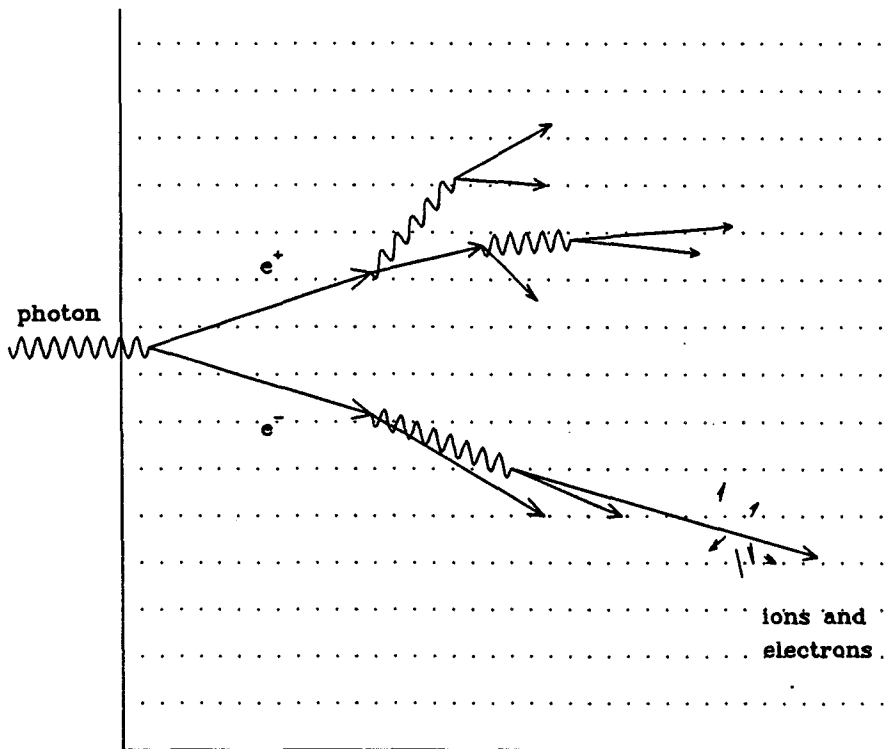
Figure 4.1: Schematic drawing of a photon-induced shower.

- radiate a Bremsstrahlung photon,

- interact directly with an atomic electron in a violent collision.

In each of these processes, the incident electron loses energy. Energy loss by ionization is dominant for incident electron energies below a GeV, and Bremsstrahlung dominates above (see figure 4.2). Violent collisions between electrons are relatively rare, and generally are neglected. [1]

The probability is high that a high energy electron will radiate a large fraction of its energy before traversing one radiation length of material. In effect, this defines the radiation length.[2] More precisely, a radiation length (denoted as X_0) is the average distance covered by an electron before it loses $1/e \approx 37\%$ of its energy:

$$-\frac{dE}{dX} = E_0 e^{-X/X_0}.$$

It depends on the material through which the electron is passing but not on the energy of the electron. A very precise formula has been derived using QED, with

---

[1] At some level they already are incorporated in the formula for energy loss due to collisions.

[2] It can be shown that the electrons loses this energy to one single photon most of the time [Hei36, sec.23].
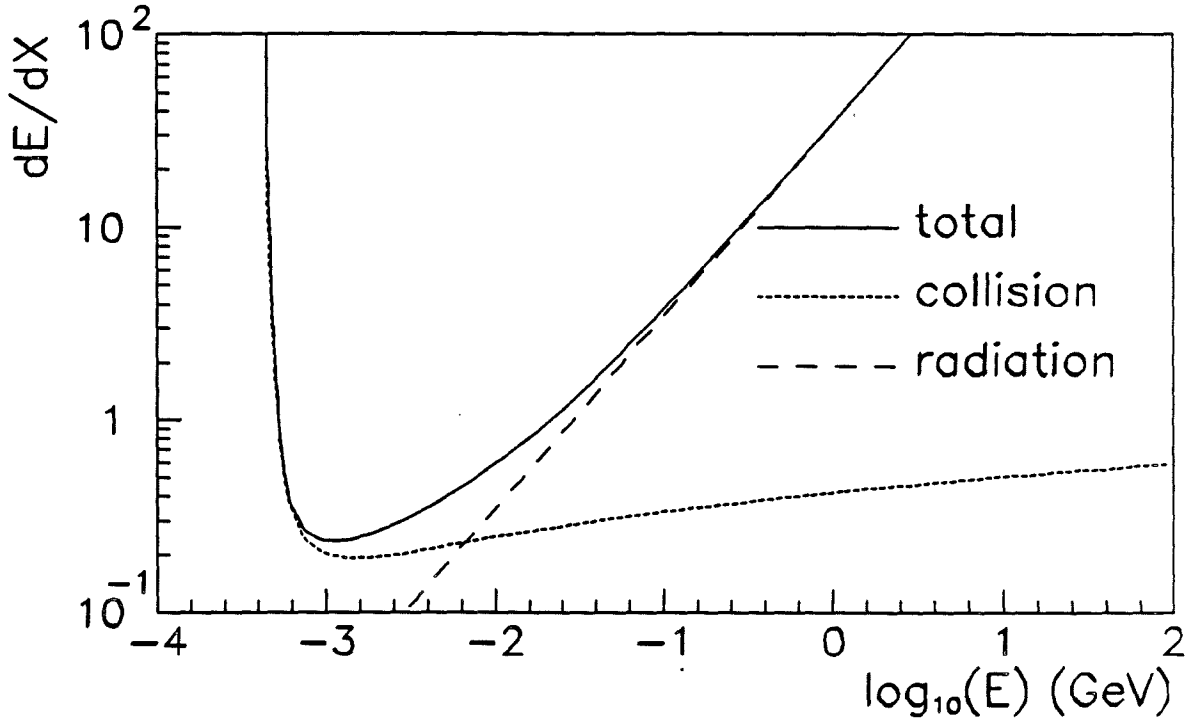
Figure 4.2: Energy loss by an electron. (after [Hei36, p.222])

assumptions about the effects of the screening of nuclear charge by atomic electrons [PDG, p.66]

$$\frac{1}{X_0} = \frac{4\alpha r_e^2 N_A Z^2}{A} \times$$

$$\left\{ \ln\left(\frac{184.15}{Z^{1/3}}\right) + \frac{1}{Z}\ln\left(\frac{1194}{Z^{2/3}}\right) - 1.202\alpha^2 Z^2 + 1.0369\alpha^4 Z^4 - \frac{1.008\alpha^6 Z^6}{1+\alpha^2 Z^2} \right\}$$

where the nucleus has charge Z and atomic number A, $\alpha = e^2/\hbar c$ is the QED coupling constant, $r_e = e^2/m_e c^2 = \alpha\hbar/m_e$ is the classical electron radius, and N_A is Avogadro's number. A good approximate formula is

$$\frac{1}{X_0} = \frac{4\alpha r_e^2 N_A Z(Z+1)}{A}\ln\left(\frac{183}{Z^{1/3}}\right)$$

As expected, the main dependence is on Z^2 (recall that the Bremsstrahlung cross section goes as Z^2).

It is worth writing the explicit expressions for energy loss due to collisions with atoms, and due to Bremsstrahlung radiation [Hei36, pp.172,220,221,225].

68

- energy loss due to collisions, nonrelativistic limit

$$-\left(\frac{dE}{dX}\right)_{\text{coll}} = \frac{3}{4}\sigma_0 N_A Z(m_e c^2)\left(\frac{m_e c^2}{E - m_e c^2}\right)\left(\ln\frac{E - m_e c^2}{IZ} + \frac{1}{2}\right)$$

- energy loss due to collisions, extreme relativistic limit

$$-\left(\frac{dE}{dX}\right)_{\text{coll}} = \frac{3}{4}\sigma_0 N_A Z(m_e c^2)\left(\ln\frac{E^3}{2m_e c^2 I^2 Z^2}\right)$$

- energy loss due to radiation ("Bremsstrahlung")

$$-\left(\frac{dE}{dX}\right)_{\text{rad}} = N_A \sigma_{\text{rad}} E$$

- in the case of no screening,

$$\sigma_{\text{rad}} = \bar{\sigma}\left(4\ln\left(\frac{2E}{m_e c^2}\right) - \frac{4}{3}\right)$$

- in the more realistic case of complete screening by atomic electrons,

$$\sigma_{\text{rad}} = \bar{\sigma}\left(4\ln\left(\frac{183}{Z^{1/3}}\right) - \frac{2}{9}\right)$$

In these expressions σ_0 stands for the Thompson cross section;

$$\sigma_0 = 2\left(\frac{4\pi r_e^2}{3}\right)$$

and $\bar{\sigma}$ is similarly a simple quantity characteristic of radiative processes in a given material,

$$\bar{\sigma} = \alpha Z^2 r_e^2$$

Numerically, $\sigma_0 = 0.665$ barns, and $\bar{\sigma} = 0.577\ Z^2$ millibarns. The ionization potential of the material is given by $I \approx 13.5\ Z$ eV.

Very slow electrons ($E < 1$ MeV) lose energy slowly by colliding with atoms and ionizing them. The greater the energy of the electron, the slighter the energy loss by ionization. High energy electrons, however, have a high probability for emitting a Bremsstrahlung photon. This is especially true for high-Z materials like lead, argon, steel, xenon, etc., because the probability is proportional to Z^2. Note also that the probability increases with the energy of the electron. The probability distribution for photon energies is fairly flat (at least it is not sharply

peaked), so it is not unlikely that the electron will lose an appreciable fraction of its energy through Bremsstrahlung. The photon intensity spectrum is given by the approximate formula [Hei36, p.225]

$$\frac{k\sigma_k}{E_0\bar{\sigma}} = \frac{k}{E_0}\frac{a}{\ln(E_0/(E_0 - k))}$$

where k is the photon energy, and a is a constant with value about 20-23.

The energy loss dE/dX for electrons shown in figure 4.2, is proportional to the total cross section. Clearly Bremsstrahlung dominates except at the very lowest energies. The expressions for Bremsstrahlung should also make it clear where the definition of the radiation length comes from.

Photon Interactions in Matter

Photons interact with matter mainly through three processes:

1. photoelectric effect. $\gamma + A \rightarrow A^+ + e^-$ (A stands for atom.) very small energies only.

2. Compton scattering. $\gamma + e^- \rightarrow \gamma' + e^-$ important for $E_\gamma < 1\text{GeV}$.

3. pair production. $\gamma + Z \rightarrow Z + e^+ + e^-$ dominant for E_γ above 3GeV.[3]

The simple expressions for these cross sections are [Hei36, pp.123,125,157,200]

- photoelectric effect, nonrelativistic limit

$$\sigma_k = 4\sqrt{2}\sigma_0\alpha^4 Z^5 \left(\frac{m_e c^2}{k}\right)^{7/2}$$

- photoelectric effect, extreme relativistic limit

$$\sigma_k = \frac{3}{2}\sigma_0\alpha^4 Z^5 \left(\frac{m_e c^2}{k}\right)$$

---

[3]At high enough energies ($E_\gamma \approx 400$ GeV) muon pair production is no longer entirely negligible.

- Compton scattering

$$\sigma = \frac{3}{8}\sigma_0 \left(\frac{m_e c^2}{k}\right) \left[\ln\frac{2k_0}{m_e c^2} + \frac{1}{2}\right]$$

- pair production, no screening

$$\sigma_{\text{pair}} = \frac{2}{9}\bar{\sigma} \left(14\ln\frac{2k}{m_e c^2} - \frac{109}{3}\right)$$

- pair production, complete screening

$$\sigma_{\text{pair}} = \frac{2}{9}\bar{\sigma} \left(14\ln\frac{183}{Z^{1/3}} - \frac{1}{3}\right)$$

Note the similarity in the cross sections for pair production and for Bremsstrahlung. These two processes are closely related — in fact they are really the same at the level of Feynman diagrams, as shown in figure 4.3. Take the Bremsstrahlung diagram. If we reverse the direction of the outgoing electron, we have an incoming positron, and the process is really electron-positron annihilation in the field of a nucleus. If next we time-reverse the entire diagram, so that the photon is incident and the electrons are outgoing, then we have the pair production diagram. This connection is important in understanding the shower multiplication process, which consists basically of an interchange between electrons and photons (almost like a plasma which is relaxing). Normally one imagines a cascade based on a particular Lorentz frame – that of the perturbing potentials. Thinking of the shower in the rest frame of the incident particle, one sees it is like an expanding gas of electrons and photons. Schematically there are three regions of photon "absorption" (see figure 4.4) corresponding to the three processes listed above (figure 4.5). Writing the usual expression for the absorption of a beam of particles, the total absorption coefficient τ can be defined.

$$N_\gamma(X) = N_0 e^{-X/\tau}$$

where $\tau = \tau_{\text{PE}} + \tau_{\text{CS}} + \tau_{\text{PP}}$. Very soft photons (region I) are absorbed quickly through the photoelectric effect, the main product being slow electrons which ionize heavily. Critical photons (region II) penetrate farthest. When they are absorbed, the end products are a low energy electron, and a secondary photon of less energy – typically one in region I. High energy photons (region III), such as the ones the energy of which we want to measure, produce a pair of electrons. The electrons tend slightly to be asymmetric, but on average are equal, so often they will have high energy also.

71
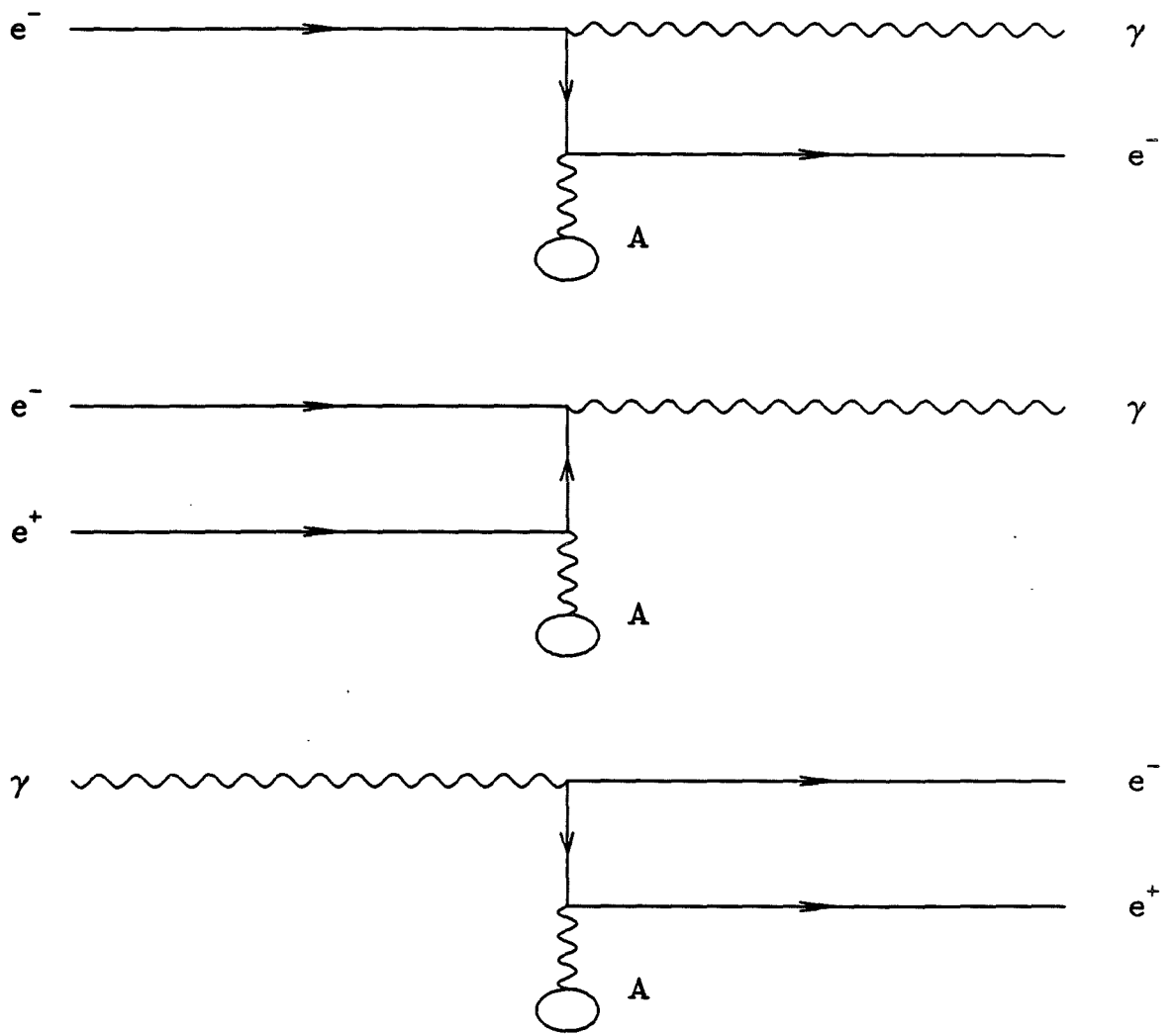
Figure 4.3: Relation between Bremsstrahlung and pair production.
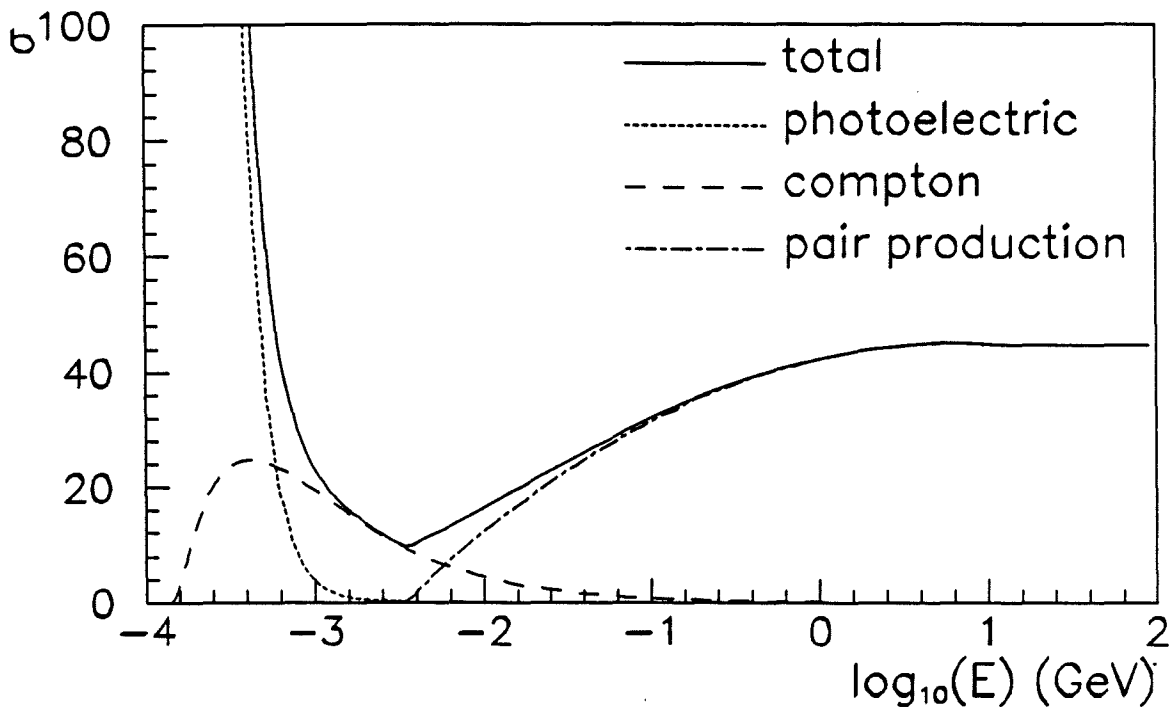
Figure 4.4: Three regions of photon absorption. (after [Hei36])

Shower Multiplication

The early stages of a shower cascade consist of alternating stages of Bremsstrahlung and pair production (see figure 4.6). As mentioned above, these are sister processes. It is only after several stages of photon-electron multiplication that large numbers of highly ionizing particles appear.

The early stages of a shower consist of a few high energy electrons and photons, which multiply, roughly one generation per radiation length. Succeeding generations penetrate to greater depth, but each generation starts with less energetic particles than the preceeding. Eventually low energy photons produce low energy electrons, which lose their energy by collisions with atoms rather than by radiation. These electrons become less and less energetic, until they stop. At the tail of the shower, only a diffuse gas of slow electrons is left, which peters out after 15-20 radiation lengths. (See depiction in figure 4.7.)

photoelectric

absorption

compton

scattering

pair

production
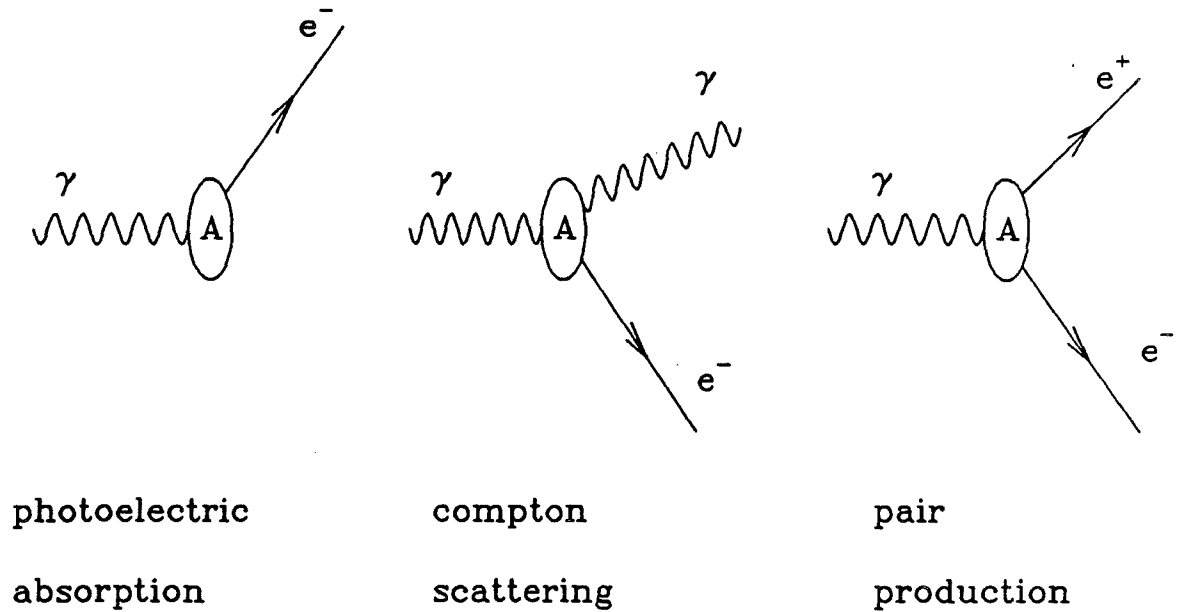
Figure 4.5: Three main processes in photon absorption.

4.1.3 Shower Fluctuations

Clearly shower generation is a stochastic process. Two identical electrons striking the calorimeter would deposit different amounts of energy (i.e., would cause different amounts of ionization) at a specific depth. Measuring the energy and shape of showers involves an intrinsic random element apart from random instrument errors, which in good calorimeters sets the ultimate limit on energy and position resolution.[4]

In the case of sampling calorimeters, the fluctuations in energy measurement are considerably larger than the intrinsic limit, due to the fact that only a tiny fraction of the ions produced contribute to the signal. The fluctuations in the exact fraction of total ionization detected by the sensitive material decreases with the thickness t of the sampling layers as $\sqrt{t}$.

---

[4]This situation can be contrasted with measuring the momentum of a track, in which case the random errors due to multiple scattering and soft photon radiation are very small (if not quite negligible) compared to the tracking errors. Put another way, measuring the energy of a shower is like trying to determine the temperature of a volume of gas containing only a few thousand molecules.
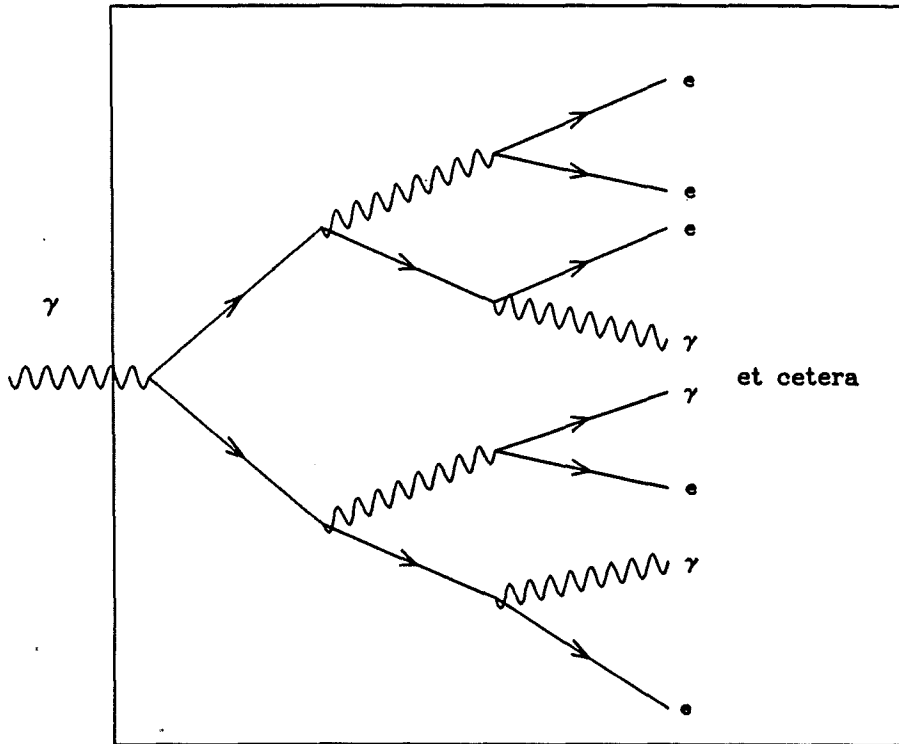
Figure 4.6: Strict stick diagram of a cascade.

The fluctuations in shower shape are smoothed to some extent in a measurement of the total shower energy. They pose significant problems, however, for measurements of the longitudinal development of a shower, useful for particle identification. Figure 4.8 shows the longitudinal profiles of three electron showers from good μe events, and three pion showers from exclusive ρ^0 events. Clearly e/π separation can be done on a statistical basis only. Figure 4.9 shows the *average* shape of electron and pion showers in the calorimeter. As explained in a later section, the statistical separation of electrons from pions is based partly on the similarity of a particular shower to one of these average shapes.

γ

high energy
electrons

medium energy
electrons and
photons

low energy
electrons
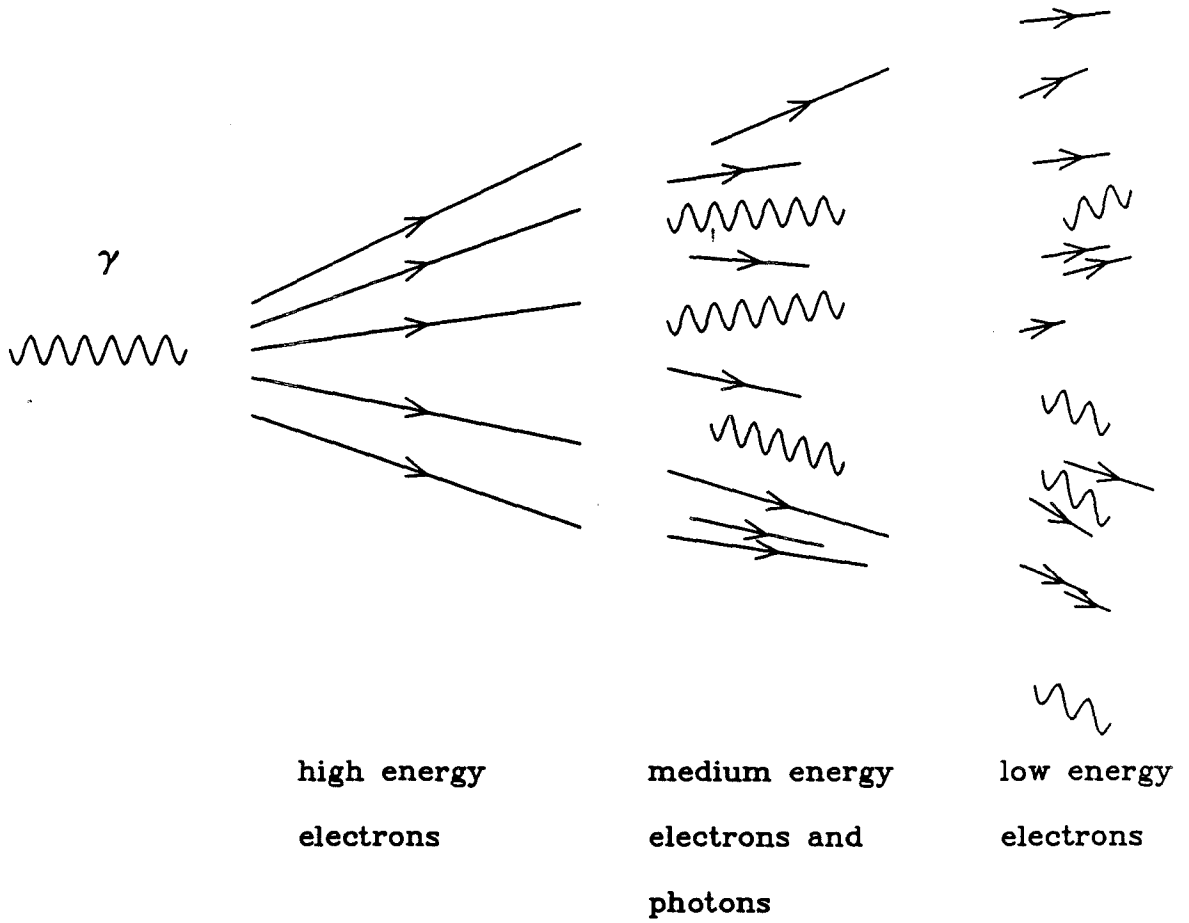
Figure 4.7: Three stages of an electromagnetic shower.
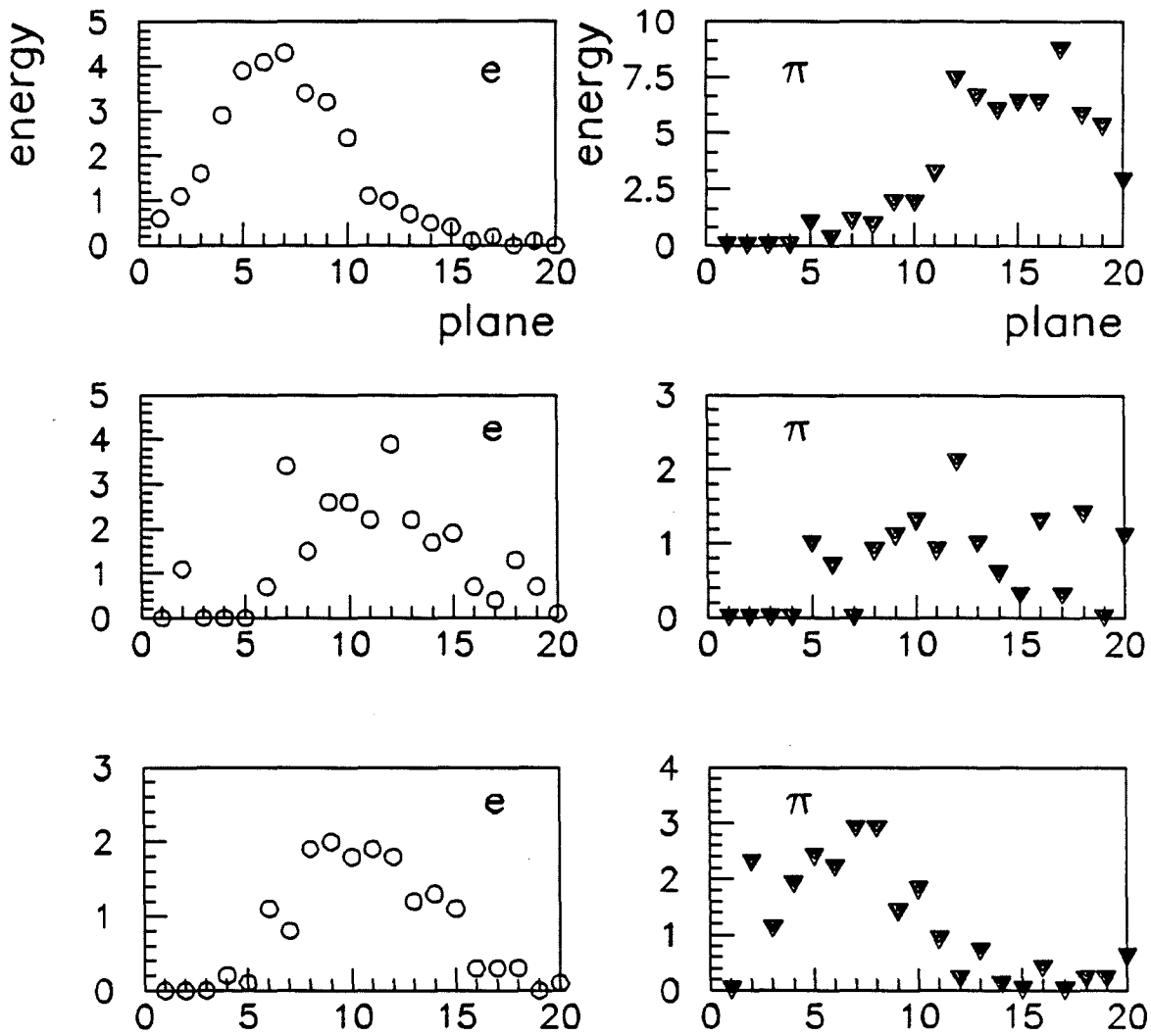
Figure 4.8: Three electron and pion longitudinal profiles. The points mark the energy (GeV) in each plane, for one shower.
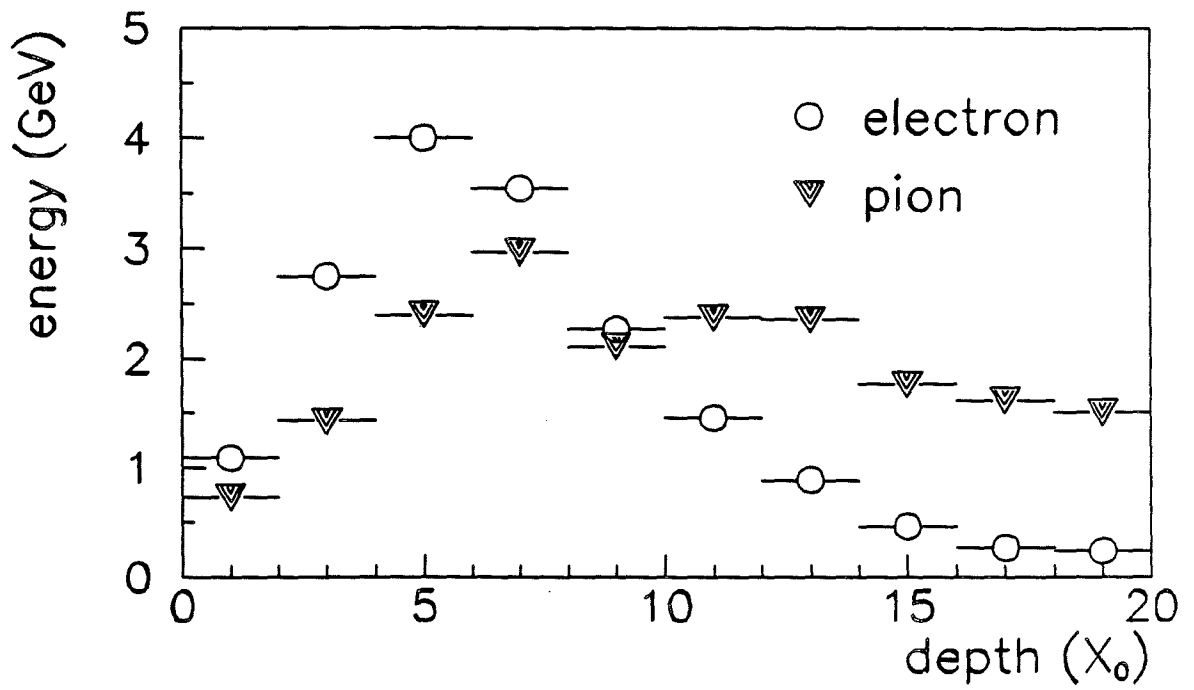
Figure 4.9: Average electron and pion longitudinal profiles. The points mark the average signal seen, for many showers.

4.2 Physical Construction

The E665 calorimeter is a simple stack of very dense material (lead) interleaved with very thin material (argon-ethane gas).[5] The lead provides the material necessary for the cascade, and the gas provides longitudinal samples of its development. The ionization produced in the gas can be measured by accelerating the freed electrons toward sense wires. To a large extent the average primary ionization produced in a gas is a constant fraction of the total ionization[6]:

$$\frac{N_{ions}^{gas}}{N_{ions}^{lead} + N_{ions}^{gas}} = \text{constant},$$

and since the total energy of the particle is proportional to the total ionization ($N_{ions}^{lead} + N_{ions}^{gas}$), the signal collected from the sense wires in the gas is proportional to the shower energy. This type of calorimeter is called "gas-sampling."

4.2.1 Lead Layers

The lead layers are glued to aluminum sheets which provide structural strength. There are twenty layers, each one radiation length thick. The lead and aluminum together (0.5 cm Pb and 0.2 cm Al) are less than a centimeter thick, but there is a small air space (a few mm) on either side of each lead plane due to the details of the hangar construction.

4.2.2 Anodes

The gas-sampling layers consist of many pieces which constitute only a fraction of a radiation length, and each intercepts only a tiny portion of the total ionization. The primary amplification of the ion signal produced by charged particles is accomplished using proportional wire tubes. The economically motivated choice was

---

[5]The relative density is about 10,000:1.

[6]A subtle "transition effect" has been identified which is manifested by rapid shifts in the equilibrium populations of photons and electrons at the boundary between a high-Z and a low-Z material [Iwa90]. This effect is minor, however, and does not cause any significant nonlinearities.

Iarocci chambers,[7] which were operated in the proportional mode.[8]

The sense wires constitute the anode. They are strung the full three meter length of the tube. The overall frame ("profile") is made of plastic, and includes walls separating the individual wires. This helps reduce anomalous ionization in a cascade produced by a slow electron travelling across several wires. All surfaces are coated with graphite, which constitutes a resistive cathode. The anode wires are held at ground, and the cathode at negative high voltage. As it turned out, wires of two different diameters were used.[9] Since the accelerating field near the wire depends on the wire diameter, two different potentials (-2 and -2.15 kV) are applied to the calorimeter, so that the gas gain is the same in all planes. One assembly of eight wires constitutes a "tube," and two tubes are housed inside a tight-fitting plastic case to make a "bitube." The wires are spaced one centimeter apart. Due to the thickness of the plastic case housing the two profiles, the *mean* separation of wires is somewhat larger: 1.05 cm/wire.

Plastic supports ("bridges") spaced at regular intervals stabilize the wires and ensure correct placement with respect to the cathode.[10] They were placed at the same position in every tube, so that they overlap in a head-on view of the calorimeter.

4.2.3 Cathodes

There really are *two* cathodes in each plane: the resistive, graphite coating inside the bitube, and additional copper sense pads taped to the outside. The purpose of the graphite is to support the electric field which accelerates the electrons. It also collects positive ions. Its resistive nature allows a transparency to fast signals, however, which can be detected by a pad external to the bitube: the cutoff frequency depends on the resistance to ground and the capacitance to the pickup

---

[7]Iarocci tubes have been described several times in the literature. See for example [Iar83]. Based on a design implemented at the Mont Blanc proton decay experiment, they have been used successfully in several other experiments, including OPAL at LEP. Our Iarocci tubes were early versions, and proved to be at times "uncooperative," and difficult to repair.

[8]The original intention was to run the tubes in limited streamer mode, thereby obviating electronic amplifiers. It was feared, however, that the unscattered beam would produce too many ions, harming the performance of the calorimeter near its center. Also, it has been observed that nonlinearities appear at relatively low energies (> 12 GeV) [Iar83, p.40].

[9]This was an error, not intentional.

[10]Prototype studies revealed significant cathode pulse height variations along a set of wires, eventually tracked down to variations in wire placement with respect to the cathode [Nic83b, Nic84e, Nic84f].

pad [Nic83a]. This property is exploited by mounting copper sense pads outside the bitube. The resistive cathode does the work of shaping the field and collecting ions, while the conducting cathode picks up the fast current pulses from avalanches – even though it is at ground potential, and is merely taped to the outside of the plastic casing.

The conducting pads are etched copper on G10 boards. There is a pad on both sides of the wire, eliminating to first order the sensitivity to wire placement [Mes84]. The signals from pairs of pads are summed passively through thin wires soldered to each and wrapped around the edge of the bitube.

The boards are mounted to a precision of roughly 1 mm on the bitube sheath. Since the position of the bitubes are well-constrained, so is that of the pads. The signals from all pads at a given (Y, Z) coordinate are summed actively, using op-amp circuits in external electronics boards.

The pads come in three sizes, chosen to give a roughly constant angular resolution for π^0 reconstruction [Nic83c]. (One can show that $\sigma_M/M \propto l_{pad}/d_{12}$, where M is the reconstructed mass, l is the length of the side of a pad, and d_{12} is the distance between the photons at the calorimeter.) Those in the central one square meter are 4 cm on a side. In the square band around these the pads are 8 cm, and in the outer band, 16 cm. This arrangement is depicted in figure 4.10.

4.2.4   Planes

Eighteen bitubes with cathode pad boards carefully taped on the outside are stacked in thin aluminum boxes, along with the amplifying and test pulsing electronics for the anode signals. The box provides the support structure for the chambers and electronics, a fairly good shield against ambient radio noise, and a gas shield in case of leaks in the bitubes. One box complete with contents is called a "plane." There are twenty planes, and eighteen bitubes in each plane, each 0.1675 m wide, so the active area of each plane is roughly 3×3 m^2. The box is rectangular, since it houses electronics in addition to the bitubes. The most upstream plane is numbered one; all odd-numbered planes are hung so that the wires are horizontal, and the even-numbered planes are vertical.

The boxes were designed so that the bitubes fit snugly; the position of the bitubes, and more importantly, the pads, should be constrained to within about 1 mm. Each box is hung from a hanger much the way the lead layers are. The hangers move longitudinally in flat grooves; special trolleys were constructed for

One Quadrant
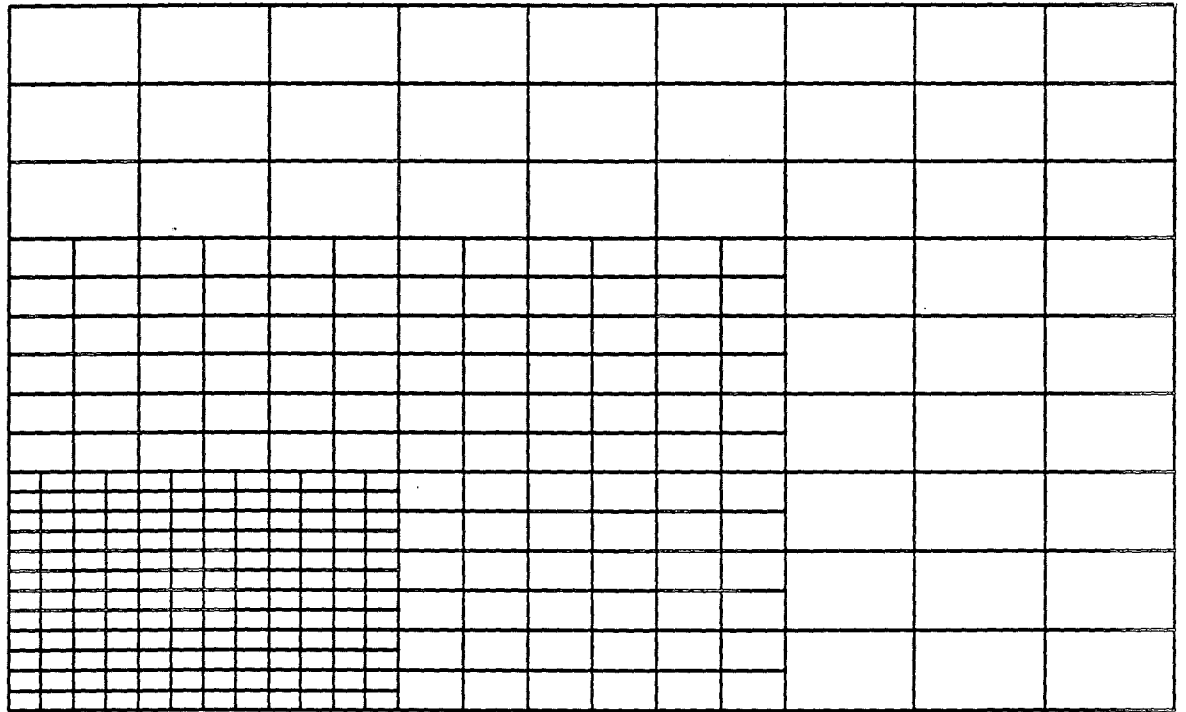
Figure 4.10: Pattern of calorimeter cathode pads.

moving one plane at a time. There is enough space to allow access to any single plane. The planes can be uncabled and removed vertically from the stack for repair, although this process is onerous. The vertical position of each plane is set by turning a bolt on a screw which attaches the plane to the hanger. The horizontal position can be varied a couple of millimeters within the flat grooves. The planes were aligned with respect to one another using an optical level; the tolerance was meant to be 1/8 inch (about 3 mm).

The high voltage for each profile (resistive cathode) is supplied through connectors at the edges of the box. There is one "Droege" supply for each plane, allowing in principle each plane to be fine-tuned for gas gain. In practice the supplies are set so that every 50 μm-wire plane runs at -2.0 kV, and every 63 μm-wire plane runs at -2.15 kV. (The anodes are at ground, and resistive cathodes are at negative potential.) These voltages are set to an accuracy of 1.5 volt.

The low voltage is supplied through single wires at one corner of each plane. The pad and bitube signals are returned through connectors at the edges of the box. All signal and supply wires for a plane are arranged carefully into bundles (called "umbilicals"), to allow uncabling in case a plane needs to be repaired.

Gas is flowed through plastic tubing at the corner of the plane. There is one input and one output line: the gas passes through the profiles serially. An air circulation system draws air over the electronics, in an effort to reduce heating problems, and to remove any traces of ethane that might leak from the Iarocci tubes.

4.2.5   Dart Planes

One small pad is 4 cm on a side, so it covers four wires in a bitube. The transverse size of a photon in pure lead is roughly 2 cm in radius, so even with the expansion due to the gas-sampling layers, it is clear that the limit on position resolution is not met using the small pads. To improve position measurement, four planes near shower maximum were specially instrumented so that individual wires could be read out. In addition to the standard bitube signals, the signal from each individual wire in the central meter of the plane, and each pair of wires in the outer meters of the plane, was amplified and digitized. These planes (numbers 4 through 7) are called "Dart" (detailed anode read-out) planes.

Prototype measurements indicated that the position resolution was about 4 mm for electrons of moderate energy; the pads have a resolution of 6 mm. (Of course,

the resolution improves as the shower energy increases.) The Dart wires were not used in earlier analyses of π^0s.

The additional amplifiers forced a more complicated arrangement of bitubes in these planes. Whereas the electronics cards in the normal planes are all at one end, in the Dart planes the bitubes have alternate orientations, so that the electronics is found on both ends of the plane. In normal planes, the gas flows sequentially through the bitubes, but there are two parallel routes for the gas in Dart planes.

4.2.6 Gas System

The importance of a constant gas gain is discussed in a later section. The calorimeter gas system is designed to provide a gas the composition of which is constant to better than 0.2% per week [Mic87]. A standard Fermilab system mixes pure argon and ethane to one percent (50% argon, 50% ethane, by volume); this particular mixing rack also supplies gas for the PTMs. Fluctuations of one percent in a day are too large, so the gas is flowed through a large buffer tank, to smooth out fluctuations. The gas volume of the calorimeter is about 60 ft^3 and the flow rate is of 2–3 ft^3/hour, so the calorimeter is flushed about once per day. The volume of the buffer tank is about 800 ft^3, which corresponds to roughly two weeks of calorimeter volumes.

Three mass flow meters are used to monitor the flow of gas: one at the input to the buffer tank, one at the input to the calorimeter, and one at the output from the calorimeter.

The Iarocci chambers leak easily, so it is important to keep a positive pressure differential between the inside and outside of the tubes. (Any oxygen leaking in will harm seriously the performance of the chambers, because the oxygen molecules pick up free electrons easily.) In fact the overpressure of the chambers with respect to the atmosphere must be slight, however, or serious leaks will develop. The output of the calorimeter is kept at 1–2 inches of water above atmospheric pressure; the pressure differential from the input to the output of the calorimeter is on the order of an inch of water. This means the absolute pressure of the amplifying gas varies rapidly, according to the weather.

The gas from the buffer tank is kept at 10 psi. A valve controls the flow into an input manifold. One line brings gas to each of the planes. A manual valve for each plane allows a matching of plane impedances, so that the flow is roughly the same in each plane. (The flow is twice as high in the Dart planes, due to the alternating

orientation of the bitubes in those planes.) The gas flows serially from one profile to the next; if an impurity were to appear at the input, it would propagate gradually from one end of a plane to the other. The output gas from each plane is brought to two exhaust manifolds, and the gas is flowed through a giant, home-brew oil bubbler, which provides the step in pressure of the calorimeter with respect to the experimental exhaust.

There is no alcohol vapor in the calorimeter gas, and there is no explicit control of the temperature. Temperature fluctuations are damped well by the tent, described next.

4.2.7   Tent

During the commissioning of the calorimeter in 1987, it was found that the connectors on the high voltage cables were hygroscopic. Unacceptably large currents were drawn on particularly moist days. To bring this under control, a tent was erected around the entire calorimeter, including electronics and high voltage supplies. Dehumidifiers were installed inside the tent, and ran all the time. As a result, there were no problems with humidity, although a few members of the collaboration had aesthetic objections to the tent. (The old tent was replaced by a new one, built by professional carpenters.) As a bonus, temperature fluctuations in the hall due to the opening of large doors in the middle of winter were successfully dampened out; the temperature inside the tent was warmer and much stabler than in the hall.

4.2.8   Electronic Readout

None of the electronics in the calorimeter is exotic (compared to the custom-designed chips for the Rich, for example), but all the systems together amounted to a considerable challenge in debugging and calibration. Some serious problems appeared during the run, as detailed in a later section. Here only a very brief overview of electronic amplification and digitization is given.

In a normal (i.e., non-Dart) plane, there are eighteen amplifier cards, one for each bitube. Each card contains two amplifiers: a low-gain, low-impedance amplifier used for regular data taking, and a high-gain amplifier, meant for measurement of the muon energy deposition.[11] The high-gain amplifiers were enabled by opening

---

[11]It was planned to use the halo muon signal for monitoring the spatial and time variations of the gas gain.

element	bitubes	small pads	medium pads	large pads
width (ns)	727	1451	1457	1421

Table 4.1: Fastbus ADC gate widths.

a magnetic relay. Unfortunately, these relays failed, and heroic efforts failed to rescue the high-gain system. The high-gain amplifiers remain dysfunctional through all three runs.

The regular amplifiers have low input impedance in order to minimize ringing of the current pulse from the electron avalanche along the anode wire. They are calibrated using a precision capacitor and a voltage source to inject a fixed charge in the input [Oli84]. The capacitor is mounted on the board, and the voltage is controlled via a "plane driver," addressable through a simple bus. These amplifiers turn out to be very stable: no appreciable drift in gain occurs over several days. They are also very uniform.

The amplifiers for the individually read-out anode wires are similar; the gain is higher since the input charge is smaller by a factor of five or ten.

The pads are summed passively; there is no amplification for the signals inside the plane.

The anode and cathode signals from the planes are gathered together in external crates called "coffins." There is one coffin in each quadrant; only the lower ones contain boards for the anode signals. These boards form anode sums which can be used for building a calorimeter trigger (e.g., the FCAL trigger). The pad boards contain circuits to sum the signals from the twenty planes corresponding to a given cathode pad; these are the "pad towers" used to find showers. The op-amp circuits avoid nasty coupling that would plague passive summers, and they keep the output signal narrow. The anode and cathode signals are delayed in order to be in time for the experimental trigger.

All signals are brought from the coffins to fastbus crates where they are digitized in Lecroy 1885 ADCs. There are two such crates, one on the west side and one on the east, and each contains thirteen ADC modules.[12] (Refer to figure 4.11.)

The gates for the ADCs are generated from the experimental trigger. The gate length is somewhat shorter for anode signals than for pad signals, but in general is about 1 μs long. A summary of measured values is given in table 4.1.

---

[12]For the 1990 and 1991 runs, ADCs for the SUM Wall were installed in these crates, also.

The Fastbus ADCs are dual-range devices with an effective resolution of fifteen bits, or 12k counts. The input is split in three pieces according to 8:1:1. Digitization of the 80% piece gives the low-range scale (about 0.05 pC per count); digitization of the 10% piece gives the high-range scale (about 0.4 pC per count). The ADC can switch between the two scales automatically. The scale is signified by a bit in the address word. A copy of this bit was installed in the data word, too [Mic86]. The ratio of the slopes for the two ranges is eight, to within one percent.[13] The pedestals vary considerably from channel to channel, but usually are very stable. The switch-over point varies from channel to channel. A sketch of the ADC response to input charge is given in figure 4.12.

Each crate is controlled by a Lecroy 1821 crate controller. The two crates operate in parallel, and send the ADC data to a third fastbus crate, located in the control room. The third crate also is controlled by an 1821 module, which communicates over a link to the event concatenation microvax. The data from the Fastbus ADCs is stored in large (4Mb) memories in the third crate. The data can be stored in these memories faster than they can be read by the microvax.

4.2.9 Several Calorimeters in One

It is worth emphasizing that the E665 electromagnetic calorimeter is really several calorimeters put together in one. There are several obvious dichotomies, which correspond to various symmetries in the design and construction of the calorimeter:

- There is an anode calorimeter and a cathode calorimeter: the total energy measured by each should be the same, within resolution.

- The odd-numbered, horizontal planes and the even-numbered, vertical planes constitute two interleaved calorimeters. They have separate low-voltage power supplies, and are read-out through distinct fastbus crates, but nonetheless should measure nearly the same energy.

- There are four identical quadrants of pads towers. Each should see the same minimum-ionizing signal, despite different external summer cards.

These dichotomies are useful when testing the performance of the calorimeter, and when tracking down systematic problems.

---

[13]This statement applied to the ADC itself. The ratio of slopes for the pads was found to be about 7.4, a fact which has not been explained. [Ram88a].

BISON 61 → concatention machine (μvax)
BISON 64 →
BISON 65 →

CAMAC

21 1892s

CALORIMETER

west   east

21 1885s   1885s 21

key

21
FB1821
segment
manager

1885s
FB1885
13 ADCs

1821s
FB1892
4 memories

Data flows from bottom to top.
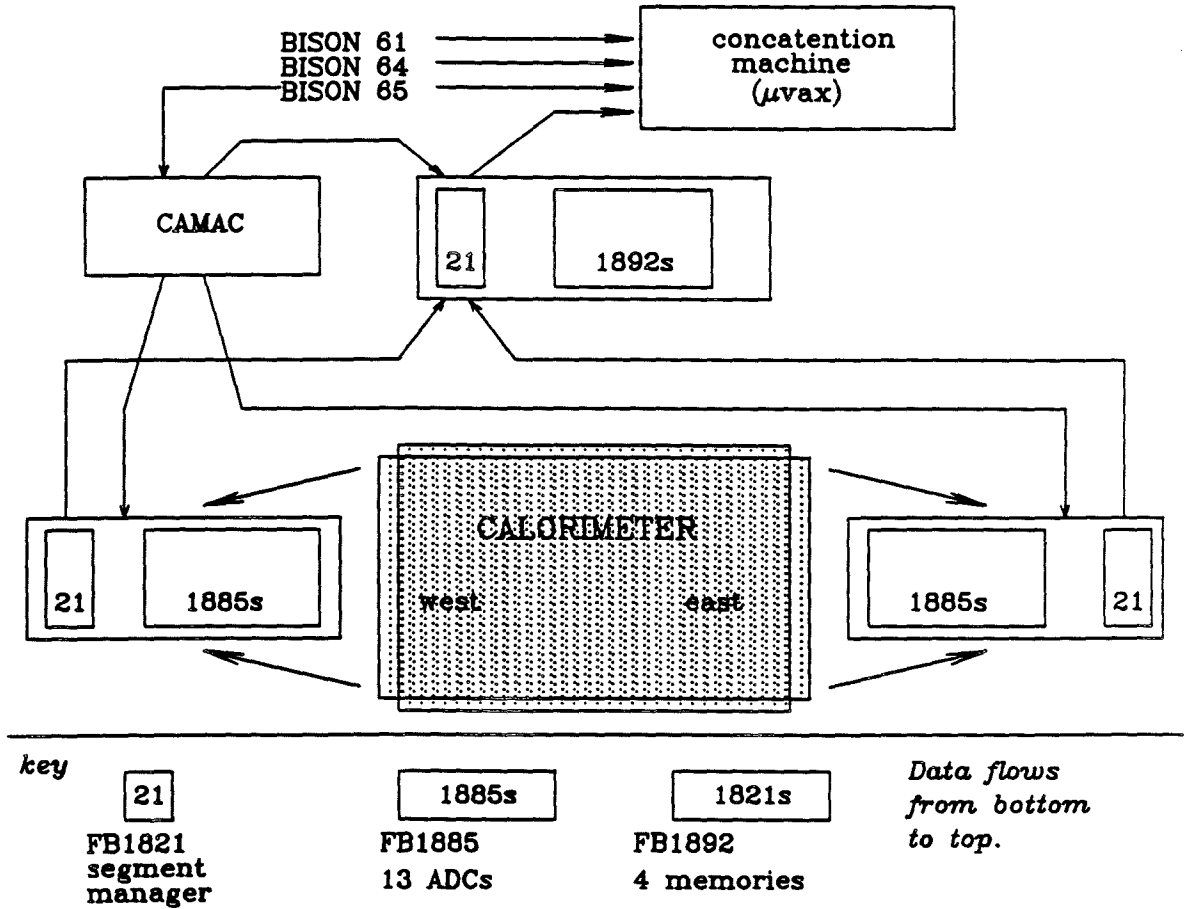
Figure 4.11: Sketch of the calorimeter Fastbus readout system.
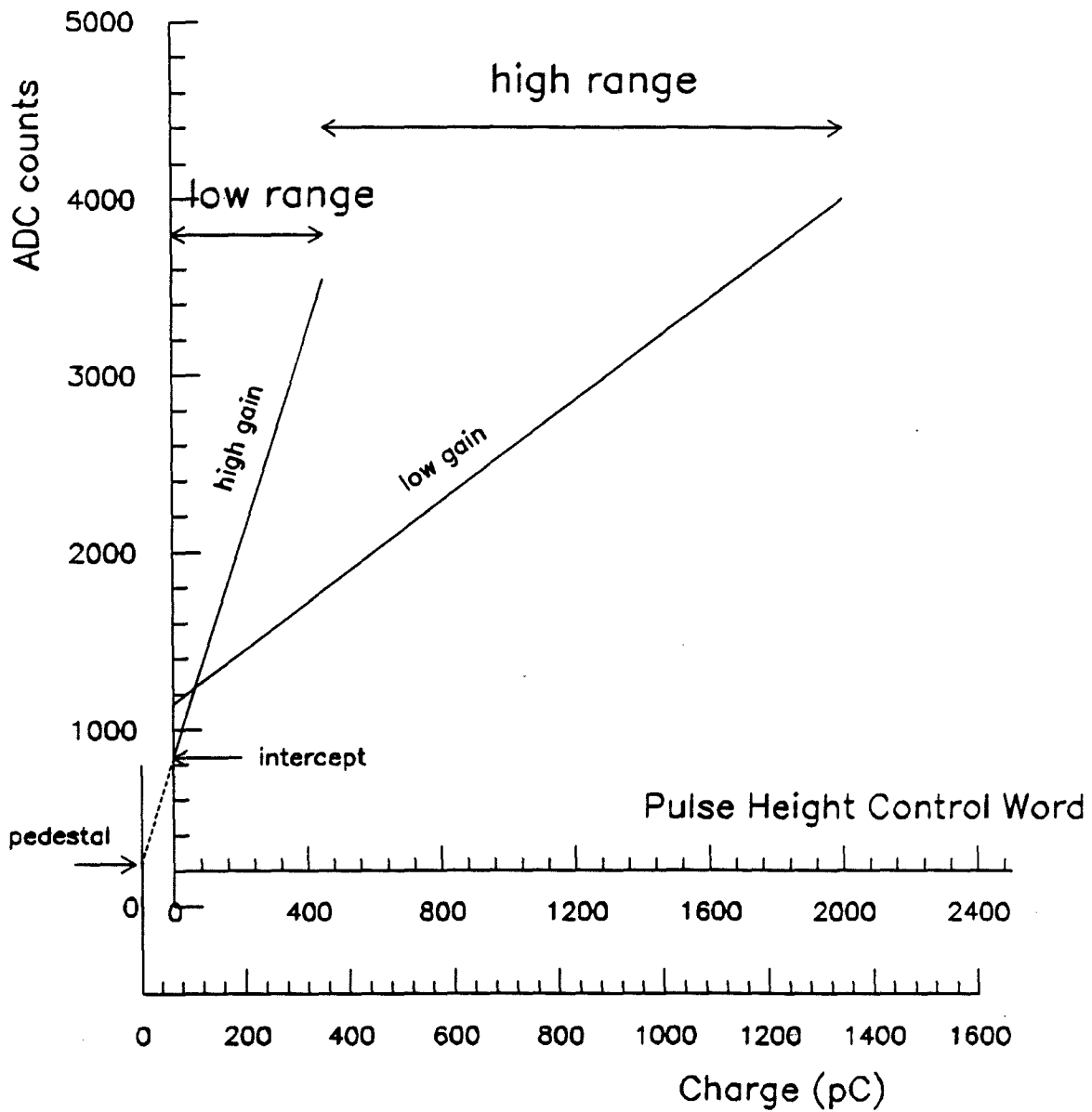
Figure 4.12: Response of a Fastbus 1885 ADC to input charge.

4.3 Monitoring

A good physics analysis requires good data. The experimenter certainly tries to build an apparatus that is stable and reliable, but all devices break occasionally, and some have time dependent performance. The most basic level of monitoring occurs when the shift crew inspects each piece of apparatus, once per shift. More refined checks are carried out by an array of online "consumer" programs, which analyze partially some of the data as it is logged to tape.[14] The most constant and automated level of monitoring is accomplished using specialized programs, running on the front-end PDP computers. These are discussed in the following sections.

4.3.1 Online PDP Tasks

Specialized PDP programs have been written to help combat systematic errors. They have two main purposes:

1. monitor the apparatus and notify the shift crew of any failures

2. calibrate the apparatus by measuring its response to known signals

The calorimeter programs perform both jobs at the same time. They interact with the calorimeter electronics or with monitoring devices through Camac, measure something, and check that the result of the measurement is as expected. If not, a message is sent to the error message screens. In any case, the measurement is sent to the Vax for logging to tape along with the data, so that it is available for physics analysis later.

The monitoring tasks run during the interspill period (when there is no beam in the hall). They are put into hibernation when regular D/A is running, to avoid clashes (particularly in Camac). When the programs generate a set of e.g. calibration data, this data is packed into an interspill event, which can be distinguished from spill events by a particular bit in the trigger mask.[15] The event buffer is a block of integer words, so floating-point numbers from calibration tasks must be handled carefully.

---

[14]Consumers are discussed in the software chapter.
[15]See the software chapter.

The size of the signal from proportional tubes is proportional to the gas gain, the gain of the amplifying electronics, and the conversion factor for the ADC. Clearly, several kinds of monitoring are required.

4.3.2 Gas Gain

The factors which can affect the gas gain are the high voltage, temperature, pressure, and gas composition. These facts can be understood by considering the avalanche process close to the wire. The dependence on the voltage comes from the acceleration of the electrons between collisions. The greater the acceleration, the greater the number of ions produced by an electron per collision. The dependence on the density comes from the total number of collisions the electron undergoes before reaching the anode wire. The higher the number of collisions, the greater the avalanche, and the larger the signal on the wire. The density of the gas is a function of the temperature and absolute pressure of the gas.

The high voltage should be very constant. Once set, the Droege high voltage supplies do not drift, and the correspondence between the setting and the actual high voltage is reproducible over many weeks. A set of Camac-controlled DACs are used to provide the set voltage. The granularity of the DAC is adjusted via a resistor network so that an accuracy of 1.5 volts is achieved. A 1 volt change in high voltage causes about a 1% change in gas gain. The monitoring voltage supplied by the Droege module is digitized in a Camac ADC; the currents are measured, too. An interactive task (HVC) is used to set voltages. Based on an a priori calibration of the Droeges against a known resistor divider, this program sets the DAC voltages, fine-tuning with respect to the levels detected by the ADCs. A monitoring task (CALDVM), running during the interspill period, reads these same ADCs, and sends the results to be logged to tape. If any of the voltages drifts by more than five volts, an error message is sent to the screens read by the shift crew. If any Droege supply trips, then an audible alarm is sounded in the control room.

The gas in the calorimeter is isobaric: measurements indicated that the difference across a plane was negligible, at normal flow rates. The pressure is barely above atmospheric, so monitoring of the changes in atmospheric pressure is required. The voltage produced by a precise pressure transducer is digitized in Camac ADCs, and the result is sent to tape by CALDVM [ODa87b]. A change in pressure by 1 mmHg causes a change in the gas gain by about one percent. The transducer and Camac ADC have a granularity of about 0.2 mmHg.

91

The temperature in the calorimeter is reasonably stable, due to the environmental control systems in the lab, and the tent. It is measured in many places, with the hope that gradients across planes or from the edges towards the center could be monitored. The current supplied by the probes is converted to a voltage, which is measured by Camac ADCs. The granularity of the probes and ADC is 0.05 degrees, corresponding to a 0.1% change in gas gain. CALDVM sends the data to tape. The monitors were calibrated before being installed [Ram87b], but it appears that the calibration changed after they were installed. Although the position gradients could not be determined, there was no difficulty in tracking the average temperature of the calorimeter, and other points.

The composition is constant (or at least very slowly varying) due to the performance of the mixing rack, and the fact that the gas is buffered in a large tank upstream of the calorimeter. Changes in composition can be detected using the data from two gas gain monitors. These chambers are home-made brass proportional tubes, inside each of which an Fe^{55} source of gamma rays is mounted [ODa87a]. One is placed at the input to the calorimeter, and the other, at the output. This allows detection of serious gas contamination due to a leak in the calorimeter. The monitors were not mounted inside the tent, which means that they are exposed to the larger temperature variations of the hall. A temperature monitor mounted in the path of the gas flow tracks these variations.

The dependence of gas gain on pressure, temperature, and high voltage was determined before the run using one of the gas gain monitors. Since the temperature variations for the gas gain monitors are different from the calorimeter, the Fe^{55} signal does not track the gas gain in the calorimeter. Corrections for changes in pressure, temperature, and high voltage are calculated for the calorimeter data specifically. Changes in gas composition can be detected by correcting the gas gain monitor data for changes in pressure and its temperature and voltage, and looking for time dependence.

The signals from the two gas gain monitors are split, and one copy is measured in a Camac ADC. The other copy is discriminated to provide a trigger and gate. The monitoring tasks CALGGM reads the ADC a thousand times, forming a histogram for each monitor, which it sends to be logged to tape.

4.3.3 Electronic Amplifiers

The electronic amplifiers are not monitored, except for the supply voltages. These are digitized in Camac ADCs, which are read by CALDVM. If any of the supply

92

voltages are incorrect, a message is sent to the shift crew. Similarly, if any of the Camac or NIM crate voltage supplies fails, a message is sent. More detailed monitoring occurs within the context of the calibration of the electronic amplifiers.

4.4   Calibration

Even in the case when there is no break down of the apparatus, much work is required in calibrating its response before the best physics analysis can proceed. Due to a lack of manpower and time, only the most basic calibrations of the calorimeter have been carried out. These are described in the following sections.

4.4.1   Gas Gain

Given a knowledge of how the actual gas gain changes as a function of pressure and temperature, the net gain of the calorimeter can be "renormalized" so that a measurement of energy deposition is true.

Gas gain calibrations are based on the changes of the spectra from the gas gain monitors as high voltage, pressure and temperature are changed [ODa87c, Nic87, Sch88a]. As the gas gain changes due to e.g. changes in pressure, the peak of the pulse height spectrum moves.

The spill data are analyzed by extracting the interspill data ahead of time, and reducing them to decoded and translated values stored on disk [Sch90c]. These files are read during the course of analysis [Sch90a], and corrections applied to the calorimeter readings. To the extent that the high voltage, pressure, and temperature readings are represented in the interspill data, variations of gas gain in time are removed.

The variation of the gas gain with pressure and temperature over a normal operating range may be represented by the formulae

$$\frac{G_1}{G_2} = (\frac{T_1}{T_2})^a$$

$$\frac{G_1}{G_2} = (\frac{P_1}{P_2})^b,$$

with $a = 6.7$ and $b = -7.7$ [FM85]. This implies that a temperature change of one centigrade degree gives a 2.3% change in the gas gain, and a one percent change

in the pressure gives gain change of 7.7%. For small changes in temperature and pressure these expressions can be linearized:

$$\frac{G(T)}{G(T_0)} = 1 + \alpha(T - T_0)$$

$$\frac{G(P)}{G(P_0)} = 1 + \beta(P - P_0)$$

where $\alpha = a/T_0 \approx 0.023$ and $\beta = b/P_0 \approx -0.0101$, to be compared with the values $\alpha = 0.029$ and $\beta = -0.0098$ obtained using the calorimeter gas gain monitors.

For the 1987-88 data, the pressure readings after calibration varied around zero; but for the temperature readings an offset $T_0 = 33.22$ degrees was subtracted.

Taking gas gain variations into account is straight forward. If the raw reading in a channel is E_i, then it is adjusted according to

$$E_i \rightarrow E_i' = A_g E_i = \frac{E_i}{\Delta_P \Delta_T}$$

where

$$\Delta_P = 1 + \beta(\delta P) \qquad \text{and} \qquad \Delta_T = 1 + \alpha(\delta T).$$

This amounts to multiplying all energies by a net scale factor, which means that determinations of the absolute normalization of the calorimeter must carefully take into account the mean value for A_g.

Example temperature and pressure variations are shown in figure 4.13.[16] The plots show that the temperature of the calorimeter changes slowly, due mostly to the insulating properties of the calorimeter tent. The change in temperature for the hydrogen data is less than 1 centigrade degree over almost 400 hours. The Xenon data was cooler, with little short-term variations but a general drift from $T = 31\,\text{deg}$ to $T = 28\,\text{deg}$ over 600 hours. The deuterium data span a much longer time period (1400 hours), which includes the time when the experiment was still green. One sees larger variations in temperature. In particular, there was one period (about one week) when the calorimeter was at its "normal" value of about 32 degrees, and the rest of the time it was cooler, about 30.5 degrees.

The pressure variations are much more dramatic than the temperature variations. In all three sets the pressure variations span the range $P_{min} \approx -13\text{mmHg}$ to $P_{max} \approx +15\text{mmHg}$, which leads to variations in $\Delta_P = \pm 10\%$. Most of the day-to-day gas gain variations come from changes in atmospheric pressure. This is clearest in the plots for the hydrogen data, but is true in general.

---

[16]A complete set of plots is given in [Sch90f].

It is worth emphasizing that the overall gas gain correction factor varies substantially over a period of several days. Even in the hydrogen data (about two weeks) this factor varies by 20%, and in the post-December deuterium data it varies almost as much.

Cross-Check using μ-e Events

Elastic μe scattering events were extracted from the data [Sch90d], and were used to calibrate and study the calorimeter. A good electron signal was obtained, as discussed in a later section. (See figure 4.37 on page 136.) The mean value for $R_{E/p} = E_{sh}/p_{tr}$ was plotted as a function of time. The mean value for A_g was also plotted; both are shown together in figure 4.14. The anti-correlation between $R_{E/p}$ and A_g is remarkable, as shown explicitly in figure 4.15.

Applying the mean values of A_g to the mean values of $R_{E/p}$ gives a stable calorimeter response as a function of time, as shown in figure 4.14. The distribution of the electron energies from μe events is improved by making gas gain corrections, as shown in figure 4.16.

Figure 4.13: Example plots of pressure and temperature readings.
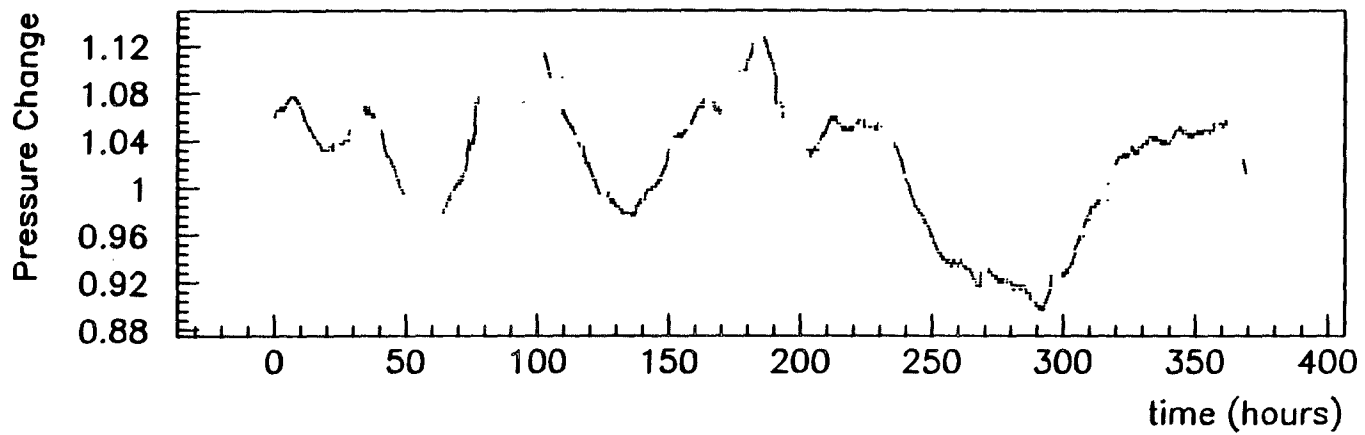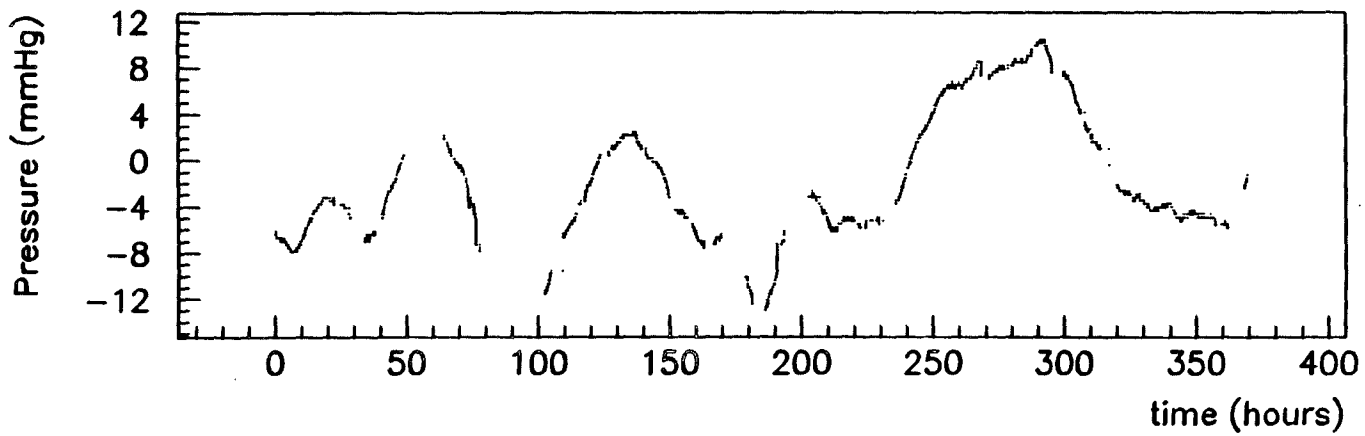
Hydrogen

PTHV.HRZH2.T
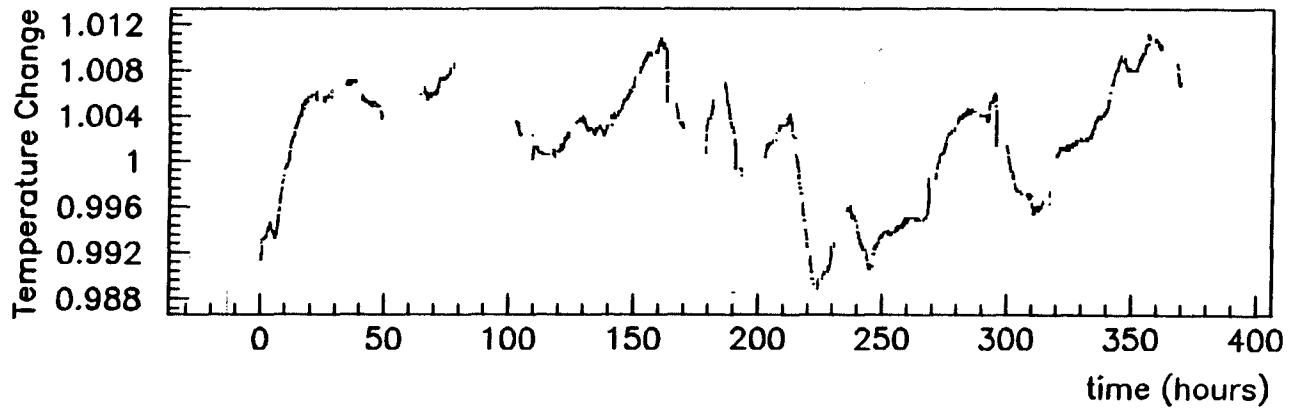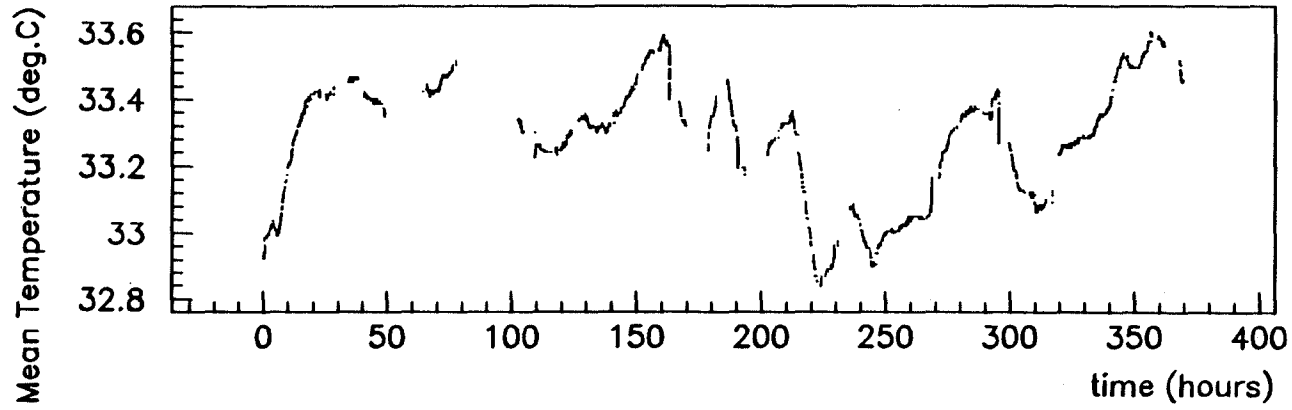
Hydrogen
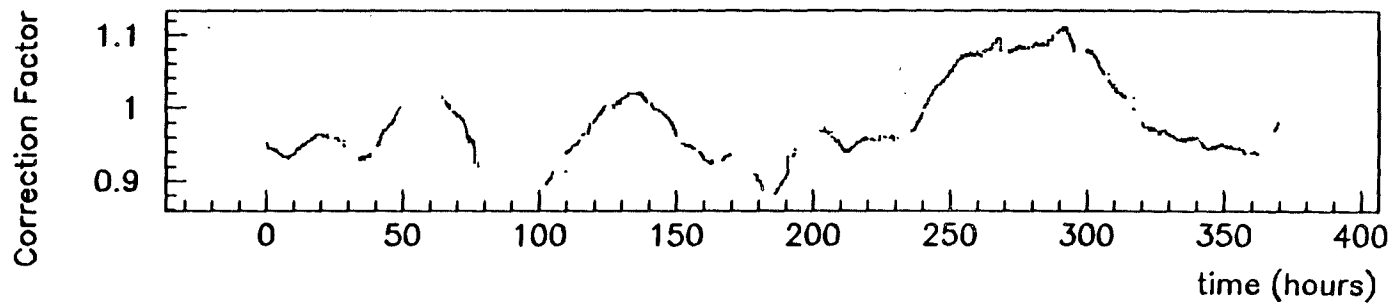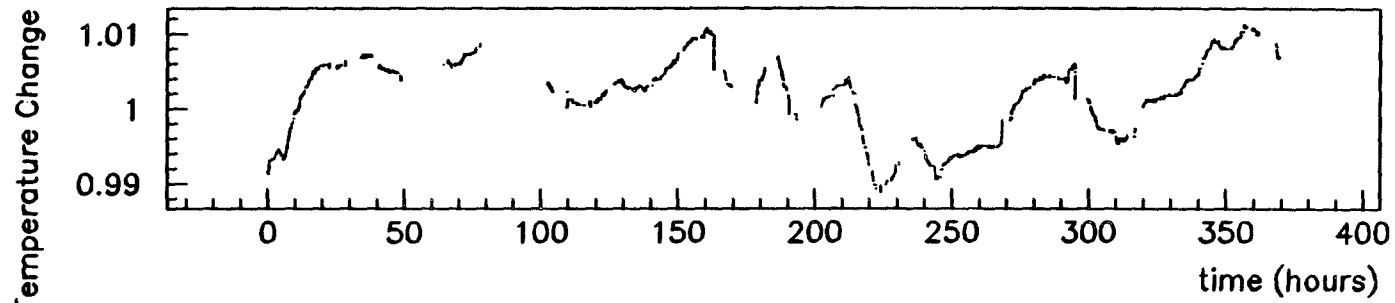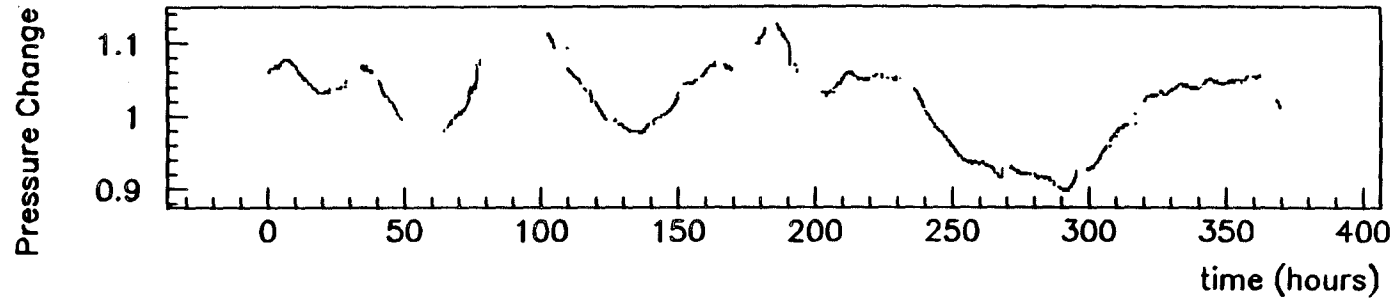
PTHV.HRZH2.T

Hydrogen   PTHV.HRZH2.T
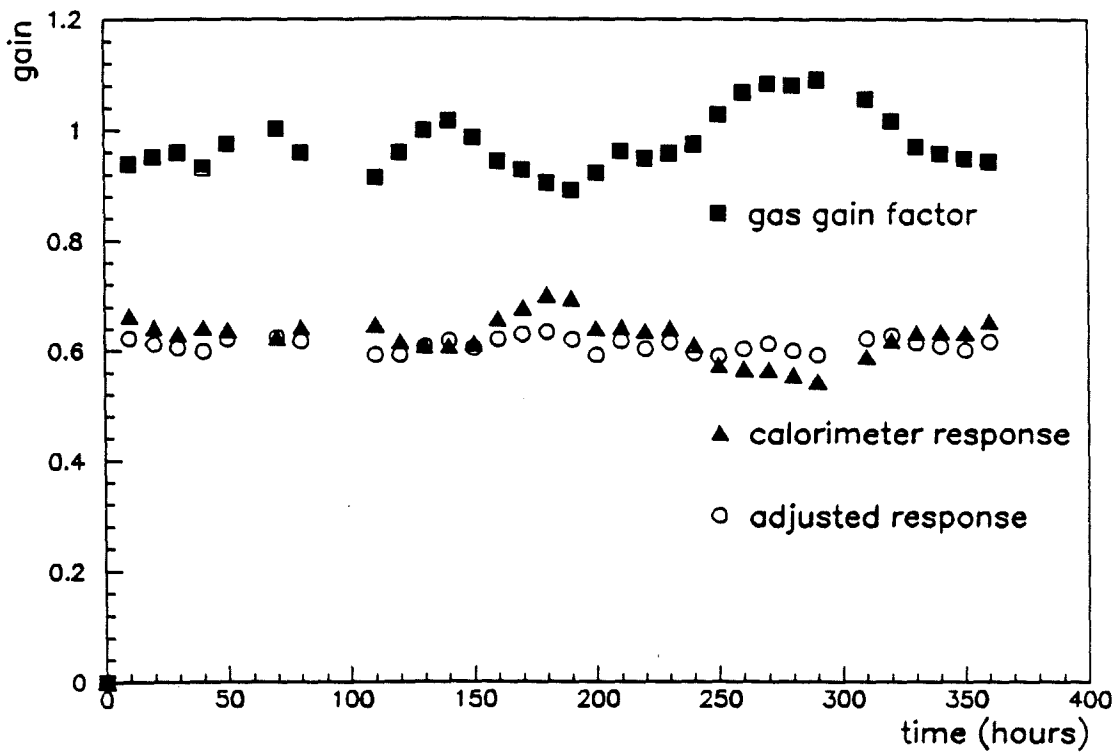
Figure 4.14: Gas gain correction A_g and mean calorimeter response $R_{E/p}$ to μe scatters over time.
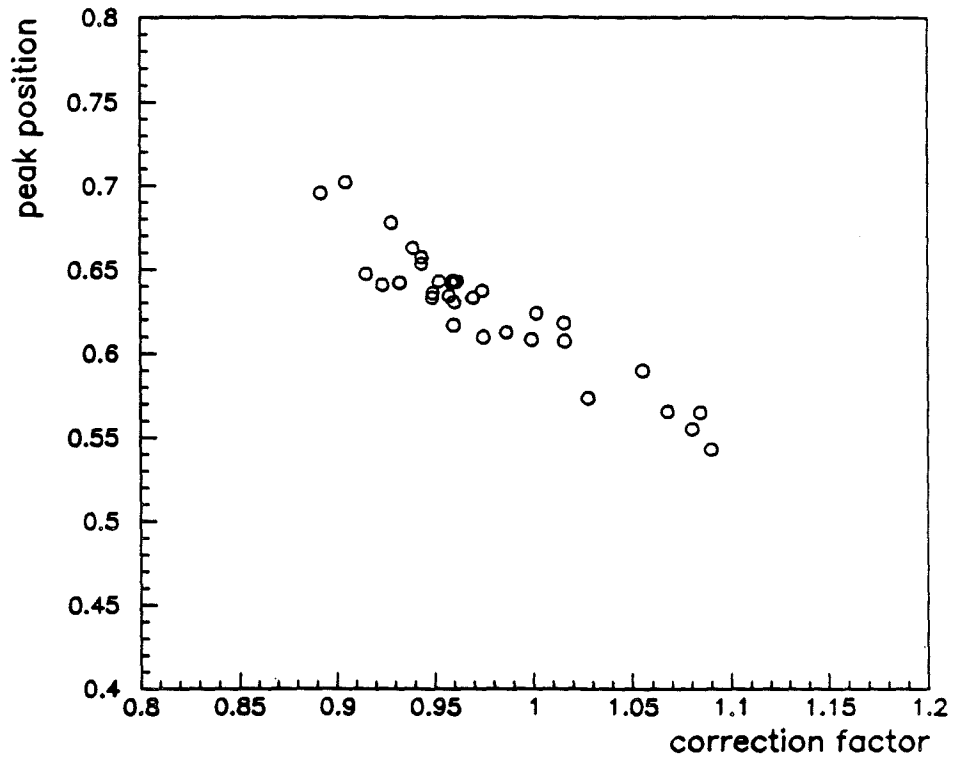
Figure 4.15: Anti-correlation of $R_{E/p}$ and A_g.
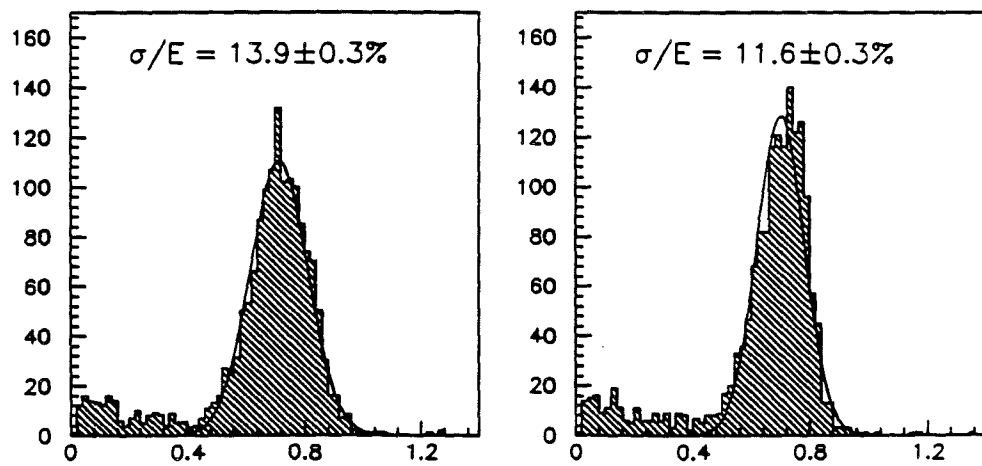
Figure 4.16: Resolution of μe energies with and without gas gain corrections.

4.4.2 Amplifier Gain

A given charge after gas multiplication near the anode wires corresponds to a definite ADC reading. This correspondence must be determined in order to analyze calorimeter data. For the purposes of calibration, the gain of the internal, low-gain anode amplifiers may be considered part of the calibration of the ADCs. This amounts to measuring the two straight lines (slope and intercept) shown in figure 4.11. It is not necessary to determine the calibration in terms of coulombs, since in the end an overall multiplicative constant for converting from ADC counts in a channel to GeV in a channel is needed, as discussed below. The goal of electronics calibration is to measure the *relative* slopes and intercepts for both ranges of all channels.

The electronics calibration consists of measuring the response of a channel at several known pulse heights, as recorded by the ADCs. If the input pulse heights are chosen judiciously, then the two ranges of the ADC will be covered. The slope and intercept are determined by a least-squares fit to two independent straight lines.

This strategy underlies the methods in calorimeter calibration programs. There are three distinct tasks: CALLOS for the bitubes ("summed anodes"), CALLOI for the individual anode wires, and CALLOP for the pad towers. Each of these runs in the interspill period, pulsing channels at fixed amplitudes, storing the results in memory, and performing linear fits. All actions are taken through Camac, including accessing the ADCs. A Fastbus-Camac interface is installed for this purpose, and there is special NIM and Camac-based control logic, to allow the generation of gates by interspill tasks, distinct from the regular gating based on the experimental trigger [Nic86b].

The calibration anode signals are generated with a voltage applied to a fixed capacitor. The pad signals are injected at input to the summing boards, rather than at the pads themselves.[17] A programmable Camac quad-pulser was used for this purpose.

The test pulse amplitudes were chosen carefully so that three points in the low range, and three points in the high range, were obtained for all channels. Time allows only three pulses at each amplitude. After the response of all channels to all six amplitudes is measured, two linear fits are calculated. The number of bad fits is counted, and if there are too many, then an error message is sent to the shift

---

[17]A program of automated capacitance testing was carried out after the calorimeter was installed, to check that the pads were connected [Nic86a].

crew.[18]

Pedestals (low range) are measured by reading the ADCs when there is zero charge at the input. Since the zero of the test pulsing devices is not known exactly, this accomplished by pulsing the pads when calibrating the anodes (thereby generating a gate for the ADCs), and vice-versa. There is an important distinction between intercept and pedestal: the intercept gives the mean ADC reading when the input control word for the pulsing device is set to zero, and the pedestal is the mean ADC reading when there is strictly zero charge at the input to the ADC. The pedestals for the high range were determined poorly in the 1987-88 run, as discussed later in this chapter.

The results of the linear fits are written to a direct access disk file. Each task compares the current values of the constants to those in the file (i.e., from the previous calibration). If too many channels have significant changes in the constants, then error messages are sent to the shift crew. After each complete calibration, a fourth task (CALSLO) sends a copy of the calibration values to the microvax for logging to tape. There are so many values that twenty interspill events are needed.[19] These events are designated by user event numbers (part of the trigger mask), allowing them to be put back together offline.

The calibration tasks are large compared to the memory of the PDP front-end, due to the arrays required for storing the results of pulsing and linear fits for all the channels. Each task must carry out tens of thousands of Camac operations, which requires a great deal of time. Consequently, they run only one at a time: a task manager, CALMAN, coordinates the activities of all the calorimeter tasks. It sets and reads flags in a global common to keep track of access to disk files and Camac modules. The sequence of tasks is tied to the spill number.

The interspill events constituting a complete set of calibration constants are skimmed from the tapes offline, and processed to reconstruct the original set of values [Sch90c]. Roughly a hundred such sets were obtained for the useful 1987-88 running period: several sets per day. There turn out to be largely redundant, due to the excellent stability of most of the electronics. A couple ADC modules tended to drift, however, as discussed in a later section.

Plots of the values for all six calibration constants are shown in figure 4.17.

---

[18]Similarly, error messages are sent if any error occurred when the Fastbus ADCs are read.

[19]The total number of values is 6 constants/channel $\times$ 96 channels/ADC $\times$ 13 ADCs/crate $\times$ 2 crates = 14976 numbers. The six constants are the low range pedestal and slope, the high range intercept and slope, the width of the low range pedestal, and the difference between the low range intercept and low range pedestal (see below).

element	l.r. slopes		slope ratio	pedestal width
	peak	sigma	peak	sigma
normal bitube	10.9	0.11	8.18	4.4 and 10.2
outer Dart	7.08	0.35	8.29	8.9 and 14.2
inner Dart	4.85	0.20	8.8	≈ 10
small pads	6.09	0.14	7.67	12.8
medium pads	6.09	0.12	7.63	13.2
large pads	6.05	0.12	7.62	13.1
Dart wires	11.7	0.21	–	–

Table 4.2: Some characteristic electronics calibration constants. The "peak" and "sigma" for the low-range (l.r.) slopes were obtained using a gaussian fit. The ratio refers to the low-range slope divided by the high-range slope; the expected value is 8.0. The pedestal width, expressed in ADC counts, was obtained from a gaussian fit.

Most distributions were roughly gaussian, allowing characterization be a mean value, and a sigma (rms). Relevant values are listed in table 4.2. The Dart constants were poor, as discussed later in this chapter. The ratio of the slope is not exactly eight, for reasons that were never completely understood. [20]

Figure 4.18 shows the fractional change of constants, from one set of constants to the next. A narrow peak at zero is obtained (note the logarithmic scale); the rms width is less then 2 %.

Using the Calibration Constants

An event gives a set of readings for all ADC channels: $\{A_i; i = 1, N_{tot}\}$, where A_i is the reading of the ith channel, and N_{tot} is the total number of channels (fixed for all events).

The electronics calibration provides the pedestals A_i^0 for every channel: this is the reading of the ADC when there is no signal at the input. There are two pedestals, one for each range of the ADC. The pedestal-subtracted values are simply $A_i - A_i^0$. Due to noise in the amplifiers and picked up along the leads, there is a width to the pedestal. The distribution of values when there is no signal is (in most cases) a gaussian, with a peak value at A_i^0.[21] In order to obtain a clean signal for purposes of finding clusters, a threshold Δ_0 is imposed on the differences

---

[20] The case of the pad slopes has been investigated [Ram88a]. The ADCs were tested carefully, and the ratio of slopes was eight to better than one percent. The different ratios obtained here reflect the performance of the electronics and/or the pulsing networks.

[21] Some important exceptions are discussed below.
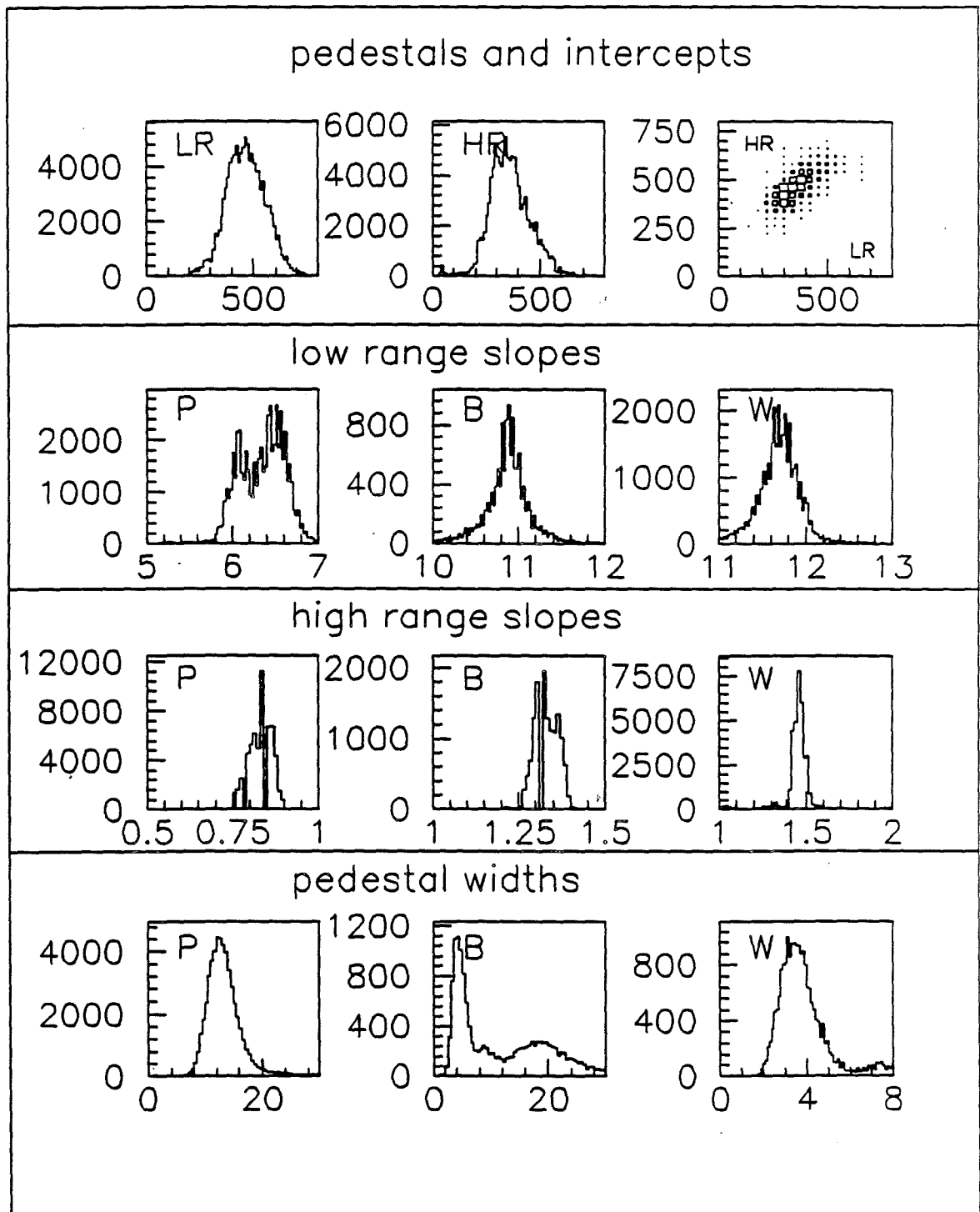
Figure 4.17: Distribution of calorimeter electronics calibration constants. The letters "LR" and "HR" stand for low-range and high-range; and, "P," "B," and "W" stand for pads, bitubes, and wires.
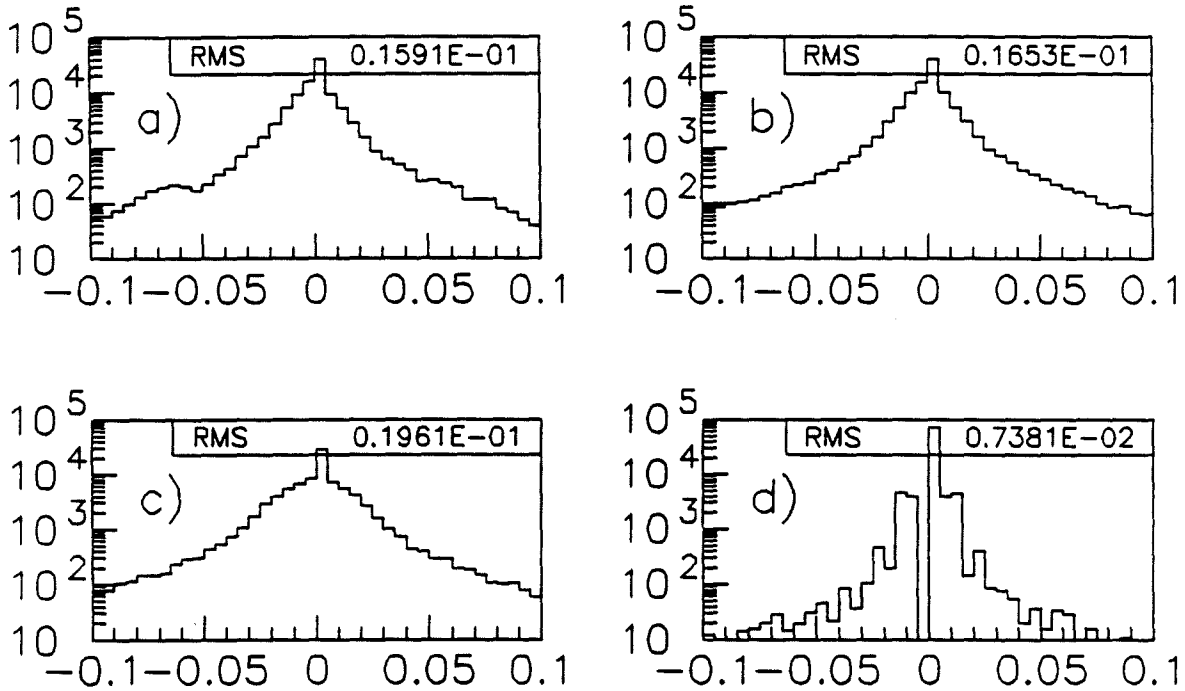
Figure 4.18: Changes of the electronics constants, one set to the next.

$A_i - A_i^0$:

$$A_i \to B_i = (A_i - A_i^0) \, \theta(A_i - A_i^0; \Delta_0),$$

where $\theta(\Delta, \Delta_0) = 1$ if $\Delta > \Delta_0$, zero otherwise. Δ_0 is the "pedestal subtraction threshold." This gives rise to a smaller set of "hit" channels, i.e., those that have a nonzero signal: $\{B_i; i = 1, N_{hit}\}$, where N_{hit} is the number of hit channels.

The calibration of the electronic amplifiers also provides a relative calibration of the gains of each channel – amplifier and ADC lumped together. Basically the slopes for each channel provide a conversion factor into "equivalent pulse heights," according to

$$B_i \to C_i = \beta_i(B_i) \, B_i.$$

The constant $\beta_i(B)$ is bivalued: it has value β_i^{low} if the reading B is in the low range of the ADC, and value β_i^{high} if it is in the high range. Since the low-impedance amplifiers are highly linear over any reasonable range, the constraint imposed by Lecroy on the ADCs translates into the condition

$$\frac{\beta_i^{low}}{\beta_i^{high}} = \frac{1}{8}.$$

The translation of B_i gives a mirror set $\{C_i; i = 1, N_{hit}\}$. At this level all

105

channels of a given type (τ = pads, bitubes, or wires) have been normalized so that the value in one is on the same scale as another. The last step is to impose an absolute scale, to convert from equivalent pulse heights to GeV per channel:

$$C_i \rightarrow E_i = \kappa^\tau C_i.$$

This gives the set of translated values $\{E_i; i = 1, N_{\text{hit}}\}$, measured in GeV per channel, which is the starting point of calorimeter pattern recognition. Note that the scale factors κ^τ are different for pads, bitubes, and anode wires, due the different gains in the amplifiers.

The total energy measured by calorimeter (pads, for example) is given by

$$E_{\text{total}} = \sum_{i=1}^{N_{\text{hit}}} E_i = \kappa^{\text{pad}} \sum_{i=1}^{N_{\text{tot}}} \beta_i(B_i) \, (A_i - A_i^0) \, \theta(A_i - A_i^0; \Delta_0).$$

There are in total five constants for one channel: $A_i^{0,\text{low}}$, $A_i^{0,\text{high}}$, β_i^{low}, β_i^{high}, and κ^τ. The first four are determined by the electronics calibration programs,[22] and the determination of κ^τ is discussed in the next section.

4.4.3   Pedestal Subtraction Threshold

Choosing the pedestal subtraction threshold Δ_0 is less trivial than one might expect. The dependence of the relative pad signal as a function of Δ_0 is shown in figure 4.19. The data are 25 GeV electron showers, from the 1990 calibration beam. Also shown is the number of pads in the shower, and the total number of hit pads in the calorimeter. For low values $\Delta_0 < 40$ counts, there are many "hit" pads in the calorimeter which do not belong to the main cluster. For high values $\Delta_0 > 70$ counts, the number of pads continues to decrease, which ultimately will effect the position and energy resolution. These considerations are illustrated in figure 4.20. The point at $\Delta_0 = 10$ counts is unreliable, because at the threshold so many pads fire that many events cannot be analyzed. In this case there might be an improvement in energy resolution as Δ_0 is decreased from 40 to 20 counts. Certainly the width of the bitube–pad signal ratio is narrower as Δ_0 decreases from large values. The position resolution definitely worsens as Δ_0 is increased from 20 to 60 counts. The values used officially are $\Delta_0 = 30$ counts for the bitubes, and $\Delta_0 = 35$ counts for the pads.

---

[22]Some information on $A_i^{0,\text{low}}$ is obtained using beam and halo events.
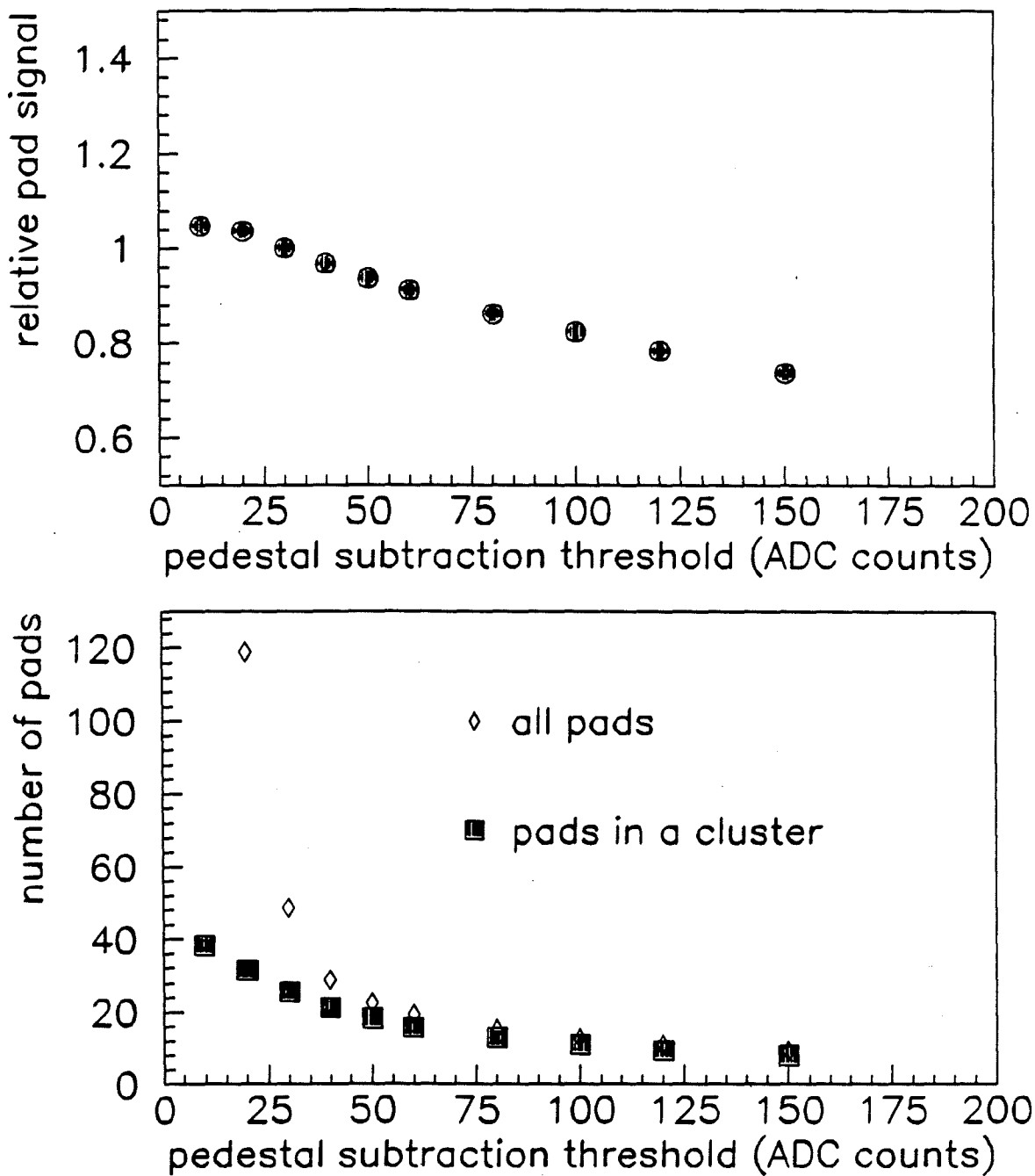
Figure 4.19: Variation of the relative signal (for 25 GeV electrons) as a function the pedestal subtraction threshold, Δ_0. The lower plot shows the variation of the number of pads in the shower (black squares), and the total number of pads in the calorimeter (open diamonds), as a function of Δ_0.
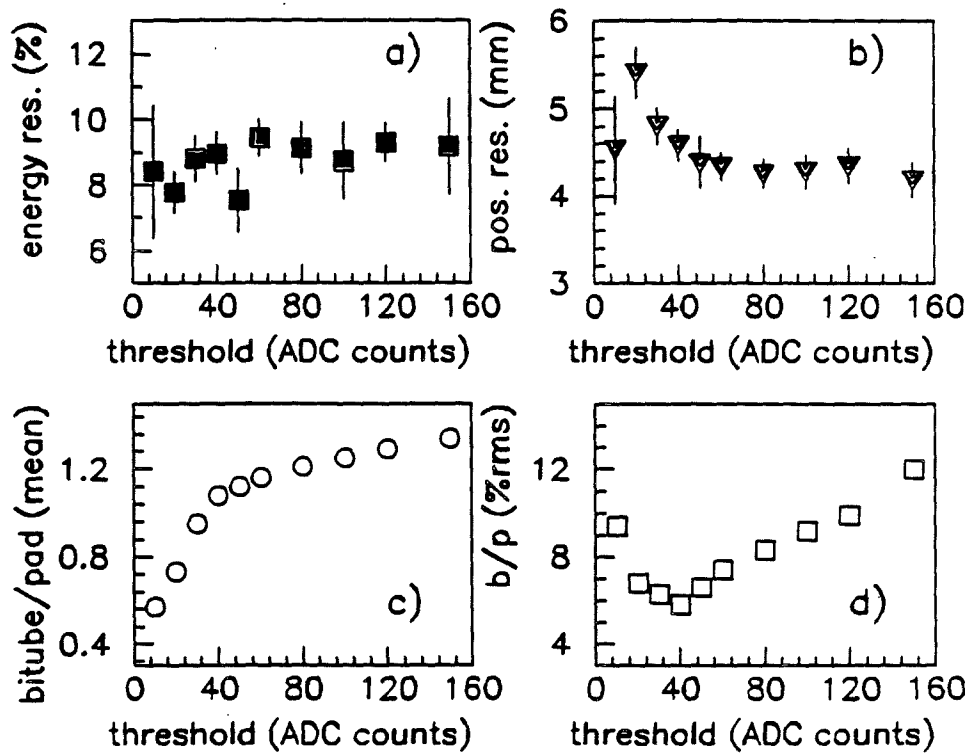
Figure 4.20: Resolution of 25 GeV showers, as a function of the pedestal subtraction threshold, Δ_0. Plot a) shows the variation of the width the E_{sh}/P_{tr} ratio as a function of Δ_0; plot b) shows the variation of the width of $Z_{sh} - Z_{tr}$. Plot c) shows the variation of the bitube–pad signal ratio, and plot d) shows the width of the ratio.

4.4.4 Absolute Scale

The parameter κ^τ describing the conversion to GeV per channel can be estimated from test beam data, but an accurate determination requires a known calibration source. Since this is an electromagnetic calorimeter, electrons and photons are appropriate.

Consider electrons which traverse the forward spectrometer, leaving a track of momentum p_e. If the set of hit channels belonging to the electron shower can be identified ($\{E_i; i = 1, N_{sh}\}$), then the total shower energy and the electron momentum should be equal:

$$E_{sh} = \sum_{i=1}^{N_{sh}} E_i = \kappa^\tau \sum_{i=1}^{N_{sh}} C_i = p_e,$$

allowing a determination of κ^τ. Electrons are obtained using a special mode of the muon beam [Sch90b].

The decay of π^0s produced in deep-inelastic scatters provides a source of low-energy photons. The invariant mass spectrum of pairs of photons shows a clear peak for π^0 decays, and the position of the peak is proportional to $\sqrt{E_1 E_2}$, where E_1 and E_2 are the energies of the two photons. Since κ^τ scales all channels, the position of this peak is proportional to κ^τ.

Electromagnetic background processes provide additions sources of electrons and photons: electrons in μe scatters, and photons in Bremsstrahlung. These tend to be at high energy, but the lower limit extends down to 40 GeV.

There are three minor difficulties in setting κ^τ:

1. The response of the calorimeter is time dependent because it varies with atmospheric pressure. The value of κ^τ deduced from one data set will be different from another, unless gas gain corrections have been handled correctly.

2. The effective value of κ^τ depends on the pedestal subtraction threshold:

$$\kappa^\tau = \frac{E_{true}}{\sum_{i=1}^{N_{sh}} \beta_i(B_i) \, (A_i - A_i^0) \, \theta(A_i - A_i^0; \Delta_0)},$$

where E_{true} is the true shower energy (e.g., the momentum of the electron track).

3. The response of the calorimeter is not linear at the highest energies, and in effect κ^τ will be substantially higher at $E_{true} = 300$ GeV than at 30 GeV.
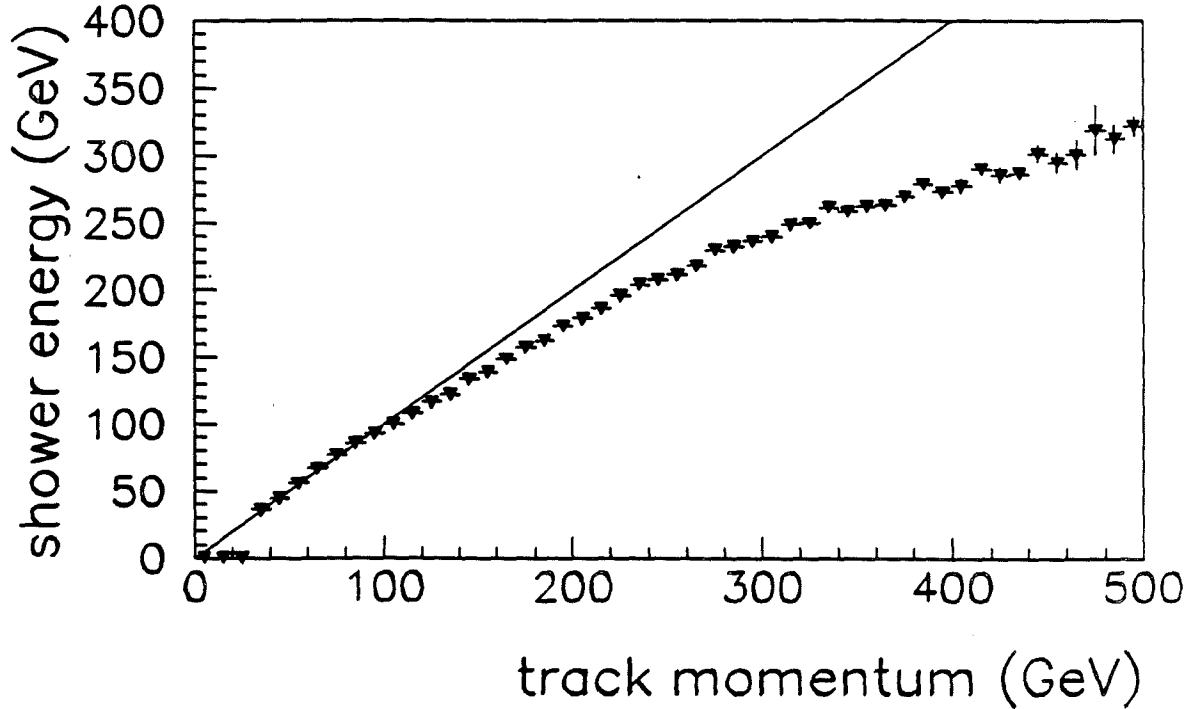
Figure 4.21: An illustration of the nonlinearity of the calorimeter. The data come from μe scatters on hydrogen.

The first item is simply a question of setting the gas gain factor A_g and the scale factor κ^r at the same point in time. (In fact these numbers are redundant.)

The dependence of the total shower energy on pedestal subtraction threshold is easy to understand. Showers are localized and have a peak (in both the transverse and the longitudinal views). As the threshold is raised, more and more channels at the periphery fall below the threshold, and are excluded from the sum. This amounts to losing some of the charge produced by the cascade; consequently, the conversion factor must be increased. A plot of κ^{pad} as a function of pedestal subtraction threshold is shown in figure 4.19 on page 107.

The full nonlinearity of the calorimeter still is not completely understood. Based on studies with prototypes in test beams, and on Monte Carlo calculations, the response was expected to be linear up to 300 GeV. The plot in figure 4.21 shows, however, that the response of the calorimeter to high-energy electrons begins to droop above 150 GeV. This problem will be discussed later in this chapter. For the purposes of setting κ^r, a maximum energy cut of 50–100 GeV is imposed.

data sample	ΔY (m)	ΔZ (m)
μe scatters, H_2	-0.01041	-0.00745
hadrons in DIS	-0.0100	-0.0069
electron beam (1990)	-0.0154	-0.0063
Ramberg	-0.0106	-0.0052
Melanson	-0.0089	-0.0064

Table 4.3: Summary of calorimeter alignment with respect to the global coordinate system. Ramberg's numbers are given in [Ramberg, p.74], and Melanson's numbers in [Mel91c].

4.4.5   Alignment

The simplest way of differentiating photons and electrons is that the latter produce tracks while the former do not. If there is an electromagnetic shower in the calorimeter and a track pointing to its center, then the shower was produced by an electron. In this sense photons are "neutral electromagnetic showers."

In order to ensure correct matching of reconstructed tracks and reconstructed shower centers, the calorimeter must be aligned within the global coordinates system. The Y and Z offsets can be determined easily with a set of electrons; hadrons cover a broader range of Y and Z and provide a check on the electron result.

For several sets of data the offsets were determined:

$$\Delta Y = Y_{shower} - Y_{track} \qquad \Delta Z = Z_{shower} - Z_{track},$$

where (Y_{shower}, Z_{shower}) are the coordinates of the center of gravity of the shower, and (Y_{track}, Z_{track}) are the coordinates of the track at the front face of the calorimeter. The results are summarized in table 4.3. Some example distributions are given in figure 4.22.
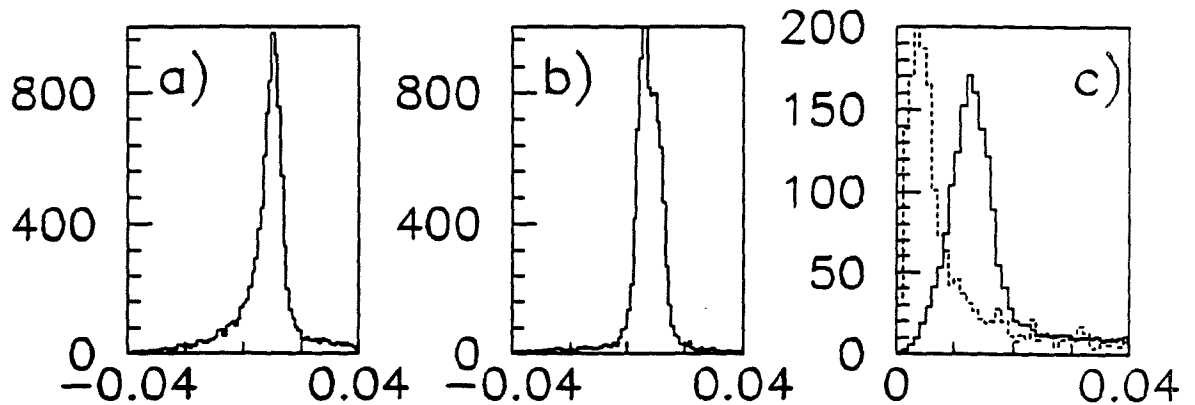
Figure 4.22: Calorimeter alignment as determined from μe data. Plot a) shows the difference $\Delta Y = Y_{sh} - Y_{tr}$, and plot b) shows $\Delta Z = Z_{sh} - Z_{tr}$. Plot c) shows the distance $D = \sqrt{(\Delta Y)^2 + (\Delta Z)^2}$, before alignment (solid line), and after alignment (dashed line). Units are meters.

4.5 Technical Difficulties

The 1987-88 run was the first serious run for experiment 665. Due to many problems with hardware, it was characterized by some to be merely an "engineering run."[23] There were several serious problems with the calorimeter which made analysis more difficult. Some of these were simple hardware problems which have been repaired, but others are endemic to the design of the calorimeter and its environment. Each problem is discussed below.

4.5.1 Bitube Oscillations

The most visible problem with the 1987-88 data is the presence of coherent noise on the bitubes for planes five and seven. This noise is quite small viewed on an oscilloscope, but large compared to the pedestal width. An example of the uncorrected "pedestal" is illustrated in figure 4.23a, and plot b shows the correlation between two channels in a plane.[24]

A clever routine was written for fixing this problem: the routine takes all raw

---

[23]Over a dozen graduate students have written successful thesis with these data, so this characterisation is at best unkind!

[24]For bitubes, 400 counts is about 1 GeV.

readings from planes five and seven, and finds a cluster of (pedestal-subtracted) values to estimate the "amplitude" of the noise for that event. A priori knowledge of the relative gains is used to provide a sharp cluster for channels which otherwise have no signal. Once the amplitude is determined, it is subtracted from *all* channels, again with adjustments for the variations in electronic gains among the channels. This scheme works well, as illustrated in figure 4.23c and d. (Plot e shows the pedestal for a normal channel.)

The effect of the bitube oscillations can be illustrated further by plotting the anode signal against the pad signal. Within the intrinsic noise in each channel (i.e., the pedestal widths), these two quantities should correlate perfectly. Figure 4.24 shows the correlation before and after the software fix.

The bitube oscillations in planes five and seven were picked up by other planes connected to the same low-voltage supplies, i.e., other odd-numbered planes. The concept of using empty channels to give the amplitude of the noise in each event was extended in a new routine to the odd-numbered planes. This improved the resolution for the anodes.

Several attempts to fix this problem during the run failed. There was one observation of noise of frequency 17 kHz. After the run, it was found that the low-voltage current drawn by the planes was past the range of some of the supplies. New linear supplies were purchased, and installed close to the calorimeter. Ground loops were eliminated. During the 1990 run, there were no signs of bitube oscillations.[25]

4.5.2   Dead Channels

As mentioned above, the electronics proved to be very reliable, with virtually no channels failing after installation. The Iarocci chambers are another matter. There were tremendous difficulties bringing some tubes into good working condition: there were several profiles which refused to hold high voltage after the planes were hung. Attempts to burn these in *in situ* failed, and they had to be turned off.[26] Unfortunately, some of the bad profiles were in the center of the calorimeter, near shower maximum. Turning these off made energy measurement and resolution a problem. A list of dead channels was compiled [Ram88b], and cross checked with the evidence in the data.

---

[25]Ashutosh Kotwal discovered a small oscillation before the beginning of the 1991 run. He fixed it by replacing one of the low voltage supplies.

[26]This means that the high voltage pin for the offending profile was disconnected.
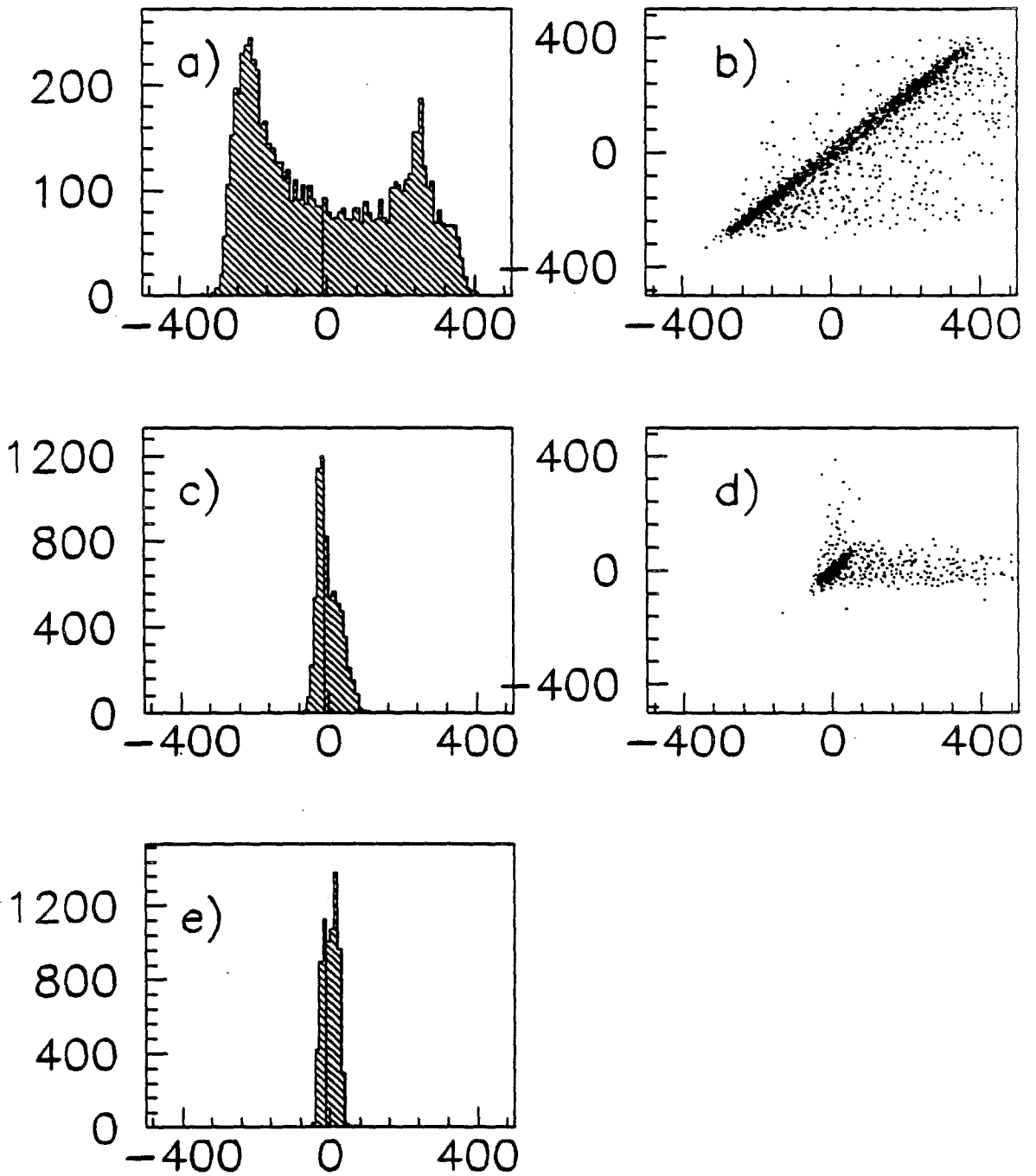
Figure 4.23: Illustration of calorimeter bitube oscillations, and the effectiveness of the software fix. Plot a) shows the raw pedestal for bitube 2 in plane 5, and plot b) shows the correlation between bitubes 2 and 4. Plot c) shows the pedestal after the software fix, and d) shows the correlation (or lack thereof). Plot e) shows bitube 5 in plane 15, indicating a normal pedestal.
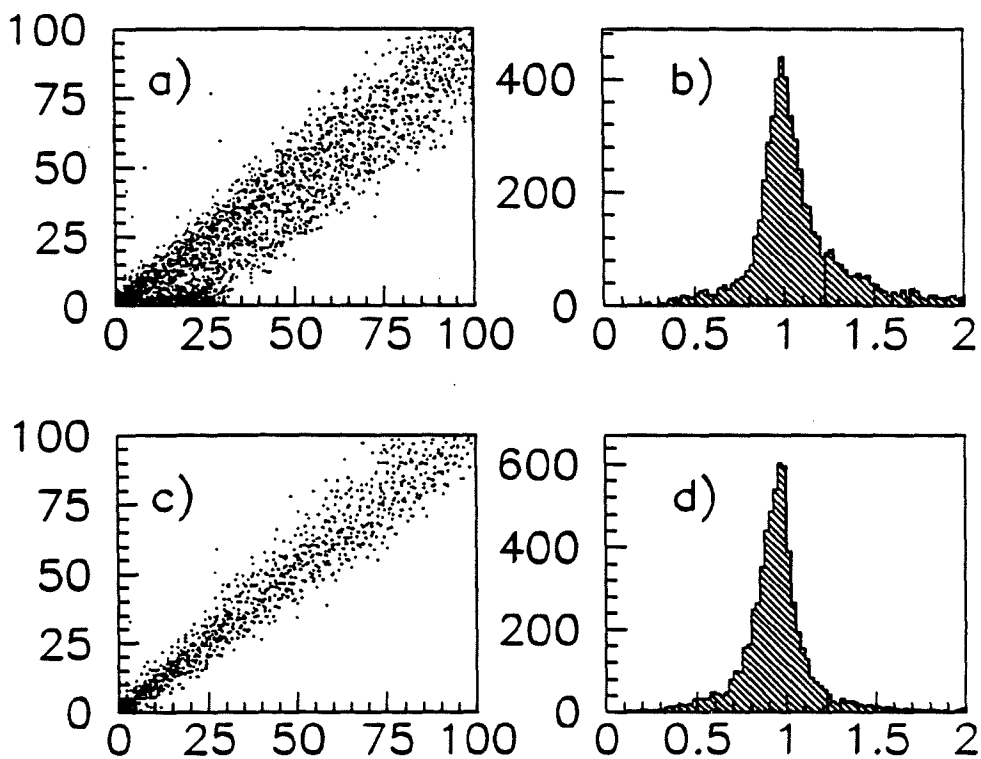
Figure 4.24: Second illustration of calorimeter bitube oscillations, and the effectiveness of the software fix. Plot a) shows the correlation between total bitube energy and total pad energy, with no bitube fix, and plot b) shows the ratio of the two. Plots c) and d) show the same quantities, after the software fix.

A small number of electronics channels did not work, and a few pads also seemed to be disconnected.

Although the map looks dismal, it is worth repeating Doug's remark about failed channels in the calorimeter [Michael, p.123]:

> "Perhaps a more positive way of looking at the functionality of the calorimeter is to list what *does* work rather than what *doesn't*. More than 98% of the Iarocci tube profiles were functional all of the way through the readout electronics (710 out of 720 profiles). More than 99% of the pad towers were functional (1180 out of 1188 [channels])."

To a certain extent, the charge missing in dead channels can be estimated from neighboring channels. Fixes for dead channels have been attempted [Ramberg, pp.95–96]. It has been shown that these fixes help produce a smooth average energy flow across the face of the calorimeter [Michael, pp.123–4].

Nearly all of the broken bitubes were repaired in 1990. One bitube (number 10 in plane 5) was fixed but then failed again after installation. A very substantial electron beam calibration set was taken to study the effects of this dead bitube [Sch90b]. A study based on these data indicated that adequate offline compensation was possible; a second attempt to fix this bitube was not undertaken.

4.5.3 Plane Four

Every second bitube in plane four was inoperational due to gas problems. This is illustrated in figure 4.25, which shows the average energy in each bitube for deep-inelastic events.[27] In retrospect there was evidence from the consumer monitoring histograms that some bitubes were dead, but it was masked by the effects of bitube oscillations, discussed above. After the run was over, this plane was opened, and it was discovered that one of the input gas tubes was pinched closed, thereby cutting off the supply of fresh gas to one half of the bitubes. An early study showed that these bitubes were dead by the time "good" data was taken (November, 1987). These bitubes are corrected as part of the dead channel correction, mentioned in the previous section.[28]

---

[27]It can be seen that bitubes 13 and 15 are dead, also.
[28]These bitubes are fully operational for the 1990 run.
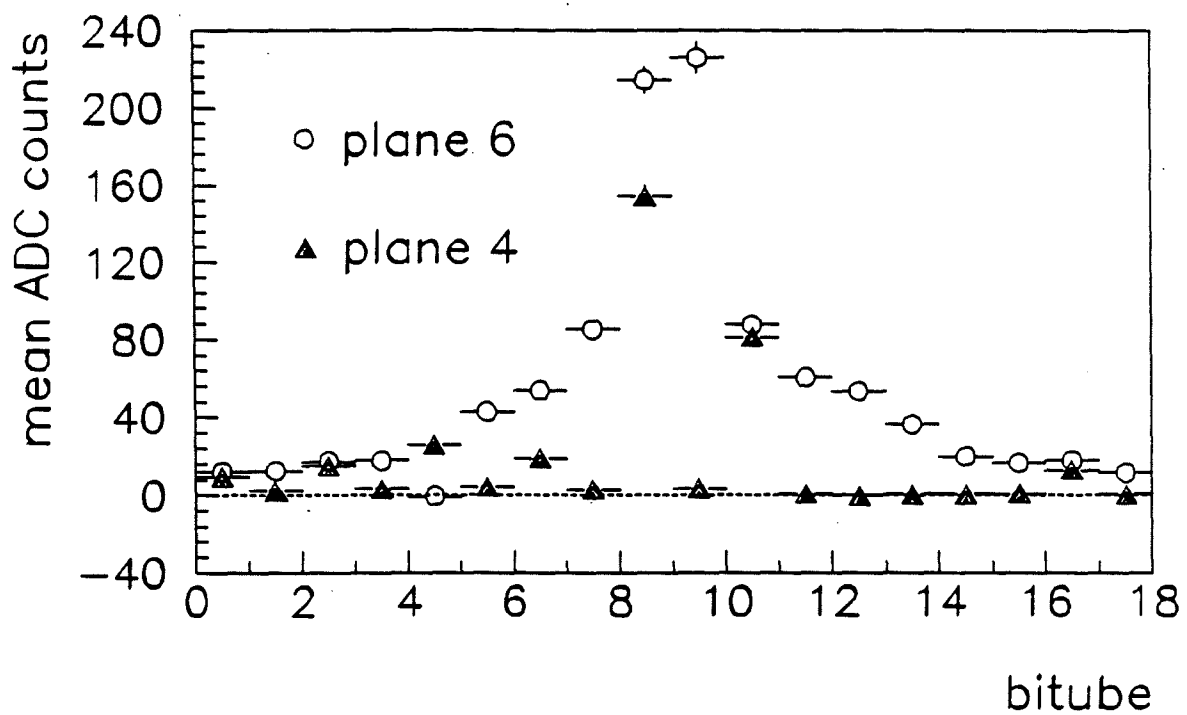
Figure 4.25: Dead bitubes in plane 4 (plot a), to be contrasted with plane 6 (plot b). These figures were made from the mean energy deposited by deep-inelastic events.

4.5.4 Drifting Pedestals

Most of the Fastbus ADCs turned out to be very stable. A couple of ADCs were found to drift and jump suddenly, however, over the course of several days. An illustration is given in figure 4.26. It was found that all channels moved together: the cause might be an change in the performance of the internal current supply which sets the pedestals. These ADCs were replaced for the 1990 run.

A jump of ten counts in one channel corresponds to 0.02 GeV in the bitubes, and 0.08 GeV in the pads. Figure 4.27 shows the shift of the muon signal in the pads before and after one of the more severe jumps in ADC number 26. Before the jump, the mean signal is 59 counts, but after it is 48 counts.

A substantial fraction of the events were triggered by halo and random-beam, which deposit virtually no energy in the calorimeter. These can be used to calculate pedestals for the low range. A series of programs were carried out to produce detailed tracking of the low-range pedestals. These pedestals were used in lieu of the pedestals produced by the interspill calibration. They agreed with the latter for nearly all channels, the significant exception being those pads and bitubes in the beam. (See discussion on beam loading below.)

4.5.5 Pedestal Widths

The shot noise in the bitube amplifiers has been estimated. Measurements show that the width of the pedestal (the total noise charge) increases as the square-root of the ADC gate width, and the capacitance at the input. For an input capacitance of 1000 pF, the "equivalent noise charge" was measured:

$$Q_{en} \text{ [fC]} = 50\sqrt{T_{gate} \text{ [ns]}}.$$

The noise for a pad tower has been calculated in a similar manner. It should be about 15 ADC counts, which agrees well with the observed pedestal width (12 counts, typical).[29] The dependence on the square-root of the gate width was confirmed.

The pedestal width degrades the energy resolution of the calorimeter. Let σ_0^{ped} be the pedestal with of a single channel, expressed in GeV. (For the pads, $\sigma_0^{ped} = 0.09$ GeV, and for the bitubes, $\sigma_0^{ped} = 0.05$ GeV.) This quantity is independent of

---

[29]Twelve ADC counts in the low range corresponds to about 600 fC.
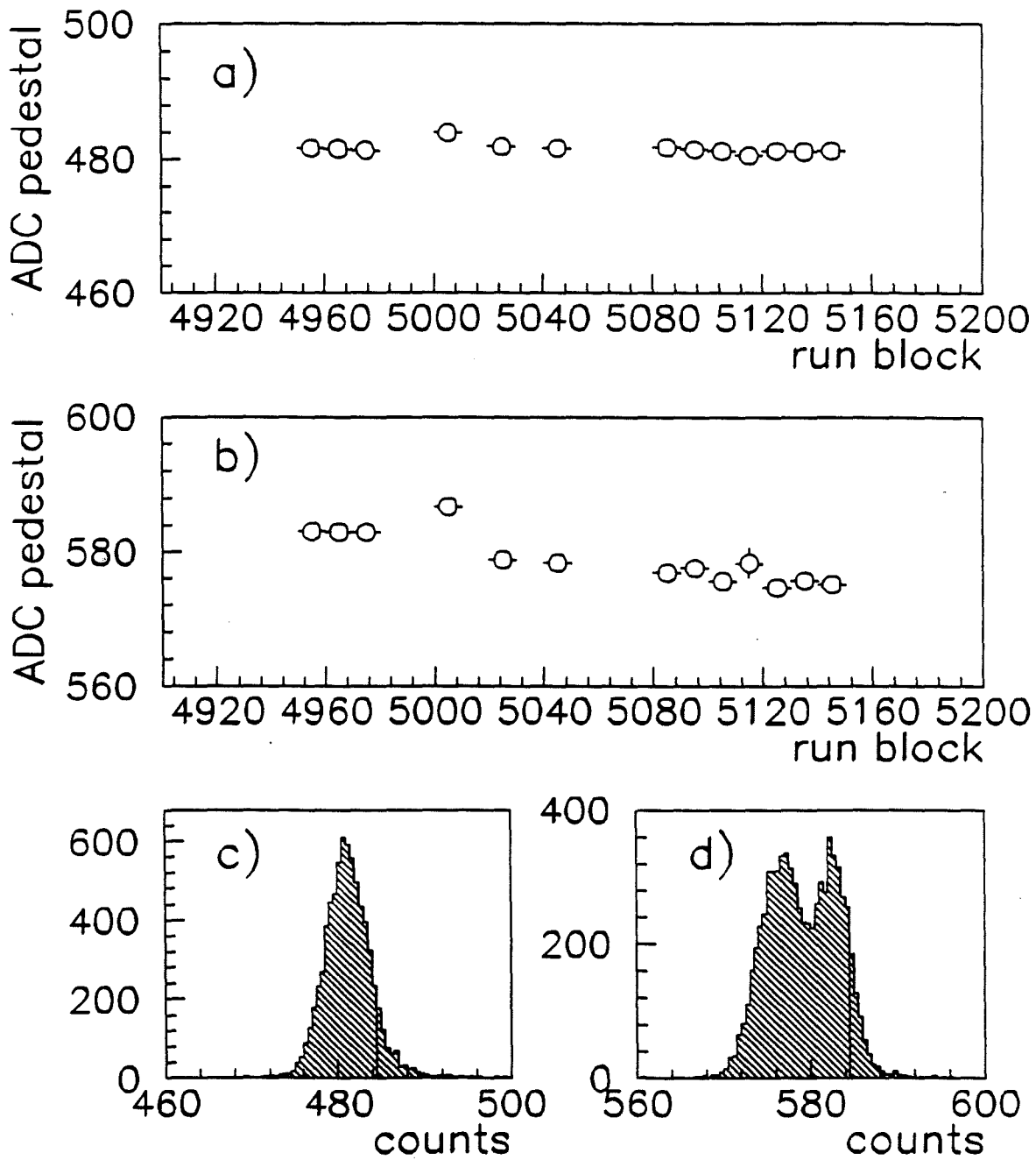
Figure 4.26: An example of a drifting fastbus ADC. The number plotted is the mean of all ninety-six channels, versus run block. Plot a) shows a typical stable ADC (number 13), and b) shows ADC 26. Plot c) shows the signal from ADC 13, summed over run blocks, and plot d) shows the same for ADC 26. Notice the two-peak structure in the latter.
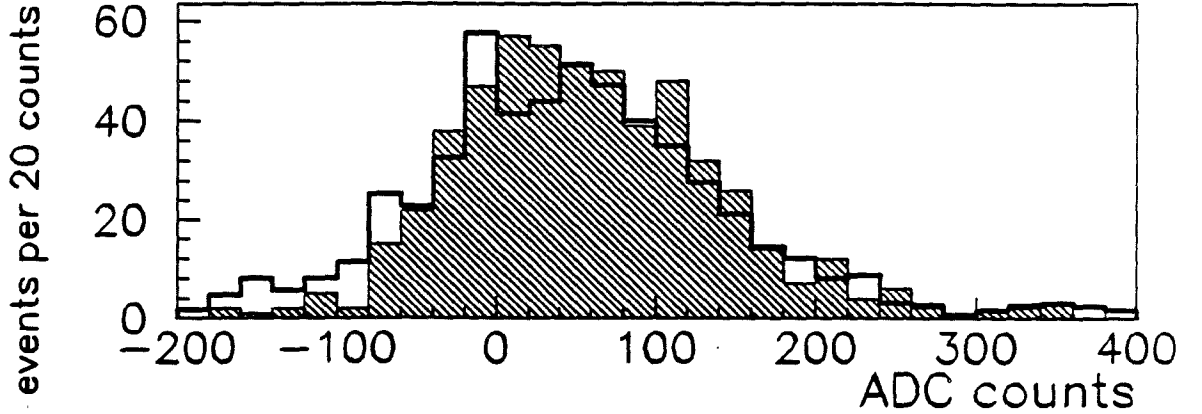
Figure 4.27: The halo muon signal changes slightly as a result of the jump in fastbus ADC number 26. The shift in the mean is 11 counts.

the energy in the channel. Assuming that the noise in two channels is uncorrelated, the total noise for N channels is

$$\sigma_{\text{tot}}^{\text{ped}} = \sqrt{\sum_1^N \sigma_0^{\text{ped}}} = \sqrt{N}\sigma_0^{\text{ped}}.$$

Typically, the energy resolution depends on $\sqrt{E}$, with E the energy of the shower. This term arises from the finite number of ionizing electrons produced in a shower. Write $\sigma^E = A\sqrt{E}$, where A is a constant depending on the characteristics of the calorimeter. Then the resolution due to the two uncorrelated terms $\sigma_{\text{tot}}^{\text{ped}}$ and σ^E is

$$\sigma^{\text{total}} = \sqrt{(\sigma_{\text{tot}}^{\text{ped}})^2 + (\sigma^E)^2} = \sigma^E \sqrt{1 + N\left(\frac{\sigma_0^{\text{ped}}}{\sigma^E}\right)^2}.$$

Unless the shower is completely contained in one channel (which does not happen for the E665 calorimeter), the resolution term σ^E depends on the number of channels N, also. (Clearly the worst resolution is achieved if only one channel is included in the shower sum; as more and more channels are included the resolution improves.) For the purposes of this illustration it can be guessed that $\sigma^E(N) = \sigma_0^E\sqrt{N}$. Then, assuming $\sigma_0^{\text{ped}} \ll \sigma_0^E$,

$$\sigma^{\text{total}} = \sigma^E \sqrt{1 + N\left(\frac{\sigma_0^{\text{ped}}}{\sigma_0^E\sqrt{N}}\right)^2} \approx \sigma^E \left[1 + \frac{1}{2}\left(\frac{\sigma_0^{\text{ped}}}{\sigma_0^E}\right)^2\right].$$

which clearly increases the effective constant $(\sigma_0^E)' > \sigma_0^E$. Approximate values (for 20 GeV electrons) are $\sigma_0^E = 300$ counts, and $\sigma_0^{\text{ped}} = 12$ counts. It behooves the calorimeter expert to keep the pedestal widths narrow!

120

The gate widths for the 1987-88 run were a bit wider than necessary, but it turns out that the actual energy resolution is dominated by other factors.

An excessively wide pedestal hinders setting a low pedestal subtraction threshold, also. (The lower the threshold, the better the resolution, so long as one is above the noise.) For most channels the pedestal has a gaussian shape, so the noise signal can be written

$$f(A) = \frac{1}{w\sqrt{2\pi}} \exp(-\frac{1}{2}\frac{A^2}{w^2}),$$

where A is the ADC reading (after pedestal subtraction), and w is the pedestal width. The function has been normalized to one, so it can be regarded as a probability distribution.[30] The mean ADC reading $\langle A \rangle$ is zero if averaged over the entire range of A, but it is nonzero if a threshold T is imposed on the distribution. The mean value $\langle A \rangle_T$ for values falling above the threshold $T > 0$ is

$$\langle A \rangle_T = \int_T^{+\infty} dA\ A\ f(A) = \frac{w}{\sqrt{2\pi}} \exp(-\frac{1}{2}\frac{T^2}{w^2}) = w^2\ f(T).$$

For a given threshold, this mean increases as w^2. Note that the width of this distribution is the same as the width of the pedestals.

The average energy for N channels will be approximately $N \cdot \langle A \rangle_T$, since pedestal fluctuations are uncorrelated. Figure 4.28 shows the total signal in the calorimeter for "empty" events, as a function of the threshold. The gaussian shape for the pads is obtained, but the bitube shape is more complicated, due to the different pedestal shapes for different groups of bitubes.

4.5.6   High Range Constants

Generally speaking the interspill calibration programs produced useful constants. However, the central bitubes in the Dart planes failed to calibrate, resulting in significant problems in offline data analysis. The low range and high range slopes can be predicted, but the high range pedestal for each channel must be measured. (Low range pedestals can be determined from random beam and halo data.)

The exact cause of the calibration failure is unknown, but the following may have played a role :

---

[30]Of course, there is a lower and upper bound, which does not effect this discussion.
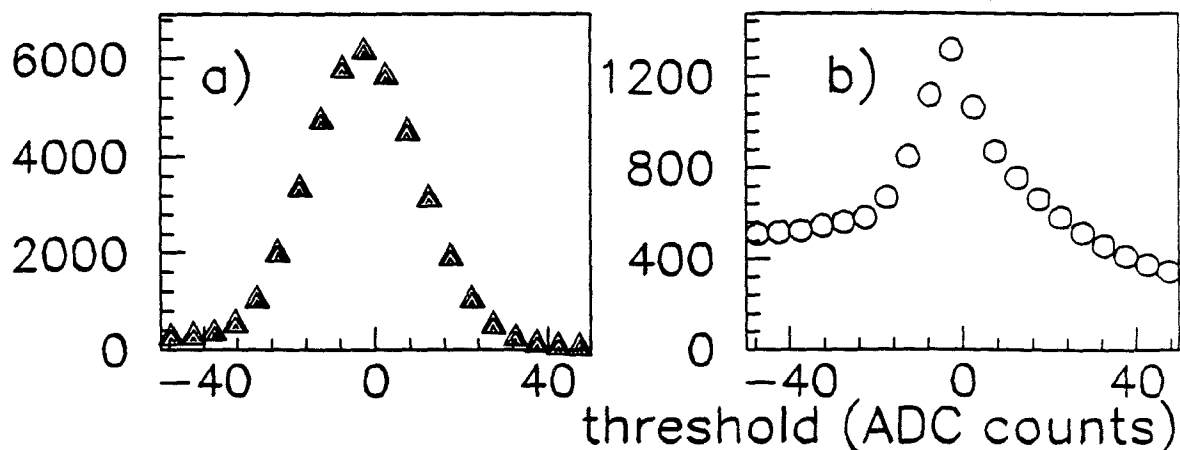
Figure 4.28: Total signal in the calorimeter, for different pedestal subtraction thresholds. Plot a) shows the pad towers, and plot b) shows the bitubes.

- Planes 5 and 7 were oscillating (± 500 low range counts) and these oscillations were picked up by planes 4 and 6.

- The electronic gain in the central dart plane bitubes is relatively small (5 versus 7 in the outer bitubes, or 11 in ordinary planes), so the pulse heights chosen for calibrating the high range may have been inappropriate for these channels.

Four constants are needed to specify the relation between the ADC reading (A), and the charge at the input (Q).

$$A = a_L + b_L Q \qquad \text{for low range readings}$$

$$A = a_H + b_H Q \qquad \text{for high range readings}$$

The values of a_L and a_H lie in the range 100 to 1000 and are uncorrelated and unpredictable. (They are, however, quite constant.) The values of b_L and b_H depend on the amplifier gain, but are constrained by Lecroy to satisfy

$$b_L/b_H = 8.00 \ (1 \pm 0.03).$$

The four constants a_L, b_L, a_H, and b_H must be measured for every channel: this is the job of the calibration tasks. A test pulse of controllable amplitude is used to vary Q. A is read out, and linear fits performed to determine the constants a_L, a_H, b_L, and b_H. The test pulse for bitube amplifiers is generated inside each plane, and in practice is very linear:

$$Q = \alpha + \beta P$$

122

name	constant	description
CALx0	$A_L = f_L(0)$	low range pedestal
CALx1	b_L	low range slope
CALx2	a_H	high range intercept
CALx3	b_H	high range slope
CALx4	$\Delta = a_L - A_L$	offset pedestal–intercept
CALx5	σ_L	low range pedestal width
CALx6	κ	conversion ADC counts to GeV

Table 4.4: Identification of calorimeter constants. The letter x stands for B for bitubes, P for pads, and W for individual anode wires. (For run 90 data, CALx2 is the *true* high range pedestal.)

where P is a control value set via Camac. The constant α is not zero, and can amount to 100 ADC counts in a given channel. This means that intercepts from linear fits to

$$A = f_L(P) \qquad A = f_H(P)$$

will not equal the true pedestals a_L and a_H, which are defined to be the ADC readings with strictly zero charge on the input. (Further details may be found in [Sch89c].) The difference

$$\Delta = a_L - f_L(0)$$

was recorded as a fifth calibration constant. It was assumed that the true high range pedestal could be obtained through

$$f_H(0) = a_H - \frac{1}{8}\Delta.$$

The low range pedestal $f_L(0)$ was determined by pulsing the pads (which generated a gate for all ADCs), and reading the bitube ADC. The width of the low range pedestal distribution was recorded as the sixth constant. (See table 4.4.)

The slope for a given channel could be estimated, and there is clear evidence that the linear fits performed by the calibration tasks correlated the values of the intercept and slope. Proper values for the slope were obtained interactively after the run was over. These were applied to correlation plots of the slope and intercept, and values for the intercept inferred. The error in this method could be easily 20 ADC counts. (Plane five presented special problems due to the apparently malfunctioning amplifiers.)

(It is worth pointing out that the option of forcing the ADCs to digitise in the low or the high range was overlooked. If this facility had been used, the true high range pedestal a_H could have

been determined the same way the low range pedestal a_L was determined. This was changed for the 1990 running period!)

4.5.7 Beam Loading

The electromagnetic calorimeter used by EMC had a hole in the center through which the beam passed. This was also suggested in the early stages of the design of the E665 calorimeter. The ionization of the gas by the beam would be substantial, leading to space charge effects which could degrade the performance of the calorimeter. Calculations showed, however, that the effects were tolerable, leading to a loss of gain of a few percent [Wil83]. Tests with a prototype showed that the gain decreased by a factor of two for a beam rate of 10 MHz [Nic84d]. Although corrections might be substantial, it is better to have the measurement (e.g., high-p_T photons) to be corrected, than to have nothing. No hole was built in the calorimeter, but the bitubes with the least resistive graphite cathodes were chosen for the center. Also, the calorimeter was placed so that the beam was centered on the boundary between two bitubes, to halve the current in each bitube produced by the beam.

The effects of the beam are evident offline even at an intensity as low as 0.5 MHz. Figure 4.29 shows the pedestals from a bitube in the beam, with beam and without it. The beam has two effects on the pedestal:

1. There is a long tail.

2. The peak position is *lower*, due to long-lived negative tail from earlier pulses.

The most significant problem for analysis was the shift in the peak pedestal position. The change in the pedestal value is typically 10 counts, which summed over twenty bitubes amounts to about 0.5 GeV. The peaks were fitted to a gaussian to determine the effective pedestal for standard running conditions.

The distortion of the energy response in this region due to the tail has not been understood, nor has it been possible to measure the loss of gain with respect to other regions of the calorimeter.

124
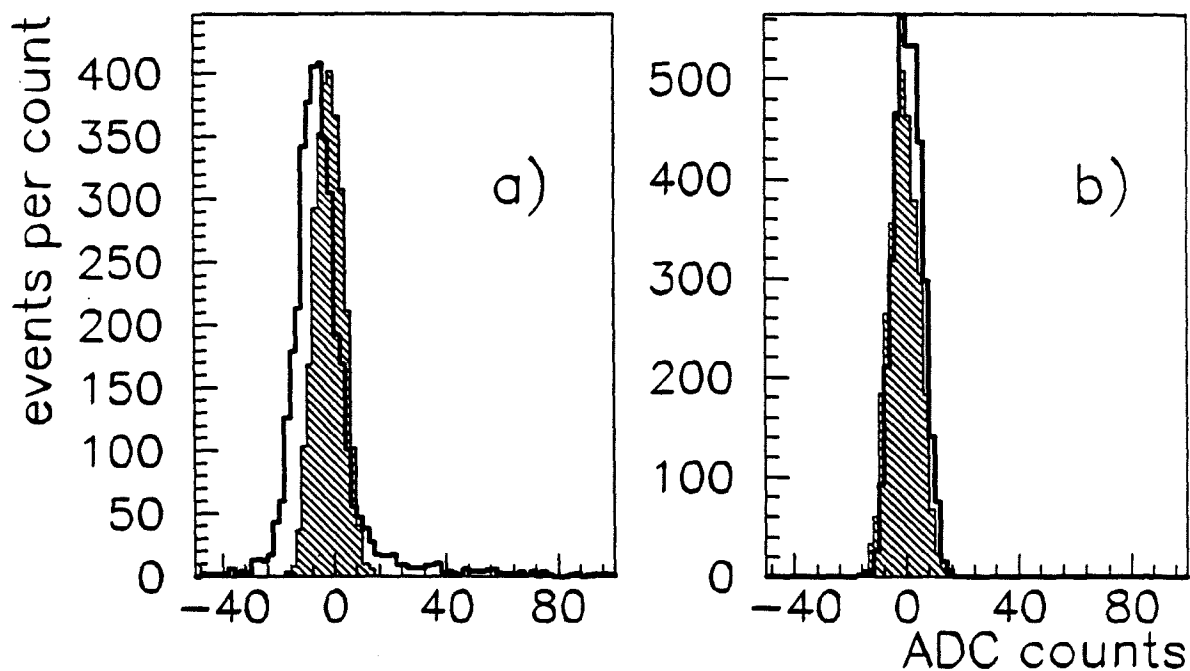
Figure 4.29: The effect of the beam on the pedestal distribution for bitubes in the beam. Plot a) shows bitube 10 (in the center of the calorimeter), and plot b) shows bitube 5 (far from the center). The shaded curve shows the signals for a pulser run (no beam present), and the thick lines show the signal for halo events. (The muon was excluded form the bitubes shown.)

4.5.8 Nonlinear Energy Response

The apparent energy reported by the calorimeter is not proportional to the energy of the photon or electron all the way to 500 GeV. This is illustrated by a plot of E_{sh} versus P_{tr} for electrons in μe events, shown in figure 4.21 on page 110. The deviation is seen more clearly in the plot of the ratio E_{sh}/P_{tr} versus P_{tr}, and of the difference $E_{sh} - P_{tr}$ versus P_{tr}, shown in figure 4.30. Plot c) shows the ratio E_{sh}/P_{tr} at 70 GeV and 370 GeV.

The nonlinearity could have several sources:

1. The amplifiers could be saturating.

2. The ADCs could be saturating.

3. The gas gain could be suffering a local suppression, due to the intensity of the particles in the center of the cascade.

4. The high-energy particles hit the center of the calorimeter. The beam loading on the central bitubes could be causing a reduced gain.

5. There could be a calibration error for the high range (such as the high range intercepts, discussed above), or the offline analysis could be faulty.

6. Part of the shower could be escaping out the back of the calorimeter.

1. The charge deposition of electrons was measured using test beam data, with the result 7.5 pC per GeV [Kun84]. He also showed that the peak energy deposition in a single plane was 40 pC, for a 50 GeV electron. The internal amplifiers were designed to be linear up to 750 pC, so the nonlinearity should not be caused by them.

2. The maximum charge digitized in the ADC (high range) is 1600 pC.

3. The shower occurs very fast compared to the drift time of the electrons toward the wire, or of the ions drifting away. There is not enough time for ordinary space charge effects to build up *inside* a single shower.

4. The beam loading is present, as shown in an earlier section. Its effects are not estimated easily.

5. Bad constants or bad code certainly could be possible.
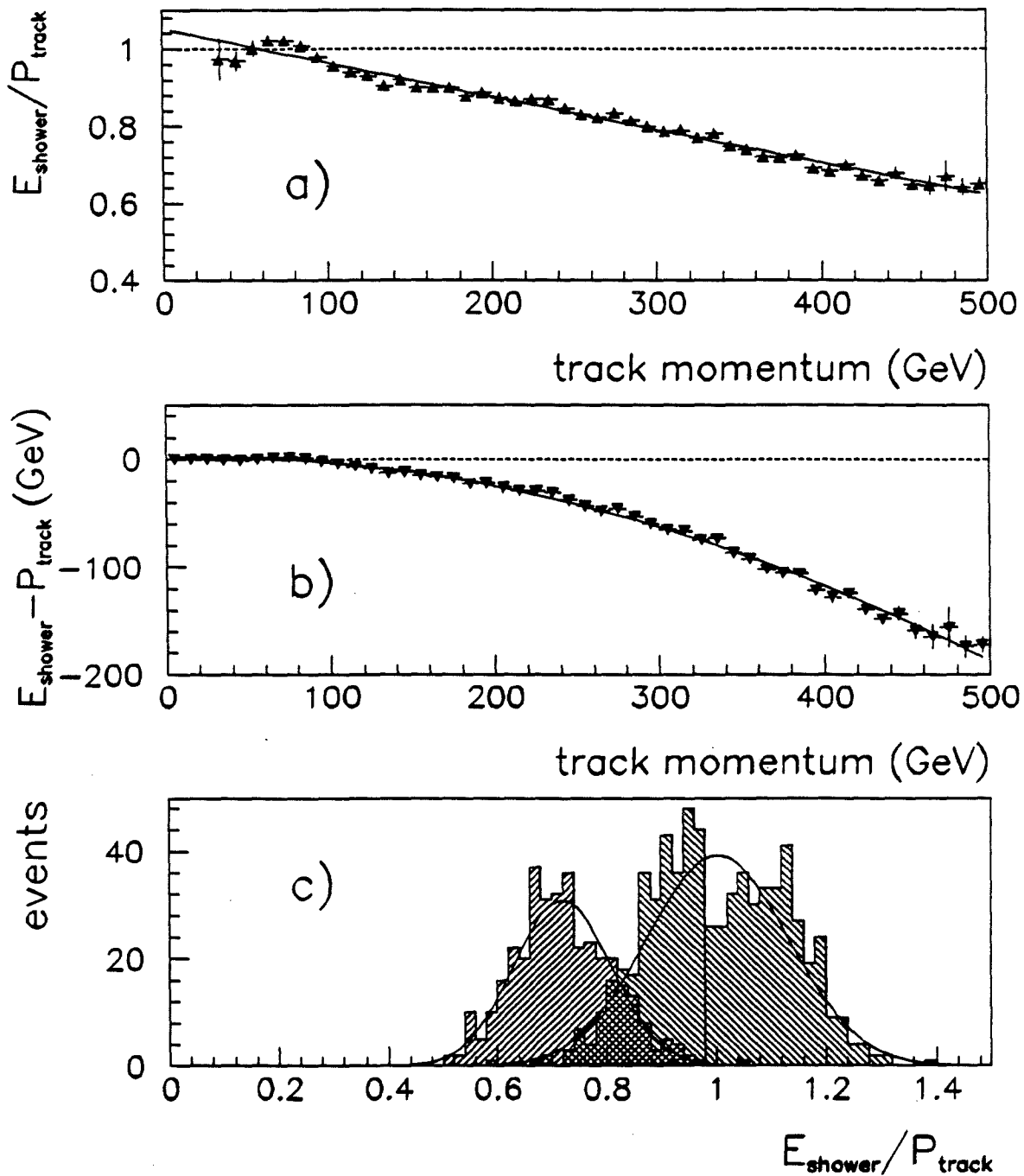
Figure 4.30: Nonlinear calorimeter energy response to μe scatters. Plot a) shows the ratio E_{sh}/P_{tr} versus P_{tr}, and plot b) shows the difference $E_{sh} - P_{tr}$. Plot c) shows the peak E_{sh}/P_{tr}, for $50 < P_{tr} < 100$ (higher bump) and $350 < P_{tr} < 400$ (lower bump).

This performance has been taken as given, and several parametrizations of the nonlinearity exist. The data shown here lead to three simple expressions:

1. direct correlation
$$E_{sh} = a_0 + a_1 P_{tr} + a_2 P_{tr}^2,$$

with $a_0 = 2.8 \pm 0.9$ GeV, $a_1 = 1.02 \pm 0.01$, and $a_2 = (-8.0 \pm 0.2) \times 10^{-4}$ GeV^{-1}.

2. "intercept" versus energy

$$E_{sh} - P_{tr} = b_0 + b_1 P_{tr} + b_2 P_{tr}^2,$$

with $b_0 = 1.6 \pm 0.8$ GeV, $b_1 = 3.1 \pm 0.1$, and $b_2 = (-8.2 \pm 0.2) \times 10^{-4}$ GeV^{-1}.

3. "slope" versus energy

$$\frac{E_{sh}}{P_{tr}} = c_0 + c_1 P_{tr} + c_2 P_{tr}^2,$$

with $c_0 = 1.053 \pm 0.007$ GeV, $c_1 = -9.0 \pm 0.6$, and $b_2 \approx 0$ GeV^{-1}.

Although this problem is interesting, very high energy electrons are not used in this analysis of ρ^0 states in this thesis, so this topic will not be investigated further.

4.6 Performance

In this section, a brief, cursory look at the calorimeter performance is given. Much of the discussion will be qualitative, as the technical difficulties discussed in the previous section tend to cloud the picture.

4.6.1 Muons

The energy deposited in the calorimeter by muons in the form of ionization amounts to 400-500 MeV. Additional energy comes from processes such as knock-on electrons, nuclear interactions, bremsstrahlung, and pair-production. The sum of these contributions should be about 2 GeV, according to calculation [Nic84a]. The muon signal should stand distinctly above pedestal.

Figure 4.31 shows the signal seen in the pads and the bitubes for halo muons. The units are pC seen by the fastbus ADCs, which is roughly the charge produced by the channel. Also shown is the distribution for channels far from the muon, which should be empty: this is a kind of pedestal. The muon can be distinguished from the pedestal easily. Table 4.5 lists a couple of interesting numbers for these plots.

If the pedestal were narrower, then the peak would be separated from the pedestal, and could be used for calibration purposes. Studies indicate that the exponential *tail* of the distributions is a good measure of gas gain. It also was observed that the tail is significantly larger than the Landau distribution, when convoluted with the pedestal.

element	pedestal		muon signal			difference
	peak	sigma	peak	sigma	mean	between peaks
bitubes	0.006	3.9	5.4	7.8	8.4	5.4
pads	0.0	2.0	2.1	2.4	2.9	2.1

Table 4.5: **Measurements of the charge collected (at the ADC) for halo muons. Units are pC.**

Some muons produce showers in the calorimeter. Figure 4.32a shows the distribution of shower energies above 0.5 GeV, produced by halo muons. The halo muon momentum distribution is given in plot b), and the ratio shower energy to track
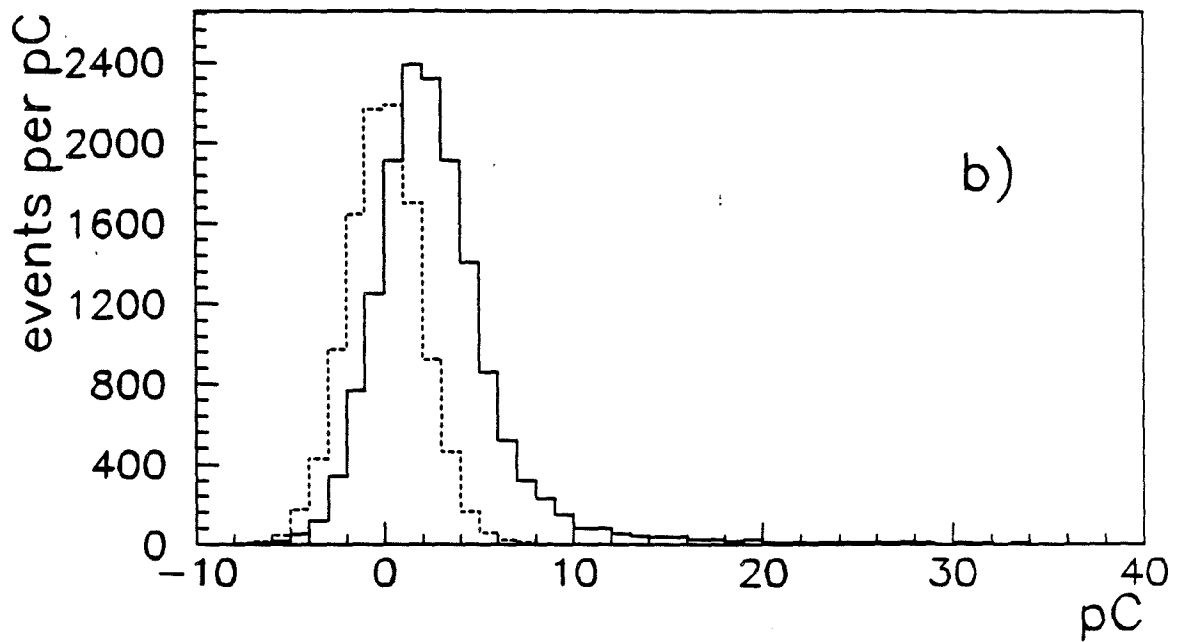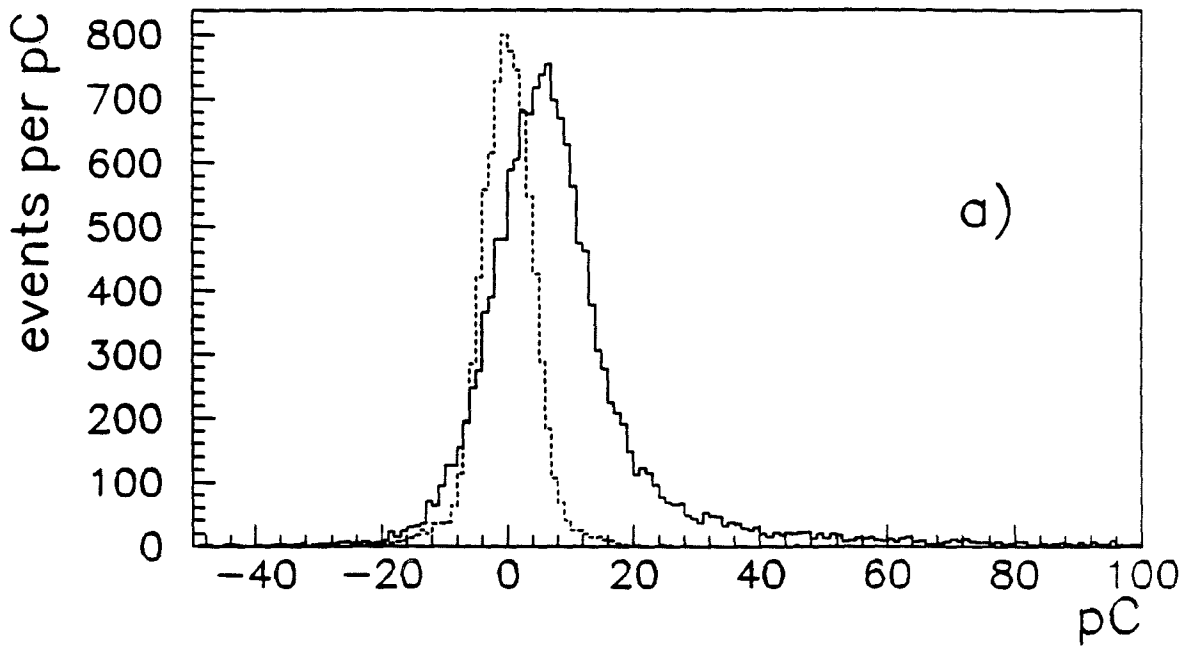
Figure 4.31: Plot a) shows the halo muon signal seen in the bitubes (solid line), together with the "pedestal" (dashed line). Plot b) shows the same for the pads. (Units are pC into the ADC.)
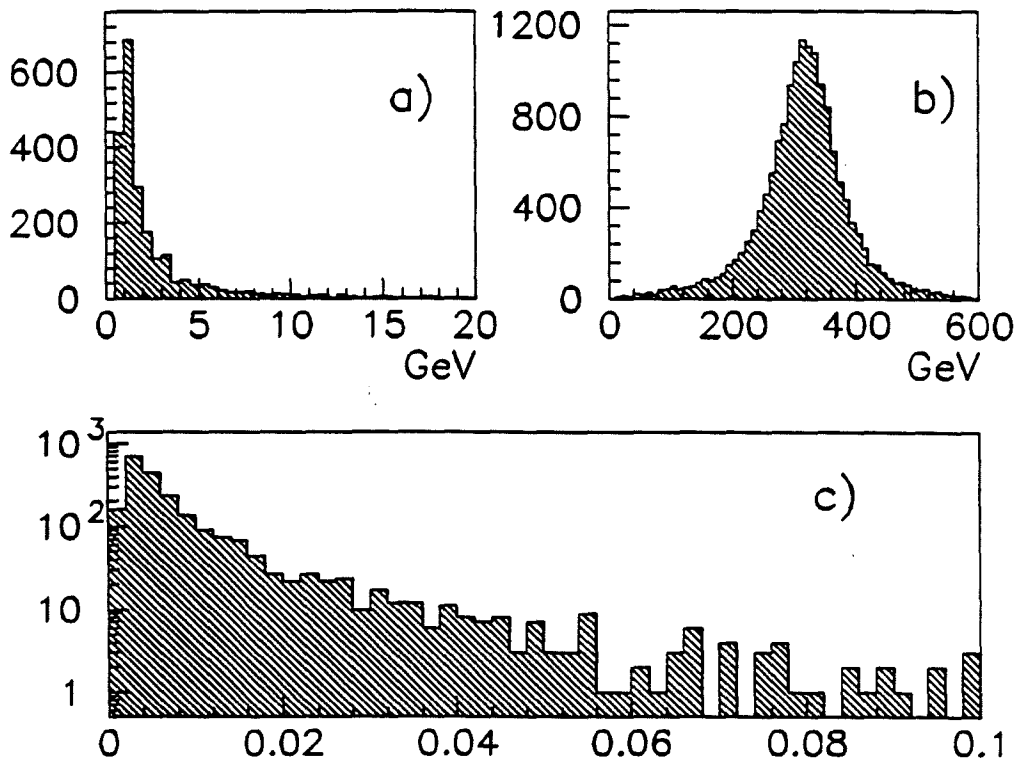
Figure 4.32: Showers produced in the calorimeter by halo muons. Plot a) shows the shower energies. Plot b) shows the muon momenta. Plot c) shows the shower energies normalized to the muon momenta.

momentum is shown in plot c). Of 15310 halo events analyzed, 2312 contained a shower greater than 0.5 GeV. This means that 2 in 13 events will have a significant shower.

4.6.2 Electrons

The electron beam data from the 1987-88 run were poor. Much better data were obtained during the 1990 running period, so these data were used for studying many aspects of the calorimeter performance.

Electrons striking the calorimeter will deposit all of their energy in a single shower. This is why they are used to set the absolute scale of the calorimeter. Figure 4.33a shows the energy of showers produced in data from a 30 GeV tune. Plot b) shows the track momenta, and plot c) shows the ratio of the shower energy to the track momentum. A narrow gaussian is seen near one. The overall scale factor κ^r is adjusted until the peak of the gaussian occurs at one.
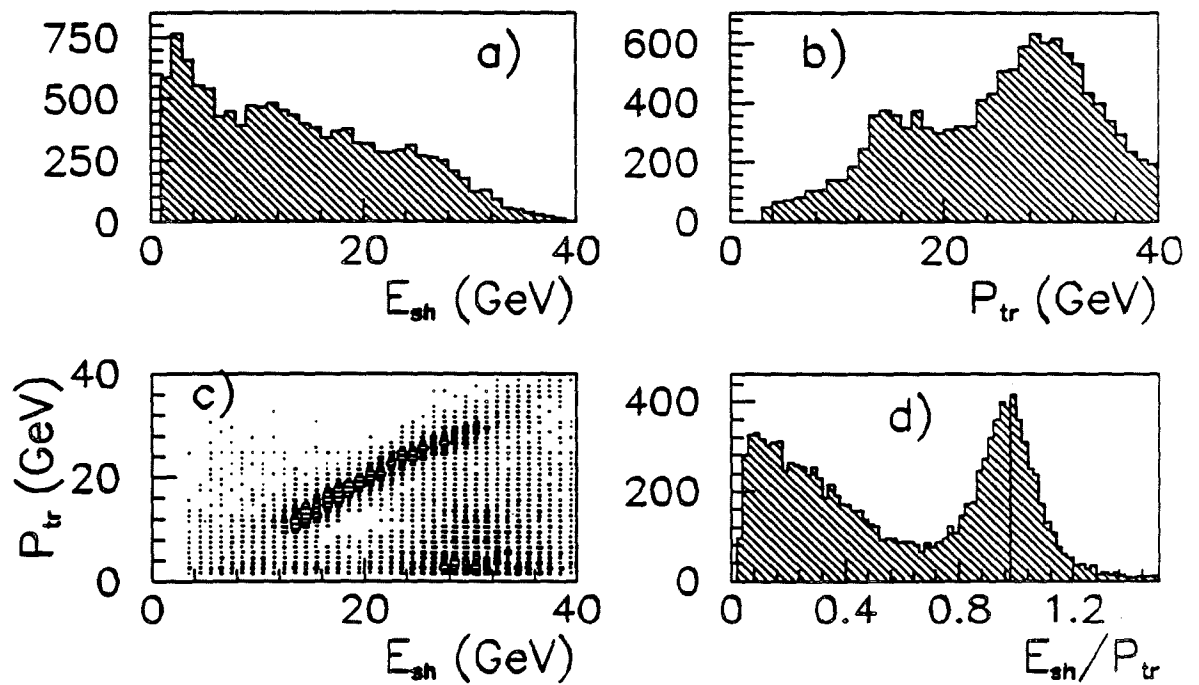
Figure 4.33: Electron showers in the calorimeter (1990 electron beam). Plot a) shows the shower energies, plot b) shows the track momenta, plot c) shows the correlation between them, and plot d) shows the shower energy divided by the track momenta.
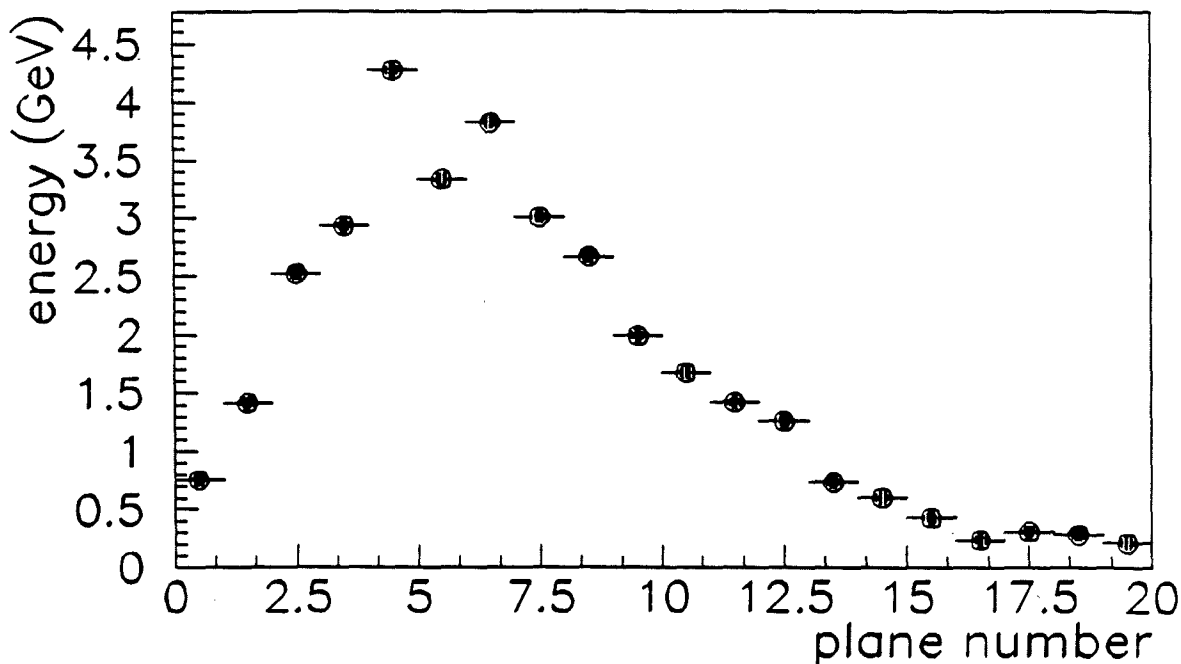
Figure 4.34: Longitudinal shower profile, from 20 GeV electrons.

Electron showers should show a characteristic longitudinal shape, on average. Figure 4.34 shows the mean longitudinal profile for 20 GeV electrons. The rapid rise for the first few radiation lengths, with a peak at a depth of 4–7 X_0, followed by a long tail, is seen. Some bumps in the curve are due to relative differenced in absolute gain, not yet compensated.

The transverse shower shapes are shown in figure 4.35. Plot a) is a two-dimensional view of the average shape. Radial symmetry is evident; plot b) shows the projections in Y and Z. The energy density varies with distance from the center as shown in plot c); this distribution goes to zero as $R \rightarrow 0$ because the surface element is $2\pi R dR$, which goes to zero. Plot d) shows the radial energy distribution, per unit area. This distribution could be fitted with a single exponential:

$$\frac{dE}{dR} = \text{const.} \times \exp(-\lambda R),$$

with the result $\lambda = 34$ m^{-1}. This corresponds to a characteristic length of $R_0 = 2.9$ cm, so most of the shower energy should be contained in about 25 pad towers. The Y and Z projections could be fitted tolerably well with exponentials, also, with the result $\lambda \approx 29.4$ m^{-1}.

Electrons do not penetrate the lead, in contrast to hadrons and muons. Fig-

133
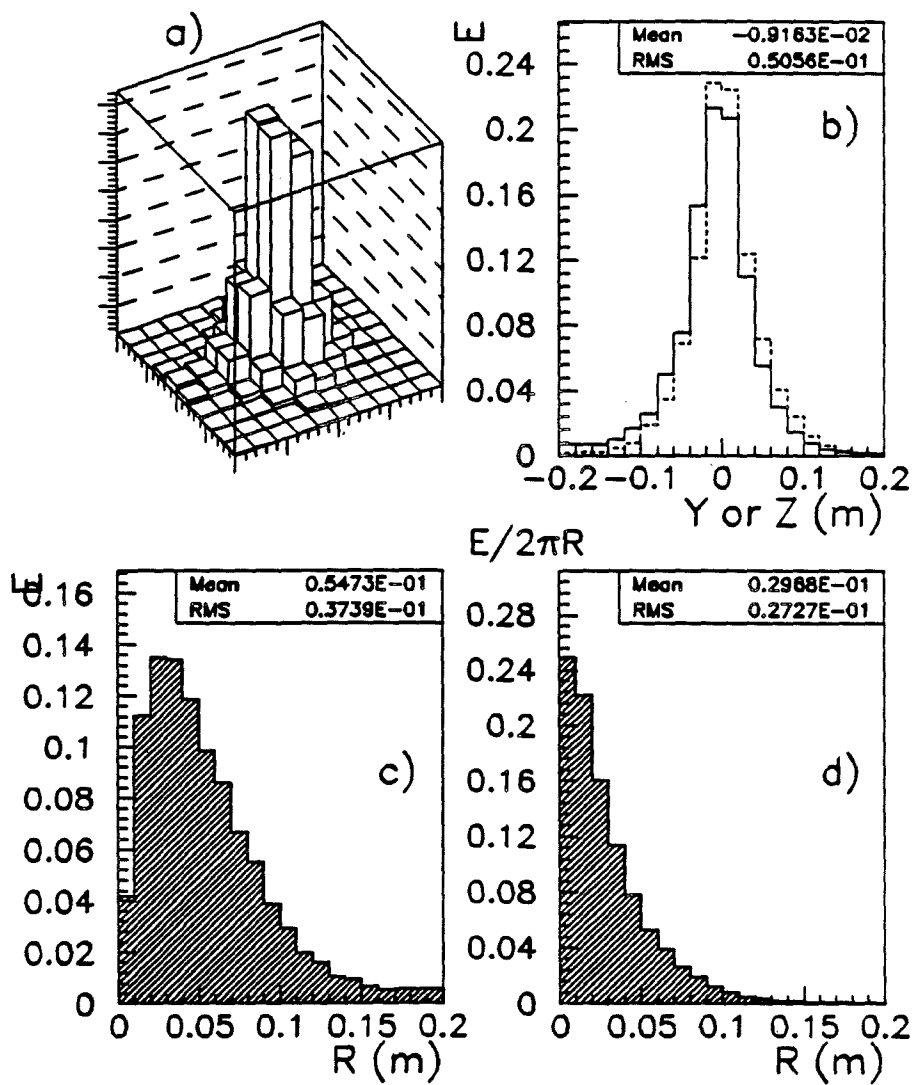
Figure 4.35: Transverse shower profile, from 20 GeV electrons. Plot a) shows the YZ distribution, with projections in plot b). Plot c) shows the density versus R, and d) shows c) normalized per unit surface area. Plots b)–d) are normalized to one.

relative frequency

0.6

0.4

0.2

0

0   5   10   15   20

1

10^{-1}

10^{-2}

10^{-3}

0   5   10   15   20
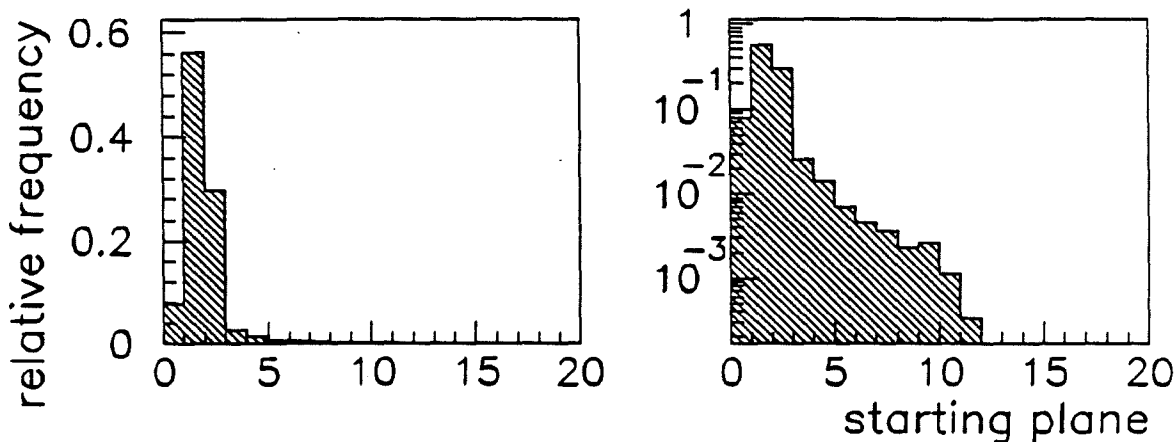
starting plane

Figure 4.36: Starting point of 30 GeV electron showers for 1990 data. a) linear scale, b) logarithmic scale.

ure 4.36 shows the staring point of electron showers, defined to be the depth ($X_{0.05}$) at which 5% of the total shower energy has occurred:

$$\frac{1}{20} = \frac{\int_0^{+X_{0.05}} dX \frac{dE}{dX}}{E_{sh}} \approx \frac{\sum_{i=1}^{X_{0.05}} E_i}{E_{sh}}.$$

4.6.3 μe Signal

Given good response to electrons, elastic μe scatters produce a distinctive signal in the calorimeter. The muon generally deposits no significant energy in the calorimeter, but the electron produces a huge electromagnetic shower. Candidate μe events were skimmed from the reconstructed events using only track criteria (one positive and one negative track, and the momentum of the latter must be at least 50% of ν) [Sch90d]. Figure 4.37 shows the spectrum shower energies for these events, and the momentum of the negative track, P_{el}.[31] A cut $0.8 < Z_{el} < 1.2$ was imposed, to help reduce the fraction of pions from deep-inelastic events. A clear correspondence between shower energy and P_{el} is observed, although they are not proportional in the high-energy region.

These events contain essentially one or two showers, as shown in figure 4.38. The number of forward tracks is two, by selection. The number of showers peaks at one, with a rapidly falling tail. Electrons sometimes radiate a photon which

---

[31]Due to the properties of the trigger, the acceptance for μe events is significant only at high-ν.
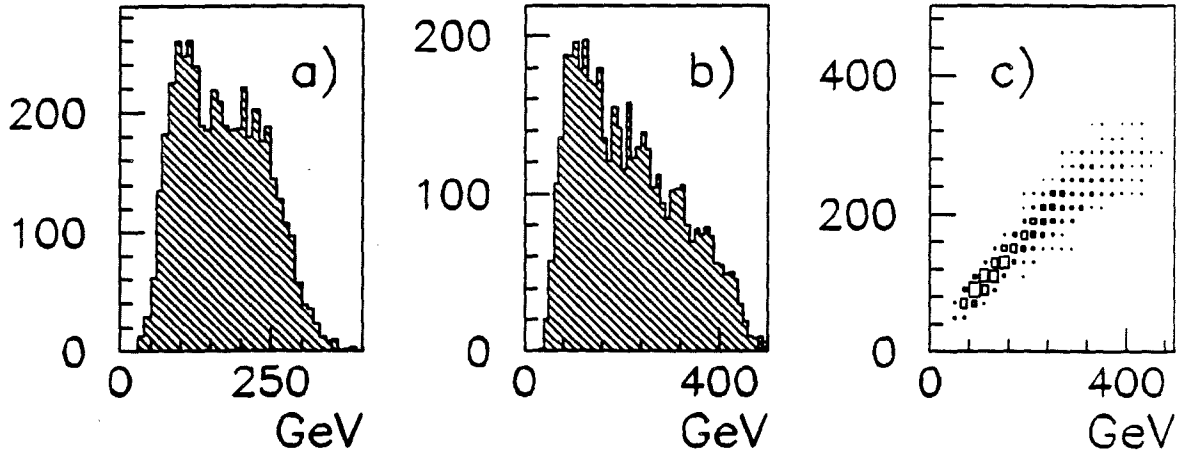
Figure 4.37: Basic signal for μe events. (SAT, hydrogen) Plot a) shows the shower energies, plot b) shows the track momenta, and plot c) shows the correlation between the two.

impacts the calorimeter at a point distinct from the electron; or the radiated photon may convert, producing two more electrons.[32] These events have the expected topology, to be contrasted with those for high-Q^2, deep-inelastic events (dashed lines).

The electron track should point to the center of the electron shower. Figure 4.39 shows the correspondence between tracks and showers. The projected Y and Z distributions are very similar, as shown in plots a) and b). The distribution of the distance between the track and the coordinates of the shower,

$$\Delta = \sqrt{(Y_{sh} - Y_{tr})^2 + (Z_{sh} - Z_{tr})^2},$$

is shown in figure 4.39c. It goes to zero as $\Delta \to 0$ because it is weighted by the surface element $(2\pi\Delta)d\Delta$. Plot d) shows this distribution, divided by $(2\pi\Delta)$.

The efficiency for the calorimeter to detect the electron in μe scatters is very high. Events from this sample were selected with the additional criteria

$$(2 \times 10^{-4}) < x_{Bj} < (7 \times 10^{-4}) \quad \text{and} \quad 0.7 < Z_{el} < 1.1,$$

$$-12 < X_{vtx} < -10 \quad \text{and} \quad D < 0.04,$$

which should produce a pure sample of μe scatters.[33] These cuts are indicated in figure 4.40a–c. The spectrum of calorimeter showers for these events is shown in plot d. Out of 4651 events so defined, none fell below the cut $E_{sh}/P_{tr} = 0.4$, indicated in plt e).[34]

---

[32] The reconstruction efficiency for downstream photon conversions is not very high.

[33] Elastic μe scatters produce a peak at $x_{Bj} = (m_e/M_p) = 5.45 \times 10^{-4}$.

[34] This estimate of the calorimeter efficiency ignores events in which fastbus failed.
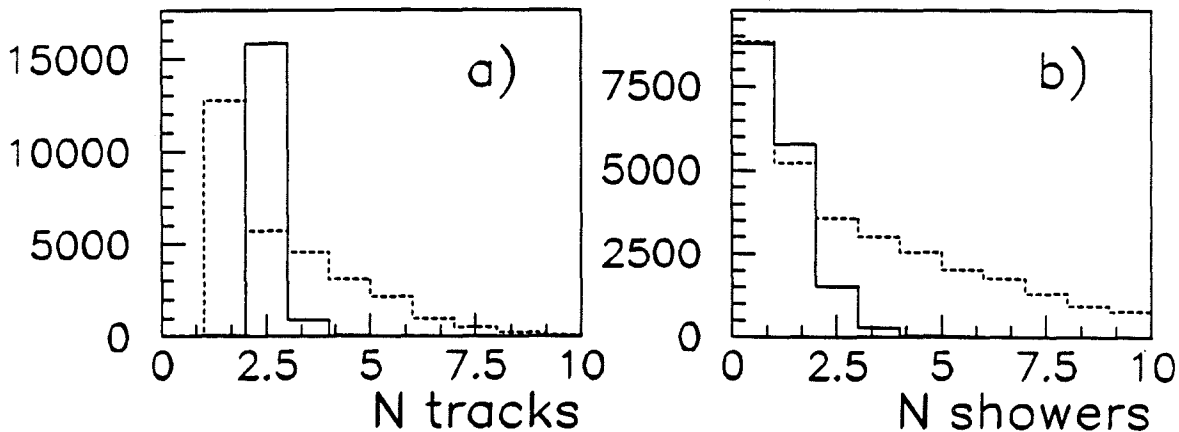
Figure 4.38: Shower and track multiplicities for μe events. Plot a) shows the track multiplicities, and b) shows the shower multiplicities. The dashed lines show the same for deep-inelastic events. (The μe events are required to have three tracks, including the two muons.)

4.6.4 $\mu\gamma$ Signal

The bremsstrahlung signal ("$\mu\gamma$ signal") is similar to the μe signal. A set of candidate events were skimmed together with the μe events. The photon emitted by the muon will have energy ν, roughly, and will produce a large shower in the calorimeter. The spectrum of shower energies, photon energies, and the correspondence is shown in figure 4.41.

The photon does not leave a signal in wire chambers, so it cannot be tracked from the vertex to the calorimeter. On the other hand, it is not deflected by the magnetic fields, so its trajectory is a straight line from the vertex. The photon is emitted at virtually zero angle to the muon, and kinematic considerations show that it is usually emitted by the beam muon.[35] The direction at the vertex of the beam muon and the scattered muon was extrapolated in a straight line to the calorimeter.

Extraction of a *target-related* bremsstrahlung signal is difficult due to the fact that the muon is scattered through a miniscule angle. Consequently, the uncertainty in the vertex position is large, and in practice a vertex cut is not very effective: there is a large background due to bremsstrahlung *downstream* of the CVM. Plots a) and b) in figure 4.42 show the Y and Z distributions of the photon

---

[35]A photon emitted by the beam lowers the center-of-mass energy for the muon-nucleon interaction, thereby increasing its probability. This is not true when the photon is emitted by the scattered muon.
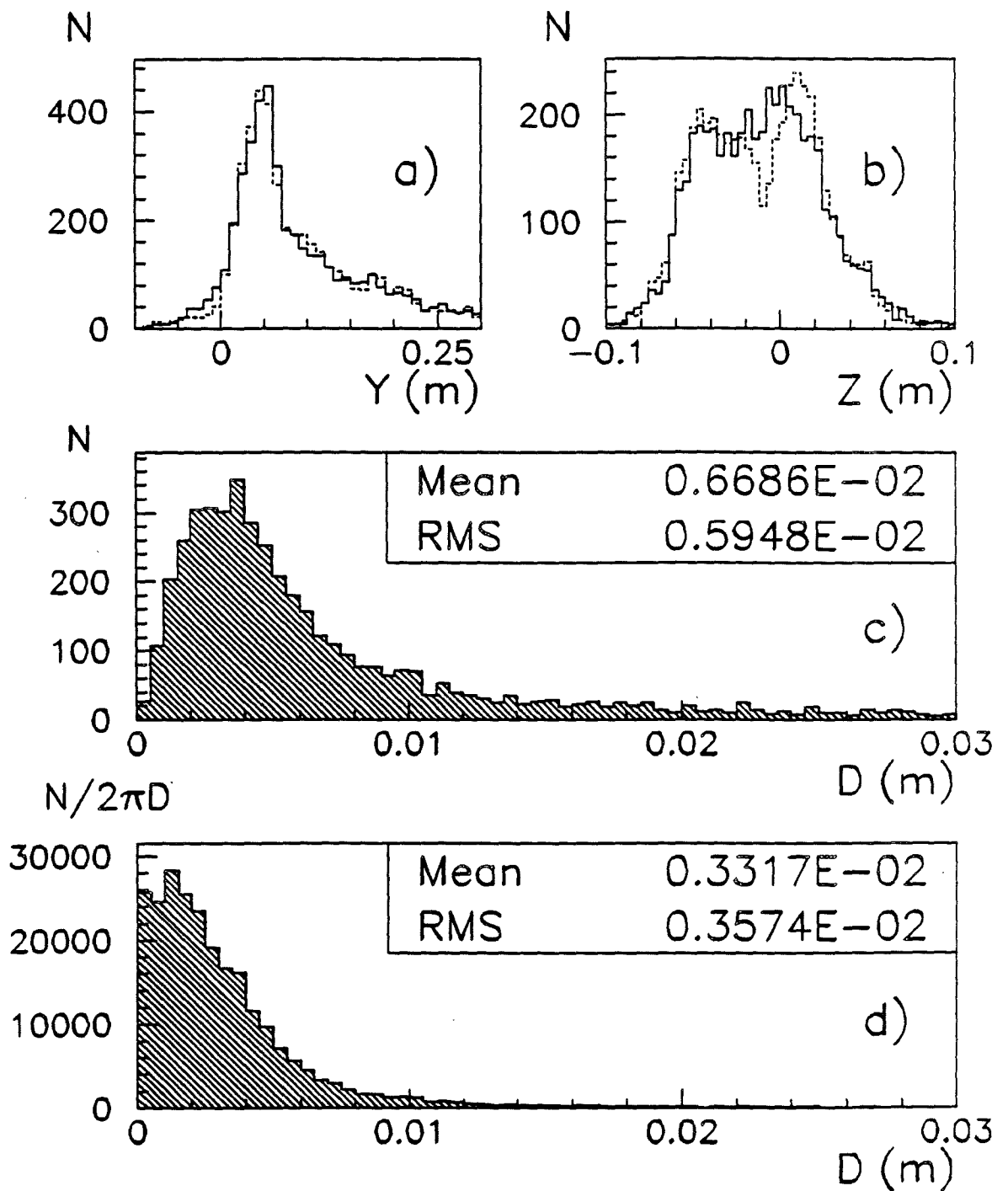
Figure 4.39: Track and shower coordinates for μe events. Plots a) and b) show the Y and Z coordinates of the showers (solid line) and tracks (dashed lines). Plot c) shows the distribution of the distance between them, Δ. Plot d) shows the distribution of Δ with the surface element $(2\pi\Delta)$ removed.
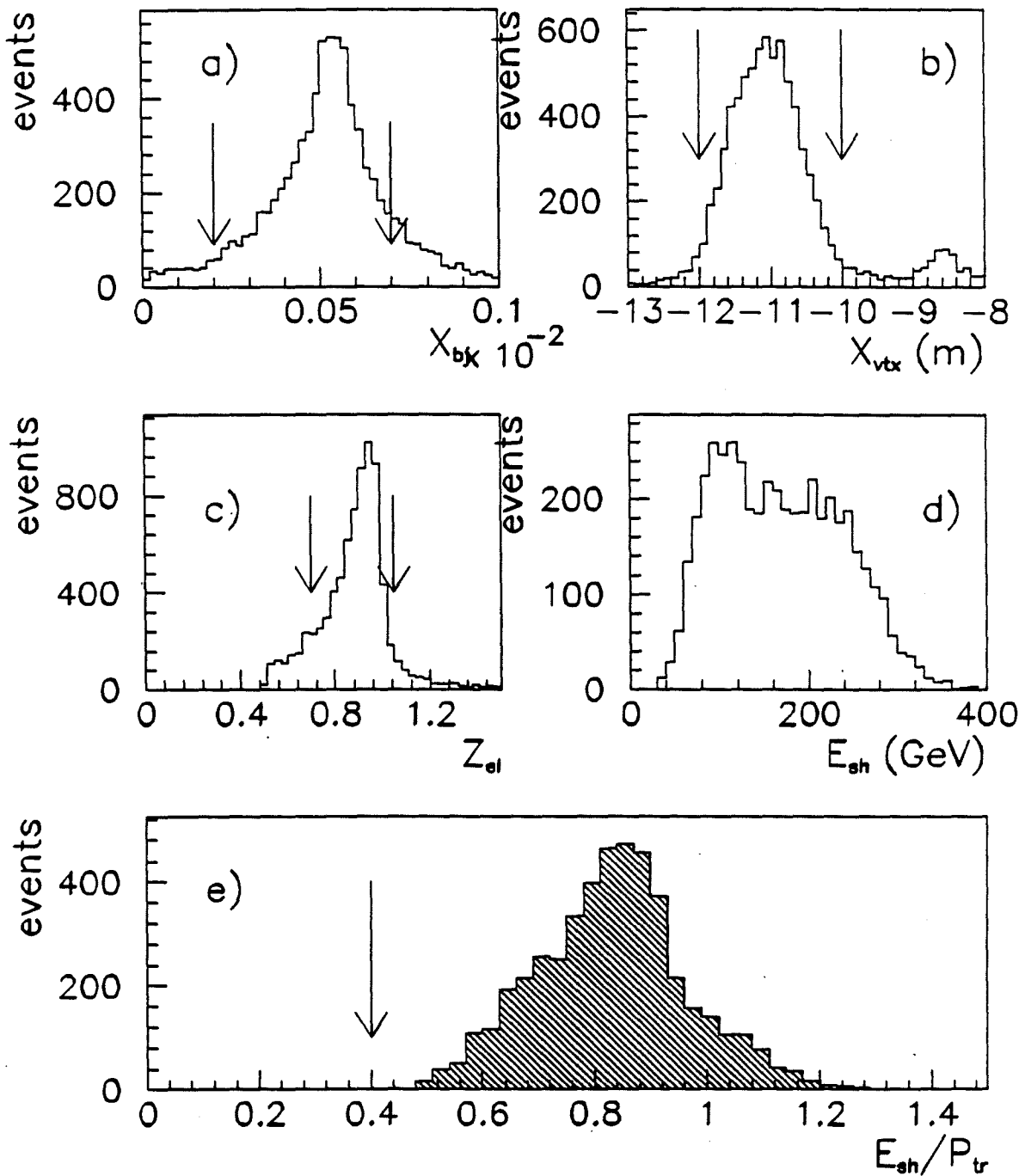
Figure 4.40: A measure of the calorimeter efficiency for μe events. (SAT, hydrogen) Plots a), b), and c) indicate the cuts on x_{Bj}, X_{vtx}, and Z_{el}. Plot d) shows the spectrum of E_{sh}, and plot e) shows E_{sh}/P_{el}, with the cut imposed for calculating the efficiency.
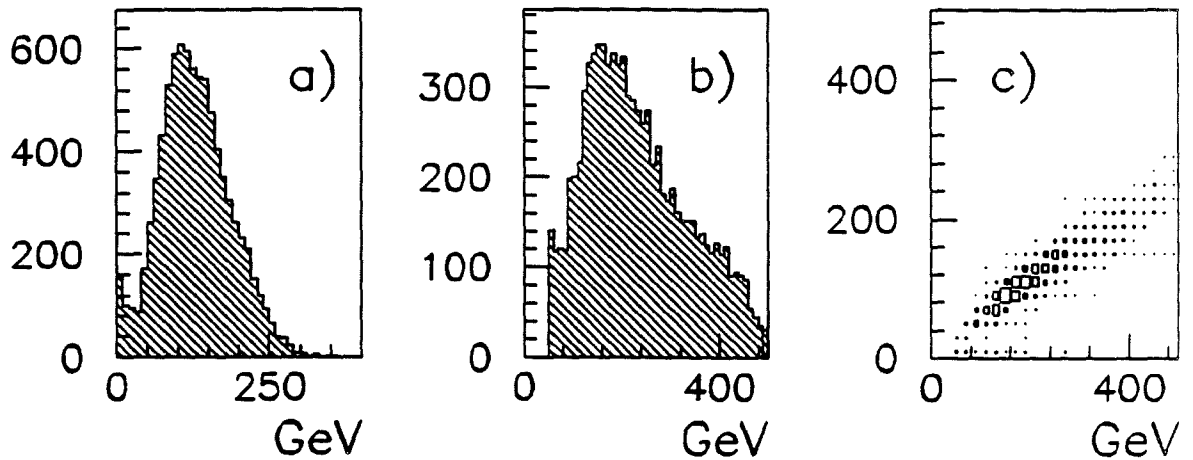
Figure 4.41: Basic signal from $\mu\gamma$ events. (SAT, hydrogen) Plot a) shows the shower energies, plot b) shows the photon energies (ν), and plot c) shows the correlation between the two.

showers. Plots c) and d) show the difference between the shower coordinates, and the projection of the beam from the vertex position to the calorimeter.

There are two components to the ΔY distribution. It turns out that the narrow peak at zero corresponds to the *downstream* bremsstrahlung, which occurs at "high" ν. Figure 4.43a shows the X_{vtx} distribution. The thin solid line is the total distribution, the shaded area is the piece corresponding to the narrow peak at $\Delta Y \approx 0$, and the thick solid line is the piece for $|\Delta Y| > 0.015$ m. The same description applies to the ν distributions, in plot b). It seems plausible that the narrow peak is due mainly to the downstream bremsstrahlung events, as indicated by 4.43a, since there is no error due to the bending of the beam in the CVM.[36] The broad distribution is the target-bremsstrahlung; it is broad because vertex position is uncertain, hence the displacement at the calorimeter due to the bending of the beam in the CVM.[37]

Figures 4.43c) and d) show the correlation between the shower center and the beam track, projected to the calorimeter. A vertex cut and an upper cut $\nu < 300$ GeV were applied. The correlation in Z, immune to the vertex uncertainty, is strong; the Y correlation is poor, due to the uncertainty of the bending in the CVM. (In fact, the difference $\Delta Y = Y_{sh} - Y_{bm}$ correlated well with the vertex position, in the magnet.)

---

[36]The difference between the muon impact point at the calorimeter projected from before and after the CVM is 6 cm.

[37]This is a rare case of where the background is a narrow peak on top of a broad signal!

140
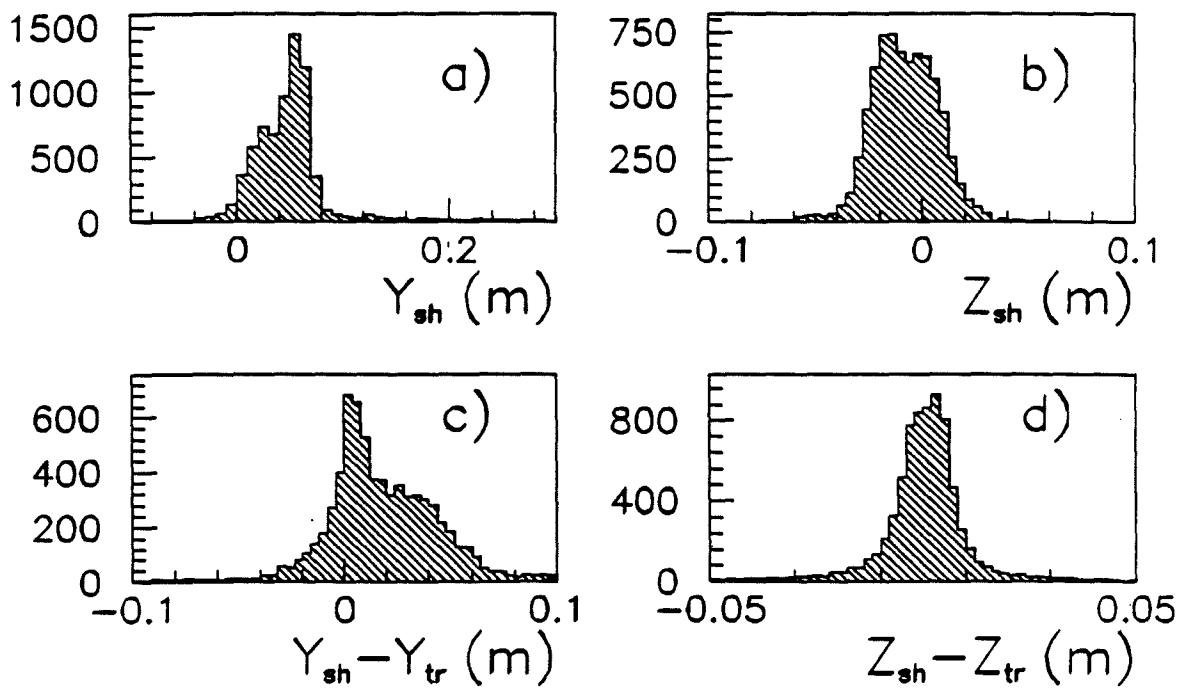
Figure 4.42: Coordinates of bremsstrahlung showers. Plots a) and b) show the Y and Z coordinates of the showers. Plots c) and d) show the differences between the coordinates of the shower and the beam, projected from the vertex to the calorimeter.
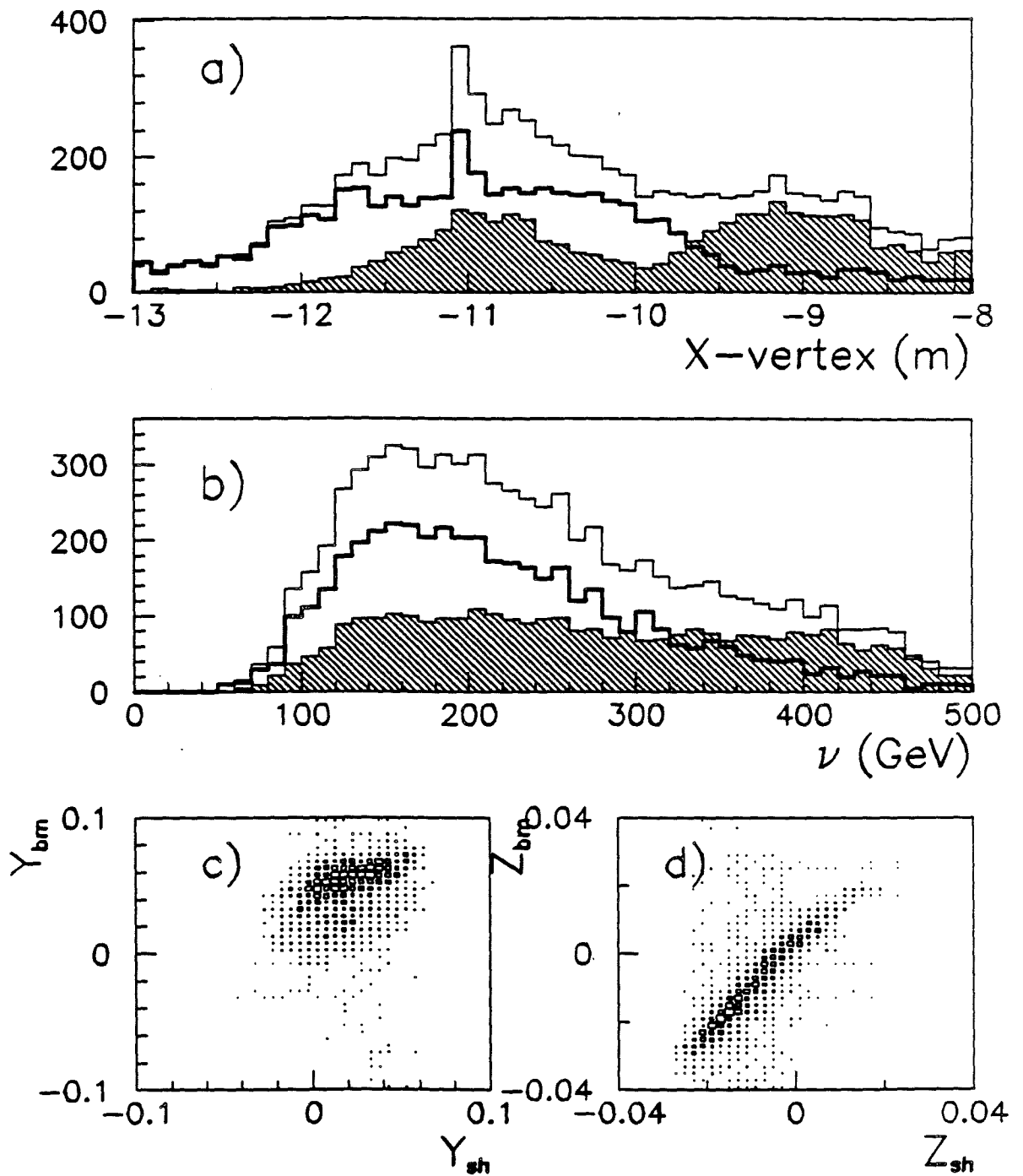
Figure 4.43: Cuts on $\Delta Y = Y_{sh} - Y_{bm}$ show a correspondence to target– and downstream–bremsstrahlung (plot a), which corresponds to low– and high–ν (plot b). Plots c) and d) show the correlations between shower and projected beam tracks, for low-ν, target events.

The distinctive signature of μe and $\mu\gamma$ events in the calorimeter have prompted many to use it as a filter against this "electromagnetic background" [Magill, Ryan, O'Day, Michael, Salvarani]. The cuts devised resemble those discussed in [Sch89d], and use a cut on E_{sh}/ν and the number of showers.

4.6.5 π^0 Signal

Deep-inelastic events are characterized by the copious production of pions. The mean total charged hadron multiplicity in E665 varies from 6 to 10 [O'Day, p.117], so the number of neutral pions should be about 4. All π^0s decay immediately into two photons, a large fraction of these (more than 60%) will strike the active area of the calorimeter. If both photons strike the calorimeter, then the invariant mass of the parent π^0 can be reconstructed:

$$m = \sqrt{E_1 E_2} \frac{d_{12}}{(X_{sh} - X_{vx})},$$

where E_1 and E_2 are the energies of the two photons, measured at X_{sh}, separated by a distance d_{12}.

The π^0 signal in deep-inelastic data was analyzed using a fraction of the LAT data [Ramberg].

4.6.6 Electromagnetic-Hadronic Event Separation

Several versions of simple calorimeter cuts exist for removing electromagnetic background events (μe scatters and bremsstrahlung) from a deep-inelastic sample. Most of these involve a cut on the calorimeter energy E_{cal}, the ratio E_{cal}/ν, and the number of showers, N_{sh}. This follows the suggestions in a study [Sch89d].

More refined cuts have been designed to eliminate two sources of electromagnetic background events. The virtual photon direction and energy is taken from the measurements of the incident and scattered muons, and, assuming it to be the starting point of an electron, the impact point at the face of the calorimeter can be estimated.[38] An empirical quantity is calculated:

$$\Delta_{DJ} = a \ E_{sh} \ \exp(-\frac{E_{sh}}{b}),$$

---

[38]A fast estimator of the electron trajectory called TRNSPT is used [Sch89a].

where the constants $a = 0.003$ m and $b = 105$ GeV were chosen by eye. If the distance D from the hypothetical electron impact point to the shower center is less than Δ_{DJ}, then the event is consistent with a μe scatter.

A similar cut is based on the co-planarity of the two muons and the photon in bremsstrahlung events. The coordinates of the shower are used to calculate a quantity called "planarity" (**P**) from the beam momentum vector $\vec{P}$, the scattered muon vector $\vec{P}'$, and the shower vector $\vec{K}$:[39]

$$\mathbf{P} \equiv (\hat{P} \times \hat{P}') \cdot \hat{K}, \qquad \text{where} \hat{P} = \frac{\vec{P}}{|\vec{P}|}, \quad \hat{P}' = \frac{\vec{P}'}{|\vec{P}'|}, \quad \hat{K} = \frac{\vec{K}}{|\vec{K}|}.$$

The planarity is a measure of the component of $\vec{K}$ perpendicular the lepton plane. (Bremsstrahlung photons and elastically scattered electrons should be in the lepton plane.) Plots of the planarity **P** versus E_{cal}/ν show a clear separation of "electromagnetic" and "deep-inelastic" events. (See figure 4.44.)

Another method of separating hadronic and electromagnetic events was devised recently, as part of a study of the muon reconstruction efficiency. One of the characteristics of deep-inelastic events is the high-p_T of the debris with respect to the virtual photon. In the horizontal plane, the distinction between low-p_T and high-p_T is not apparent due to the bending of particle trajectories by magnetic fields. In the vertical plane, however, p_T maps directly onto displacement. A deep-inelastic event has a larger spread of energy in the vertical direction than an electromagnetic event.[40]

The calorimeter showers provide a picture of the hadronization of the event, albeit only partial. A crude measure of the energy flow in an event can be formed from the position and energies of all showers. One can define two simple variables from the first and second moments of the shower coordinates:

$$F_Y \equiv \langle Y^2 \rangle_E - (\langle Y \rangle_E)^2 \qquad \text{and} \qquad F_Z \equiv \langle Z^2 \rangle_E - (\langle Z \rangle_E)^2,$$

where

$$\langle Y \rangle_E = \frac{\sum_{i=1}^N E_i\, Y_i}{\sum_{i=1}^N E_i} \qquad \text{and} \qquad \langle Y^2 \rangle_E = \frac{\sum_{i=1}^N E_i\, Y_i^2}{\sum_{i=1}^N E_i},$$

ditto for the Z moments. (Y_i, Z_i) are the coordinates and E_i the energy of the ith shower, and the sum extends over all N clusters in the calorimeter. Note that the

---

[39]The direction of shower vector $\vec{K}$ is taken to be along a straight line from the vertex to the center of the shower.

[40]This idea was the basis for the SAT secondary and monitoring filters, discussed in the software chapter. It also was used in a highly-selective calorimeter-based event filter, for obtaining a sample of enriched deep-inelastic events [Sch89b].
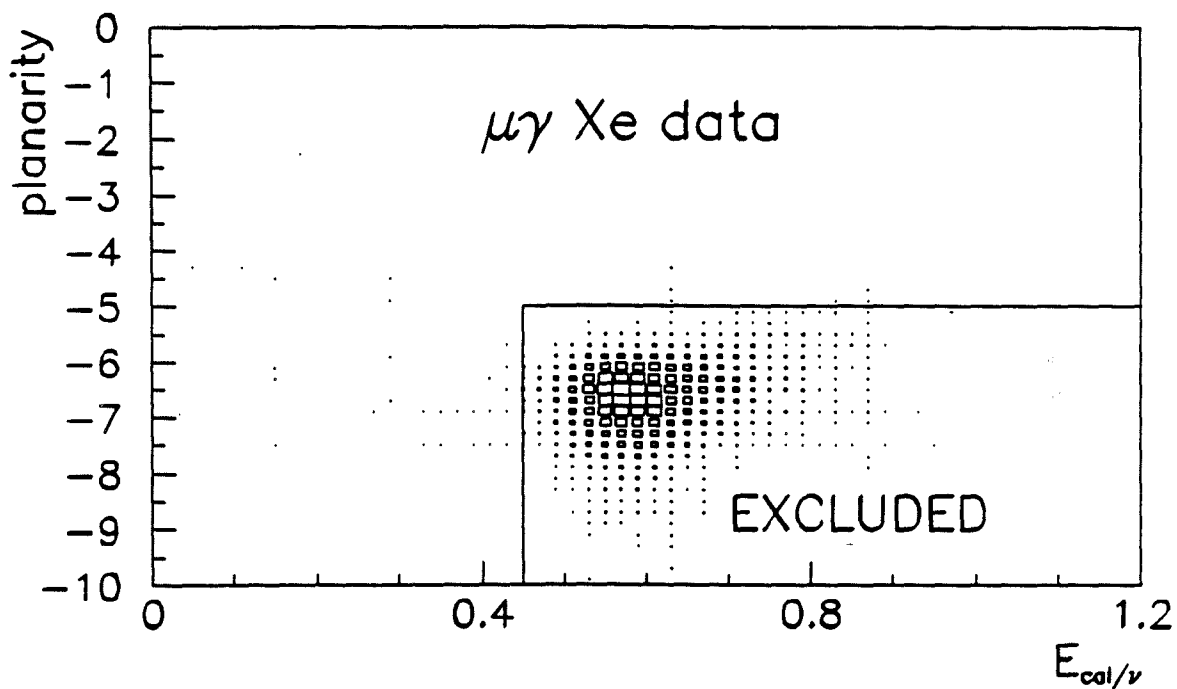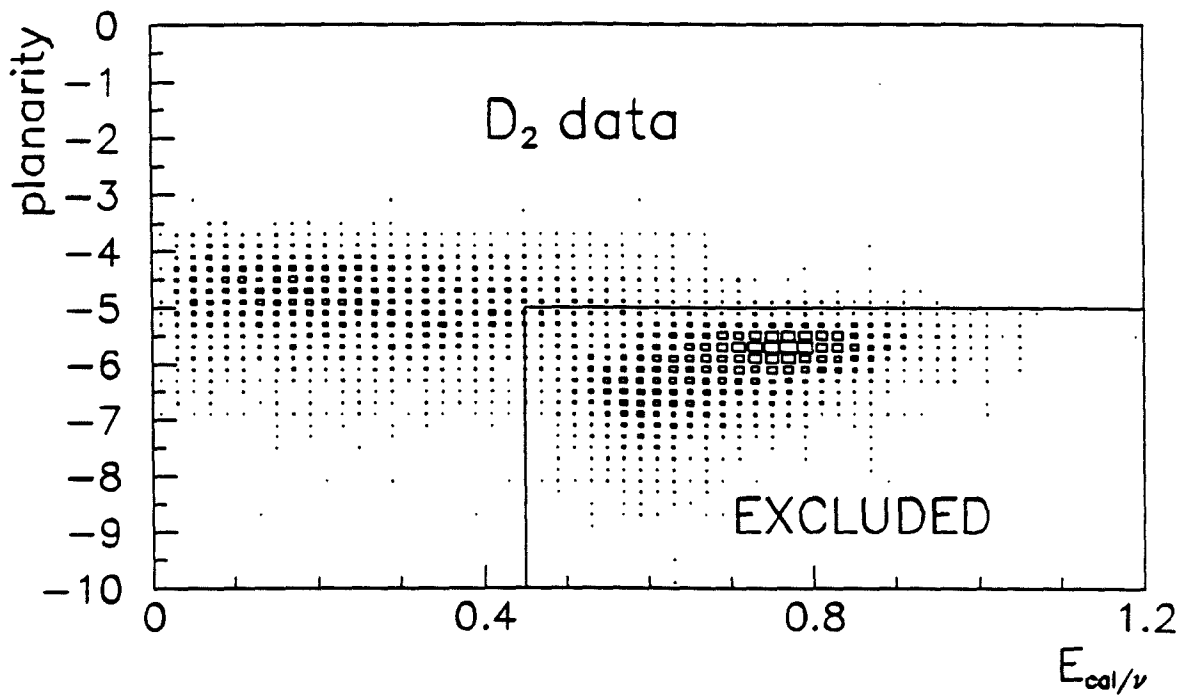
Figure 4.44: An example of the effectiveness of the planarity cut. (Plot kindly provided by Jaffe.)

variables F_Y and F_Z are independent of any track quantities; there is no sensitivity to track reconstruction, including the muon.

Figure 4.45 shows the distributions for F_Y and F_Z. Plot a) shows F_Y for deep-inelastic (i.e., multi-hadron) events (dark curve), and for μe events (shaded histogram). The light curve shows a distribution from raw PTMV events. Plot b) shows the same for F_Z. The magnetic field disperses the charged particles horizontally, causing an unclear separation of hadronic and electromagnetic events in F_Y. The quantity F_Z, however, gives a clear separation.

A cut of $F_Z = 10^{-6}$ was chosen, to differentiate between deep-inelastic and electromagnetic events. Plot 4.45c shows the track multiplicity and d) shows the ratio E_{CAL}/ν, above and below this cut. The differentiation is good.

4.6.7   Linearity

The linearity of the calorimeter is difficult to establish. A set of 1990 electron beam events were selected, with a tune energy of 35 GeV. Cuts were applied to select electrons, and the shower energy plotted versus the track momentum. Figure 4.46a) shows the result, together with a linear fit. The χ^2 of the fit is not good, and there is a significant nonzero intercept. Adding a quadratic term gives a much better fit, as shown in plot b). Based on these two plots, it is hard to say that the shower energy is proportional to the track momentum; the nonlinearity $1 - E/P$ is several percent at 50 GeV!. Further evidence that E_{sh} is not proportional to P_{tr} is shown in figure 4.46: the "intercept" $(E_{\mathrm{sh}} - P_{\mathrm{tr}})$ is energy dependent, as is the "slope" $(E_{\mathrm{sh}}/P_{\mathrm{tr}})$. The track momentum correlates strongly with the impact point, as shown in the figure, but the ratio $(E_{\mathrm{sh}}/P_{\mathrm{tr}})$, is relatively flat.

On the other hand, one can look at cross–sections of the shower-track correlation, and look for a shift in $E_{\mathrm{sh}}/P_{\mathrm{tr}}$. Figure 4.47 shows this ratio for a) $15 < P_{\mathrm{tr}} < 22$, and b) $30 < P_{\mathrm{tr}} < 35$. The gaussian peaks are equal within errors. The quadratic fit shown in figure 4.46 would suggest

$$\frac{E_{\mathrm{sh}}}{P_{\mathrm{tr}}} = -\frac{0.509}{P_{\mathrm{tr}}} + 1.182 - (7.46 \times 10^{-3})P_{\mathrm{tr}},$$

which has a value of 1.015 at $P_{\mathrm{tr}} = 18.7$ GeV, and a value 0.926 at $P_{\mathrm{tr}} = 32.1$ GeV. The two plots display different tails beyond the non-gaussian peak, which may be responsible for the curvature in figure 4.46. The different tails might be due to the different fractions of hadrons and electrons at different energies about the basic

146
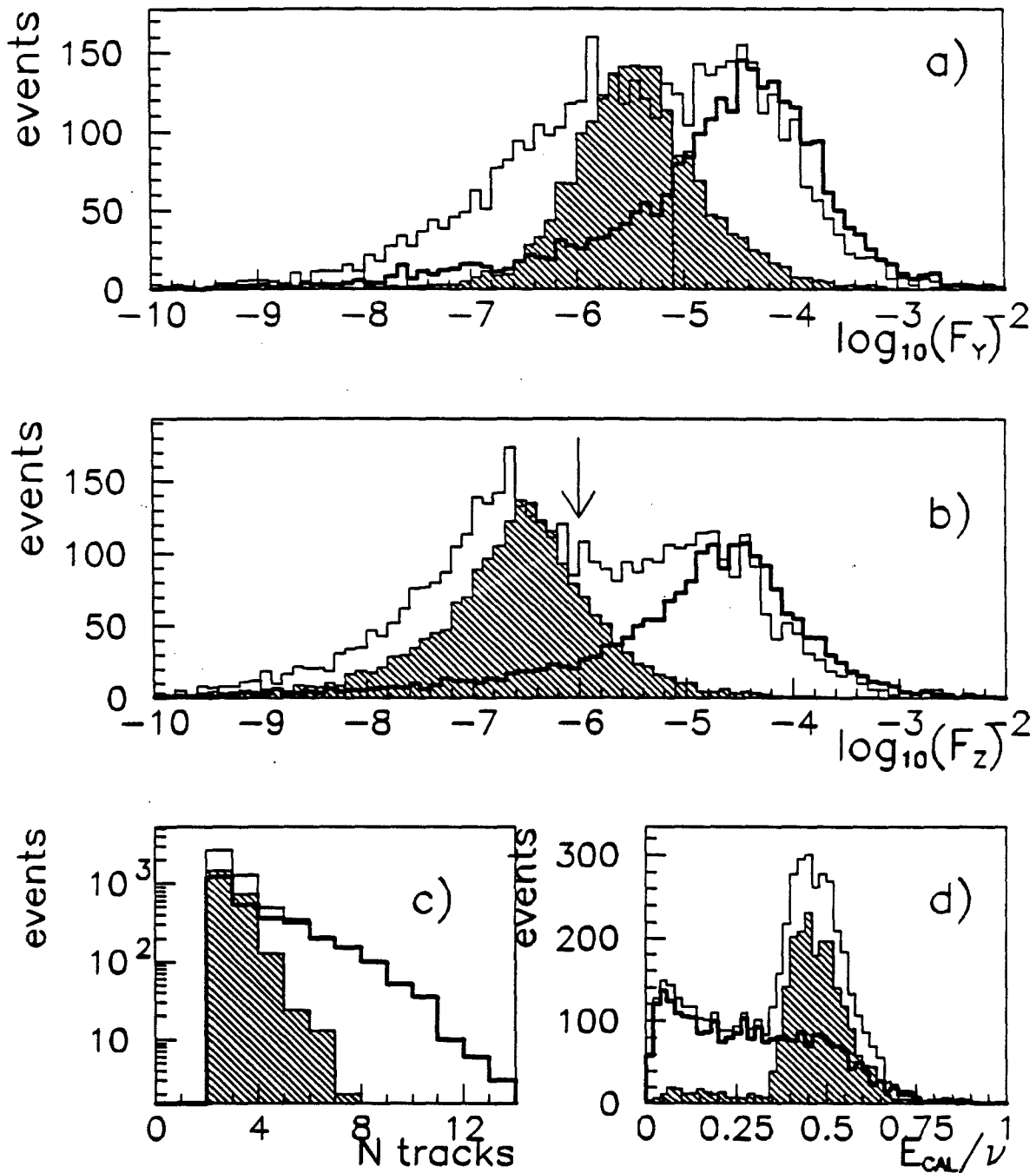
Figure 4.45: Distributions of the energy flow variables a) F_Y and b) F_Z, for electromagnetic events (shaded area), deep-inelastic events (heavy line), and unfiltered PTMV events (light line). Plot c) shows the track multiplicities obtained for a cut at $F_Z = 10^{-6}$, and plot d) shows the ratio E_{CAL}/ν.
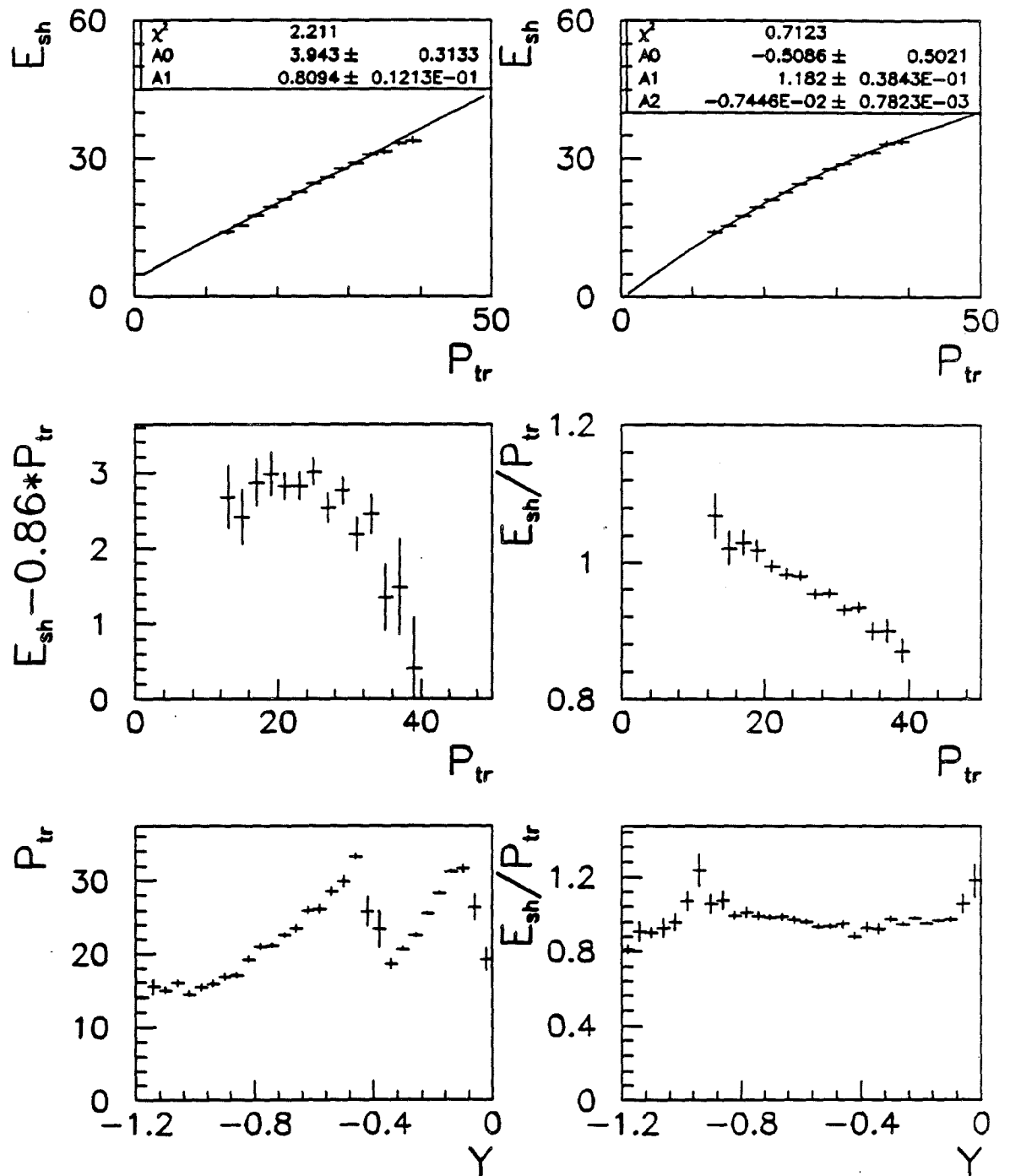
Figure 4.46: Apparent nonlinearity at low shower energies.

tune (35 GeV).[41]

Another tune at 15 GeV contains a high fraction of electrons, leading to a gaussian peak for E_{sh}/P_{tr}, as shown in figure 4.47b. This peak is lower due to lower gas gain.

4.6.8 Energy Resolution

The energy resolution of the calorimeter was first measured to be [Ramberg, p.72]

$$\frac{\sigma^E}{E} = 0.07 + \frac{0.44}{\sqrt{E}}.$$

This measurement was made using electron beam data, and bremsstrahlung events. Bremsstrahlung data have been used, also, and the results agreement with this value [Mel91d].

This result was disappointing, since the analysis of test beam data gave $\sigma^E/E \approx 0.3/\sqrt{E}$. Why is there a flat offset, and why is $\sigma^E \cdot \sqrt{E} \approx 0.44$ rather than 0.3? Several unwanted effects could be contributing to this problem.

- There were several dead bitubes in the calorimeter. The charge collected will vary according to which bitubes are sampled, so a sum over all will be broader than just one.

- There could be errors in gas gain corrections.

- There could be errors in the calibration of electronics constants at the level of pedestal subtraction, or gain correction.

- There could be errors in the high voltage settings.

- There could be excessive noise in the electronics.

- There could be nonlinearities.

All of these and other possibilities have been investigated, with none of them giving a clear explanation for the resolution. Many of these items have been handled

---

[41]Of course this could not explain the nonlinearity at high energies, as depicted in figure 4.21 on page 110.

Plot a) fit results:

χ^2		1.327	
Constant	29.60 $\pm$		2.034
Mean	0.9693 $\pm$	0.5830E$-$02	
Sigma	0.1107 $\pm$	0.5555E$-$02	

Plot b) fit results:

χ^2		0.8191	
Constant	42.38 $\pm$		2.810
Mean	0.9622 $\pm$	0.4412E$-$02	
Sigma	0.7672E$-$01 $\pm$	0.3962E$-$02	

Plot c) fit results:

χ^2		1.659	
Constant	113.4 $\pm$		3.557
Mean	0.9050 $\pm$	0.3034E$-$02	
Sigma	0.1186 $\pm$	0.2453E$-$02	
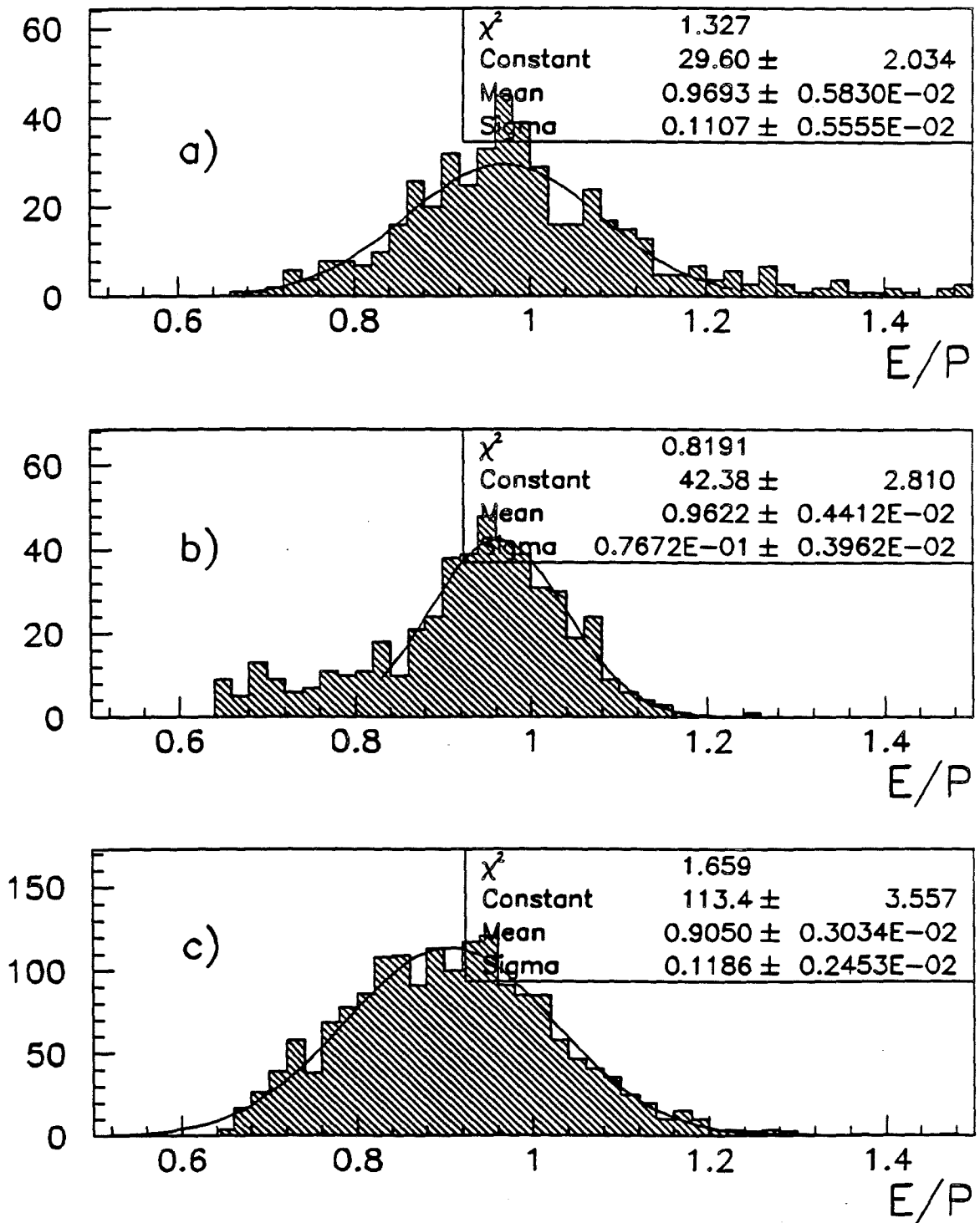
Figure 4.47: The ratio E_{sh}/P_{tr}, plotted for a) $15 < P_{tr} < 22$, and b) $30 < P_{tr} < 35$. Plot c) shows the same peak, for a different tune.

better in the 1990 run, so there is a hope that the energy resolution will be better for those data.

An illustration of the energy resolution as a function of energy is given in figure 4.48. The top plot shows the variation of the fitted gaussian width of the ratio $G = E_{sh}/P_{tr}$ as a function of P_{tr}, for 1990 electron beam data. The curve is simply $\sigma/E = 0.44/\sqrt{E}$. The middle plot shows the energy resolution measured from 1988 μe scatters. Ramberg's curve is displayed also; it is clear that a basic constants term such as 0.07 is needed to describe these data. The bottom plot shows an attempt to combine the μe and electron beam data; the latter clearly are lower than the former, so an *ad hoc* offset of 5% was added to the electron data, so that they join the μe data. The dashed curve is Ramberg's measurement, and the dash-dotted curve shows $0.05 + 0.44/\sqrt{E}$. There may be an indication that there is an additional term $\sigma/E \propto 1/E$.

Although the energy resolution is an important parameter for describing the calorimeter, it is difficult to determine because the gain of the calorimeter varies with position (due to e.g., dead bitubes), and the energy of reference electrons correlates with position. This may one of the main reasons why the resolution is poorer than expected.

4.6.9 Position Resolution

Some indication of the position resolution is given by the plots in figure 4.22. The measured resolution (using simple gaussian fits to the histograms) is summarized in table 4.6.

data sample	σ_Y (mm)	σ_Z (mm)
μe scatters, H_2	2.93 ± 0.11	3.88 ± 0.03
hadrons in DIS	10.7 ± 0.4	9.26 ± 0.24
Ramberg	10.3	10.3

Table 4.6: Measurements of the calorimeter position resolution.

There is an energy dependence to the position resolution, as shown in figure 4.49: the higher the shower energy, the better the position resolution.[42] The μe data show evidence of a double peak structure at high energies, due to the quantization of the coordinates from the pads. The intrinsic resolution certainly

---

[42]This explains the different position resolution obtained by different people.
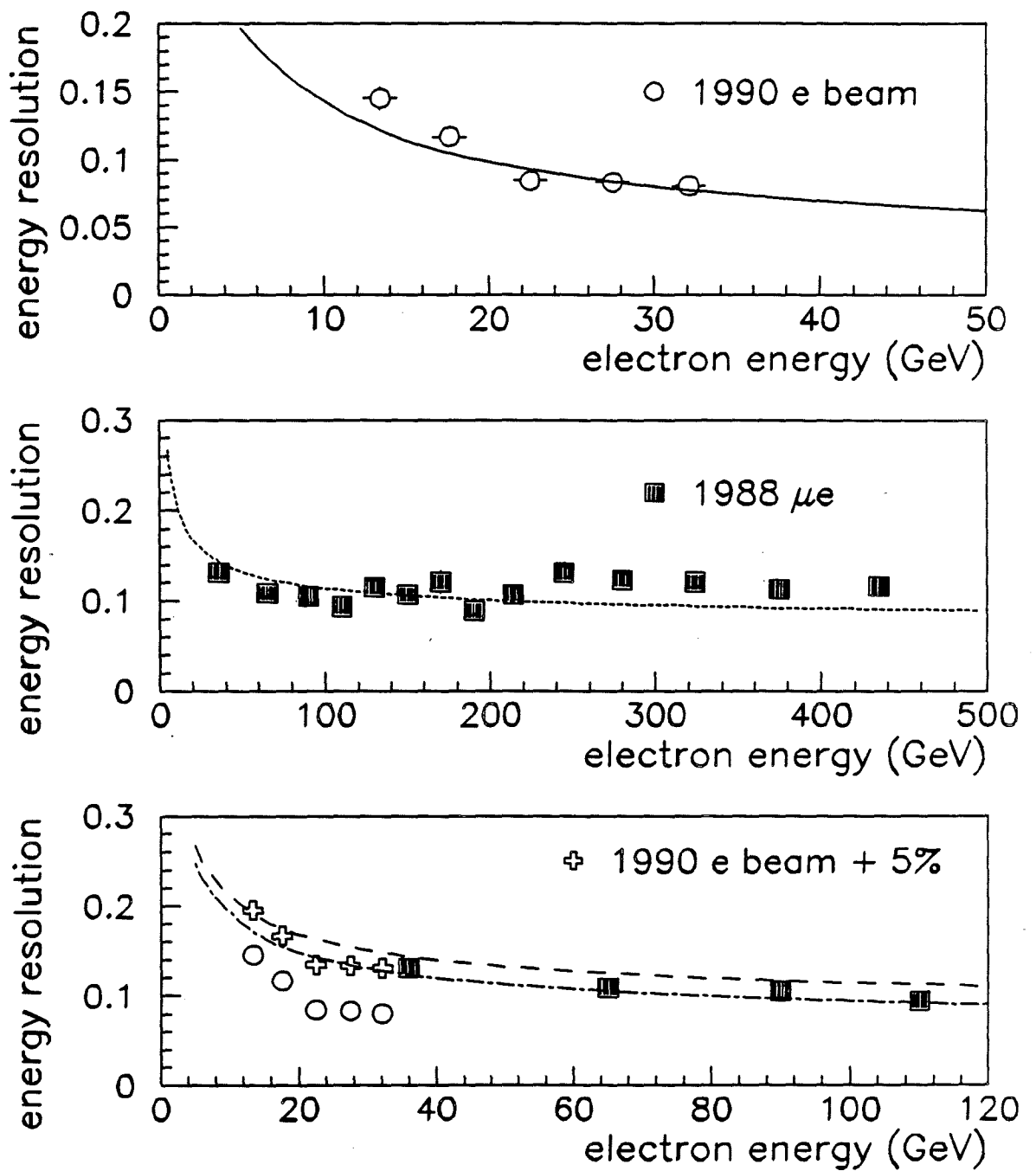
Figure 4.48: Calorimeter energy resolution, measured using 1990 electron beam data, and μe data from 1988.
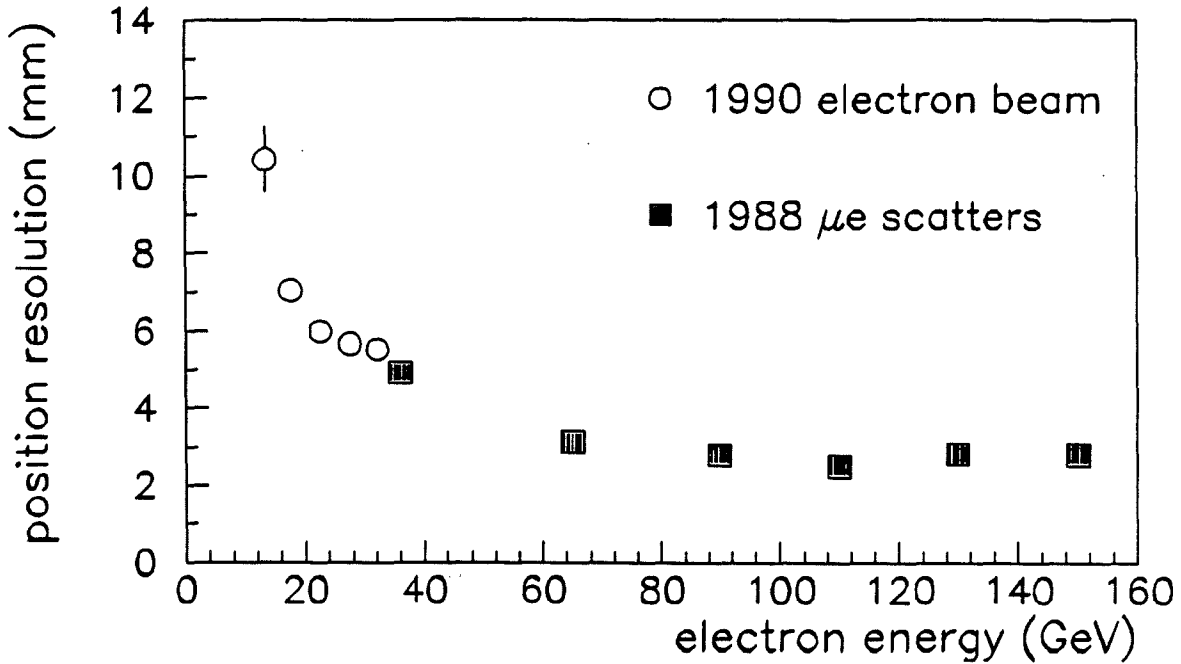
Figure 4.49: Improving spatial resolution as a function of energy.

decreases below 3 mm; at one point the two peaks were fitted separately, given $\sigma = 1.4$ mm at $P_{\mathrm{tr}} = 324$ GeV.

4.6.10   Longitudinal Profiles

Electrons should produce a smooth longitudinal profile, which changes in shape only slowly: the parameters vary as $\ln E$. Figure 4.50 shows longitudinal profiles for two incident energies, from 1990 electron beam data. The standard parametrization for the longitudinal shape is

$$\frac{dE}{dX} = E \; \frac{\beta^\alpha}{\Gamma(\alpha+1)} \; X^\alpha \; e^{-\beta X}.$$

The maximum of this function occurs at $X_{\mathrm{max}} = \alpha/\beta$, and the center of gravity at about $X_{\mathrm{cog}} = X_{\mathrm{max}} + 1$. The parameters α and β are expected to vary logarithmically with electron energy, and so the center of gravity increases slowly with energy, too. This can be seen in figure 4.50b. Another illustration is given in figure 4.51. The fit to figure b) is quadratic:

$$\text{center of gravity} = c_0 + c_1 P_{\mathrm{tr}} + c_2 P_{\mathrm{tr}}^2,$$
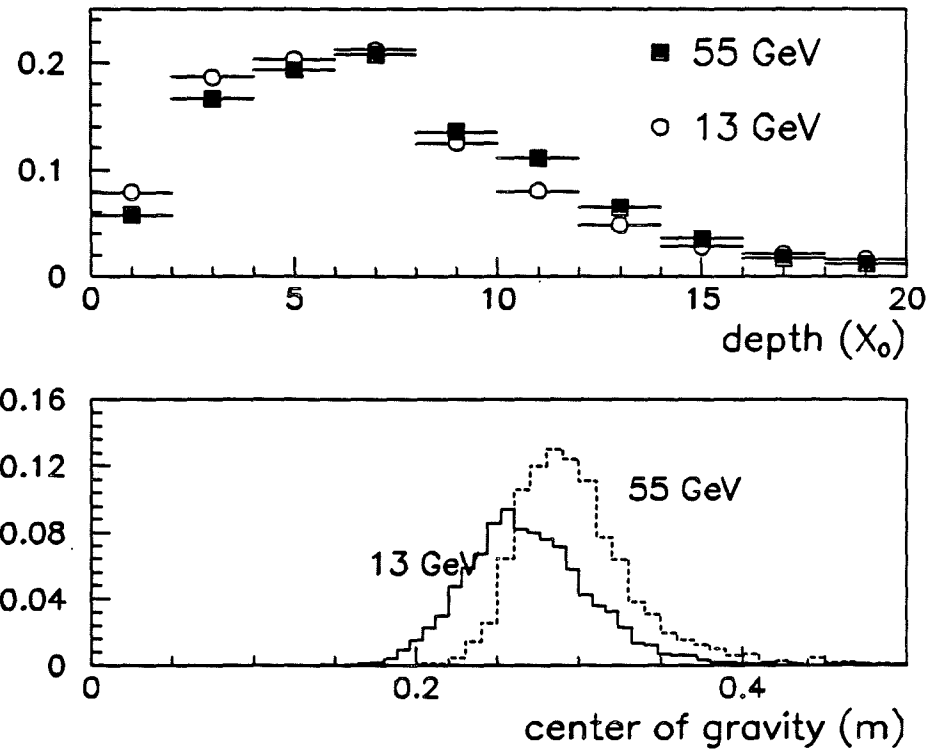
Figure 4.50: Electron longitudinal profiles at two different energies. Plot a) shows the energy deposition per two planes. Plot b) shows the longitudinal center of gravity.

mean longitudinal center of gravity
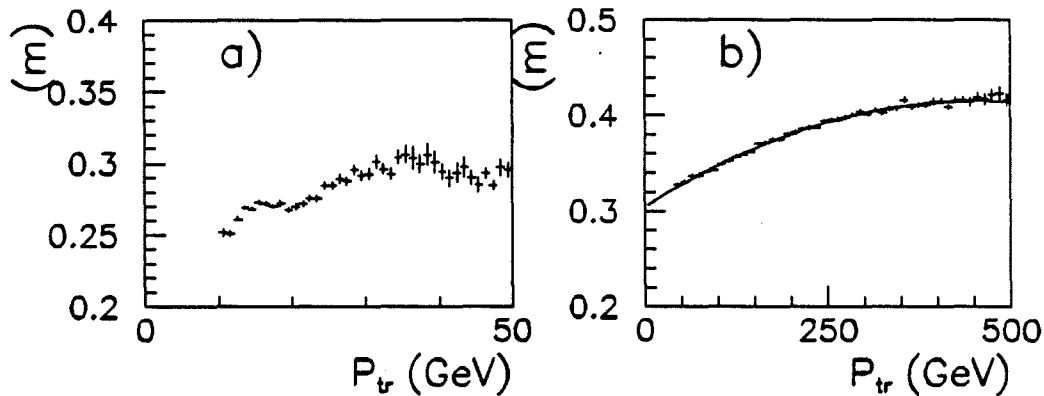
Figure 4.51: Slow increase in the longitudinal center-of-gravity as a function of energy, a) for electron beam events, and b) for μe events. The quadratic fit is described in the text.

with $c_0 = 0.304 \pm 0.001$ m, $c_1 = (4.87 \pm 0.12) \times 10^{-4}$ m/GeV, and $c_2 = (-5.36 \pm 0.25) \times 10^{-7}$ m/GeV^2.

4.7 Electron-Hadron Separation

The calorimeter can be used for particle identification to the extent that it can separate electrons from hadrons and muons, and photons (neutral electromagnetic showers) from everything else. In the following sections, several variables which may distinguish between electromagnetic and hadronic variables are presented.

4.7.1 Shower Energy and Track Momentum

Electrons always are absorbed in the calorimeter, while hadrons usually pass through, or at most deposit a small fraction of their energy in the calorimeter. Figure 4.52 shows the shower energy plotted versus track momentum, a) for electrons, and b) for pions.

The most straight forward discriminator between electrons and hadrons is the ratio $\phi = E_{sh}/P_{tr}$, expected to peak at one for electrons, and at zero for hadrons. Distributions of this variable are shown in figure 4.52c.

155
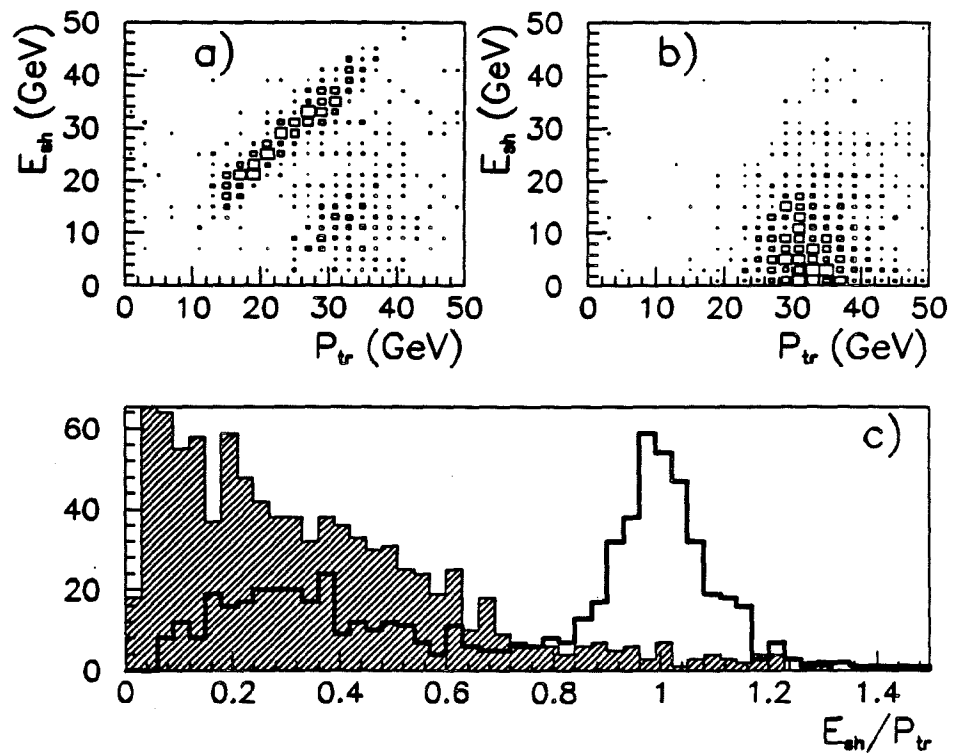
Figure 4.52: Distributions of the shower energy plotted versus track momentum, a) for electrons, and b) for hadrons. Plot c) shows the ratio $\phi = E_{sh}/P_{tr}$, for electron candidates (solid line), and hadron candidates (shaded histogram).

4.7.2 Shower Shapes

The difference between the longitudinal shapes for electrons and hadrons was mentioned at the beginning of this chapter. An illustration was given in figure 4.9, on page 78. The difference is striking, and reflects the fact that electrons are interacting electromagnetically, and that their shower behavior is governed by the radiation length; while, hadrons are interacting hadronically, and the shower behavior is governed by the interaction length.

Many measures can be invented to differentiate between electromagnetic and hadronic longitudinal shower shapes. For example, the ratio of the energy in the back half of the calorimeter to that in the front half is quite different for the two:

$$B \equiv \frac{\sum_{i=1}^{10} E_i}{\sum_{i=11}^{20} E_i}$$

which is about 2/3 for electrons, but extends to much larger values for hadrons. The distribution for B is shown in figure 4.53.

Another measure is the (longitudinal) center-of-gravity, defined to be

$$\Lambda \equiv \int_0^{+\infty} dX \, X \, \frac{dE}{dX} \approx \sum_{i=1}^{20} i \, E_i.$$

Distributions of Λ are shown in figure 4.53.

Electron showers begin within the first two layers, while hadron showers can begin anywhere in the calorimeter. The starting point $X_{0.05}$, mentioned earlier, can be a good discriminator between electrons and hadrons. It can be defined, for example, as the depth up to which 5% of the total shower energy has been deposited:

$$\frac{1}{20} = \frac{\int_0^{+X_{0.05}} dX \, \frac{dE}{dX}}{E_{sh}} \approx \frac{\sum_{i=1}^{X_{0.05}} E_i}{E_{sh}}.$$

See figure 4.53 for distributions of $X_{0.05}$.

Hadronic showers tend to be more diffuse, more spread out laterally, than electron showers. The "breadth" might help distinguish between them:

$$\Pi \equiv \frac{\sum_{k=1}^{N} r_k E_k}{\sum_{k=1}^{N} E_k},$$

where the sum is over pads $\{k = 1, \ldots, N\}$ in a cluster (shower), and r_k is the distance of the kth pad from the center of the cluster. The breadth Π is for electrons and hadrons is plotted in figure 4.54.

157
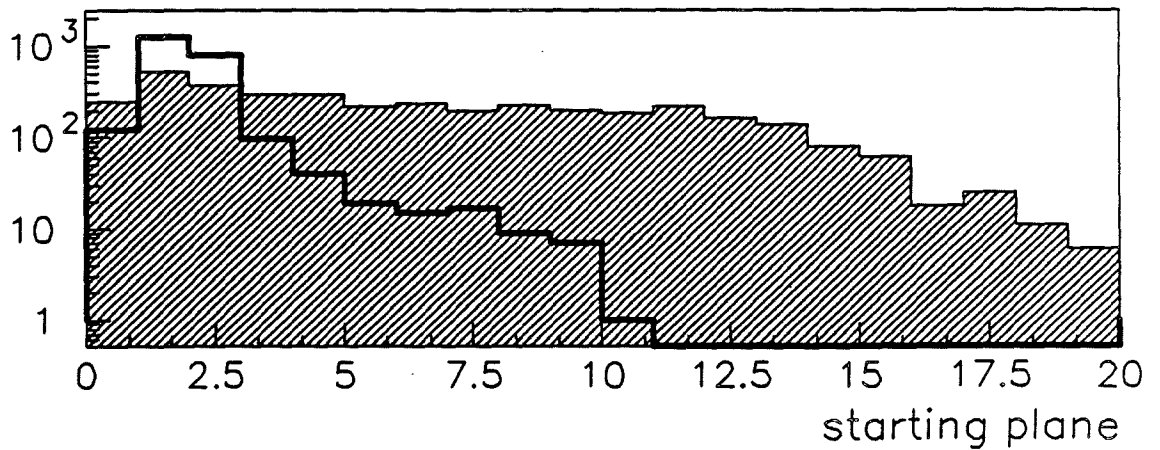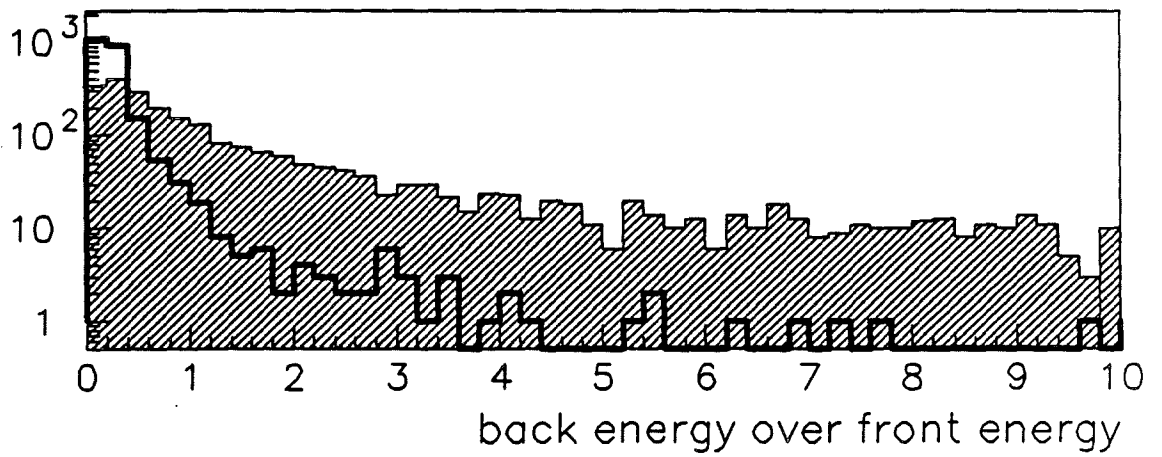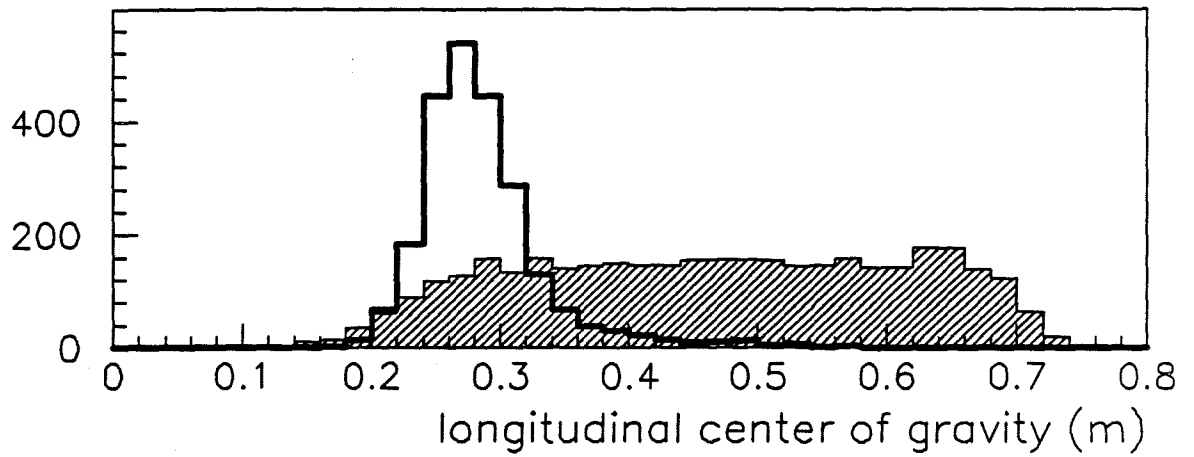
Figure 4.53: Distributions shower shape parameters, for electrons and hadrons. The shaded area indicates hadron distributions, and the thick solid line indicates electrons.

variable		cut value
shower energy over particle energy	ϕ	0.7
center-of-gravity	Λ	0.35
back energy over front energy	**B**	1.5
starting point	$X_{0.05}$	6.0
breadth	Π	0.04
mean energy per pad	η	0.9

Table 4.7: Summary of cuts for separating electrons and hadrons.

In a similar sense, the number of pads per GeV of energy can distinguish electrons and hadrons:

$$\eta = \frac{N}{E_{sh}}$$

is shown for electrons and hadrons in figure 4.54.

A slow, logarithmic rise in most of these shower shape variables has been observed. (See figure 4.51, for example.) If greater sensitivity is required, then taking this rise into account will be necessary.

4.7.3 Cuts

The distributions of shower shapes and of $\phi = E_{sh}/P_{tr}$ indicate where cuts for separating electrons and hadrons should be made. Values were chosen by eye, and are listed in table 4.7.

4.7.4 Photons

At the relatively crude level developed here, photons may be regarded as "neutral electromagnetic showers," which means that they pass all the shower shape cuts for electrons, and do not match any track.

4.8 Neutral Energy Jets

As was stated at the beginning of this chapter, the primary motivation for building the calorimeter was its enhancement in studies of hadronic jets. The calorimeter
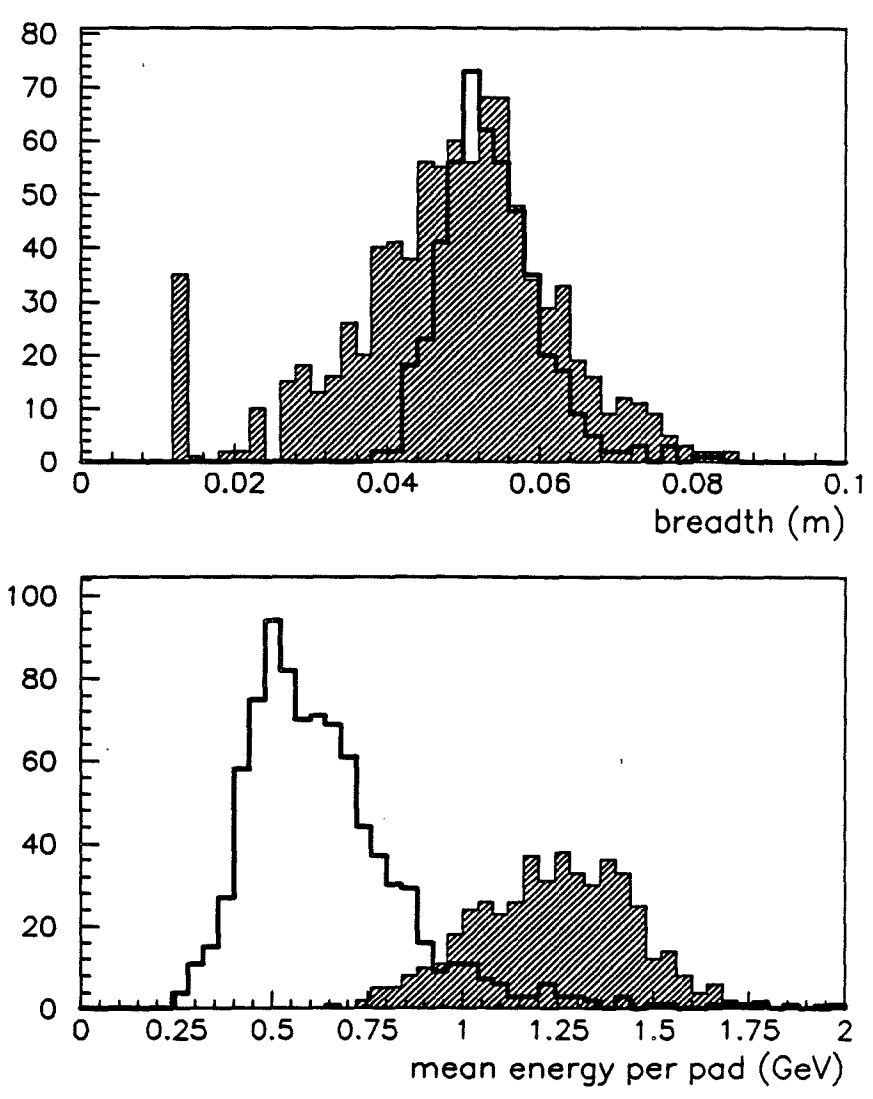
Figure 4.54: Distributions shower shape parameters, for electrons and hadrons. The shaded area indicates hadron distributions, and the thick solid line indicates electrons.

information has been applied quite successfully to that end, despite the many technical difficulties described above [Michael]. He found that the addition of neutral energy to the determination of jet axes was a very important step, eliminating the need for any severe multiplicity cuts, such as those imposed in other analyses [Jansen]. This is certainly one of the biggest successes for any single detector in E665.

4.9 Analysis Code

This section provides a brief overview of the calorimeter analysis code. The progress of an event from raw form to physics quantities is depicted in figure 4.55. First the data is decoded, and then translated. Translation involves several steps, including corrections for gas gain, dead channels, and oscillations. The translated data present the normalized readings for pattern recognition (cluster finding). After showers have been located, their shape parameters are calculated. All information about the clusters is stored in the LGLB banks. The cluster descriptions are used for sundry physics purposes, such as electron/hadron separation, photon identification, end event characterization. A subset of the clusters pass photon cuts, and are the basis for π^0 reconstruction and jet studies.

Overviews of the organization of code in E665 can be found elsewhere. The basic decoding routines are kept in the UDPAM, and the rest is in the EAPAM. Code for processing interspill calibration and monitoring data is stored in the CPAM.

4.9.1 Decoding

Decoding calorimeter raw data is the same in principle as for other detectors,[43] except that the calorimeter "DMA" is really a complete subevent, containing a complete fastbus data buffer. There is the standard header at the beginning. Two sections follow the header, one for each fastbus crate. There are a few words at the beginning and end of each section, containing the run and event correlator module words. These words for the east crate are checked by the concatenation machine, and it is important that the words from the west crate be checked offline.

After the correlator words come the ADC data. Since the calorimeter did not operate in zero-suppressed mode, there are ninety-seven words per ADC: ninety-six data words (no addresses) and one separator word, which contains the ADC error status. There are thirteen ADCs per crate.[44]

The decoding routine extracts the fastbus subevent from the entire event using calls to standard routines. It marches through the event, checking run and event numbers, and looking for the separator words at the proper places. It checks the

---

[43]See the software chapter

[44]For the 1990 run, an ADC was added to each crate for the SUM Wall signals. The decoder was modified to reflect this run dependence.

```
┌─────────────────────────────────────────────────┐
│                    raw data                      │
└─────────────────────────────────────────────────┘
                         │
                         ▼
┌─────────────────────────────────────────────────┐
│                    DECODE                         │
│           extract and unscramble DMA              │
└─────────────────────────────────────────────────┘
                         │
                         ▼
┌─────────────────────────────────────────────────┐
│                   TRANSLATE                       │
│        subtract pedestals, fix oscillations       │
│        apply electronics and gas gain factors     │
│        correct for dead channels                  │
└─────────────────────────────────────────────────┘
                         │
                         ▼
┌─────────────────────────────────────────────────┐
│              PATTERN RECOGNITION                  │
│              find pad clusters                    │
│              measure shower shapes                │
└─────────────────────────────────────────────────┘
                         │
                         ▼
┌─────────────────────────────────────────────────┐
│             PARTICLE IDENTIFICATION               │
│             select photon candidates              │
│             designate electrons                   │
│             reconstruct two−photon masses         │
└─────────────────────────────────────────────────┘
                         │
                         ▼
┌─────────────────────────────────────────────────┐
│                    physics                        │
└─────────────────────────────────────────────────┘
```
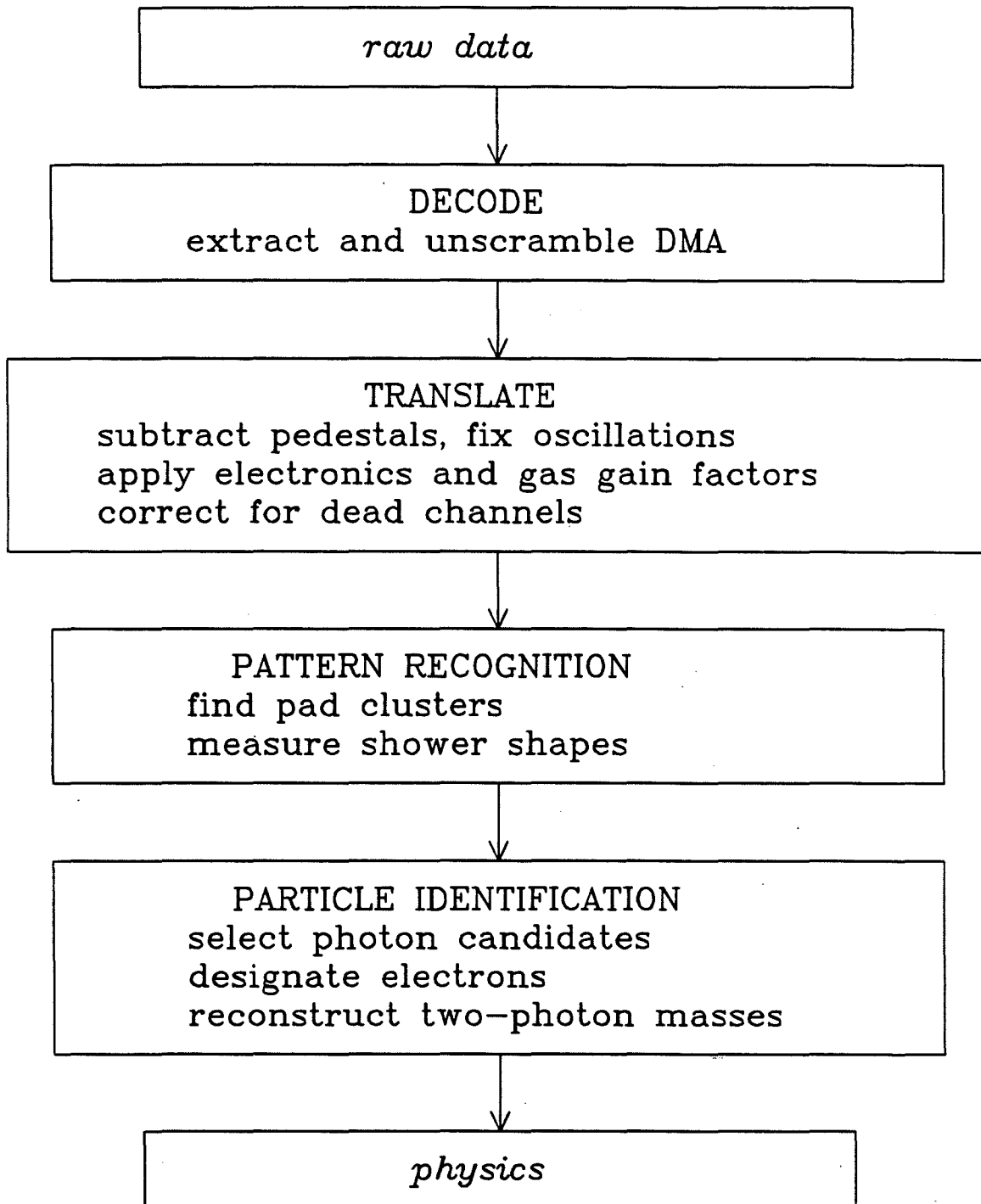
Figure 4.55: Flow diagram of calorimeter analysis.

separator words for any error status. Each ADC digitizes either pads, bitubes, or individual anode wires; which element depends on the slot number. For a given element, a routine to map the channel number onto the offline numbering scheme for pads, bitubes, or wires. The reading for the given element is stored in an array. After all channels in all ADCs have been processed, the arrays are transferred to LDEC banks.

4.9.2 Translation

The first step in translation is to subtract pedestals. The range bit for each word in the LDEC banks is checked, and the appropriate pedestal subtracted.[45]

The pedestal-subtracted values can be massaged by the routines for removing bitube oscillations. These must be run after pedestal subtraction, and before electronics gains are applied.

Next the electronics gains are applied. If the reading in a given channel is in the low range, and is below the pedestal subtraction threshold, then the channel is ignored (it's considered empty). Otherwise, the appropriate slope is applied to the pedestal-subtracted reading, according to the range bit. Also applied is the absolute scale factor, κ^r. The values for non-empty channels are stored in the LCOR bank.

Next a gas gain correction factor is calculated, based on the current pressure and temperature. (These readings are stored in a disk file, which is then read into memory, and stored in long-lived Zebra banks [Sch90a].) All channels are scaled by this correction factor.

(A plane-dependent correction for changes in high voltage can be calculated, and applied to bitube channels, but in practice this was not done for the 1987-88 run.)

Finally, adjustments to the translated data are made for known dead channels. At a simple level, the dead channels must be added to the list of hit channels if their neighbors (longitudinal for bitubes, transverse for pads) have fired. The correction becomes slightly intricate in practice because the addition of a bitube must result in the increase of the energy of pads above it, *if* the bitube high voltage was disconnected. If the amplifier was at fault, then the pads do not need to be

---

[45]There is a subtlety regarding high range pedestals, discussed earlier in this chapter. For details, see [Sch89c].

adjusted. The situation becomes more complex when more than one shower hits a dead bitube. In the end, no simple prescription is completely satisfactory.

4.9.3 Calibration Constants

Several data files are read by the calorimeter analysis code. These contain basic or supplementary calibration constants. All are formatted files that can be modified with an editor. No file is opened and left open; its contents are stored in common blocks or Zebra banks.

The electronics calibration constants are stored in files named FEEnnnnn, where nnnnn is the run block number. These are copies of the direct-access files the interspill calibration tasks use. They are organized around ADCs, and must be rearranged in accordance with the offline numbering scheme. The file FEB00000 contains special high-range constants, created to amend the lack of high-range intercepts in some channels, as described earlier. Similarly, the low-range pedestals produced from halo events are stored in the FEAnnnnn files.[46]

The file LVSCON contains the calibration constants for the pressure transducer, temperature probes, and high voltage supplies. These constants are used when making the pressure and temperature files, called FEPnnnnn and FETnnnnn. These files are condensed records of the reading stored in interspill events. There are several steps to making them, as described in [Sch90c]. The high voltage supply calibration constants are stored in FEBnnnnn files, and the voltages themselves are listed in FEVnnnnn.

The list of dead channels is given in the file CALDEAD.

Important analysis parameters may be changed in the file CALPARAM, and the options available in analysis are steered through the CALCTL file.

4.9.4 Cluster Finding

Originally the intent was to find clusters using the pad towers and bitube towers separately. A sophisticated routine was written for finding pad clusters. It starts by finding a seed pad, and searching for a local maximum. Given a local maximum,

---

[46]There are four programs, PEDA, PEDB, PEDC, and PEDD, for obtaining good low-range pedestals. These have been released in the example calorimeter area.

all contiguous pads with enough energy are associated with the local maximum. Other local maxima are sought; pads can be associated to more than one cluster. When all locally maximum pads have been built into clusters, the algorithm enters an arbitration stage. In this stage the energy in pads belonging to two or more clusters is assigned to those clusters based on the distance of the pad from the estimated cluster centers, and on the energies of those clusters. At the end of the arbitration stage, cluster positions and energies are recalculated.[47]

An alternative routine for finding clusters of pads was written [Ramberg, p.98]. It employed techniques from network theory, but lacked an "arbitration" stage, and was less successful at finding overlapping showers.

Efforts to write a routine for finding bitube clusters never succeeded. The main obstacles are the coarse granularity of the bitubes, and the substantial probability that the pattern of showers on the face of the calorimeter will lead to ambiguous cases. These ambiguities may be overcome by trying to match projections based on amplitudes. This approach would be very difficult, however, with dead bitubes, and was therefore not developed.

The individual anode wires were installed to help locate the centers of showers more accurately. This capability was never developed.

The final list of clusters are a copy of the pad clusters found by the Nickerson or the Ramberg routines. These clusters are mapped onto bitube towers to obtain measures of the longitudinal shower shape. The clusters and shape parameters are stored in the "energy glob" bank, LGLB.

4.9.5   Particle Identification

The shower shapes are stored in the LGLB bank are the basis for electron-hadron separation, as described later. Parametrizations are used to estimate the probability that each shower is electromagnetic or hadronic, according to a certain set of cuts. These probabilities are stored in the LGLB bank.

A simple attempt to match showers with tracks is made, with the result stored in the LGLB bank. Ambiguities are ignored.

---

[47]The original version of this routine, used in other 1987 analyses, did not handle correctly the case in which a pad belonged to three clusters. This lead to nonsense results (e.g., showers of negative energy). The bug eventually was fixed [Sch91a].

A subset of the clusters in the LGLB bank pass the photon cuts. These are copied to the LPHO bank, along with estimates of the uncertainty of the kinematic quantities of the candidate photons.

All distinct pairs of photons are used to calculate invariant masses, according to the formula

$$m = \sqrt{E_1 E_2} \frac{d_{12}}{(X_{sh} - X_{vx})}.$$

The LPIZ bank is filled with these masses.

4.9.6   Monte Carlo Simulation

Test beam data were studied extensively, to derive parametrizations of showers, *and* their fluctuations. The plan was to generate fake showers with accurate, empirical average and fluctuating energy densities [Nic84c, Nic84b]. The battle against systematic effects in the real calorimeter, and in other aspects of E665 analysis, left no time for more work in this direction. No useful simulation of showers in the calorimeter using parametrizations was realized.

Extensive studies of showers using GEANT were carried out, with several interesting results [Ram87a], but it was never clear to what extent the GEANT model resembled reality. (Certainly the technical difficulties discussed in this chapter were not simulated.) Another problem with using GEANT was the expense: a single shower can require a tens of MIPs to generate.

Simulations of the most basic response of the calorimeter were first described in [Michael]. Known resolution functions were applied to Monte Carlo photons striking the calorimeter. The smeared photons were used for calculating acceptances, etc.

These techniques have been developed further [Mel91c, Mel91d, Mel91a]. Although only the *response* of the calorimeter (i.e., parts of the LGLB bank) is being simulated, not the calorimeter information itself (i.e., the input to clustering routines). It is hoped that this will be adequate for understanding the contribution of calorimeter clusters to jet determinations.

4.10 Poetic Endeavors

Upon the occasion of the completion of the twentieth plane, the calorimeter crew celebrated with champagne (of course), and original limericks. The best was composed by Ramberg, quoted here in full [CAL]:

"It's E665 that I like the least,"
said St. John, though he was deceased.
"It's the numbers I fear,
cuz God said in my ear,
that it's one step away from the beast."

Chapter 5

Software

The days when particle physics could be done with a ray of sunlight and a prism have passed – we do not even count scintillations on a screen any more. Instead signals yielded by sophisticated apparatus are recorded on magnetic tape, and processed using equally sophisticated computer programs. We attempt to describe the methods used to record data while the beam was zipping through the hall, and those used for reconstructing the events, much later on.

5.1   Online Software and Data Acquisition

The quality of the data available for offline analysis is a strong function of the online data acquisition system. The system put together by E665 was relatively complex, consisting not only of standard devices for extracting information from the apparatus, but also highly automated data logging programs. Monitoring of the apparatus and the data occurred at several levels.

5.1.1   Camac and Fastbus Devices

The wire chambers, scintillators, calorimeter, and other detectors produce electrical signals in response to charged and neutral particles. These signals must be collected and recorded on tape (the function of online data acquisition), so that they can be used to reconstruct the original event (the function of offline data analysis).

Camac and Fastbus modules are used to interface the detecting devices to the data acquisition computer. The modules fall into three broad categories:

Latches record the fact that a signal passed above a given threshold.

ADCs digitize the amplitude of a signal.

TDCs digitize the time elapsed between a start (e.g., trigger) time and the arrival of a signal.

All these modules are organized in a series of crates which constitute branches and which are connected to a computer bus. In this sense they are peripheral devices just like a tape drive or printer.

Each module is specified by a unique address (B, C, N), where B = branch, C = crate, and N = slot number in the crate. Most modules respond to more than one command, each specified by a function code, F. Sometimes parts of a module can be specified by a subaddress, A. In order to extract the data stored in a module, a computer program causes the (B, C, N, F, A) words to appear on the bus, along with a strobe signal. The designated module responds by placing its data on the bus, which the program then reads and stores in a buffer. To set up the module for the next event, a similar (B, C, N, F, A) code is put on the bus, but in this case no data is read.[1]

5.1.2   Triggers and Spill Structure

The read-out of all the Camac and Fastbus modules is initiated by a trigger – this is one of its primary purposes. There are supposed to be two steps to the trigger – in fact, two trigger signals. This was the plan (see figure 5.1) :

1. The "level one" trigger was preliminary – it indicated that relatively loose requirements were satisfied by the event. This signal caused all Camac and Fastbus modules to block further input, and digitize any signals present at their inputs.

2. If more stringent trigger requirements were met, then a "level two" trigger was produced, which caused the online computers to begin reading out the

---

[1]This description neglects details about LAMs, Q- and X-status, but schematically applies to both Camac and Fastbus systems.

Camac and Fastbus modules. If these requirements were not met, then a "fast reset" signal was sent to all modules, and the block on further input was removed.

In fact, due to problems with the hardware, the second level trigger selection was not present for either large-angle or small-angle trigger. As indicated in figure 5.1, the level two trigger signal was just a copy of the level one trigger. E665 ran with a "simple" scintillator trigger, of one level only.

Triggers occurred only when beam was in the hall – and not just because there was otherwise no beam in the hall. The beam was delivered during a spill lasting a little over twenty seconds. The beam was spilled once every minute (actually, 57 seconds). The state of Camac and Fastbus, and the front-end environment was bimodal : there was a spill period during which standard data acquisition proceeded exclusively, and an interspill period, during which a variety of monitoring and calibration tasks had a chance to run. During the interspill period, triggers were gated off, and during the spill period, interspill tasks were suspended.

The signal for spill/interspill states was provided by the accelerator, and was called an "A-interrupt" in the context of the Bison Box devices and associated software. The triggers constituted "B-interrupts." The A-interrupts caused spill setup tasks to execute, and interspill tasks to hibernate. At the end of a spill, they caused spill summary devices to be read. B-interupts caused Camac commands to be executed which acquired the data from the apparatus.

5.1.3   Monitoring

Analysis of experimental data must deal with two kinds of errors – statistical *and* systematic. As a consequence, it is not enough merely to log events to tape: the performance of the apparatus and other experimental conditions must be monitored concurrently. By taking important variations into account, systematic effects can be reduced. Sometimes this is done explicitly, as when the calorimeter gas gain is adjusted for changes in pressure. More subtle effects must be studied also, such as the efficiency of a wire chamber as a function of time. To provide the data for the necessary studies, monitoring data are logged to tape along with the true physics events. These data also are packaged as events. In simple cases such events are similar to physics events; only the trigger mask is different.[2] For example, halo muon events are logged to tape for the purpose of monitoring chamber

---

[2]The trigger mask is explained later.
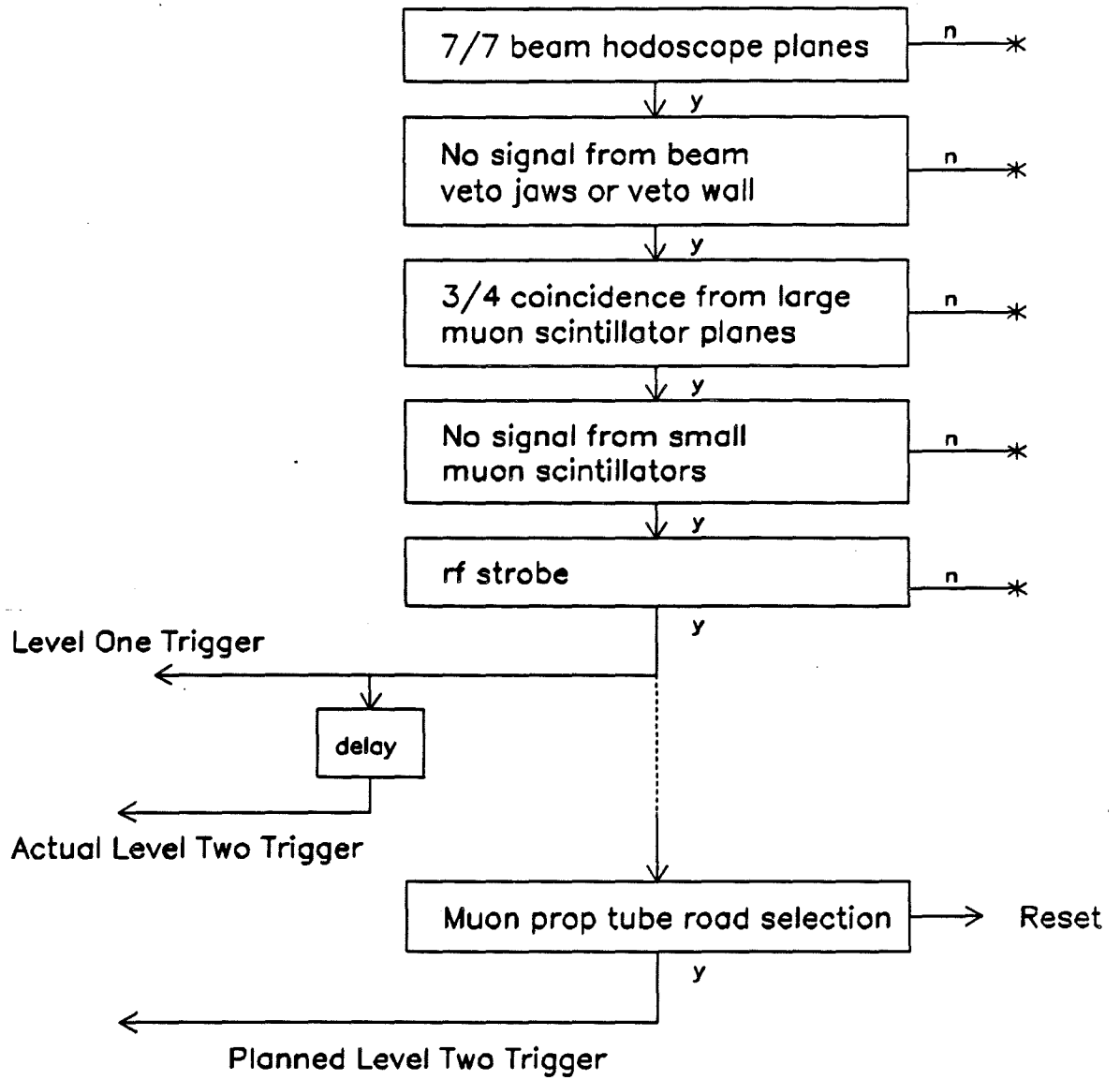
Figure 5.1: Flow chart showing the LAT decision tree. The SAT decision tree was similar.

performance.

Other kinds of monitoring data are generated between spills when the detector is quiet. These data are packed into interspill events, which are logged to tape as they come.

If a serious systematic problem appears during data taking (e.g., a detector fails), then one assumes skeptically that the data cannot be corrected for the resulting effects. Such data are considered worthless, so it is important to detect such failures as soon as they arise. For this purpose special monitoring programs are run concurrently with regular data acquisition, to check the status of detectors, and ring alarms as soon as anything goes wrong (e.g., when a high voltage supply fails).

5.1.4 Online Data Acquisition System

As part of the online data aquisition ("D/A") system, we have

- The D/A programs running on the front-end machines, which read out Camac and Fastbus modules upon receipt of a level-two trigger. When readout is complete, each machine sends the data in the form of a "singleton event" over a link to the microvax.

- On the microvax, the singleton events are collected by the Event Builder, which concatenates them, and puts them in an event pool.

- The Tape Logger program takes all events from the pool, and writes them to tape.

- The Buffer Manager controls the sample of events in the pool, deleting events only after they have been logged to tape.[3] It also sends a subset of the events to another pool, on the Vax 780.

- Monitoring programs, generically called Consumers, access the event pool on the Vax 780 to check that the events are sensible. For example, the Unpack Consumer checks that the Camac DMAs for all detectors are correct; and the Event Display shows pictorally what events "look like." The other consumers analyze data from specific detectors, to show any shift occurring on the scale of several hours.

---

[3]This was not exactly true during the 1990 run.

- An offline program called Data Validation was run on recent tapes. It made extensive histograms and summaries which helped to spot long term drifts in detectors, and to document the performance of the apparatus.

- On various local cpus, specific repetitive monitoring and calibration tasks run during the quiet period between spills. Some of these simply alert the shift crew of any problems by sending short warning messages to a screen. Others provide actual calibration data which is logged to tape for use in offline analysis.

This system is depicted schematically in figure 5.2.

5.1.5 Trigger Masks

When raw tapes written during data taking are processed offline, each event is identified by its trigger mask, which is a set of 128 bits written in a fixed location in each event. By deciphering these bits, the event can be classified according to trigger type if it is a spill event, or according to detector group if it is an interspill event (see table 5.1).

The trigger mask was derived directly from hardware input registers on each bison box (a hardware device mounted on the PDP front-end machines). Analysis of the data depended critically on these bits. A secondary copy of the trigger bits was recorded in a set of Camac latches. Agreement between the bison bits and the latch bits was found to be perfect [Bha88]. The bison bits are assumed to be perfectly reliable.[4]

5.2 Offline Event Reconstruction

The events stored on raw tape were reconstructed using the "PTMV" program, as described below. This program required much cpu time to reconstruct even simple events.[5] To optimize the use of cpu, the data was passed through two stages of selection. The first was called the "SPLIT," and the second, the "FILTER."

---

[4]Measurements of the trigger efficiencies depend on these bits.

[5]In 1987, deep-inelastic data required about three seconds per event, on the Amdahl. This number is expected to increase substantially for the new 1990 and 1991 data.

174
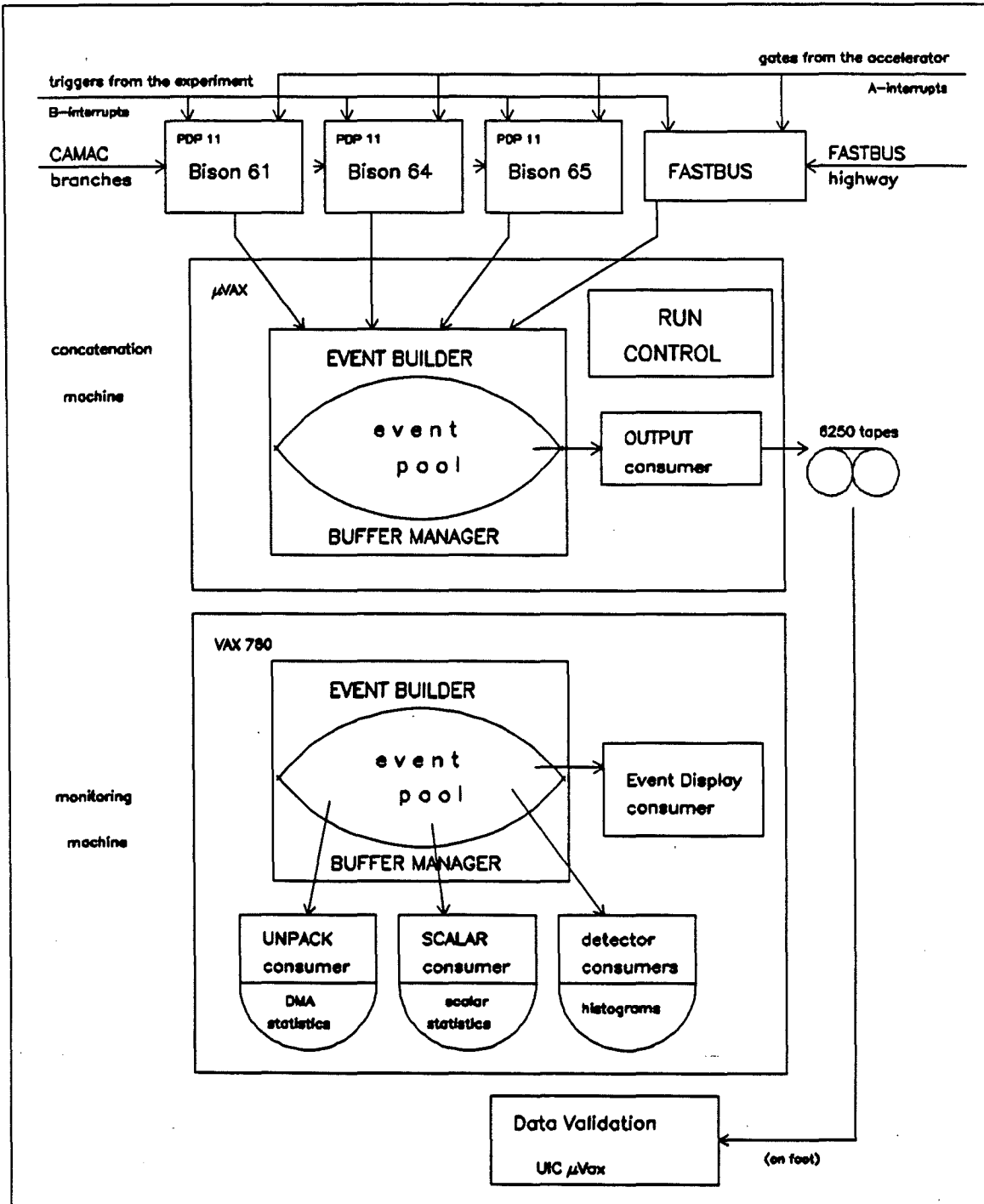
Figure 5.2: Principle components of the online system

event type	source name	categories
spill	CONC	LAT
		SAT
		HALO
		FCAL
		RBEAM
		RSAT
interspill	BI61, or	BOS
	BI64, or	EOS
	BI65	C0
		C1
		CAL
		DC
		RCH
		TOF
		PCV
		PCN
		PCF
unknown	–	–

Table 5.1: Categories encoded in the trigger mask. (The trigger names are explained in the apparatus chapter.)

5.2.1   The SPLIT

A large fraction of the triggers were monitoring events of various kinds. It seemed worthwhile to split the events according to their trigger type:

1. Studies using e.g. halo muon events would require fewer tape mounts.

2. Certain detector analyses requiring interspill data could proceed.

3. The tapes used for studies would not be the originals. If a tape were lost, it could be regenerated.

4. The input to event reconstruction would be free of non-physics triggers, making production more efficient.

5. The tape format used by the online system ("FSIO") would be replaced by a more robust and better controlled format ("Zebra").

The data split program did no analysis beyond decoding the trigger mask, and simple items like the run and event numbers. It was nonetheless a very sophisticated program due to the multiple stream i/o required. It was run on the Amdahl. At that time this cpu was new, and E665 was virtually the only user. Nevertheless, the complete Split required seven months; the program was written from July through November, 1988, and production proceeded from November through January, 1989.

5.2.2   The FILTER

Even after the SPLIT was completed, it was clear that event reconstruction offline, still was performing badly [Mel88b, Mel88c, Mel89c, Mel89b]. It was becoming clear that some of the key chambers had operated at lower efficiency than expected. It was decided that new approaches to pattern recognition were needed, and that a few designated experts would require several months to write the new code. In the mean time, the tapes containing physics triggers (SAT and LAT) were to be filtered, to produce a more concentrated sample of physics events, for eventual production.

Filter Schemes

There were several months of meetings about the FILTER before a workable program was written. The discussions centered on two important issues:

1. How boldly does one want to eliminate background? The tradeoff is between the amount of background eliminated, and the amount of signal lost.

2. What means does one use to differentiate background and signal? Different means have different systematics. A more powerful cut is expected to have a higher systematic.

In the end, five filters were devised and implemented – three for the LAT and three for the SAT, with one in common. There was a hierarchy among them such that the most conservative had highest priority. "Conservative" here means that the code eliminated the fewest valid triggers, where a valid trigger was any kind of interaction in the target. The attitude was that no precision measurement (such as the deep inelastic cross section) should be jepordized.

The SAT and LAT shared a common "primary filter."[6] This filter used the existing pattern recognition and track fitting to identify events in which the muon passed through the experiment without interacting, so that they could be rejected. Anything else with a beam track was passed. This was the essence of the FILTER project.

An enriched sample of deep-inelastic events was expected to be helpful in the development of pattern recognition, and in the bootstrapping of certain analyses. To provide these samples, a "secondary filter" was devised. For the LAT, this consisted of checking the identified muon trajectory behind the steel absorber. If it passed outside a certain vertical stripe (which tended to be flooded with μe and Bremsstrahlung events), then the event was marked as a DIS candidate. The SAT secondary filter employed the calorimeter. Cuts were applied on the overall shape and magnitude of the energy deposited in the cathode pad towers, to build an anti-Bremsstrahlung filter. The primary and secondary filters were a two-step system, but the decision to reject an event was made by the primary filter only.

In parallel to the primary and secondary filters, there were "monitoring filters" the purpose of which was to provide a check on the performance of the primary filter. They were less conservative, cutting out more background but losing more

---

[6]There were a few differences in detail. See below.

signal. Some additional events were accepted if the monitoring filter declared them good, but *no* event passed by the primary filter was rejected if the monitoring filter claimed it was bad. The monitoring filters could add events to the output stream, but not take any away.

To be useful, the monitoring filters had to be independent of the primary filter. For the LAT, roads using PTM hits were constructed which were based on scattered muon trajectories from Monte Carlo studies. Target pointing was the key to this filter [ODa88a, ODa88b, ODa88c]. For the SAT, the calorimeter information available to the secondary filter was used to construct a crude energy-flow filter.[7]

In the next section, we concentrate on the primary filter, since this filter determined the events used in analysis.

Primary Filter

The physics triggers used during the 1987-88 run required that the muon be significantly deflected from its initial path, determined by the beam hodoscopes. Neither the SAT or the LAT employed any trigger elements in the forward spectrometer or target region, so they could not differentiate between muons which interacted in the target and those which interacted in the calorimeter or the hadron absorber.[8] The latter constituted a significant background, which was, however, easy to remove. This was accomplished by comparing the muon trajectory before and after the target.

The resolutions of the beam and forward spectrometers were certainly good enough to differentiate between a muon which interacted in the target, and one which did not. This statement was made precise by measuring the difference in track parameters for random beam events as measured in the beam and forward spectrometers [Bha89]. The values are consistent with zero, within the known resolution of the spectrometers.[9] The primary filter checked whether each event is consistent with "no interaction in the target," which meant that all measured quantities $(\Delta y, \Delta z, \Delta y', \Delta z', \alpha, \Delta p)$ had to be within about three sigma of zero. The cut values are listed in table 5.2. If consistent, then the event was rejected;

---

[7]Electromagnetic events deposit energy in a horizontal band; deep-inelastic events deposit events more evenly, especially vertically. Bremsstrahlung and μe events have an obvious signature in the calorimeter – a single large electromagnetic shower.

[8]The calorimeter alone provides two hundred times more "target" than the hydrogen or deuterium targets.

[9]The beam as measured at PBT4 was propagated through the CVM to the point at which the forward spectrometer fit was reported.

quantity	rms values from RBEAM	LAT cut value	SAT cut value
Δy (mm)	0.36	1.0	1.5
Δz (mm)	0.36	1.0	1.5
$\Delta y'$ (mr)	0.13	0.39	0.50
$\Delta z'$ (mr)	0.03	0.09	0.25
angle α (mr)	0.095	0.29	0.54
Δp (GeV)	19.2	50	50

Table 5.2: Cuts for the LAT and SAT primary filters.

otherwise it was retained.

An additional source of background came from out-of-time beams, and beam veto counter inefficiencies. Both of these backgrounds were easily reduced to negligible levels by requiring that six or seven beam hodoscope planes fired [Kun89a, Kun89b].

The actual decision tree was fairly complicated. For the LAT, the following tests were made, in this order:

1. Reconstruct the beam. Unless there is exactly one in-time and no out-of-time events, reject the event.

2. If the χ^2-probability for the beam track fit is greater than 1%, *and* the momentum is less than 300 GeV, then reject the event.

3. Decode the PSA data. If there are hits in fewer than three planes, then accept the event. (No PSA hits means the muon probably was deflected out of the beam.)

4. Reconstruct tracks in the forward spectrometer (no wide angle tracks). If there are more than one track found, or if there are no tracks found, then accept the event.

5. If there is exactly one forward spectrometer track, then fit it. If the χ^2-probability is less than 1%, then accept the event.

6. Try to match the beam and the single forward spectrometer tracks. If the event is consistent with "no target interaction," then reject it. Otherwise, keep it.

The SAT primary filter was quite similar. There were three main differences:

180

1. Demand exactly one in-time beam, but allow any number of out-of-time beams.

2. Require the event to satisfy the logic of the SAT. This requirement eliminated many events taken with the hydrogen target due to hardware problems in the SAT beam definition.

3. Require evidence of a muon track behind the hadron absorber. Since there had been no muon requirement in the trigger, a significant fraction of SAT events consisted of hadrons, which formed a small contamination of the beam.[10]

A schematic showing typical primary filter performance is given in figures 5.3 and 5.4.

Filter Efficiencies

As discussed above, the purpose of the monitoring filter was to provide a check on the primary filter. Determination of the primary filter inefficiency is simple: one simply counts the fraction of *good* events accepted by the monitoring filter but rejected by the primary filter. Events satisfying these criteria were chosen to estimate the filter inefficiency:

1. one in-time beam track, no out-of-time beam tracks

2. reconstructed primary vertex, with $(-12.5 < X < -9.5)$ meters

3. exactly two tracks other than the muon, of opposite charge

4. the momenta must satisfy $(p_1 + p_2)/\nu > 0.5$

The result is summarized in table 5.3. Since these inefficiencies are so small, no correction is made to the yield.

These measurements also allow a determination of the loss of beam flux due to the first requirement. The LAT monitoring filter made no requirements on the beam, but the primary filter demanded exactly one in-time beam, and no out-of-time beams. Relaxing requirement 1) above, the loss in hydrogen due to this requirement is $21 \pm 1\%$.

---

[10]The pion and electron contamination has been estimated to be 10^{-6} [Car91].
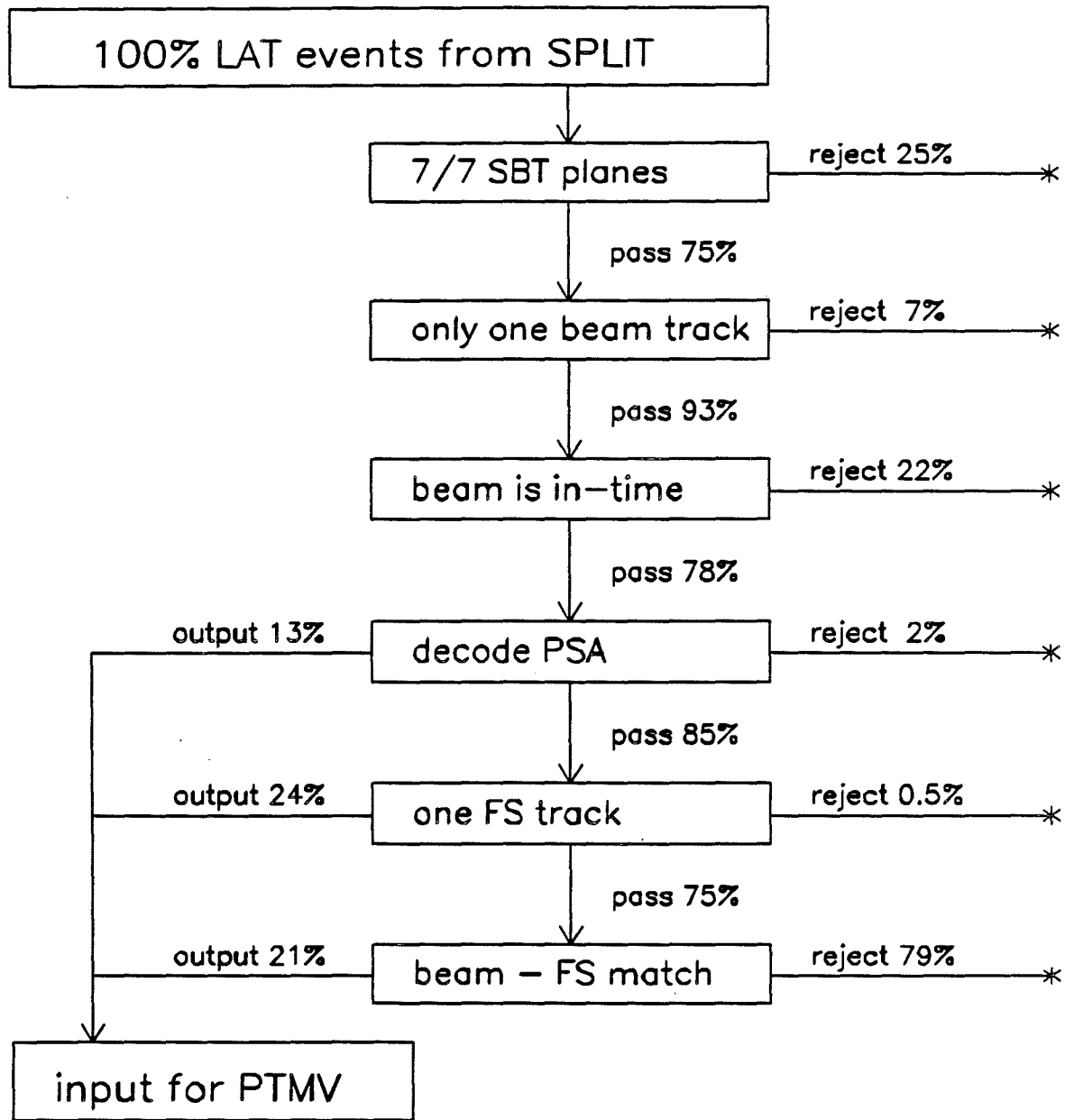
Figure 5.3: An example of LAT primary filter performance.
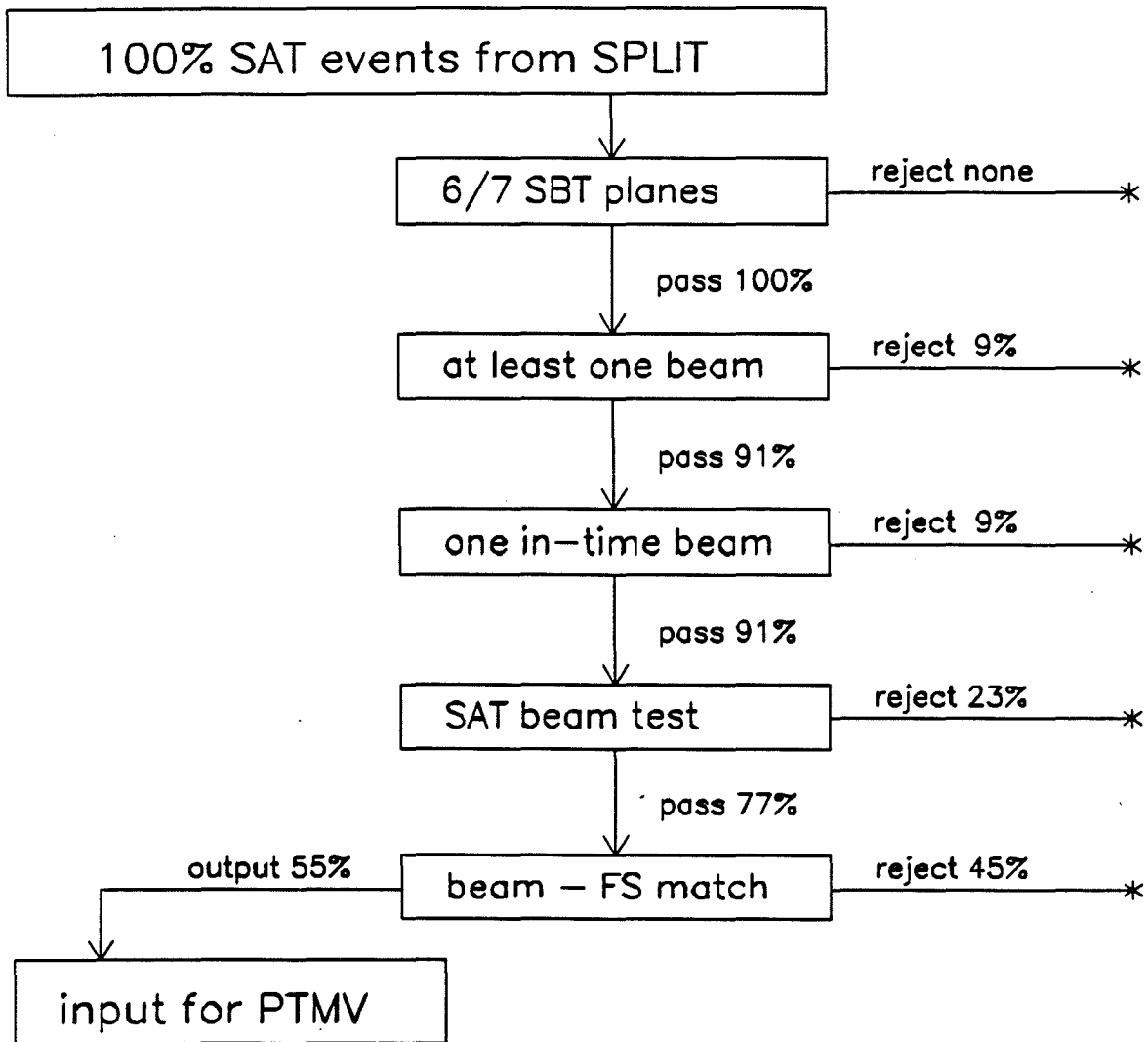
Figure 5.4: An example of SAT primary filter performance.

trigger	number passing cuts	missed by primary filter	inefficiency
SAT	402	4	1.0 ± 0.5 %
LAT	704	1	0.2 ± 0.2 %

Table 5.3: Measurement of the LAT and SAT primary filter efficiencies.

(A second measurement of the filter inefficiency was made using events satisfying simpler criteria [SA91a]. The candidate failures were scanned, and one genuine μe scatter found which was rejected by the LAT primary filter. From this scan the filter inefficiency is 0.2 ± 0.2%.)

5.2.3 Event Reconstruction

"Event Reconstruction" generally means inferring the charged particle trajectories and vertices in an event from hits in chambers.[11] E665 broke this task into four steps:

1. Sort wire chamber hits into lists corresponding to particle trajectories – **Pattern Recognition**

2. Fit each candidate track to a sophisticated model incorporating detailed maps of magnetic fields – **Track Fitting**

3. Identify muons by matching a fitted forward spectrometer tracks to track projections behind the hadron absorber – **Muon Matching**

4. Find the primary and any secondary vertices using a fit procedure – **Vertex Fitting**

Fortunately, it was possible to combine all four steps in one program on the Amdahl; this program was called "PTMV." Each step is sophisticated, and of primary importance, so we discuss each one in some detail.

---

[11] Particle identification and neutral energy measurement were special jobs to be run after events had been reconstructed. Neither particle ID nor calorimeter analysis was ready for production in 1989.

5.2.4   Decoding and Translation

Before any event reconstruction can proceed, the coordinates of the hits in chambers must be determined from the raw data.[12] This process occurs in two steps, called "Decoding" and "Translation."

An event consists of four subevents, one from each front-end machine (three PDPs and Fastbus). Each subevent starts with twenty header words, containing pointers to the first event in each DMA. (Recall that a DMA is simply a block of data words read out for a given detector.) There is an overall event header which contains pointers to the first word in each subevent.

All raw events consist of one block created under a unified D/A scheme, so a small number of utility routines could be used to extract the DMAs for all detectors. For each detector, a specialized routine for reorganizing the data words is needed, because the readout scheme for each detector is different.[13] These routines report the data in a sensible fashion, e.g., a list of hit wires in ascending order.

Once the data words are organized properly, conversion to physical units (e.g., from wire number to a coordinate in space) can take place. For wire chambers and hodoscopes this is straight forward, since only a reference point and the wire or hodoscope spacing are needed. For drift chambers and the time-of-flight counters, second-order corrections are needed due to the high precision of these instruments. Calorimeter translation involves several steps, as discussed in the calorimeter chapter.

Decoding the data requires knowledge of the hardware. Translation, however, requires a *calibration* of the hardware. In the case of wire chambers and hodoscopes, this means aligning all detectors with respect to one another. This is done using an iterative procedure [Bhatti, pp.64–68]. The surveyed positions of the third and fourth beam station are used to set the system of global coordinates [BW89]. A rough check on the alignment is provided by comparing the track fitting residuals observed for sets of chambers with the expected chamber resolution, as shown in table 5.4.

Unfortunately, a systematic discrepancy between the beam spectrometer and forward spectrometer remains, prompting a systematic investigation of the alignment and magnetic fields in both spectrometers. The "ν-offset" problem is discussed in detail in the analysis chapter.

---

[12]Technically, this is done as part of pattern recognition, for reasons of efficiency.

[13]There is in fact a fair amount of generalization at this level of decoding, too.

chamber	residual sigma	residual mean	(wire spacing)$/\sqrt{12}$
PBT	0	0	290
PCV	710	18	580
PCN	820	-13	870
PCF	640	30	580

Table 5.4: Some examples of measured chamber resolutions. The cluster size was constrained to be one. Units are microns.

5.2.5 Pattern Recognition

The goal of pattern recognition is to take hits recorded in wire chambers, which are reported chamber by chamber, and reorganize them into lists of hits corresponding to the trajectories of real charged particles. In order to accomplish this efficiently, as much knowledge of the *physically allowed* trajectories is used as possible. For example, trajectories are expected to follow straight lines in field-free regions, and they generally must point back to the target.

Algorithms

The "PR" part of PTMV consists of many "processors" (pieces of code performing a specific task by following a fixed algorithm) operating at different levels.[14] Some processors are limited to a specific set of chambers – they take hits and form track primitives such as space points or local line segments (projections). Others take these track primitives and form complete or nearly complete tracks. Only the latter are retained for output; track primitives usually are discarded at the end of an event. Each of the PR processors is described in detail in [Ryan].

PR starts with track segments in groups of chambers. Here, hits from PCN and the DCs are expected to fit straight lines. Hits from PCV and each PCF triplet are expected to fit three-dimensional space points only, since these chambers are in regions of nonzero magnetic fields. The PSA hits were fitted to space points because there is so little extent along the track that a straight line fit would be meaningless. There are only two views of PTM hits, so these are fitted to straight lines.

For the vast majority of physics topics, the kinematics of each event must be known. The kinematics of each event depend on the beam energy E_0, on the energy

---

[14]A glossary of processor names is given in table 5.6, and diagrams indicating the role played by each processor are given in figure 5.5.

of the scattered muon E_1, and on the polar scattering angle θ_{sc}. The azimuthal scattering angle ϕ_{sc} is important when looking for polarization effects. The four quantities $(E_0, E_1, \theta_{sc}, \phi_{sc})$ can be determined only if both the beam and scattered muons have been reconstructed. It makes sense, then, to require evidence of a reconstructable beam and scattered muon before attempting to reconstruct all of the other tracks. If no beam is found, then the event is rejected. Otherwise, the number of found straight line segments in the muon chambers (PTMs) was checked. If there was not at least one segment in both the horizontal and vertical views, then the event was rejected. Otherwise, pattern recognition for the forward spectrometer was performed.

In part for historical reasons, PR begins by taking straight line segments found in the DCs and PCNs, and linking them inside the CCM. Since the momentum of the candidate trajectory is not known yet, roads are defined through the PCF chambers inside which hits are searched. If enough PCF hits are found, then the track is kept. Note there is a requirement that the track, viewed horizontally, point to the target region.

After all tracks consisting of DC-PCN segments matched in the CCM have been found, the hits belonging to these tracks are dropped. Generally, segments in the PCN remain. These are projected into the PCFs, and possible short tracks found. The search roads used at this stage are larger than when the DC line segments can be used to help constrain the track.

After PCN-PCF tracks have been found, space points in the PSAs are formed. The PCN-PCF tracks are extrapolated to the PSA chambers, using a parabolic approximation to the helical path.[15] Spacepoints falling inside a two-dimensional window are added to the track. This is the way many high-energy tracks are found; this processor is vital for analyzing the SAT data [Magill, pp.62–67].

It was found that the PCF chambers were generally more efficient during the 1987-88 run than the PCN chambers. In the non-bend view, there is also greater redundancy. For these reasons a processor was written which took sets of PCF space points and formed curved track primitives. Each of these were projected into the PCN chambers, to pick up any unused hits.

Any new tracks formed at this stage again were projected to the PSAs, looking for spacepoints.

---

[15]The oft utilised routine is called DHFIT3, and was written by Silhacène Aïd. John Ryan discusses the use of this routine in his thesis [Ryan, pp.87-88].

processor	all tracks	muons	positive pions	negative pions
MU	81 (84)	95 (94)	78 (81)	69 (78)
HD	19 (16)	5 (6)	22 (19)	31 (22)
DC-MA	13 (13)	4 (5)	19 (20)	16 (19)
PC	41 (33)	52 (44)	36 (29)	34 (25)
PF	28 (20)	49 (40)	17 (9)	17 (10)
PS-MS	46 (40)	88 (80)	27 (18)	23 (17)
SF-SN	59 (67)	47 (56)	63 (71)	66 (75)
MD	35 (46)	8 (16)	45 (59)	52 (63)
PV-MV	41 (62)	43 (65)	44 (61)	37 (61)

Table 5.5: Fraction of tracks (in percent) found by various processors in pattern recognition. Data is from SAT. The numbers in parenthesis pertain to Monte Carlo.

Any short tracks consisting of PCN-PCF segments were projected through the DCs. Any DC hits consistent with an approximation to the helical trajectory were added to the track.

Finally, all tracks were projected to the PCV chambers, located near the vertex magnet. Space points formed from PCV hits were added to tracks based on a straight-line fits including hits from PCN.

(Processors for finding wide-angle tracks were run after forward spectrometer PR was completed. These used space points in PCV and the PTAs. The multiplicity of these tracks was low, and they were not used in this analysis, since their momentum was not determined.)

All of the above steps were performed *twice*. For the first pass the local fit cuts were tight because the goal was to find the scattered muon trajectory, which was expected to be stiffer than most other tracks. (The cross section falls as $1/\nu$). In the second pass the cuts were loosened to find weaker tracks lacking hits, or having larger curvature.

Table 5.5 lists the fraction of tracks found by each processor, for the SAT ρ^0 sample. As can be seen, the most important combinations of processors were SN-SF and PS-MS. (Inclusive deep-inelastic data are different, due to the different momentum spectrum of hadron tracks.)
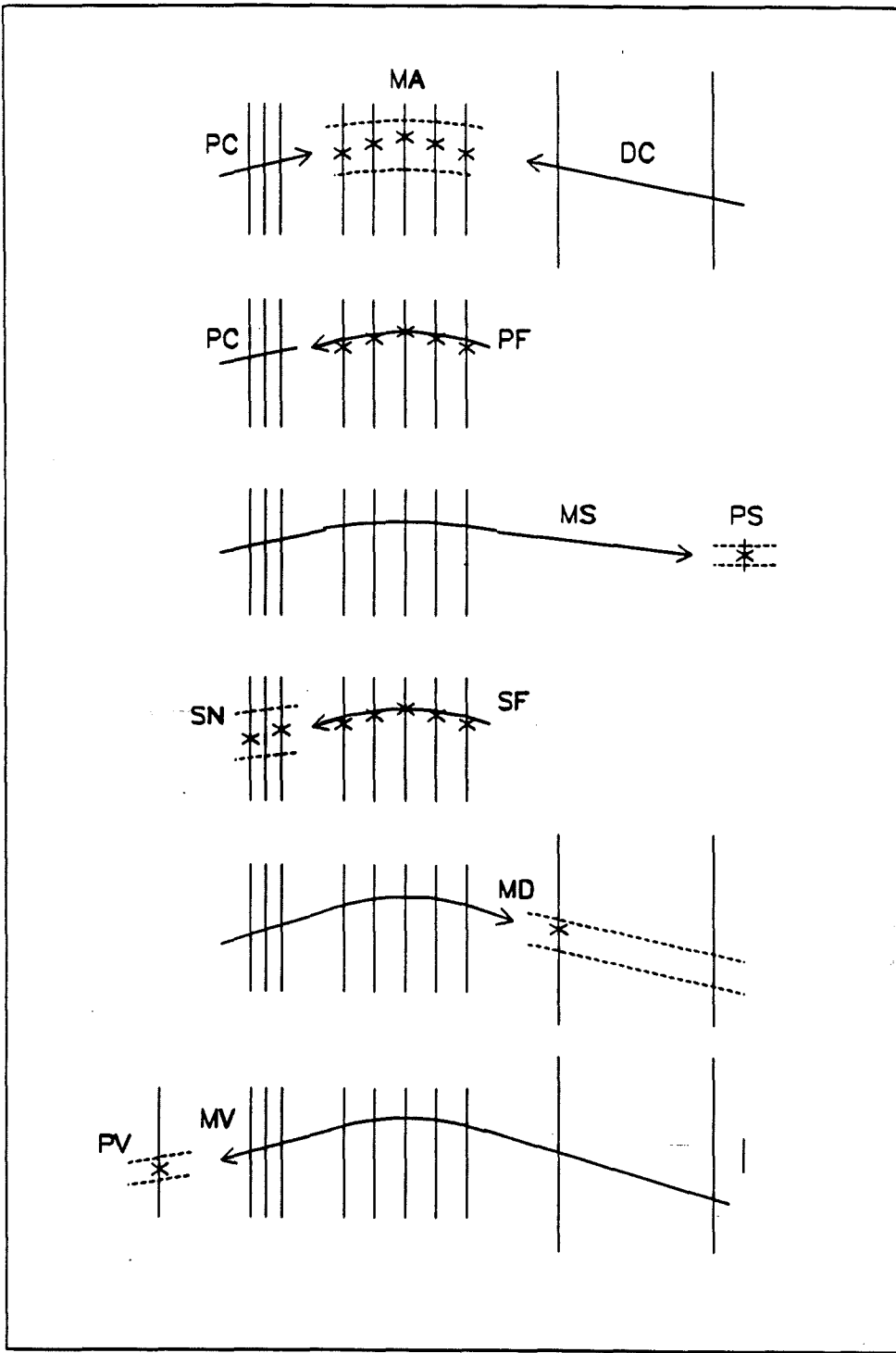
Figure 5.5: Schematic diagram of processors in Pattern Recognition.

processor name	description
PB	Find beam tracks. (space points, then projections)
SB	Match beam track with hodoscope hits.
PM	Find muon lines behind the hadron absorber.
DC	Find straight line segments in the DCs.
PC	Find straight line segments in the PCs.
MA	Match segments from DC and PC, adding PCF hits.
PF	Project PC lines into PCF and pick up hits.
PS	Find space points in the PSAs.
MS	Match PC-PCF tracks with PSA space points.
SF	Construct curved space lines from PCF hits.
SN	Add PCN hits to SF space lines.
MD	Match PC-PCF tracks with unused DC hits.
PV	Find space points in the PCVs.
MV	Add PCV space points to complete tracks.
MU	Execute the Muon Pass of PR.
HD	Execute the Hadron Pass of PR.

Table 5.6: Glossary of Processors in Pattern Recognition

Remarks

All forward spectrometer tracks must have hits from PCN and PCF. Originally the keystone of pattern recognition was to be the PCN chambers, but because of the inadequate efficiency and redundancy of these chambers, more exotic algorithms starting with spacepoints in PCF were developed. The PCF chambers are sufficiently redundant that less than perfect performance did not hamper seriously track reconstruction. The DCs are efficient (if noisy), apart from certain dead regions. Finding spacepoints in the PSAs also is efficient, owing to the high redundancy in these chambers.

A certain degree of ambiguity always exists in finding tracks in wire chambers. It can be reduced to negligible levels by using enough planes spaced not too far apart. In the case of tracks found by extrapolation from the PCFs to the DCBs and PSAs, the ambiguity was not negligible. The extrapolation was not well enough constrained to pick out the correct hits every time. Muons scattered at small angles are lost when the MS processor incorrectly links a PCN-PCF track to a spacepoint in the PSA, when the true track passed through the DCBs. The MS processor runs before MD, with no arbitration between them, resulting in a bias. The result is tracks which cannot be linked to the muon projections behind the hadron absorber.

Although a full track fit is reserved for the TF program, local fits play a major role in most PR processors. It was found just prior to PTMV production that tuning the cut values for these local fits is crucial to the performance of pattern recognition.[16] Major improvements in reconstruction efficiency were gained simply by adjusting certain cut values.[17]

The plethora of PR processors is partly a consequence of the hodge-podge of chambers employed in E665. Each set of chambers is internally consistent and sensible, but no two different sets share common views (aside from Z) or wire spacings. This fact encouraged the strategy of finding track primitives in each set of chambers, and then trying to combine primitives from different detectors into tracks or portions of tracks. More modern approaches to track reconstruction employ network theory, or combined pattern recognition – track fitting algorithms, both of which put all hits on equal footing rather than forcing groupings according to detector type.

---

[16]This point was stressed by John Ryan, who together with Doug Jansen did most of the parameter tuning.

[17]Unfortunately, some of the parameters were entered into control files incorrectly, leading to an impaired performance of the PC processor [Rya91].

It appears that the practice of dropping hits from found tracks, making them unavailable for other possible tracks later, hindered track reconstruction. In particular, if two tracks have the same Z projection, then only one is found. This leads to an inefficiency for reconstructing e^+e^- pairs from gamma conversions, an inefficiency for reconstructing μe scatters, and an inefficiency for $\pi^+\pi^-$ pairs from ρ^0 decays when the decay plane is horizontal.[18]

The efficiency of event reconstruction is discussed in the chapter on analysis. Estimates of the efficiency of individual processors can be found in [Ryan].

5.2.6 Track Fitting

The goal of track fitting is to estimate the actual trajectory followed by a real particle given a list of the coordinates of hits it left behind in the wire chambers. The trajectory is expressed at a fixed plane (X position) in terms of the coordinates (Y, Z) of the intersection point of the trajectory and the plane, the track direction $(Y', Z') = (dY/dX, dZ/dX)$ at that point (X, Y, Z), and the momentum of the particle (technically, the inverse of the momentum, $(1/p)$).

Concepts

Determination of the trajectory relies on understanding the motion of the particle in magnetic fields. In regions of homogeneous magnetic fields (with no electric fields) the trajectory is helical with the axis of the helix parallel to the magnetic field vector. In projection the helix will look like a circle the radius of which will be proportional to (p/B) (where B is the strength of the magnetic field: $B = |\vec{B}|$). In field-free regions the track will be a straight line (i.e., a circle of infinite radius).

If a particle enters a region of length L in which the magnetic field is constant, and is not captured (i.e., has a high enough momentum such that $R > L$), it will emerge with an angular deflection θ which is related to the radius of curvature and the length of the magnetic field:

$$L = 2R\sin\frac{\theta}{2} \approx R\theta \qquad \text{for small } \theta$$

---

[18]The electron pairs are important in jet analyses using neutral energy flow. The μe scatters are a major background in analyses of nuclear shadowing.

192

giving $\theta \propto (1/R) \propto (1/p)$. At the conceptual level, measuring the track momentum amounts to measuring the deflection of a particle after it has passed through a known magnetic field.

A crude version of track fitting would consist simply of fitting the track in field-free regions to straight lines (thereby obtaining the position and slopes of the trajectory), and calculating the track momentum from the angular deflection of the track. This model for track fitting provides an easy guide for gauging the precision of dipole spectrometers. We apply it to the E665 beam and forward spectrometers.

Beam Spectrometer

The main components of the beam spectrometer are sketched in figure 5.6. The wire spacing is one millimeter, so the typical resolution on one coordinate will be about $\sigma = 0.3$ mm. The lever arm on the upstream side of the NMRE analysing magnet is about 30 m, so the precision on the slope for the straight line fit is roughly 10 μr. The lever arm on the downstream end is about 20 m, so the precision on that side is about 15 μr. Adding these figures in quadrature gives 18 μr.[19] The magnet is tuned to bend the beam through about 3 mr, so the relative error on the measurement of the bend angle is (18 μr/3 mr) $\approx 6 \times 10^{-3}$. Since the fractional error on momentum is the same as the fractional error on this angle, this amounts to about 3 GeV for a 500 GeV beam track. Track fitting gives the value 2.5 GeV.

The bend in NMRE is so small that the trajectory as viewed in the ZX plane can be taken to be a straight line. The resolution on the inclination of the track in this view would be (0.3 mm/50 m) ≈ 6 μr. The value claimed by track fitting is 4.8 μr.

Forward Spectrometer

The forward spectrometer is more complicated than the beam spectrometer. As indicated in figure 5.7, there are several sets of chambers with varying resolutions. Conceptually, a straight line is obtained from some combination of PCN, PCF1, and PCV, and another from the DCs or PSAs. The angular resolution of PCN alone is poor – about 1 mr. If PCF1 is included, this falls to 0.5 mr, or if PCV is included, 0.1 mr. Because of the large lever arm between DCA and DCB, the angular resolution they provide is far better, about 0.01 mr.

---

[19]The net angle of deflection is the sum of the angles of each straight line fit (for small angles), and the measurements of the two straight line projections are independent.
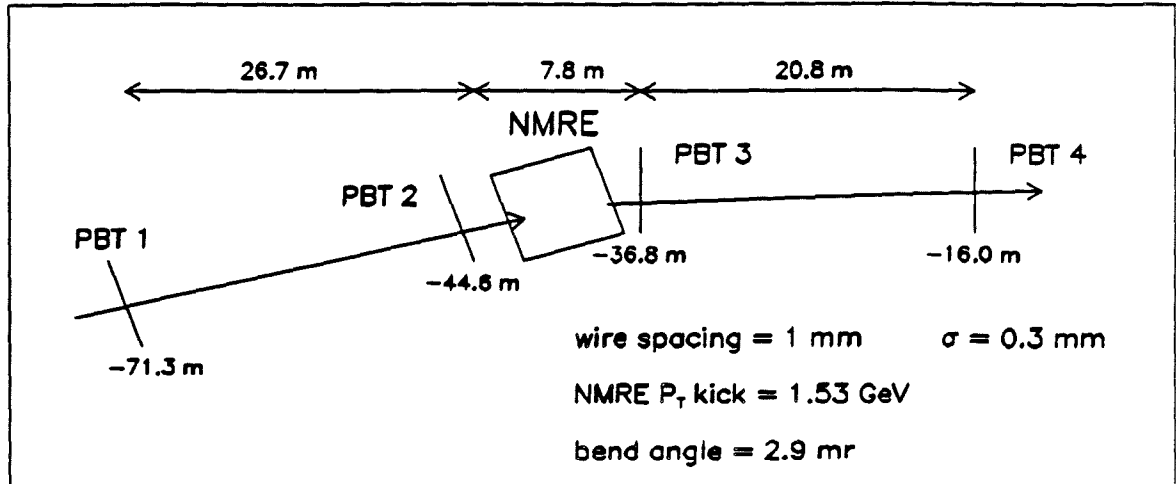
Figure 5.6: Schematic view of the beam spectrometer.

The resolution on momentum is dominated by the resolution on the slope of the track on the upstream side of the CCM. The bend angle of the CCM will be roughly (2 GeV/p), or about 10 mr at $p = 200$ GeV. The relative error on the bend angle, and on the momentum, will be about (0.2 mr/10 mr) = 0.2%, which amounts to 4 GeV for the 200 GeV track. The observed value is 3.2 GeV.

The assumption that the track is a straight line in the ZX plane is not well justified for low momentum tacks [Bak89], nonetheless it is approximately true for a 200 GeV track. Ignoring the fact that the PCF chambers contribute to the fit in Z, a track with PCN and PSA hits will have an angular resolution of 50 μr; the estimate from track fitting is more like 25 μr. Taking PCV to be the endpoint instead of PCN gives the value 25 μr, however, the real gain in resolution probably comes from the fact that the PCF chambers help constrain the fit.

Quintic Spline Fits

The model described in the last section is over-simplified; the track parametrization actually used in the track fitting code uses a quintic spline model referenced

194
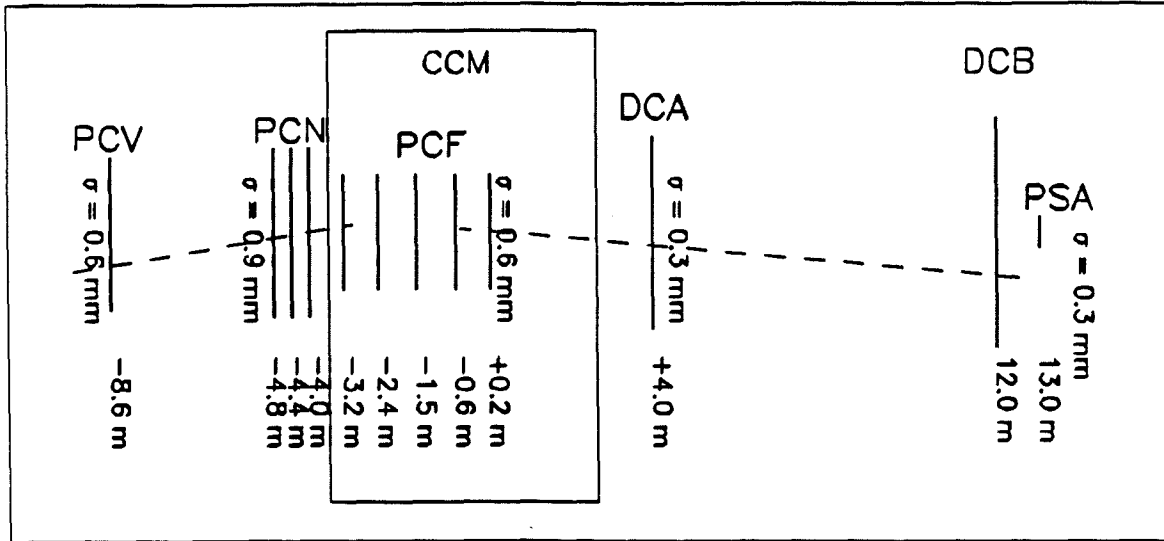
Figure 5.7: Schematic view of the forward spectrometer.

to a detailed map of the CCM field [Sal86, Salvarani]. The hits supplied by pattern recognition are subjected first to local fits. As in pattern recognition, some detectors are fitted to straight lines, and others to point fits. Effective Y and Z coordinates are calculated from these fits, and used as input to the quintic spline fit. A system of five linear equations incorporating the physical motion of a charged particle in the magnetic field is solved using matrix methods, yielding the "spline coordinates" $(Y, Z, Y', Z', 1/p)$ for the track, and the full covariance matrix for these parameters.[20] Once the fit is completed, and the energy known, the errors are modified to take multiple scattering into account.

Rescue, Superrescue, and PCV Hunt

Studies showed that the correspondence between Monte Carlo truth tracks and reconstructed tracks was poor.[21] In particular, there were many tracks with a momentum greater than the energy in the event, ν. As track reconstruction improved,

---

[20]In fact there are iterative steps taken here, in which the slope of the track in the PCF chambers is adjusted as the fit improves.

[21]These studies were carried out by Uwe Ecker and Alex Salvarani.

195

the number of tracks with $z = p/\nu$ greater than one decreased. Contributing to this improvement were three special track fit algorithms.

The Rescue and Superrescue algorithms reject hits on a track which have very large normalized residuals.[22] A complete quintic spline fit is performed. If the χ^2-probability is below 5%, the detector with the largest *normalized* residual is dropped, if its normalized residual is greater than three.[23] A full spline fit is performed on the reduced track, and another detector plane dropped, if its normalized residual is greater than three. If there are no planes with such a large residual, then the Rescue procedure is exited. If the limit of three iterations is reached without obtaining a valid χ^2-probability, and if the track contains PCV hits, then it enters the Supperrescue procedure. If there are no PCV hits on the track, then the rescue is continued, up to a limit of ten residuals. If at some point during Rescue the number of degrees of freedom for the quintic spline falls to zero, then Rescue is halted, and the track fit declared a failure.

That tracks failing Rescue often contain wrong PCV hits. The PCV chambers are far from PCN, and given the angular resolution of PCN, pattern recognition sometimes associate wrong PCV hits with a track. This shows up as a kink in the linear upstream portion of the track which the Rescue procedure can not handle: it simply strips away the points from the other chambers without fixing the kink. In Superrescue, the original track is revived, *without* the PCV hits. A spline fit is performed, and if necessary, Rescue.

The PCV Hunt procedure is an echo of the MV processor from pattern recognition. It is run after the full spline fit, and after the Rescue and Superrescue procedures. Tracks with no PCV hits are extrapolated from the PCN to the PCV chambers, if the χ^2-probability for the spline fit is at least 1%. The track momentum is known, so the curvature of the track in the fringe fields of the CVM can be taken into account.[24] The complete set of PCV hits is examined, and if at least three PCV hits are consistent with the original track, then they are added, and the full spline fit repeated.[25]

The fact that a track entered Rescue, whether it failed, and the detectors that are dropped, are recorded for each track. PCV Hunt activity is also recorded. The frequency of these processors for exclusive ρ^0 events is summarized in table 5.7.

---

[22]This is similar to truncating the non-Gaussian tails of a distribution to obtain a more reliable estimate of the peak.

[23]The hits of a single detector plane are dropped, not the generalised coordinates calculated from the local fits.

[24]The change in the horizontal direction can be as large as several millimeters.

[25]The search window was twice the chamber resolution, or about 1.2 mm.

track type	entering Rescue	PCV Hunt
scattered muon	27% (30%)	20% (18%)
positive pions	29% (26%)	16% (13%)
negative pions	22% (24%)	14% (11%)

Table 5.7: Fraction of tracks modified by the Rescue and PCV Hunt procedures. Virtually no tracks failed rescue. The numbers in parenthesis refer to Monte Carlo, the others to SAT hydrogen data.

Digression on χ^2 and Normalized Errors

The function called χ^2 is the sum of the squares of normalized residuals. By construction it is parabolic near its minimum. Finding the values of the free parameters of the model by minimizing χ^2 yields good results if the residuals are normally distributed. Although measurement of a track coordinate by a wire chamber is quantized and therefore not gaussian, inclusion of the coordinates from many (redundant) chambers nonetheless gives residuals which are nearly gaussian. Since the precision of the measurement is finite, different determinations of the same track will yield a distribution of values for minimized χ^2, and for the free parameters of the model. If the residuals are gaussian, then this distribution of the χ^2 values is known, allowing a determination of the probability that a given value of χ^2 will occur. This means that a plot of the probability of the observed values of χ^2 should be flat between zero and one. This fact is an important tool when looking for systematic effects. Example χ^2-probability distributions for SAT data and Monte Carlo are shown in figure 5.8.

Another important tool is the distribution of normalized errors on fit parameters. If the value of a fit parameter is known a priori on a case by case basis (e.g., because the data is generated from a Monte Carlo program, or because an independent and more accurate determination of the parameter is available), then the actual error normalized by the estimated error should be normally distributed. The "actual error" is the difference between the a priori ("truth") value and the measured ("reconstructed") value. The "estimated error" is obtained by propagating the known errors on the measurement (e.g., the measured accuracy of chambers) through the functional form assumed in the model to the particular parameter under consideration. If the fitted value is systematically too high, then the peak of the normalized error will be greater than one; the value of the peak indicates the significance of the shift. If the errors are systematically underestimated, then the rms width of the normalized error distribution will be greater than one.

This technique of plotting the normalized error was used to verify the performance of track fitting as described in the next section.
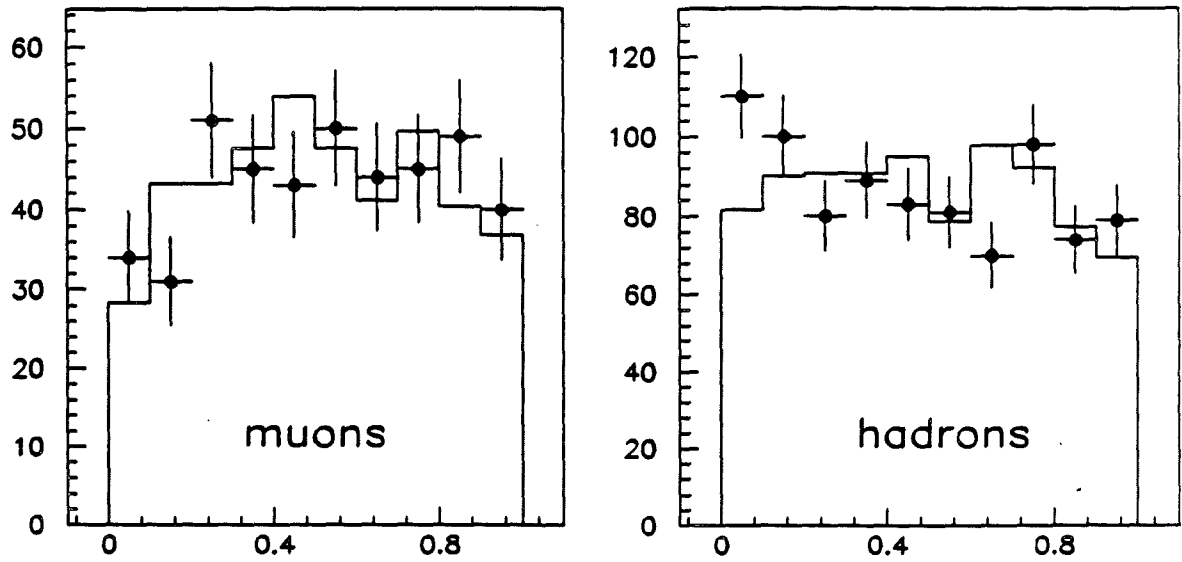
Figure 5.8: Distribution of the probability of χ^2 from track fits to forward spectrometer tracks. The points are data and the histogram is Monte Carlo.

Verification of Tracking Errors

Estimation of the errors on the track parameters can be done analytically; they depend on sums over the coordinates and the chamber resolutions. A check that the estimation is correct is carried out easily using Monte Carlo data. In this case the track parameters are known, so the actual error and the estimated error can be compared.

First some notation should be defined. For parameter α, let α_{true} be its a priori value, and α_{recon} be the value obtained from the fit. The "actual error" in a given case is

$$\Delta\alpha \equiv \alpha_{true} - \alpha_{recon}.$$

Let the estimated error obtained from the fit be σ_α, and define the "normalized error" (in some contexts called the "normalized residual") to be the *dimensionless* quantity

$$\eta_\alpha \equiv \left(\frac{\Delta\alpha}{\sigma_\alpha}\right).$$

If α_{recon} and σ_α are both correct, then the distribution of η_α should be a gaussian with zero mean and unit variance – even if σ_α is a function of α.

(The χ^2 function is really just a sum of $(\eta_\alpha)^2$, and so gaussian errors in $\Delta\alpha$ allows a determination of optimal parameters from χ^2 — it corresponds to finding the peak in $\exp(-\chi^2/2)$.)

The actual and normalized errors for all track parameters are shown in figure 5.9 for beam muons, and figure 5.10 for scattered muons. In general the distributions are quite good, with the exception of the beam Y coordinate, which has non-gaussian structure.[26] Based on these plots (and on the checks described in other sections), we trust the track fitting program to reporting valid estimates of the errors on the track fit parameters.

Measured Resolution on Track Parameters

An indication of track resolution has been given in previous sections. The relative error on momentum is expected to be proportional to the momentum; in fact it

---

[26]This anomaly has been explained by Alex Salvarani to be a consequence of the paucity of hits in the horizontal view. (One of the PBT Y chambers was inefficient.)
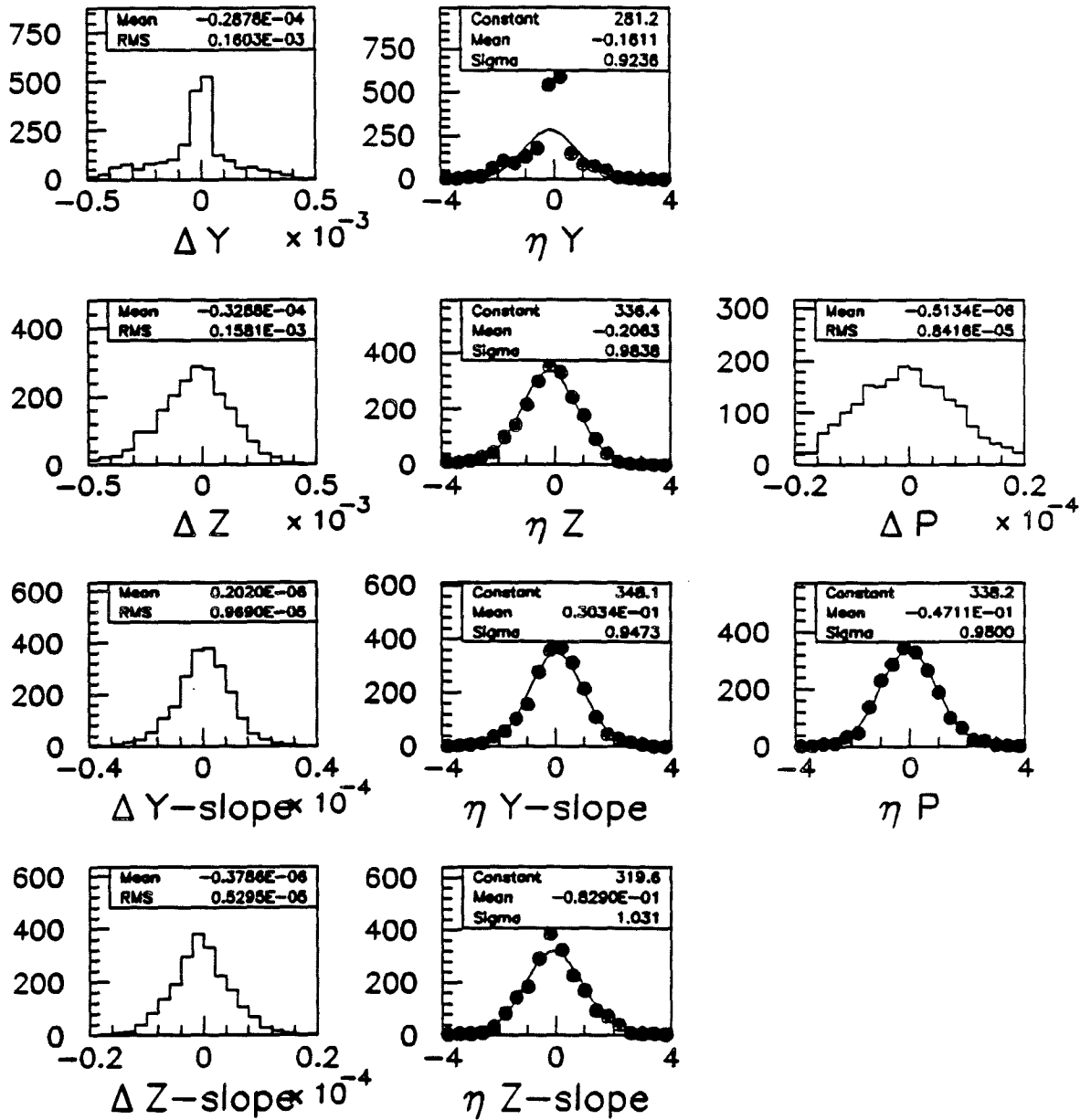
Figure 5.9: Test of the track errors for the beam as reported by track fitting. The actual error is $\Delta\alpha$, and the normalized error is $\eta\alpha$, as explained in the text.
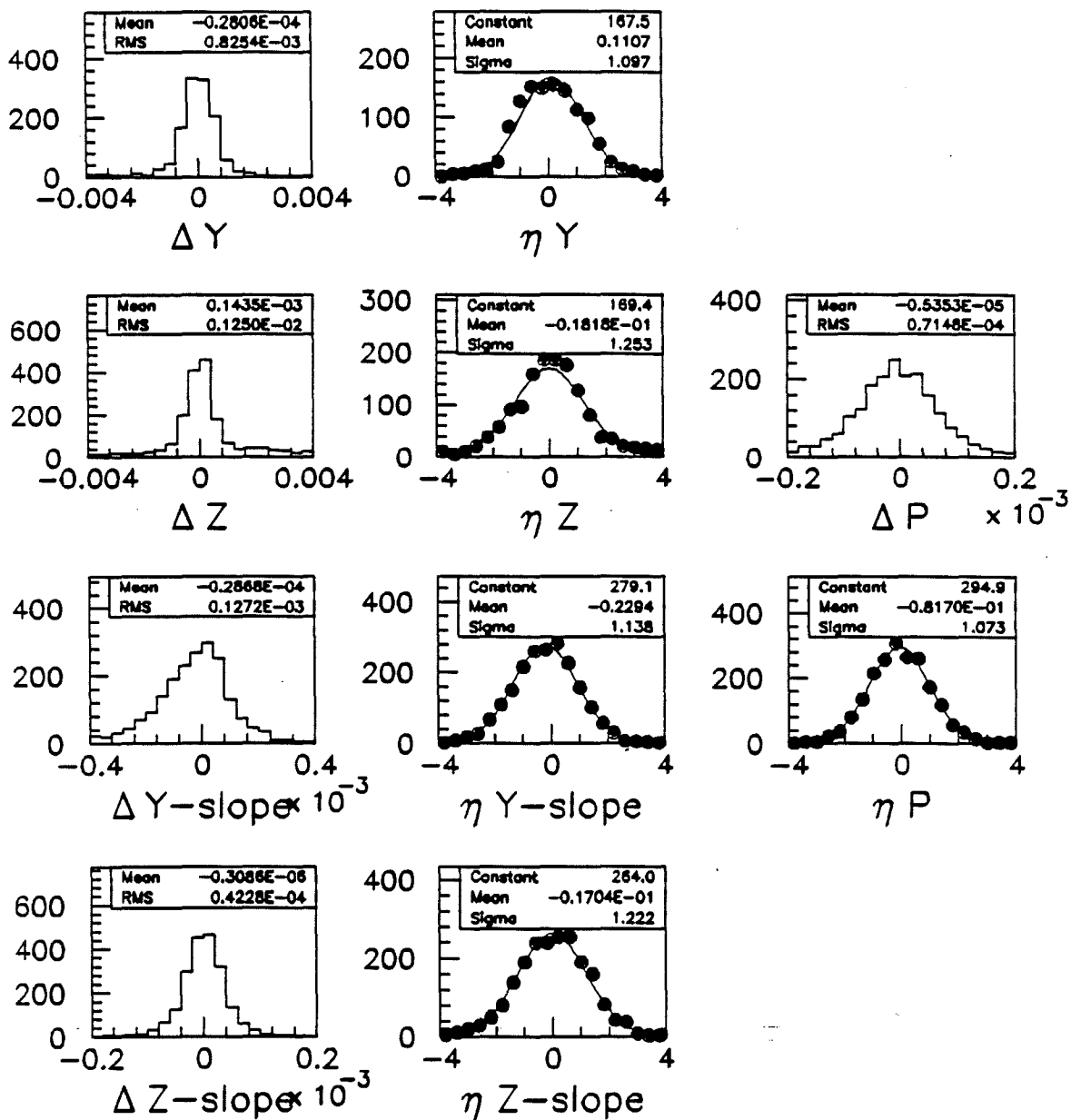
Figure 5.10: Test of the track errors for the scattered muon.

resolution	typical value	intercept a	slope b
σ_p/p	10^{-2}	2×10^{-3}	5×10^{-5}
$\sigma_{y'}$	10^{-4}	6×10^{-5}	2×10^{-3}
$\sigma_{z'}$	2×10^{-5}	8×10^{-5}	4×10^{-3}

Table 5.8: Summary of track resolution for the SAT sample. Linear relations are explained in the text.

depends linearly on the momentum (see figure 5.12)

$$\frac{\delta p}{p} = a_p + b_p \, p.$$

The estimated (absolute, not relative) error on a track slope depends linearly on the slope,

$$\sigma_{y'} = a_y + b_y \, y'$$
$$\sigma_{z'} = a_z + b_z \, z',$$

as depicted in figure 5.11. A summary is given in table 5.8.
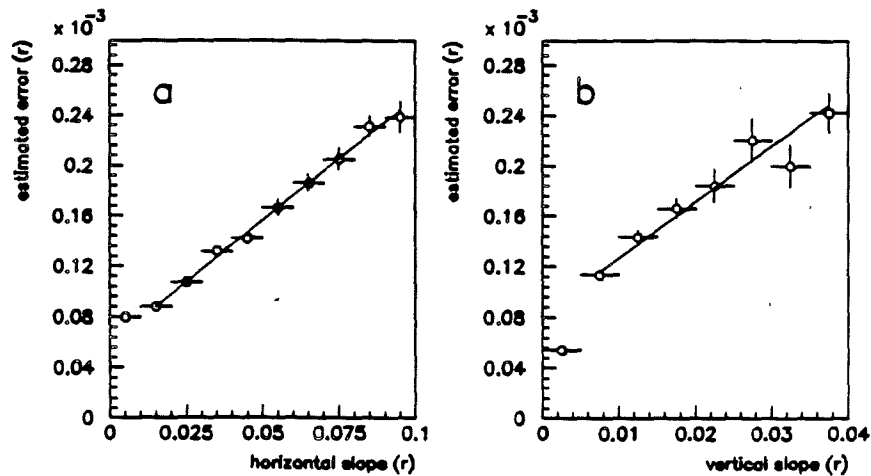
Figure 5.11: The error on the slope depends linearly on the slope. Plot a shows $\sigma_{y'}$ versus y', and b shows $\sigma_{z'}$ versus z'.

Simple Check on Track Resolution

It was argued in an earlier section that the momentum of a track is inversely proportional to the angular deflection of the track in the CCM field

$$p \propto \frac{1}{\theta}$$

degrees of freedom	intercept a_0	slope a_1	χ^2
9	$(1.77 \pm 0.20) \times 10^{-3}$	$(6.14 \pm 0.12) \times 10^{-5}$	1.1
11	$(1.93 \pm 0.11) \times 10^{-3}$	$(4.72 \pm 0.10) \times 10^{-5}$	2.2
13	$(1.69 \pm 0.10) \times 10^{-3}$	$(3.54 \pm 0.10) \times 10^{-5}$	1.4

Table 5.9: Linear fit parameters for track momentum resolution: $\sigma_{(1/p)}/(1/p) = a_0 + a_1\, p$.

which implies that the fractional errors on p and θ are proportional:

$$\frac{\delta p}{p} = -\frac{\delta\theta}{\theta} \propto p,$$

so the relative resolution on the momentum is proportional to the momentum. One expects the constant of proportionality to depend on the number of detectors contributing to the fit. A plot of $\sigma_{(1/p)}/(1/p)$ versus p is given figure 5.12, for nine, eleven, and thirteen degrees of freedom. A linear fit was performed for each set, and the fit parameters are reported in table 5.9.

Note the nonzero intercepts (approximately 1.6×10^{-3}) reported from these fits. These can be compared to the contribution to $\delta\theta$ from multiple scattering.[27] Roughly speaking, $\delta\theta^{\mathrm{MS}} = k/p$ with k a constant, so $\delta\theta^{\mathrm{MS}}/\theta \propto \delta\theta^{\mathrm{MS}}p = k \approx 1.6$ mr. Taking 200 GeV to be a typical track momentum, we find $\delta\theta^{\mathrm{MS}} \approx 10\ \mu r$, which is in the right order of magnitude for multiple scattering in the forward spectrometer itself.[28] Multiple scattering also contributes to the intercepts depicted in figure 5.11.

The effective angular resolution can be measured from a histogram of the quantity $\sigma_{(1/p)}/(1/p) - a_0 - a_1 p$. In the case of eleven degrees of freedom, a Gaussian distribution is obtained with a fitted sigma of 0.4 mr. This compares well with the estimates 0.2 - 0.5 mr obtained from the simple model described earlier. Taking $\delta\theta \approx 0.4$ mr, and estimating $\theta = p_T^{\mathrm{CCM}}/p \approx 2/p$, we find $\delta p/p \approx 2 \times 10^{-4}\ p$ which is within a factor of three of the values measured for the slope, a_1.

Correlations of Track Parameters with Position

It is interesting to note how strongly the track parameters are correlated in the lab. Tracks were chosen for which the fit was reported at the PCV plane, and plotted

---

[27]More details can be found in [Salvarani, appendix A.9].

[28]The air and wire chambers from the PCVs to the DCs amount to a few tenths of a radiation length.
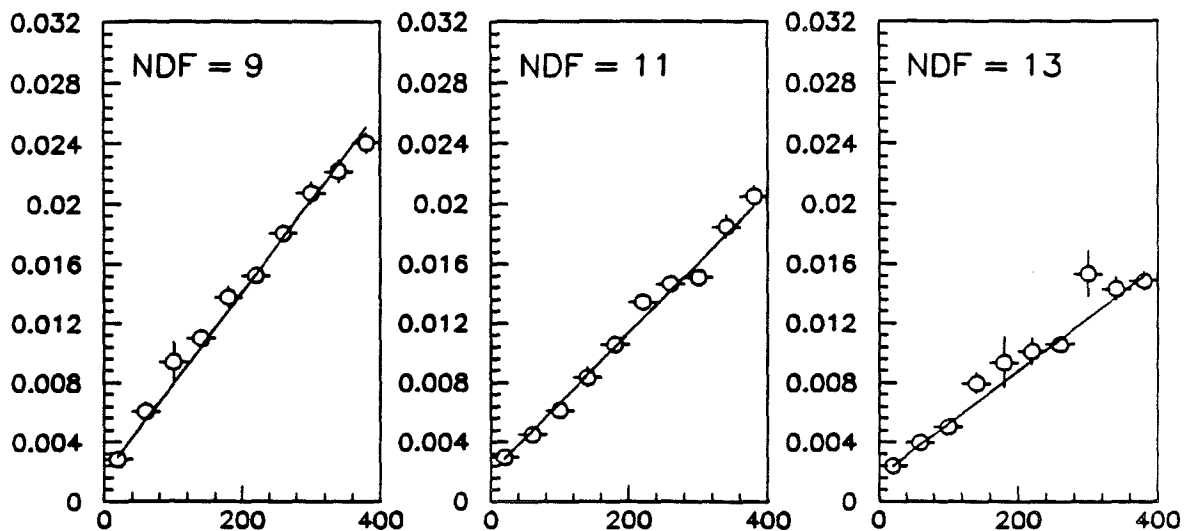
Figure 5.12: Track resolution for the scattered muon, for different degrees of freedom.

track parameters.[29] As depicted in figure 5.13, the inclination of a track can be predicted by its position in the chamber. Plots a and b show that positive and negative tracks are well separated in the horizontal coordinate. There is no separation in the vertical coordinate. There are strong correlations with momentum, also, as depicted in figure 5.14. (Only the horizontal coordinate is shown.)

This behavior is easy to understand. In the vertical view, the track impact point depends only on the vertical slope. The horizontal slope matters for the horizontal view, also, but the important factor is the bending of the tracks in magnetic field, which gives the sharp separation between positive and negative tracks. Neglecting the horizontal slope and the dependence on vertex position, the impact point and slope should be proportional to $(1/p)$. This expectation is confirmed by the behavior $p \propto 1/y$ and $p \propto 1/y'$, as seen in figure 5.14.

These correlations are not unimportant because they tie features of the wire chambers (such as dead regions) to primary tracks quantities. For this reason, it is important to model chamber efficiencies in two dimensions with as much care as possible.[30]

---

[29]Similar plots are obtained for tracks reported at the PCN plane.

[30]The chamber efficiency models are discussed later in this chapter.
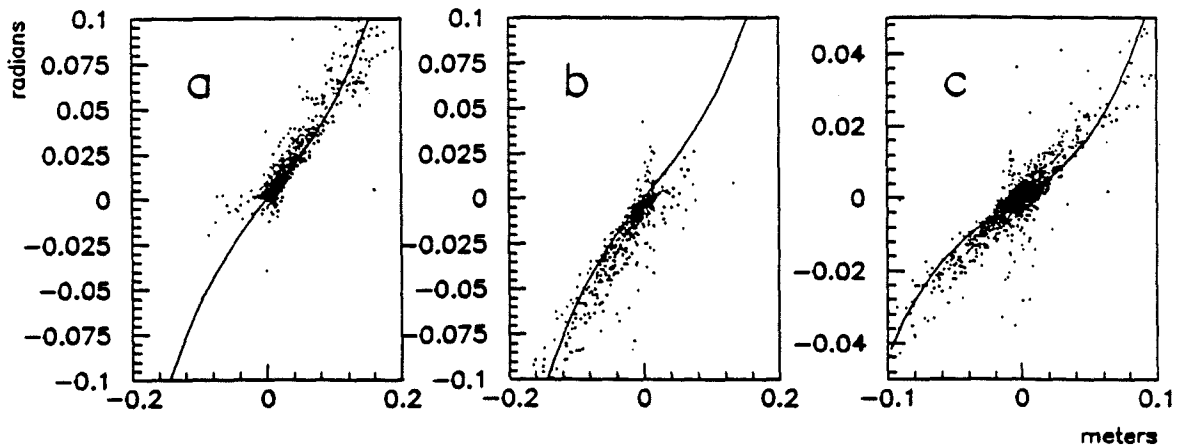
Figure 5.13: The correlations between track slope and position, as reported at the PCV chambers. Plot *a* shows y' versus y for positive pions, and plot *b*, for negative pions. Plot *c* shows z' versus z for all pions. The curves are third-degree polynomial fits.
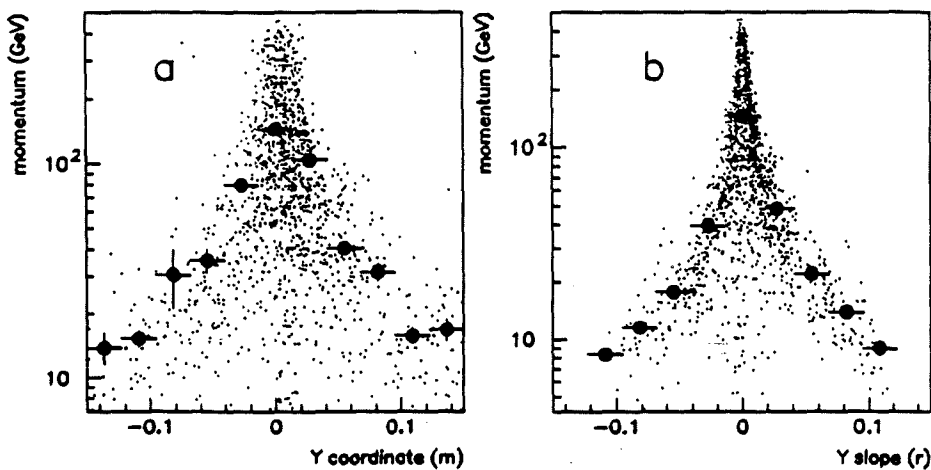

Figure 5.14: The correlations between momentum and the horizontal position, as reported at the PCV chambers. Plot *a* shows p versus y, and *b* shows p versus y'.

5.2.7 Muon Match

The goal of muon match is to identify candidates for the scattered muon.[31] The technique is simple in principle: all combinations of straight-line projections behind the hadron absorber are compared to all forward spectrometer tracks. Those matches satisfying simple criteria are designated as muons.

The muon chambers (PTMs) and the small muon hodoscopes (SMSs) contain only horizontal and vertical elements, so unless there is exactly one horizontal or vertical projection, an ambiguity arises which only can be resolved using forward spectrometer tracks.

Point-match and Intersection-match

There are two methods used to match forward spectrometer tracks with pairs of muon chamber lines [Ant89b]. In the first, which we will call the point-match method, the FS track is extrapolated along a straight line to the back of the hadron absorber. A set of χ^2 values is calculated for each candidate match:

$$\chi^2_\alpha \equiv \left(\frac{\alpha_{\text{FS}} - \alpha_{\text{PTM}}}{\sigma_\alpha} \right)^2$$

where $\alpha = y, z, y', z'$, and $\sigma^2_\alpha = (\sigma^{\text{PTM}}_\alpha)^2 + (\sigma^{\text{MS}}_\alpha)^2$. The errors on the forward spectrometer tracks are not propagated to the plane of the χ^2 test. The effects of multiple scattering in the calorimeter and hadron absorber are not negligible,[32] $\sigma^{\text{MS}}_\alpha$ is meant to include some measure of the error due to muon interactions in the calorimeter and hadron absorber. The standard formula for the Gaussian approximation to multiple scattering is used. A match was accepted if all χ^2_α were smaller than the cut value of 40. This cut is very far away from the observed peak, which for $\alpha = z$ or z' stops at about 10. For $\alpha = y$ or y', there is a long tail extending well past 40 [Ant89a]. In the case of multiple matches, the match with the lowest χ^2 was taken, and the others abandoned.[33]

Although most muons are identified using the point-match method, some fail due to large-angle scatters in the absorber or calorimeter. A second method of

---

[31]If there is more than one candidate, then the vertex processor chooses the one which makes the best fit with the beam muon.

[32]The guassian approximation to the multiple scattering distribution indicates that the rms angular deviation of a 100 GeV muon is roughly 2 mr, and the rms positional deviation is a couple of millimeters.

[33]Technically, they were recorded in an extension of the muon projection list, but the vertex processor handled only the match with the lowest χ^2.

muon matching (the "intersection-match method"), was devised which allowed for a kink in the muon trajectory. In this method, the intersections of straight-line extrapolations of the forward spectrometer and muon chamber tracks are calculated in the horizontal and vertical views separately. If the X positions of these intersections agree to within 8 cm, and if these positions fall within the range covered by the calorimeter and the hadron absorber, then the match is accepted. In the case of multiple matches, the match giving the smallest angle of scatter is kept.

Both methods of muon match start with downstream straight line segments in the forward spectrometer. If the found muon track contains no drift chamber and no PSA hits, then no match is made, and the event is lost (assuming there were no other muons in the event).

Efficiency of the Muon Match

It has been estimated from Monte Carlo that the muon match was over 99% efficient [Anthony, p.91]. These Monte Carlo studies did not, however, include catastrophic muon interactions in the steel. The muon match efficiency was measured from data, by scanning events satisfying these criteria [SA91a, SA91b]:

- There could be one in-time beam, no out-of-time beams.

- The single in-time beam must be fitted.

- There must be at least two FS tracks.

- There must be one positive track, reaching the DCs, with nonzero momentum.

- There must be at least one muon line in each view.

Muon match was said to have failed if there was no identified muon in the event. After scanning one hundred events, found seven genuine failures were found, out of about 376 candidates. The muon match inefficiency is estimated to be $1.9 \pm 0.7\%$.

Efficiency of the Muon Line Reconstruction

Sometimes muon line pattern recognition finds the wrong lines in the PTMs due to noise hits, or low multiplicity. From a scan, this was estimated to happen $2.4 \pm 0.8\%$ of the time [SA91a].

Loss of events occurred when the muon causes showers in the steel or concrete absorbers. These showers can flood the PTMs and SMSs, making it impossible to reconstruct any muon lines. A visual scan showed this rate to be negligible [SA91a].

5.2.8 Vertex Fit

Given fitted tracks, including the beam and (candidate) scattered muon, the final step in event reconstruction is to find the primary vertex, and secondary vertices, if any. This was carried out by the vertex procedure in three steps:

1. Find the "$\mu\mu$ vertex," taking the beam and scattered muon only.

2. Using the $\mu\mu$ vertex as a starting point, find the primary vertex by adding appropriate hadron tracks and refitting.

3. Take any hadron tracks not fitted to the primary vertex, and attempt to find secondary vertices.

The $\mu\mu$ Vertex

The $\mu\mu$ vertex is fundamental. If the found beam and scattered muon tracks are incompatible, then no $\mu\mu$ vertex can be found, and event reconstruction is aborted.

The "Convex" search method is used for the $\mu\mu$ vertex and for the primary vertex [Wit81a]. First the tracks provided by the track fit are swum to a common point. Then the tangents to the trajectories (which are curved) are calculated at that point, and the point is found which minimizes the perpendicular distances from all tangents to that point. The coordinates for this point can be calculated explicitly due to the fact that the tracks have been approximated by their tangents. The tracks are swum to the new point, and the tangents recalculated. The process is repeated until the change in vertex position from iteration to iteration is small enough, or if the χ^2 of the vertex is too large for too many iterations. Each calculation involves inversion of a weight matrix, which can be used to calculate a generalization of the χ^2 function [Wit81b]:

$$\chi^2 = \sum_i \left\{ \sum_\alpha \frac{(\alpha_V - \alpha_i)^2}{\sigma_{\alpha_i}^2} + 2 \sum_\alpha \sum_{\beta \neq \alpha} \frac{(\alpha_V - \alpha_i)(\beta_V - \beta_i)}{\sigma_{\alpha_i \beta_i}^2} \right\}$$

where α and β run over the cartesian coordinates X, Y, Z; i denotes the tracks, and V the found vertex. The covariances are calculated from the fit; they refer to errors on the vertex position, not errors on the tracks. Note that the track momenta are not varied in this process.

(If the covariances $\sigma_{\alpha_V \beta_V}$ were neglected, then this χ^2 function would reduce to a kind of distance-squared:

$$\chi^2 = \sum_i \sum_\Delta \left(\frac{\Delta_i}{\sigma_{\Delta_i}} \right)^2,$$

where Δ is simply the perpendicular distance from the track to the vertex point, and σ_Δ is the estimated error on Δ due to uncertainty in the vertex position.)

Vertices with Hadrons

The algorithm for finding the primary vertex uses the same Convex search procedure, but it is complicated by the fact that only some of the hadron tracks belong to the primary vertex. (Hadron secondary interactions and decays produce tracks which do not point to the primary vertex.) Part of the job of vertex fitting is to determine which hadron tracks belong to the primary vertex, and which are merely "close."

To begin, all hadron tracks are included in the search for the primary vertex. If the resulting χ^2 probability is smaller than 10^{-3}, then the fit is rejected. The track with the largest normalized residual (Δ/σ) is dropped, and another attempt is made. Tracks are dropped in this fashion until an acceptable χ^2 probability is obtained. After that a last attempt is made to add the dropped tracks: they are attached to the vertex if the χ^2 probability remains acceptable. Those tracks which are included in the fit are considered to come from that vertex, and are said to be "fitted." All other tracks are called "close" tracks. A track can be fitted to one vertex only.

Secondary vertices are searched using any tracks not fitted to the primary vertex. There can be any number of outgoing tracks in a secondary vertex, and either zero or one ingoing track. Clearly the ability to find a secondary vertex improves as the distance between the primary and secondary vertex increases.

Neutral two-prong vertices (called "V-zeros") are special. They are produced by decays of K^0s and Λs, and by the conversion of real photons.[34] They can

---

[34]The neutral resonances ρ^0, ϕ, ω, J/ψ, etc., are very short lived, so their decay products

occur at large distances from the primary vertex. All tracks are considered when searching for V-zeros, even those already fitted to the primary vertex. If a fitted track together with another track forms a V-zero, and if the invariant mass of the pair is consistent with known neutral long-lived particles, then a neutral vertex is formed from the pair, and the track originally fitted to another vertex is detached from that vertex. Monte Carlo and data both show that the number of V-zeros in exclusive ρ^0 events is negligible.

Normalized Distance to the Vertex

An important quantity in the vertex fit is the normalized distance to the vertex, defined as

$$d_N = \left(\frac{\Delta}{\sigma_\Delta}\right)$$

where Δ is the perpendicular distance from the track to the vertex point, and σ_Δ is the estimated error on Δ. A plot of d_N for all tracks ("fitted" and "close") is shown in figure 5.15. The shaded portion of the histogram shows d_N for fitted tracks only. Although there is no explicit cut on Δ or d_N,[35] the vertex fit procedure clearly attaches tracks to the primary vertex with $d_N < 4$. Figure 5.15 also shows the absolute distances of tracks to the vertex (Δ); the shaded regions shows that fitted tracks are usually within a centimeter of the vertex.

Track Errors at the Vertex

Since the target was placed inside the vertex magnet, the track inclinations reported by track fitting are different than those expected at the point of interaction. Part of the function of the vertex processor is to swim all tracks to the vertex, and report the primary three-momenta of the reconstructed trajectories there. In addition, it must report the estimated errors on these quantities. The routine used for this purpose is called VTRACK, and it performs several functions:

- It traces the ray.

- It propagates errors, mixing components of the covariance matrix due to simple extrapolation, and due to the bending of the track by the magnetic

---

should be fitted to the primary vertex, barring secondary interactions.

[35]The maximum values for these quantities were set to impossibly large values – effectively, no cut at all.
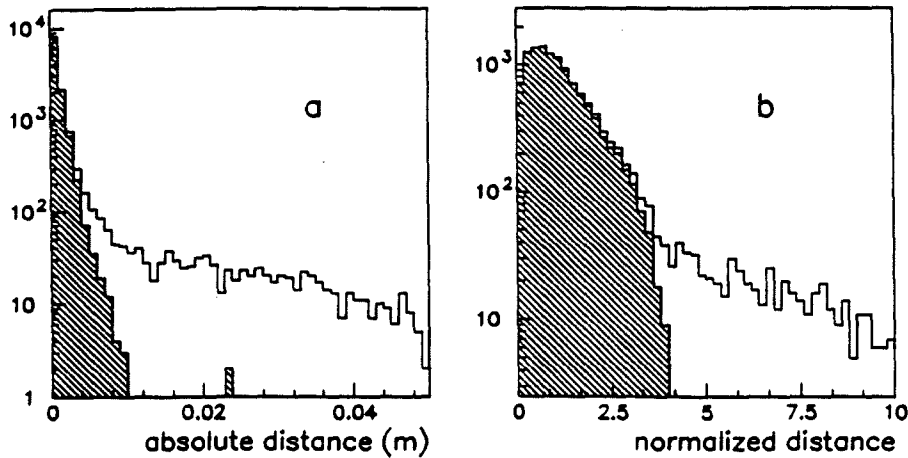
Figure 5.15: Distribution of absolute and normalized distance to the primary vertex, for tracks in the exclusive ρ^0 sample. The shaded region indicates tracks fitted to the vertex.

field.[36]

- It adjusts the errors to take multiple scattering and energy loss into account.

Note that the track momentum is *not* changed during swimming.

Track parameters at the vertex are discussed in the analysis chapter.

Efficiency of Vertex Reconstruction

It is important to know the success rate of vertex reconstruction. Given a valid beam and scattered muon, how frequently is a primary vertex found? Fifty events with no primary vertex were scanned [SA91a]. In all cases the vertex was lost due either to errors in track reconstruction, or to impossible topologies. The latter refers to events in which the muon radiated a large-energy photon downstream of the PCN chambers, causing a false determination of its momentum. When the track is swum through the CVM field, it does not meet the beam trajectory. The incidence of genuine failures of vertex fitting is negligible.

---

[36]In general the errors can get larger or smaller in magnitude, especially in the bend plane coordinate and slope.

5.2.9 The PTMV Production

As explained above, the PTMV production was the main event reconstruction program for E665. It was an amalgamation of pattern recognition, track fitting, muon match, and vertex fitting put together in one program. It read the output of the Filter programs, and tried to reconstruct every event. All events were written out.

Two simple cuts were applied in the earliest stages of pattern recognition.

1. There must be at least one in-time beam.[37]

2. There must be at least one muon projection behind the hadron absorber, or event reconstruction was aborted.

If these two requirements were met, then full pattern recognition was run, followed by track fitting, muon matching, and vertex fitting.

5.2.10 Calorimeter Analysis

Calorimeter analysis is completely independent of all other detectors — it can be run before or after PTMV.[38]

The most used implementation of standard calorimeter analysis is found in the Data Reduction ("DR") program [BWJES]. Loose event selection criteria were combined with standard calorimeter analysis. The reconstructed events written out by PTMV contain a sizable fraction of "uninteresting" events which can be eliminated by simple kinematic cuts. Since the calorimeter analysis was relatively fast, a reasonable DR project could be carried out easily. Most students have used the output of the DR tapes for their analyses. However, the exclusive neutral meson sample used in this analysis was skimmed directly from the PTMV output tapes, as discussed in the Analysis chapter.

---

[37]A beam is "in-time" if at least one beam hodoscope element fired in each of seven stations, indicating that the reconstructed track corresponds to the correct bucket, not an earlier one.

[38]This fact was used to help check the efficiency of deep-inelastic event reconstruction. Also, recent analysis of nuclear shadowing rely on the calorimeter information for eliminating μe and bremsstrahlung background rather than on tracking.

The details of calorimeter analysis and performance are given in the calorimeter chapter.

5.3 Monte Carlo Simulations

Many aspects of event reconstruction are not difficult to understand using simple pencil-and-paper calculations. For example, rough estimates for track resolution were given in the section on track fitting. These estimates are useful as checks on the event reconstruction, and as guides for understanding. Serious analyses, however, require more rigorous determinations of resolutions and efficiencies. For this purpose Monte Carlo techniques are widely employed.

The idea is to simulate the input to event reconstruction programs, and see how well the events are reconstructed. This requires an approximate knowledge of the real event distributions, and an exact knowledge of the apparatus. This suggests a dichotomy of tasks:

1. Generate "truth" tracks meant to mimic what nature provides in the real data.

2. Simulate the response of the apparatus to the truth tracks.

E665 has divided the task into two parts along these lines. Task one is carried out by the first stage Monte Carlo, and task two by the second stage.

5.3.1 First Stage Monte Carlo

Most distributions studied in E665 have been measured before, to some degree of accuracy. This means that fairly concrete expectations for the results of analysis exist. These expectations form the basis of the first-stage Monte Carlo. In particular, public software packages based partly on theoretical prejudices and partly on empirical parametrizations have been implemented to cover the two main steps of event generation:

1. generation of primary particles at the point of interaction

2. simulation of the trajectories, decays, and secondary interactions of particles as they traverse the apparatus

The first step embodies the "physics" of the events, so an appropriate software event generator must be chosen for the analysis. For example, the well-known LUND model is used in E665 to generate ordinary deep-inelastic events. Other available generators include μe scattering (with no primary radiation) and muon Bremsstrahlung. Also, there is an interface to GAMRAD for LUND events. There are non-physical generators, used for measuring reconstruction efficiency or trigger acceptance.

None of these generators simulates exclusive neutral meson production. A special Monte Carlo generator called RHOGEN has been written for this purpose, and is discussed in detail in the next section.

The realistic passage of particles from the interaction point to the calorimeter is carried out using GEANT. This package simulates the effects of magnetic fields and matter on the particles, and also particle decay. It requires faithful maps of the magnetic fields, and basic representations of the apparatus.[39] Fortunately the physics generator and GEANT are well-separated in the E665 Monte Carlo, making the implementation of the custom-made exclusive ρ^0 generator straight forward.

GEANT can simulate most interactions of particles passing through matter, however, some processes require too much cpu time. In order to to generate a large sample of events in a reasonable amount of time, only muons were propagated beyond the front face of the calorimeter and the hadron absorber. Hadrons, electrons, and pions were stopped; no showers were simulated. Only multiple scattering was taken into account in the propagation of muons through the calorimeter and hadron absorber; bremsstrahlung, elastic μe scattering, and muon-nucleon interactions were neglected. As a consequence, the trigger efficiency was poorly represented in the Monte Carlo data. Special studies were carried out to determine the muon "self-veto" probability, using real data. These studies are presented in the analysis chapter.

---

[39]Originaly EMC code was used, which lacked several important effects, such as secondary interactions outside the target, and pair production bremsstrahlung in the apparatus. Several people worked hard to implement the more realistic simulation provided by GEANT, including Shuichi Kunori, Erik Ramberg, Silhacene Aid, and Steve O'Day.

5.3.2 The Exclusive ρ^0 Generator

Most analyses of hadrons in deep-inelastic scattering focus on inclusive distributions. The LUND model of fragmentation can be used for the acceptance corrections needed in these analyses. The topology of exclusive reactions, however, is quite different than that modeled in the LUND Monte Carlo. In exclusive ρ^0 events, for example, the "fragmentation" consists of two oppositely-charged pions, which together take up nearly all of the energy lost by the muon. Typically they are fast, forward-peaked, and of course correlated. In order to model such events for the purposes of studying the reconstruction efficiency, a special Monte Carlo generator (RHOGEN) was written.

The E665 Monte Carlo was based originally on code inherited from EMC, but since has been altered substantially (e.g., it has been fitted into GEANT). Despite its complexity, the first stage Monte Carlo retains some conceptual simplicity.

1. The beam is generated first. The Monte Carlo beams are taken from beam triggers in the real data, and the hits in chambers are smeared to simulate real chamber resolution. GEANT is used to choose an interaction point.

2. Control is passed to the "event generator," which determines the primary interaction. This entails picking random values for the event kinematics (e.g., Q^2 and ν) according to an assumed distribution. In the case of parton scattering, the LUND is used to decide which parton absorbs the photon emitted by the muon, and to fragment this parton into primary hadrons. These hadrons are then listed in the truth bank, MTRU. In the case of muon-electron scattering, the kinematics are worked out from a random value for the energy transfer, ν. (LUND is not needed.) In the case of exclusive neutral meson production, custom-written code determines the kinematics, and the decay distributions and mass of the resonance.

3. GEANT takes over the event, and swims each of the primary particles it finds in the MTRU bank through the apparatus, allowing random reinteractions of hadrons, photon conversions, etc. When additional particles are generated, these are automatically placed in the MTRU bank. Vertex and track banks are also generated.

Generation of simulated exclusive ρ^0 events simply involves producing a list of primary particles, that is, a scattered muon, a virtual photon, the scattered target nucleon, the ρ^0 resonance, and the two decay pions. GEANT handles the mundane aspects of the event generation, and the second stage Monte Carlo simulates the responses of the apparatus.

215

General Considerations

The purpose of this generator is to provide fake events resembling closely real ones so that the effects of the apparatus on the measurement of physics quantities can be determined. There are three important aspects to the generation:

- kinematics (the cross section)

- resonance mass

- resonance decay

The cross section used is a standard form taken from the Vector Dominance Model:

$$\frac{d^3\sigma}{dQ^2\, d\nu\, dt} = \sigma_0 \Gamma \left(\frac{m^2}{Q^2+m^2}\right)^2 \left(1 + \epsilon\frac{\xi^2 Q^2}{m^2}\right) e^{-b|t|} \qquad (5.1)$$

In this equation, E_0 is the muon beam energy, and $\nu = E_0 - E_1$ the energy lost by the muon. The momentum transfer from the muon is Q^2, and t is the momentum transfer to the target (e.g., a proton). The factor Γ represents the effective virtual photon flux, and ϵ is the virtual photon polarization:

$$\Gamma = \frac{\alpha}{8\pi}\frac{W^2 - M^2}{E^2 M^2 Q^2}\frac{1}{1-\epsilon}$$

$$\frac{1}{\epsilon} = 1 + \frac{2(Q^2 + \nu^2)}{(4EE' - Q^2 + Q^2_{\min})}\frac{Q^2}{Q^2 - Q^2_{\min}}.$$

There are two free parameters:

$$b = b(Q^2) \qquad \text{the diffractive slope parameter}$$
$$\xi^2 = \text{a constant determining } R = \sigma_L/\sigma_T.$$

In this generator, E_0, ν, Q^2, and t are taken to be the primary kinematic variables: they are chosen randomly and independently. (Of course, checks for kinematic bounds are made.)

The mass distribution of the ρ^0 resonance has been studied in great detail. Naively one expects it to follow a relativistic Breit-Wigner form. It turns out, however, that phase space and quantum mechanical effects cause mass-dependent modifications. For the purpose of generating Monte Carlo ρ^0 events, a distribution based on the Söding model is used:

$$N(M) = A\, R(M) + B\, I(M)$$

216

$$R(M) = \frac{MM_\rho\Gamma(M)}{(M^2 - M_\rho^2)^2 + M_\rho^2\Gamma^2(M)}$$

$$I(M) = \frac{M^2 - M_\rho^2}{(M^2 - M_\rho^2)^2 + M_\rho^2\Gamma^2(M)}$$

$$\Gamma(M) = \left(\frac{M}{M_\rho}\right)\left(\frac{M^2 - 4m_\pi^2}{M_\rho^2 - 4m_\pi^2}\right)^{3/2}\Gamma_\rho.$$

Standard values are used for the resonance parameters: $M_\rho = 0.770$ GeV and $\Gamma_\rho = 0.153$ GeV. The relative strength of the interference term is set to $B/A = -0.1$, and the distribution $N(M)$ is normalized to one over the range $2m_\pi = 0.28$ GeV to $2m_\pi + 10\Gamma_\rho = 1.81$ GeV.

Other mass shapes are available, including a simple Breit-Wigner resonance, and a gaussian, used for generating exclusive ϕ events.

The code for generating decay distributions was written with the ρ^0 in mind: the model is of a massive neutral particle decaying into a pair of charged particles. In reality the decay distribution follows spherical harmonics determined by the spin of the resonance, but in this Monte Carlo the distributions are simple functions of the polar (θ) and azimuthal (ϕ) decay angles. Several options for the polar decay distribution are available, including

$$\frac{dN}{d\cos\theta} = \frac{1}{2}, \text{ or } \frac{3}{2}\cos^2\theta, \text{ or}$$

$$= \frac{3}{4}\sin^2\theta, \text{ or } \frac{3}{4}[(1-r) + (3r-1)\cos^2\theta],$$

where r is a free parameter with value between zero and one. The azimuthal decay distribution is

$$\frac{dN}{d\phi} = \frac{1}{2\pi} \text{ or } \frac{1}{\pi}\sin^2 2\phi.$$

The different distributions can be chosen at run time by setting values in a control file. The ρ^0 data are generated using the Söding mass formula, and various decays distributions. The ϕ data are generated using the gaussian mass distribution, and transverse polarization.

There are physics assumptions inherent in this model. The events are assumed to be exclusive: no "extra" pions are generated, and QED radiative effects are ignored. Options to generate exclusive π^0 events and photon conversions are defined, but the distributions for the cross section and the decays are not modified accordingly – they will be incorrect for these particular cases.

Preliminary Trigger Tests

The Q^2, ν, and t ranges over which events are generated are chosen to match those seen in the real data. The trigger acceptance, however, is essentially zero for the low-Q^2, low-ν region of the kinematic plane. In order to avoid running the GEANT portion of the first stage and the second stage Monte Carlo for events in this region, preliminary trigger tests were devised which allowed discarding events after kinematics were chosen. There are two types of tests:

1. A simple contour in the (Q^2, ν) plane defined a region of zero acceptance.

2. A fast estimator of the impact point of the scattered muon at the focal plane is used to define an idealized version of the trigger veto.

There are uncertainties in both methods, so in both cases conservative limits were set. There is a separate version for SAT and for LAT data.

The kinematic contour was chosen based on preliminary studies of trigger acceptance. An event was accepted if

$$E' < E'_{\text{max}} = A + B\theta^2,$$

with $A = 320$ GeV for SAT, 150 GeV for LAT, and $B = 300$ GeV/(mr)^2 for SAT, 35 GeV/(mr)^2 for LAT. These contours were picked to be inside the contour for one percent acceptance.

The fast estimator (TRNSPT) of the scattered muon trajectory uses simplified forms for the CVM and CCM fields. The net effect of the bending of the field on the particle trajectory is expressed in simple analytic forms. A kind of transfer function is built up from sums and products of matrices describing the trajectory of the scattered muon between magnets and inside magnets. This function transports the muon from the vertex point to a point in a plane downstream of the CCM, e.g., the trigger focal plane. The transport depends on the vertex position and the momentum vector of the scattered muon. Details are given in [Sch89a].

In the case of the SAT, the beam is transported to the focal plane, to define a veto region. The scattered muon is transported next. If it strikes the veto region, then the event is discarded. The LAT veto region is fixed for all events. These veto regions are smaller than the actual one, by a boundary about one centimeter wide.

The final trigger test is done after the hodoscope signals have been simulated in the second stage Monte Carlo. The beam requirement, veto definitions, and positive muon signal for the LAT are checked exactly as defined in the hardware. The trigger acceptance for the kinematic regions of interest is quite low, extending below ten percent where the cross section rises rapidly. The preliminary trigger test based on the estimated muon impact point at the trigger focal plane saves enough time to double the yield of SAT events generated per job, and increase the LAT yield by a factor of five.

Program Flow in RHOGEN

The main event generator is called RHOGEN.[40] This routine starts with a beam momentum vector and vertex point, and produces the primary particles of the interaction. There are six basic steps, as shown in figure 5.16.

1. Generate a value for the resonance mass. (RHOGEM)

2. Generate values for the kinematic variables (Q^2, ν, t). (RHOGEK)

3. Generate scattering and decay angles $(\theta_{sc}, \phi_{sc}, \theta_{qk}, \phi_{qk}, \theta_{dk}, \phi_{dk})$. (RHOGED)

4. Calculate the momentum vectors and energies in the lab for all primary particles. (RHOGEP)

5. Store kinematic quantities in standard banks.[41] (RHOGEB)

6. Apply preliminary trigger tests. (RHOPTR)

The code is internally documented; technical details may be gleaned from a listing of the pamfile. A cradle for generating events is called SPRAY, and was run on the Amdahl. Comparison of the real and simulated data is given in the analysis chapter.

---

[40]There are several routines for reading constants files, printing banks, calculating functions, and filling histograms, which will not be discussed here. The code resides in the "RHPAM."

[41]A special bank called MRHO is filled containing a copy of all quantities calculated in RHOGEN.
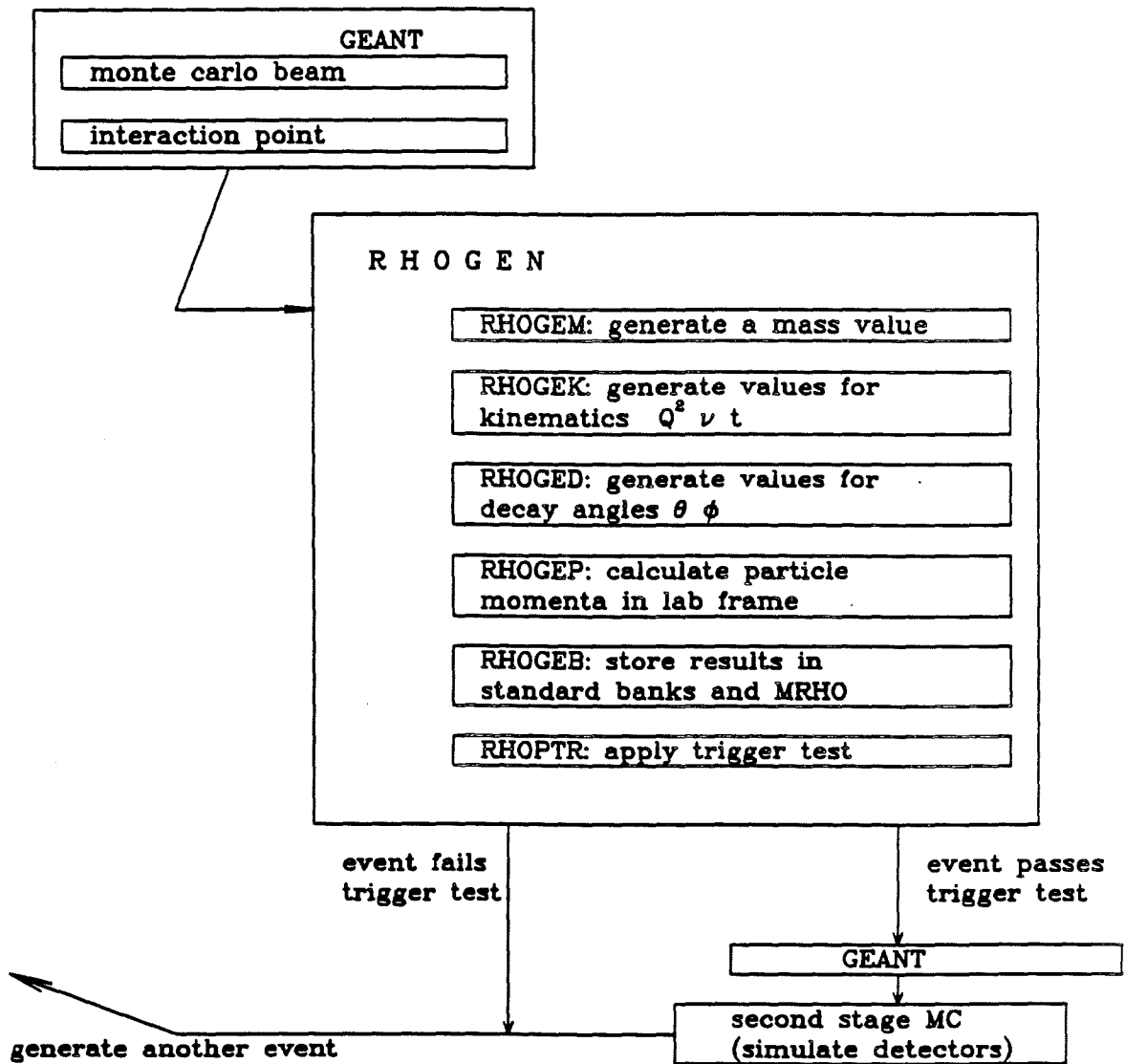
Figure 5.16: RHOGEN flow diagram

5.3.3 Second Stage Monte Carlo

The tracks generated by the first stage Monte Carlo are nearly detector independent; they are influenced only by magnetic fields and material volumes. In order for the simulated data to be useful, it must be made to resemble the real data more closely. For example, the effects of the finite aperture of wire chambers must be imposed, so that corrections for geometric acceptance can be calculated. The actual resolution and efficiency of chambers also must be simulated, in order to study the potential losses of tracks and events due to the performance of the hardware, and the requirements of the software.

In the second stage Monte Carlo, the precise position and spacings of wire chambers and hodoscopes are used to calculate the ordinal number of hit wires and scintillators, for simulated tracks. Hits are deleted randomly, according to measured efficiencies and dead regions. Finally, various kinds of noise hits are simulated, and added to the lists of hits generated from the simulated tracks. The result is a data set identical in format to the real data. The event reconstruction program (PTMV) can process these data without modification, which ensures a rigorous test of its capabilities.[42]

Alignment

The probability of reconstructing a track depends in its trajectory through the chambers; it must pass within the active area of several of them. In order to measure this probability accurately, the precise position and size of the chambers must be used. Similarly, in order to digitize the coordinates of tracks within the aperture of a wire plane correctly, the position of the first wire in the plane, of the wire spacing, and of the orientation of the wires must be known. These quantities were measured carefully for the purposes of event reconstruction; the alignment constants used by PTMV are the same as those used by the second stage Monte Carlo.

The apparatus was aligned carefully, but a residual error always remains. This error is important if it is large enough to contribute to the error used in track fitting. The alignment was refined until the error was not larger than one-tenth of the wire spacing; recall that the resolution of a wire plane is about 30% of the wire spacing. Tests of the alignment were conducted as part of a study of

---

[42]The only part of the analysis chain which is not tested is decoding; the DMAs on the raw tapes have no parallel in the Monte Carlo data. An error in one of the decoders was not simulated, and was handled directly [Sch91c, Sch91d], as discussed in the analysis chapter.

the momentum measurement, with the result that the residual alignment errors in most cases are considerably smaller than the stated tolerance. Exceptions are discussed in the analysis chapter, to the extent that they influence the analysis. An intractable alignment error should be simulated in the Monte Carlo, in oder to understand its effect. Since the basic alignment is quite good, no alignment errors are simulated.

Chamber Efficiencies and Dead Regions

A limiting factor in the reconstruction of tracks is the loss of hits due to hardware inefficiencies. The ionization of gas in a chamber is a stochastic process, as is its amplification near the wire. If a chamber is operating under less than optimal conditions, it may happen that a track will produce no signal. Electronic circuits sometimes malfunction, resulting in the loss of a signal. Ideally these occurances are very rare, but realistically the probability that a hit is "missing" may be as high as 20%. If enough chambers are inefficient, then some tracks will not produce the hits needed by reconstruction, and will be lost. These losses were quite significant in 1987-88, due to problems with certain chambers. The simulation of chamber inefficiencies is one of the most important tasks of the second stage Monte Carlo.

The efficiency of most chambers is not constant across the aperture. Some chambers are built with deadened regions through which the beam passes, for example. Others require support wires which effect the efficiency of the chamber. Sometimes an electronics card fails, causing the loss of all signals from a group of wires. The beam may damage a section of a chamber, due to the high rate of ionization, leading to films and deposits on wires which block the collection of electrons freed by ionization. It was shown earlier in this chapter that track parameters are correlated with position in chambers (see figures 5.13 and 5.14), hence with specific dead regions, whether intentional or accidental. Special features of all planes must be determined carefully, and incorportated in the Monte Carlo, so that it mimics the real data sufficiently well.

Early studies of chambers showed significant effects due to support wires in PCF, and the dead regions of the drift chambers. Later, the time-dependent efficiency of the PCN chambers was shown to correlate with the efficiency for reconstructing straight-through beam tracks. Before the production of Monte Carlo data could proceed, the dead regions of all chambers had to be delineated, and the average efficiency of each plane (outside the dead regions) measured.

Tracks from reconstructed deep-inelastic data were used as trial tracks for each

wire plane. If a given plane was not necessary for the reconstruction of a track, then the track could be used to test its efficiency. It was assumed that the efficiencies of all planes on the track are uncorrelated, so that the probability that a given plane contributes to the track is independent of whether other planes contributed.[43] Ntuples and two-dimensional histograms were filled with detailed efficiency maps. Major features were reduced to analytic forms, based on known construction techniques and details of the design. For example, a double-ring structure was observed in the PCN chambers, caused by a segmented resistive cathode. Vertical stripes were clearly visible in the drift chamber efficiency maps, due to the nonconducting strips used to bisect the horizontal planes. These and other features have been described [RSB90, Ryan]. The dead regions of the drift chambers are important for the reconstruction of tracks in exclusive ρ^0 decay, so they were measured carefully [Sch90e].

A direct manifestation of chamber efficiencies is the number of planes contributing to the scattered muon track. Figure 5.17 shows the number of planes from each forward spectrometer group contributing to the scattered muon track. The data are high-Q^2, deep-inelastic events from hydrogen, and are represented by the points with errors. The Monte Carlo data are represented by the histograms, which were normalized to the data with respect to the number of entries. The agreement is fairly good, if not perfect. The Monte Carlo tracks have slightly too many hits from PCV and the DCs, and too few from PCN and PCF. They have too many degrees of freedom, but the difference is not large: $\langle NDF \rangle_{\text{data}} = 12.2$, and $\langle NDF \rangle_{\text{MC}} = 12.4$.

If the reconstruction of the muon track were independent of the number of planes from a given detector, then the distribution of planes with hits would follow a binomial distribution: the probability P_m that m planes fire out of a maximum of n is

$$P_m = C_m^n \; \epsilon^m \, (1 - \epsilon)^{n-m},$$

where ϵ is the efficiency of an individual plane, and $C_n^m = n!/m!(n-m)!$ is the binomial coefficient. N tracks may give a distribution of planes firing, with k_m the number of times m planes fired; $k_0 + \cdots + k_n = N$. The probability that the distribution $\{k_i\}$ is observed is

$$L = p_0^{k_0} p_1^{k_1} \cdots p_n^{k_n} = \Pi_{m=0}^n \left[C_m^n \epsilon^m (1 - \epsilon)^{n-m} \right]^{k_m}.$$

The observed distribution approximates the most likely one, so the typical plane efficiency ϵ may be estimated by maximizing the likelihood, L. In practice it is

---

[43]At the time these chamber efficiencies were measured, this assumption seemed valid. Later studies of reconstruction efficiency indicated that tracks were lost in a manner suggesting *correlated* inefficiencies; this loss is discussed in the analysis chapter.

chamber	estimated efficiency		measured efficiency	mean number of hits		maximum number
	data	MC	efficiency	data	MC	number
PCV	0.66	0.71	0.85	3.8	4.3	6
PCN	0.77	0.71	0.89	9.8	9.5	12
PCF	0.90	0.86	0.90	14.0	13.5	15
DCA	0.76	0.75	0.95	6.4	6.3	8
DCB	0.75	0.83	0.95	6.5	7.0	8

Table 5.10: A comparison of plane efficiencies in real and simulated data. The "estimated efficiency" refers to the binomial error calculation in the text.

easier to work with the "log-likelihood,"

$$L \equiv -\ln \mathrm{L} = -\sum_{m=0}^{n} k_m \ln C_n^m + m \ln \epsilon + (n-m)\ln(1-\epsilon).$$

The estimated value for ϵ is the one at which the first derivative of L is zero, leading to

$$\epsilon = \frac{\sum_{m=0}^{n} m k_m}{n \sum_{m=0}^{n} k_m}.$$

Values for k_m were taken from the distributions in figure 5.17, and values for ϵ calculated. The result is listed in table 5.10. The values are considerably lower than the true efficiencies because the distributions are not quite binomial: they are strongly influenced by the minimum number of hits required to reconstruct the track. Nonetheless the agreement between real and simulated data is acceptable; the worst disagreement is in the DCBs.

Noise

There are two kinds of noise (i.e., extra chamber hits) to be simulated:

1. background noise, such as might result from spurious signals from amplifiers and latches, and

2. track-related noise, such as hits caused by delta rays.

The background noise is relatively flat, when measured with respect to track impact points at a chamber. If caused by malfunctioning electronic circuits, it is uncorrelated with track position. If caused by the remains of tracks from earlier buckets, then it is correlated weakly with tracks in the current bucket. The second
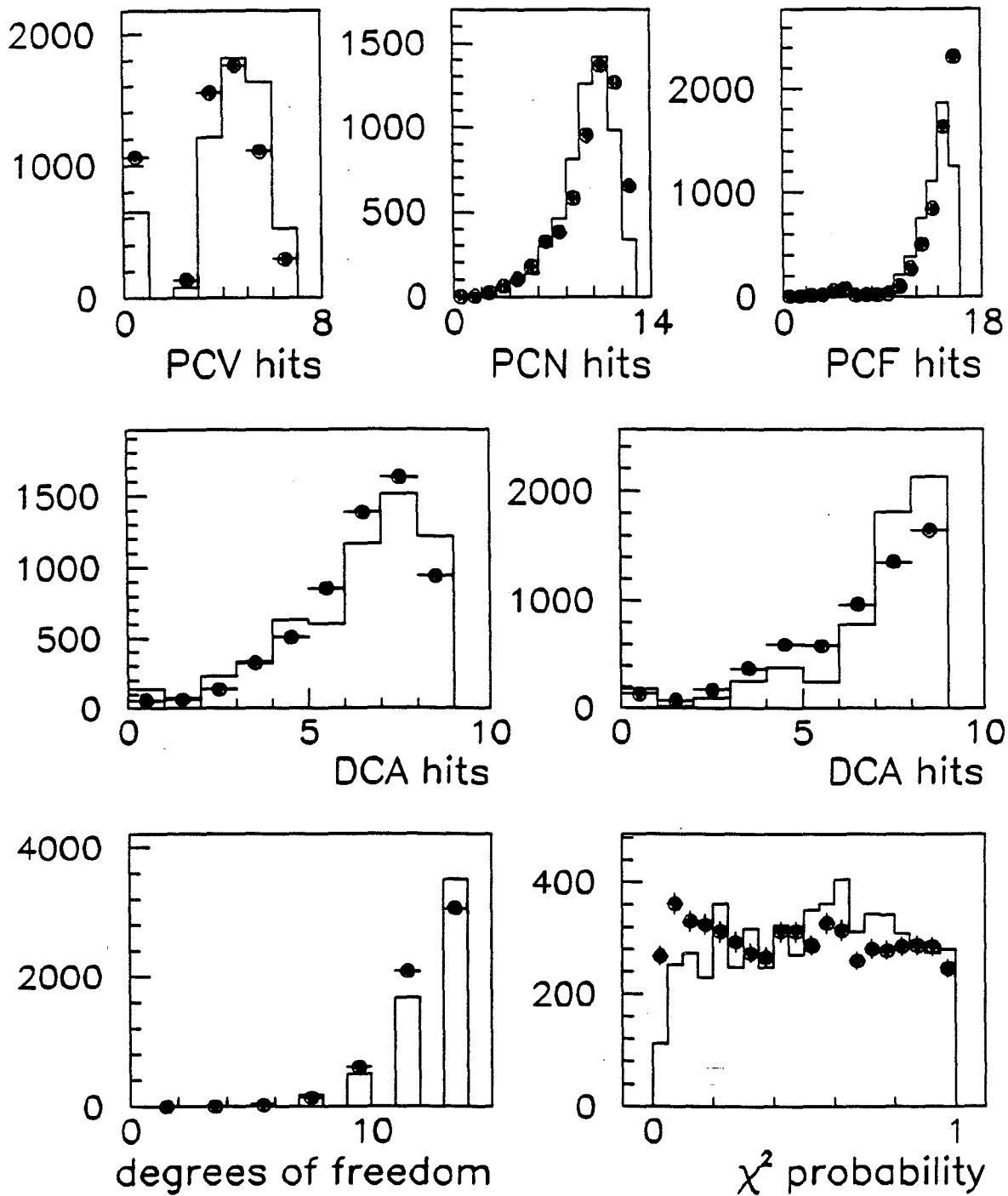
Figure 5.17: Number of planes in each detector contributing to the scattered muon track. Real data from LAT hydrogen are represented by solid circles; the simulated data are represented by the histograms, which have been normalized to the real data.

stage Monte Carlo adds hits to chambers independent of coordinate. The number of hits added is scaled to the number of hits from the simulated tracks, as was suggested after an early study of unused hits from data.

A series of plots shown in figure 5.18 shows that there are very many hits in data not used in track reconstruction. The distributions in Monte Carlo do not match the data. Nonetheless, since hits that are not correlated with the tracks to be reconstructed are unlikely to play a role in reconstruction efficiency, this simulation is thought to be adequate.

The track-related noise is more important. Large-angle delta rays may cause a cluster of wires to fire in place of one. Tracks passing through halfway between two wires may fire both, leading to a cluster of two hits. These clusters clearly influence track reconstruction, and must be handled correctly. During translation, clusters of wires are divided into clusters of one and two wires. Each cluster is treated as a single hit by pattern recognition, and track fitting. It is important to simulate the distribution of one-wire and two-wire clusters accurately. Studies of data lead to an empirical prescription for generating clusters in the Monte Carlo.[44] Figure 5.19 on page 232 shows the one-wire and two-wire residual distributions for data and Monte Carlo. The Monte Carlo mimics the data well. The similarity of the χ^2-probability distribution, shown in figure 5.17, depends on the quality of this simulation.

Missing Simulation

Some potentially important detector effects are wholly omitted in the second stage Monte Carlo.

- There is no simulation of intensity effects. For example, there are no stale tracks in the Monte Carlo, and no local loss of efficiency due to high beam fluxes. The Monte Carlo resembles the real data in the limit of zero intensity (infinite time between buckets).

- Only the latch information for hodoscopes is simulated. No pulse height or timing effects, such as the propagation of light through scintillator, are mimicked. The SMS latches were inefficient, but plainly they performed well as veto counters. This is not reflected in the Monte Carlo.

---

[44]John Ryan and Alex Salvarani tuned the model.

226

PBT
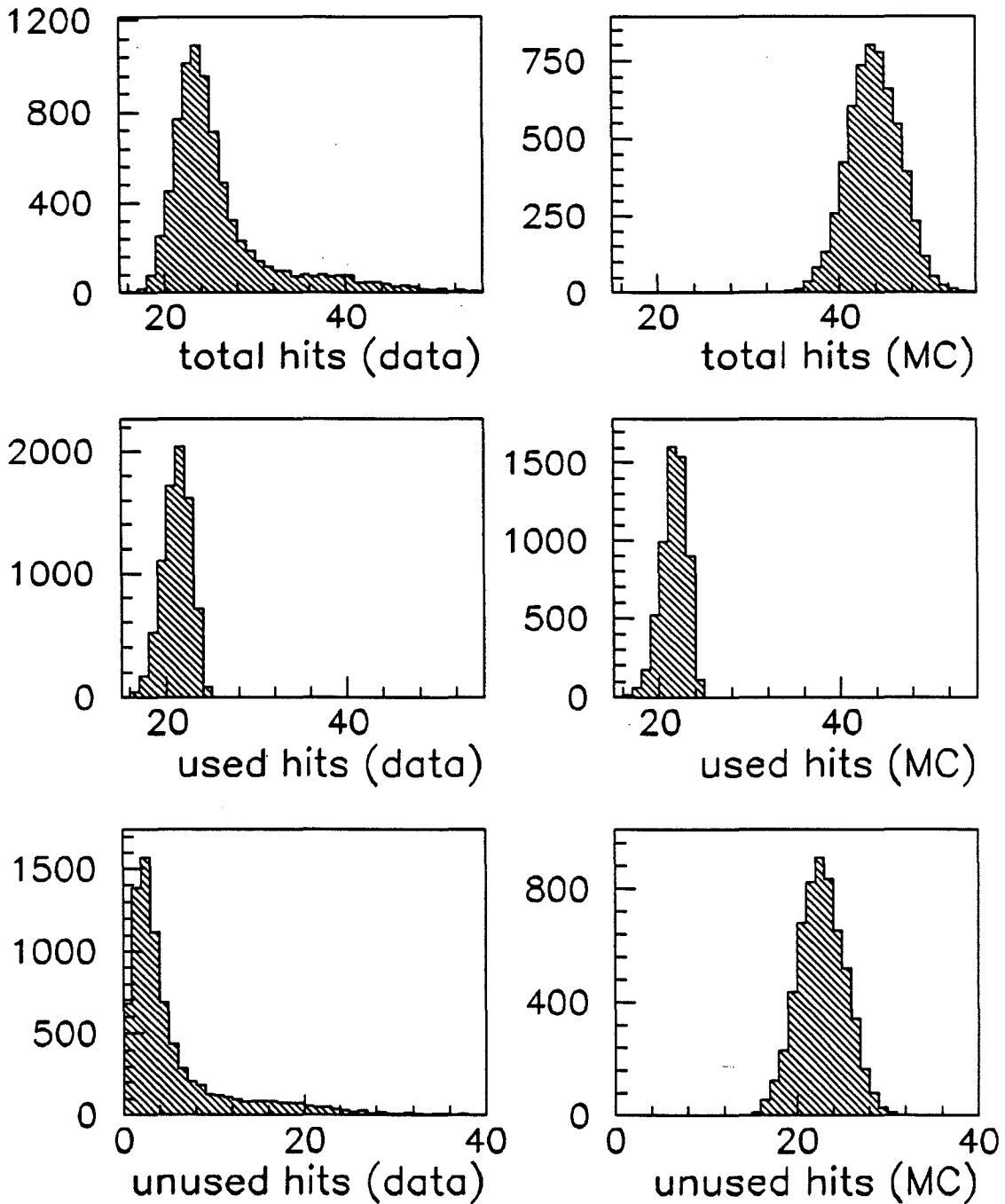
Figure 5.18: Background noise hits in data and Monte Carlo, for a series of wire chambers. The top plots show the total number of hits per event, the middle plots show the number of hits used per event, and the bottom plot shows the number left over.

PCV

total hits (data)

total hits (MC)

used hits (data)

used hits (MC)

unused hits (data)

unused hits (MC)

PCN

total hits (data)

total hits (MC)

used hits (data)

used hits (MC)

unused hits (data)

unused hits (MC)

PCF

total hits (data)

total hits (MC)

used hits (data)

used hits (MC)

unused hits (data)

unused hits (MC)

DCA

total hits (data)

total hits (MC)

used hits (data)

used hits (MC)

unused hits (data)

unused hits (MC)
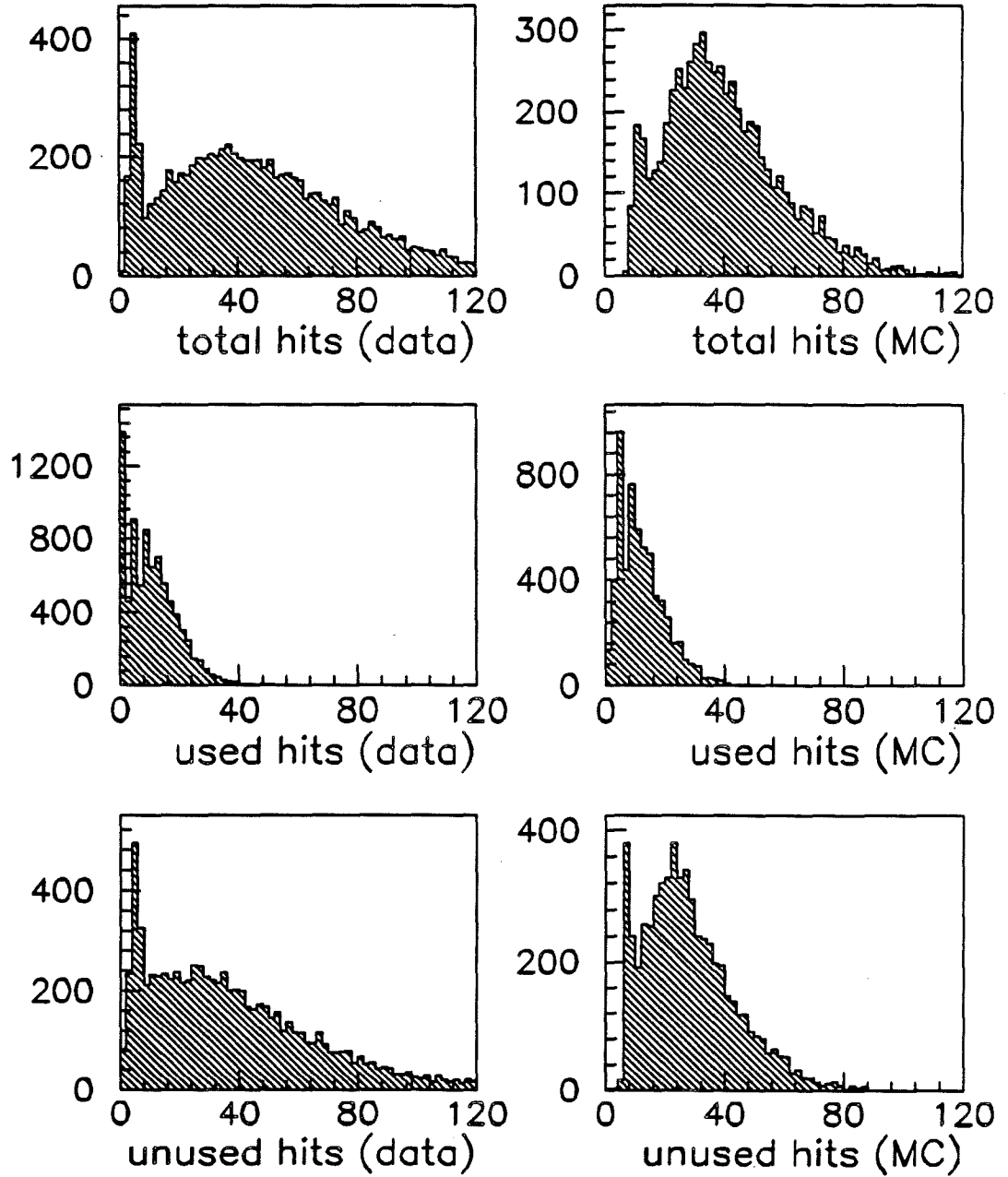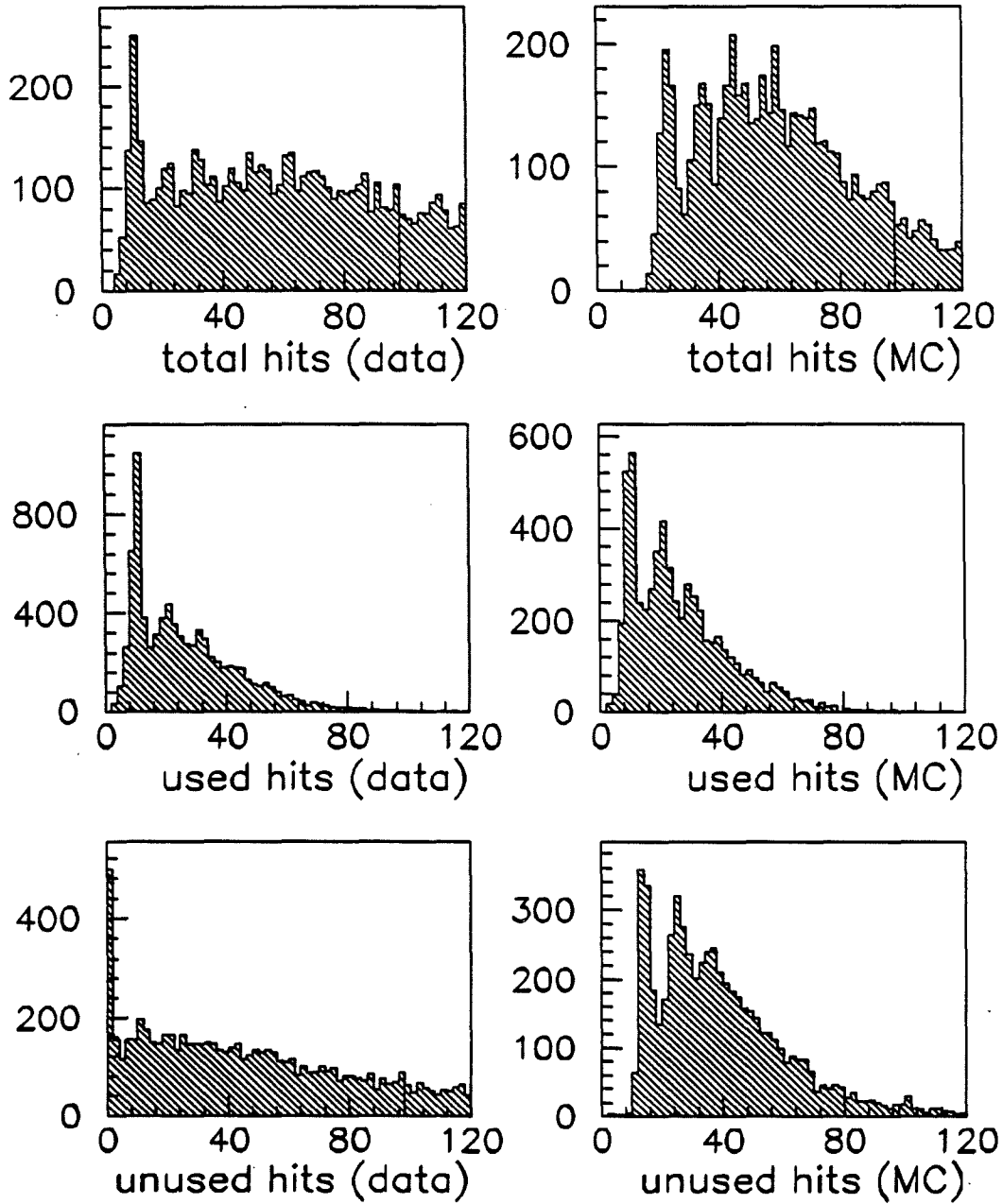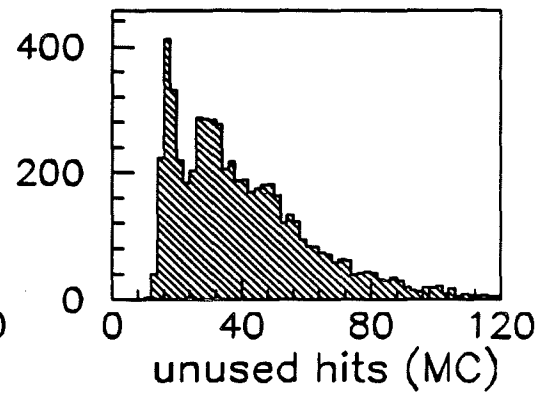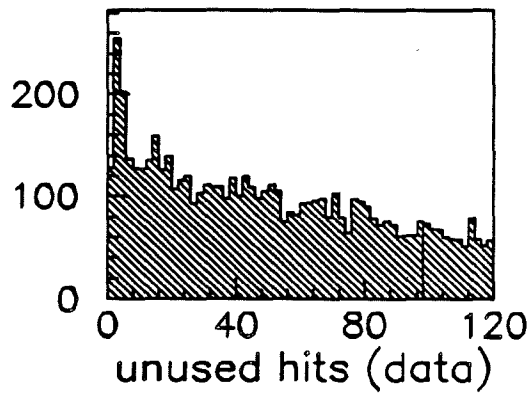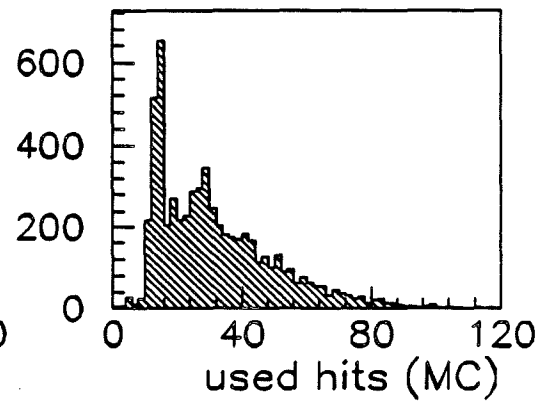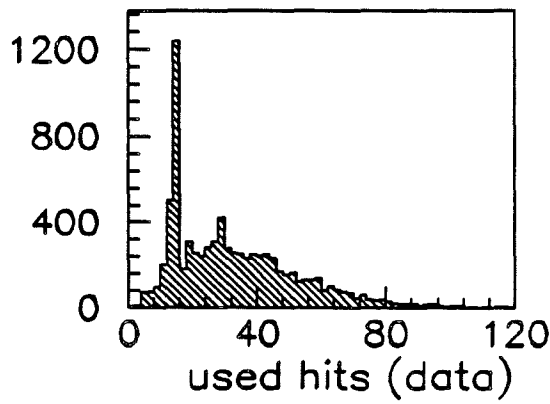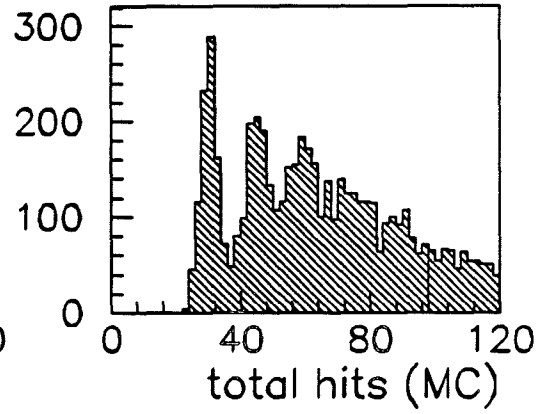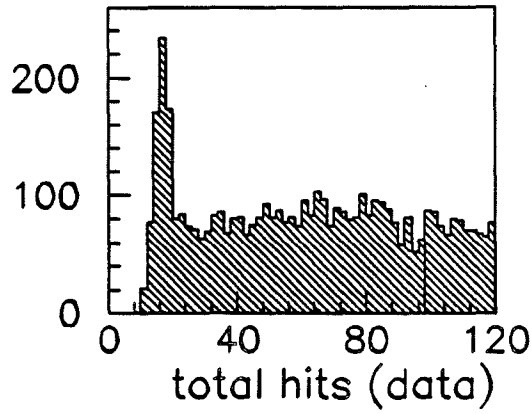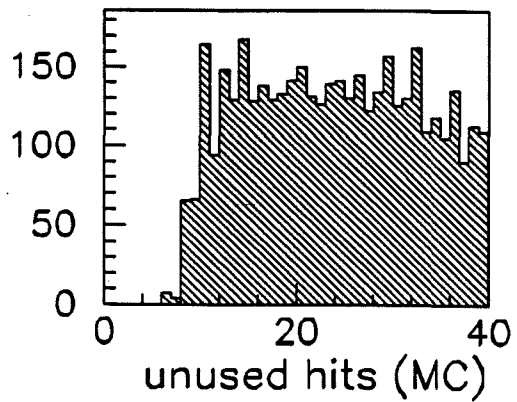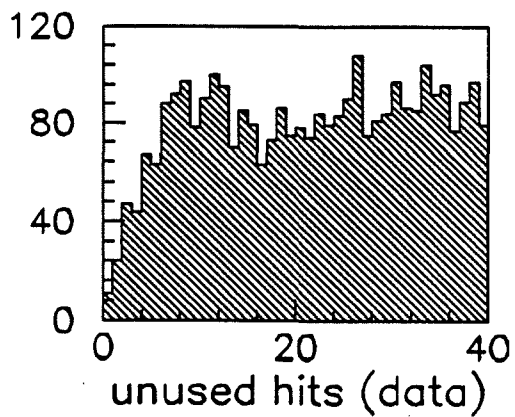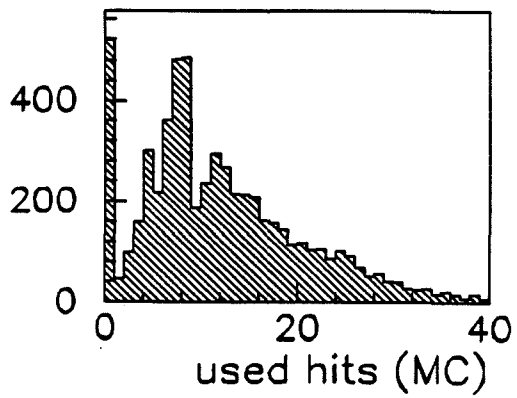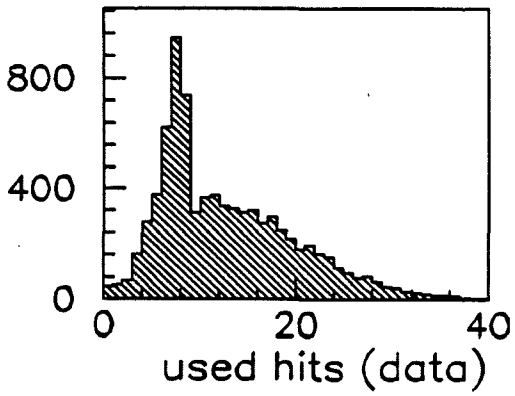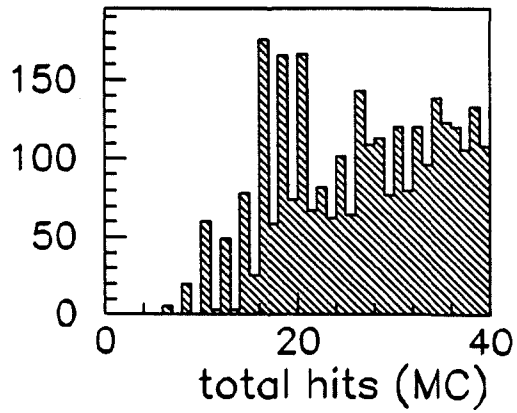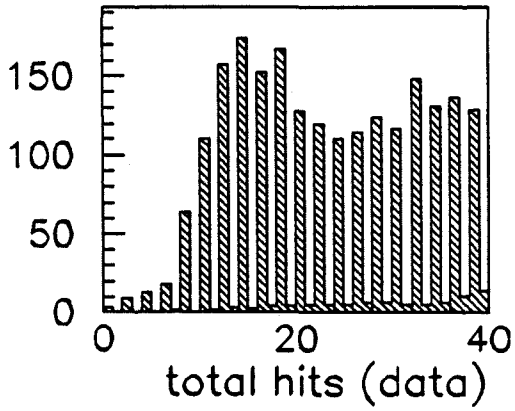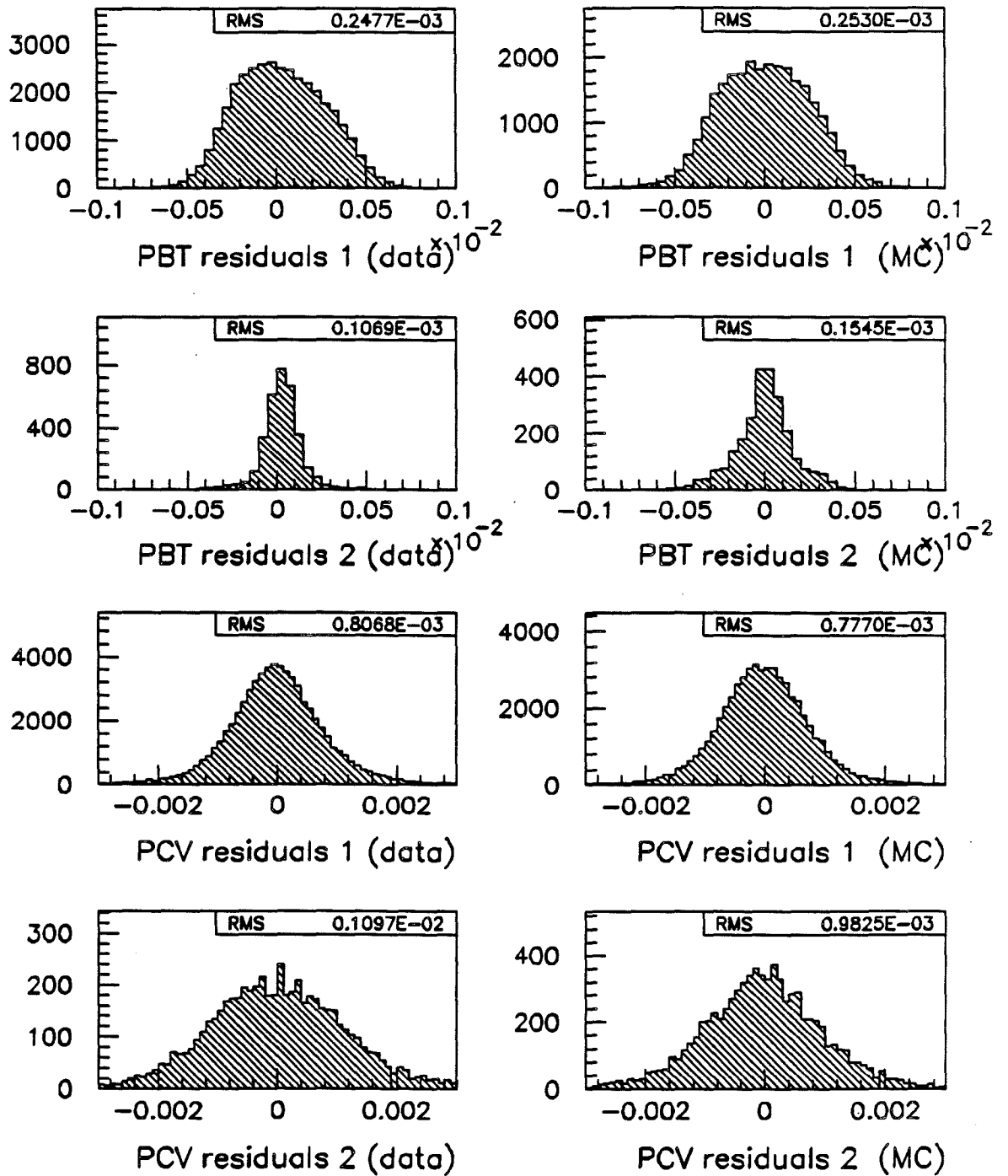
Figure 5.19: Residuals for a series of chambers, plotted for one-wire and two-wire clusters. The Monte Carlo was tuned to resemble the data.
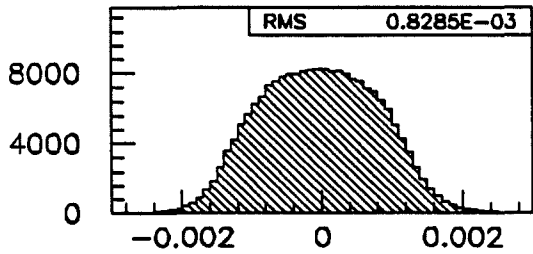
RMS 0.8285E-03

PCN residuals 1 (data)
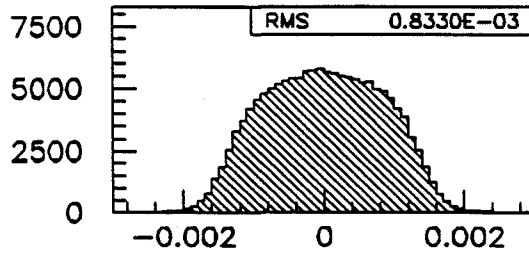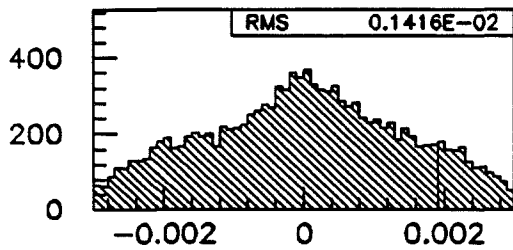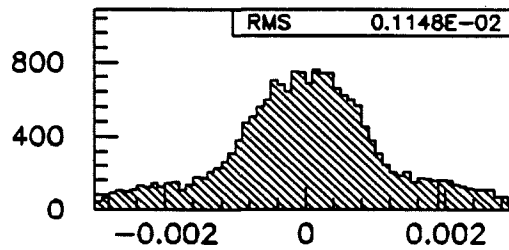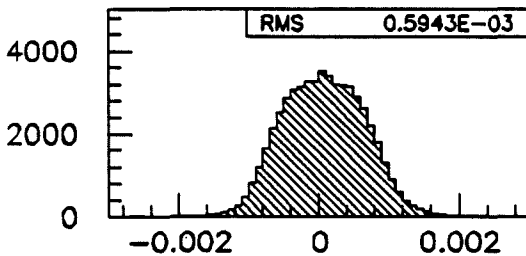
RMS 0.8330E-03

PCN residuals 1 (MC)

RMS 0.1416E-02

PCN residuals 2 (data)

RMS 0.1148E-02

PCN residuals 2 (MC)

RMS 0.5943E-03

PCF residuals 1 (data)

RMS 0.6093E-03

PCF residuals 1 (MC)

RMS 0.8244E-03

PCF residuals 2 (data)

RMS 0.8201E-03

PCF residuals 2 (MC)

RMS   0.6679E-03

DC residuals (data)

RMS   0.7168E-03

DC residuals (MC)

RMS   0.5055E-03

PSA residuals (data)

RMS   0.3170E-03
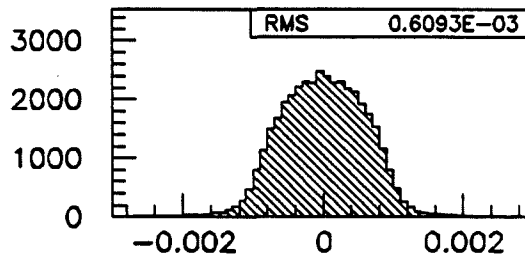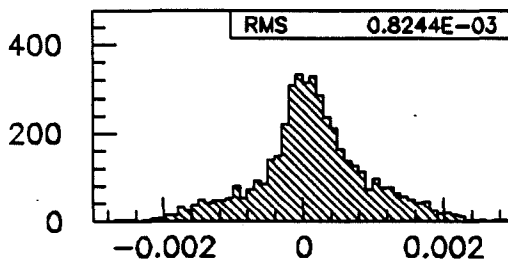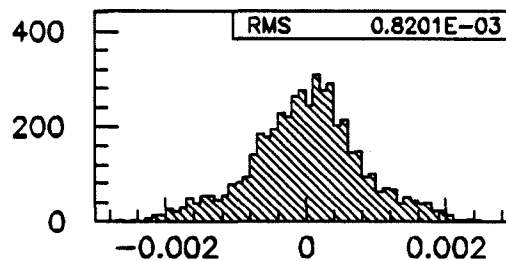
PSA residuals (MC)
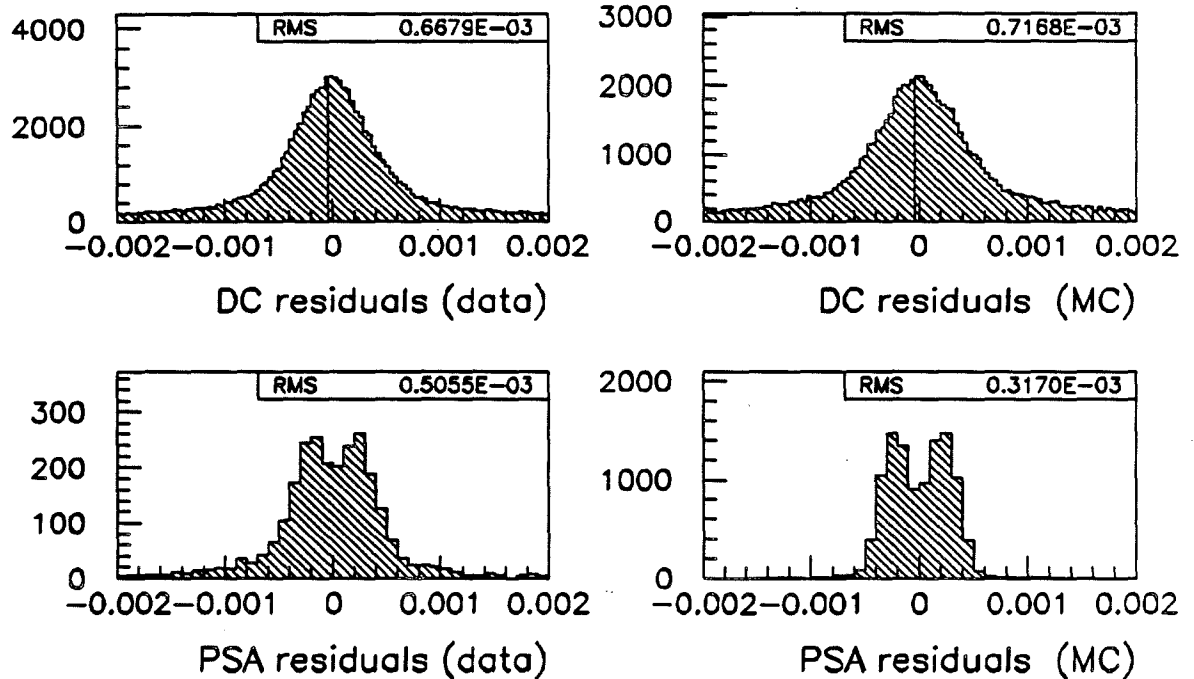
- The second stage Monte Carlo simulates hits in all wire chambers and hodoscopes, but does not simulate any data from the cherenkov counters, the time-of-flight counters, or the calorimeter.

Intensity effects appear to be negligible. The trigger efficiency was determined from the data, and a simulation in the Monte Carlo was deemed unnecessary. Simulation of particle identification was not needed.

The missing items in the second stage Monte Carlo do not compromise its usefulness. The small-angle and large-angle trigger requirements can be tested in Monte Carlo data as well as in real data. Muon tracks in Monte Carlo events passing these requirements resemble those reconstructed in the real data, as illustrated in figure 5.20. Standard kinematic cuts were applied to obtain equivalent samples of muon tracks, for example, $Q^2 > 2.5$ GeV^2, and $y_{Bj} < 0.8$. The target is hydrogen. The real data are represented by the symbols, and the Monte Carlo data by the histograms. The shapes match fairly well. An asymmetry in the Z coordinates of the muons in data which is not reproduced by the Monte Carlo. It is caused by an inefficiency for triggering on muons scattered downward, and effect not included in the simulation. This inefficiency is described in the analysis chapter.

234

Since the Monte Carlo is used only for correcting losses due to finite acceptance and inefficiency, its performance is adequate.
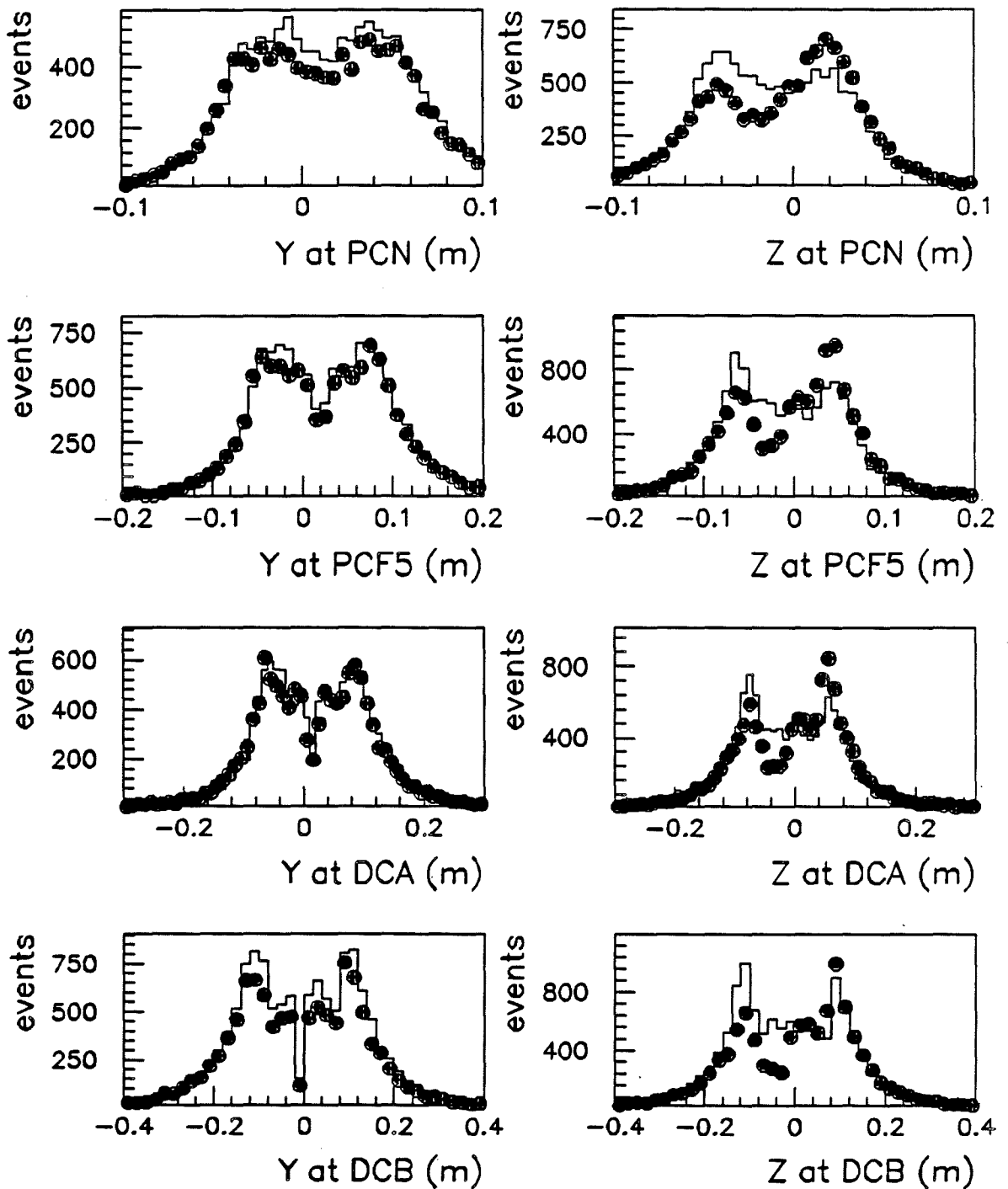
Figure 5.20: Comparison of track coordinate distributions in data (solid circles) and Monte Carlo (histogram). The latter have been normalized to the former. These muon are taken from standard deep-inelastic events on hydrogen.

Chapter 6

Analysis

6.1 Event Selection

Events are selected on the basis of track information. Several cuts are required in order to acquire a pure sample of exclusive ρ^0 events; these will be developed through the course of this chapter. A short synopsis is nonetheless useful.

The key selection is topological: the incident and scattered muons and the pions from the decay of the ρ^0 must be present. This means there can be only a single, in-time track in the beam spectrometer, a single, scattered muon, and one positive and one negative hadron track in the forward spectrometer. No other tracks are allowed. (The recoiling target is too slow to be detected in the spectrometer.)

The goal is to isolate a sample of *exclusive* events. Particles produced in addition to the pions from decay are excluded by demanding that the two pions take up all of the energy lost by the muon:

$$E_1 + E_2 = \nu.$$

In order to ensure good resolution on the invariant mass, on decay variables, and on the momentum transfer to the target, the pion tracks are required to be fitted to the primary vertex.

Additional cuts on kinematics vary depending on the context, but the basic sample satisfying the above criteria amounts to approximately one thousand events.

6.2 Validation of the Monte Carlo

The Monte Carlo data are used to calculate the loss of events and tracks. They are also used to study the resolution of kinematic and physics quantities resulting from the finite aperture of the apparatus, and its actual performance. It is important to check that the simulated data mimic the real data sufficiently closely. Several comparisons are presented in this section.

The plots shown in this chapter follow the convention that real data are represented by symbols, while the simulated data are represented by solid lines. Except where noted, the Monte Carlo histograms are normalized to the data histograms, according to the number of entries within the bounds of the plot.

6.2.1 Phase Space of the Beam

The Monte Carlo uses quasi-real beam events for the simulation: tracks that were reconstructed successfully are stored in a disk file. For each simulated event, the first stage Monte Carlo reads one beam track from the file, and smears the recorded impact points to simulate the resolution of the PBTs. The result is a close replica of the real beam, as depicted in figure 6.1.

These distributions were made using LAT and SAT events from hydrogen; good agreement is found for other targets. The limits of the phase space of the LAT beam are set using the veto jaw counters (SVJ); the sharp cutoffs in the Y coordinate are a clear indication of the SVJ placement. The SAT beam is narrower, because only the central SBT counters were used in the definition of acceptable beam trajectories. As a consequence, the SAT momentum bite is narrower than that of the LAT. The track fit quantities are imperfectly reproduced by the Monte Carlo: there are more degrees of freedom than in the data. In addition, the relative resolution,

$$\text{relative resolution} \equiv \frac{\sigma_{1/p}}{(1/p)},$$

is *higher* in the simulated data than in the real data.

The important quantities for physics analysis are the beam momentum, and the coordinates and angles of the beam as it enters the vertex region. These are adequately reproduced by the Monte Carlo simulation.

The loss of beam flux due to failures of pattern recognition are determined from

238

the data directly, so there is no need to simulate events with multiple beams.

The files used in the Monte Carlo were made before it was shown that the beam momentum is measured incorrectly: it is too high by approximately 7 GeV. This error is discussed in detail later in this chapter. The real data were corrected for this effect, but the Monte Carlo beam files were not regenerated. The distributions presented in figure 6.1 were made without removing the 7 GeV offset in the data.

The plots shown in figure 6.1 show that the SAT beam and the LAT beam are quite different. More detailed comparisons are given in [Sch91e].

6.2.2 Interaction Points

A comparison of the reconstructed vertex coordinates for simulated and real exclusive ρ^0 events is given in figure 6.2. There is evidence in the data for vertices in the PCV chambers, located at about -8.6 m. These vertices are not found in the simulated data, because the Monte Carlo program limits primary vertices to the target. The PCV vertices are easily eliminated. The target vertices are shown in the figure, also. The requirement that there be two hadrons in addition to the scattered muon results in a distribution of reconstructed vertices which increases toward the downstream end of the target. This feature can be explained by the acceptance of the pions [1], and is perfectly reproduced by the Monte Carlo. The Y and Z distributions reflect the phase space of the beam.

The resolution on the X position of the primary vertex is represented accurately in the simulated SAT data, but it is less perfect in the LAT data. Nonetheless, the agreement is adequate.

6.2.3 Primary Interaction

The primary interaction is the starting point of Monte Carlo simulation, and the end point of event reconstruction. It is keystone of data analysis. If the Monte Carlo mimics reality, then comparisons of reconstructed trajectories at the primary vertex should evidence no significant differences between simulated and real data.

Distributions of basic track quantities Y', Z', and P for the scattered muon and


[1]Pion acceptance is discussed later in this chapter
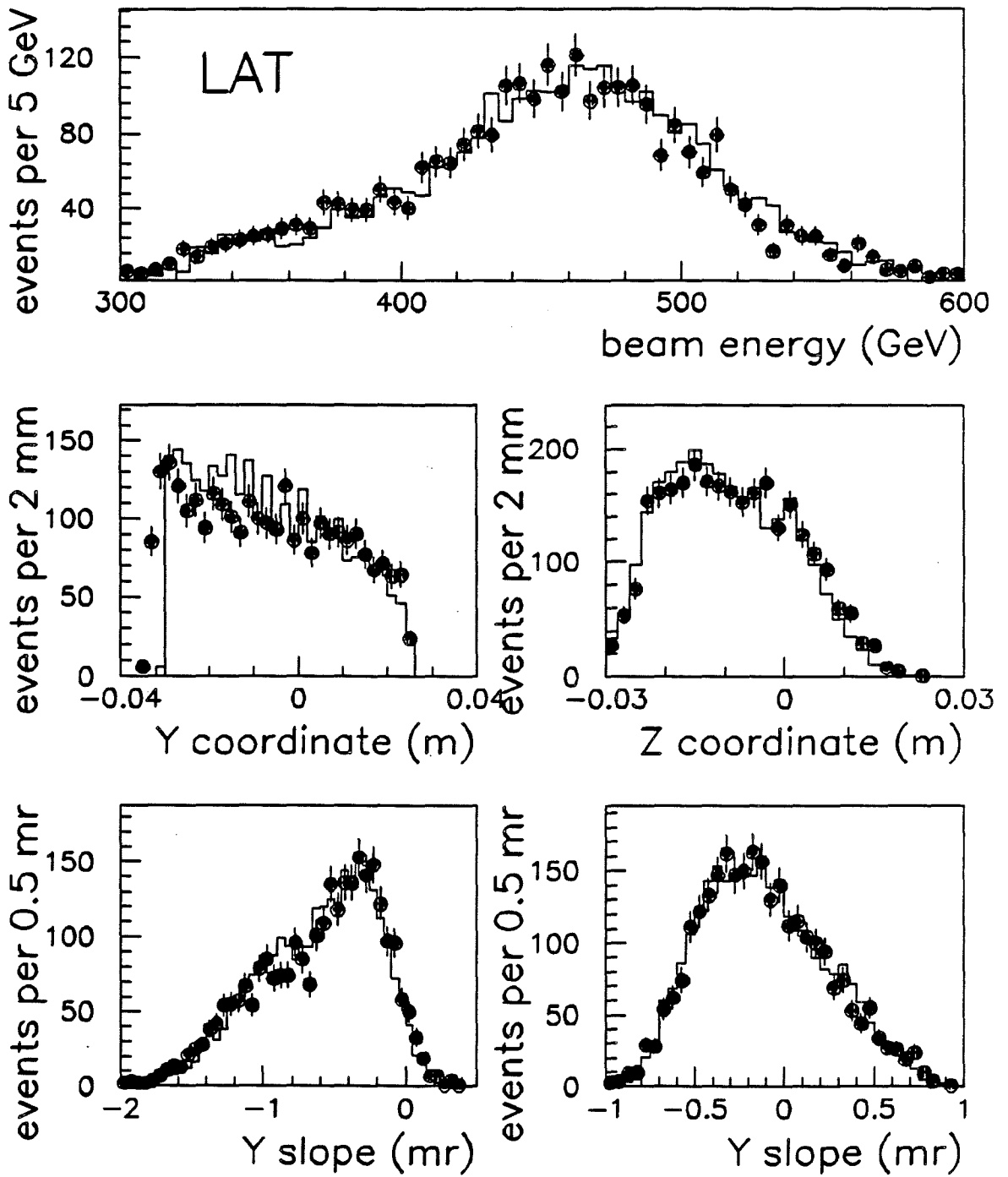
Figure 6.1: Comparison of the beam simulated by the Monte Carlo, and the real beam, for LAT and SAT events in hydrogen.

SAT
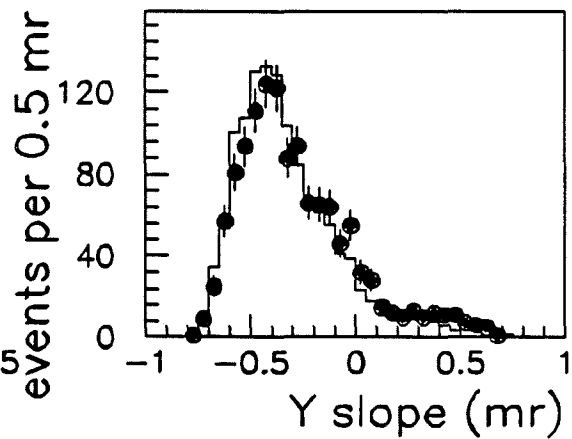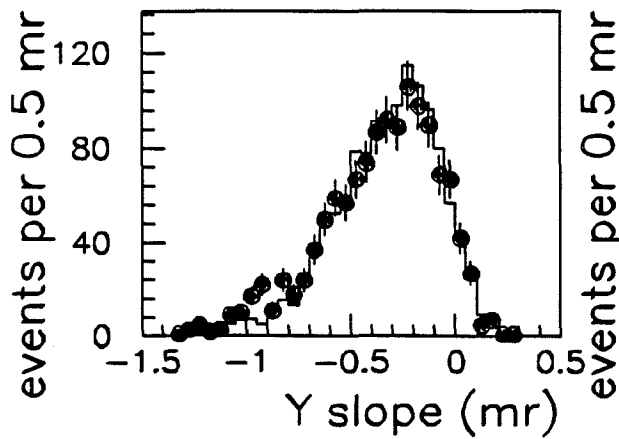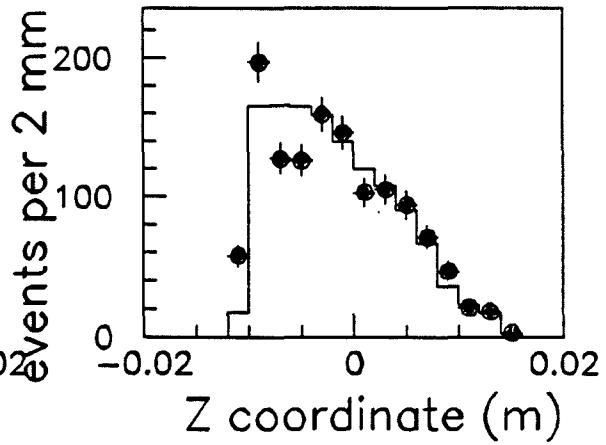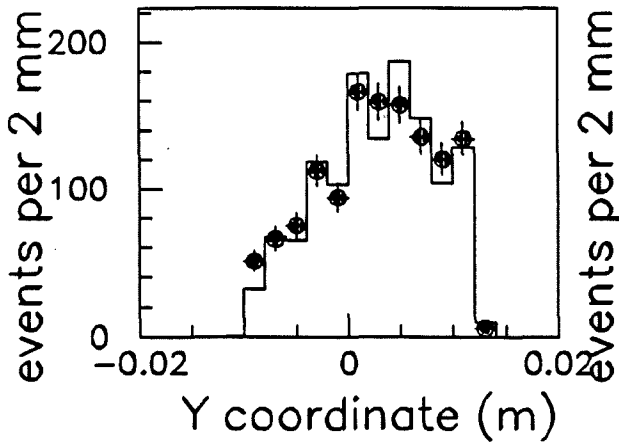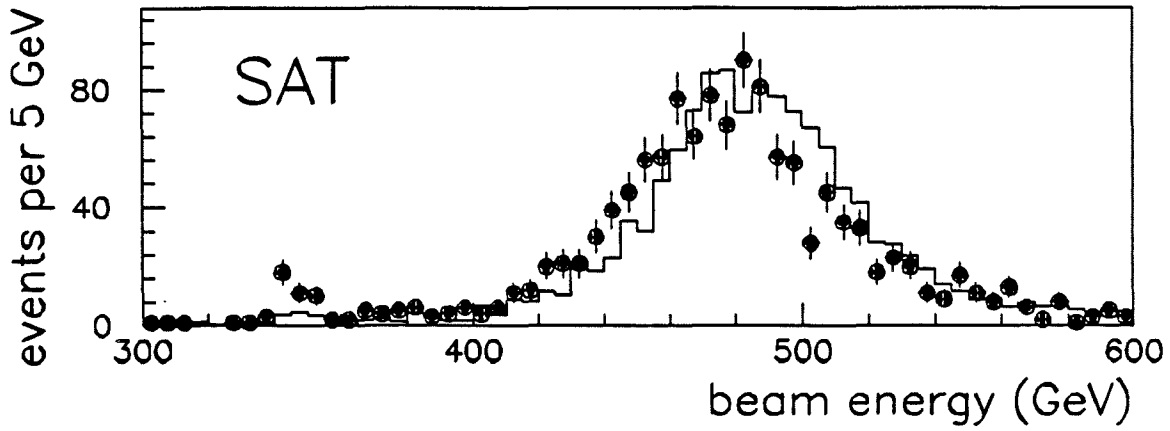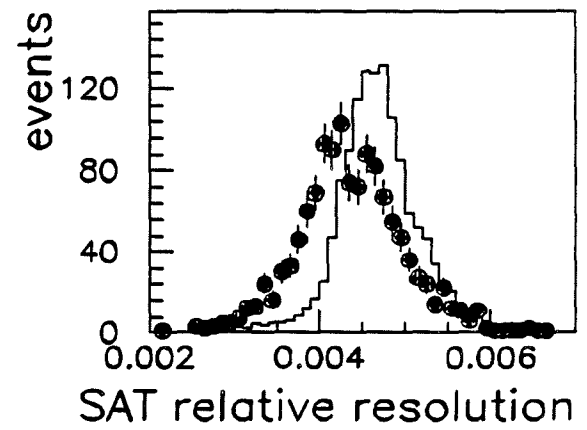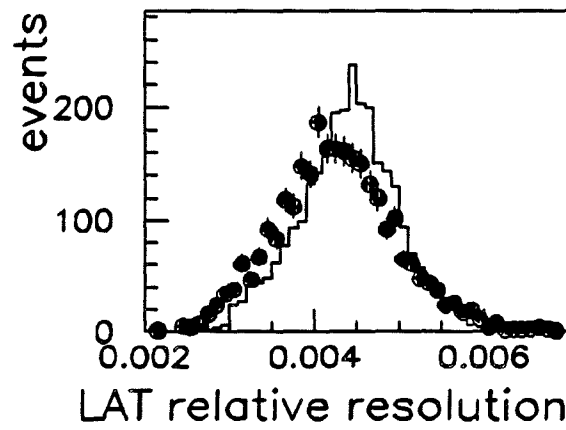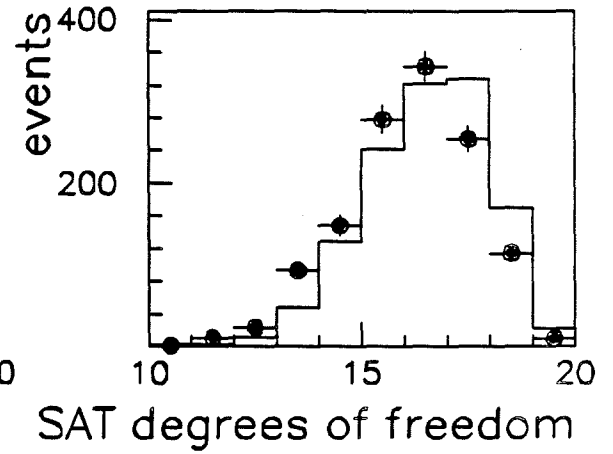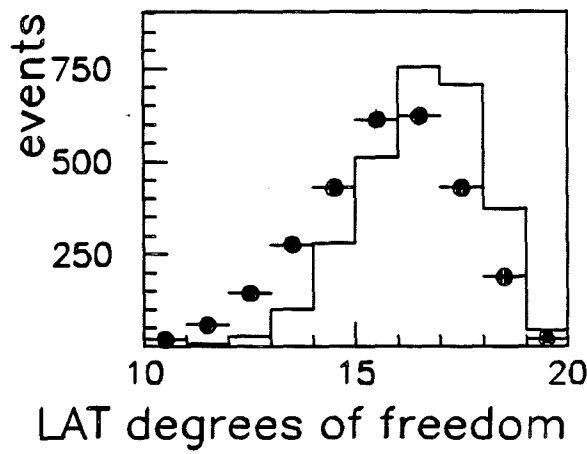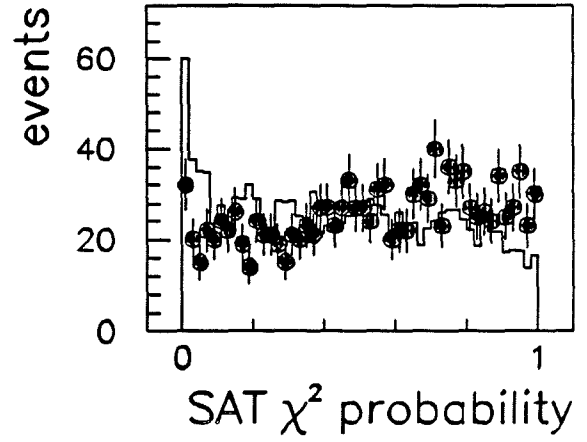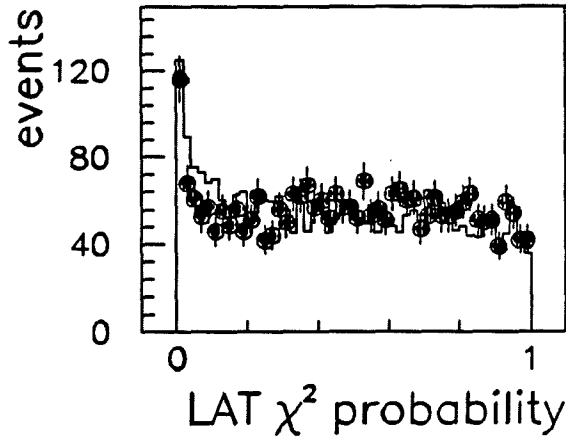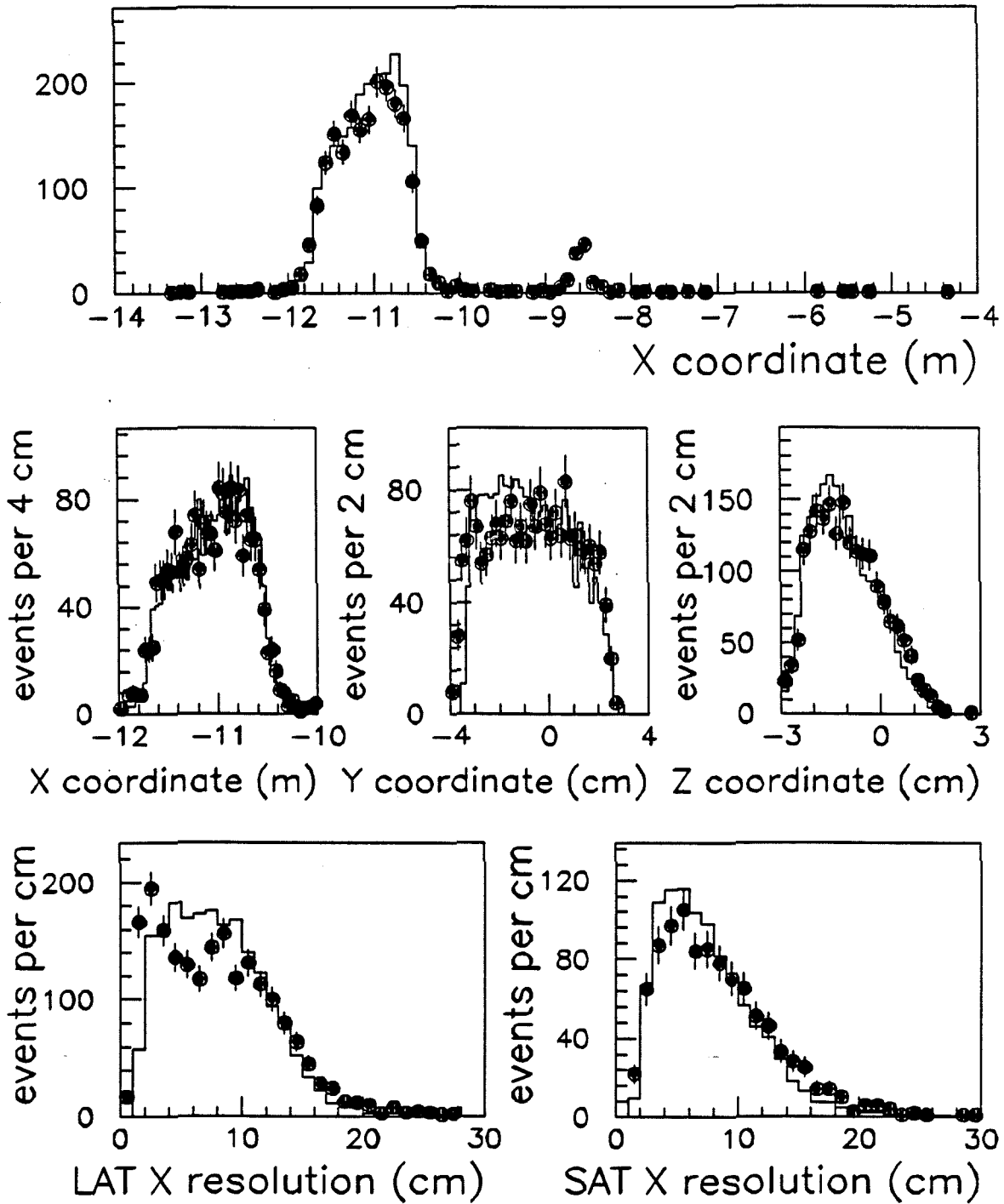
Figure 6.2: Comparison of vertex distributions for simulated and real data.

the positive pion in LAT and SAT data are given in figure 6.3. The negative pion distributions are indistinguishable from the positive pion distributions, so they are not shown.

In the LAT data, significant differences are evident for the scattered muon. Two effects in the real data cause these differences:

1. The muon self-veto probability is not simulated in the Monte Carlo.

2. The real LAT was inefficient for muons scattered downward, toward negative Z coordinates. This effect is not simulated.

These important effects are discussed later in this chapter.

The pion appears to be well simulated in the Monte Carlo. A small difference in the momentum spectrum probably follows from the differences in trigger conditions.[2]

For the scattered muon and the pion, the degrees of freedom and χ^2-probability distributions are reasonable.

The simulated SAT data agrees with the real data quite well. (The SAT hardware performed well; these data appear to be free of sundry odd effects and asymmetries.)

6.2.4   Tracks through the Chambers

Given that the primary interaction is simulated adequately, it remains to show that the paths of the muon and pions through the apparatus also are simulated adequately. Corrections for reconstruction losses depend on the correspondence between simulated and real data.

The importance of accurate maps of chamber efficiency has been mentioned before. There are two aspects to chamber efficiency: the delineation of dead regions, and the measurement of "outer" efficiencies, away from the dead regions. The former is very important to the performance of track reconstruction; the latter, to track fitting.

---

[2]The pion momentum is strongly correlated with ν, because these events are exclusive.

LAT data
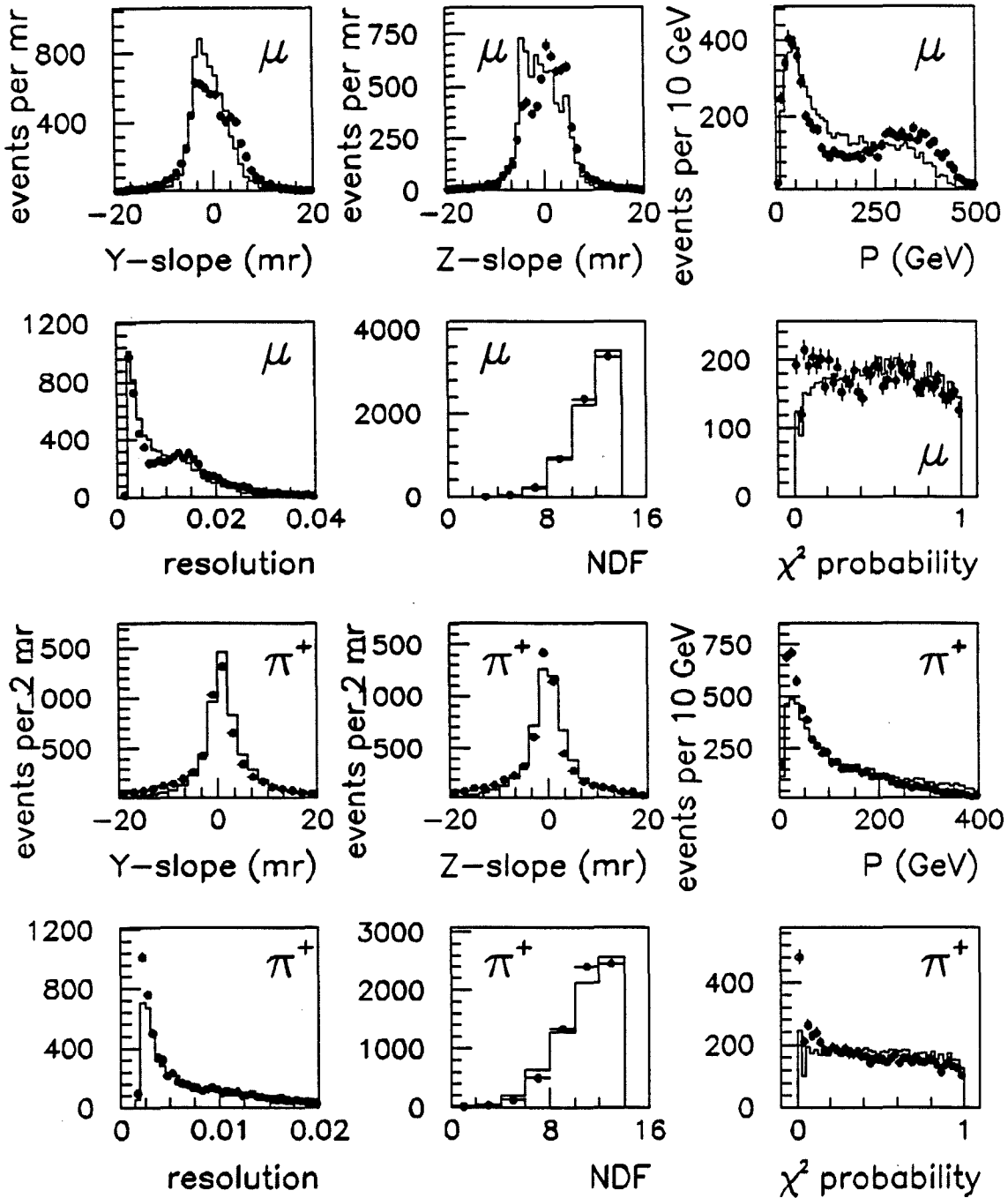
Figure 6.3: Comparison of track quantities at the primary interaction point, for simulated and real data. Distributions are made for LAT and SAT data separately.

246
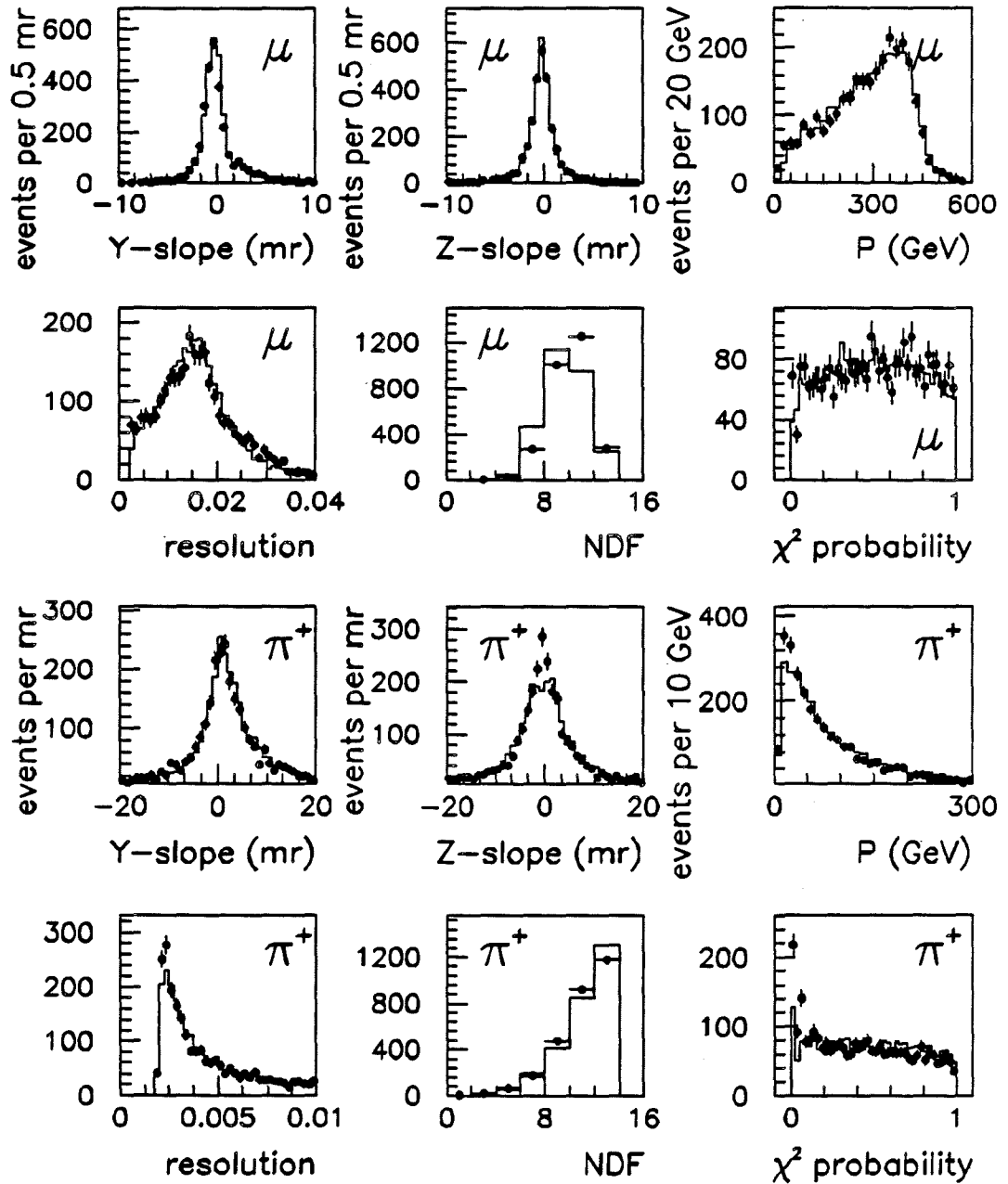
The number of hits on a track plays a role in the track fit: the greater the number of hits, the greater the degrees of freedom, hence the fit is better constrained, and the resolution of track parameters improves. Better resolution for tracks results in better resolution for derived quantities, such as Q^2, ν, the invariant mass, and t. The plots in figure 6.3 indicate that the number of degrees of freedom in the data is accurately reproduced by the Monte Carlo; the relative resolution on the momentum is reproduced also. This agreement follows from the correctness of the outer efficiencies.

The dead regions of chambers are best represented by two-dimensional plots, such as those found in [RSB90, Sch90e]. Gross features can be seen in one-dimensional plots, as shown in figure 6.4. The distribution of tracks at several forward spectrometer planes is shown, for the scattered muon, the positive pion, and the negative pion, separately. LAT data is shown first, followed by SAT data.

The LAT comparisons are obscured by the trigger effects mentioned in the previous section. Nonetheless, the agreement between simulated and real data is fairly good. The SAT comparisons are very good, in particular, for the pions. The dead regions in the center of the drift chambers appear to be well represented by the Monte Carlo; the PSA distributions also agree.

The number of planes from each chamber group contributing to scattered muon and pion tracks is shown in figure 6.5. Again, agreement is not perfect, but seems to be adequate. There are too few hits from PCN and PCF, and perhaps too many from DCB. The relative height of the zero hits and the nonzero hits portions of the DC and PSA histograms is a measure of the size of the dead regions. Here the agreement between Monte Carlo and real data is very good.

The correlation between position and momentum was mentioned in the software chapter. Figure 6.6 illustrates the correlation of the mean momentum of the scattered muon, positive pion, and negative pion with horizontal position in the PCN chambers. The agreement between simulated and real data is good, except for positive pions and muons which pass on the east side of the chambers (negative Y coordinate). Few events are in those bins, so the mean momentum is not well determined: the discrepancy is not considered serious.

These distributions indicate that the response of the apparatus to the tracks in the forward spectrometer is simulated well. This conclusion was reached also in [Aïd, Bhatti].

LAT scattered muons
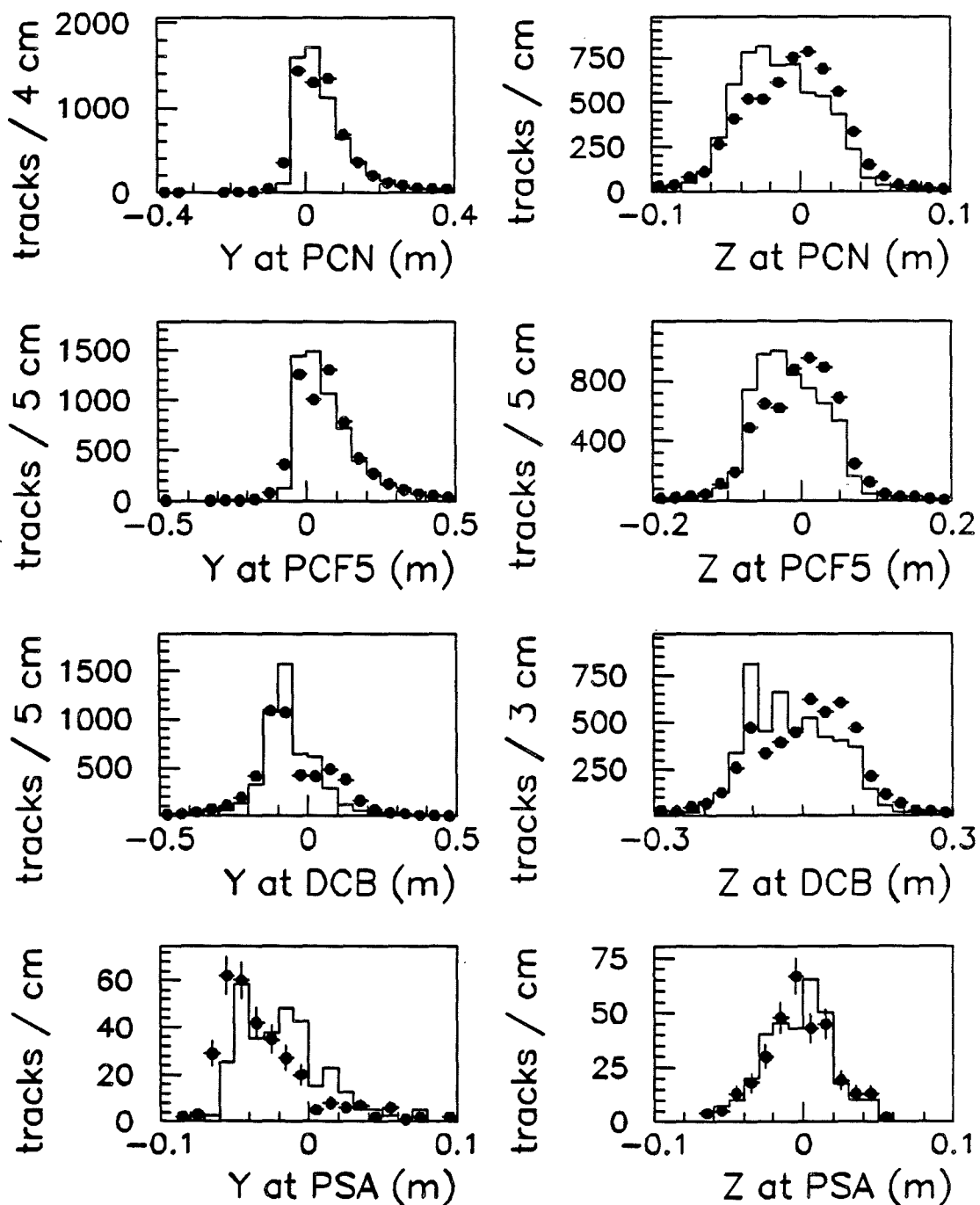
Figure 6.4: Comparisons of track distributions in simulated and real data, at four locations in the forward spectrometer. Shown separately are scattered muons, positive pions, and negative pions from LAT data, followed by the same for SAT. (six pages)

LAT positive pions
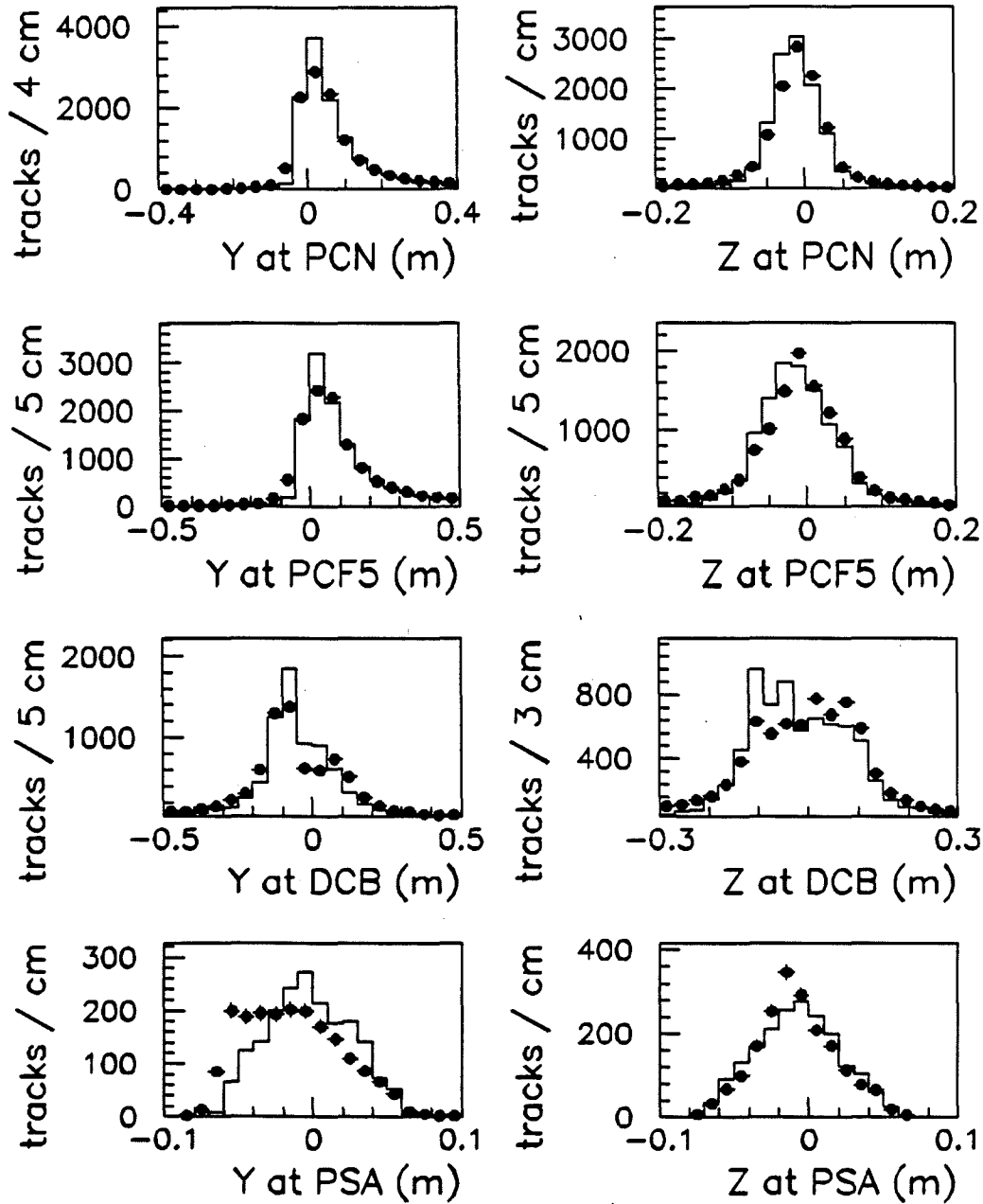
LAT negative pions
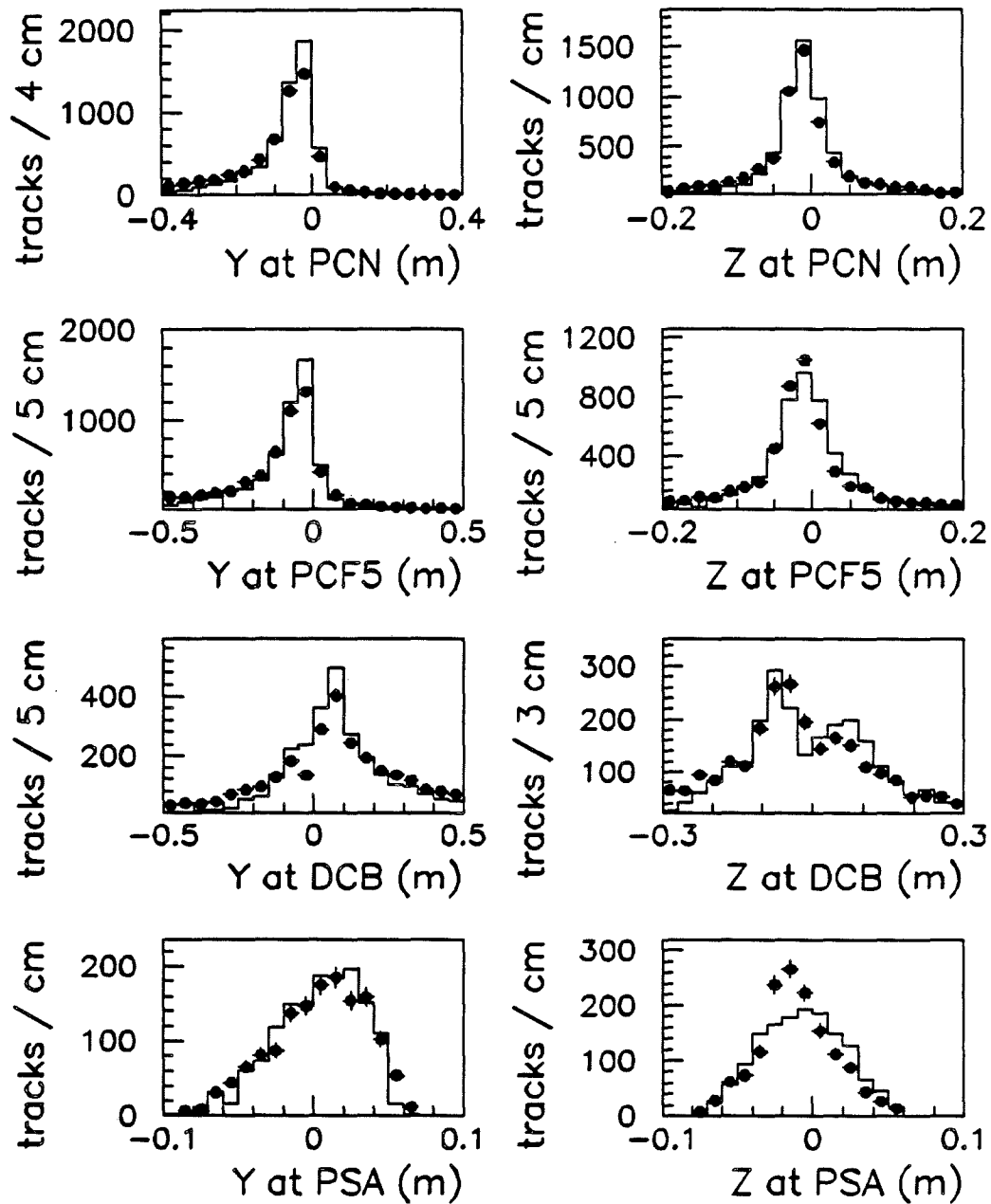
SAT scattered muons
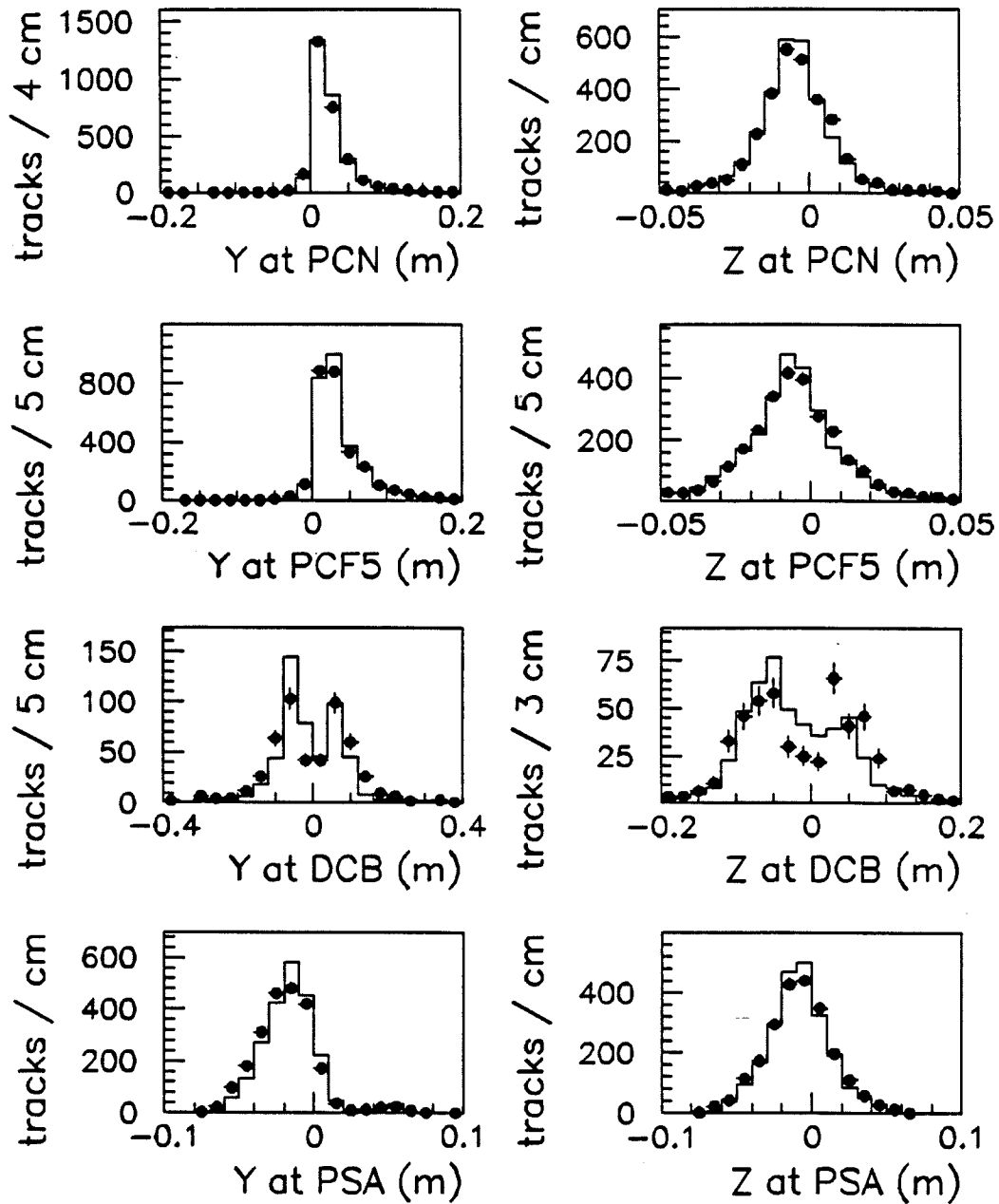
SAT positive pions
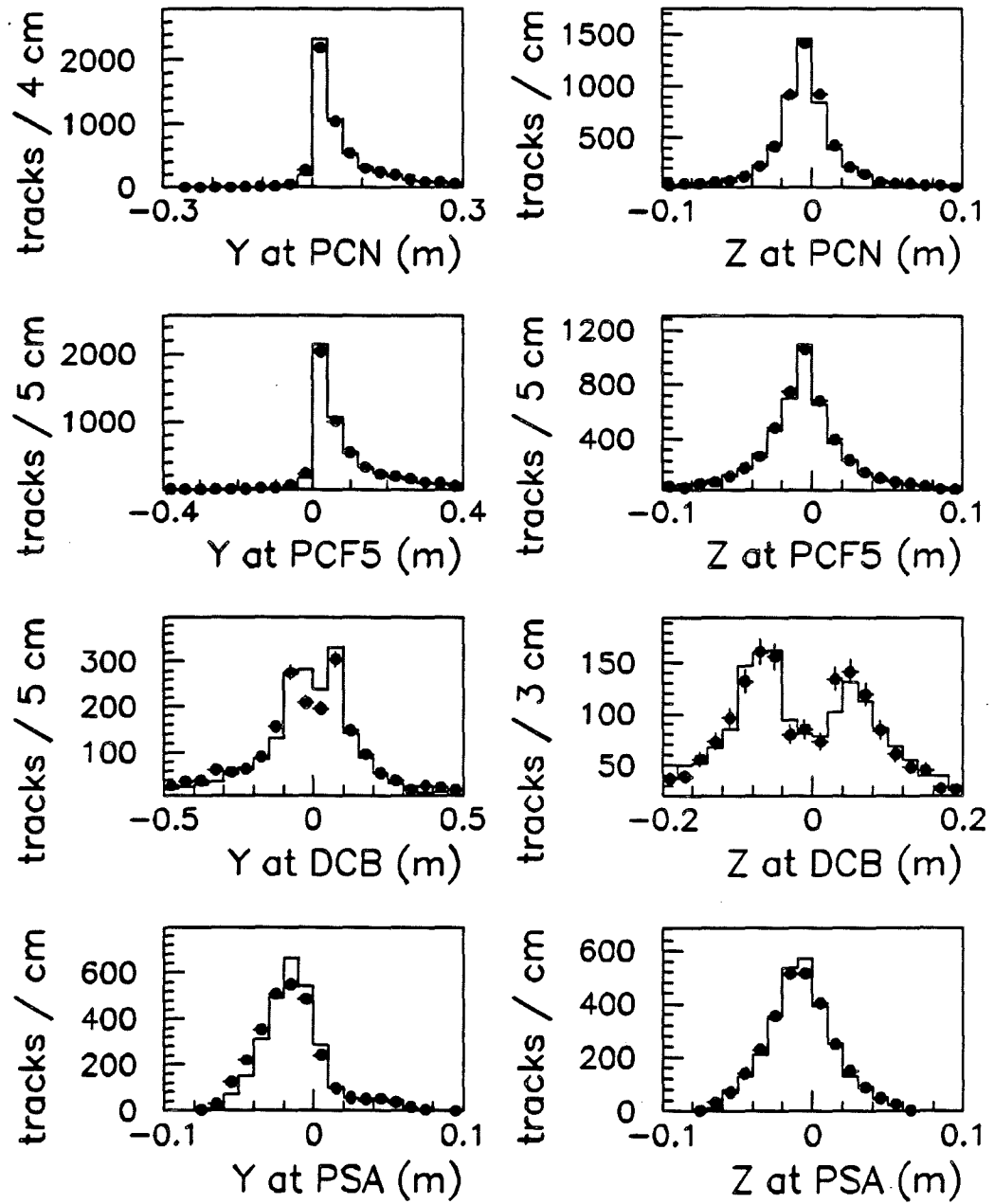
SAT negative pions
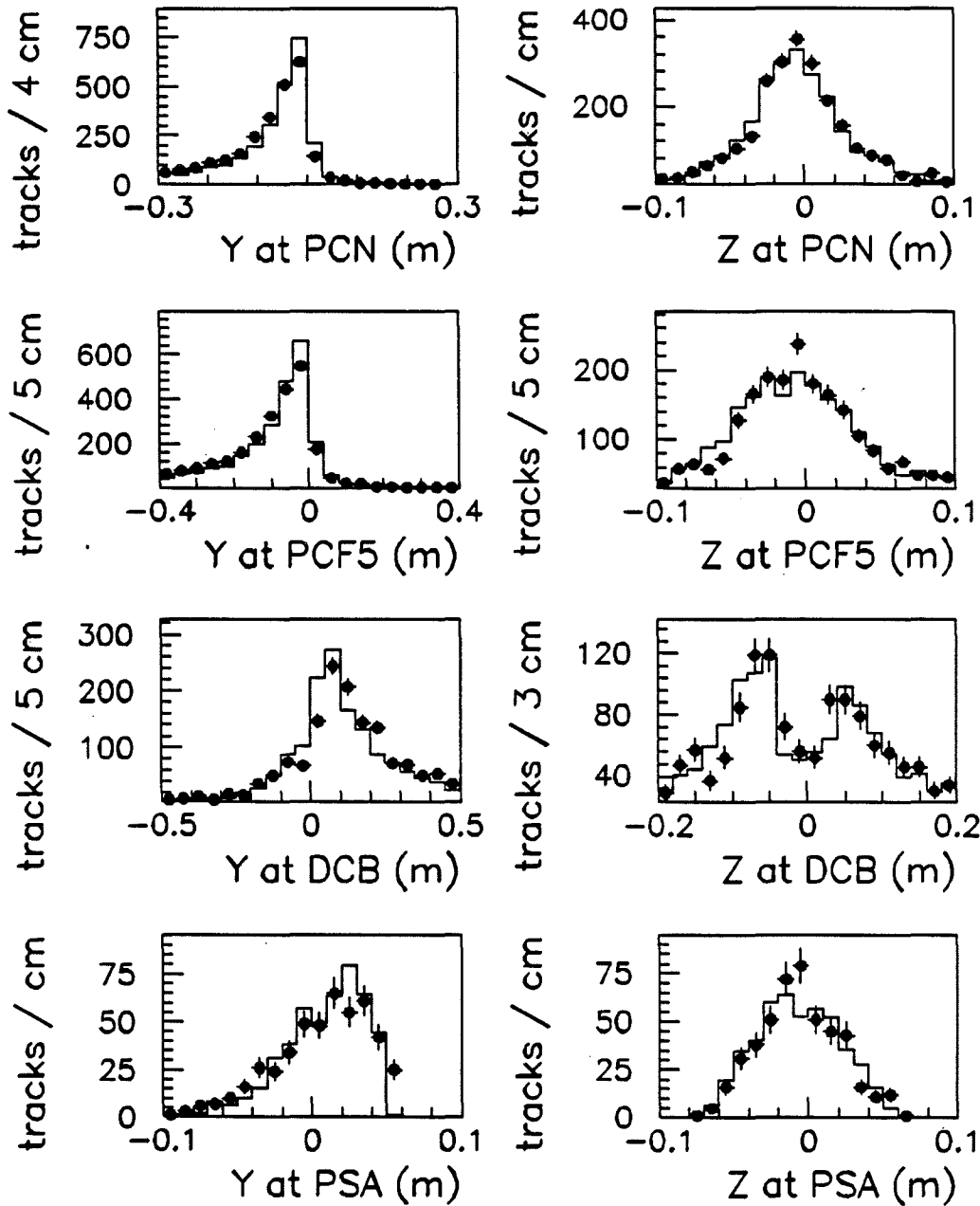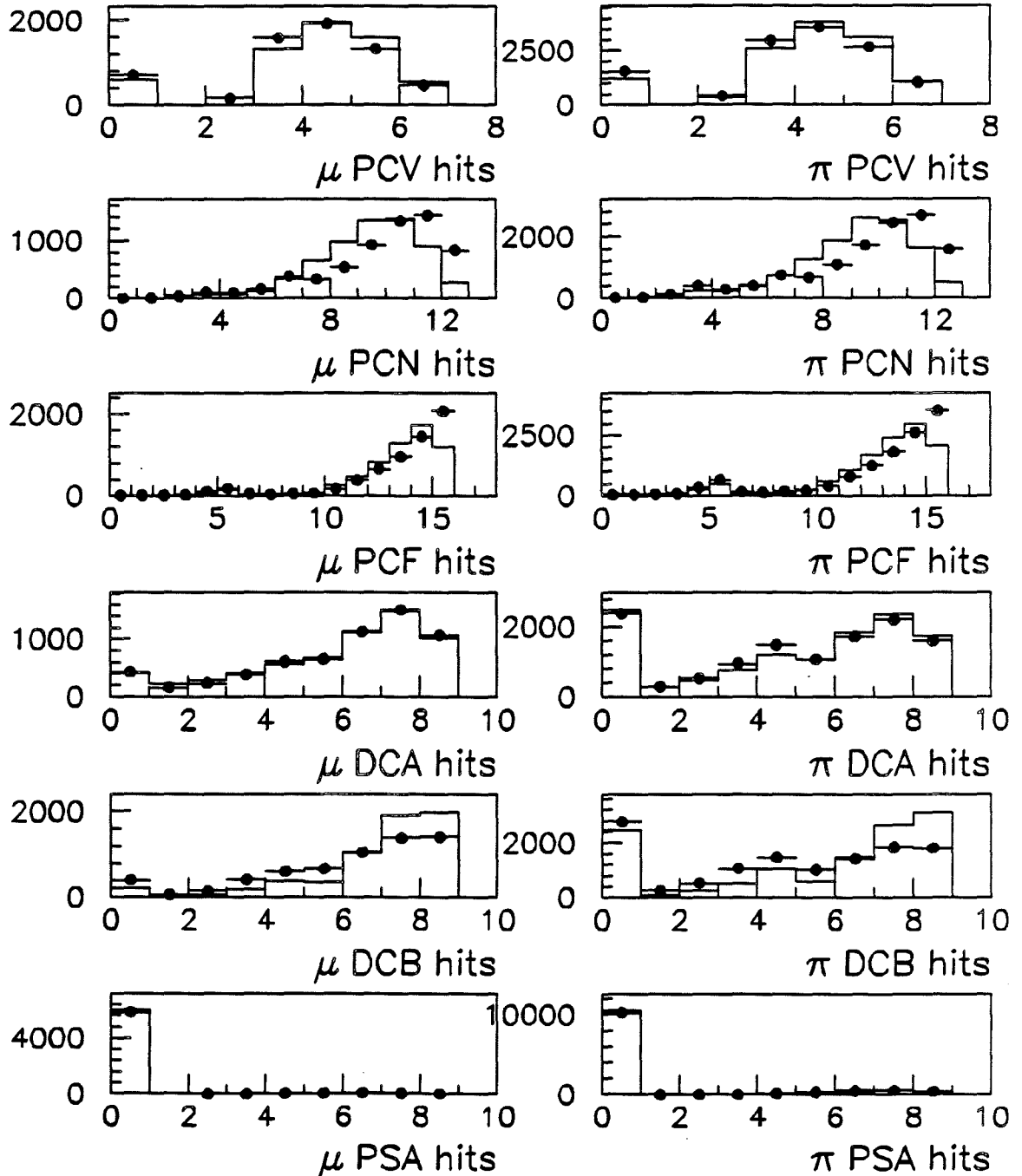
Figure 6.5: Comparison of chamber hit multiplicities for simulated and real data. Muons tracks are shown on the left, and pion tracks on the right. LAT and SAT data are shown separately.

SAT data

μ PCV hits

π PCV hits

μ PCN hits

π PCN hits

μ PCF hits

π PCF hits

μ DCA hits

π DCA hits

μ DCB hits

π DCB hits

μ PSA hits

π PSA hits
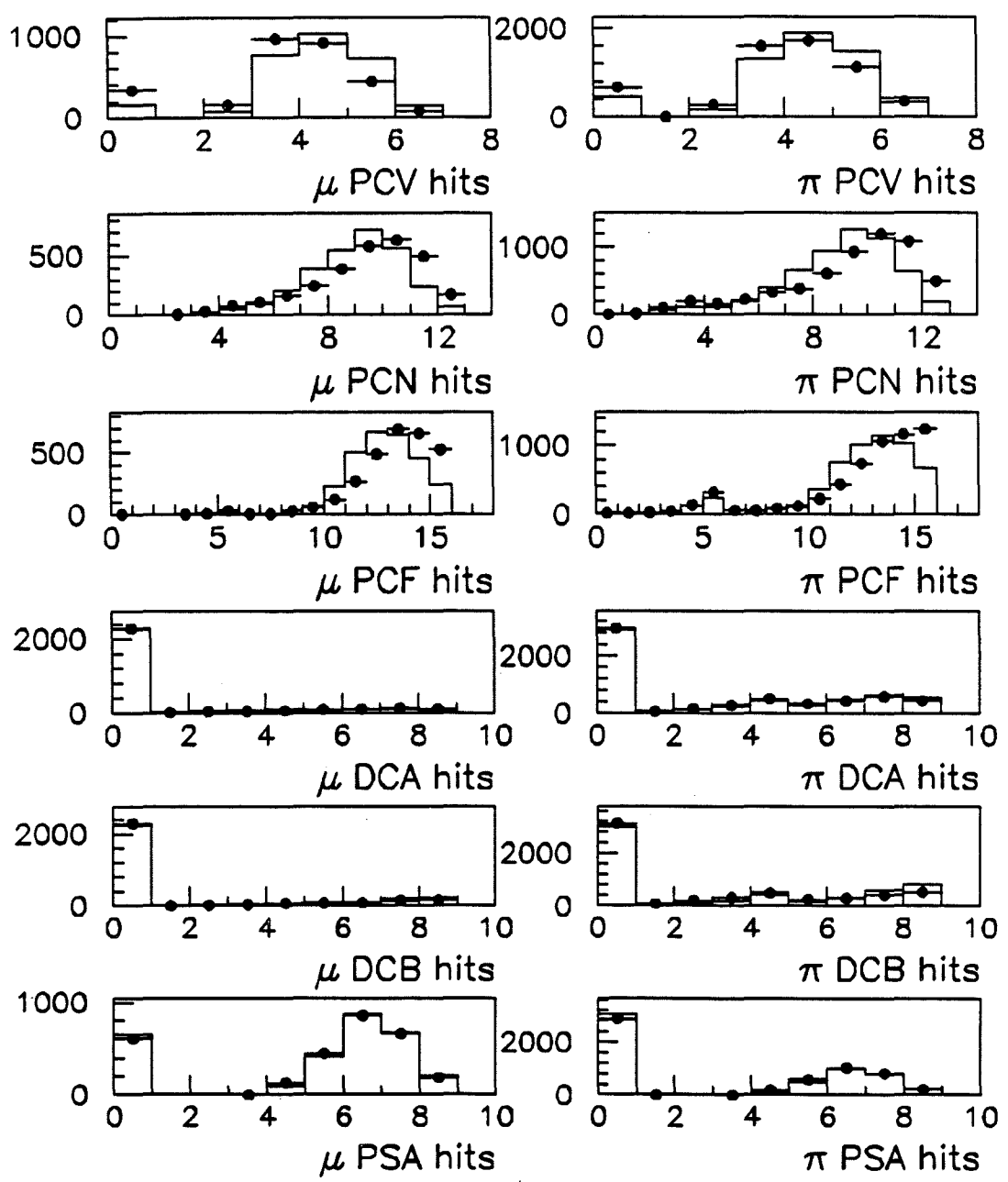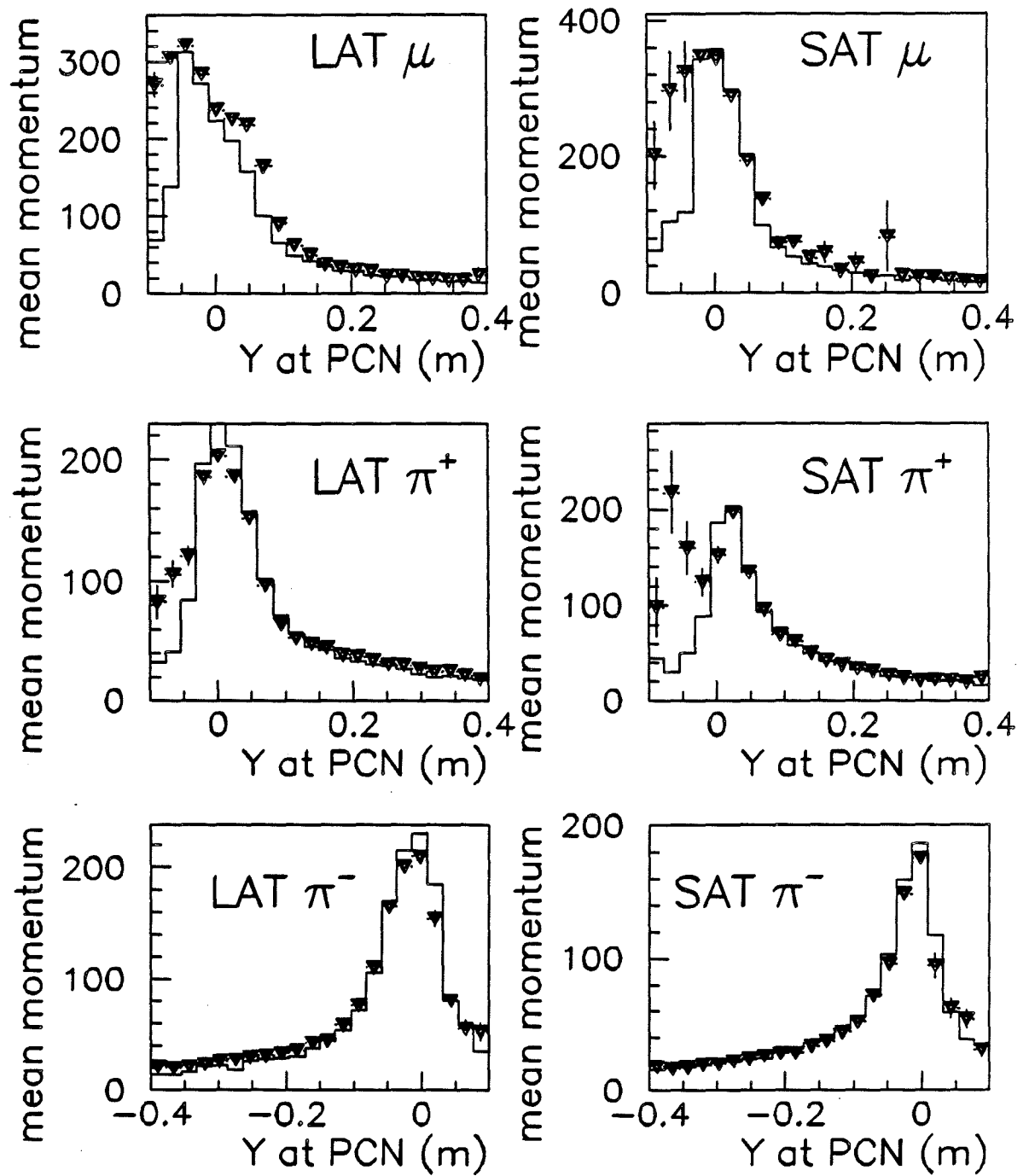
Figure 6.6: Comparison of the mean momentum versus position at PCN for real and simulated data.

6.2.5   Vertex Reconstruction

The tracks reconstructed in the forward spectrometer must be propagated back to the primary vertex, which itself is inferred from the forward spectrometer tracks. The distributions of the vertex fit parameters should be the same for simulated and real data. Comparison of the number of degrees of freedom and the χ^2–probability distribution for the vertex fit is given in figure 6.7. The agreement is close, if not perfect. Also shown is the number of fitted tracks and close tracks. The total number of tracks was constrained to be four. Even in the Monte Carlo data, tracks sometimes are not fitted to the primary vertex. The distribution of X coordinates is shown, also.

6.3   Resolution

6.3.1   Momentum Errors

Momentum resolution was discussed in the software chapter. Its quadratic dependence on momentum follows from the fact that the resolution of a coordinate by a wire chamber is a constant independent of the coordinate. The resolution of the track slope consequently is constant, as is the difference between two slopes: σ_θ = constant, independent of θ. Momentum is inversely proportional to this difference:

$$P \propto \frac{1}{\theta} \quad \Rightarrow \quad \frac{\delta P}{P} = -\frac{\delta\theta}{\theta} \quad \Rightarrow \quad \sigma_P \propto \sigma_\theta P^2.$$

This quadratic dependence of the estimated momentum error on momentum is illustrated in figure 6.8. These plots were made using tracks from the SAT exclusive ρ^0 data. The error shown is the mean value of the estimated error from the track fit. The error on the beam momentum is seen to be better than that of the scattered muon, by about a factor of five. The error on pion momentum is about the same as that of the scattered muon.

The dependence of the momentum error on momentum was fitted to a second order polynomial:

$$\sigma_P = a + bP + cP^2,$$

for LAT and SAT events, real and simulated. The results are summarized in table 6.1. The agreement between the simulation and the real data is reasonably good except for the beam. Note that the constant term a is nonzero statistically,

257
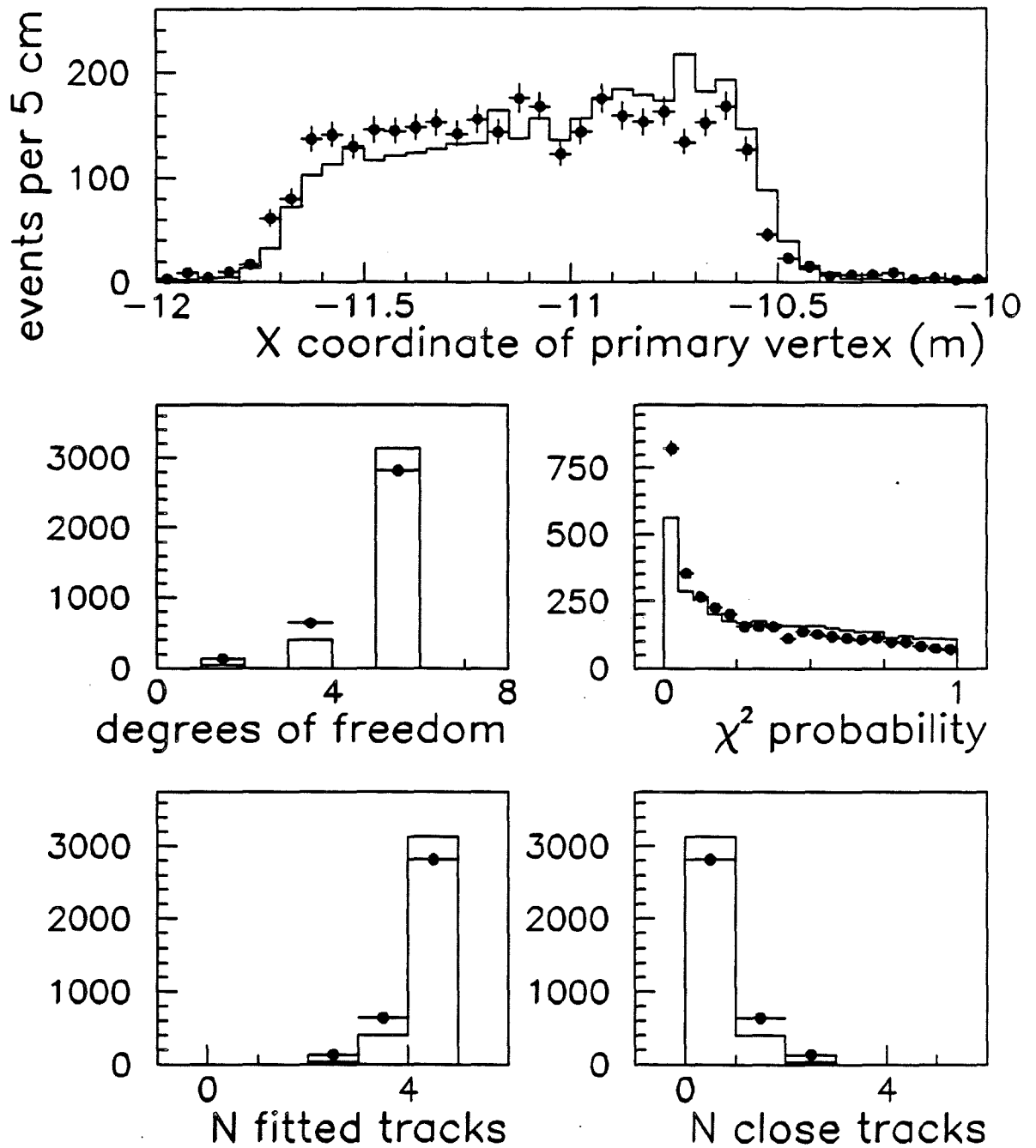
Figure 6.7: Comparison of vertex fit parameters, for simulated and real LAT data.
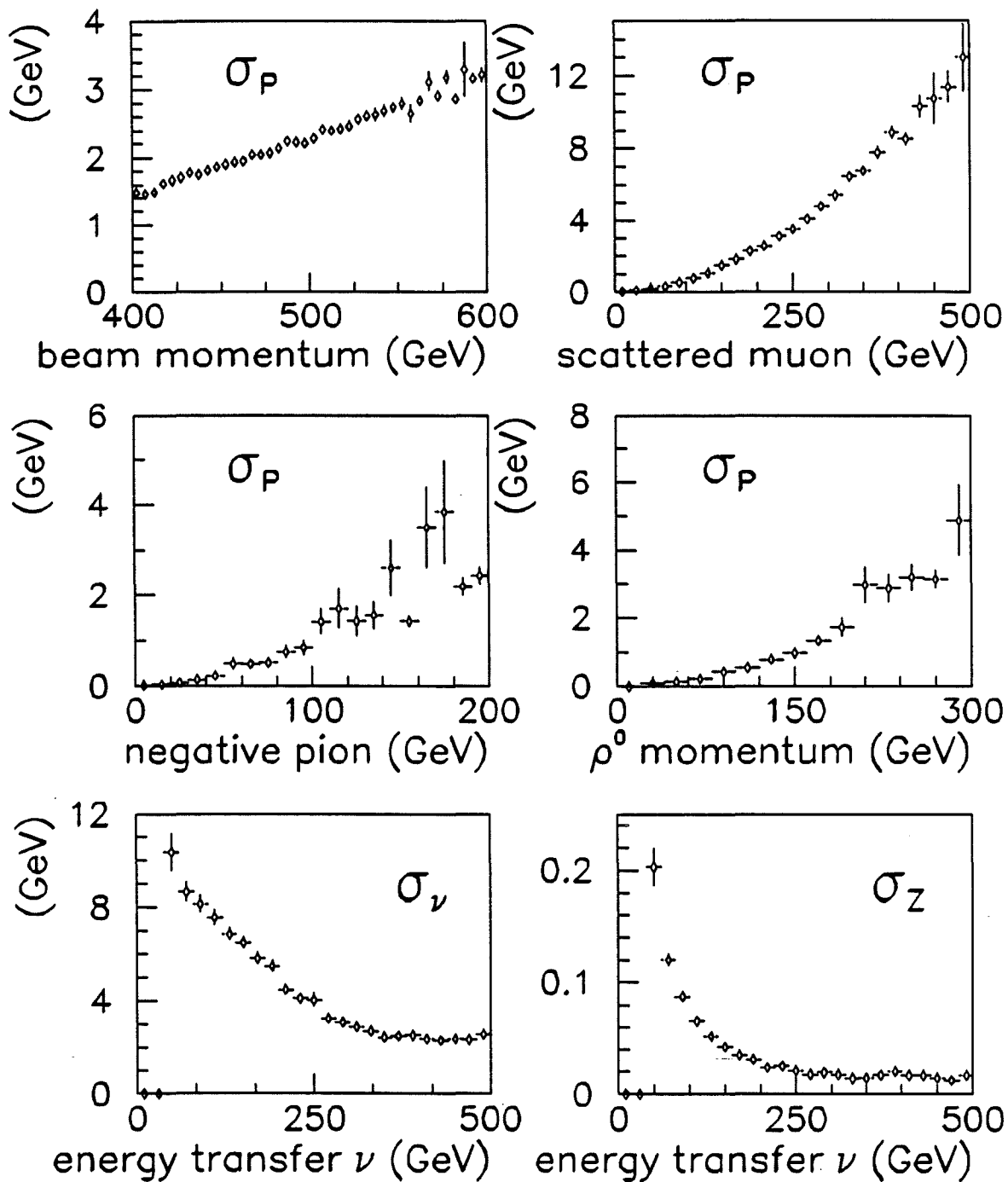
Figure 6.8: Estimated absolute error on momentum for SAT data, plotted versus momentum. Also shown is the dependence of σ_Z as a function of ν.

track	sample	a (GeV)	b $(\times 10^{-3})$	c $(\times 10^{-6}$ GeV$^{-1})$	χ^2
beam muon	LAT data	1.19 ± 0.04	-4.68 ± 0.16	14.0 ± 0.2	1.6
	LAT MC	-0.01 ± 0.01	0.20 ± 0.03	9.3 ± 0.1	1.3
	SAT data	-1.11 ± 0.05	4.95 ± 0.18	3.7 ± 0.2	1.0
	SAT MC	-0.12 ± 0.02	0.60 ± 0.04	8.9 ± 0.04	1.5
scattered	LAT data	0.020 ± 0.002	0.93 ± 0.11	52.1 ± 0.9	1.6
muon	LAT MC	0.022 ± 0.001	0.74 ± 0.06	50.5 ± 0.3	4.1
	SAT data	0.017 ± 0.003	1.30 ± 0.23	52.1 ± 1.1	0.9
	SAT MC	0.000 ± 0.003	1.51 ± 0.11	49.1 ± 0.4	4.8
negative pion	LAT data	0.010 ± 0.001	0.83 ± 0.28	80.3 ± 6.3	1.5
	LAT MC	0.018 ± 0.004	0.92 ± 0.40	84.8 ± 5.7	1.2
	SAT data	0.014 ± 0.002	0.18 ± 0.34	97.1 ± 8.3	0.6
	SAT MC	0.038 ± 0.006	-1.35 ± 0.41	113.5 ± 6.4	0.9

Table 6.1: **Measured mean estimated momentum errors, expressed as parameters in a quadratic fit.**

but is negligible compared to the others. The linear term also is nonzero, but is dominated by the quadratic term for momenta above 10 GeV.

The energy transfer is the difference between the beam energy and the scattered muon energy: $\nu = E_b - E_s$. The difference between the energy and the momentum of forward particles ($P > 5$ GeV) is much smaller than the error on the momentum, so in this case $\nu = P_b - P_s$ to a very good level of approximation.[3] The statistical measurement errors on the beam momentum and the scattered muon momentum are uncorrelated, so

$$\sigma_\nu = \sqrt{\sigma_{P_b}^2 + \sigma_{P_s}^2}.$$

In order to understand the qualitative behavior of σ_ν, the approximations $\sigma_{P_b} = \sigma_b P_b^2$ and $\sigma_{P_s} = \sigma_s P_s^2$ can be used, giving

$$\sigma_\nu = \sqrt{\sigma_b^2 P_b^4 + \sigma_s^2 P_s^4} = \sigma_b P_b^2 \sqrt{1 + \left(\frac{\sigma_s}{\sigma_b}\right)^2 (1-y)^4},$$

where $y = \nu/P_b$. Since $\sigma_s > 5\sigma_b$, the one can be neglected for small enough y, giving

$$\sigma_\nu \approx \sigma_s E_b^2 (1-y)^2 = \sigma_s (E_b - \nu)^2.$$

The error on ν decreases with increasing ν, as expected. (Basically, it is a reflection of the error on the momentum of the scattered muon, since the error on the beam momentum is relatively small.) This is seen in the plot in figure 6.8. The mean error was fitted to a quadratic form,

$$\sigma_\nu = a + b\nu + c\nu^2,$$

---

[3]Approximations of this sort are not made in the computer programs used in this analysis.

with values listed in table 6.2.

A similar calculation can be carried out for the ρ^0 momentum $P_\rho = P_1 + P_2$, where P_1 is the momentum of the positive pion, and P_2 is the momentum of the negative pion. Writing $\sigma_P = \sigma_0 P^2$ for the two pions (σ_0 is a constant), the result is

$$\sigma_{P_\rho} = \sigma_0 \sqrt{P_1^4 + P_2^4}.$$

In the case $P_1 = P_2 = P_\rho/2$, this becomes

$$\sigma_{P_\rho} = \frac{\sigma_0}{2\sqrt{2}} P_\rho^2.$$

The plot in figure 6.8 illustrates this dependence. A quadratic fit for σ_{P_ρ} was performed, giving the values listed listed in table 6.2. These values also indicate that the momentum error for the ρ^0 is smaller than that of a single pion at the same momentum.

The energy fraction of the pion pair is

$$Z_{\text{pair}} \equiv \frac{P_1 + P_2}{\nu} = \frac{P_\rho}{\nu}.$$

If $Z_{\text{pair}} = 1$ then the event is characterized as "exclusive." The estimated error on Z_{pair} follows from the errors on P_1, P_2, and ν:

$$\sigma_Z = \frac{1}{\nu} \sqrt{\sigma_{P_1}^2 + \sigma_{P_2}^2 + Z_{\text{pair}}^2 \sigma_\nu^2} = \frac{1}{\nu} \sqrt{\sigma_{P_\rho}^2 + Z_{\text{pair}}^2 \sigma_\nu^2}.$$

Using the approximations above for σ_ν and σ_ρ, and taking $Z_{\text{pair}} \approx 1$, this becomes

$$\sigma_Z = \frac{1}{\nu} \sqrt{\frac{\sigma_0^2}{8} \nu^4 + \sigma_s^2 (E - \nu)^4}.$$

For small ν, the error on ν dominates, and σ_Z decreases with ν. At large ν, the error on P_ρ becomes important, so σ_Z increases with $P_\rho \approx \nu$. This behavior is seen in figure 6.8. The minimum error on Z_{pair} occurs at $P_\rho \approx 350$-400 GeV, with the value of $\sigma_Z = 1.5\%$.

An empirical fit for σ_Z as a function of ν was performed using the function

$$\sigma_Z = a + b/\nu + c\nu,$$

with the results listed in table 6.2.

quantity	sample	a (GeV)	b ($\times 10^{-3}$)	c ($\times 10^{-6}$ GeV^{-1})	χ^2
σ_ν	LAT data	10.50 ± 0.09	-45.1 ± 0.4	59.7 ± 0.6	2.8
	LAT MC	9.35 ± 0.05	-37.8 ± 0.3	49.8 ± 0.4	3.8
	SAT data	11.93 ± 0.18	-46.3 ± 1.1	55.4 ± 1.6	0.8
	SAT MC	12.11 ± 0.10	-45.9 ± 0.7	54.7 ± 1.2	2.2
σ_{P_ρ}	LAT data	0.03 ± 0.03	-0.20 ± 0.41	41.2 ± 1.8	1.4
	LAT MC	0.04 ± 0.02	-0.96 ± 0.47	51.0 ± 1.8	1.8
	SAT data	0.04 ± 0.03	0.80 ± 0.60	34.9 ± 2.4	1.5
	SAT MC	0.01 ± 0.02	0.10 ± 0.56	51.8 ± 2.3	2.0
σ_Z	LAT data	-4.09 ± 0.34	9.76 ± 0.40	80.7 ± 6.2	2.6
	LAT MC	-3.24 ± 0.21	8.29 ± 0.21	80.5 ± 4.6	3.3
	SAT data	-3.93 ± 0.35	10.8 ± 0.4	65.9 ± 6.6	1.3
	SAT MC	-4.55 ± 0.24	11.5 ± 0.2	97.6 ± 6.3	1.4

Table 6.2: Mean estimated error for ν, P_ρ, and Z_{pair}, expressed as parameters in a quadratic fit.

6.3.2 Total Energy Cut

The focus of this thesis analysis is *exclusive* ρ^0 production, that is, on events in which a ρ^0 meson is produced and nothing else. The conservation of energy is used as a primary selection criterion: all available energy should be taken up by the ρ^0. If E_b and E_s are the energy of the muon before and after the interaction, P_0 and P_0' the energy of the target, and $E_\rho = E_1 + E_2$ the energy of the ρ^0, then for exclusive events,

$$E_b + P_0 = E_s + P_0' + E_\rho,$$

$$E_\rho = E_1 + E_2 = \nu + \frac{|t|}{2M} \approx \nu,$$

$$Z_{\text{pair}} \equiv \frac{E_1 + E_2}{\nu} \rightarrow 1.$$

The Mandelstam variable $t \equiv (P - P')^2$ is the four-momentum-squared absorbed by the target; it is typically a fraction of a GeV,[4] so the term $t/2M$ is negligible compared to the energy available for the hadronic final state, ν.

A cut on Z_{pair} is used to select events in which no appreciable energy is lost to unobserved particles, such as slow hadrons or photons. The resolution of Z_{pair} is finite, however, and the inelastic background extends up to the limit $Z_{\text{pair}} = 1$. The

---

[4]The fact that t is small is a consequence of the fact that the target nucleon is left intact by the interaction, which requires that the cross section for the process include an elastic form factor, which falls rapidly at large momentum transfers.

raw distributions of Z_{pair} for real LAT and SAT data are shown in figure 6.9. All of the events contain exactly two forward tracks besides the muon, one negative and one positive, with the primary vertex in the target. A sharp peak at $Z_{pair} = 1$ is evident, but there also is a broad background falling to zero near $Z_{pair} = 1$. There is no such background in the simulated data; the peak at $Z_{pair} = 1$ is completely isolated.

The goal is to reject as much inelastic background as possible, without losing too much of the peak. It also is important to avoid kinematic biases which enter because the error on Z_{pair} varies with ν, as discussed earlier in this chapter.

For ideal exclusive events, $Z_{pair} = 1$ exactly. In real events Z_{pair} will differ from one for three reasons:

1. The momentum of the pion and muon tracks is not measured exactly; errors on these quantities result in an error on Z_{pair}.

2. One of the pions undergoes secondary interactions which changes its energy before or during the measurement.

3. The event is not exclusive.

It was shown in the software chapter that the errors estimated in the track fitting program are correct, so these can be propagated to an estimated error on Z_{pair}. A check that the error is estimated correctly can be made by plotting the normalized error, defined earlier as the actual error divided by the estimated error. Since the true value of Z_{pair} is one (theoretically), the actual error is $1 - Z_{pair}$, and the normalized error is

$$X \equiv \frac{1 - Z_{pair}}{\sigma_Z},$$

where $\sigma_Z = \sqrt{\sigma_1^2 + \sigma_2^2 + \sigma_\nu^2}$ is the estimated error on Z_{pair}. The actual error $(1 - Z_{pair})$ is definitely not gaussian, as shown in figure 6.10, but the normalized error is close to gaussian. (The curve shown is the unit gaussian.) A small deviation can be seen for $Z_{pair} < 1$, which comes from the energy loss of pions as they traverse the target and apparatus. Although this tail is statistically significant, it can be ignored: the loss of events due to a cut on this tail can be calculated from Monte Carlo, and is small.

The inelastic background creates a large tail at large values of the normalized error, X, as depicted in figure 6.11. The distribution of simulated data is essentially gaussian, with almost no entries past $X = 5$. The real data, however, exhibit a
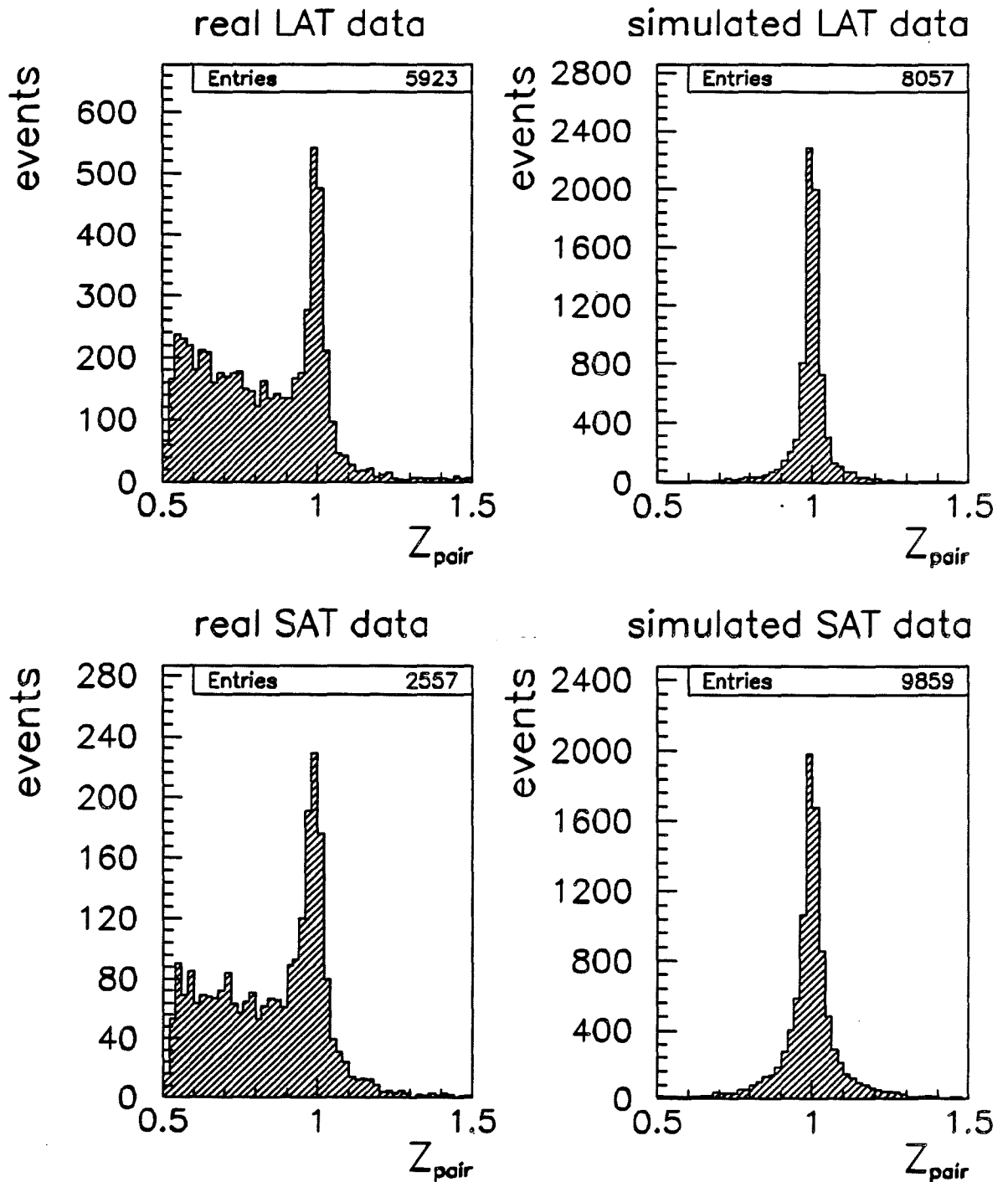
Figure 6.9: Raw distributions of $Z_{pair} = (E_1 + E_2)/\nu$, for real and simulated data.
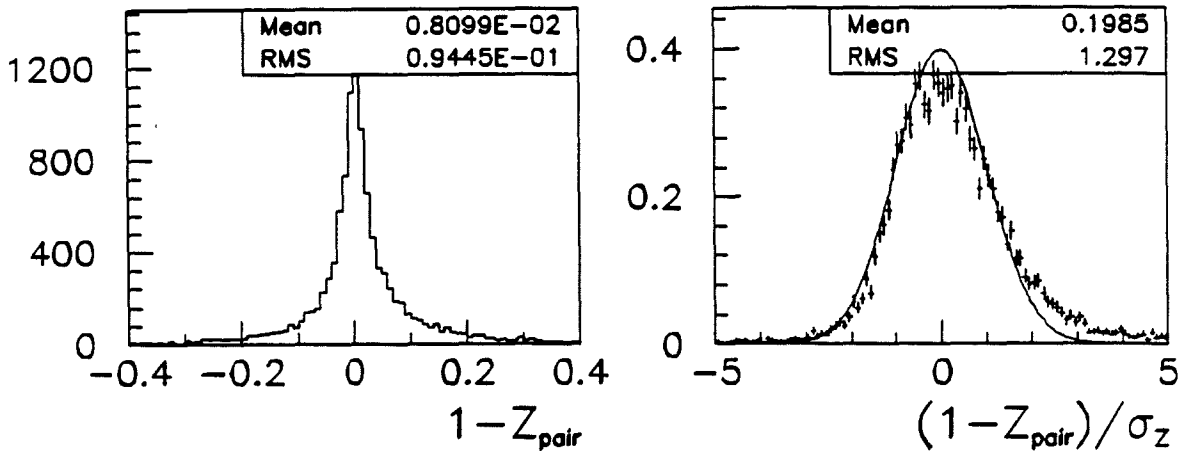
Figure 6.10: Distributions of Z_{pair} residuals from simulated data. The plot on the left shows the actual error on Z_{pair}, and the other plot shows the distribution of the normalized error. The curve is a gaussian with zero mean and unit variance.

large exponential tail extending past $X = 30$. The relatively simple form of these distributions makes them amenable to a series of empirical fits, as follows:

1. The peak at $X = 0$ is fit to a gaussian plus a constant term. Although the exact value of the mean and width varies with the upper limit of the fit, the same behavior is seen with the signal from the simulated data. The peak in real data has the same shape as the simulated peak.

2. The peak is subtracted from the total histogram, the result representing the inelastic background. This distribution is fitted readily by an exponential.

3. The entire spectrum is fitted to the sum of a signal and a background term. The choice of background term is somewhat arbitrary; the tail is definitely exponential, but it seems natural to force the background to go smoothly to zero at $X = 0$. A seven-parameter function is used, specifically:

$$N(X; A, \mu, \sigma, B, \kappa, \gamma, C) = S(X; A, \mu, \sigma) + B(X; B, \kappa, \gamma, C) \qquad (6.1)$$

$$S(X; A, \mu, \sigma) = A \exp\left[-\frac{1}{2}\frac{(X - \mu)^2}{\sigma^2}\right]$$

$$B(X; B, \kappa, \gamma, C) = B\,X^\gamma \exp(-\kappa X) + C \qquad \text{for } X > 0,$$
$$= C \qquad \text{for } X < 0.$$

4. The values for the signal peak and width are consistent with $\mu = 0$ and $\sigma = 1$, so the fit is repeated with these parameters fixed. The resulting values are listed in table 6.3.
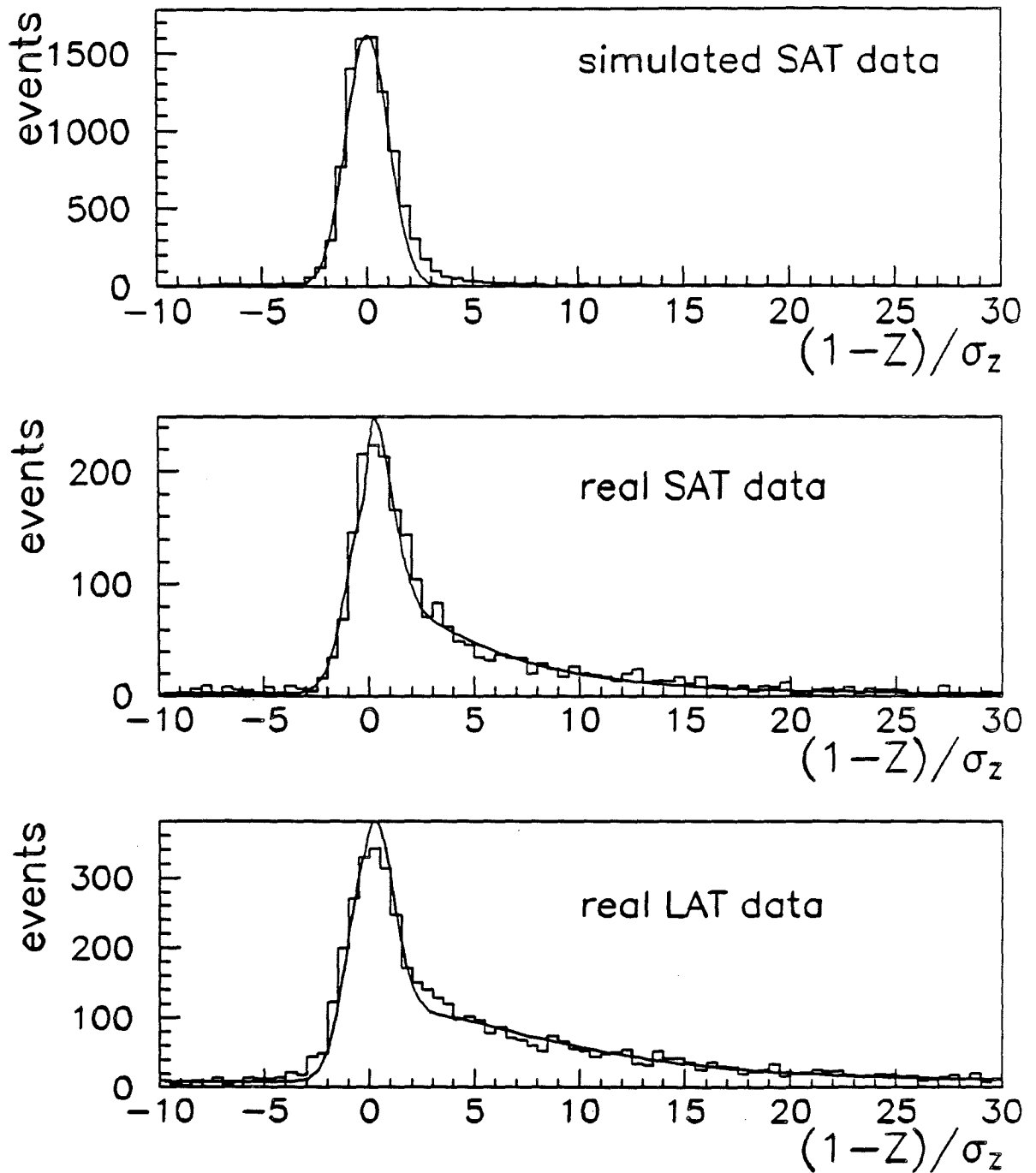
Figure 6.11: Distribution of the normalized error $X = (1 - Z_{pair})/\sigma_Z$, for Monte Carlo and real data. The curves are fits described in the text.

sample	A	B	κ	γ	C	χ^2
SAT	178 ± 10	97 ± 11	0.223 ± 0.020	0.205 ± 0.120	2.7 ± 0.3	1.7
LAT	337 ± 11	100 ± 8	0.165 ± 0.012	0.410 ± 0.078	8.9 ± 0.7	2.3

Table 6.3: Results of a five-parameters fit to the normalized error distributions, $X = (1 - Z_{\text{pair}})/\sigma_Z$. The function is explained in the text; the gaussian peak was fixed at zero, and its variance at one.

Figure 6.12 shows the nature of the fit; the dotted line represents the signal gaussian, the dashed line represents the background term, and the solid line shows the sum of the two.

Data simulated using the LUND model of deep-inelastic interactions can be compared to the background obtained from the five parameter fit, as shown in figure 6.13. The plots on the left are made using real SAT data; those on the right are simulated data. Clearly there is no elastic peak at $Z_{\text{pair}} = 1$ in the LUND data: the LUND model does not simulate exclusive neutral vector meson production! A comparison of the distribution of $X = (1 - Z_{\text{pair}})/\sigma_Z$ for the background derived
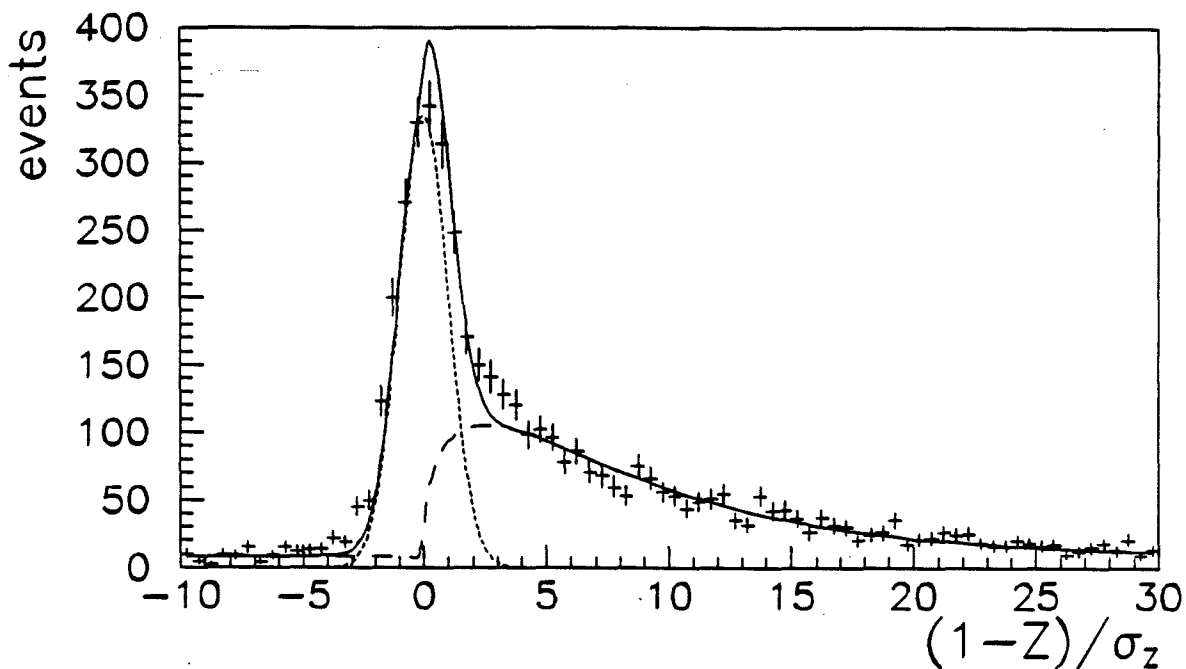

Figure 6.12: The signal and background terms are shown explicitly, for the LAT data. The dotted gaussian curve represents the signal, and the dashed curve represents the inelastic tail. The solid curve is the sum of the two.

from the real data, and for the LUND data is given in the second row of plots. They are similar. The SAT distribution is sharper at $X \approx 1$ than the LUND; the LAT distribution (not shown) closely resembles the SAT.

The LUND data were fitted to the background function discussed above, with results that agree with those obtained from the real data. The values for κ and γ, which determine the basic shape of the background term, are compared in the third row of the figure. The values are reasonably consistent.

The similarity of the LUND distributions to the background inferred from the data lends credence to the latter. Since the LUND is just a model, however,[5] it will be used for purposes of *comparison* – quantitative results will be derived from the real data directly.

The fit function (equation 6.2) provides an estimate of the amount of background contaminating the event sample. The number of signal and background events obtained using a lower cut X_{min} and an upper X_{max} is

$$N_S(X_{min}, X_{max}) = \int_{X_{min}}^{+X_{max}} dX \, S(X; A, \mu, \sigma)$$

$$N_B(X_{min}, X_{max}) = \int_{X_{min}}^{+X_{max}} dX \, B(X; B, \kappa, \gamma, C).$$

These may be regarded as functions of X_{min} and X_{max}. A natural choice for the lower cut is $X_{min} = -5$. The upper cut is more interesting. Figure 6.14 shows four quantities plotted as a function of X_{max} :

$$\text{"total signal"} \equiv \frac{N_S(-5, X_{max})}{N_S(-5, \infty)},$$

$$\text{"total background"} \equiv \frac{N_B(-5, X_{max})}{N_B(-5, \infty)},$$

$$\text{"background/signal"} \equiv \frac{N_B(-5, X_{max})}{N_S(-5, X_{max})},$$

$$\text{"background fraction"} \equiv \frac{N_B(-5, X_{max})}{N_S(-5, X_{max}) + N_B(-5, X_{max})}.$$

The background is close to zero for $X_{max} = 0$, but half of the signal is lost for this cut. The entire signal is obtained for $X_{max} = 3$, but the background is 35% of the total.[6] For X_{max} up to about 1.5, the increase in the signal is faster than the

---

[5]This model is not necessarily completely valid at the edges of kinematic space, such as for $Z \to 1$.

[6]Ultimately, the ratio of the background over the signal approaches 1.4.
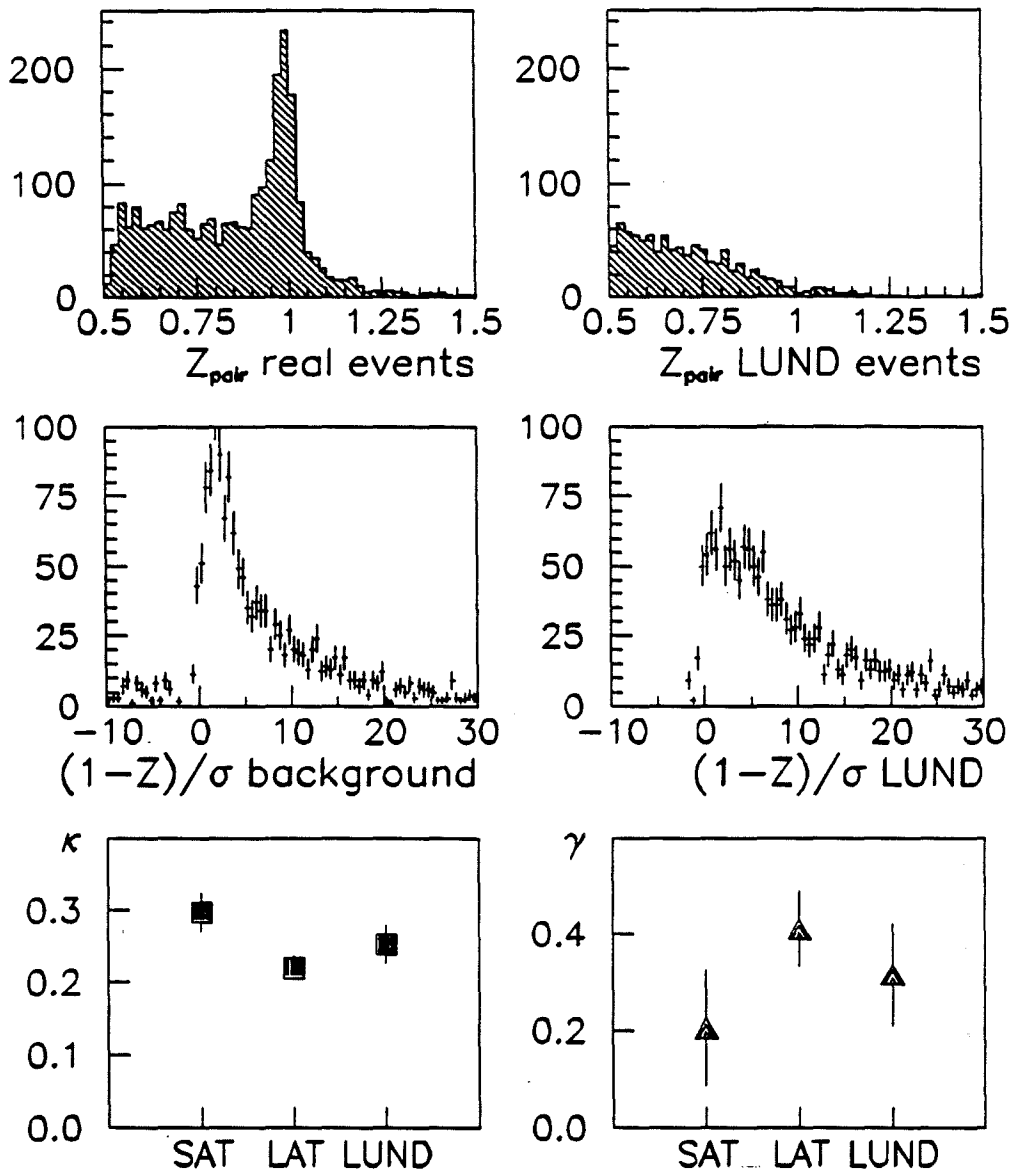
Figure 6.13: Comparison of Z_{pair} distributions from real SAT data, and low-Q^2 data simulated using the LUND Monte Carlo program. The signal term fitted to the data was subtracted from the total to give the deduced real background, which can be compared to the LUND model. The bottom plots compare the values of fit parameters κ and γ from real SAT and LAT data, and from LUND.

background fraction. A reasonable choice for cut is $X_{max} = 1$, for which 85% of the signal is retained, with a background fraction of 19%. It is important to test the sensitivity of the results of this physics analysis to the choice of X_{max}. To this end, an alternate value of $X_{max} = 0.2$ is chosen, for which the total signal is 59%, and the background fraction is 9.1%.

Given these considerations, three cuts on energy conservation are defined:

1. $0.9 < Z_{pair} < 1.1$,

2. $-5 < \frac{(1-Z_{pair})}{\sigma_Z} < 1$,

3. $-5 < \frac{(1-Z_{pair})}{\sigma_Z} < 0.2$.

The effect of these three cuts on the Z_{pair} spectrum is shown in figure 6.15. Plot a) shows the events accepted by the first cut; clearly a fair amount of background remains within the cut. Plot b) shows the effect of the other two cuts. Cut 2 results in a narrow peak centered on one; the third cut, because of its strict upper bound, is asymmetric.

6.3.3 Angular Resolution

Invariant mass depends on both the pion energies and the angle between the tracks, at the vertex:
$$M^2 = (p_1 + p_2)^2 = 2m^2 + 2E_1 E_2 - 2\vec{p_1} \cdot \vec{p_2}.$$

The estimated error on the mass is derived from the momentum resolution (discussed earlier) and the resolution of the track angles, in particular, on

$$H \equiv \cos\theta = \frac{\vec{p_1} \cdot \vec{p_2}}{|\vec{p_1}||\vec{p_2}|} = \frac{1 + y_1' y_2' + z_1' z_2'}{\sqrt{1 + (y_1')^2 + (z_1')^2}\sqrt{1 + (y_2')^2 + (z_2')^2}}.$$

Estimated errors on y' and z' are reported by track fitting; these are propagated to obtain an estimated error on H.

Some understanding of the errors on H and M is gained using simulated data. A comparison of simulated and real data distributions for y', z', $\sigma_{y'}$, $\sigma_{z'}$, $\langle \sigma_{y'} \rangle$ versus y', and $\langle \sigma_{z'} \rangle$ versus z', for the negative pion is given in figure 6.16. The agreement is good. Note that these are the reconstructed quantities reported at the primary vertex. The tracks were traced through the vertex magnetic field and

upper cut on $(1-Z)/\sigma$

total signal — — — — total background

background/signal   background fraction
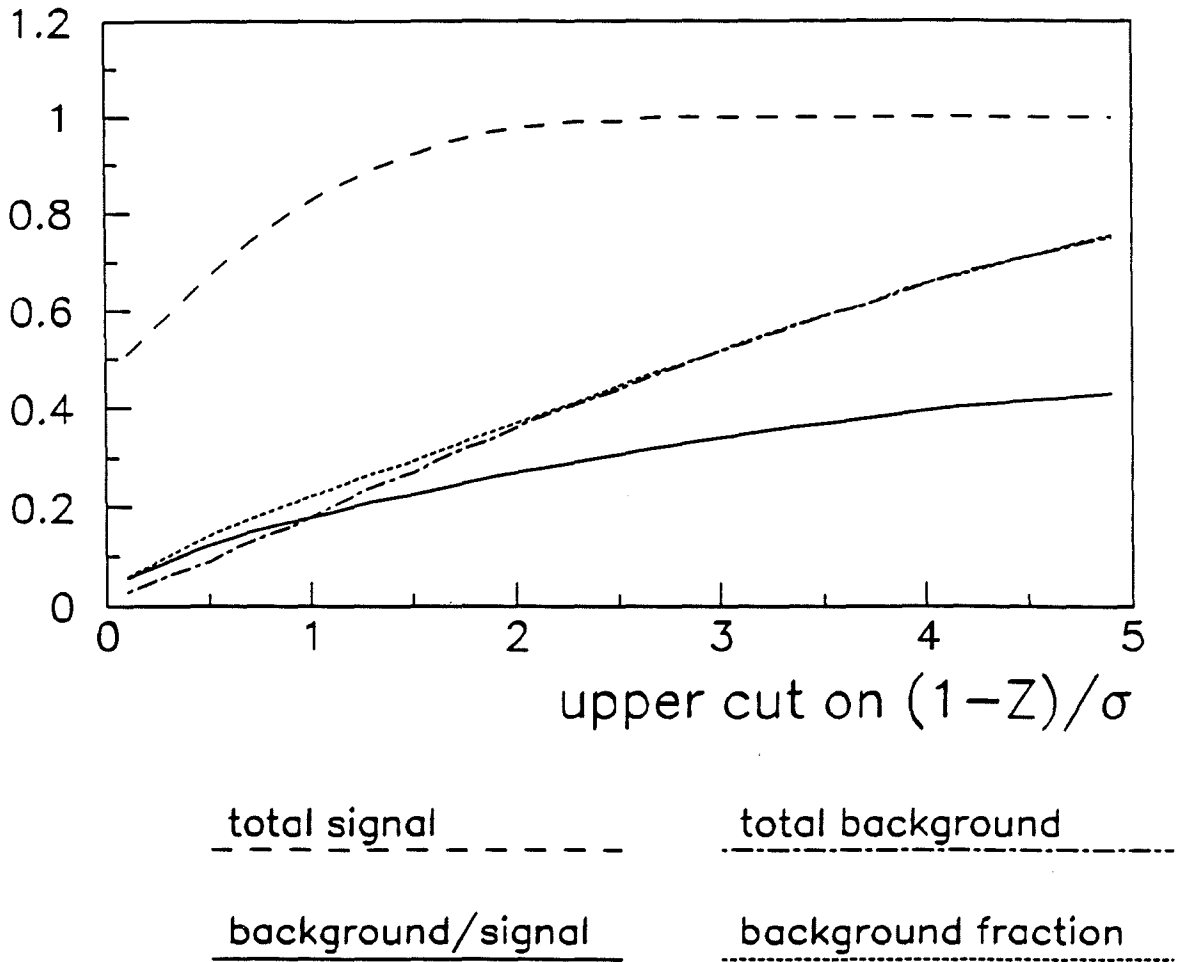
Figure 6.14: Variation of the signal and background retained as a function of X_{max}. The terms are defined in the text.

271
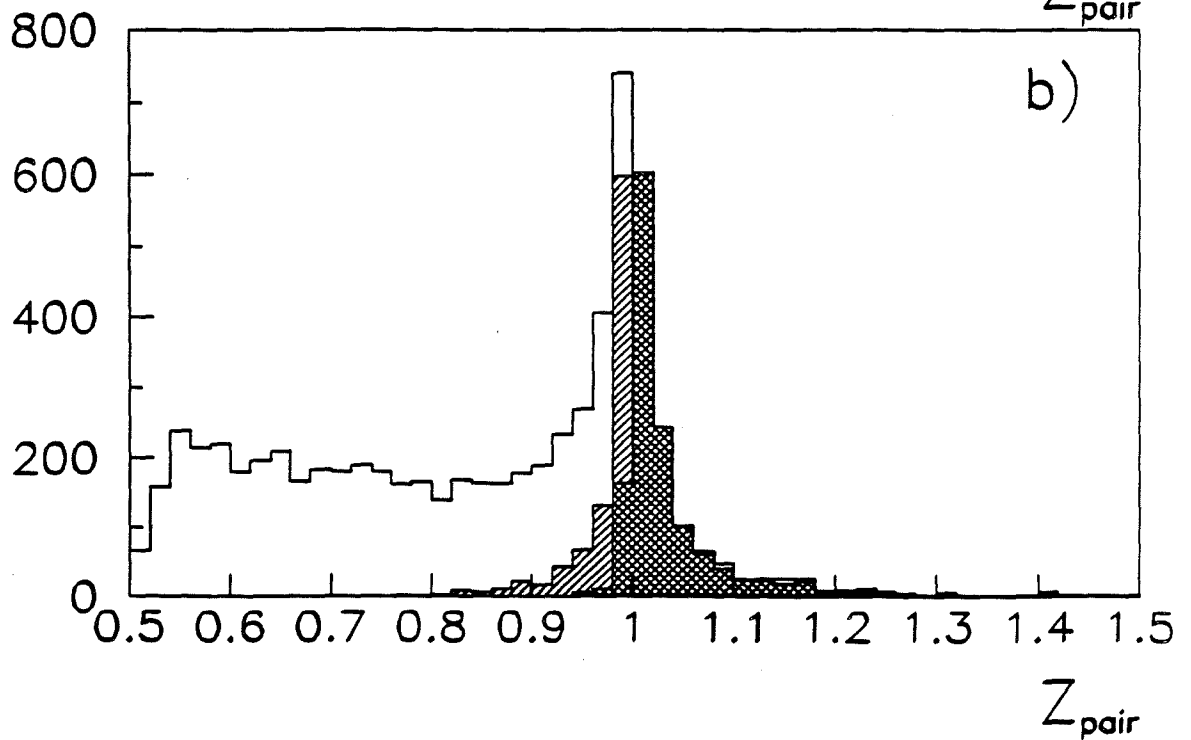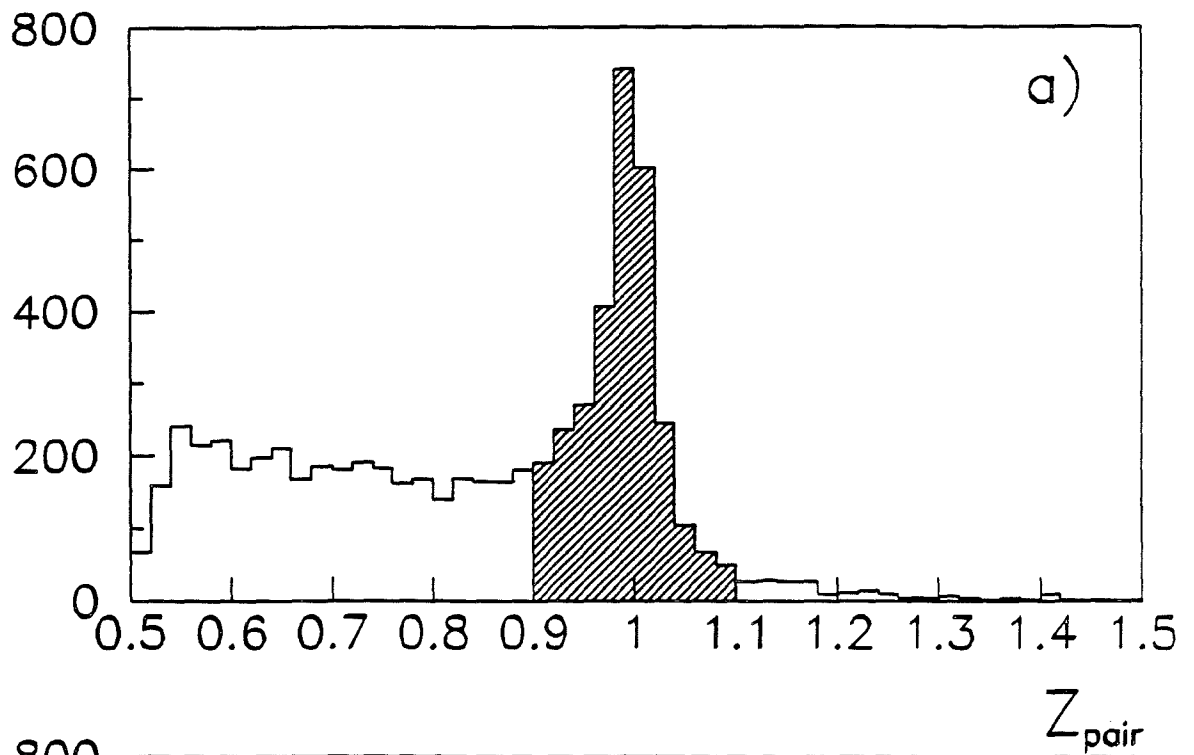
Figure 6.15: Effect of the three Z_{pair} cuts. Plot a) shows the events retained by the first cut (shaded area). Plot b) shows the events retained by the second cut (hash lines with positive slope), and the subset of these which pass the third cut (hash lines with negative slope).

target to the fitted vertex.[7] These quantities are meant to match the trajectories of the primary interaction, hence there is little difference between y and z (horizontal and vertical).

The estimated errors $\sigma_{y'}$ and $\sigma_{z'}$ for both pion tracks are propagated to obtain the estimated error σ_H, assuming no correlated errors between the tracks. A comparison of simulated and real data distributions for $(1 - H)$ and $\sigma_H/(1 - H)$ is given in figure 6.17. The resolution on $(1 - H) \approx \theta^2/2$ is poor when the two tracks are very nearly parallel. For most tracks, however, the resolution is approximately 10%.

Although the estimated errors $\sigma_{y'}$ and $\sigma_{z'}$ are nearly the same (see figure 6.16), the actual errors

$$\Delta y' = y'_{\text{recon}} - y'_{\text{true}} \qquad \Delta z' = z'_{\text{recon}} - z'_{\text{true}}$$

("recon" stands for "reconstructed") are quite different, as shown in figure 6.18. The actual error $\Delta y'$ is distinctly larger than $\Delta z'$ (top two plots). The distribution of the normalized error $(\Delta y'/\sigma_{y'})$ is too wide: the variance is almost four, while for $(\Delta z'/\sigma_{z'})$ it is 1.2. The wider distribution for $\Delta y'$ is the result of the lurking variable $\Delta X = X_{\text{recon}} - X_{\text{true}}$, i.e., the actual error on the reconstructed vertex position.

All charged tracks curve inside the magnet. Since the target was placed inside the CVM for the 1987-88 running period, the tracks curve at the vertex point. As a consequence, the horizontal track angle (y') reported at the primary vertex varies with the position of the reconstructed vertex. An error on the vertex position is estimated in the vertex fitting program, however, this error is not included in the estimated error for y'. The actual vertex error ΔX for exclusive ρ^0 events is shown in figure 6.18; the distribution of normalized errors $(\Delta X/\sigma_X)$ is gaussian with a variance of 1.3.

The effect of the lurking variable ΔX is shown in figure 6.19. The top plot shows the variation of the mean normalized error $\eta_{y'} \equiv \langle \Delta y'/\sigma_{y'} \rangle$ and $\eta_{z'} \equiv \langle \Delta z'/\sigma_{z'} \rangle$ as a function of the actual error ΔX. The linear dependence of $\eta_{y'}$ on ΔX is simply the small-angle approximation to a rotation in the horizontal plane. The significance is high: $\eta_{y'} \approx 5$ for $\Delta X = 10$ cm, which occurs not infrequently as seen in the fifth plot in figure 6.18. There is no effect in z because the magnetic field has little effect on the vertical projection of the trajectory.

The second plot in figure 6.19 shows that the width of the distribution of the

---

[7]A check of the precision of the trace can be found in [Sch91b].
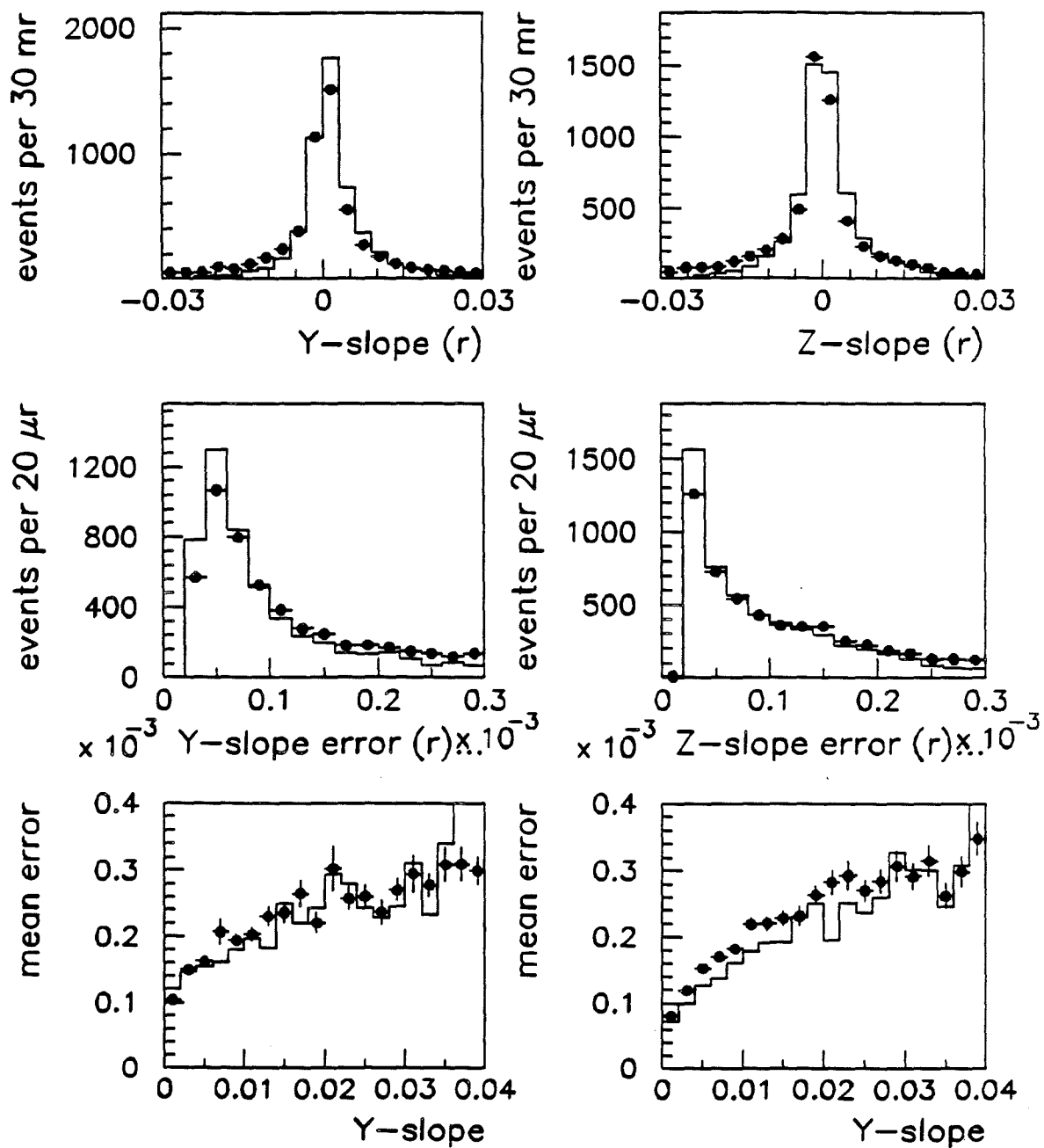
Figure 6.16: Comparison of simulated and real data, showing the distribution of track angles and their resolution, for negative pions in LAT data.
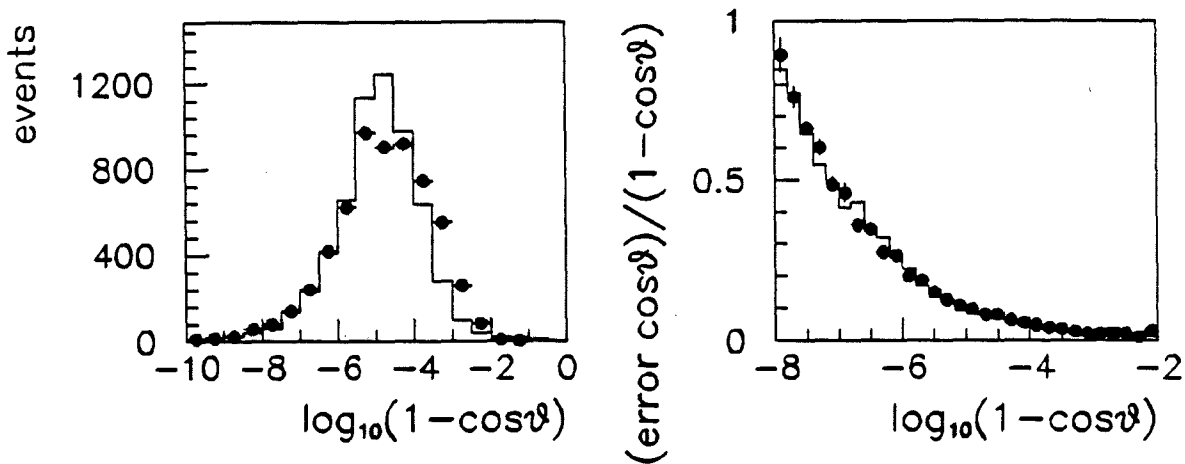
Figure 6.17: Comparison of the angle between the pion tracks for simulated and real data. Also shown is the resolution of $1 - \cos\theta$.

normalized error can be reduced below $\sigma = 1.5$ by taking the limit $|\Delta X| \to 0$.[8]

The variable ΔX lurks behind the error on $H = \cos\theta$, also. For a particular measurement, one can write

$$y'_{\text{meas}} = y'_{\text{true}} + r + D(\Delta X),$$

where r represents the small errors due to finite track resolution. The error $D(\Delta X)$ arises because the trajectories are curved at the primary vertex; y' is a function of X_{meas}, so the error $\Delta y'$ varies with $\Delta X = X_{\text{meas}} - X_{\text{true}}$. The errors r are essentially gaussian, so

$$\langle r \rangle = 0 \quad \Rightarrow \quad \langle y'_{\text{meas}} \rangle = y'_{\text{true}} + D(\Delta X).$$

The error $D(\Delta X)$ satisfies $D(0) = 0$, and, since the target is in a region where the magnetic field is nearly homogeneous, $D(-\Delta X) = -D(\Delta X)$:

$$D(\Delta X) \approx q \frac{P_T^{\text{CVM}}}{P} \frac{\Delta X}{L^{\text{CVM}}},$$

where $P_T^{\text{CVM}} \approx 1.54$ GeV is the p_T-kick of the CVM, and $L^{\text{CVM}} = P_T^{\text{CVM}}/B_0^{\text{CVM}}$ is the effective length of the magnet. The charge of the track is $q = \pm 1$.

The error on y' induces an error on $H = \cos\theta$, and ultimately on the invariant mass. The errors $D(\Delta X)$ from the two pions add because they have opposite

---

[8]The plot shows the distribution of the absolute value of the normalized error, $|\eta_{y'}|$. Since the mean of the normalized error is zero, the mean of $|\eta_{y'}|$ is proportional to the width of the original distribution: $\langle |\eta_{y'}| \rangle = \sigma\sqrt{2/\pi} = 0.789\sigma$.
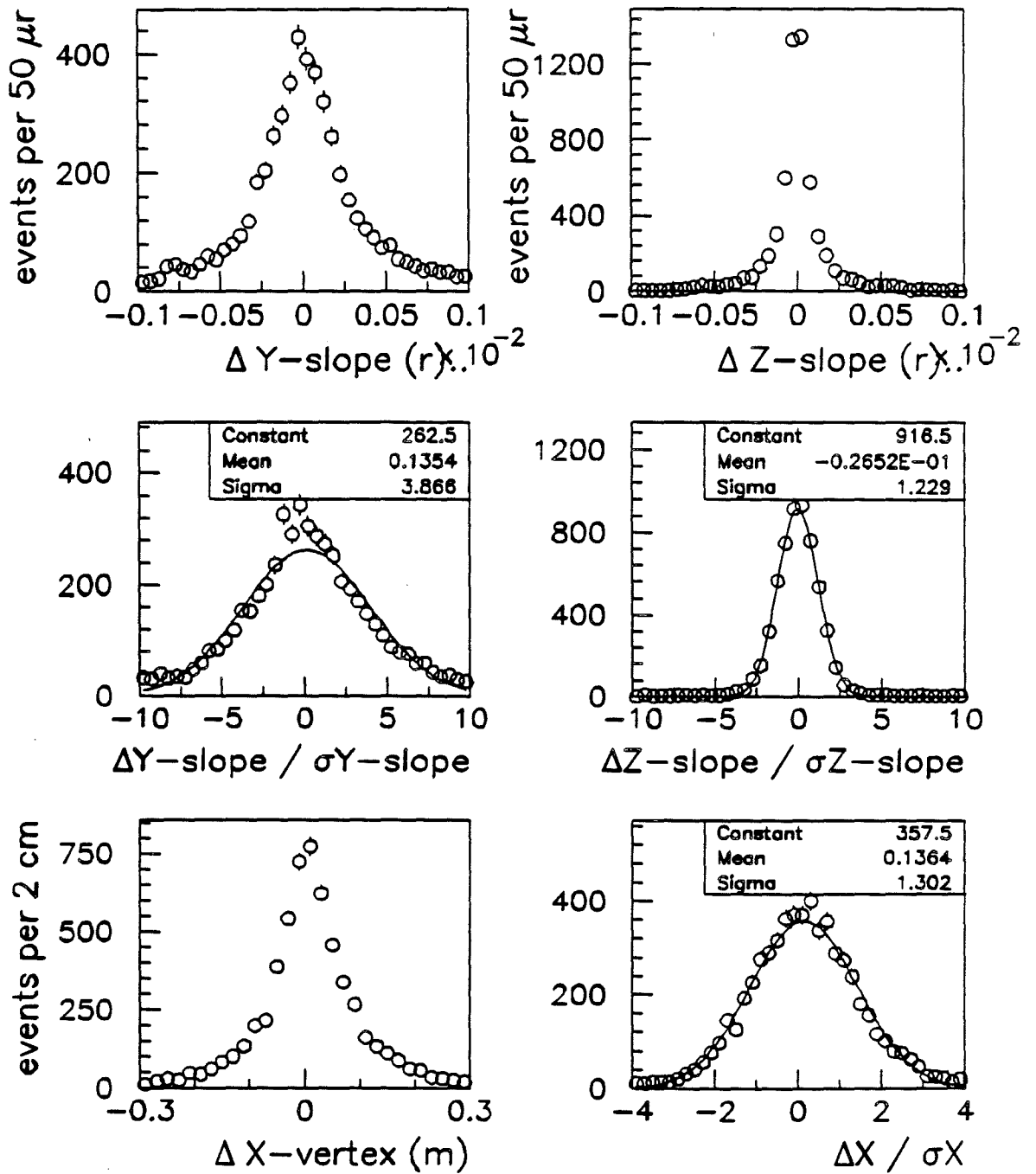
Figure 6.18: Actual errors on track angles ($\Delta y'$ and $\Delta z'$), and normalized errors ($\Delta y'/\sigma_{y'}$ and $\Delta z'/\sigma_{z'}$), for negative pions in exclusive ρ^0 events. Also shown is the actual and normalized errors for the X coordinate of the primary vertex. The fits are gaussian.
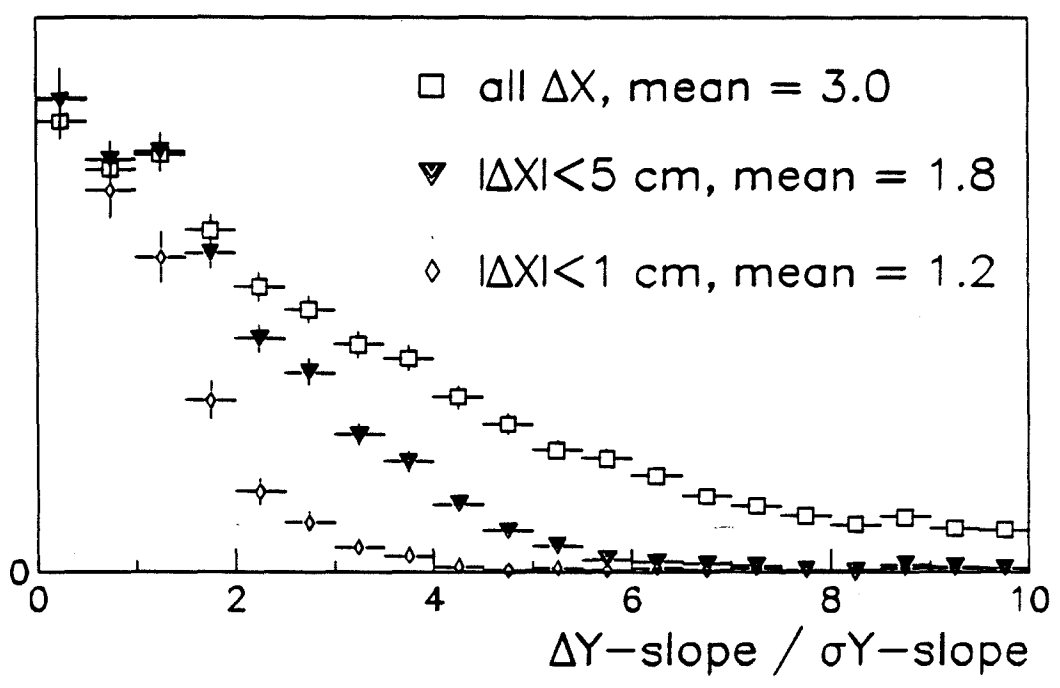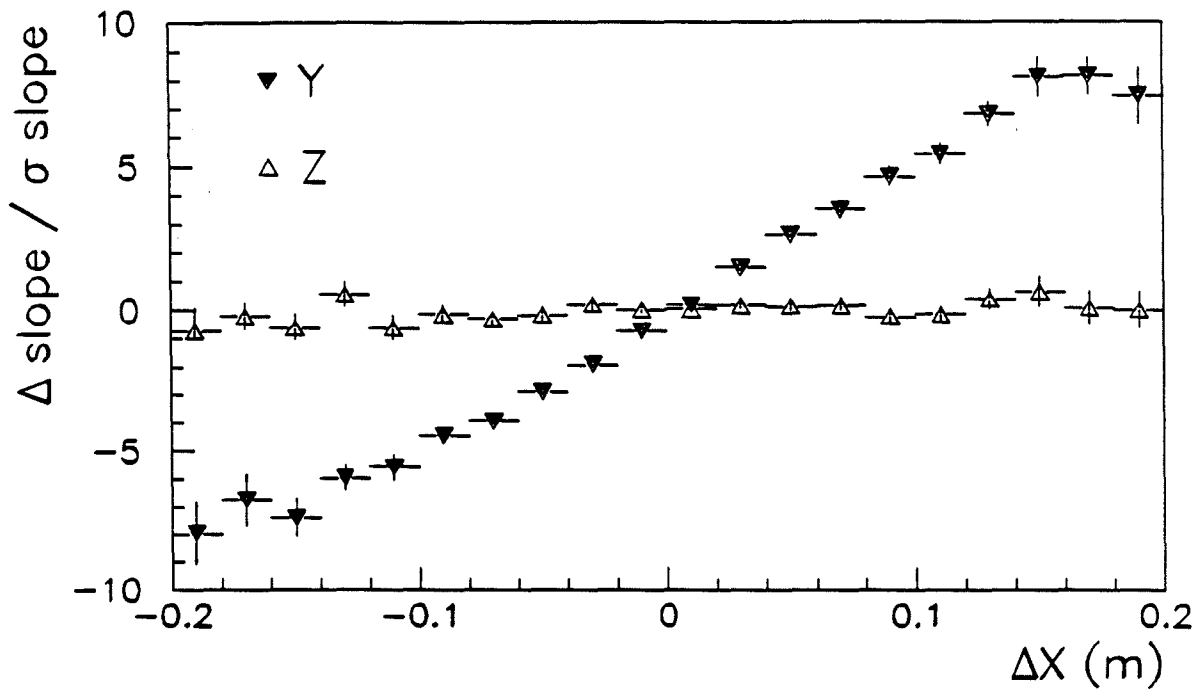
Figure 6.19: The top plot shows the variation of the normalized error on the track angles ($\eta_{y'} \equiv \langle \Delta y'/\sigma_{y'} \rangle$, and $\eta_{z'}$) with the actual error $\Delta X = X_{\text{recon}} - X_{\text{true}}$. The bottom plot illustrates how the distribution of $\eta_{y'}$ becomes narrower as $|\Delta X|$ is reduced.

charge; this can be contrasted with the case of Q^2, in which vertex errors ΔX have little effect because the muons both are positive.[9]

The error ΔX can be considered a parameter; $H = H(\Delta X)$. The approximate behavior of $H(\Delta X)$ can be calculated using Taylor's expansion,

$$H'(\Delta X) \approx H(0) + H'(0)(\Delta X),$$

where

$$H' = \left(\frac{\partial H}{\partial y_1'}\right)\frac{\Delta y_1'}{\Delta X} + \left(\frac{\partial H}{\partial y_2'}\right)\frac{\Delta y_2'}{\Delta X}.$$

It easily can be calculated that

$$\frac{\partial H}{\partial y_1'} = \frac{(1 - (y_1')^2)(y_2' - y_1') - y_1' z_1'(z_2' - z_1')}{\sqrt{1 + (y_1')^2 + (z_1')^2}\sqrt{1 + (y_2')^2 + (z_2')^2}} \approx y_2' - y_1',$$

to lowest order in y' and z'. Clearly $(\partial H/\partial y_2') \approx y_1' - y_2'$, so

$$\begin{aligned}
\Delta H = H'(0)(\Delta X) - H(0) &= (y_2' - y_1')\Delta y_1' + (y_1' - y_2')\Delta y_2' \\
&= (y_2' - y_1')\left(\frac{1}{P_1} + \frac{1}{P_2}\right)\left(\frac{P_T^{\mathrm{CVM}}}{L^{\mathrm{CVM}}}\right)(\Delta X).
\end{aligned}$$

In the case $P_2 = P_1$ and $y_2' = -y_1'$, the effect is maximal: $\Delta H = -4y'\Delta y'$. For $P_2 \gg P_1$ and $y_2' \ll y_1'$, $\Delta H = -y_1'\Delta y_1'$.

The actual and estimated errors on $H = \cos\theta$ are shown in figure 6.20 for LAT exclusive ρ^0 events. The variation of the mean absolute value of the normalized error $\eta_H = \Delta H/\sigma_H$ with the absolute value of the actual error $|\Delta X|$ is shown also. If there were no error on the X coordinate of the vertex, then the resolution would reach its optimal value. Some measurements of errors on H are given in table 6.4.

The inaccuracy of the vertex position is a result in part of the inaccuracies of the track angles. The vertex position is inferred from the intersections of trajectories in the horizontal and vertical planes. The larger the angles between tracks, the better is the vertex resolution. This dependence is illustrated in the last plot in figure 6.20, where the mean value of the absolute value of the actual error $\langle|\Delta X|\rangle$ is plotted versus the true angle between the pion tracks; $(1 - \cos\theta) \approx \theta^2/2$. Thus, the larger the true angle θ, the smaller the error on X, and hence the smaller is the error on the reconstructed angle. (See figure 6.18.)

---

[9]In fact, the error on Q^2 vanishes for $P_t = P_b$, whereas the error on $M_{\pi\pi}$ reaches its maximum magnitude for $P_1 = P_2$.
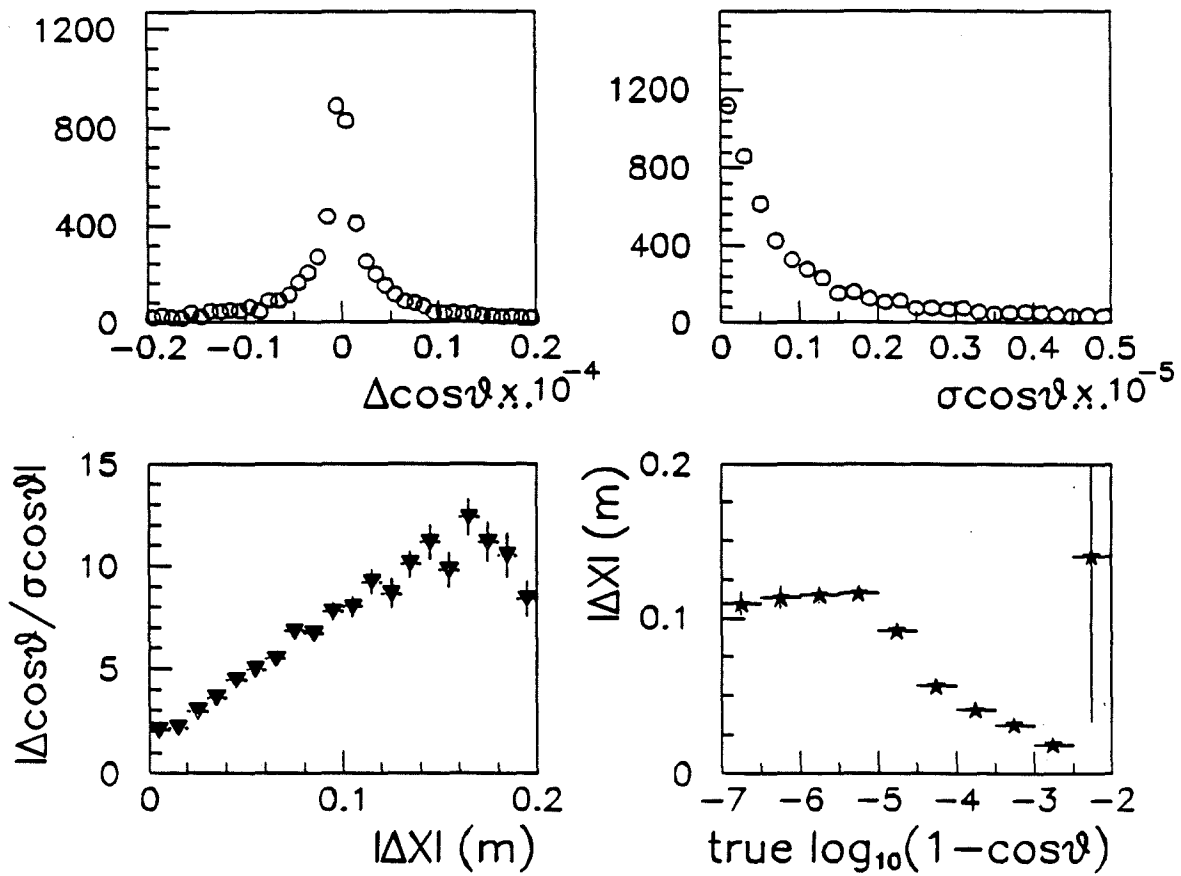
Figure 6.20: Actual and estimated errors on the angle between two tracks, $H = 1 - \cos \theta$. Also shown is the correlation between the mean absolute normalized error and the lurking variable, $|\Delta X|$, and the connection between the latter, and the pion opening angle.

item	LAT mean	LAT rms	SAT mean	SAT rms
$\sigma_{\cos\theta}$	2×10^{-6}	-	2×10^{-6}	-
$H_{measured}$	41×10^{-6}	-	62×10^{-6}	-
H_{true}	38×10^{-6}	-	57×10^{-6}	-
$H_{measured} - H_{true}$	1.2×10^{-6}	15.4×10^{-6}	0.9×10^{-6}	21.0×10^{-6}
$(H_{measured} - H_{true})/\sigma_{\cos\theta}$	0.40	6.25	0.57	6.79
$\|y_1' - y_2'\|$	8.5×10^{-3}	10.5×10^{-3}	11.2×10^{-3}	12.4×10^{-3}
$\|z_1' - z_2'\|$	8.2×10^{-3}	8.7×10^{-3}	9.6×10^{-3}	9.6×10^{-3}
$\sqrt{2(1 - \cos\theta)}$	7.6×10^{-3}	7.9×10^{-6}	9.6×10^{-3}	8.8×10^{-6}

Table 6.4: Measured errors on the angle between the pion tracks, for simulated LAT and SAT exclusive ρ^0 events.

6.3.4 Secondary Interactions

The pions from the ρ^0 decay must travel through a non-negligible amount of material in order to be detected. In addition to the target itself, there are the wire chambers, the cherenkov counters, and the air in the hall. The largest concentration of matter upstream of the RICH detector is the target itself. The pions can interact electromagnetically or hadronically, leading to an imperfect correspondence between their trajectories at the primary vertex, and those measured in the forward spectrometer. The electromagnetic interactions cause small angle deviations, which are taken into account when the track is fitted; the errors from multiple coulomb scattering in fact are smaller than those from the coordinate measurements. Energy loss by bremsstrahlung or inelastic electromagnetic interactions is negligible. Hadronic interactions are more damaging: the pion often loses a large fraction of its energy to several secondary particles, and sometimes is not reconstructable. Clearly events in which one of the pions undergoes a secondary interaction must be discarded. These losses cannot be taken into account in track or vertex fitting; however, estimates of the rate of secondary interactions are not difficult to calculate, and the Monte Carlo can be used to investigate the details of "marred" events.

The probability of pion interaction in a length of material L is

$$P(L) = 1 - \exp(-\frac{L}{L_H}) \quad \text{where} \quad L_H = \frac{1}{N_{Av}\rho\sigma}.$$

The inelastic pion-nucleon cross section comprises 85% of the total for hydrogen and deuterium; values from [PDG] are listed in table 6.5; these are also expressed in terms of inelastic and total interaction lengths. The probability that one of the two pions reinteracts in the target depends on the mean path length in the

quantity	hydrogen	deuterium
$\sigma_{total}^{\pi N}$ (mb)	38.7	73
$\sigma_{inel.}^{\pi N}$ (mb)	33	61
$L_{total}^{\pi N}$ (m)	6.11	2.82
$L_{inel.}^{\pi N}$ (m)	7.18	3.38
mean path between vertices (m)	0.38	0.38
probability either π interacts (%)	12.2	25.4
probability either π interacts elastically (%)	1.8	3.8

Table 6.5: Summary of cross sections and probabilities for secondary interactions in the target for hydrogen and deuterium. The cross sections are taken from [PDG].

target; a simple calculation shows that if L_T is the length of the target, then the mean distance travelled by a pion in the target is $L_T/3$. Using the empirical values for the interaction length listed in table 6.5, and the value $L_T = 1.15$ m, the probability that a given pion reinteracts in the target is 12.7% for deuterium, and 6.1% for hydrogen. When the pion reinteracts, the interaction is inelastic 85% of the time. There are two pions in these events, so the probability that one or more pions reinteracts is twice the probability that a particular pion reinteracts: 25.4% for deuterium, and 12.2% for hydrogen. Fortunately, most of the events in which a pion has reinteracted in the target are easily identified, because the interaction usually is inelastic, leading to several additional particles, and a significant energy loss of the original pion: a cut on the total number of reconstructed tracks and on the total energy in the event eliminates most of these events. The number of events with pions interacting elastically, comprising 3.8% of the deuterium sample, and 1.8% of the hydrogen sample, can be reduced somewhat by demanding that all tracks be fitted to the primary vertex.

The Geant Monte Carlo, which uses the Geisha package to describe hadronic interactions, gives results in accordance with these estimates.[10] The mean distance between primary and secondary vertices in the target is 0.36 m, and the probability that a pion reinteracts in the target is 14.8% for hydrogen, and 30.3% for deuterium, in fair agreement with the values listed in table 6.5. According to the Monte Carlo, a pion reinteracts downstream of the target and upstream of the Rich detector 12.5% of the time.

Events in which a pion reinteracts inelastically, losing much of its energy and producing additional particles, are easily eliminated with three cuts:

1. *topology cut:* There should be exactly two pions in the event, one positive and one negative.

---

[10]A discussion of the Geisha package can be found in [Salvarani, appendix B].

cut	hydrogen			deuterium		
	total	target	spectrometer	total	target	spectrometer
none	12900	1318	1684	8200	1592	955
topology	5487	116	322	3253	86	174
energy	4744	70	179	2824	45	112
vertex	4218	47	117	2531	30	79
all cuts / no cuts	0.327	0.036	0.069	0.309	0.019	0.083

Table 6.6: Summary of the effect of cuts meant to eliminate events in which a pion reinteracts. The heading "target" means that the pion reinteraction occurred in the target; "spectrometer" means that the reinteraction occurred outside the target, but upstream of the Rich. More than half of these occurred downstream the center of the CCM. The cuts are applied successively. These numbers were obtained from LAT Monte Carlo events.

2. *energy conservation cut*: All of the energy lost by the muon should be taken up by the pions.

3. *vertex cut*: The beam muon, scattered muon, and the two pions should be fitted to the primary vertex.

The result of applying each of these cuts is listed in table 6.6. The topology cut removes the bulk of the events in which a pion reinteracts, but the energy conservation and the vertex cuts help reduce the fraction of "marred" events without significantly reducing the number of "pristine" events. In the end, 31–32% of the events pass these cuts, with only 1% with pions which reinteract in the target, and a total of 4% which reinteract before reaching the Rich detector. The error on the mass for these events is the same as for events with no reinteractions: approximately 60 MeV (rms). These cuts reduce the effects of secondary interactions to a negligible level.

The loss of events with no pion reinteractions due to these cuts is described in table 6.7. Monte Carlo events were selected in which there were no secondary interactions, and the three main cuts were applied. The largest loss, due to the topology cut, occurs because events are not reconstructed completely. The other two cuts reduced the topologically correct events by 19%; it can be shown that the events removed are often not reconstructed completely correctly, so that the loss is compensated by the increased quality of the sample.

Some of the properties of secondary interactions are illustrated in figures 6.21–6.23. The first plot in figure 6.21 shows that in most events there is only one vertex – the primary vertex. Although the loss of events in deuterium is significant, the targets still are basically "thin" to pions. When there is a secondary interaction

cut	hydrogen events	fraction surviving	deuterium events	fraction surviving
none	8856	1.000	5040	1.000
topology	4553	0.512	2694	0.534
energy conservation	4085	0.461	2412	0.480
vertex	3719	0.420	2228	0.442

Table 6.7: Events lost due to mass cuts, based on events from LAT Monte Carlo. The cuts are successive.
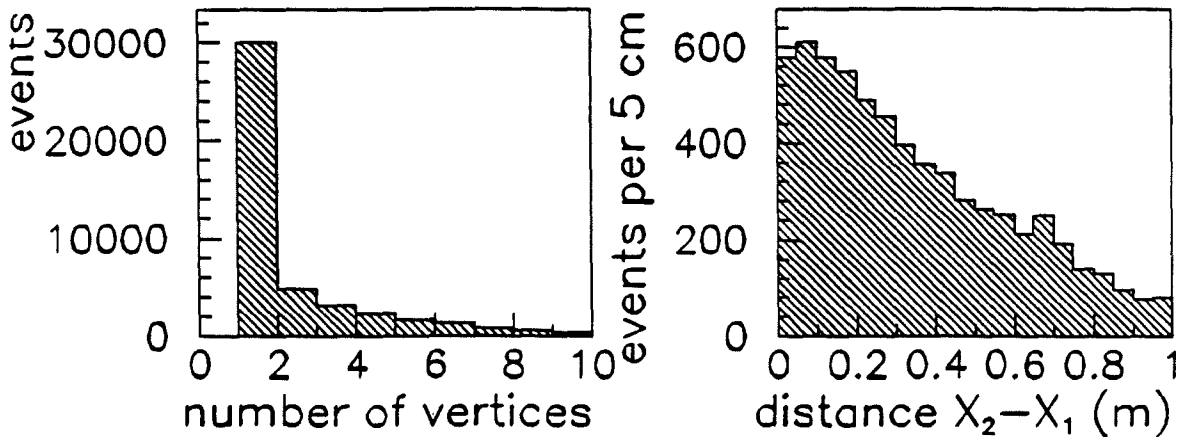
Figure 6.21: True vertices in simulated LAT events. The first plot shows the number of vertices per event, and the second shows the separation between primary and secondary vertices, when both are in the target.

in the target, it is likely to be close to the primary vertex, as illustrated in the second plot in figure 6.21. The mean distance is about 36 cm; when normalized to the uncertainty on the position of the primary vertex it is 9.4 cm.

The plots in figure 6.22 show that there are two kinds of pion reinteraction, characterized by large and small energy losses. The mean energy loss for all secondary interactions is 95 GeV, but for events with a fractional energy loss less than 50%, the mean energy loss is only 5 GeV. The change in the vertical slope also contains two components: a narrow peak at zero, and a broad base.

The pion reinteractions are reflected in the distribution of the number of reconstructed tracks, as shown in figure 6.23. The first plot shows that there is a significant number of events with fewer or more than four tracks; a simple topology cut requiring four reconstructed tracks clearly will eliminate many of the events in which a pion has reinteracted. After this cut, the number of tracks fitted to the primary vertex is shown in the second plot; there are a few events in which
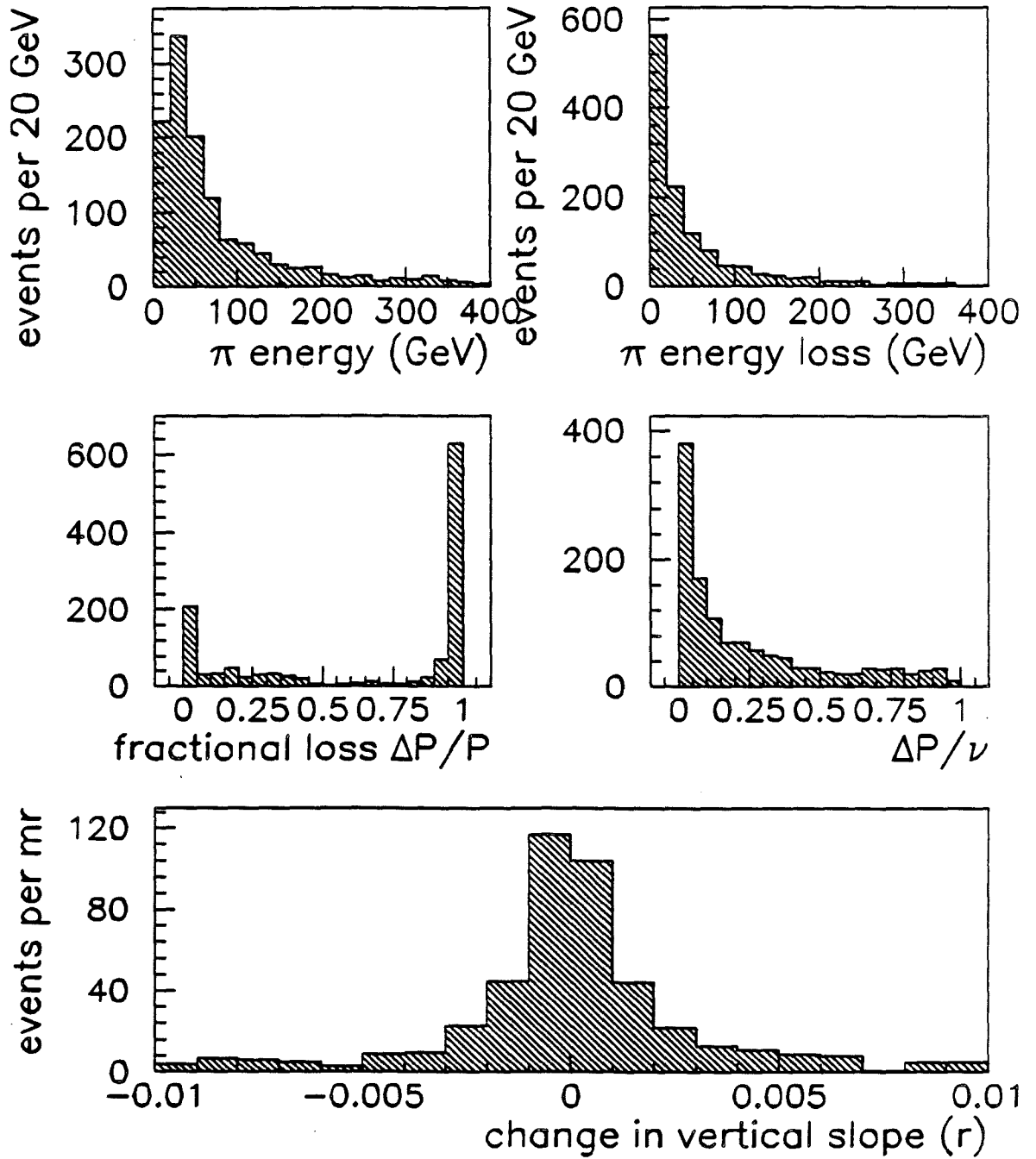
Figure 6.22: Energy lost by pions in simulated LAT events.
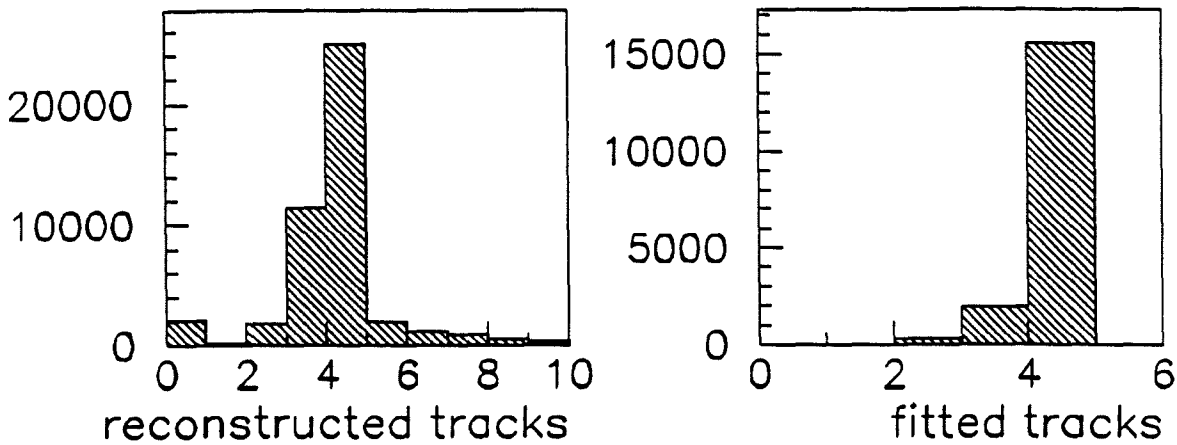
Figure 6.23: The first plot shows the number of reconstructed tracks in simulated LAT events. The second shows the number of fitted tracks for those events with exactly four reconstructed tracks.

one or both of the pions do not belong to the primary vertex. Eliminating these events improves the purity of the remaining sample, and the accuracy of the mass measurement.

The characteristics of events with and without pion reinteractions are displayed in figure 6.24. The shaded histograms show the distributions obtained from simulated LAT events in which the pions did not interact. The heavy line histogram shows the same quantities for events in which at least one of the pions reinteracted. Both samples have been normalized to one; the shape is of interest. The first plot shows that there is a net energy loss due to pion reinteractions; in fact, the region $Z_{pair} < 0.7$ is dominated by events in which a pion reinteraction has occurred. The second and third plots show that the secondary interactions distort the mass shape significantly.

In the last two plots, D stands for the distance from a reconstructed track to the primary vertex at the point of closest approach; σ is the uncertainty on this quantity. The fourth plot shows the distribution of D/σ averaged over all four tracks, and the fifth plots shows the distribution of the largest value occurring in an event. The vertex cut, in which all four tracks are required to be fitted to the primary vertex, causes a cutoff on $\langle D/\sigma \rangle$ at 2.2, and on $(D/\sigma)_{max}$ at 4.
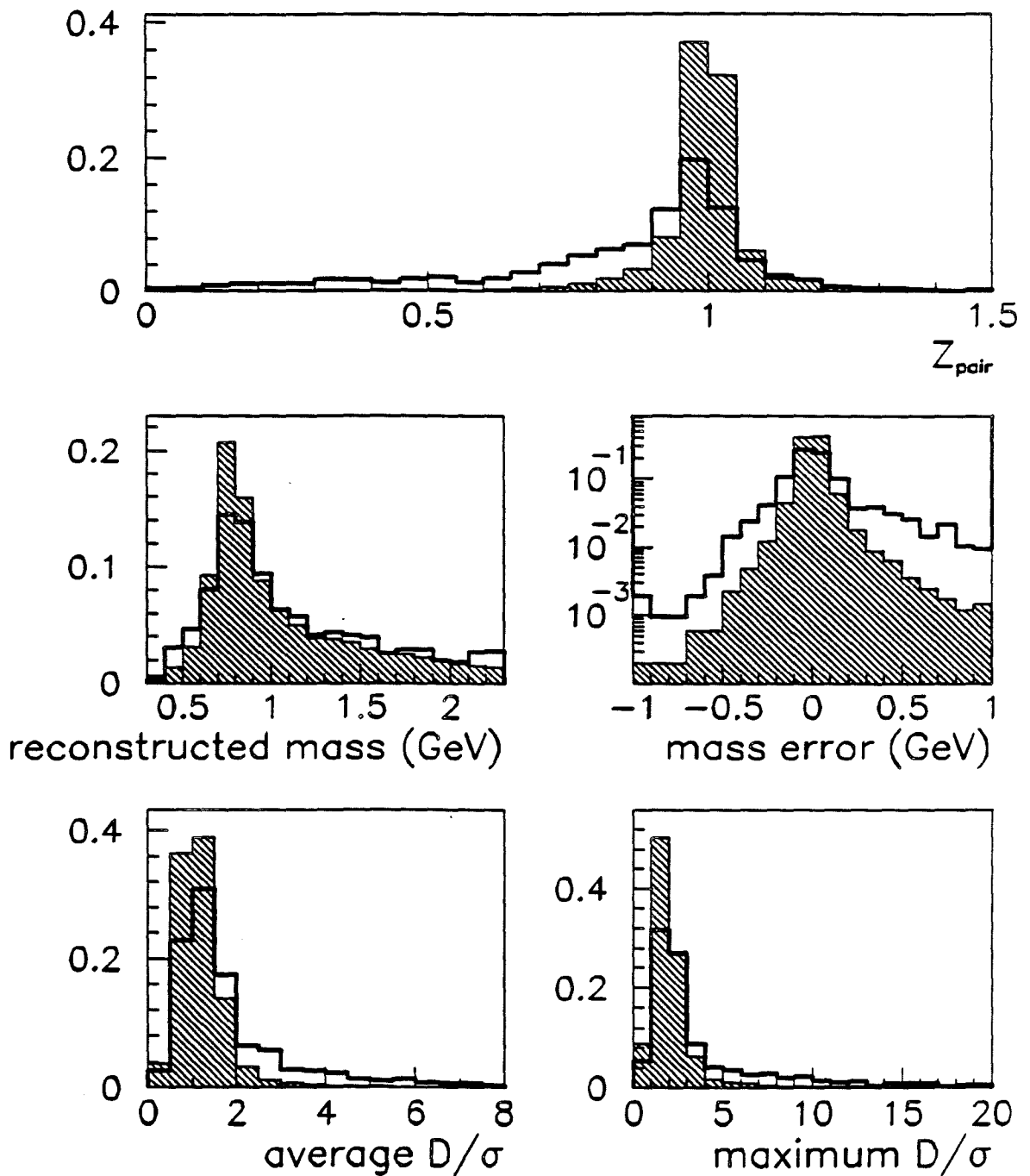
Figure 6.24: A comparison of certain event quantities for events with pion reinteractions (heavy line), and without (shaded histogram). All histograms were normalized to one.

6.3.5 Multiple Coulomb Scattering

The pions undergo many small angle scatters as they pass through the target, which can distort the angles of the tracks reconstructed at the vertex. Under certain assumptions, the distribution of the track deviations is gaussian. The standard formula for the rms plane angle of the deviation is [PDG]

$$\theta_0 = \frac{0.0141\text{GeV}}{p\beta} \sqrt{\frac{L}{L_R}} \left(1 + \frac{1}{9} \log_{10} \left(\frac{L}{L_R} \right) \right), \tag{6.2}$$

where L is the length and L_R is the radiation length of the material through which the particle is passing. Given the target vessels used in 1987-88, this works out to be

$$\theta_0 \approx \frac{46 \ \mu r}{P} \text{ for the hydrogen target,}$$

$$\approx \frac{50 \ \mu r}{P} \text{ for the deuterium target, and}$$

$$\approx \frac{141 \ \mu r}{P} \text{ for the xenon target.}$$

On average this angle is less than 1 μr for pions in exclusive ρ^0 events. Since the mean opening angle between the pions is on the order of 10 mr, this error is negligible.

6.3.6 Mass Resolution

The invariant mass of a pion pair is never measured exactly correctly. The error $\Delta M \equiv M_{meas} - M_{true}$ arises from several sources:

1. Measurement of the pion trajectories (momentum and angle) in the forward spectrometer is imprecise.

2. The track inclination in the horizontal plane is incorrect because the reconstructed primary vertex position is not exactly correct.

3. Tracks are reconstructed erroneously.

4. The pions reinteract in the target or in the apparatus.

5. The alignment of the chambers is in error, or the magnetic fields are not mapped correctly.

The first three items are essentially stochastic, and give rise to a finite mass resolution; generally the average error is expected to be zero. The last two items can produce nonzero shifts in measured quantities, such as the mass; they are responsible for potential systematic errors. Track resolution and pion reinteractions have been discussed earlier in this chapter. Track reconstruction will be discussed in greater detail later, as will the possibility of systematic errors due to chamber misalignment and incorrect magnetic field maps.

Most of the issues in mass resolution have been discussed in previous sections. The estimated mass error is shown in the first plot of figure 6.25. The second plot shows that it increases steadily as the true mass increases. The third plot shows that the normalized error is too large; this is due to the error on the primary vertex position, ΔX. The variation of the absolute normalized error with the lurking variable ΔX is shown in the fourth plot.

One important point that must be mooted is the fact that the invariant mass is positive definite — it has a rigorous minimum value of $2m_\pi$ no matter how badly tracks might be reconstructed. This follows from the fact that, in the context of offline analysis, the energy of the pion is strictly greater than its momentum, no matter what the momentum resolution is.[11] Consequently, the distribution of measured mass values relative to a given true value has a strict lower bound, and a distant upper bound given by the center of mass energy. This lower bound approaches the center of the distribution as the true mass approaches zero. Eventually it is comparable to the estimated error on the mass, at which point the average error becomes significantly different from zero.

These points are illustrated in figure 6.26. The first plot shows that the actual error on the mass peaks at zero, with a fairly rapid falloff; the second plot shows that the falloff comes to an abrupt end for negative errors. (Note that the true mass value has been restricted to small values.) The mean of this error is significantly greater than zero, but it approaches zero as the true mass increases; the extent of the error depends on the mass resolution, and on insidious effects such as pion reinteractions and pattern recognition failures.

Figure 6.27 shows how the mean error increases as $M_{true} \to M_{min} = 0.2791$ GeV; unfortunately, it is not negligible across the mass resonance.

Most events are reconstructed with a reasonable error on the mass, as shown by the peak at zero in figure 6.26. The position of this peak and its width, estimated using a gaussian fit, are constant as a function of the true mass, as shown in

---

[11] This would not be the case if there were *separate* measurements of the pion momentum and energy.
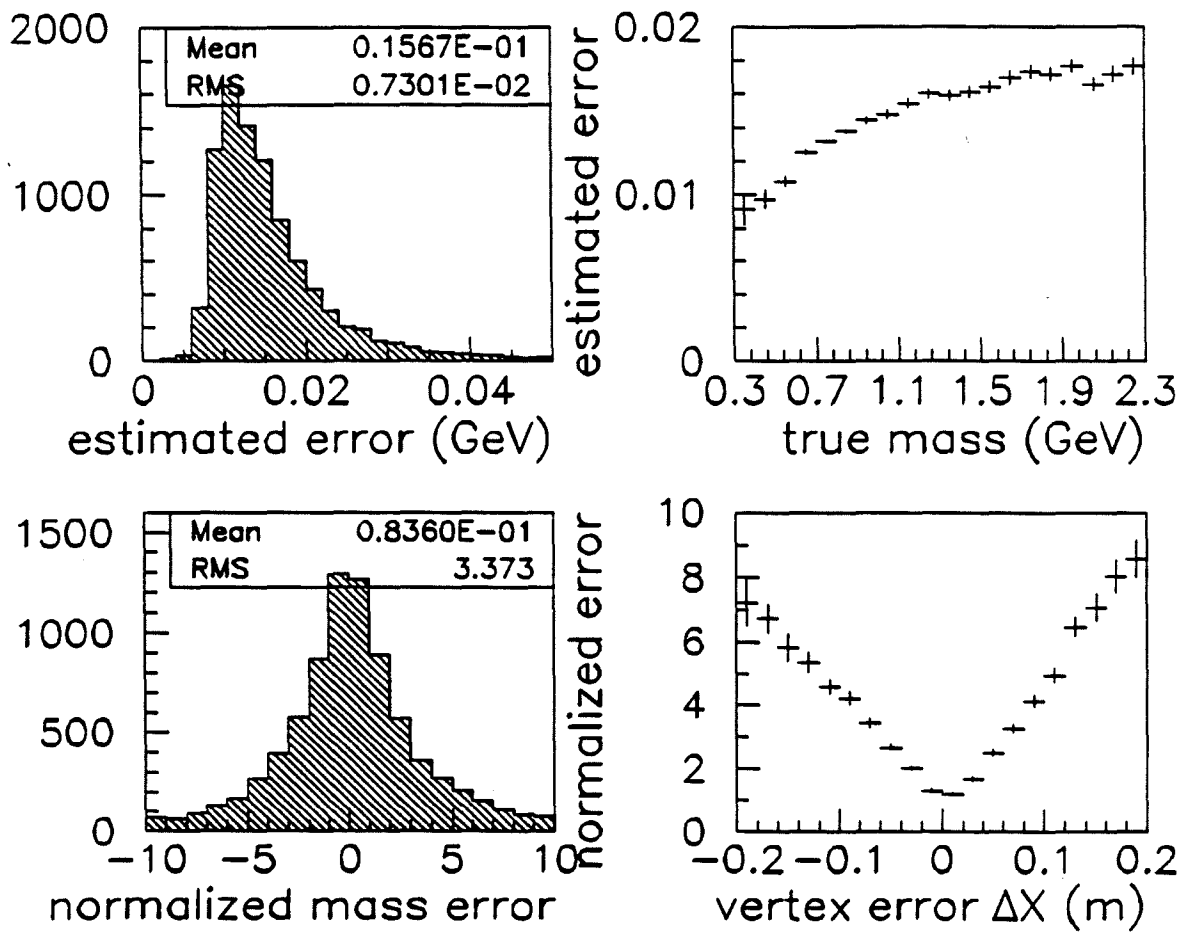
Figure 6.25: Estimated error on the mass. The first plot shows the distribution of σ_M, obtained from the track parameters. The second plot shows its variation with the true mass. The third plot shows the normalized error, and the last plot shows the variation of the normalized error on the actual vertex error, ΔX.

$M_{true} < 0.6$ GeV
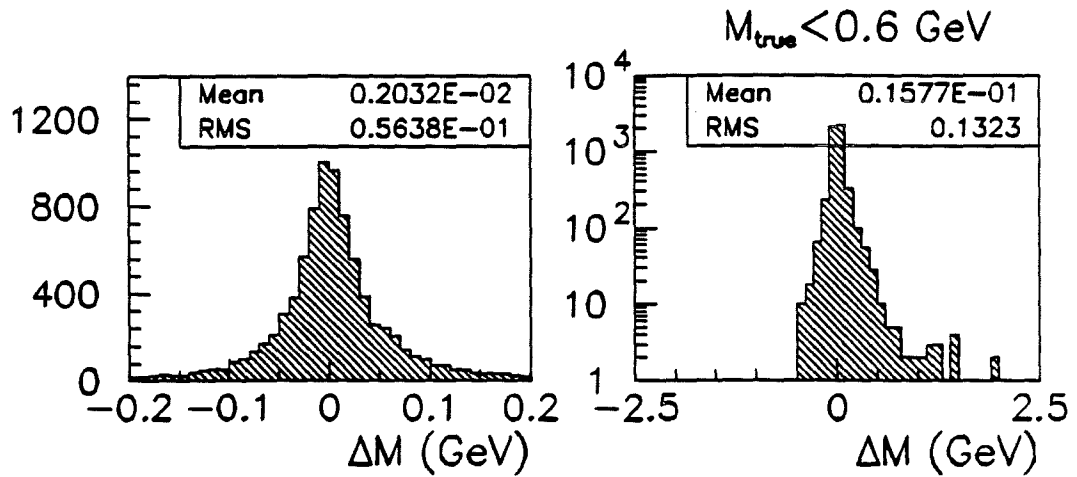
Figure 6.26: Actual errors on the mass. The first plot shows the central peak at zero. The second shows that the mass errors are abruptly cut off due to the absolute lower bound, $M_{meas} > M_{min}$.

figure 6.28. The mean rms error is 35 MeV, which is 4.7% of the ρ^0 mass (770 MeV). This value is about twice the mean estimated error, shown in figure 6.25.

There are two significant components in the relation between M_{meas} and M_{true}:

1. $M_{meas} \approx M_{true}$

2. $M_{meas} \approx M_{peak} \approx 0.75$ GeV

The first component is desirable: it allows a measurement of the true mass distribution, in principle. The second component is undesirable: it amounts to a "fallout" of "shadow" from the resonance peak to other values of the mass. (Of course, the shadow is larger closer to the peak than farther.) This structure is illustrated in figure 6.29a, and in figure 6.30.

A useful presentation of the mass smearing is shown in figure 6.29b, in which the actual error $\Delta M \equiv M_{meas} - M_{true}$ is plotted as a function of the measured (smeared) mass M_{meas}.[12] The double-axis structure still can be seen in this plot.

The implication is that a set of events with measured mass near 1 GeV consists of two subsets: those with true mass near 1 GeV (to within about 0.05 GeV), and those with true mass near the peak at 0.75 GeV. This structure is not easy

---

[12]This plot is the same as plot a), rotate by 45 degrees, and flipped about $\Delta M = 0$. Another representation is given in figure 6.31 on page 296.
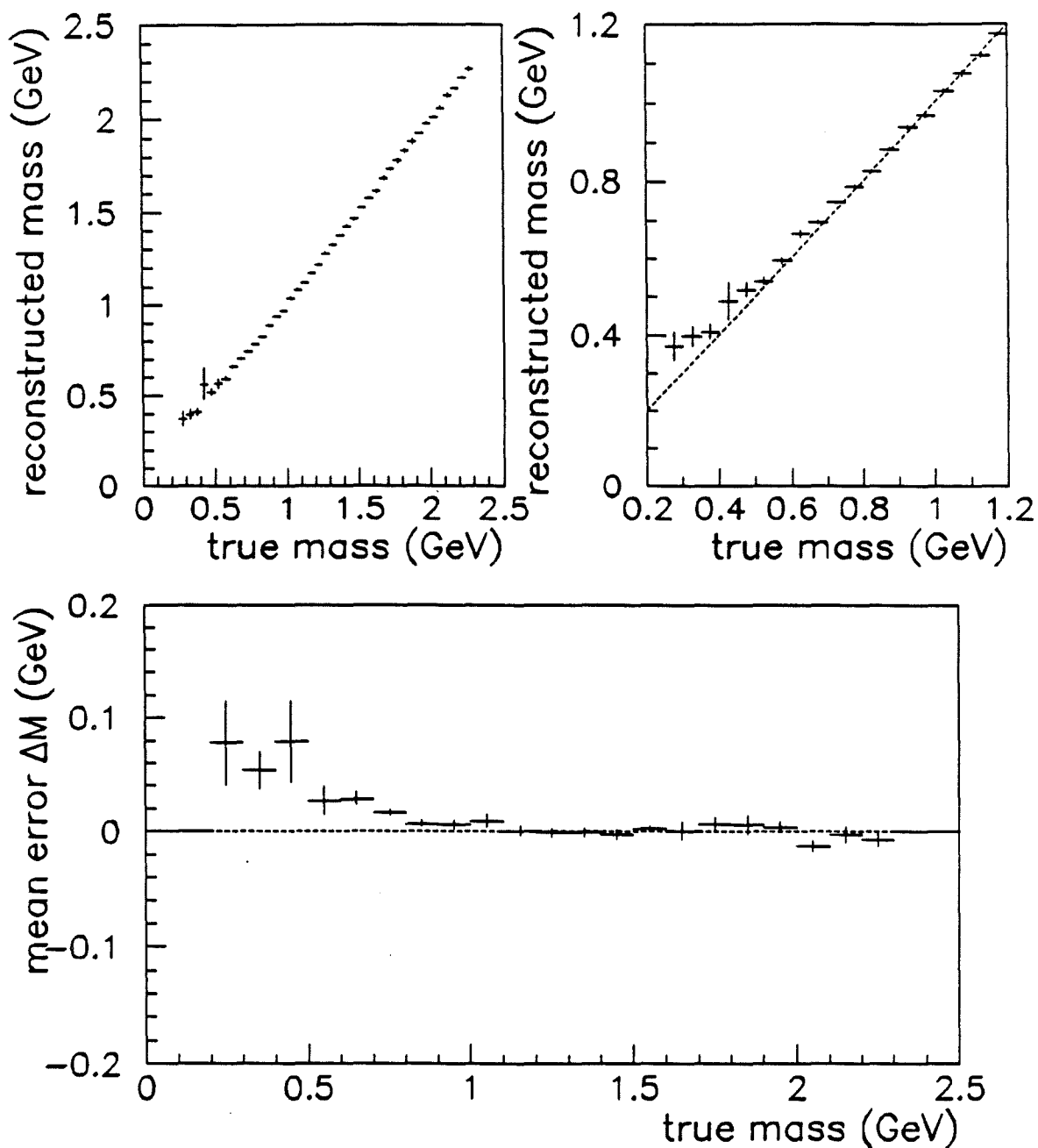
Figure 6.27: The first two plots show the mean reconstructed mass plotted versus the true mass. A small deviation is evident for $M_{\text{true}} < 0.8$ GeV. The third plot shows clearly an increase in the mean error as $M_{\text{true}} \rightarrow M_{\text{min}}$. Note that the typical mass resolution is less than 0.02 GeV, and the bin width is 0.1 GeV.
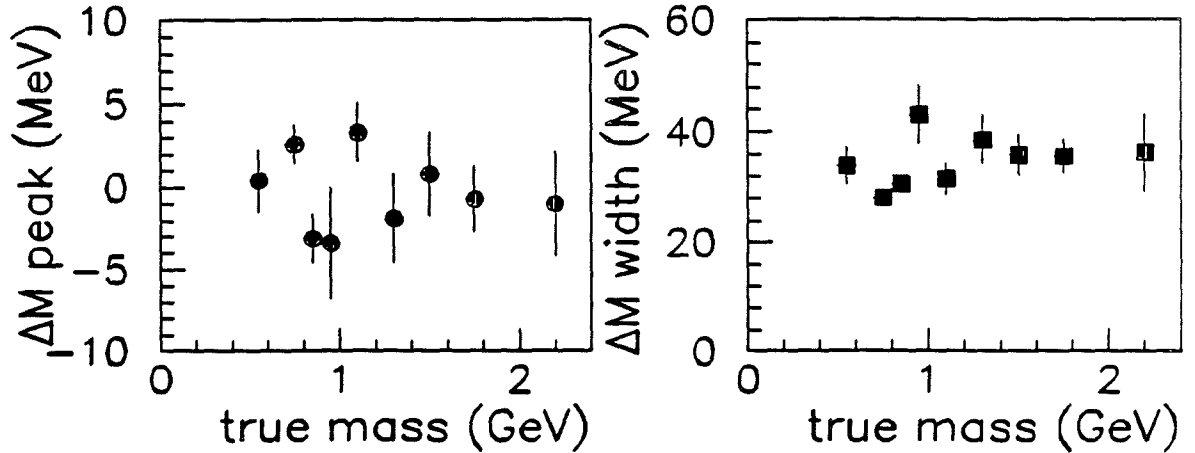
Figure 6.28: Peak actual mass error, mean (first plot), and rms (second plot), shown as a function of the true mass. The mean rms error is 34.8 MeV.

to disentangle, and it requires a lot of simulated data, in order to determined the precise relation between M_{meas} and M_{true}.[13] To this end, a "fast" Monte Carlo program was written, as an alternative to the "full" Monte Carlo.[14]

6.3.7 Fast Monte Carlo

As discussed in the previous section, the relation between the error on the mass and the reconstructed mass is not simple for two reasons:

1. The mass errors are significant, and are distributed asymmetrically. They extend from $\Delta M = -M_{true}$ to values as large as 5–10 GeV.

2. The true distribution is peaked at a value distinctly above threshold.

A plot of the actual mass errors $\Delta M = M_{meas} - M_{true}$ versus M_{meas} is shown in figure 6.31. The top plot shows the actual values, while the bottom plot shows the variation of the mean error versus the reconstructed value. The odd S-shaped curve is a result of the "shadow" of the peak in the true distribution; this shadow can be seen in the top plot in the figure along the line $\Delta M = M_{meas} - 0.77$ GeV. It would be absent if the true distribution were monotonic, and would be negligible if the resolution were better. Clearly the mean error depicted in the bottom plot tends

---

[13]Figures 6.29 and 6.30 were generated from 10^5 Monte Carlo events.

[14]Although not part of the original plan, this fast Monte Carlo allowed checks and studies of parameters that never would have been possible with the full Monte Carlo, based on Rhogen.
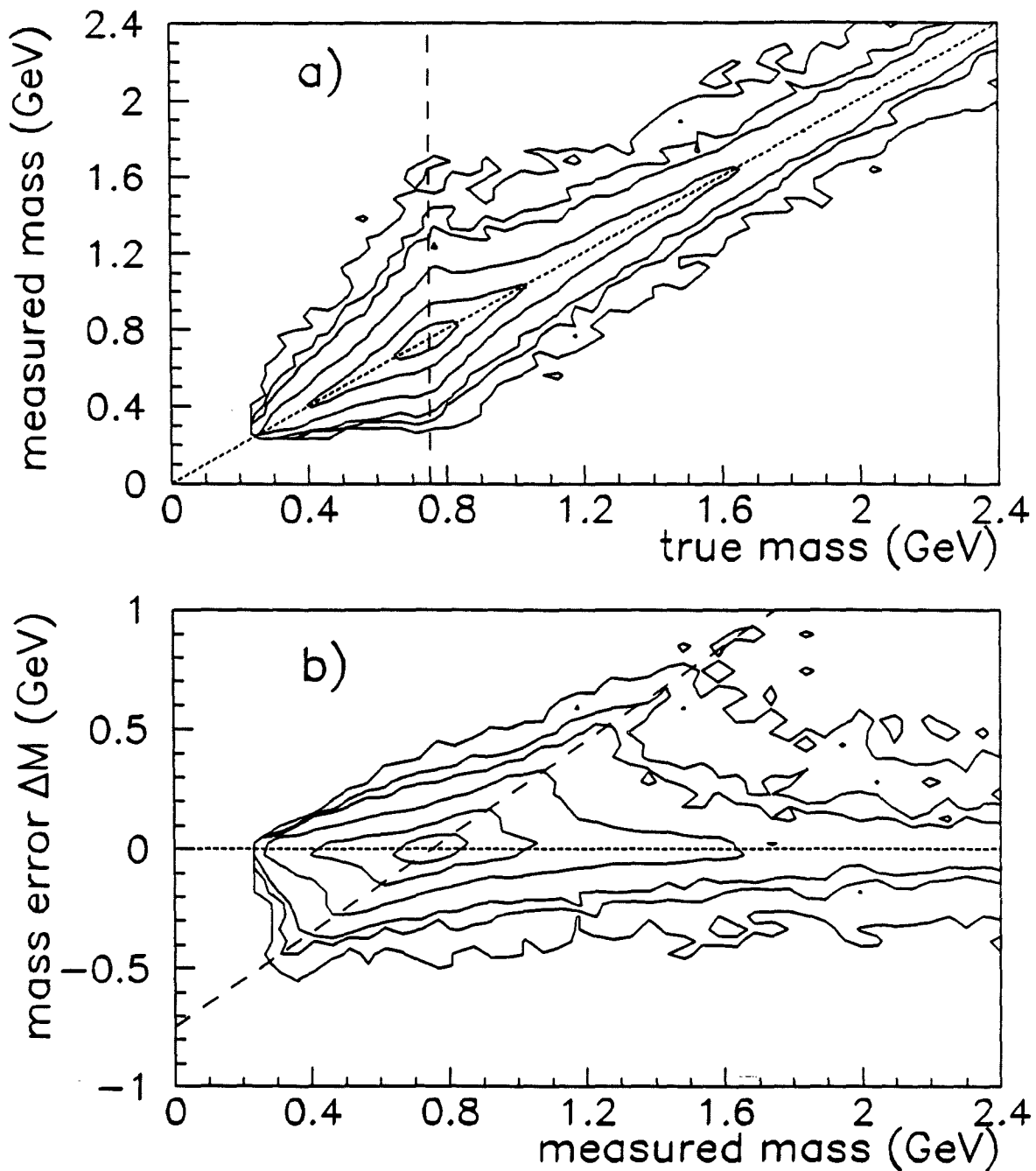
Figure 6.29: Mass measurement errors, showing (approximate) logarithmic contours. Plot a) shows the shape of the distribution of M_{meas} versus M_{true}. Plot b) shows the actual error $\Delta M = M_{meas} - M_{true}$ versus M_{meas}. The dotted line indicates the events reconstructed with little error, and the dashed line indicates the "shadow" of the true resonance peak.
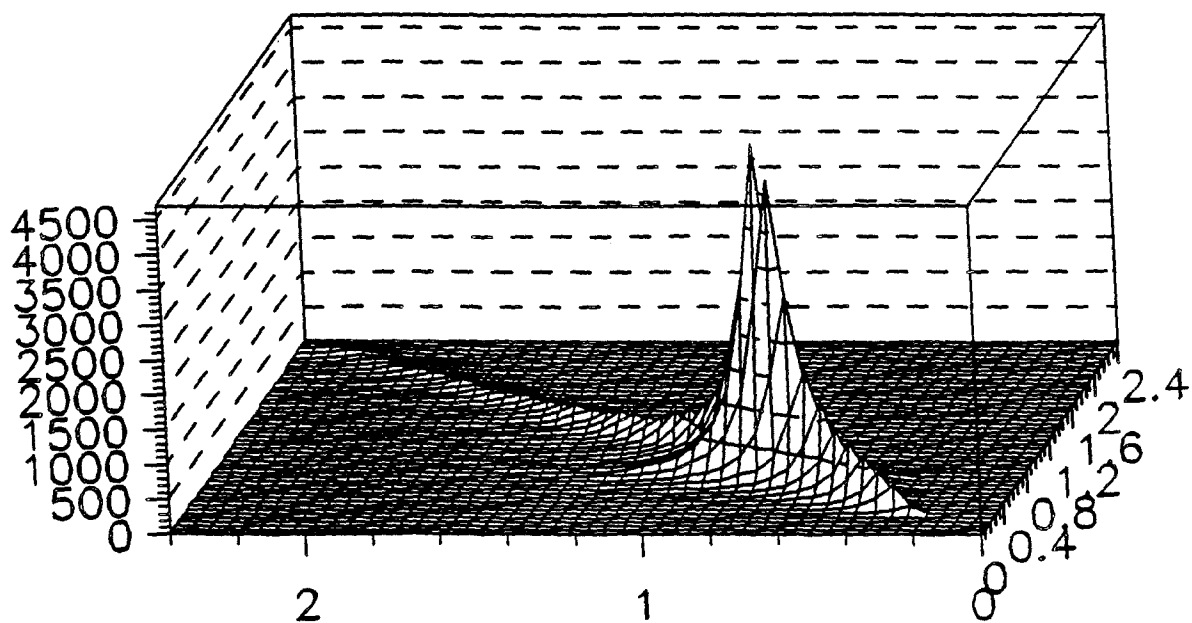
Figure 6.30: Another representation of the mass measurement error; figure 6.29a plotted in three dimensions. The long tail corresponds to the diagonal dotted line in the other plot, the short tail is the "fallout" from the mass peak.

to make the mass peak wider than it "should be." The effect is quite significant: if the binning is 0.1 GeV, then some bins are shifted in effect by one bin width! (Also, recall that the nominal ρ^0 resonance width is 153 MeV.)

The problem is to reconstruct the true mass distribution, given a measured distribution and some knowledge of the distortions of the true mass distribution by errors. If the true distribution is represented by function $F(M_{true})$, the measured distribution by $G(M_{meas})$, and the probability of measuring M_{meas} when the true value is M_{true} by $K(M_{meas}, M_{true})$, then

$$F(M_{meas}) = \int dM_{true}\ G(M_{true})\ K(M_{meas}, M_{true}).$$

This convolution is a particular type of Fredholm equation, and often is studied in the context of linear integral equations.[15] Experiment provides $F(M_{meas})$, and Monte Carlo can be used to estimate $K(M_{meas}, M_{true})$. The goal is to determine $G(M_{true})$.

The basic features of the kernel $K(M_{meas}, M_{true})$ can be seen in figure 6.31. There is a peaked distribution at $M_{meas} = M_{true}$, with long tails extending to large values of $\Delta M = M_{meas} - M_{true}$. The tail is truncated at negative values of ΔM, but there is no real limit for large values of ΔM. The central peak is easy to handle, but the long, asymmetric tail causes problems. For the purposes of unfolding, it must be well-determined, otherwise the statistical fluctuations in the measured spectrum can be amplified beyond manageable levels.

It is not possible to generate enough simulated events using the full Monte Carlo (Rhogen) to determine these tails, due to the limited cpu resources and time available. The events obtained, however, are enough to allow empirical determination of the errors on the tracks, expressed in terms of fitted parametrizations. It has been shown that the simulated data match the real data in most respects reasonably well; for the purposes of understanding the mass smearing, the kernel $K(M_{meas}, M_{true})$ can be determined by propagating the empirical errors on the pion tracks to the invariant mass.

A simple Monte Carlo program is used to perform the error propagation. The true mass distribution and a given decay distribution are generated randomly, and boosted into the lab frame using the observed distribution for the ρ^0 energy. The pion momenta and track angles are calculated, and smeared according to empirical parametrizations. The smeared mass is calculated, and correlated with the true mass.[16] This "fast" Monte Carlo can generate a million (M_{meas}, M_{true}) pairs in

---

[15] The Fredholm equation is discussed in [Ryan, Salvarani].

[16] This technique is tantamount to performing the convolution integral using "Monte Carlo Integration."
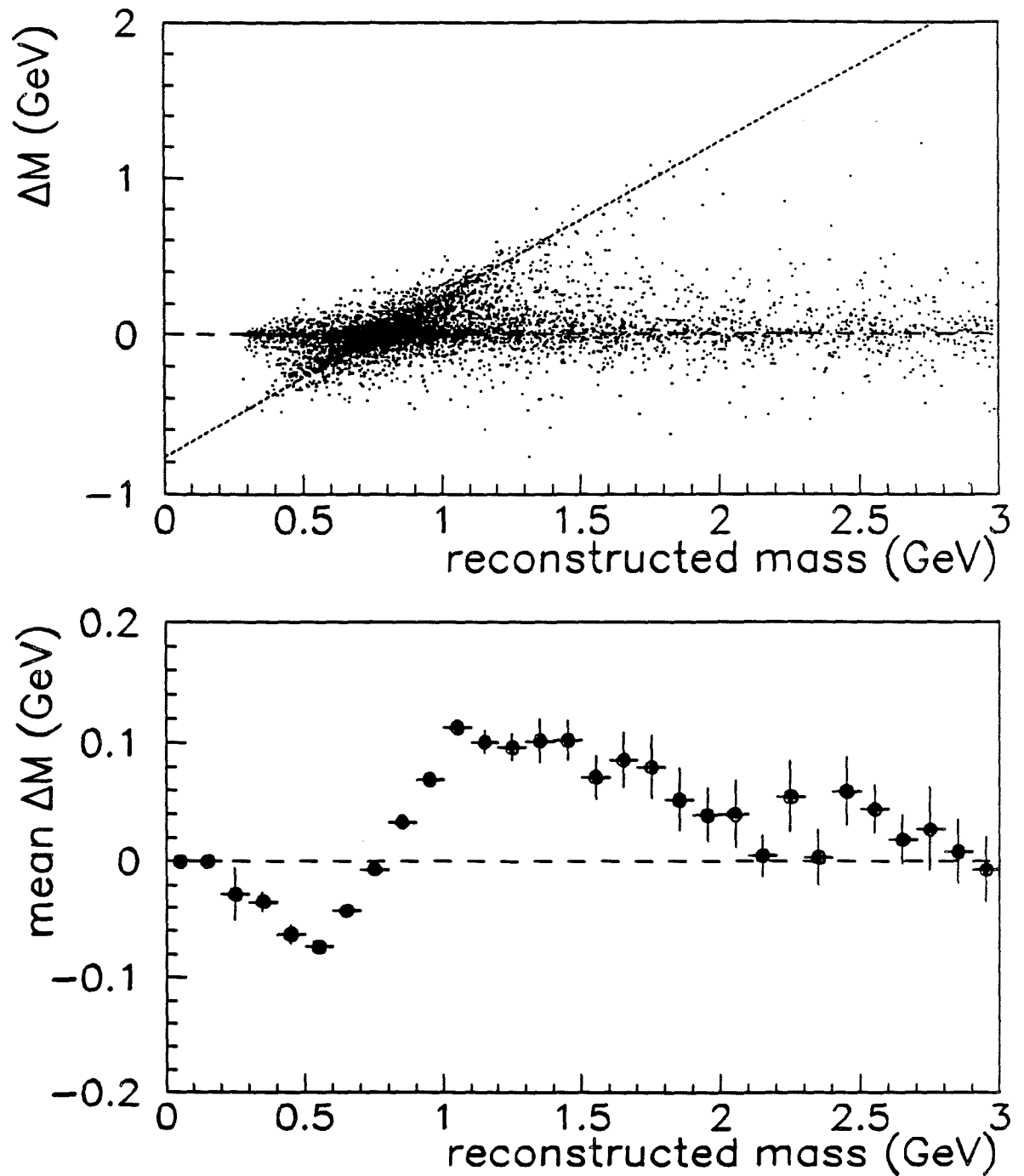
Figure 6.31: Two plots illustrating the effect of non-negligible mass errors. The top plot shows the actual values (M_{true}, M_{meas}), with the slanted line indicating the "shadow" of the mass peak. The bottom plot shows that the mean error varies significantly as a function of reconstructed mass.
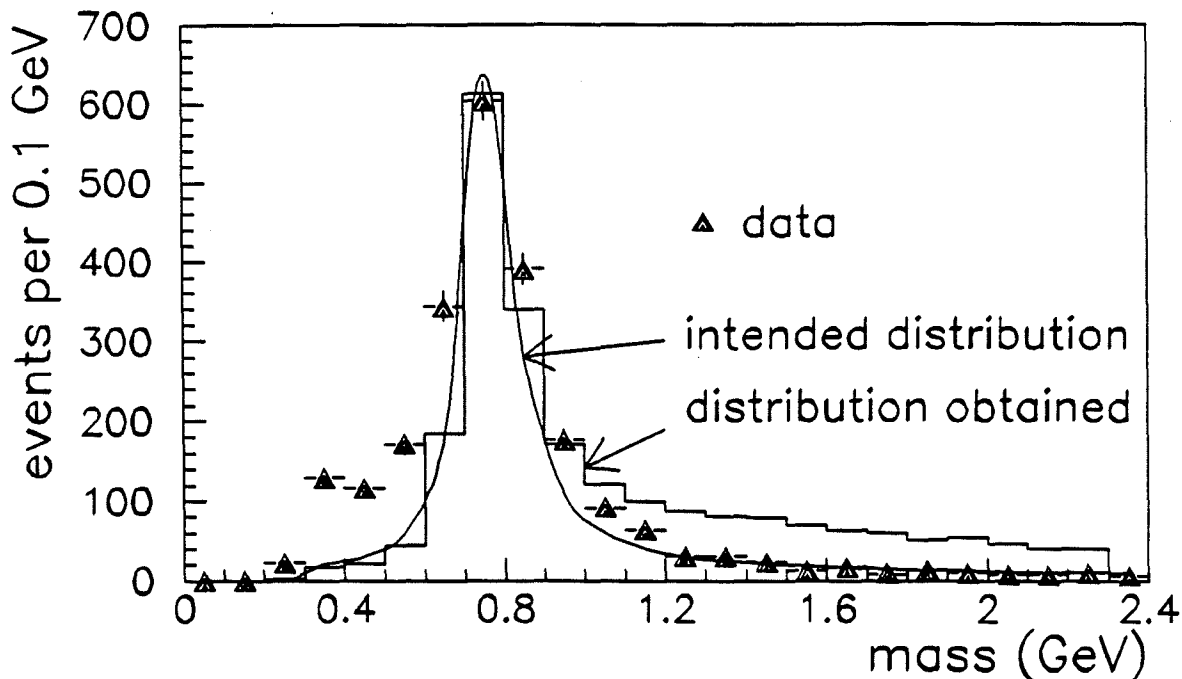
Figure 6.32: Erroneous Monte Carlo mass distribution. The smooth curve indicates the intended shape of the true mass distribution, and the histogram shows the distribution actually obtained. There is a clear excess at high values of the mass. The points represent real data.

four hours on the Vax; the original "full" Monte Carlo required weeks of running on the Amdahl to generate forty thousand events.

In fact there was an error in Rhogen which caused a significant distortion of the mass and kinematic distributions, as illustrated in figure 6.32. Although the software bug was found and could be fixed easily, it was not possible to regenerate the events using the full Monte Carlo. The effect of the bug, however, was studied using the fast Monte Carlo, first with the distorted mass distribution, then with the correct mass distribution. This is illustrated in figure 6.39.

Several empirical distributions are required as a priori input for the fast Monte Carlo:

1. ρ^0 *energy.* The Lorentz boost from the ρ^0 center-of-mass to the lab frame is a function of the $E_\rho \approx \nu$. The distributions from LAT and SAT data are shown in figure 6.33, and are represented by the parametrizations:
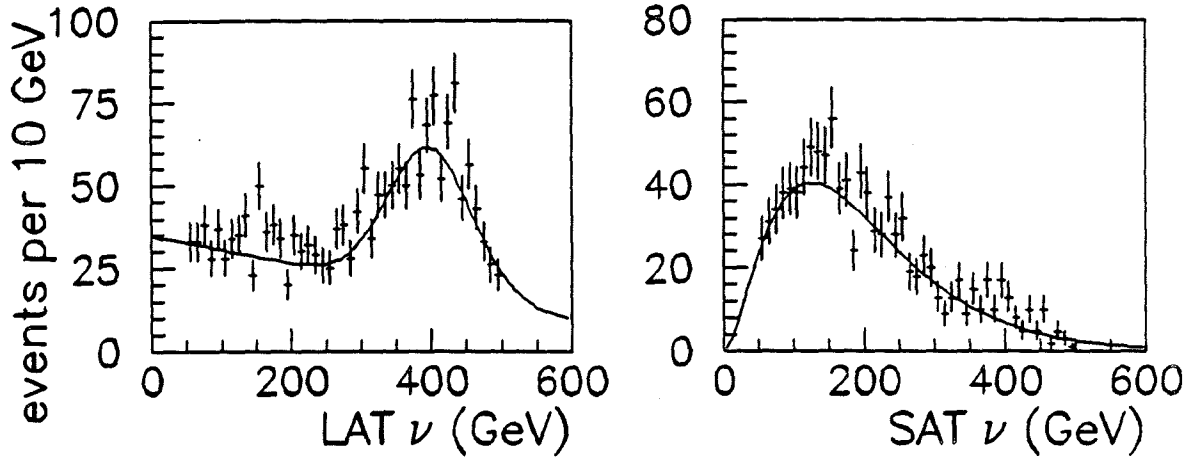
Figure 6.33: Energy distribution of ρ^0 events, from real LAT and SAT data. The smooth curves indicate the empirical parametrization used to represent the ρ^0 energy in the fast Monte Carlo.

- LAT

$$\frac{dN}{d\nu} = A + B\nu + C\exp\left[-\frac{1}{2}\left(\frac{\nu - \mu}{\sigma}\right)^2\right],$$

with $A = 34.8\pm2.8$, $B = (-4.2\pm1.7)\times10^{-2}$, $C = 43.2\pm4.8$, $\mu = 398\pm4$, and $\sigma = 60.0 \pm 7.3$.

- SAT

$$\frac{dN}{d\nu} = A\nu^B \exp(-C\nu),$$

with $A = (5.8\pm2.1)\times10^{-2}$, $B = 1.71\pm0.09$, and $C = (1.37\pm0.06)\times10^{-2}$.

2. *vertex error.* The lurking variable ΔX is a source of significant error, as discussed in previous sections. It can be described by an exponential function:

$$\frac{dN}{d\Delta X} = A\exp(-\lambda|\Delta X|),$$

with $\lambda = 12.6 \pm 0.03$ m^{-1} for both LAT and SAT data.

3. *momentum resolution.* A fit to $\sigma_{1/P}$ versus $1/P$ was made using the quadratic form ($S \equiv 1/P$, in GeV):

$$\sigma_S = a + bS + cS^2,$$

with the result $a = (57.4 \pm 0.9) \times 10^{-6}$, $b = (0.29 \pm 0.10) \times 10^{-3}$, and $c = (20.5 \pm 2.3) \times 10^{-3}$. The fit for LAT and SAT data are the same, within errors.

4. *angular resolution.* Linear fits were performed to $\sigma_{y'}$ versus y' and $\sigma_{z'}$ versus z', with the result

- y': $a = (117 \pm 3) \times 10^{-6}$, $b = (7.0 \pm 0.4) \times 10^{-3}$,
- z': $a = (77 \pm 3) \times 10^{-6}$, $b = (13.7 \pm 0.6) \times 10^{-3}$.

The fit for SAT data was the same, within errors.

5. *rotation with ΔX.* For small enough displacements ΔX, the change on the horizontal slope $\delta y'$ is approximately linear:

$$\delta y' = \frac{P_T^{\mathrm{CVM}}}{P} \frac{\Delta X}{L^{\mathrm{CVM}}} \approx 0.01(\Delta X)$$

for $P \approx 50$ GeV. The positive and negative pions were fitted to linear functions of ΔX, with the result

- π^+: $a = (-68.2 \pm 13.2) \times 10^{-6}$, $b = (8.18 \pm 0.21) \times 10^{-3}$,
- π^-: $a = (+52.1 \pm 12.0) \times 10^{-6}$, $b = (-7.38 \pm 0.20) \times 10^{-3}$.

With a mean pion momentum of 97 GeV, this can be reexpressed as

$$\delta y' = q \left[a + \frac{B}{P}(\Delta X) \right],$$

with $a = -6 \times 10^{-5}$ and $B = 0.66$. The charge of the pion is $q = \pm 1$.

6. *reconstruction efficiency.* The full Monte Carlo shows that there is a loss of events at low values of the invariant mass, as shown in figure 6.34. These data can be fitted by the exponential function

$$\epsilon(M) = A + B \exp(-CM),$$

with the result

- LAT: $A = 0.345 \pm 0.004$, $B = -0.50 \pm 0.12$, $C = 4.1 \pm 0.5$;
- SAT: $A = 0.330 \pm 0.009$, $B = -0.16 \pm 0.09$, $C = 3.0 \pm 0.9$.

7. *decay distribution.* Based on earlier analyses of the exclusive ρ^0 events in the E665 data, a predominantly transverse polarization was chosen to represent the real data. Writing

$$W(X) = \frac{3}{4} \left[(1 - r) + (3r - 1)X^2 \right],$$

with $X \equiv \cos\theta$, and $0 < r < 1$: pure transverse polarization corresponds to $r = 0$, while longitudinal polarization is given by $r = 1$. The shape of $W(X)$ for different values of r is shown in figure 6.35. The value $r = 0.25$ was chosen somewhat arbitrarily; with this value the momentum spectrum of the pions matches the real data quite well, as shown in figure 6.36.

reconstruction efficiency
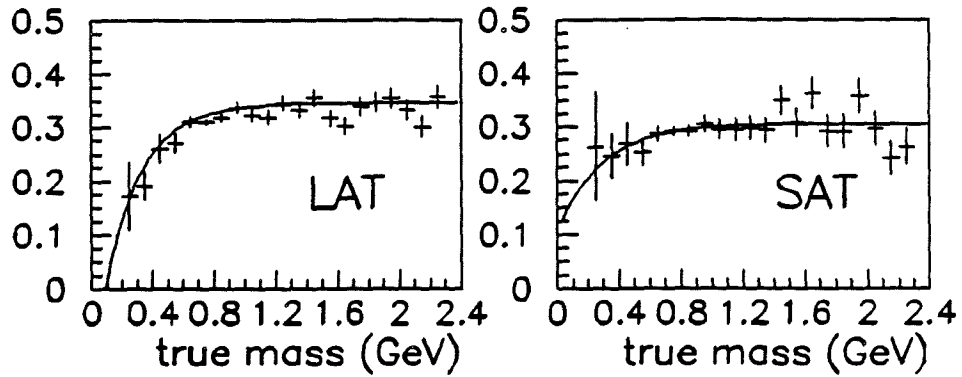
Figure 6.34: Reconstruction efficiency for LAT and SAT ρ^0 events, as determined from the full Monte Carlo. The curves illustrate the parametrization used in the fast Monte Carlo.
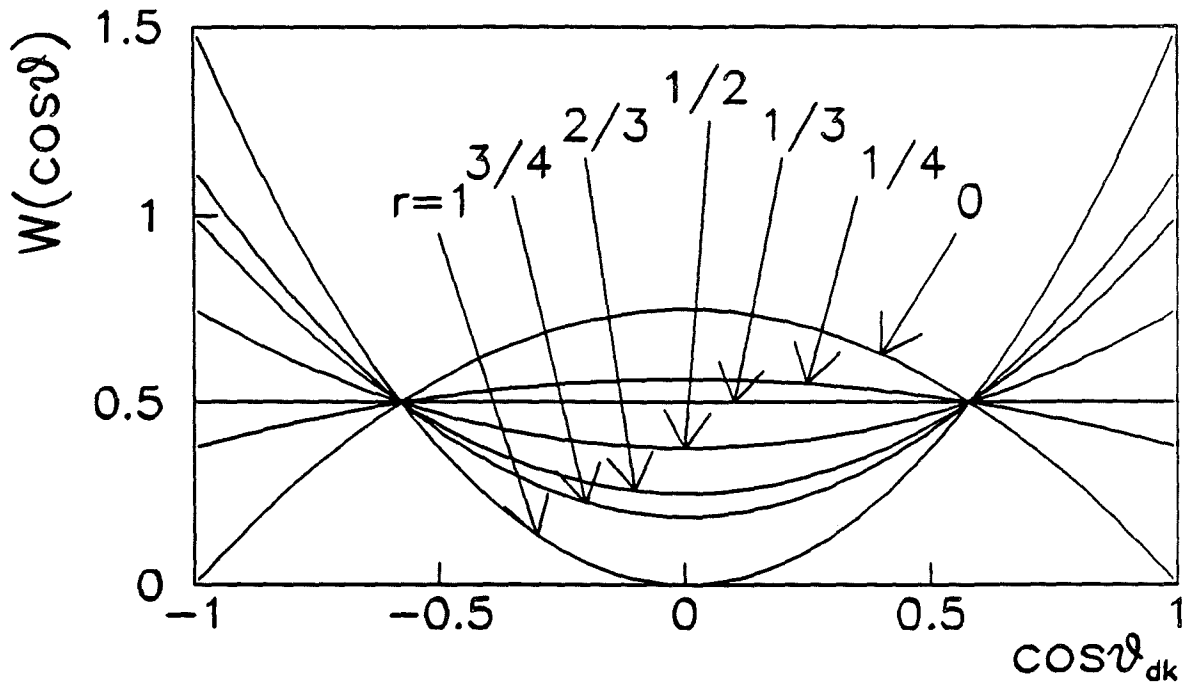

Figure 6.35: The shape of the decay distribution function $W(\cos\theta)$ varies as a function of the parameter r. $r = 0$ corresponds to transverse polarization, and $r = 1$, to longitudinal.

A few plots showing the validity (and the limits) of the fast Monte Carlo are necessary. Figure 6.36 shows the observed momentum and angle distributions and those generated by the fast Monte Carlo, for LAT and SAT data. The agreement is quite good, though there are slight differences in detail. Figure 6.37 shows the distributions for ΔM, comparing the fast Monte Carlo (histogram) to the full Monte Carlo (open points). Again, the agreement is good.

The main concern is the mass smearing. The results for the full Monte Carlo and fast Monte Carlo are shown in figure 6.38. In this case, the fast Monte Carlo employed the same *incorrect* mass distribution obtained in the full Monte Carlo. The two can be distinguished primarily by the fact that the statistical precision of the fast Monte Carlo is far greater than that of the full Monte Carlo.

Figure 6.39 compares the mass smearing, as represented by a plot of $\langle\Delta M\rangle$ versus M_{meas}, for the wrong mass distribution depicted in figure 6.32, and the correct mass distribution. It is clear that the bug is significant: the mean error at $M_{meas} \sim 1$ GeV is twice as large when the correct distribution is used as when it is not. This can be understood as a delicate balance between the "shadow" of the true mass peak across the reconstructed mass spectrum (see figure 6.31 on page 296), and the tail above the peak, reconstructed at approximately the correct value.

The sensitivity of the correction to the decay distribution is shown in figure 6.40. The three curves represent $\langle\Delta M\rangle$ plotted against M_{meas}, for three parameter values $r = 0$, 1/2, and 1. The difference is small, quite negligible in the neighborhood of the peak. This is true because the long tails of the ΔM distribution arise primarily from the ΔX distribution, and not from the details of the momentum and angular resolution.

This fast Monte Carlo is used to determine the relation between observed and true mass values, under the primary assumption that the true mass distribution is reasonably close to the relativistic Breit-Wigner shown in figure 6.32.

An attempt to unsmear the data is described in a later section. First, two cuts applied to the data must be described.

6.3.8 ϕ Meson Cut

There is a small bump near threshold for the data displayed in figure 6.32, not modelled by either Monte Carlo. These events are the "reflection" of the ϕ meson,
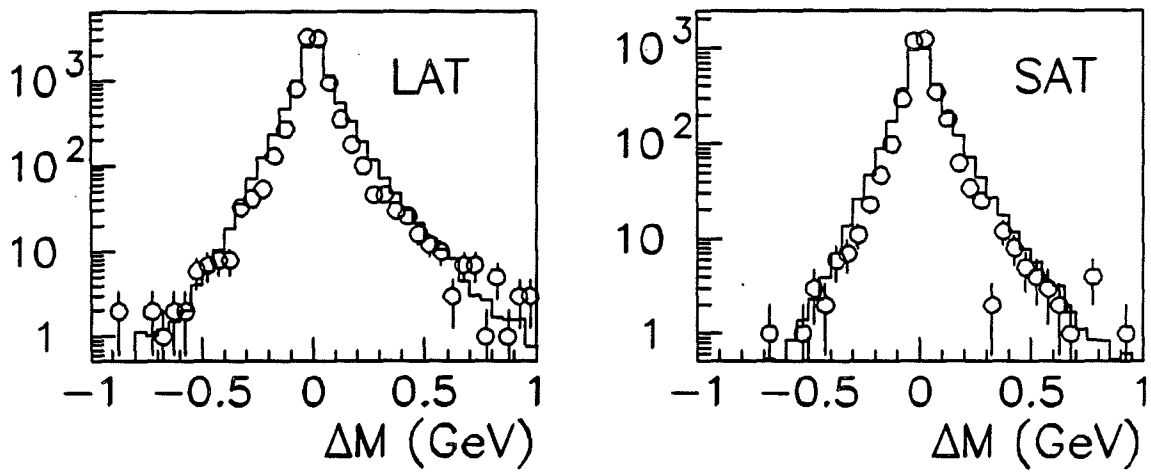
Figure 6.37: Comparison of fast and full Monte Carlo ΔM distributions, for LAT and SAT data.
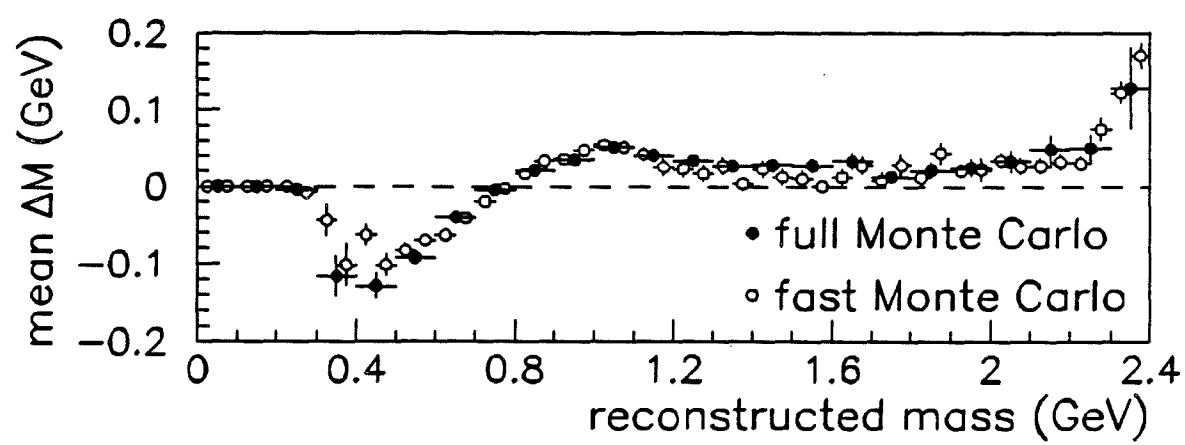

Figure 6.38: Comparison of the mean mass error plotted versus the reconstructed mass, as obtained from the full and the fast Monte Carlos.
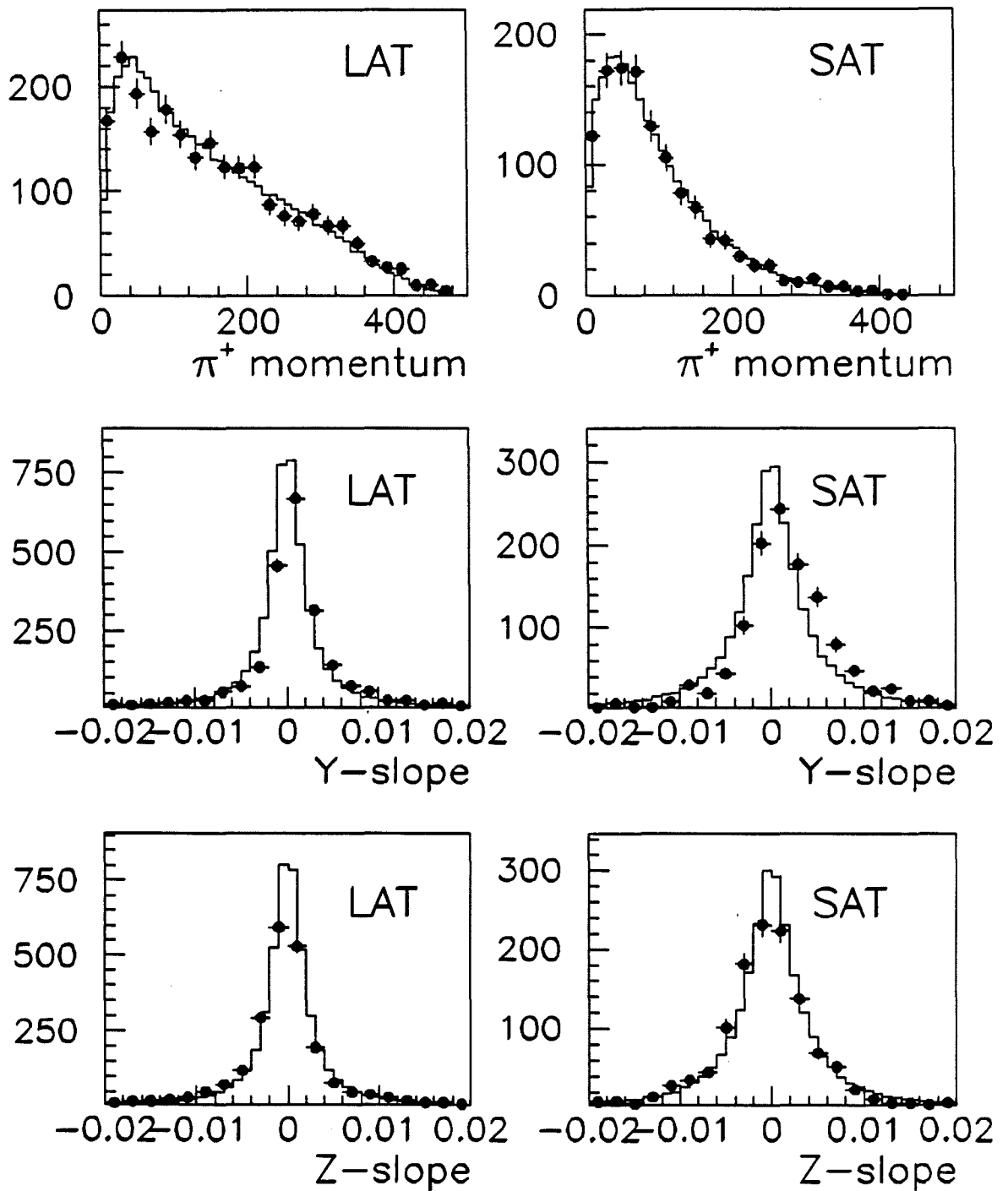
Figure 6.36: A comparison of the track distributions obtained from the fast Monte Carlo, and real data.
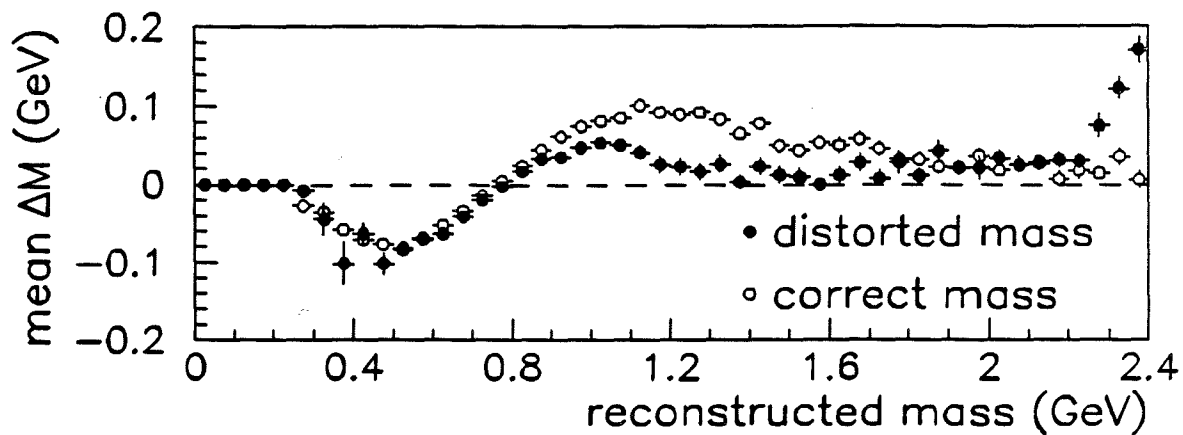
Figure 6.39: Comparison of the mean mass error, plotted versus the reconstructed mass, for the correct and the incorrect mass distributions.
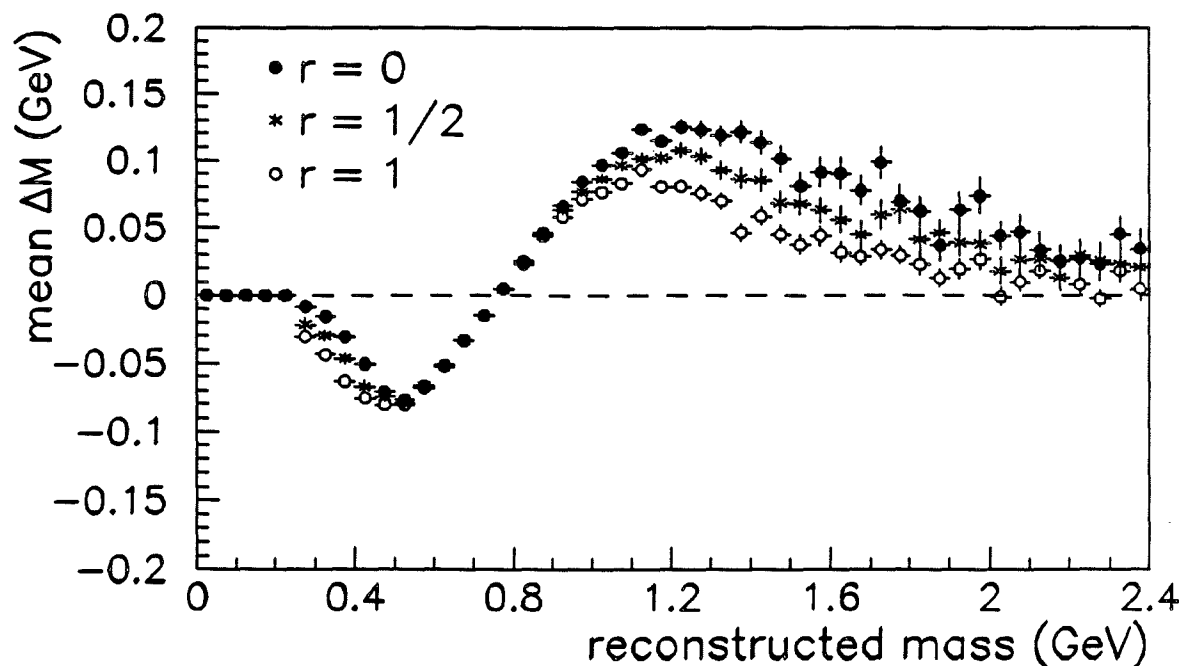

Figure 6.40: The mean mass error plotted versus the reconstructed mass, as obtained from the fast Monte Carlo, for three values of the decay parameter r.
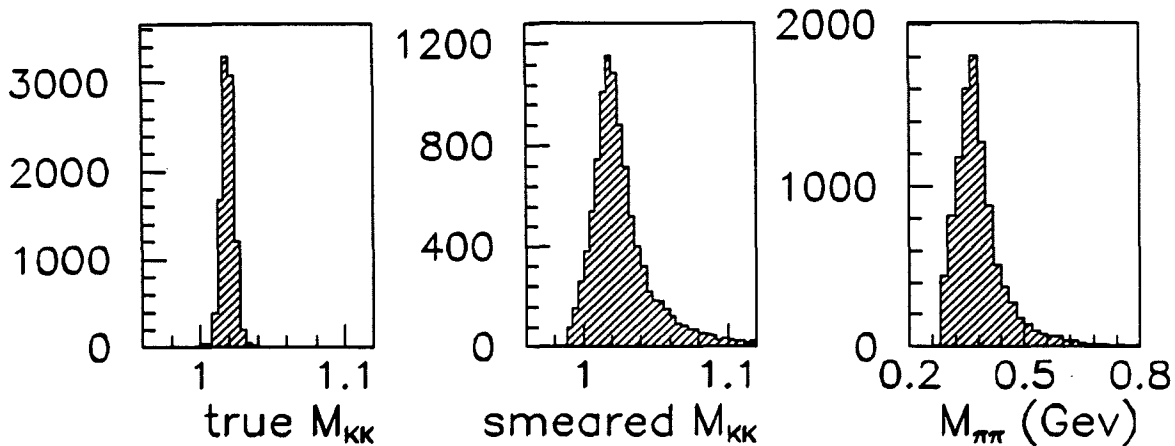
Figure 6.41: Fast Monte Carlo Simulation of the ϕ mass distribution. The first plot shows the true mass distribution, and the second shows the mass distribution after smearing. The third plot shows the reflection of the smeared ϕ events in the two-pion invariant mass spectrum.

which decays into a charged kaon pair half of the time. Since it is not possible to separate pions and kaons for this analysis, the ϕ decays can be excluded only by a mass cut: the invariant mass of the two hadron tracks is calculated, assuming the hadrons to be kaons. If the mass is consistent with the ϕ mass, then the event is discarded.

These considerations are illustrated in figure 6.41. Events were generated using a version of the fast Monte Carlo based on empirical distributions acquired for the ρ^0 simulation. The true mass was described by a gaussian, and the decay products were kaons. The first plot shows the true mass distribution, and the second plot shows the mass calculated from the smeared kaon tracks quantities. The third plot shows the reflection of the ϕ peak in the two-pion invariant mass spectrum: the invariant mass of these events was calculated assuming the hadrons to be pions. Most of the events fall between threshold at $2m_\pi = 0.279$ GeV, and 0.5 GeV. They do not pose a difficult background to remove; the ϕ production rate is much smaller than the ρ^0 rate, so the number of ϕ decays falling under the ρ^0 peak is negligible.

To eliminate possible ϕ events, a simple mass cut is applied: all ρ^0 events must satisfy

$$M_{KK} > 1.06 \text{ GeV},$$

where M_{KK} is the invariant mass of the hadron tracks assuming them to be kaons. The effect of this cut on the two-pion invariant mass spectrum is shown in figure 6.42. As expected, the spectrum above $M_{\pi\pi} \sim 0.6$ GeV is unaffected, but the
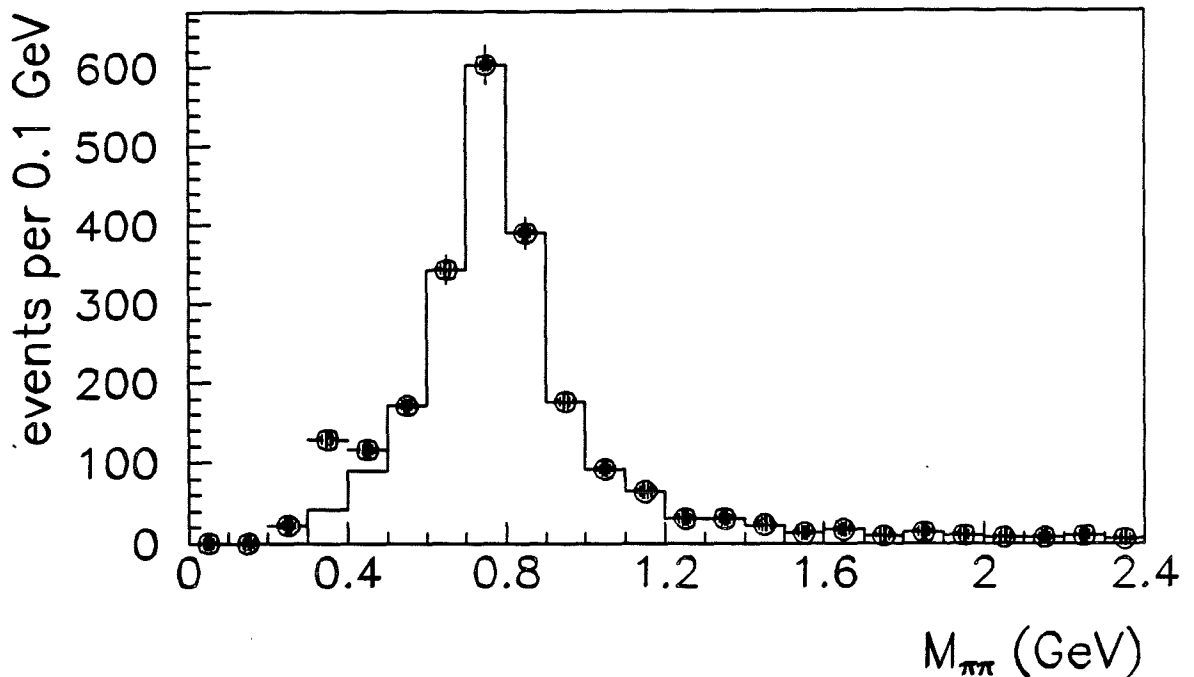
Figure 6.42: The effect of the ϕ cut can be seen in the region of 0.3–0.5 GeV. The bump near threshold is removed by this cut.

bump at $M_{\pi\pi} \sim 0.4$ GeV is eliminated. The cut applied to the real data removes 5.9% of the events.

The ϕ reflection can be mimicked using the fast Monte Carlo data. Figure 6.43 shows the $M_{\pi\pi}$ spectrum obtained for ρ^0 decays with a 5% admixture of ϕ decays. This spectrum closely resembles the data.

The ϕ cut removes some legitimate ρ^0 events. Applying this cut to the fast Monte Carlo data, the loss is plotted as a function of the smeared mass in figure 6.44.

6.3.9 Electron Cut

The separation of electrons and hadrons was discussed in the calorimeter chapter. The cuts listed in table 4.7 (page 159) are used to differentiate electrons and hadrons. The effect of possible electrons from photon conversions would appear at low mass values, because the opening angle between the electrons would be very
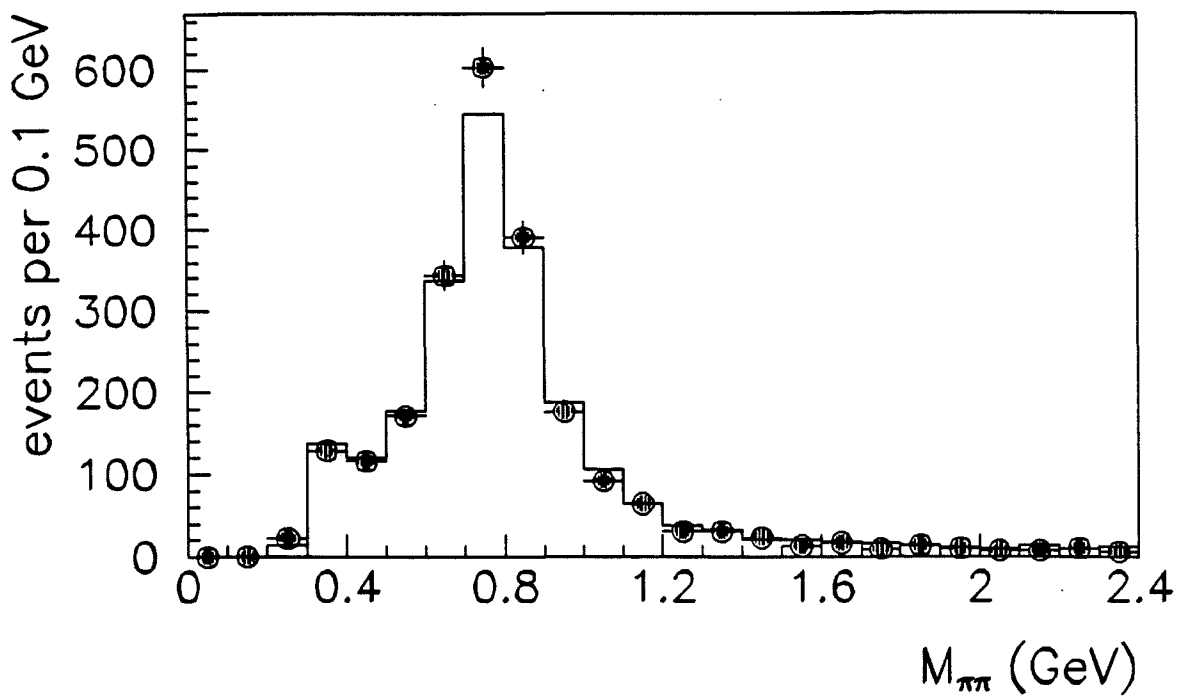
Figure 6.43: Comparison between a combination of ρ^0 and ϕ fast Monte Carlo data, and real data.
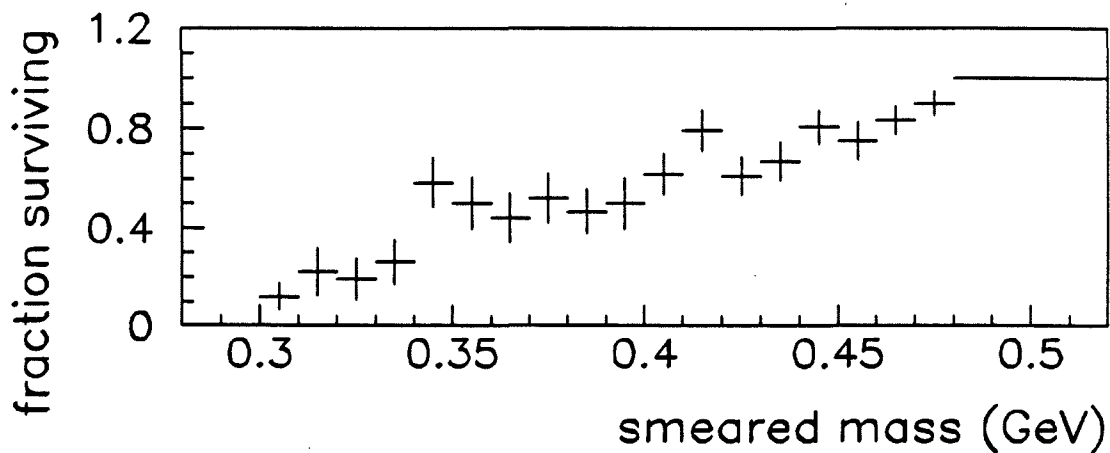

Figure 6.44: Events surviving the ϕ cut, according to the fast Monte Carlo simulation, plotted as a function of the smeared two-pion mass.
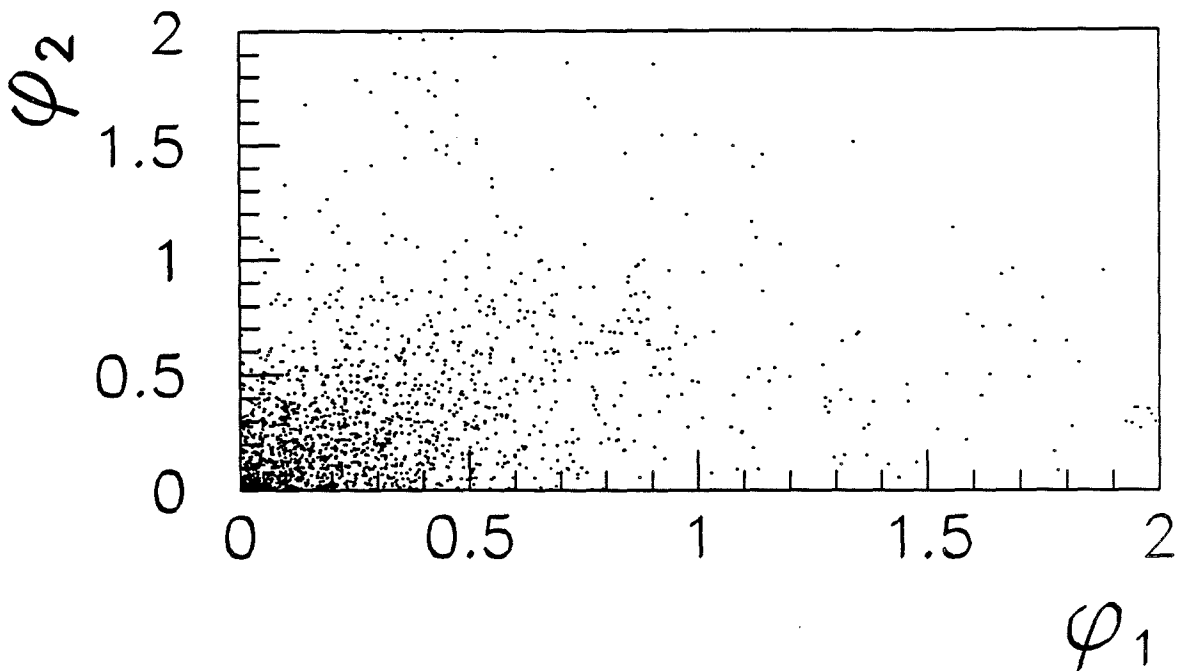
Figure 6.45: The values for (ϕ_1, ϕ_2) for the two "hadron" tracks in the exclusive ρ^0 events. ($\phi = E_{sh}/P_{tr}$.)

small: $M^2 \approx 2m^2 + E_1 E_2 \theta^2$.

The most powerful indicator of an electron shower is the ratio of the shower energy to the track momentum: $\phi_i = E_i/P_i$ ("1" $\Rightarrow \pi^+$, "2" $\Rightarrow \pi^-$). Electrons from a photon conversion will show large values of ϕ_i. Figure 6.45 shows the values of the pair (ϕ_1, ϕ_2) for the exclusive ρ^0 events passing the cuts described previously. There is no indication of an enhancement near $(\phi_1, \phi_2) = (1,1)$ – in fact, no indication of any correlation between ϕ_1 and ϕ_2 at all. Nonetheless, an "electron cut" is easily defined, to exclude electrons:

$$\phi_1 < 0.7 \quad \text{and} \quad \phi_2 < 0.7.$$

The distribution of ϕ_2 is shown in figure 6.46, and the π^- momentum distribution, also. There is no sign of any momentum bias for this cut. The electron cut removes 21% of the events.

Figure 6.47 shows the distribution of the two-pion invariant mass before (solid circles) and after the electron cut (open circles). The former has been normalized
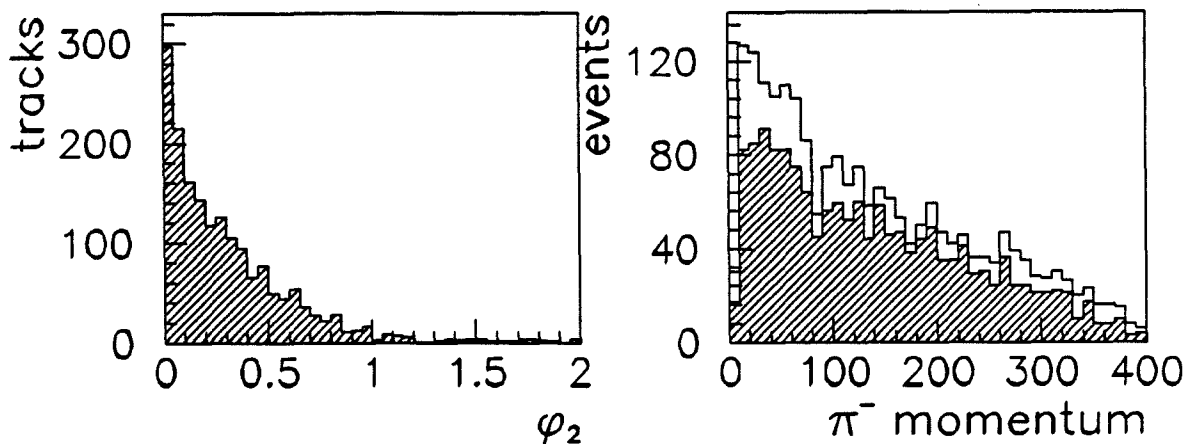
Figure 6.46: The first plot shows ϕ_2. The electron cut excludes events with $\phi > 0.7$. The second plot shows the π^- momentum before (open histogram) and after (shaded histogram) the electron cut.

to the latter. The electron cut removes events at low values of the invariant mass.

6.3.10 Mass Background

The exclusive ρ^0s must be selected from a large sample of ordinary inelastic events. The resolution of the pion momenta is good enough to resolve a sharp peak at $Z_{\mathrm{pair}} = 1$, but is not good enough to reduce the background under the peak to a negligible level. (See figure 6.15 on page 272.) The mass spectrum contains a contribution from these events which certainly is nonresonant, but also is not flat.

Events from the interval $0.5 < Z_{\mathrm{pair}} < 0.7$ were selected from the data to represent the background. All other cuts were the same. The resulting distribution is shown in figure 6.48a, with a curve representing a fit to the function

$$\frac{dN}{dM} = A\,(M - 2m_\pi)^B\,\exp(-C(M - 2m_\pi)).$$

The values of the parameters from the fit are $B = 1.44 \pm 0.09$ and $C = 3.94 \pm 0.20$.

For comparison, the mass spectrum from events simulated using the Lund Monte Carlo program which passed all exclusive ρ^0 cuts, including the cut $0.9 < Z_{\mathrm{pair}} < 1.1$, is shown in figure 6.48b. The real data are shown also, normalized to the Lund events. The shapes are quite similar. For this analysis, the background
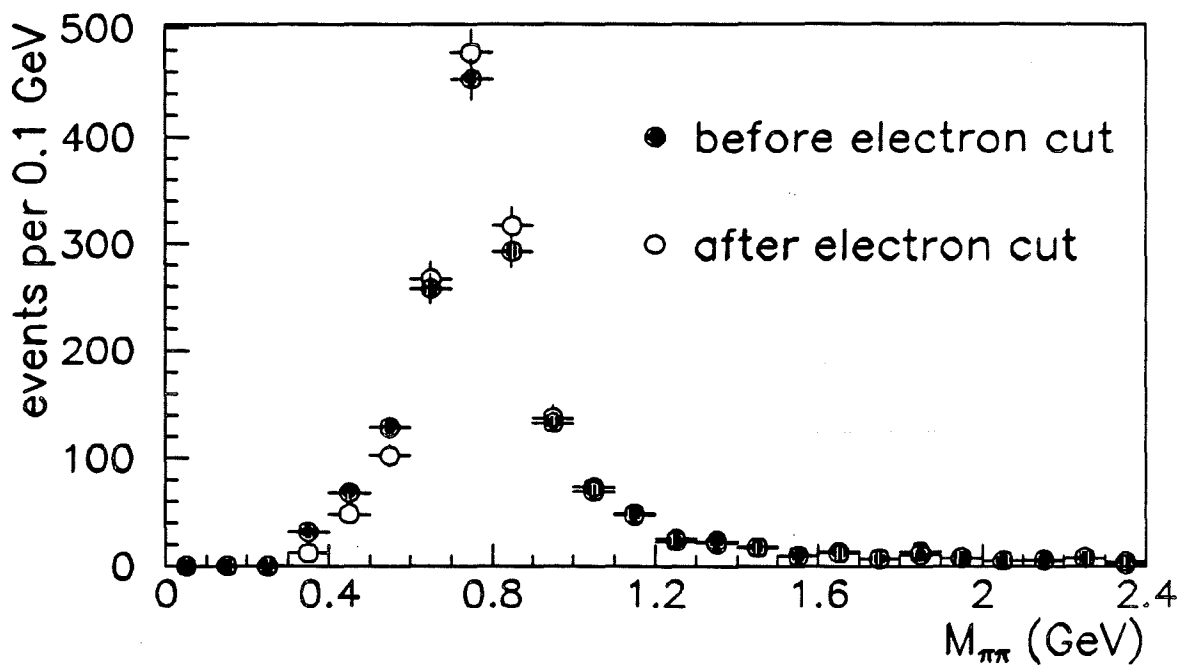
Figure 6.47: A comparison of the shape of the two-pion invariant mass distribution, before and after the electron cut.
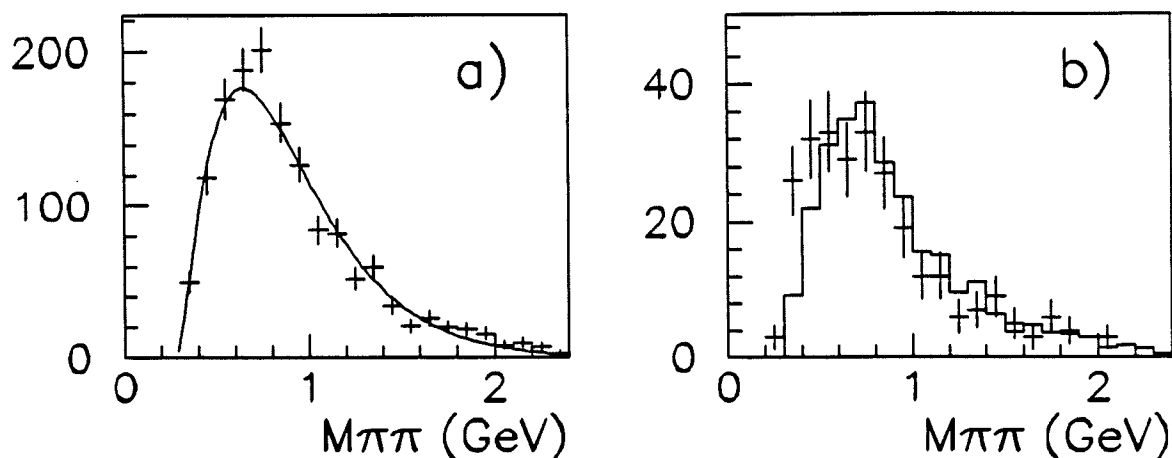
Figure 6.48: Mass background. Plot a) shows the distribution of events for $0.5 <$ $Z_{pair} < 0.7$, with a fit to the background function. Plot b) shows a comparison of events simulated using Lund (points), and the background from real data (histogram, normalized to the points).

distribution as represented by the parametrization above is used. It is included in the fast Monte Carlo simulation of the mass smearing.

The presence of the background broadens the mass peak. Assuming that it contributes 20% of the entries in the mass distribution, a background subtraction can be carried out easily. Figure 6.49 shows the change in the ρ^0 peak from data, after background subtraction.

6.3.11 Attempted Deconvolution

The need for a deconvolution of the mass spectrum was discussed briefly in an earlier section (see page 295). An unsuccessful attempt to derive the true mass distribution from the measured distribution is described briefly in this section, as an aid to future analyses of ρ^0s in E665.

The plot in figure 6.29 shows the contours of the kernel. The smearing is nontrivial, as also can be seen in figure 6.50a, which compares the true, smeared, and unsmeared mass distributions. The simplest approach to this problem takes the plot of the kernel, represents it as a matrix, and applies the matrix inverse to the observed distribution. Briefly, given

$$F(M) = \int_{T_1}^{T_2} dT \, G(T) \, K(M, T),$$
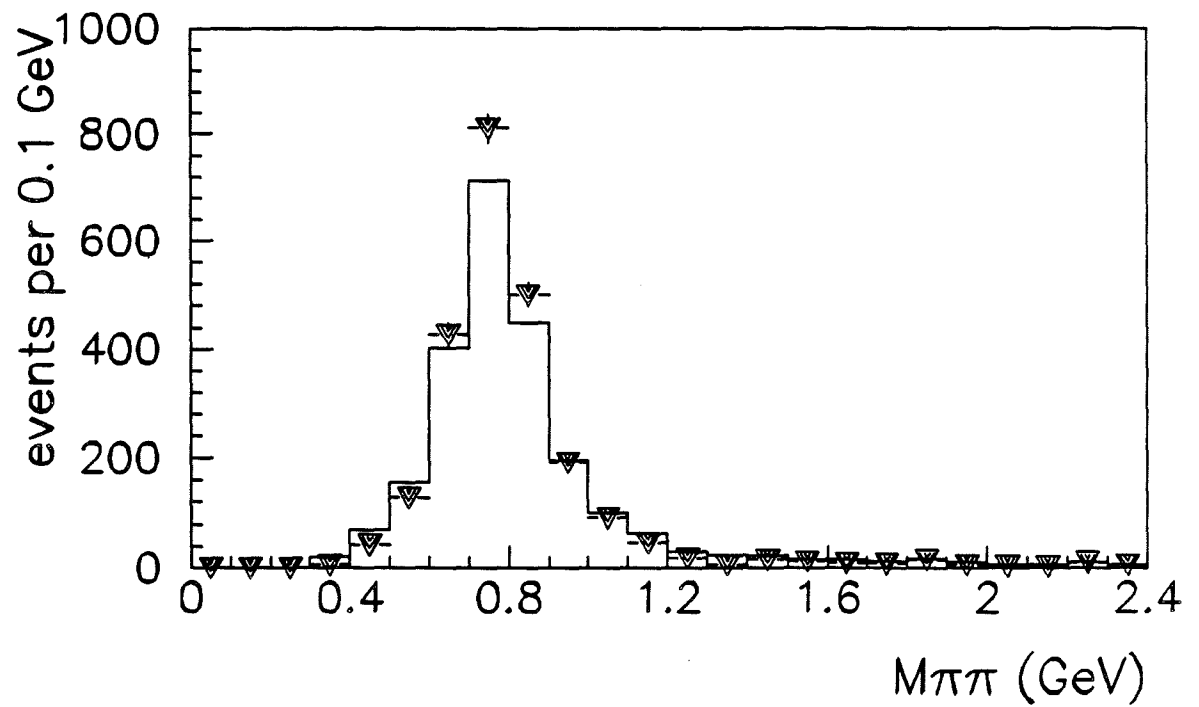
Figure 6.49: Mass spectrum before background subtraction (histogram), and after (black triangles). Both histograms contain the same number of entries.

introduce bins:

$$F_i \equiv \int_{M_{i-1}}^{M_i} dM\ F(M)$$

where $M_i = M_0 + i\Delta$; Δ is the bin width. Then, in an unsophisticated manner,

$$
\begin{aligned}
F_i &= \int_{M_{i-1}}^{M_i} dM \int_{T_1}^{T_2} dT\ G(T)\ K(M,T)\\
&= \sum_j \int_{T_{j-1}}^{T_j} dT\ G(T) \int_{M_{i-1}}^{M_i} dM\ K(M,T)\\
&= \sum_j \int_{T_{j-1}}^{T_j} dT\ G(T) K_i(T)\\
&\equiv \sum_j K_{ij} G_j,
\end{aligned}
$$

with

$$G_j = \int_{T_{j-1}}^{T_j} dT\ G(T) \quad \text{and} \quad K_{ij} = \int_{T_{j-1}}^{T_j} dT \int_{M_{i-1}}^{M_i} dM\ K(M,T).$$

Solution of the convolution equation would be accompanied by inverting the matrix, $\mathbf{K}$:[17]

$$\vec{G} = \mathbf{K}^{-1}\ \vec{F}.$$

The F_i are identified with the bins of a histogram of the observed mass spectrum, and the G_j are the true spectrum. The matrix K_{ij} is based on the plot from Monte Carlo of M_{meas} versus M_{true}, subject to the normalization condition

$$\sum_i F_i = \sum_j G_j.$$

A million fast Monte Carlo events were used to fill a 24×24 grid of M_{meas} against M_{true}. The mass threshold $M_{\text{min}} = 0.2791$ GeV was subtracted from both axes, to avoid singularities resulting from identically zero rows and columns in the matrix K_{ij}. The matrix was inverted using standard routines. Vectors $\vec{G}$ (the smeared mass distribution) and $\vec{F}$ (the true mass distribution) also were generated. The "unsmeared–smeared" distribution, given by

$$\vec{G'} = \mathbf{K}^{-1}\ \vec{F},$$

was calculated. It is compared to the true distribution in figure 6.50a. The agreement is quite good. A fit to the unsmeared distribution retrieves the parameters of

---

[17]Not all convolution equations can be solved in this manner; the separation in the integral over T of $G(T)$ and $K(M,T)$ is an approximation.

the model. The slight deviations at the peak and at threshold are due the coarse binning used (0.1 GeV); the details of the structure of the kernel where the two axes meet is lost (see figure 6.31a on page 296).

It remains to apply the inverted kernel to the observed mass distribution. The result is poor, as shown in figure 6.50b: the measured distribution (histogram) is smooth and well-behaved, but the deconvoluted spectrum (points) is jagged, and peaked too sharply. A fit using the Söding model gives $M_\rho = 770 \pm 1$ MeV, and $\Gamma_\rho = 55 \pm 8$ MeV, which is much too small.

The poor performance results from the slight difference between the observed and simulated spectrum, shown in figure 6.51. Plot a) shows that the real spectrum actually is narrower than the simulated; the mass smearing evidently is overestimated by the Monte Carlo. The inverted kernel squeezes the peak to make it narrower and taller. It squeezes the real data too much because it is based on a simulated peak that is too wide.

Better methods for solving the convolution equation are known. For example, the kernel matrix can be diagonalized, and the observed spectrum expanded in terms of its eigenvectors. Unwanted high frequency components resulting from meaningless statistical fluctuations can be suppressed. Another method consists of expanding the observed spectrum and the kernel in terms of a suitable set of orthonormal functions (e.g., Laguerre polynomials including the exponential factor), and solving the linear equations relating the coefficients of the expansion to relate the true to the observed distribution. Unfortunately, there was not enough time to pursue these possibilities.

6.3.12 Monte Carlo Fit

Since the attempt to deconvolute the mass spectrum failed, another approach to determining the true mass distribution was tried. The parameter of interest is the strength of the interference term, f:

$$\frac{dN}{dM} = R(M) + f\, I(M)$$

$$R(M) = \frac{M M_\rho \Gamma(M)}{(M^2 - M_\rho^2)^2 + M_\rho^2 \Gamma^2(M)}$$

$$I(M) = \frac{M^2 - M_\rho^2}{(M^2 - M_\rho^2)^2 + M_\rho^2 \Gamma^2(M)}$$

314
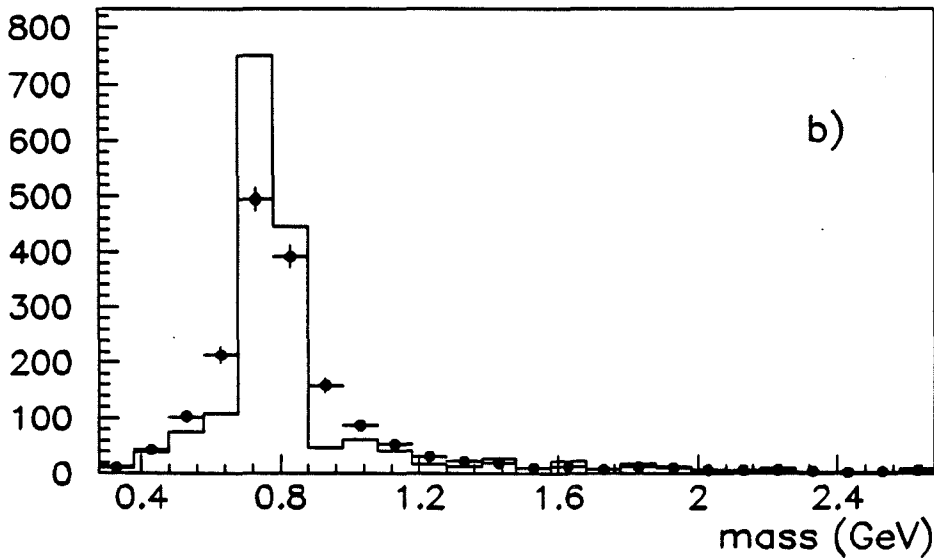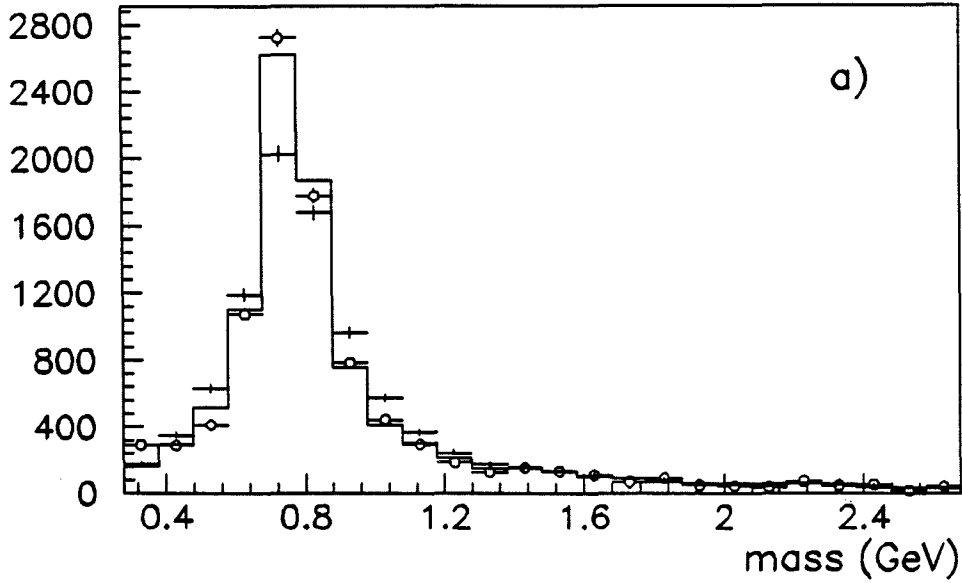
Figure 6.50: Deconvoluted mass distributions. Plot a) shows the simulated data; the histogram is the true mass distribution, the crosses are the smeared distribution, and the open circles are the unsmeared distribution. Plot b) shows the real data; the points show the observed spectrum, and the histogram, the result of applying the inverted kernel determined from the simulated data.
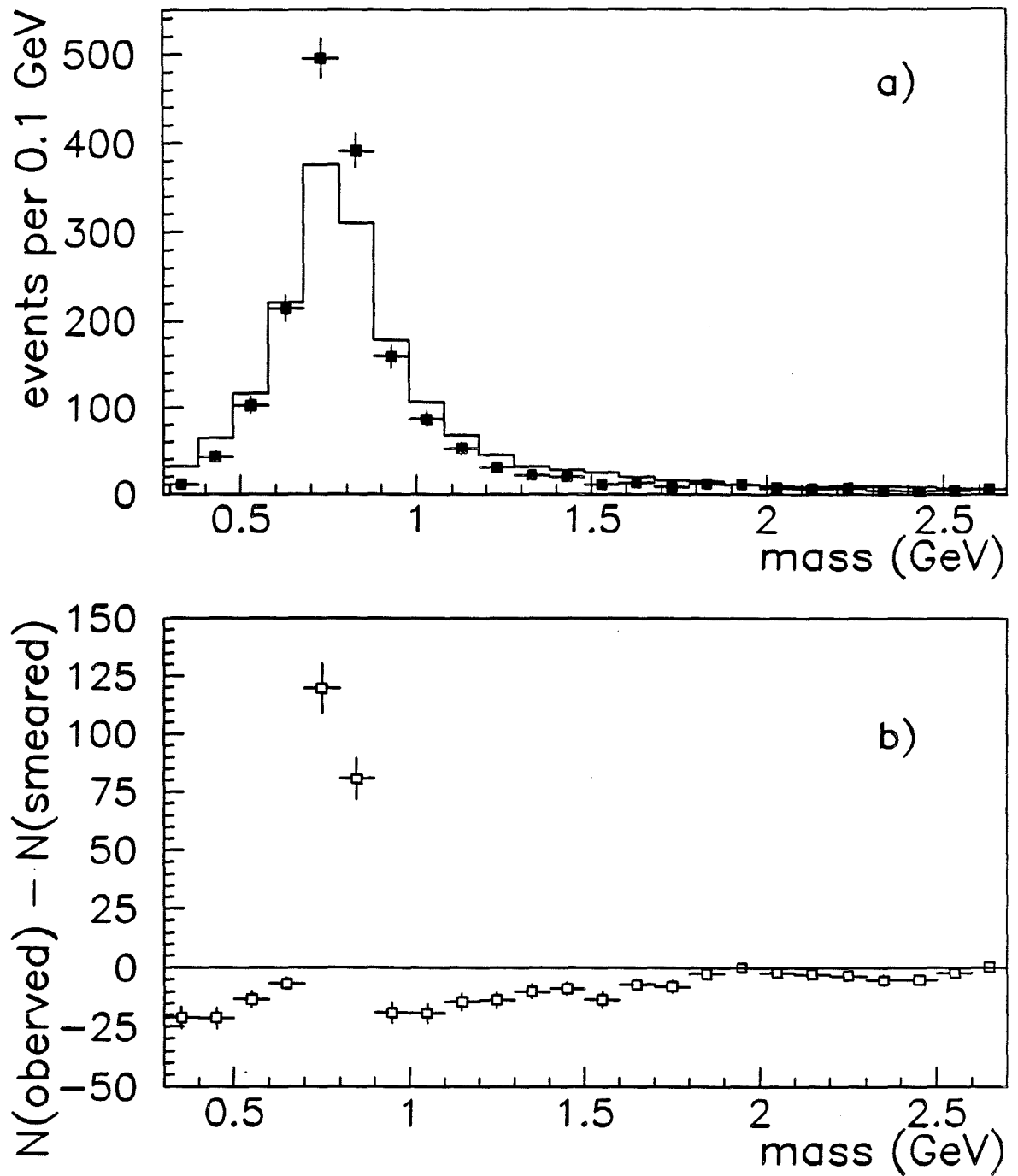
Figure 6.51: A comparison of the smeared simulated mass distribution, and the real distribution. In plot a) the two are compared directly. The difference between them is shown in plot b).
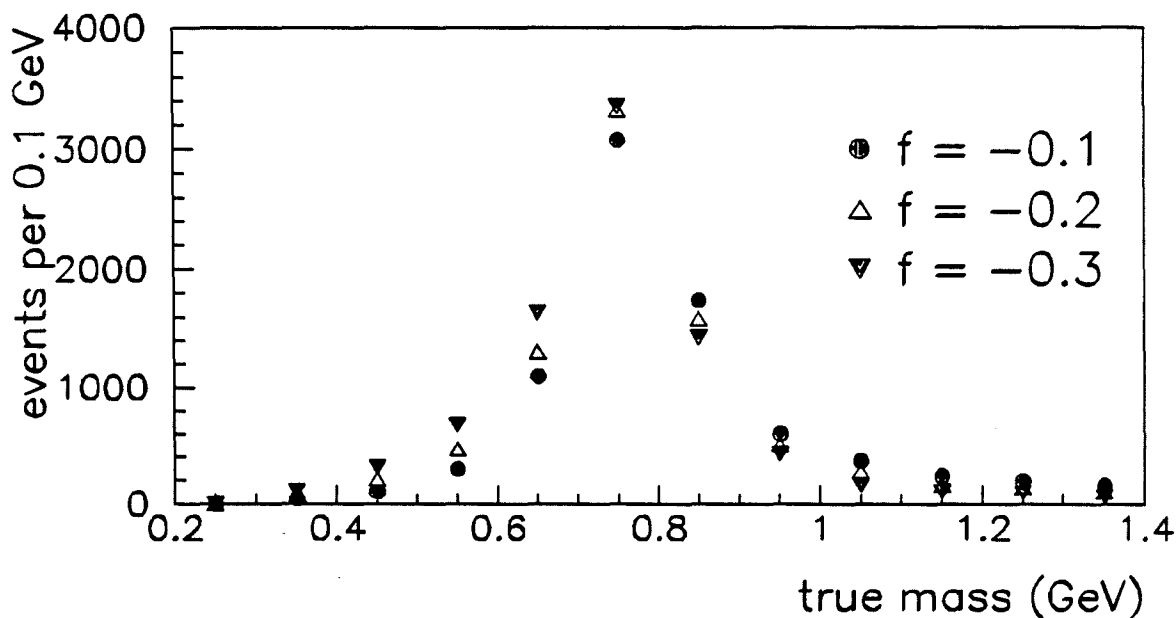
Figure 6.52: Variation of the true mass shape, for different values of the strength of the interference term, $f = -0.1$, -0.2, and -0.3.

The parameter is negative: $f < 0$. The shape of the true distribution changes with f as illustrated in figure 6.52: the shoulder on the low side of the peak increases as the magnitude of f increases, and the actual peak shifts to lower values.

The technique is to generate several distributions of the smeared mass, for several values of f. (The fast Monte Carlo is used.) For each value, the simulated histogram is normalized to the data histogram, and a χ^2 is calculated between the histograms:

$$\chi^2 \equiv \sum_i \frac{(D_i - S_i)^2}{(D_i + S_i)},$$

where the sum is over the bins $i = 1, \ldots, 24$, the data histogram is D_i, and S_i is related to the original simulated mass histogram $S_{i,0}$ by

$$S_i = S_{i,0} \left(\sum_i D_i / \sum_j S_j \right),$$

so that $\sum_i S_i = \sum_j D_j$. A set of histograms S_i^n are generated, for $n = 1, \ldots, N$ values of the interference strength, $f = f_1, \ldots, F_N$. For each value, χ^2 is calculated, leading to a set of values $\chi^{2(n)}$. The best value of f is the one which gives the minimum χ^2.
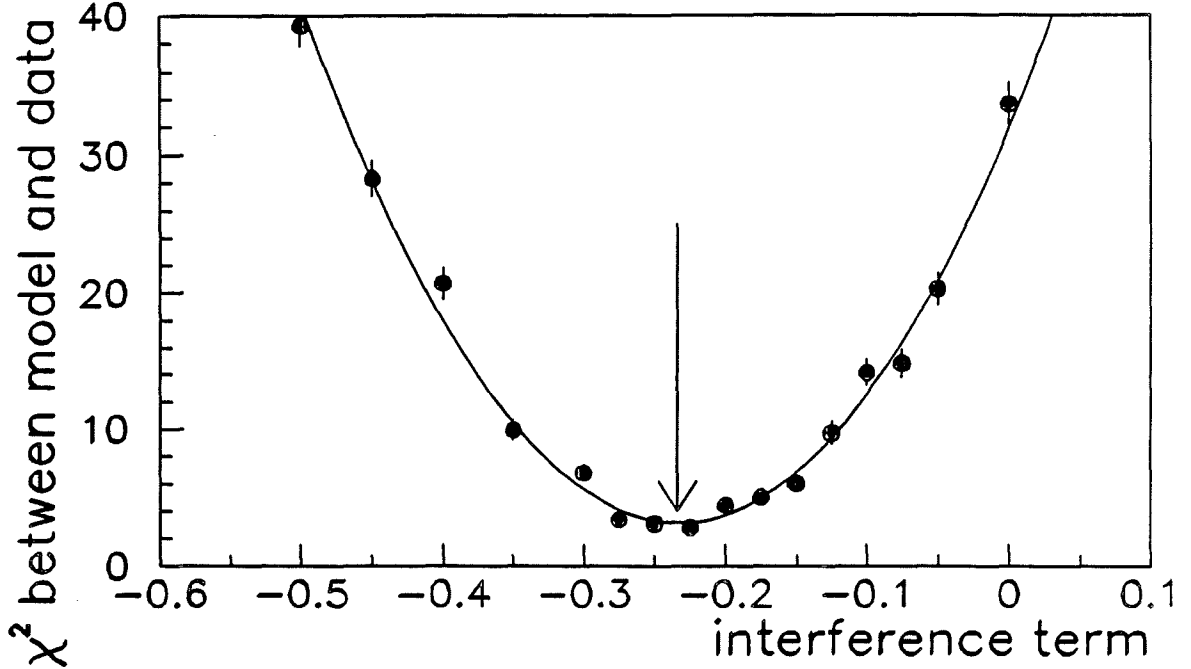
Figure 6.53: The variation of χ^2 with the strength of the interference term. The curve is a fit to the points, with the arrow indicating the minimum.

To start, all events are used to make a data histogram, such as the one displayed in figure 6.51 on page 316. Sixteen values for f are chosen, between $f = 0$ and $f = -0.5$. The resulting values for χ^2 are shown in figure 6.53, plotted against the values for f. A clear parabola is obtained, which is fitted easily by a quadratic polynomial. The minimum of the parabola gives the best value for f, as indicated by the arrow. At that point, χ^2 is close to one.

There is a statistical uncertainty on the optimal value for f which is not obvious at first. There are approximately 2200 entries in the range $0.3 < M_{\pi\pi} < 2.0$ GeV, over which χ^2 is calculated; there are just under ten thousand simulated events. The statistical uncertainty in the data is responsible for a statistical uncertainty in χ^2 at each point: a variation in the contents of each bin D_i by a normal amount $\sqrt{D_i}$ leads to a variation in the value of χ^2. To evaluate this uncertainty, twenty-five virtual copies of the data histogram are made, which differ only by random variations of the contents in each bin.[18] For the same model histogram S_i, twenty-five values for χ^2 were calculated for each of these twenty-five copies. The variance

---

[18]Technically, the real histogram is used as a model for a routine which generates random numbers based on a histogram; calling this routine approximately 2200 times results in a virtual copy of the original histogram.

of the χ^2 values is used as the statistical uncertainty on the central value, indicated by the error bars in figure 6.53. The statistical uncertainty in the optimal value for f was obtained by using the twenty-five virtual copies of the original histogram, and finding twenty-five optimal values. The variance of these values is taken to be the statistical uncertainty on the optimal value, due to the single real distribution. In the example shown in figure 6.53, this result is $f = -0.232 \pm 0.006$. The optimal value of f is the one obtained from the real distribution.

The discussion in the next chapter of the interference term includes its dependence (or lack thereof) on Q^2 and ν. Due to the properties of the trigger at low acceptance, Q^2 and ν are correlated. Since the track errors depend on ν, the mass smearing varies from one bin to the next. In an extension of the program combining the fast Monte Carlo and the χ^2 optimization, the ρ^0 energy distribution is generated from the ν distribution obtained empirically for each Q^2 or ν bin. This ensures the best match between simulated and real data, within the limitations of the fast Monte Carlo program.

6.3.13   Mass Distributions from LAT and SAT

There is a slight difference between the mass distribution obtained from the LAT and from the SAT data, as illustrated in figure 6.54. The plots are normalized to the same number of entries. The SAT distribution falls systematically higher than the LAT at mass values below and at the peak; above the peak the SAT is lower than the LAT. All cuts are the same, but the kinematic distributions are somewhat different.[19] Two different energy conservation cuts are shown; the difference is the same in both cases.

This difference would suggest that the interference term might be different for the two data sets (see figure 6.52). However, the difference between the two data sets seems to persist even when limited to overlapping kinematic regions. The full Monte Carlo simulation gave no clues about the source of the discrepancy. The difference indicates a systematic error in the mass measurement, and will be discussed further in the next chapter.

---

[19]The SAT data are found at very low Q^2, and fairly low ν, while the LAT data are found at higher Q^2 and high ν.
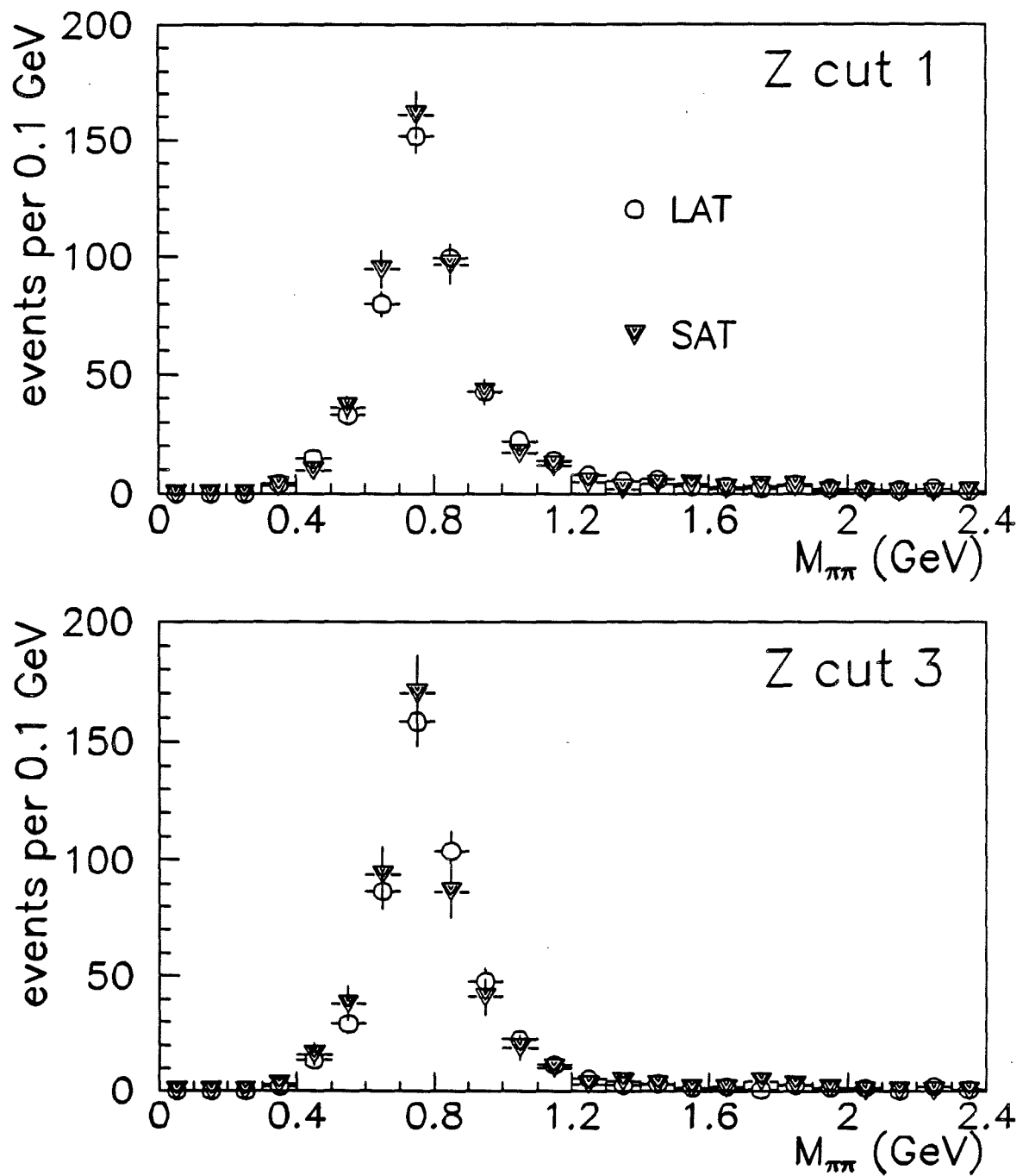
Figure 6.54: Mass distributions from LAT and SAT, for two cuts on Z_{pair}: 1) $0.9 < Z < 1.1$, and 3) $-5 < (1 - Z)/\sigma$. A small difference between the SAT and LAT data is visible.

number of LAT events	942
number of SAT events	535
total number of events	1477

Table 6.8: Number of events from hydrogen and deuterium satisfying all mass cuts.

6.3.14 Mass Statistics

The events used for the mass fits must satisfy these requirements:

1. one in-time beam, no out-of-time beams

2. exactly four fitted tracks (including beam and scattered muons)

3. a reconstructed primary vertex, with

   (a) $-12 < X_{vtx} < -10$ m

   (b) four fitted tracks

   (c) no close tracks

4. no missing energy (3 variations)

   (a) $0.9 < Z_{pair} < 1.0$, or

   (b) $-5 < (1 - Z_{pair})/\sigma_Z < 1$, or

   (c) $-5 < (1 - Z_{pair})/\sigma_Z < 0.2$.

5. $0 < M_{\pi\pi} < 2.4$ GeV

6. $M_{KK} > 1.06$ GeV

7. $E_{sh}/P_{tr} < 0.7$ for both pion tracks

8. $0.01 < Q^2 < 10$ GeV^2 and $40 < \nu < 600$ GeV.

The second energy conservation cut is used by default. All raw data from the hydrogen and deuterium targets were combined. Events from the LAT sample with the SAT bit set were excluded (12%), as were events from the SAT sample with the LAT bit set (6.7%). The number of events surviving all cuts are listed in table 6.8. Figure 6.55 shows the Q^2 and ν distributions of these events. Although the kinematic regions covered by the LAT and the SAT are different, both together give a fairly flat coverage of ν and $\log Q^2$, allowing convenient choices for Q^2 and ν bins.
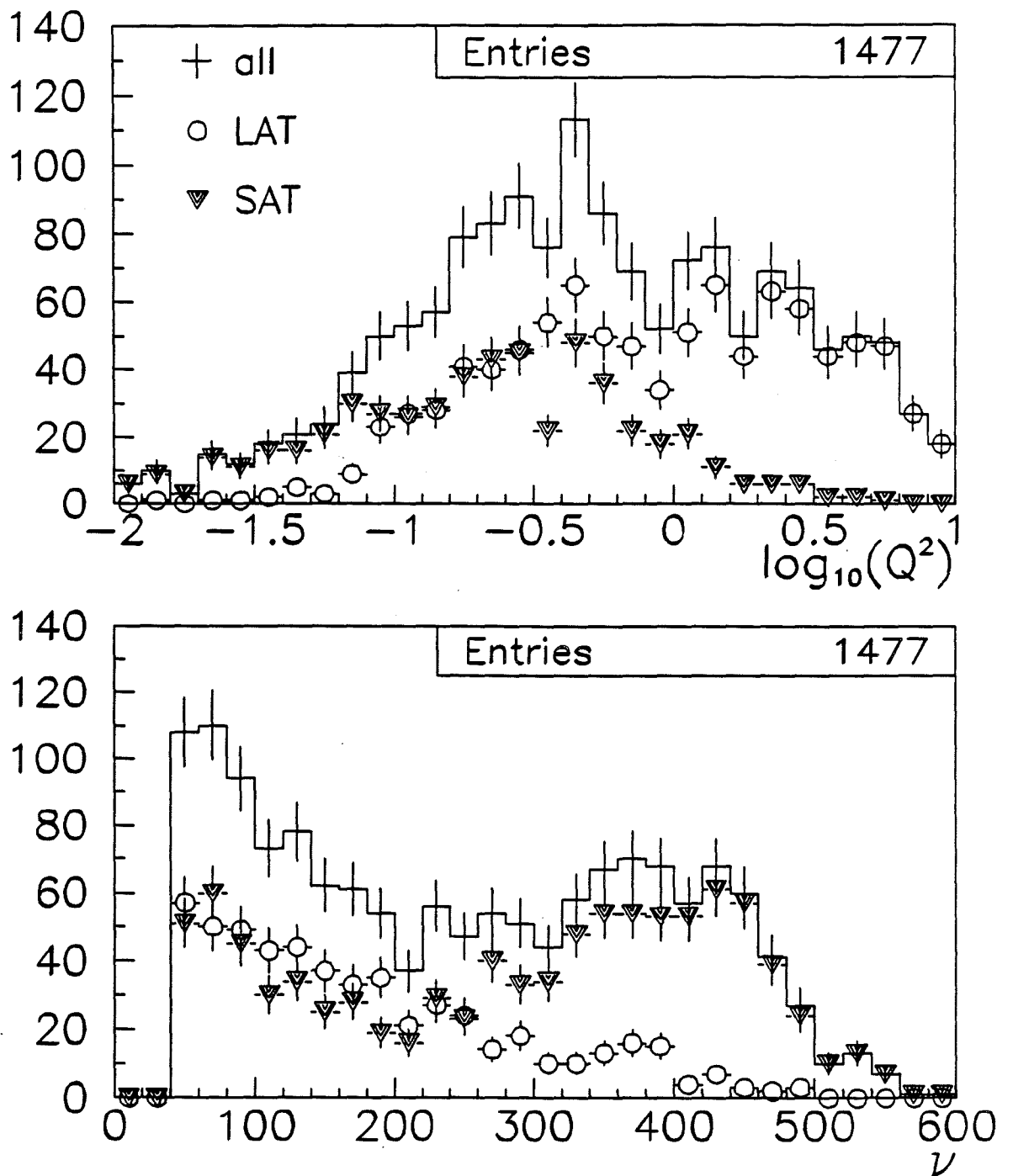
Figure 6.55: Kinematic distribution of events satisfying the mass selection cuts.

6.4   Decay Distributions

The angular distribution of the decay pions is interesting because the ρ^0 is a vector particle. The pions have equal energy and opposite momenta in the ρ^0 rest frame; they are collinear and the axis they define is called the decay axis. The distribution of the angles of this axis with respect to the quantization axis reflects the ρ^0 polarization. Several experiments have shown that the polarization is particularly simple if the quantization axis is taken to be the direction of the recoil nucleon in the hadronic center-of-mass frame; this Lorentz frame and coordinate system is called the "helicity frame." The angle θ is the polar angle of the decay axis with respect to the quantization axis, and ϕ, the azimuthal angle, measured with respect to the plane defined by the virtual photon and the outgoing ρ^0 meson (i.e., the "production plane"). The polarization vector of the virtual photon lies in the plane defined by the incident and scattered muons (the "lepton plane"); its angle with the production plane is called Φ. The results from experiments using polarized real photons have shown a striking dependence on the angle between the decay plane and the photon polarization vector, i.e., on $\psi \equiv \Phi - \phi$.

The direction, energy, and mass of the virtual photon is given by the difference of the incident and scattered muon four-momenta. If the target is assumed to be a nucleon, then it is easy to calculate the boost to the hadronic center-of-mass frame, in which the incoming virtual photon and nucleon have equal and opposite momenta. The mass, energy, and direction of the scattered ρ^0 is given by the two pions. Since the reaction is assumed to be elastic in the sense that the direction of the momentum of the nucleon is changed (it absorbs no energy), the quantization axis is given by the ρ^0 momentum vector (which must be opposite that of the recoiling nucleon). A second Lorentz boost along this axis to the ρ^0 rest frame allows a determination of the angles of the decay axis with respect to the quantization axis. The polar angle θ is zero if the positive pion is parallel to the quantization axis in the ρ^0 rest frame.

The azimuthal angle ψ is determined by finding the normals to the lepton plane and the decay plane; ψ is the angle between the normals. It is positive if the projection of the normal to the decay plane onto the scattered muon vector is positive; otherwise, it is negative. (In fact negative values are translated by 2π to lie in the range $\pi \to 2\pi$.)

The collisions between the virtual photon and the target nucleon are quite energetic: $W = \sqrt{s}$ ranges from 10 to about 30 GeV. The γ factor of the boost from the ρ^0 rest frame into the lab is between 50 and 1000! It turns out that despite these large boosts, the angular and momentum resolution of the two muon

and the two pion tracks is good enough to allow direct measurement of the decay distributions, without the complicated smearing patterns discussed in connection with the mass distribution. Furthermore, the large boosts from the rest frame into the lab frame generally is enough to put both pions into the acceptance of the forward spectrometer.

The track resolution has been discussed extensively already. There is one more effect in the data, however, that is important for the analysis of the decay distributions, as discussed in the next section.

(In the rest of this chapter, studies of reconstruction and resolution are based on the full Monte Carlo simulation, not any "fast" version. These studies were complicated by the fact that the pion energies were incorrect, leading to incorrect calculation of Lorentz boosts. This problem was handled by recalculating the pion energies from their three-momenta.)

6.4.1   Positive Pions through the PSAs

A check of the reconstruction of $\cos\theta$ reveals a significant problem with events in which the positive pion is detected in the PSA chambers. As illustrated in figure 6.56, $\cos\theta$ can be measured accurately when the positive pion is measured using the DCs. When it goes into the PSAs, however, a severe distortion sometimes occurs. Careful examination of some of the faulty events indicated three sources for this distortion:

1. The cluster size for the PSAs was restricted to one. If two contiguous wires were hit, then only one was used on the track. The momentum of PSA tracks is very sensitive to the position of these hits; a shift of 0.5 mm is enough to cause a significant error on the track momentum, which pulls the reconstructed vertex away from its correct position, leading to an incorrect invariant mass (because the tracks are in the CVM field), and incorrect Lorentz boosts.

2. Some of the tracks which reach the PSAs pass just outside of the dead region in the upstream DCs. These hits are not associated with the track by pattern recognition, resulting in poorer momentum resolution.

3. Some tracks contain incorrect hits from PCV.

These reconstruction errors are subtle, and cannot be detected by looking at the usual measures of track quality (χ^2, number of degrees of freedom, etc.), nor can

the events be rejected based on any vertex criterion. In all cases, the actual error on the vertex position was large, indicating that the error on track quantities was magnified by the vertex magnetic field, as discussed earlier in this chapter.

It is not clear why only the positive pion is relevant: there is no distortion when the negative pion passes through the PSAs. Perhaps the reconstruction of the scattered muon (which is positive) interferes with that of the positive pion.

Some further illustrations of the problem are given in figure 6.57. The mean error increases with ν because the probability that the positive pion passes through the PSAs increases with its momentum. Since the positive pion has larger momentum if $\cos\theta > 0$, the error $\Delta\cos\theta = (\cos\theta)_{\text{recon}} - (\cos\theta)_{\text{true}}$ is evident for $\cos\theta > 0$, and is absent for $\cos\theta < 0$. Events with $\nu > 300$ GeV and $\cos\theta > 0$ display a broad distribution in the error on the vertex position, ΔX, most of which is due to PSA tracks.

The bad values for $\cos\theta$ could be rejected only by rejecting events in which the positive pion passes through the PSAs. This draconian measure comes at a high cost, however: the otherwise smooth acceptance in $\cos\theta$ becomes severely distorted, as discussed later. The events were analyzed with and without a cut excluding positive pions which pass through the PSAs. Any difference between the measurements was taken as a measure of systematic error.

6.4.2   Resolution on $\cos\theta$

The PSA reconstruction produces wide error distributions. If events in which the positive pion passes through the PSAs are rejected, then a sharp correlation between reconstructed and true $\cos\theta$ is obtained. The error

$$\Delta\cos\theta = (\cos\theta)_{\text{recon}} - (\cos\theta)_{\text{true}}$$

is small, as shown in figure 6.58. It is nearly zero on average, with am rms width of about one percent. It increases slowly with ν. (Recall that $\langle|\Delta\cos\theta|\rangle$ is proportional to $\sigma_{\cos\theta}$.)

6.4.3   Acceptance of $\cos\theta$

Not every recorded event is reconstructed. Losses occur due to geometry, hardware, software, and analysis requirements. Ideally, the losses are constant as a function
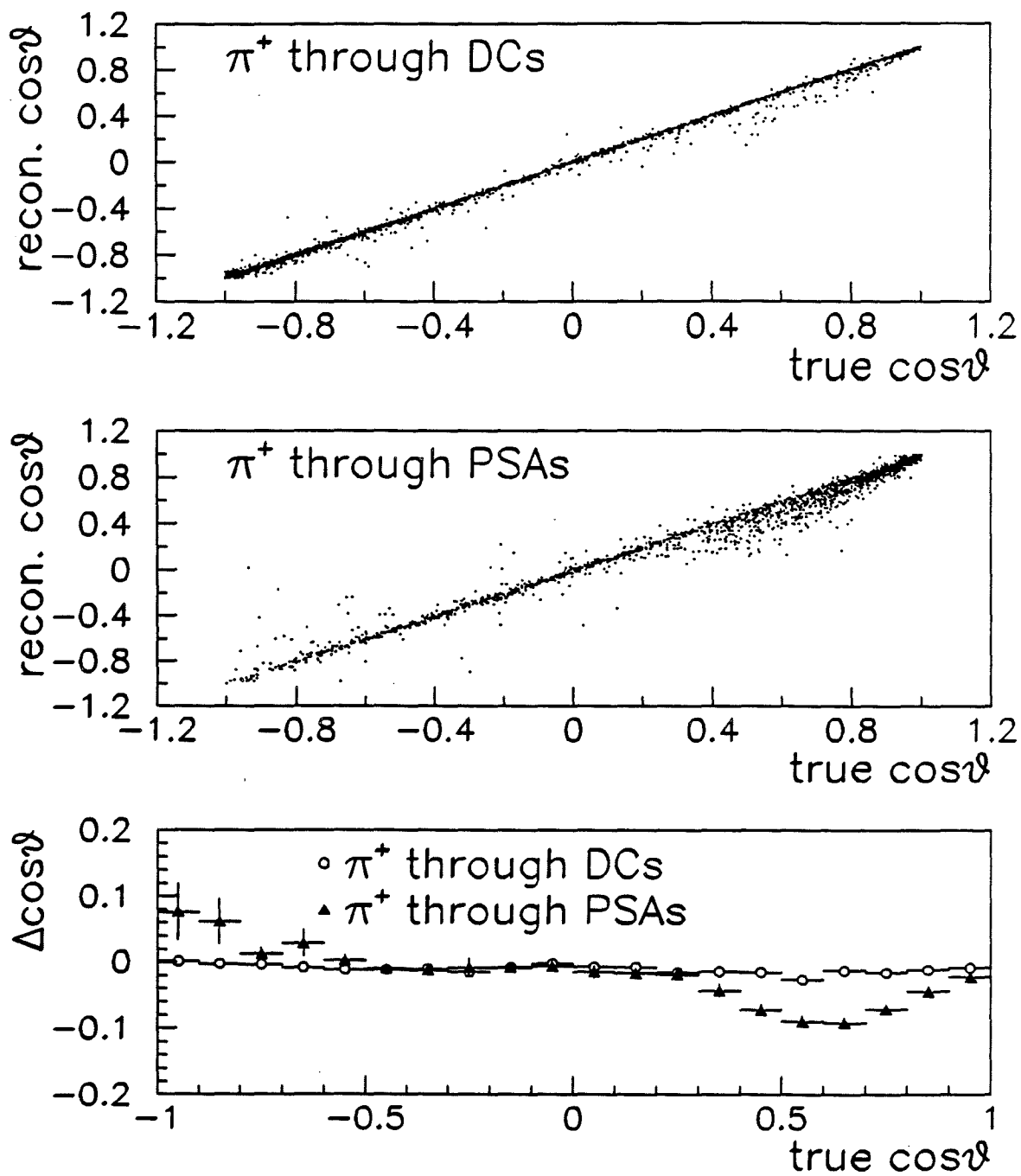
Figure 6.56: Correlation of reconstructed and true $\cos \theta$, for events in which the positive pion passes through the DCs, or the PSAs. The third plot shows the mean error $\Delta \cos \theta$, plotted versus the true value.
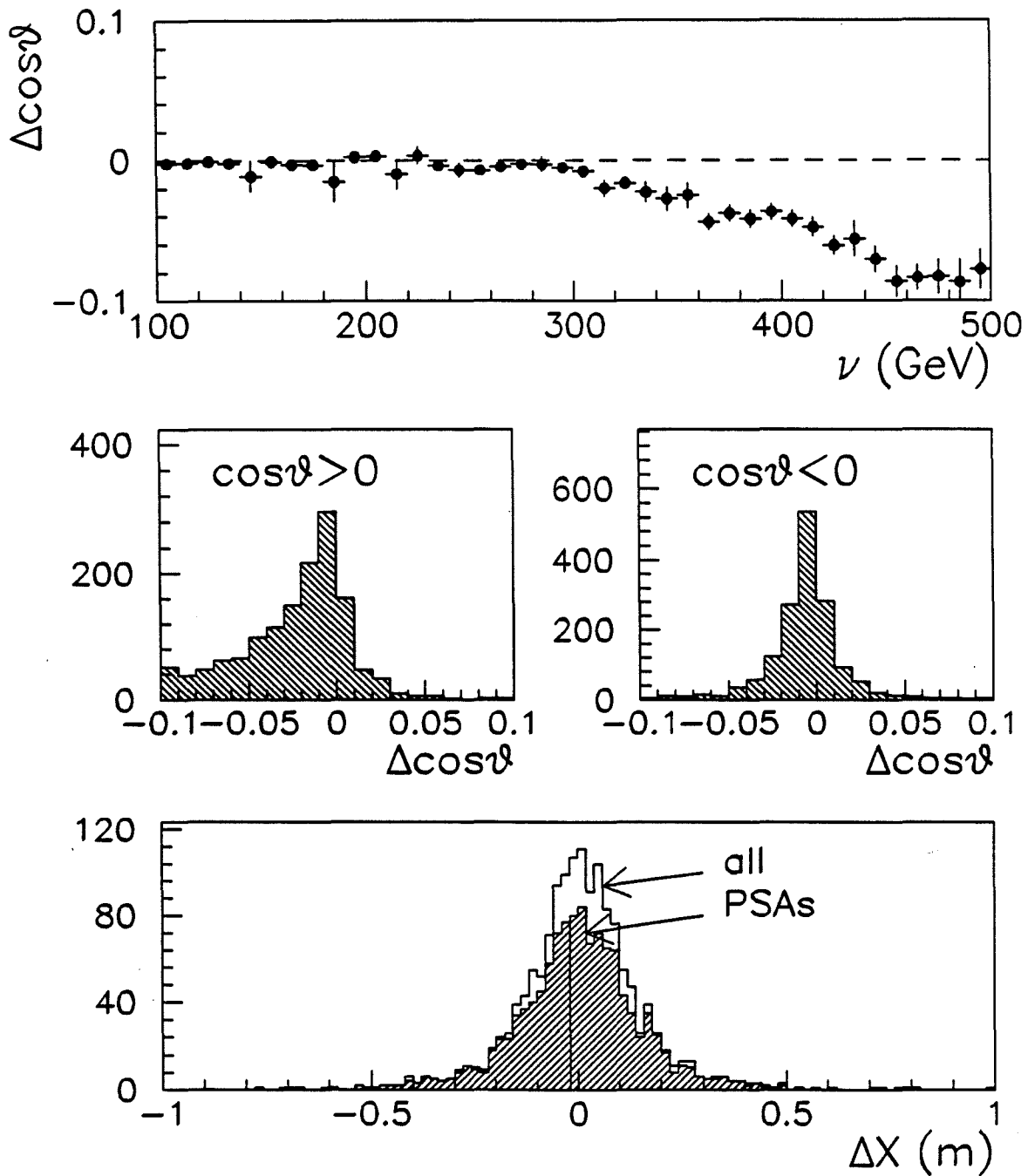
Figure 6.57: Further illustrations of the PSA reconstruction problem. The mean error $\Delta \cos \theta$ increases with ν, and is worst when the positive pion is forward. The PSA tracks in the faulty region contribute to the broad distribution in the error on the vertex position.
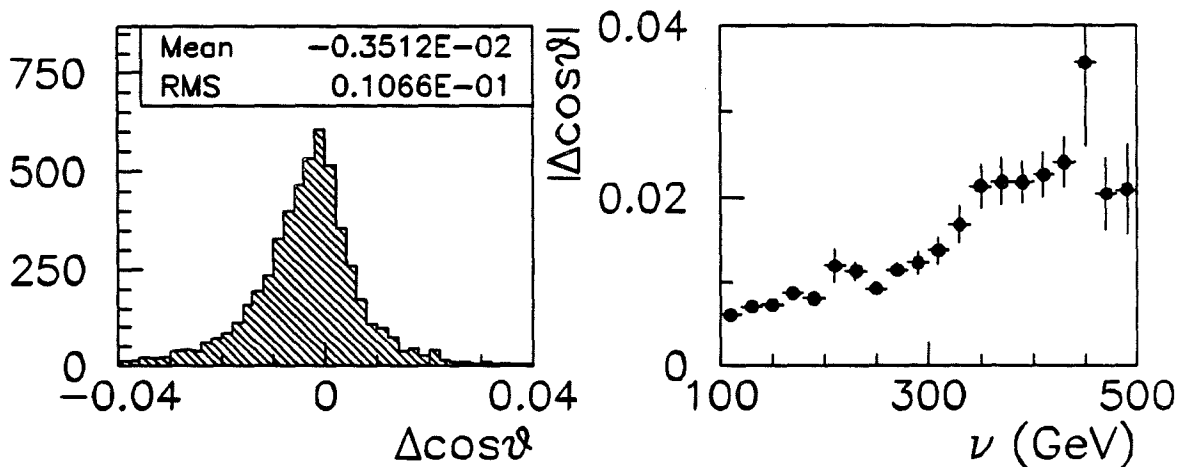
Figure 6.58: Resolution on cos θ, determined from Monte Carlo data, when the PSA reconstruction problem is avoided.

of all analysis variables. Realistically, losses occur, and must be taken into account. The variation of the fraction of events lost as a function of one or more variables is called "acceptance," as if the combination hardware–software–analysis passed events only with a certain probability. There are five basic pieces to acceptance:

1. *Geometry.* Losses occur because one or more required tracks pass outside of the active region of necessary chambers. The geometric acceptance is that obtained when the hardware and software are perfect, and the analysis places no cuts on analysis variables. It is usually responsible for the main features of the net acceptance.

2. *Chamber Efficiency.* Chambers do not register hits in every plane for every track. The detection of tracks is a stochastic process, and the probability that ionization leads to a registered hit is less than one. Furthermore, real chambers are imperfect, and may malfunction. (Several chambers in E665 functioned poorly.) If enough hits are missing, then the track cannot be reconstructed.

3. *Pattern Recognition.* Tracks constitute a very small fraction of the set of all combinations of all hits from all chambers. Practical algorithms for finding valid tracks are limited by the need for speed, and usually fail to reconstruct a small set of tracks which produced an adequate set of hits in the chambers. Beyond the inherent limitations of pattern recognition algorithms, which in principle can be calculated, human errors occur as the code is written. These are incalculable, and can only be taken into account by running the code on Monte Carlo data.

328

4. *Track Fitting.* Track fitting procedures involve cuts on statistical distributions to reject bad tracks; these cuts reject a small number of good tracks, also.

5. *Vertex Fitting.* Vertex fitting also rejects a small number of correctly reconstructed events, due to quality cuts.

The strongest factor in the acceptance should be the geometry, as is the case here. The basic chamber aperture is known from surveys. Dead regions are mapped from the data. The magnetic fields play an important role, also.

The hardware efficiencies, defined as the probability that a hit will occur when a track passes through a plane at chamber coordinate θ, were measured from reconstructed tracks [RSB90, Sch90e]. The inefficiencies were assumed to be uncorrelated, and variations with beam intensity were neglected.[20] The data were divided into several periods, and the outer efficiencies of every plane measured for the different periods. These numbers are used in the detector simulation.

The efficiency of pattern recognition algorithms and code is discussed in detail in [Ryan]. It varies with the detectors involved, and the algorithms used. Overall, the probability that a scattered muon in the forward spectrometer is reconstructed, given adequate hits, is 90–95%. The probability that a hadron is reconstructed, is 80–85%.[21] Given this individual efficiency, the net efficiency for reconstructing a complete ρ^0 event is less than 60%.

If a track is found correctly by pattern recognition, then the probability that it will not be fitted is negligible. Some incorrect tracks will be rejected, and others will be harmed or distorted by the Rescue, Superrescue, and PCV-Hunt procedures.

Measurements from Monte Carlo and real data show that the loss of events due to failures in the vertex fitting are negligible.[22]

The geometric acceptance boils down to the probability that a track with a given momentum, direction, and charge will reach the PCF chambers at the center of the CCM. If it starts out parallel to the x-axis, then it emerges from the CVM

---

[20]Evidence has been found that there might be correlated inefficiencies in the drift chambers. The number of hits on a track was found to vary with the beam intensity.

[21]The scattered muon is usually the stiffest track, and thus easier to find. It is found first, before any hits have been removed.

[22]If the tracks are found and/or fitted incorrectly, however, then the reconstructed vertex may be in the wrong place inside the vertex magnet, leading to large errors in the track parameters. These events may be rejected by analysis cuts.

at a horizontal angle $\theta_{\text{CVM}} \propto 1/P$. It travels along a straight trajectory until it enters the CCM, at which point it is bent back toward the x-axis. A simple calculation shows that the horizontal impact point depends quadratically on the vertex position, and inversely on the track momentum. The PCF chambers are 2 m wide. Given the placement and strength of the CVM and CCM, this width corresponds to the impact point of a 9 GeV track, which emerges from the CVM at an angle of approximately 100 mr. (This track will pass about 10 cm from the x-axis at PCV, and about 60 cm at PCN.)

The minimum momentum for a track to reach PCF depends on its initial direction, in addition to its momentum. For example, the height of PCF is 1 m, which corresponds to an angle at the vertex of only 30 mr. In general, the geometric acceptance will depend on the track momentum, the direction angles y' and z', and the vertex position.[23] Instead of a sharp cutoff at 9 GeV, a shoulder is observed, the details of which depend on the physics process generating given distributions in y' and z'. The overall acceptance for ρ^0 events, plotted as function of the slowest pion, is shown in figure 6.59.

Although the geometric acceptance is responsible for the acceptance knee at low momentum, less pronounced features at high momentum are due to the limitations of pattern recognition. Figure 6.60a shows the acceptance of ρ^0 events plotted as a function of the pion momenta. There is a slight dip in the region $P = 150 \to 300$ GeV, due in part to interference between the MD and MS processors. Otherwise the acceptance is quite flat, and nearly the same for positive and negative pions. A cut to reject events in which the positive pion passes through the PSA severely distorts the acceptance, as shown in figure 6.60b.

The determination of $\cos\theta$ requires both pion tracks to be reconstructed. The momentum of each track depends on $\cos\theta$. Ignoring the component perpendicular to the boost axis, and terms of order $1/\gamma$,

$$P_{\pm} = \gamma[\beta E_0 \pm P_0 \cos\theta]$$

$$\approx \frac{\nu}{2}\left[1 \pm \sqrt{1 - \left(\frac{m_\pi}{M_\rho/2}\right)^2}\cos\theta\right],$$

$$\cos\theta \approx \frac{p_+ - p_-}{\nu}\left(\frac{M_\rho}{\sqrt{M_\rho^2 - 4m_\pi^2}}\right).$$

One of the two pions will be slow if $|\cos\theta|$ is large, or if ν is low. The worst acceptance problem occurs for $|\cos\theta| \to 1$, and $\nu \to 0$, as illustrated in figure 6.61. Fortunately, the problem is minimized by requiring $\nu > 100$ GeV.

---

[23]See also [Jansen].
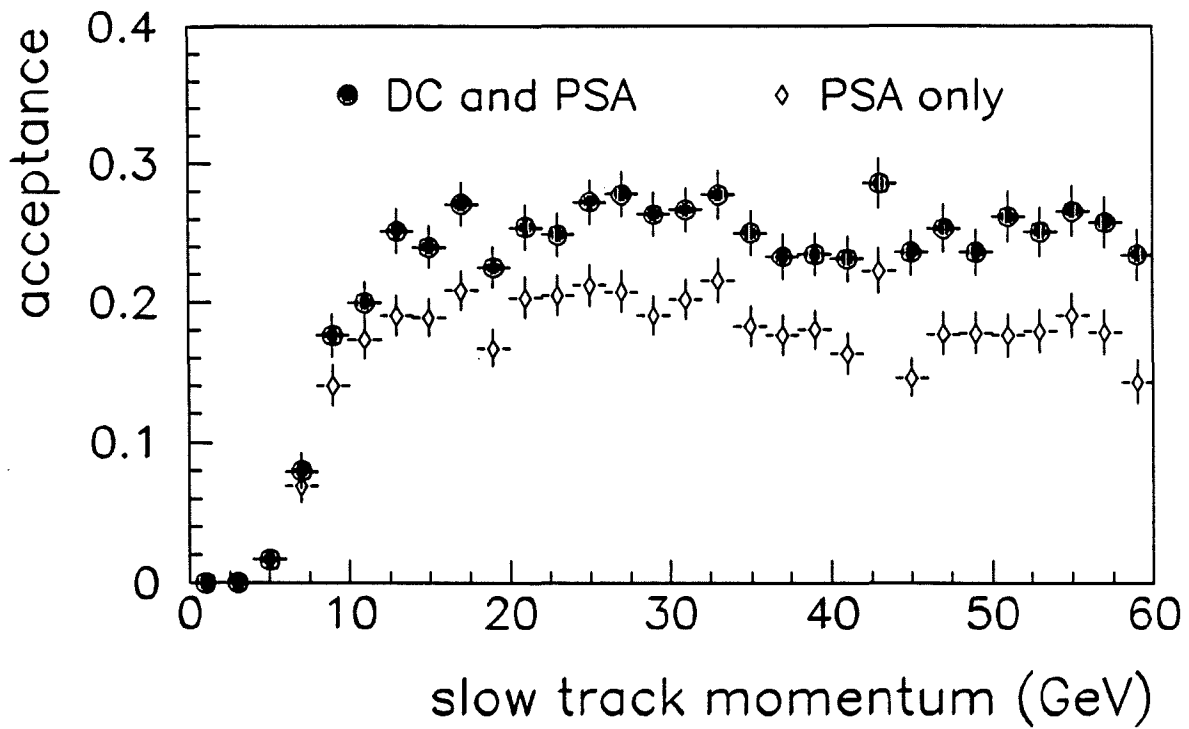
Figure 6.59: Complete ρ^0 acceptance as a function of the momentum of the slowest pion. The requirement that the positive pion pass through the PSA does not effect the shape of the distribution in this range.
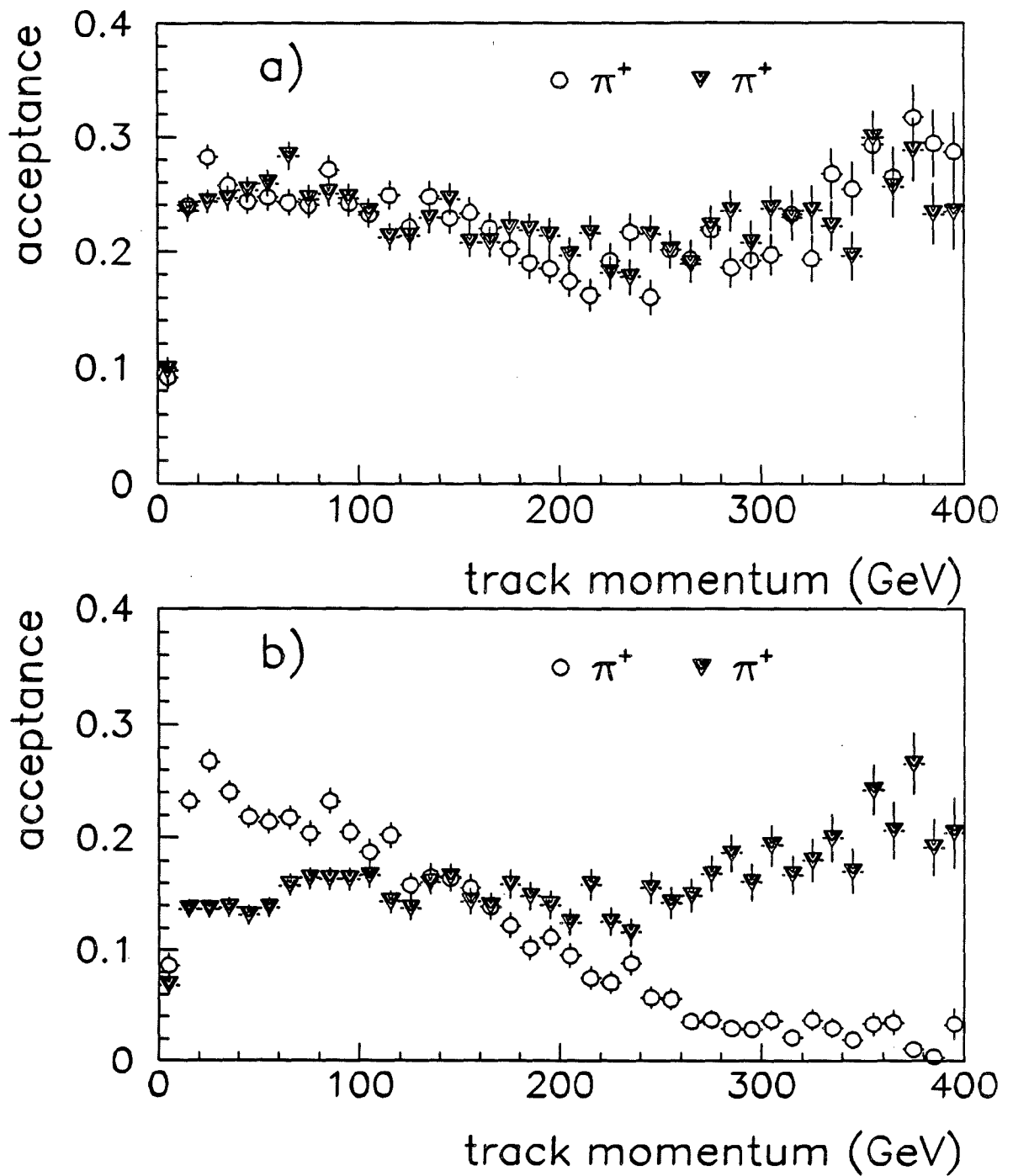
Figure 6.60: Acceptance as a function of the pion momenta. a) Positive pion allowed
to pass through PSAs, b) not allowed.
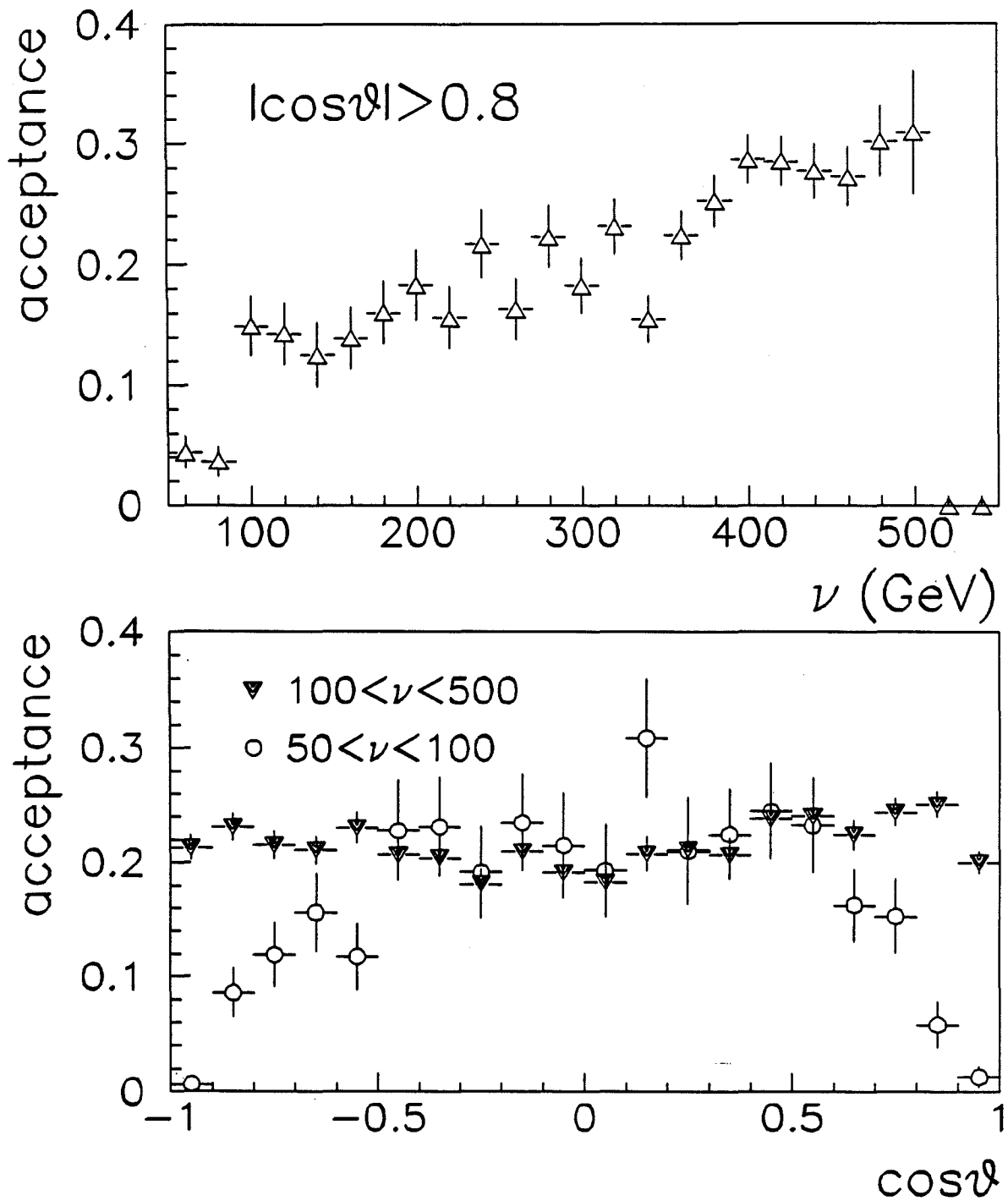
Figure 6.61: Acceptance of large $|\cos\theta|$ as a function of ν. The variation with $\cos\theta$ is worst for $\nu < 100$ GeV.

Since the acceptance at the extremes of $\cos\theta$ depends on ν, it is important that the Monte Carlo mimic the ν distribution of the data well. A comparison of the accepted events plotted as a function of ν for real and simulated data is shown in figure 6.62. Despite an error in the Rhogen code distorting the Q^2 distribution, the basic shape of the ν distribution in data is reproduced by the Monte Carlo.

The acceptance after requiring $\nu > 100$ GeV is not perfectly flat, when plotted as a function of $\cos\theta$, as shown in figure 6.63a. There remains a small loss at large $|\cos\theta|$, due to the fact that boosts help less and less as $|\cos\theta| \to 1$.[24] There is a dip in the center, which reflects the dip in the track acceptance for $P = 150 - -300$ GeV, shown in figure 6.60a (page 332).

If events in which the positive pion passes through PSA are rejected, then the acceptance is poor when $\cos\theta > 0$, as shown in figure 6.63b. If the flatness of figure 6.63a follows from the similarity of the positive and negative pion acceptances in figure 6.60a, then the disparity in 6.60b leads to the slanted acceptance in 6.63b.

The acceptance plots in figure 6.63 contain statistical variations which should be smoothed out. This is accomplished by fitting the histogram. The function required is defined over the interval $-1 < X < 1$, where $X \equiv \cos\theta$. Since the distributions are smooth, they might be fitted by polynomials. It is easier to use orthogonal systems of polynomials. The Legendre polynomials are appropriate for this situation. The histograms are fitted to a function

$$A(X) = \sum_i^N a_i P_{n_i}(X).$$

The solid curve in figure 6.63 shows the results of a fit using Legendre polynomials of orders 0,1,2,3,4; the dotted line shows the fit using orders 0,1,2,3,4. The fit results are listed in table 6.9. The fits are equally good, and vary little over the entire range. Fits with fewer terms resulted in poor χ^2, and additional terms tended to cause indeterminant matrices (i.e., were superfluous). The fit with terms 0,1,2,3,4 was chosen.

6.4.4 ρ^0 Polarization from Fits

Three bins in Q^2 were chosen for measuring the ρ^0 polarization from the polar decay distribution. For each of these, two acceptance plots were generated ("flat" and "sloped"), and fitted to the sum of four Legendre polynomials, as discussed in

---

[24]Even for $\nu = 300$ GeV, the energy of the negative pion is only 10 GeV, if $\cos\theta = -1$.
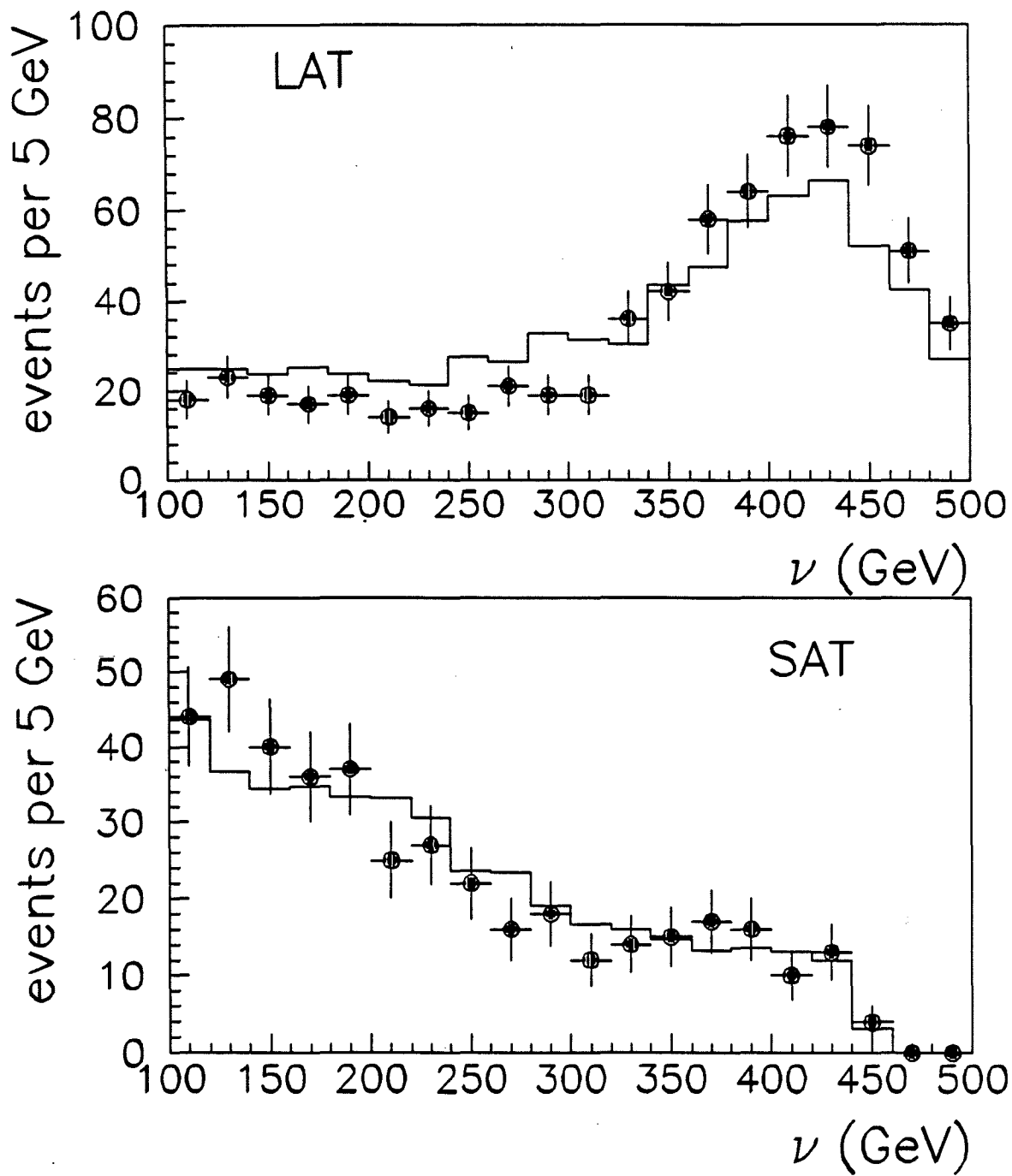
Figure 6.62: A comparison of accepted events, as a function of ν, for real and simulated data.
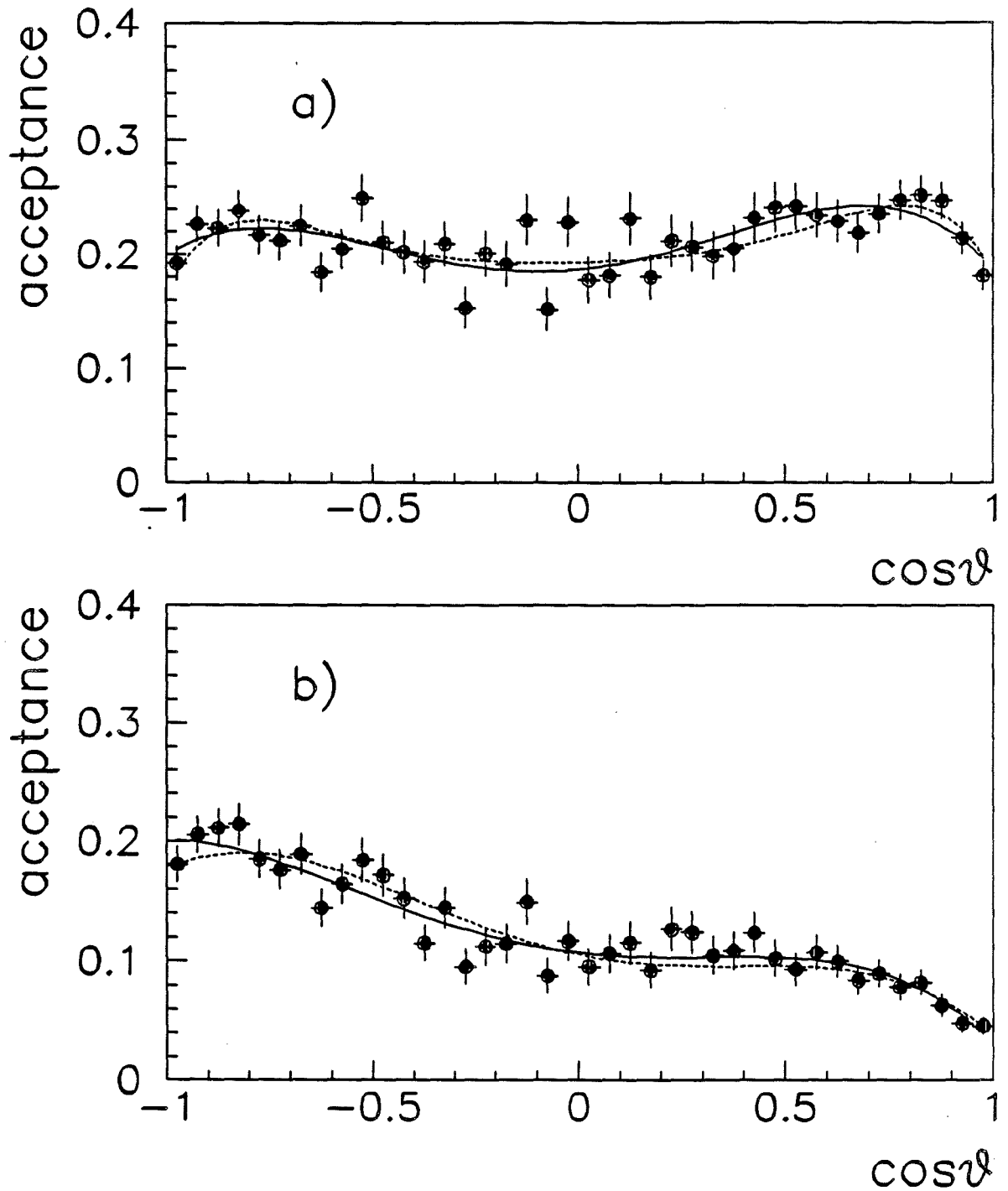
Figure 6.63: Two fits to the $\cos\theta$ acceptance. Plot a) shows the acceptance with $\nu > 100$ GeV. Plot b) shows the acceptance if $\nu > 100$ and PSA tracks are rejected.

term ($\times 10^{-2}$)	$\nu > 100$ GeV	$\nu > 100$ GeV and no PSAs
0	12.3 ± 0.2	21.1 ± 0.3
1	-6.7 ± 0.3	1.0 ± 0.3
2	1.5 ± 0.4	2.0 ± 0.2
3	-1.9 ± 0.3	-1.6 ± 1.2
4	-2.3 ± 0.5	-3.9 ± 0.2
χ^2	1.0	1.2
0	12.3 ± 0.4	21.1 ± 0.3
1	-6.9 ± 0.3	0.8 ± 0.3
2	1.2 ± 2.0	2.0 ± 0.1
4	-2.9 ± 0.9	-3.7 ± 0.4
6	0.2 ± 1.2	-1.9 ± 0.3
χ^2	1.3	1.2

Table 6.9: Acceptance for $\cos\theta$ fitted to two sums of Legendre polynomials.

the previous section. A minimum ν cut of 100 GeV was imposed, and the sloped acceptance plot and input distribution were generated by rejecting events in which the positive pion passed through the PSAs. For each Q^2 bin, three distributions were formed:

a "Flat" raw distribution, with no acceptance correction.

b "Flat" raw distribution, with "flat" acceptance correction.

c "Sloped" raw distribution, with "sloped" acceptance correction.

The distributions are normalized to one, and were fitted to the function

$$W(\cos\theta) = \frac{3}{4}[(1-r) + (3r-1)\cos^2\theta].$$

The results are shown in figure 7.1, and summarized in table 6.10.

The raw distribution (a) is very similar to the corrected distribution (b), because acceptance is nearly flat. After correcting for the acceptance loss, distribution of events with no positive pions in PSA (c) match the others. Within the statistical precision of these data, the result is the same, regardless of which acceptance correction is used.

The parameter r can be determined from the second moment of $\cos\theta$:

$$r = \frac{5}{2}\langle\cos^2\theta\rangle - \frac{1}{2}.$$

337

Q^2 range	plot	events	$\langle Q^2 \rangle$	$\langle \nu \rangle$	r	χ^2
0.01–0.4	a	549	0.18	317	$(6.7 \pm 2.4) \times 10^{-2}$	2.2
	b	549	0.18	317	$(7.6 \pm 2.5) \times 10^{-2}$	2.4
	c	241	0.17	258	$(10.7 \pm 3.4) \times 10^{-2}$	1.1
0.4–1.5	a	383	0.79	341	0.27 ± 0.04	1.1
	b	383	0.79	341	0.23 ± 0.04	0.9
	c	164	0.82	266	0.35 ± 0.06	0.5
1.5–20	a	327	4.3	243	0.48 ± 0.04	1.1
	b	327	4.3	243	0.51 ± 0.04	1.1
	c	252	4.7	211	0.56 ± 0.05	1.1

Table 6.10: Fit results for the ρ^0 polarization measured for three ranges of Q^2.
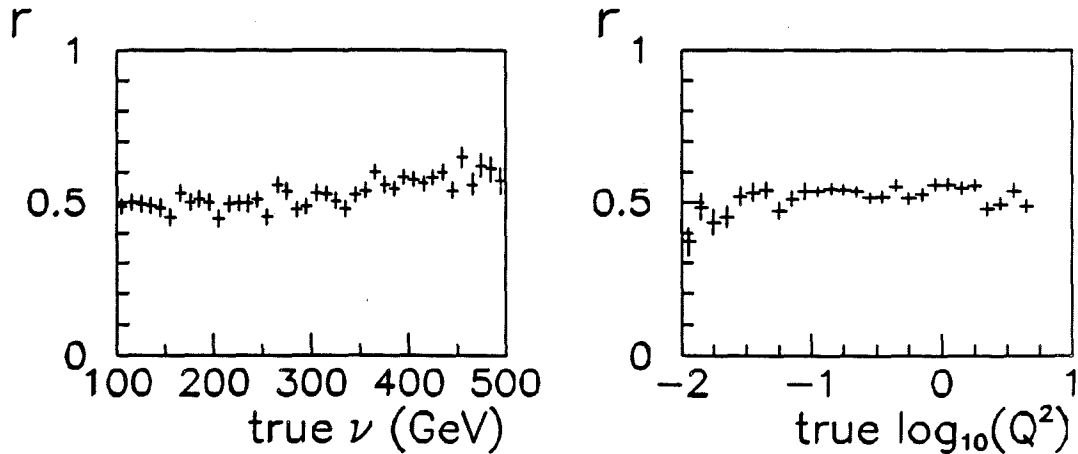
Figure 6.64: Variation of r, calculated from truth quantities, as a function of ν and $\log Q^2$.

It was set at value $r = 0.5$ for the Monte Carlo, but due to the bug mentioned earlier, its effective value changes slightly as a function of ν (and hence, Q^2), as shown in figure 6.64.

6.4.5 ρ^0 Polarization from Moments

The three plots in figure 7.1 show that the polar decay distribution, integrated over the azimuthal angle ψ, can be described by the density

$$W(\cos \theta, r) = \frac{3}{4}[(1 - r) + (3r - 1)\cos^2 \theta].$$

If SCHC is valid, then r represents the longitudinal polarization of the ρ^0. It can be expressed as a linear function of the second moment:

$$r = \frac{5}{2}\langle\cos^2\theta\rangle - \frac{1}{2}.$$

Since the distribution depends only on the one parameter r, no other moments are needed. Plotting r as a function of other quantities is easy.

It is worthwhile determining whether r varies with ν. The trigger acceptance is characterized by contours of constant scattering angle,[25] which induces a correlation between Q^2 and ν. A variation of r (or any other physics quantity) with Q^2 could be a reflection of its dependence on ν. Further, it might be a reflection of the ν dependence of the $\cos\theta$ acceptance.

There are roughly the same number of events in the interval $100 < \nu < 300$ GeV and $300 < \nu < 500$ GeV. The variation of r with Q^2 is checked using data from these two intervals. Figure 6.65a shows the variation of $\langle\nu\rangle$ with $\log Q^2$, for all selected events from LAT and SAT, combined. The points are the real data, and the histogram, simulated data after reconstruction. The agreement is adequate. Figure 6.65b shows the variation of r with $\log Q^2$. It rises smoothly in the real data, while the simulated data is nearly constant.[26] This indicates that the variation of r with Q^2 is not a consequence of the acceptance. Figures 6.65c and d show the variation of $\langle\nu\rangle$ and r with $\log Q^2$, for data in the interval $100 < \nu < 300$ GeV. r climbs, while $\langle\nu\rangle$ remains flat. Figures 6.65e and f show the data in the interval $300 < \nu < 500$ GeV. The increase of r with Q^2 is the same as in the low-ν interval, even though these events are marred by the PSA reconstruction problem.

Another depiction of the independence of r from ν is given in figure 6.66. The top plot shows the variation of r with ν, for $Q^2 < 0.8$ GeV. The second plot shows the same, for $Q^2 > 0.8$ GeV. The variation with ν is negligible, while the cut on Q^2 has a strong effect. The third plot compares the dependence of r on $\log Q^2$, for three intervals in ν.

For a given beam energy, the photon polarization parameter ϵ depends on Q^2 and ν, although the dependence on Q^2 is very weak:[27]

$$\epsilon = \left\{1 + \frac{2(Q^2 + \nu^2)}{Q^2}\tan^2\frac{\theta}{2}\right\}^{-1} \approx \frac{(w+1)^2 - (w-1)^2}{(w+1)^2 + (w-1)^2},$$

---

[25]In fact there is a slight distortion of the trigger acceptance due to the "target–length effect," and due to the fact that the veto spot is rectangular.

[26]There is a slight variation of r with ν in the Monte Carlo, as shown in figure 6.64.

[27]$Q^2_{\min}$ is neglected.
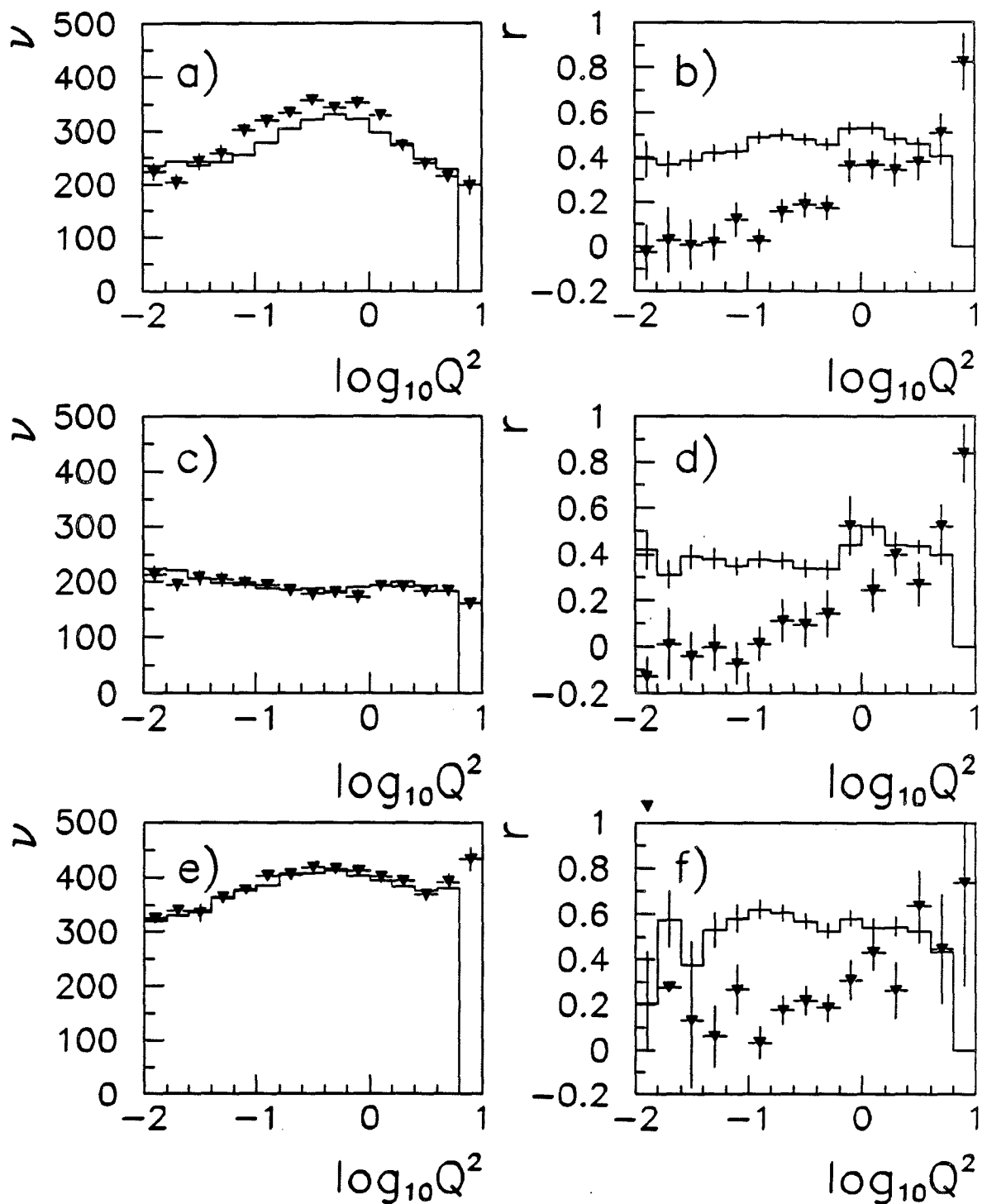
Figure 6.65: Variation of ν and r with Q^2. Plots a and b were made for $100 < \nu < 500$ GeV, c and d for $100 < \nu < 300$, and e and f with $300 < \nu < 500$ GeV. The plots on the left show $\langle \nu \rangle$ versus $\log Q^2$, and on the right, r versus $\log Q^2$. The points are real data; the histogram, simulated.
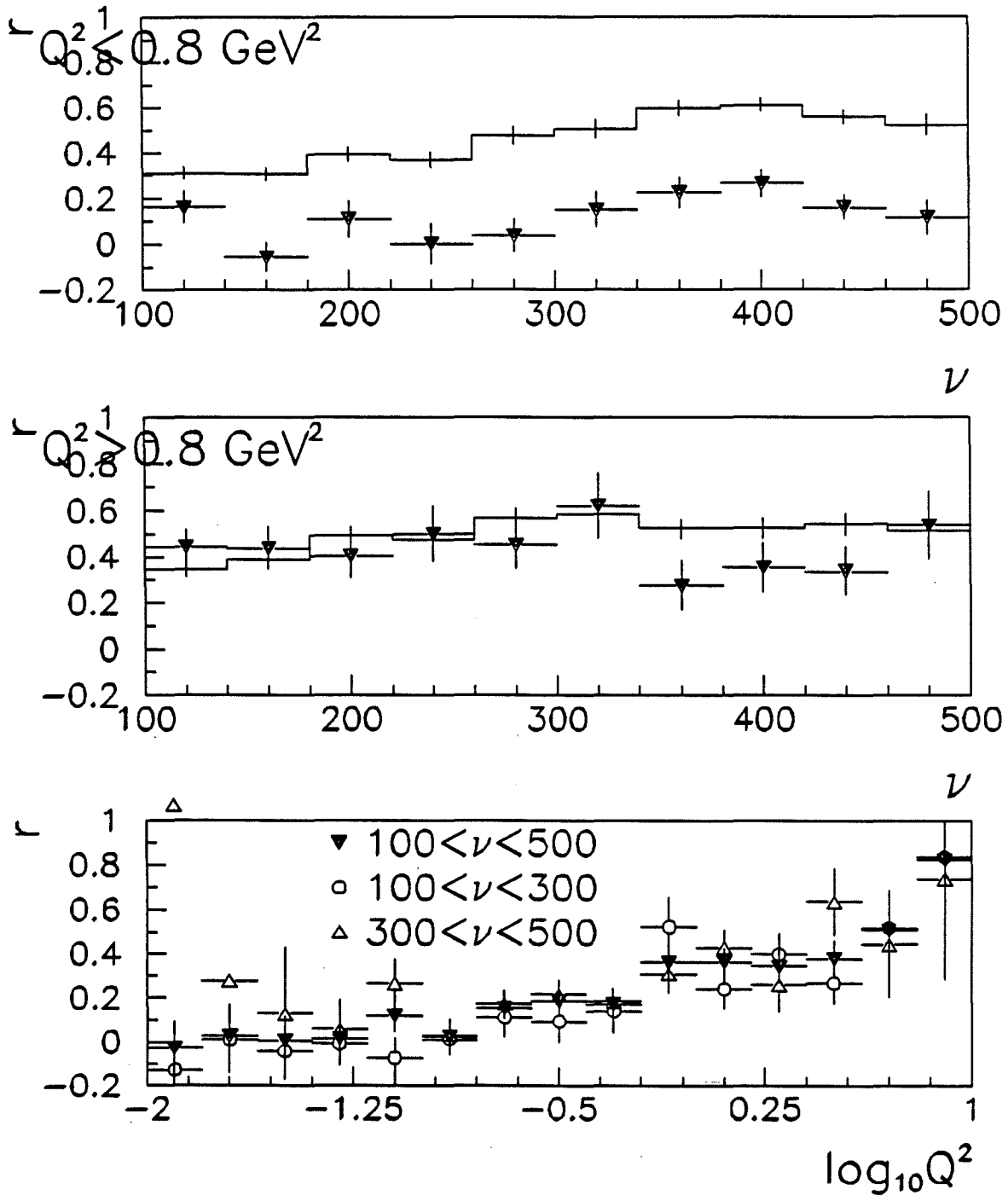
Figure 6.66: Variation of r with ν. The top plot is made with the cut $Q^2 < 0.8$ GeV^{-2}, the second, with $Q^2 > 0.8$ GeV^{-2}. The bottom plots compares r with $\log Q^2$, for three ν intervals.
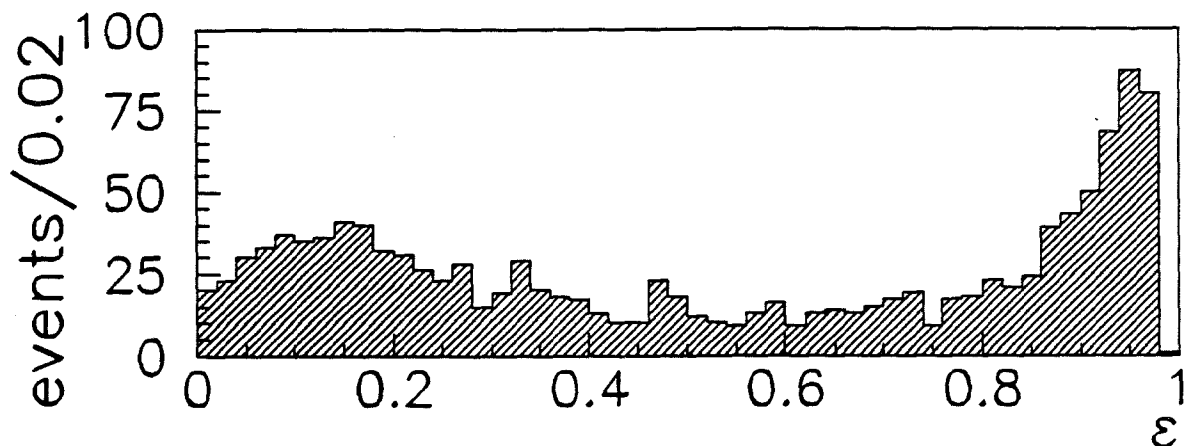
Figure 6.67: Distribution of the photon polarization parameter ϵ.

where $w \equiv E'/E = 1 - y_{Bj}$. The distribution of ϵ for these data is shown in figure 6.67. The fact that r does not depend on ν implies that it is independent of ϵ also. The variation of $\langle\epsilon\rangle$ with $\log Q^2$ is shown in figure 6.68a. It is small for the high-ν interval, and large for the low-ν interval, as shown in plot b. The slight variation of r with ϵ, shown in figure 6.68c, is a reflection of the slight variation of Q^2 with ϵ, shown in plot d. (This variation is a consequence of the trigger acceptance, not of any physics.)

6.5 Azimuthal Angle ψ

The angle ψ is the angle between the decay plane and the lepton plane. It is calculated from the normals to these planes, as described in an earlier section.

The analysis of the azimuthal angle is more difficult than of the polar angle, for two technical reasons:

1. The smallness of the angles between the muons, and between the pions, makes measurements of the normals to these planes inexact, especially given the large Lorentz boosts involved. The resolution is exacerbated by the fact that the vertex is inside a magnetic field, which couples errors on ψ to errors on the vertex position.

2. ψ is a multi-valued function of the normal vectors. Nonvanishing reconstruction errors tie ψ with $2\pi - \psi$, as illustrated in figure 6.69. Fortunately, $\cos\psi$ and $\cos 2\psi$ are immune to this problem.

342
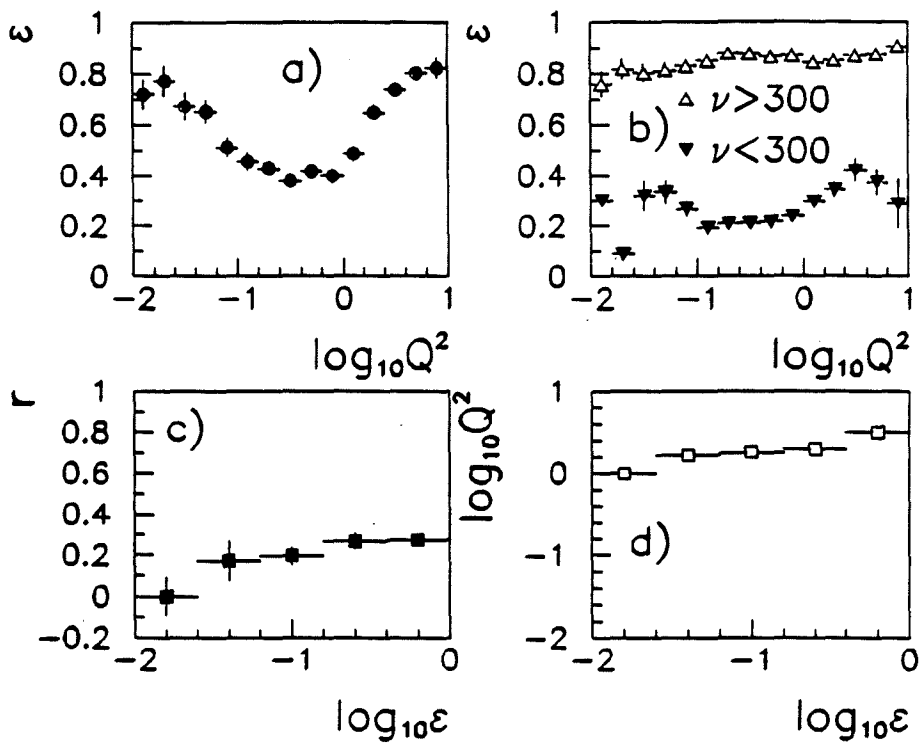
Figure 6.68: Plot a shows the variation of $\langle \epsilon \rangle$ across the range of $\log Q^2$. Plot b shows the same, for low and high ν. Plot c shows the slight variation of r with epsilon, which is a reflection of the slight variation of $\langle \log Q^2 \rangle$ with ϵ, shown in plot d.
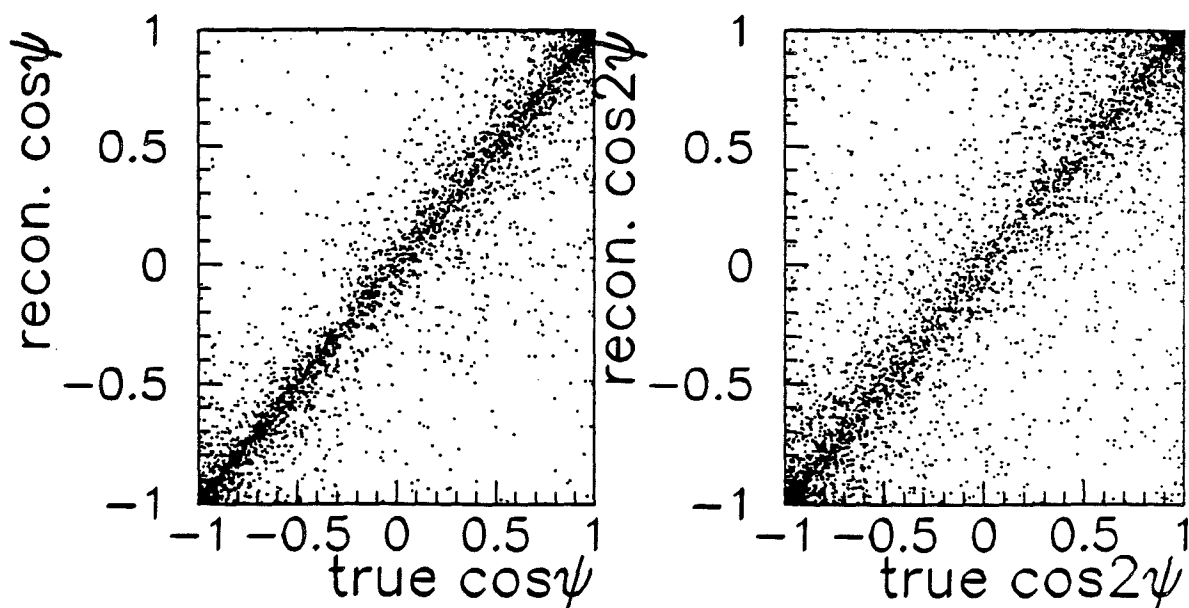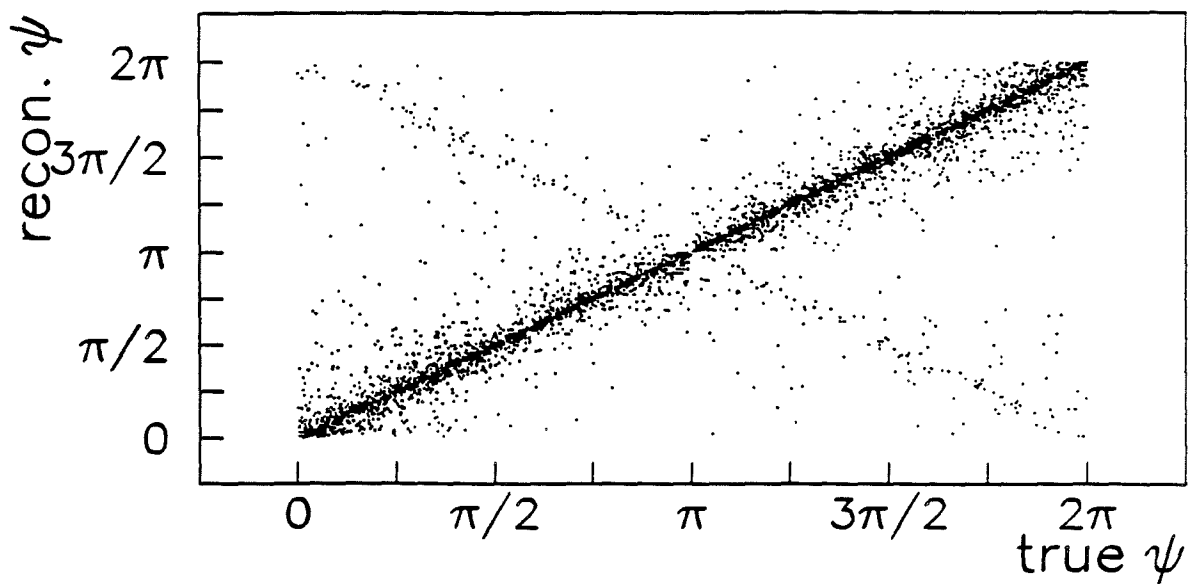
Figure 6.69: The correlation and anticorrelation between the reconstructed and the true values for ψ.

The actual errors on ψ and $\cos\psi$ are shown in the first two plots of figure 6.70.

The acceptance for ψ is flat, as shown in the bottom plot of figure 6.70.

6.6   Momentum Transfer t

Exclusive ρ^0 production by real photons is a diffractive process, which means that the cross section falls rapidly with the momentum transfer squared to the target:

$$\frac{d\sigma}{d|t|} = \sigma_0(Q^2, \nu)e^{-b|t|}$$

where

$$t \equiv (P - P')^2 = (q - v)^2 = (\nu - E_\rho)^2 - (\vec{q} - \vec{v})^2$$

P, P' are the four-momenta of the target before and after the interaction, q is the four-momentum of the photon, and v the four-momentum of the outgoing vector meson. The vector q is calculated from the measured four-momenta of the beam and scattered muons: $q = l - l'$. The four-momentum of the ρ^0 is calculated from the measured momentum of the forward spectrometer tracks: $v = P_1 + P_2$. The energy component is calculated assuming that the tracks are pions.

The resolution on t is dominated by the resolution on ν. As in the case of the invariant mass, the error distribution is asymmetric; the mean error is nonzero at low ν, as shown in figure 6.71. Both the mean error and the width of the error distribution can be decreased by a cut on ν; the mean error is negligible, and the resolution improves by over a factor of two, by demanding $\nu > 200$ GeV, as shown in figure 6.71. For these events, the rms error is $t_{rms} = 0.06$ GeV^2. A Gaussian fit to the central peak gives $\sigma_t = 0.02$ GeV^2.

The inelastic background is an important issue in the measurement of the t distributions, because its distribution is expected to be much flatter. If the contamination is too large, then the apparent slope will be much smaller than the true slope.

The background can be studied in isolation using variations of the energy cut and the invariant mass cut. It also is interesting to check the t distribution of the events generated by the Lund Monte Carlo. Four representations of the background are presented in figure 6.72.

345
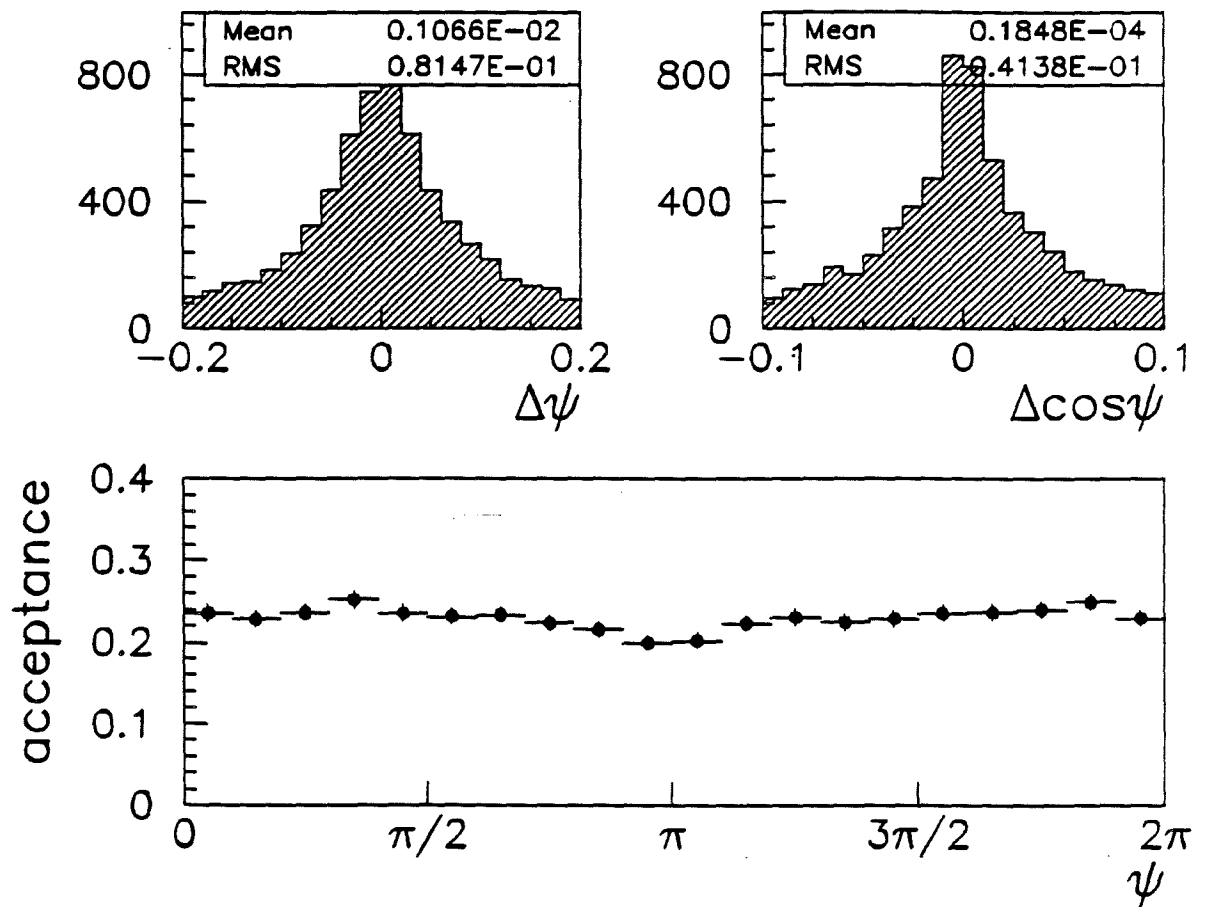
Figure 6.70: Resolution of ψ and $\cos\psi$, and the acceptance, plotted as a function of ψ.
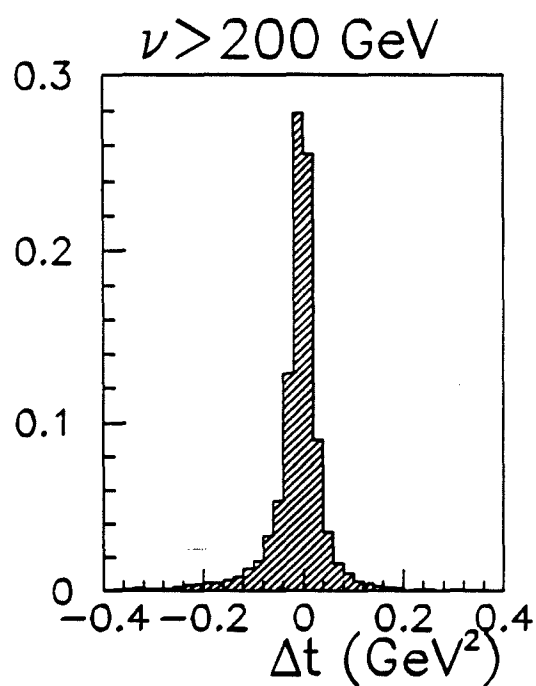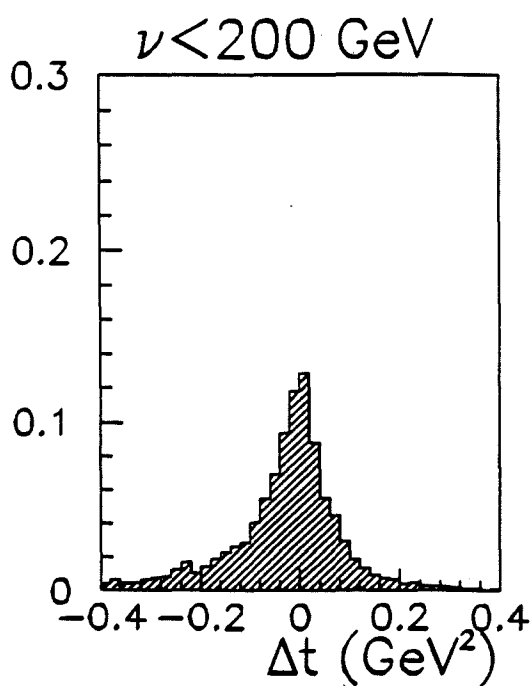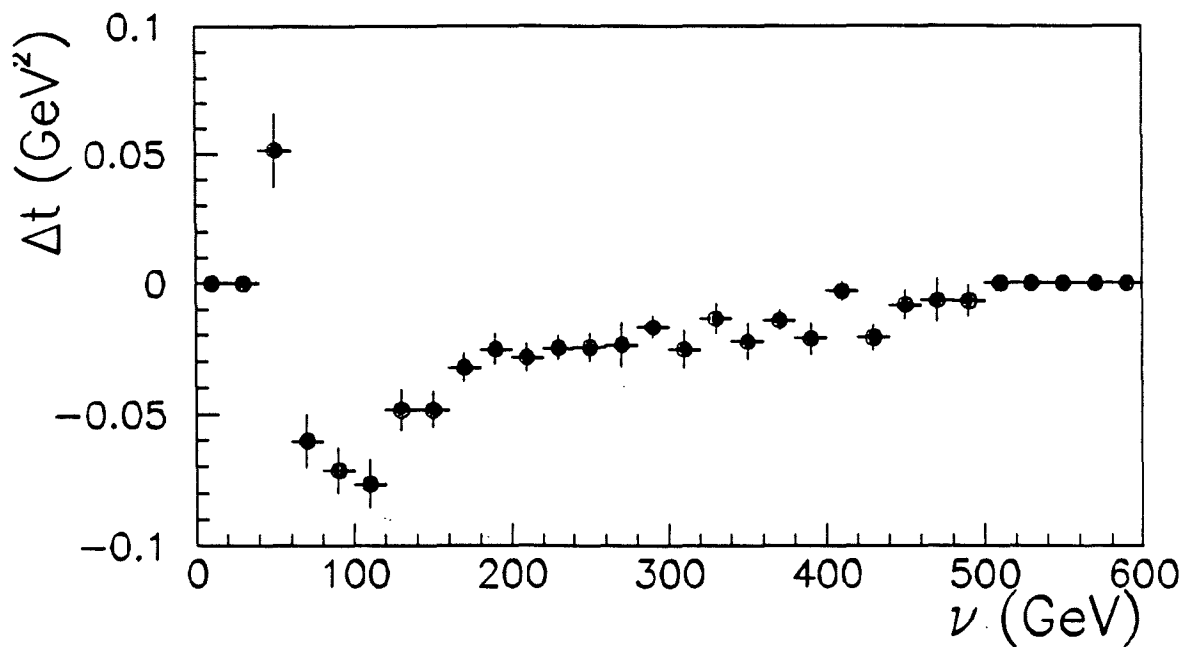
Figure 6.71: The top plot shows the mean error on t plotted as a function of ν. The bottom plots show the improvement of the resolution after a cut $\nu > 200$ is imposed.

a In addition to the mass cut, these events satisfy the converse of the energy conservation cut:

$$\frac{1 - Z_{\text{pair}}}{\sigma_Z} < -5 \quad \text{or} \quad \frac{1 - Z_{\text{pair}}}{\sigma_Z} > 1.$$

The distribution is exponential, with a slope of $b = 0.5$.

b Similar to a), these events satisfy an anti-exclusive energy conservation cut:

$$Z_{\text{pair}} < 0.85 \quad \text{or} \quad Z_{\text{pair}} > 1.05.$$

The distribution is exponential, with a slope of $b = 0.4$.

c These events satisfy

$$Z_{\text{pair}} > 0.5 \quad \text{and} \quad M_{\pi\pi} > 1.4,$$

and display an exponential slope of $b = 0.3$.

d This distribution was made from Lund Monte Carlo events.

These distributions are similar, and compared to the selected exclusive ρ^0 events, quite broad in t. The bottom plot in figure 6.72 compares the t distributions for signal and background.

The finite t resolution distorts the t distribution, in particular, producing entries with $-t < 0$ GeV, as shown in figure 6.73. Further, the presence of a nearly flat background reduces the apparent value of the slope parameter, and increases the mean value of $-t$, illustrated in figure 6.74. This plot was made including a 10% background with $b = 0.5$, and using the measured error distribution on t. Although the distribution of the smeared variable t does not match that of the input variable exactly, it is the same for $-t > 0.1$ GeV^2. In this calculation, the effect of the t resolution and of the background was reduced to less than $\Delta b = 0.5$ if the smeared distribution was fitted to an exponential plus a constant term, for $-t > 0$. The mean smeared t is nearly equal to the mean true t.

The acceptance as a function of t is shown in figure 6.75. It is flat, so no corrections for acceptance are needed.

Since the background is crucial to the study of the t distributions, a check using two energy conservation cuts is useful. Two variations of this cut were discussed earlier in this chapter:

348
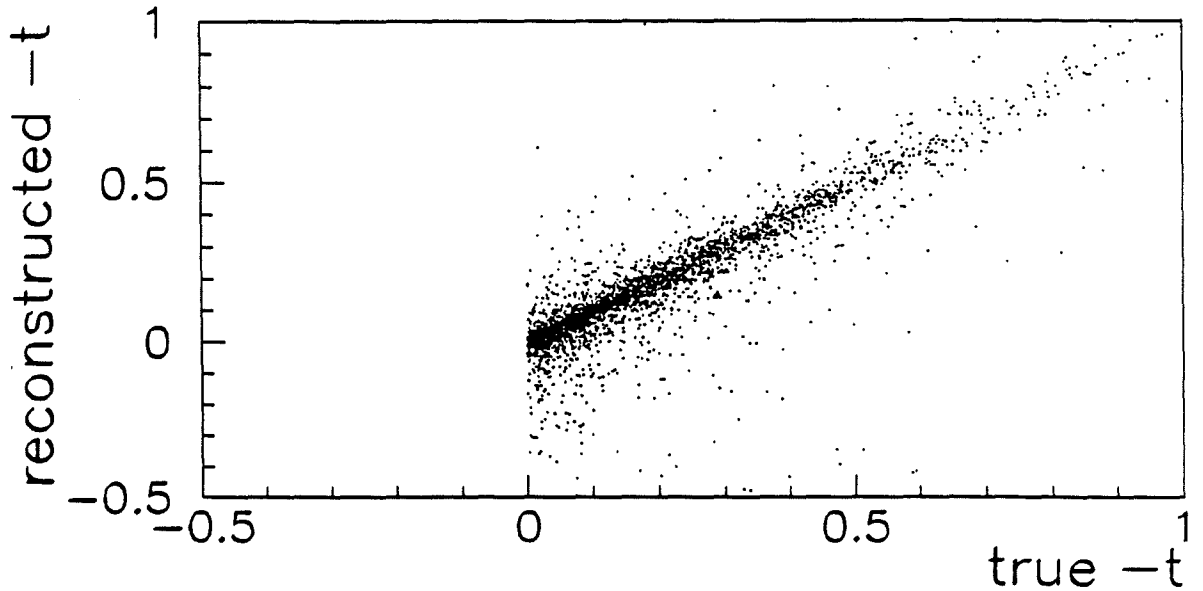
Figure 6.73: Reconstructed versus true $-t$, for selected events with $\nu > 200$ GeV.

1. Z_{pair} cut 1:

$$-5 < \frac{1 - Z_{\text{pair}}}{\sigma_Z} < 1,$$

2. Z_{pair} cut 2:

$$-5 < \frac{1 - Z_{\text{pair}}}{\sigma_Z} < 0.2.$$

The $-t$ distributions for three Q^2 bins, for these two cuts, are shown in figure 6.76. A minimum cut of $\nu > 200$ GeV has been imposed. Each of these can be fitted with an exponential for $-t > 0$,

$$\frac{dN}{-dt} = A e^{bt} + C,$$

with the results listed in table 6.11. The cut on ν has already reduced the background to a small level, as reflected in the fact that the the tighter cut on Z_{pair} has only a small effect. Without the inclusion of the constant term C, the values for b are about 1 GeV^{-2} lower. If the fit excludes the first bin $0 < -t < 0.05$ GeV^{-2}, then the results for the b slope are the same, within errors.

350
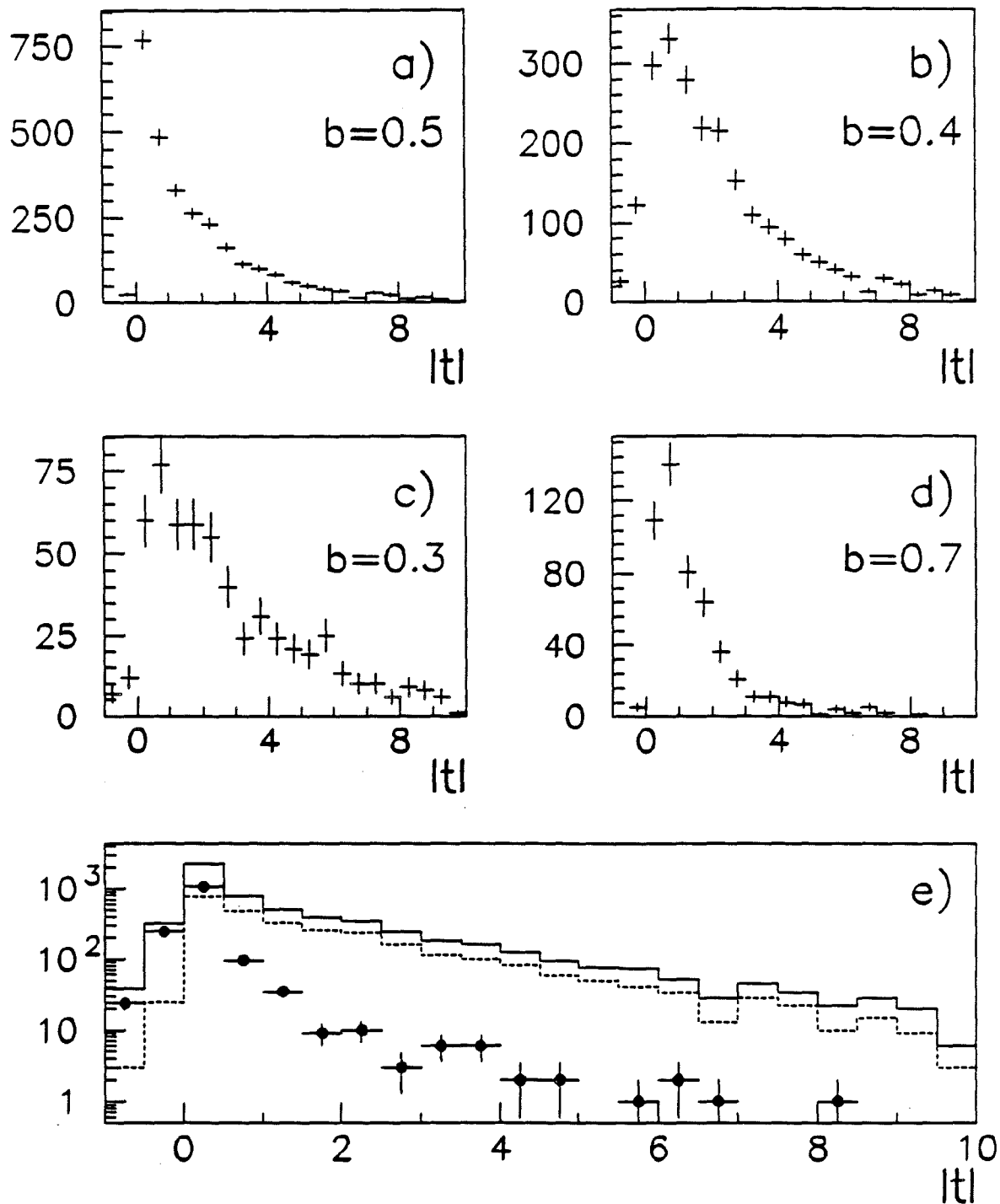
Figure 6.72: Four different estimates of the shape of the background in the $|t|$ distributions, explained in the text. In the bottom plot, the points are the selected events, the dotted line background (type a), and the solid line, the total.
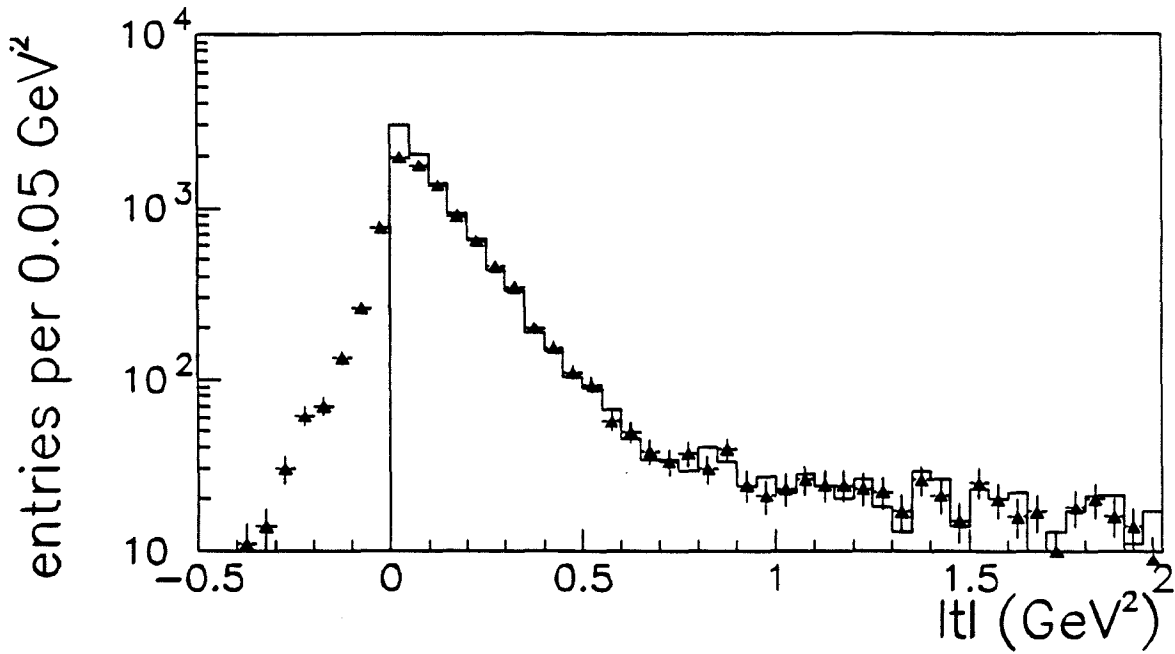
Figure 6.74: Comparison of input t distribution, including background, and smeared t distribution.

Q^2	Z_{pair} cut 1			Z_{pair} cut 2		
range	A	b	C	A	b	C
0.01–0.4	170 ± 14	9.6 ± 0.7	1.5 ± 0.5	107 ± 12	10.0 ± 1.0	1.5 ± 0.6
0.4–1.5	114 ± 11	8.9 ± 0.8	1.0 ± 0.6	68 ± 9	9.0 ± 1.2	0.9 ± 0.6
1.5–20	30 ± 5	7.1 ± 1.5	1.4 ± 0.6	24 ± 6	8.4 ± 2.2	0.9 ± 0.5

Table 6.11: Fit parameters for fits to t distributions, for three ranges of Q^2.
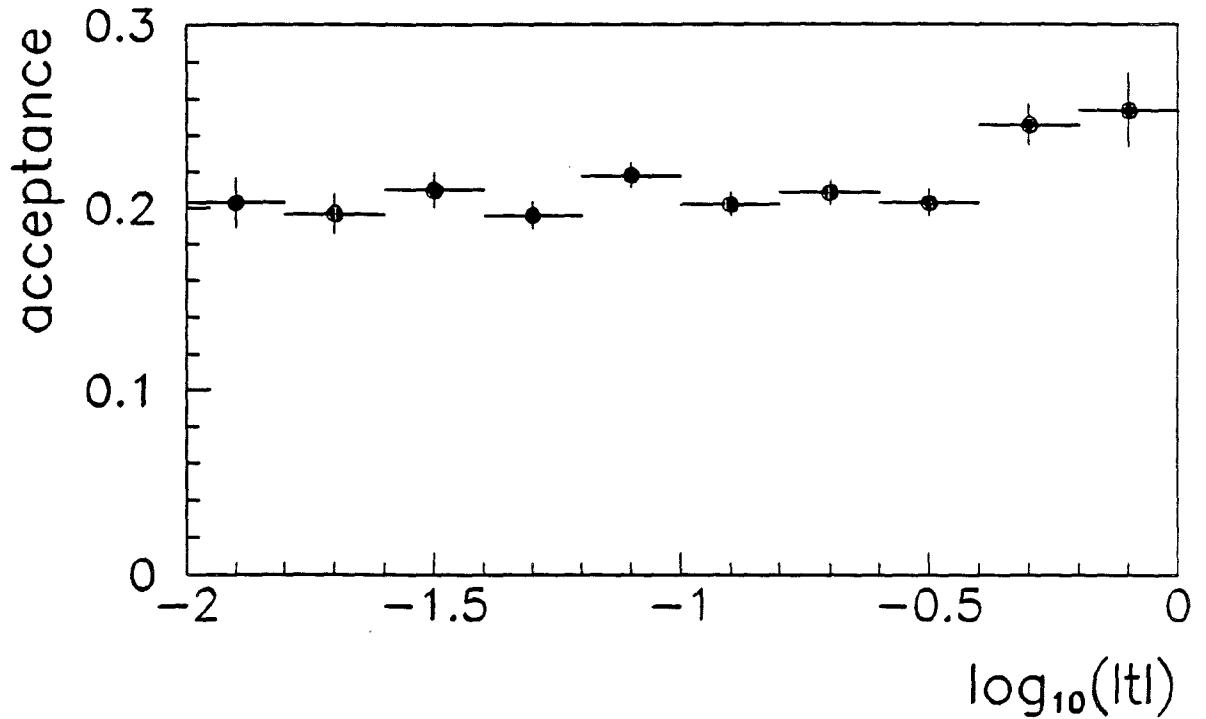
Figure 6.75: Acceptance plotted against log $|t|$.

The effect of the Z_{pair} cut, and of the reduction in background, can be seen in figure 6.77. The mean value of $-t$ is plotted against log Q^2. It appears to increase with Q^2 (which corresponds to the $-t$ distribution flattening out), if the looser of the two cuts is used. When the background is reduced, however, the increase is gone, and the slope parameter becomes independent of Q^2.

The mean value of $-t$ is plotted as a function of the invariant mass in figure 6.78. The Z_{pair} cut 1 was used.
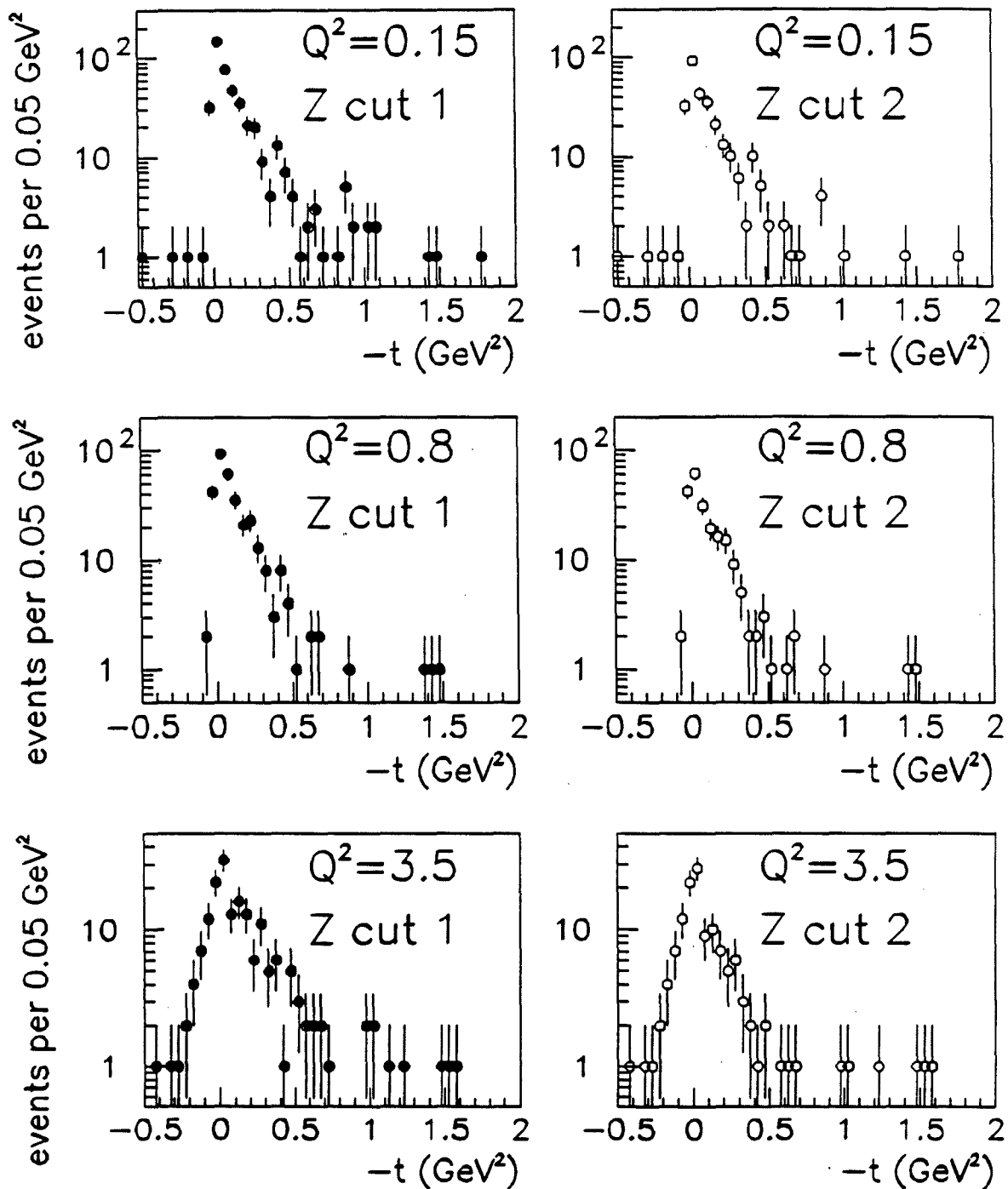
Figure 6.76: A comparison of the t distributions for three bins in Q^2, for Z_{pair} cuts 1 and 2.
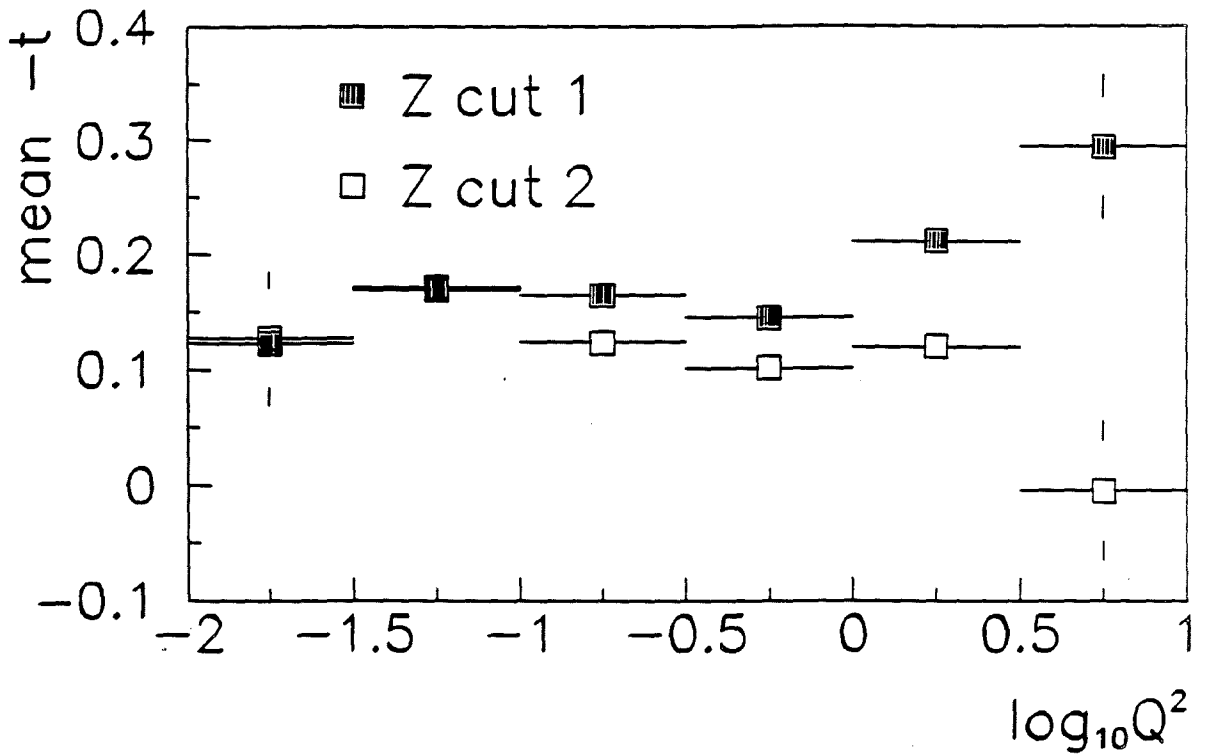
Figure 6.77: Mean $-t$ versus $\log Q^2$, for the two Z_{pair} cuts discussed in the text. There is a requirement $\nu > 200$ GeV.
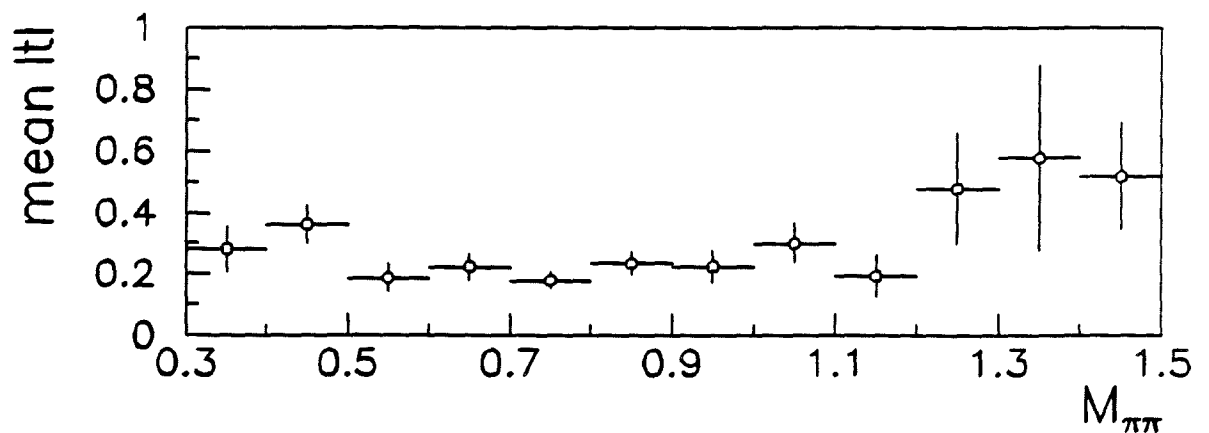
Figure 6.78: Mean $-t$ plotted versus the invariant mass. Z_{pair} cut 1 was used.

Chapter 7

Results

7.1　Mass Fits

The method of finding the optimal value for the interference term was discussed in the previous chapter. The results of that method applied to E665 data are presented here.

The values for the strength of the interference term, f, are listed in table 7.1. The data were binned first in Q^2, then in ν, to look for a variation of f with these variables. As seen from the values in table 7.1, there is no variation with Q^2 or ν. Since there is no dependence on Q^2, and none on ν, all data are combined to give the final result:

$$f = -0.31 \pm 0.10 \pm 0.15,$$

where the first error is statistical, and the second is systematic.

7.2　Decay Distributions

The polarization of the ρ^0 can be determined statistically by measuring the decay distribution of the pions in the ρ^0 rest frame. It is a vector particle, so its wavefunction can be expressed as a sum over $J = 1$ spherical harmonics:

$$\Psi = A_{-1}Y^1_{-1}(\theta,\phi) + A_0 Y^1_0(\theta,\phi) + A_{+1}Y^1_{+1}(\theta,\phi).$$

355

f versus Q^2									
Q^2 range (GeV^2)	interference f	σ_f	N_ρ	Q^2 (GeV^2) mean	rms	ν (GeV) mean	rms	x_{Bj} ($\times 10^{-3}$) mean	rms
$0.01 < Q^2 < 10$	-0.315	0.005	1477	1.30	1.79	250	142	5.9	11.4
$0.01 < Q^2 < 0.1$	-0.301	0.010	198	0.06	0.03	240	105	0.16	0.13
$0.1 < Q^2 < 0.25$	-0.290	0.010	271	0.17	0.04	284	134	0.46	0.40
$0.25 < Q^2 < 0.6$	-0.371	0.010	346	0.40	0.10	290	154	1.1	0.9
$0.6 < Q^2 < 1.6$	-0.329	0.010	291	1.02	0.39	273	148	3.3	3.0
$1.6 < Q^2 < 10$	-0.240	0.010	371	3.84	1.90	177	119	18.9	17.9

f versus ν									
ν range (GeV)	interference f	σ_f	N_ρ	Q^2 (GeV^2) mean	rms	ν (GeV) mean	rms	x_{Bj} ($\times 10^{-3}$) mean	rms
$40 < \nu < 600$	-0.305	0.005	1477	1.30	1.79	250	142	5.9	11.4
$40 < \nu < 100$	-0.335	0.010	312	2.1	2.3	70	17	17.3	19.7
$100 < \nu < 150$	-0.196	0.010	178	1.7	2.1	124	13	7.6	9.1
$150 < \nu < 250$	-0.381	0.010	269	1.4	1.9	198	30	3.9	5.3
$250 < \nu < 350$	-0.383	0.010	252	0.9	1.4	300	29	1.7	2.5
$350 < \nu < 430$	-0.277	0.010	267	0.8	1.1	388	23	1.0	1.4
$430 < \nu < 600$	-0.223	0.010	199	0.7	0.8	470	33	0.7	0.6

Table 7.1: Measured interference strength f for bins in Q^2 and bins in ν.

Since the decay of the ρ^0 into two pions is hadronic, parity is conserved, and the angular distribution of the pions will be given by the modulus of the ρ^0 wave function. If the ρ^0 is polarized transversely ($J_z = \pm 1$, as measured with respect to a given axis), then the polar angle of the decay axis will be distributed as $\sin^2 \theta$, and the azimuthal angle, as $\cos^2 \phi$. If the polarization is longitudinal, however ($J_z = 0$), then the polar angle will be distributed as $\cos^2 \theta$, and the azimuthal angle distribution will be flat. These distributions can be obtained directly from the pion momentum vectors at the vertex.

A careful, and now completely standard, presentation of the decay distribution in terms of θ and ψ is given in [SW73]. Assuming no significant lepton polarization, and assuming s-channel helicity conservation (SCHC), the decay density is:

$$W(\cos\theta, \psi) = \frac{1}{1 + \epsilon R} \frac{3}{8\pi} [(1 + \epsilon \cos 2\psi) \sin^2 \theta + 2\epsilon R \cos^2 \theta$$
$$- \sqrt{2\epsilon(1 + \epsilon)R} \cos \delta \sin 2\theta \cos \psi]. \tag{7.1}$$

In this expression, $R = \sigma_L/\sigma_T$ is the ratio of longitudinal to transverse cross sections. Within s-channel helicity conservation (SCHC), it is related to the ρ^0

polarization r according to

$$R = \frac{1}{\epsilon} \frac{r}{1 - r}.$$

Within the context of the vector dominance model,

$$R = \xi^2 \frac{Q^2}{N_\rho^2},$$

that is, it increases linearly with Q^2. The parameter δ measures the relative phase between the amplitudes for the production of transverse and longitudinal ρ^0s.

A real photon with $Q^2 = 0$ cannot be polarized longitudinally. The virtual photons absorbed by the target nucleons, however, can acquire a longitudinal polarization because they are massive: $Q^2 > 0$.[1] If the polarization of the virtual photon is preserved by the interaction, as expected if it is mediated by a pomeron, then the longitudinal polarization of the photon may appear in the decay distribution of the pions. Although the polarization of the photon is mainly transverse unless the energy transfer is large ($y_{\text{Bj}} \rightarrow 1$), the cross sections for the absorption of transverse and of longitudinal photons are independent; the latter perhaps growing rapidly as a function of Q^2.

Several studies of exclusive ρ^0 production with real photons have shown that the ρ^0 is pure transverse in the "helicity frame," independent of the invariant mass and of the momentum transfer t. This is the nucleon–ρ^0 center-of-mass frame, and the ρ^0 momentum vector is taken to be the axis of quantization. Studies with virtual photons indicate that this still is true for $Q^2 < 1$ GeV^2. If the soft, hadronic component of the photon wave function dominates at low Q^2, but eventually is replaced by the hard, point-like interactions of the bare photon as Q^2 increases above 1 GeV^2, does the net polarization fade away?

7.2.1   Polar Decay Distribution

The polar decay angle θ is measured in the ρ^0 rest frame. $\cos \theta$ is the cosine of the angle between the momentum vector of the positive pion and the quantization axis.

The data have been divided among three Q^2 bins:

$$0.01 < Q^2 < 0.4 \qquad 0.4 < Q^2 < 1.5 \qquad 1.5 < Q^2 < 20 \text{ Gev}^2,$$

---

[1] In fact they have negative invariant mass.

Q^2 range	$\langle Q^2 \rangle$	r
0.01–0.4	0.2	$(7.6 \pm 2.5) \times 10^{-2}$
0.4–1.5	0.8	0.23 ± 0.04
1.5–20	4.3	0.51 ± 0.04

Table 7.2: Fit results for the ρ^0 polarization measured for three ranges of Q^2.

and the distribution of the polar decay angle plotted for each bin. These distributions are displayed in figure 7.1. They were fitted to an expression representing the normalized decay density integrated over the azimuthal angles:

$$W(\cos\theta, r) = \frac{3}{4}[(1-r) + (3r-1)\cos^2\theta],$$

with r the free parameter in the fit. The results are summarized in table 7.2.

The polarization parameter r also can be determined from moments of the polar decay distribution, as plotted in figure 7.2. The three values from the explicit fits are shown, also.

Plainly, the polarization parameter increases from $r = 0$ at very low Q^2, to $r > 0.5$ at higher Q^2. This signifies a shift in the polarization of the ρ^0 from transverse polarization near photo-production, to longitudinal polarization in the "deep–inelastic" ($Q^2 > 1$ GeV^2, $W \gg 1 - 2$ GeV^2) regime.

This shift does not increase with a change in the polarization of the virtual photon, as it is independent of the photon polarization parameter, ϵ. This fact is illustrated in figure 7.3, where the value of r, determined using the moments technique, is plotted versus ϵ. It essentially is flat; the level is tuned by varying Q^2. The bottom two plots show graphically that transverse ρ^0 polarization (concave down), and longitudinal polarization (concave up), depend on the range of Q^2, not on ϵ.

7.2.2 Azimuthal Decay Distribution

The azimuthal angle ϕ about the quantization axis is the angle between the decay plane and the production plane. Similarly, Φ is the angle between the production plane and the lepton plane. Since the polarization vector of the virtual photon lies in the lepton plane, the distribution of the angle between the decay plane and the lepton plane, $\psi = \phi - \Phi$, is studied. If the full decay density (equation 7.1) is integrated over $d(\cos\theta)$, then a simple expression for the ψ decay distribution is
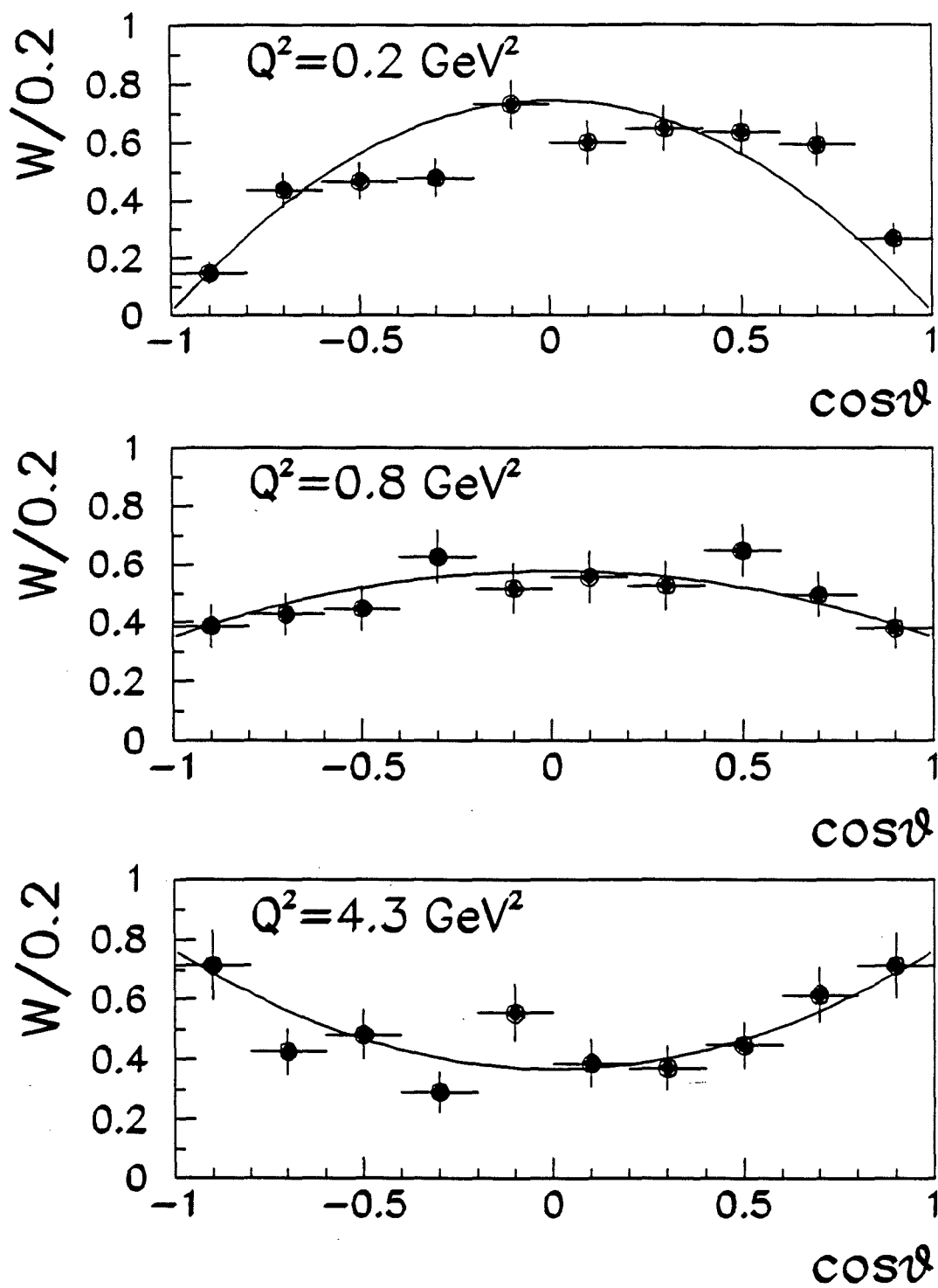
Figure 7.1: Distribution of $\cos\theta$, where θ is the polar decay angle, for three Q^2 bins.
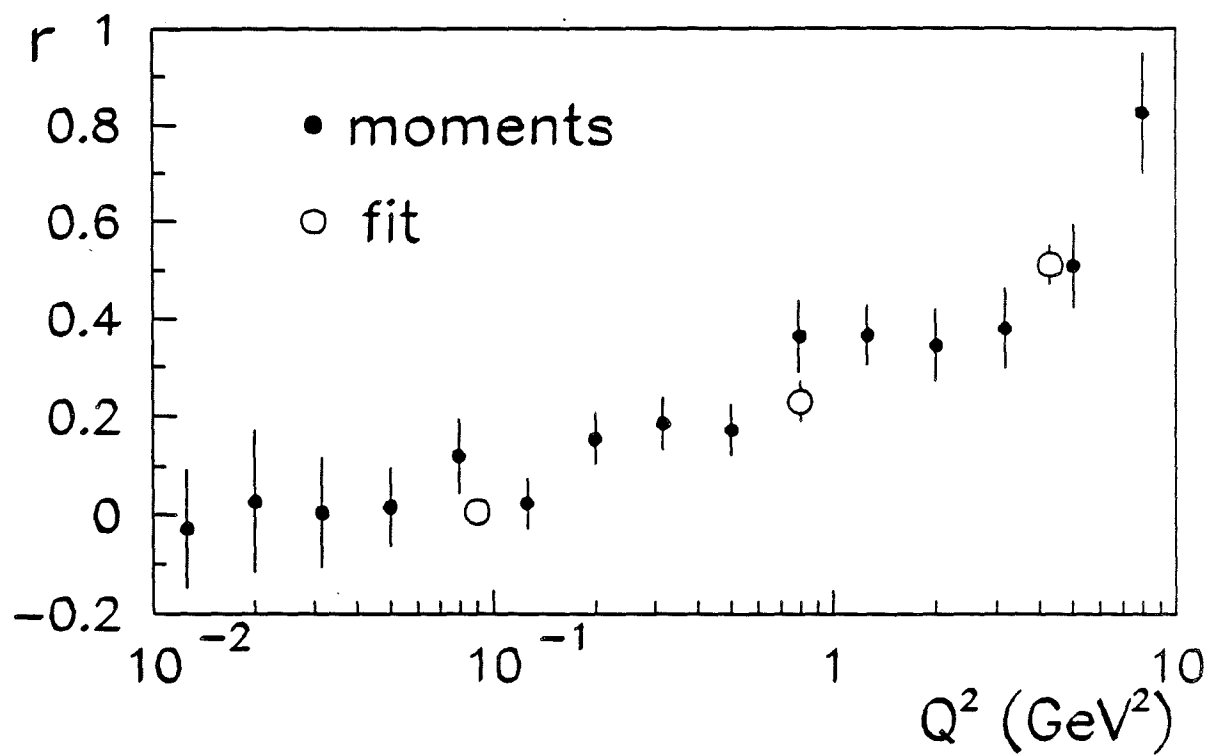
Figure 7.2: Increase of the polarization parameter r with Q^2. The three open circles are the values obtained form the fit.
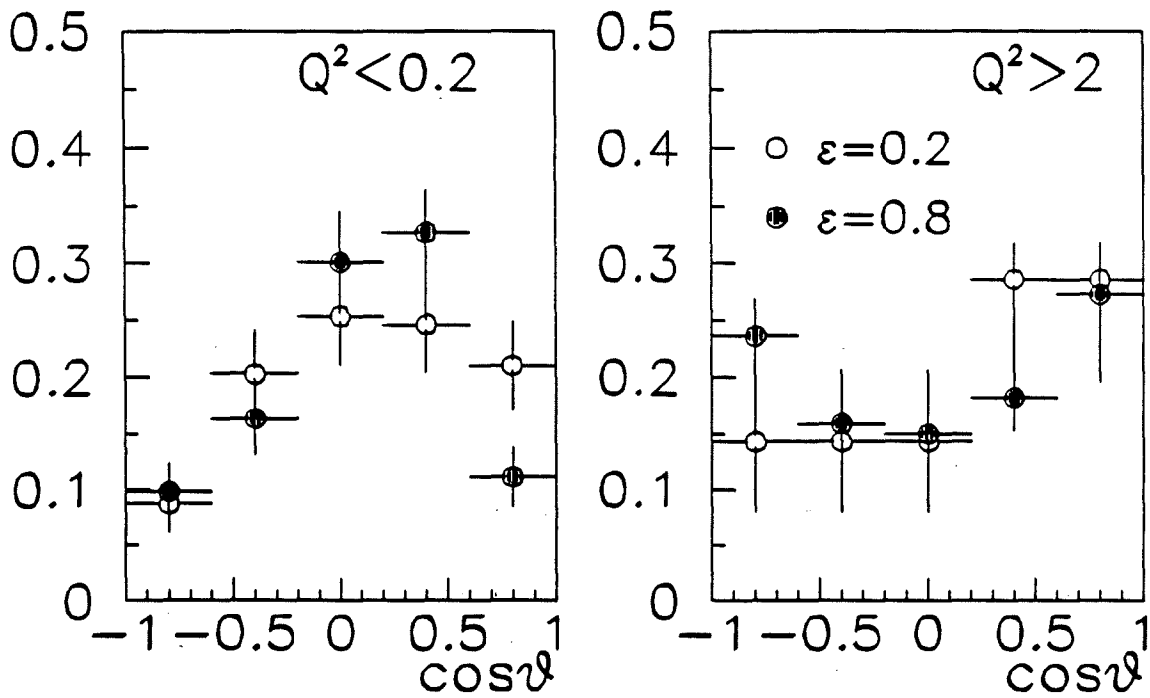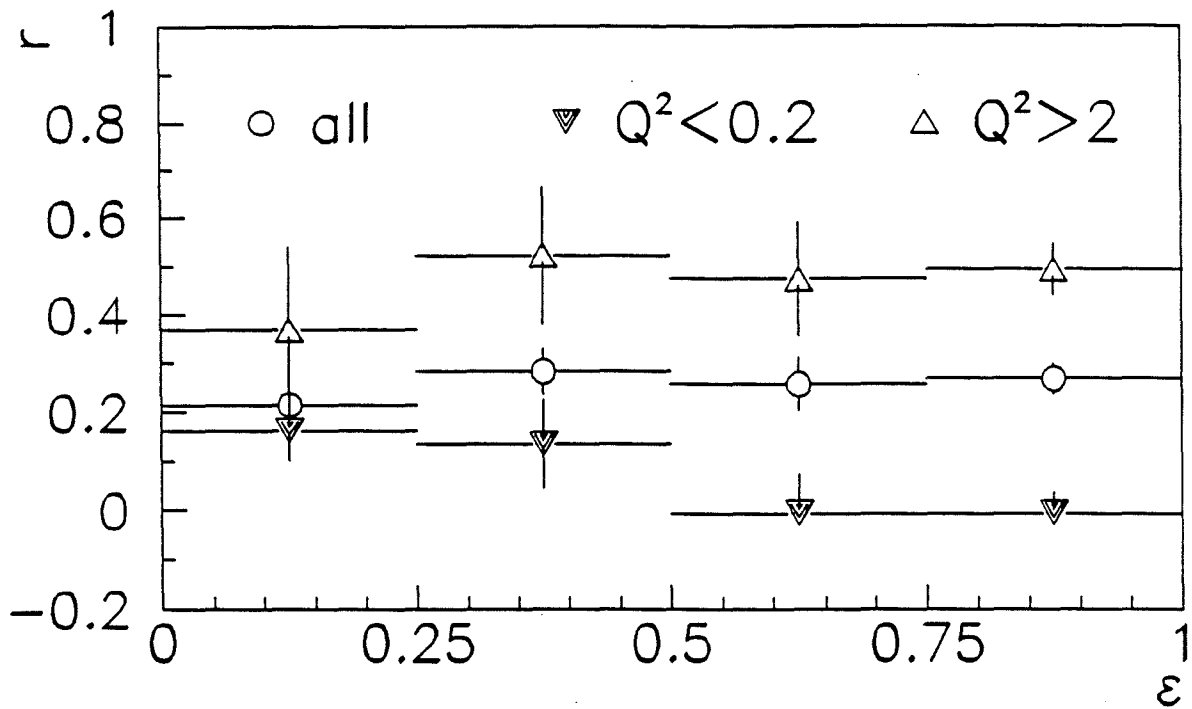
Figure 7.3: Illustration that the variation of r depends on Q^2, not ϵ.

found:

$$W(\psi, \epsilon, R) = (1 + \epsilon R) \left[1 + \frac{\epsilon}{1 + \epsilon R} \cos 2\psi \right].$$

The distribution of ψ is shown in figure 7.4, along with a fit to the expression

$$N(\psi) = A(1 + b \cos 2\psi),$$

where $A = 62 \pm 2$, and $b = 0.32 \pm 0.03$.

The longitudinal-transverse interference term may be isolated by weighting the events with $\cos \theta$, in which case the density becomes

$$W(\psi, \epsilon, R)|_{\cos \theta} = -\frac{1}{15} \sqrt{2\epsilon R(1 + \epsilon)} \cos \delta \ \cos \psi.$$

The distribution in ψ when the events are weighted by $\cos \theta$ is shown in figure 7.5, along with a fit to the expression

$$N'(\psi) = A + B \cos \psi,$$

with $A = 3.0 \pm 0.2$ and $B = 17.2 \pm 0.3$.

7.2.3 Two-Dimensional Decay Distribution

Since the resolution on $\cos \theta$ and on ψ is good, it is possible to show the distribution of events for $\cos \theta$ and ψ jointly. The data were divided into two extreme bins: $0.01 < Q^2 < 0.2$ GeV^2, for which $\langle Q^2 \rangle = 0.09$ GeV^2, and $2 < Q^2 < 20$ GeV^2, for which $\langle Q^2 \rangle = 3.5$ GeV^2. The two-dimensional distributions for these two bins are displayed in figure 7.6. A change takes place, in that for virtual photons near mass shell, there is little correlation between ψ and $\cos \theta$: the distribution resembles $\sin^2 \theta \cos 2\psi$. For higher Q^2, however, a separation takes place, in which ψ near π correlates strongly with $\cos \theta \to -1$, and ψ near 0 or 2π correlates with $\cos \theta \to 1$. Physically, this indicates that the positive pion "prefers" the scattered muon over the beam muon. Projections of the ψ distribution for $\cos \theta > 0$ (positive pion is forward), and $\cos \theta > 0$ (positive pion is backward), are shown in figure 7.7.

These densities in fact follow expectations within the expression 7.1; figure 7.8 shows the change in the distribution as R, expected to be proportional to Q^2, increases.
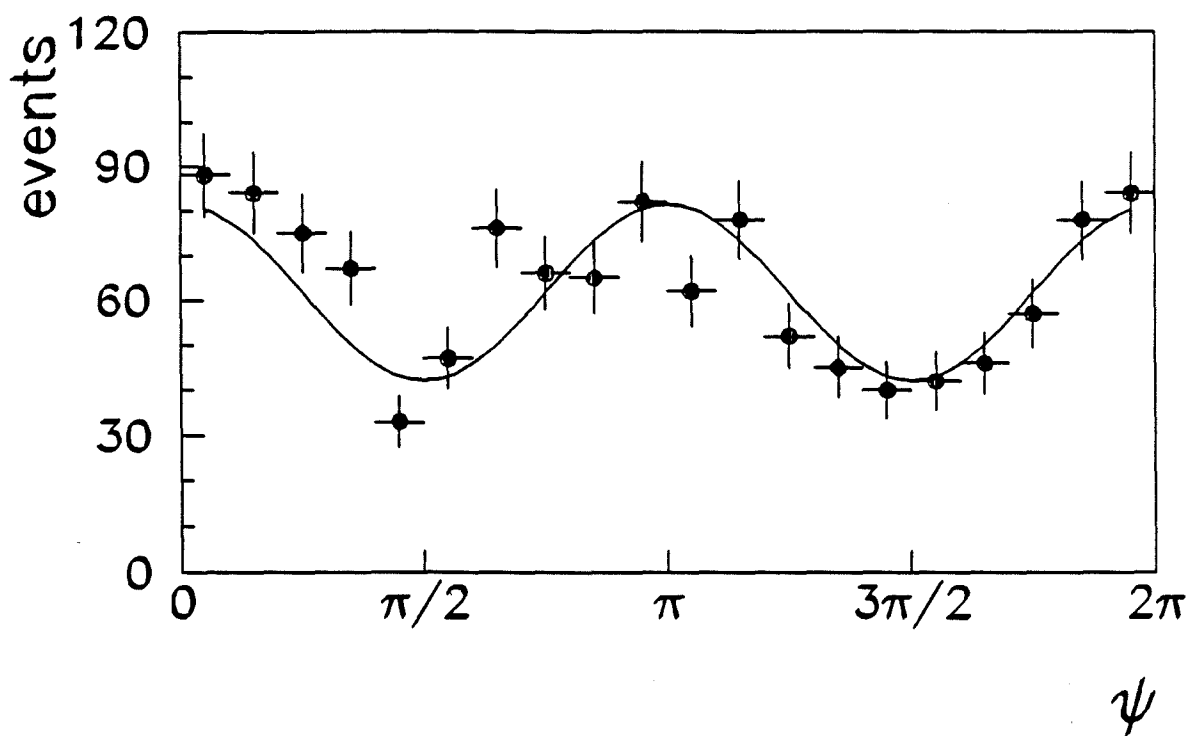
Figure 7.4: Azimuthal decay distribution, with a fit to $A(1 + b \cos 2\psi)$.
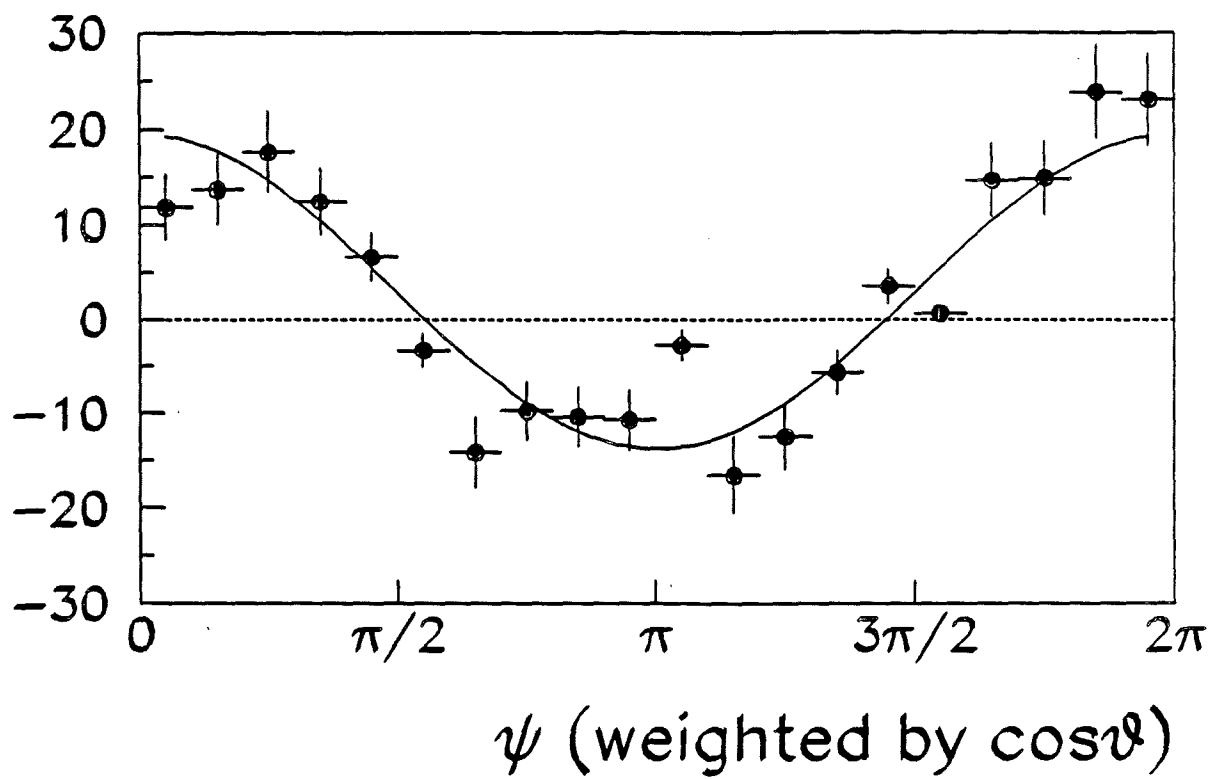
Figure 7.5: Azimuthal decay distribution, weighted by $\cos\theta$. The curve is a fit to $A + B\cos\psi$).
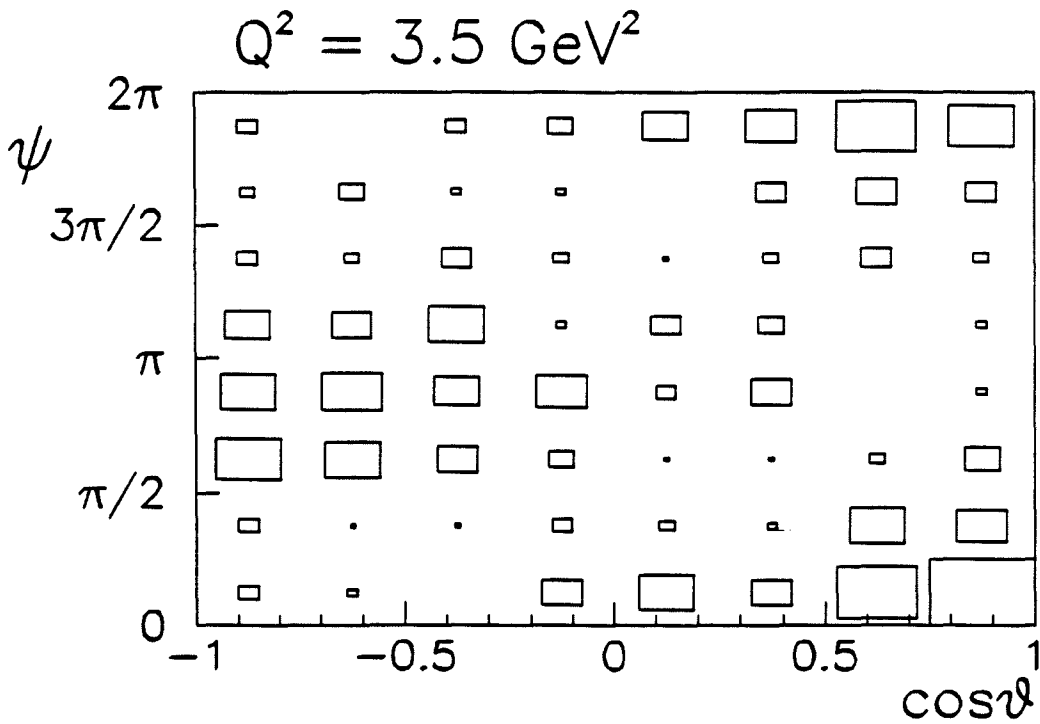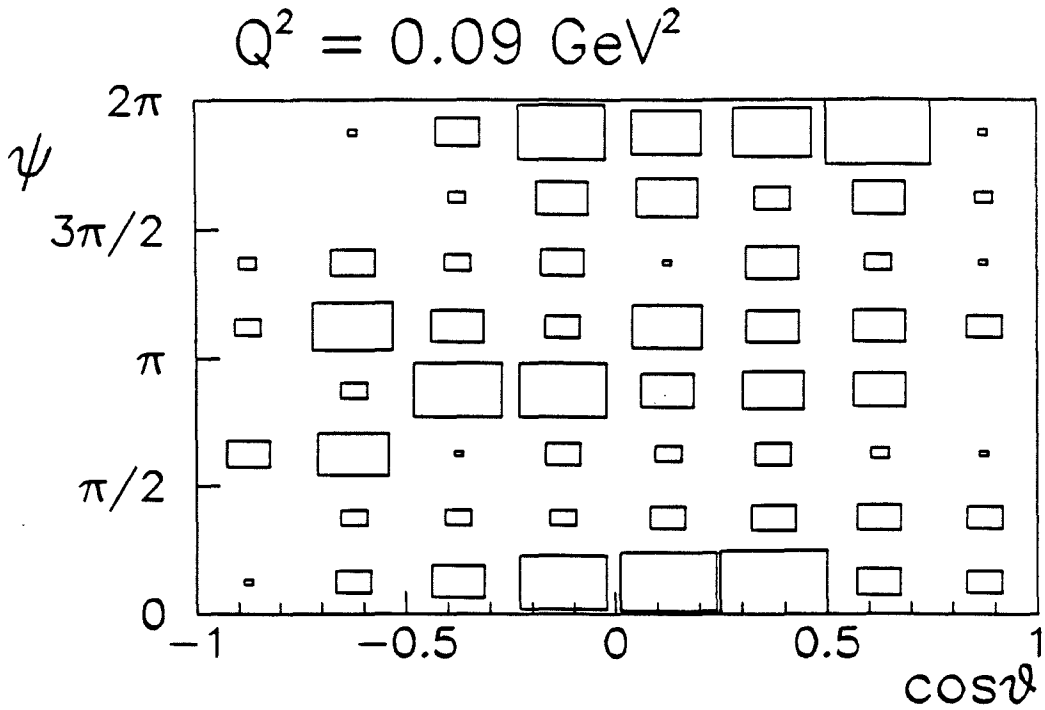
Figure 7.6: Two-dimensional decay distributions (ψ versus $\cos\theta$), for two extremes in Q^2.
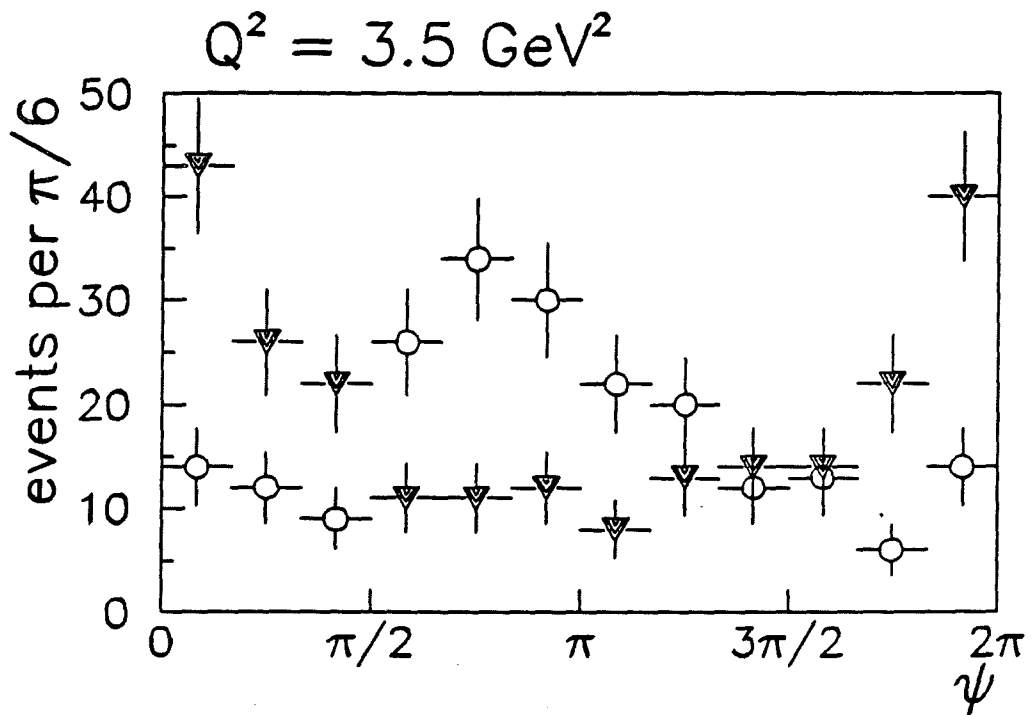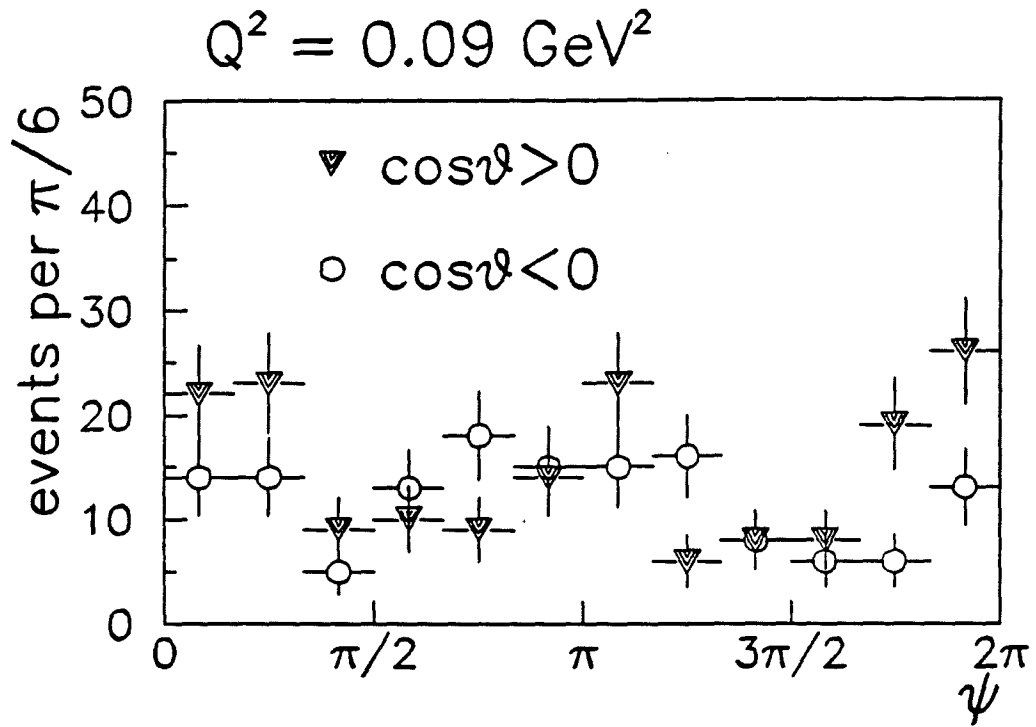
Figure 7.7: Two-dimensional decay distributions projected for $\cos\theta < 0$ and $\cos\theta > 0$, for both Q^2 bins.
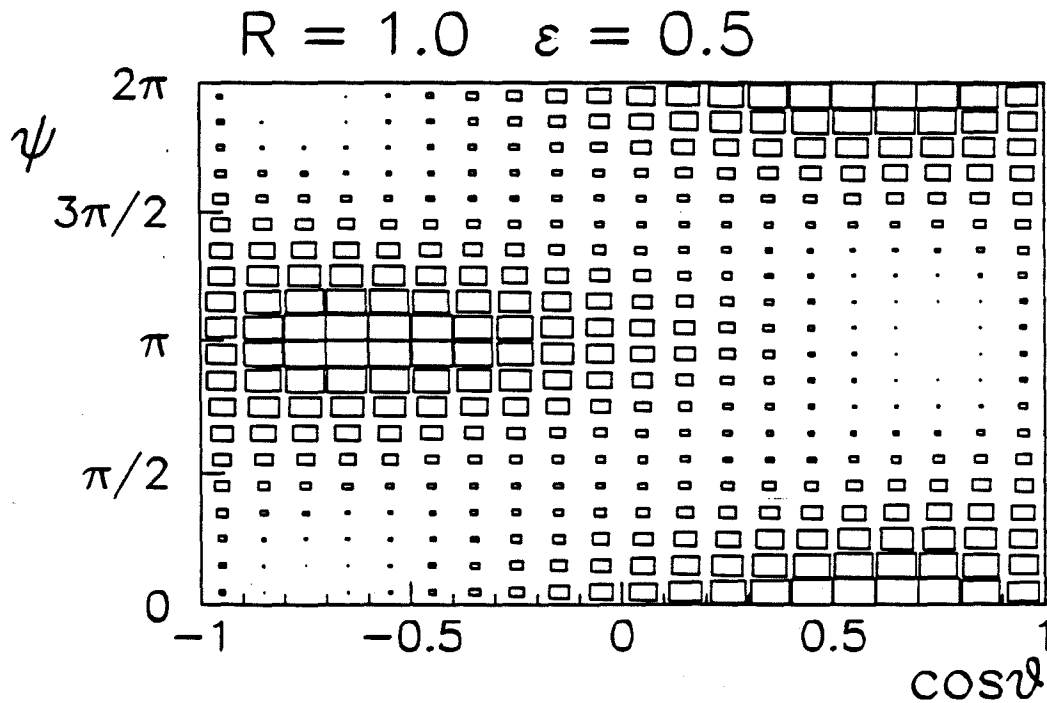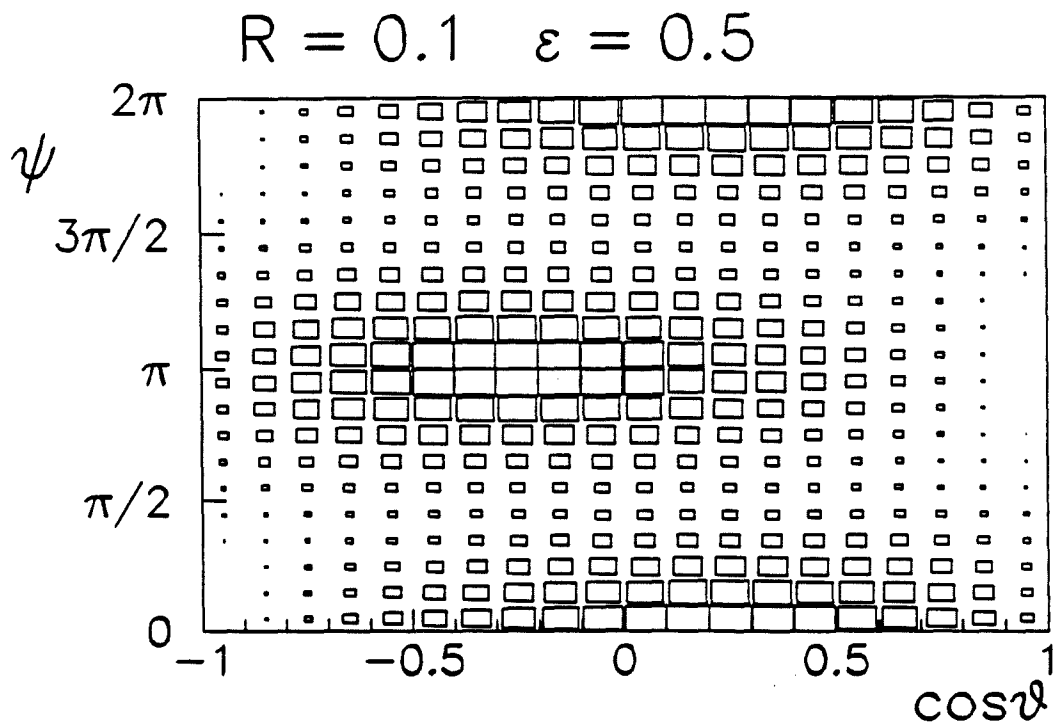
Figure 7.8: Two-dimensional decay density, for two values of R, according to expression 7.1. $(\cos \delta = -1.)$

| Q^2 range (GeV^2)	mean Q^2 (GeV^2)	slope parameter b (GeV^{-2})
0.01–0.4	0.2	10.0 ± 1.0
0.4–1.5	0.8	9.0 ± 1.2
1.5–20	3.8	8.4 ± 2.2

Table 7.3: Slope parameter b for three Q^2 bins.

7.3 Momentum Transfer t

Exclusive ρ^0 production by real photons is a diffractive process: the cross section is peaked in the forward direction, meaning that it falls rapidly with the momentum transfer to the target:

$$\frac{d\sigma}{d|t|} = \sigma_0(Q^2, nu)e^{-b|t|}$$

where

$$t \equiv (P - P')^2 = (q - v)^2.$$

P, P' are the four-momenta of the target before and after the interaction, q is the four-momentum of the photon, and v the four-momentum of the outgoing vector meson.

Experiments have shown that the value of the slope parameter b falls in the range $8 - -10$ GeV^{-2}, which is similar to the values observed in elastic pion-proton scattering. This similarity is one of the basic motivations for the Vector Dominance Model.

According to experiment, exclusive ρ^0 production by virtual photons at low Q^2 is also a diffractive process. There are suggestions that the slope parameter b should decrease with Q^2; that the photon "shrinks" with Q^2, as the soft hadronic structure becomes less and less significant, and the hard, point-like nature of the photon emerges. An analysis published by the EMC [Aub85, Ash88] indicates that the slope parameter falls to a value of about two, for $Q^2 > 5$ GeV^2. This result has caused some controversy [Cud90].

These data were divided among three Q^2 bins, and using the tight energy conservation cut, and demanding $\nu > 200$ GeV, three relatively clean distributions in $-t$ are obtained, as shown in figure 7.9. These can be fitted by the form

$$N(-t) = A \ \exp(bt) + C,$$

with the results listed in table 7.3.
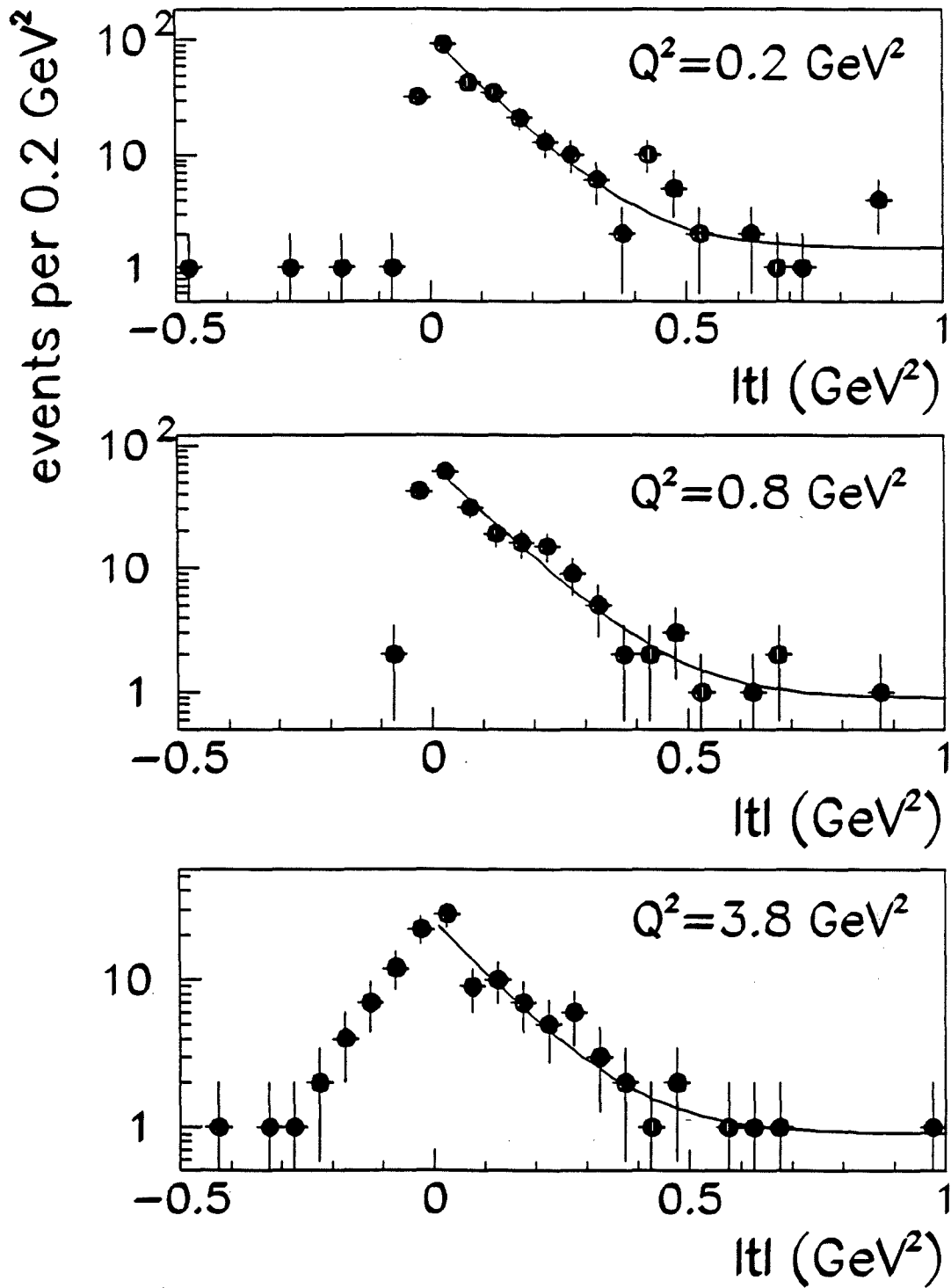
Figure 7.9: Distributions of the momentum transfer t, for three bins in Q^2. The curves are exponential fits with a constant background term, and are restricted to $-t > 0$.

These values are somewhat higher than those observed in experiments on hydrogen due to the contamination of coherent ρ^0 production off the deuteron. This contamination is expected to decrease with Q^2, due to the fall-off of the deuteron elastic form factor. Nonetheless, it is clear that the slope parameter does not decrease to a value of $b \approx 2$ GeV^{-2}, as reported by [Aub85].

7.4 Conclusions

Production of exclusive ρ^0 and ϕ mesons has been observed in the inelastic scattering of high energy muons on hydrogen and deuterium targets. The invariant mass distribution requires the presence of a term representing the interference between the resonance and the continuum production of two-pion states. The strength of this interference term appears to remain constant with Q^2 and ν.

The polarization of the ρ^0 is seen to change from a transverse polarization at low Q^2, to a dominantly longitudinal polarization at high Q^2. The azimuthal decay distribution has the form $\cos 2\psi$. The interference between the transverse and longitudinal terms is observed in the decay distribution.

The production of ρ^0 mesons is a diffractive process, even at high Q^2, where the virtual photon is expected to behave as a point-like probe. Little, if any, shrinkage is observed.

Bibliography

[ABBHHM]   ABBHHM Collaboration (DESY). Photoproduction of meson and baryon resonances at energies up to 5.8 GeV. *Physical Review*, 175:1669–1696, 1968.

[Aïd]   Silhacène Aïd. *Measurement of the ratio of neutron cross-section to proton cross-section in muon deep inelastic scattering at 490 GeV*. PhD thesis, University of Maryland, September 1991.

[Ada86]   Mark Adams. SAT MWPCs. memo BT020, E665, July 1986.

[Ada89]   Mark Adams. In-time change SB. talk ST0203, E665, June 1989.

[Ada90]   M. R. Adams *et.al.* E665 Collaboration. A spectrometer for muon scattering at the Tevatron. *Nuclear Instruments and Methods*, A291:533–551, 1990.

[Ant89a]   Perry Anthony. Muon mathing. software talk ST0149, E665, February 1989.

[Ant89b]   Perry Anthony. The utility match pam (UMPAM). document SW082, E665, April 1989.

[Anthony] Perry Lee Anthony. *Bose-Einstein Correlations in Deep-Inelastic Muon Scattering*. PhD thesis, Massachusetts Institute of Technology, September 1990.

[Ash88]   J. Ashman *et.al.* (EMC). Exclusive ρ^0 and ϕ production in deep inelastic muon scattering. *Zeitschrift für Physik*, C39:169, 1988.

[Ast82]   D. Aston *et.al.* (CERN). Photoproduction of ρ^0 and ω on hydrogen at photon energies of 20 to 70 GeV. *Nuclear Physics*, B209:56–76, 1982.

[Aub85]   J.J. Aubert *et.al.* (EMC). Exclusive ρ^0 production in deep inelastic $\mu - p$ interactions. *Physics Letters*, 161B:203–210, 1985.

371

[DL87]   A. Donnachie and P. V. Landshoff. Exclusive rho production in deep inelastic scattering. *Phys.Lett.*, B185:403–406, 1987.

[Eck73]   V. Eckardt *et.al.* (DESY). Electroproduction of ρ^0 mesons at $0.3 < Q^2 < 1.5$ GeV^2 and $1.7 < W < 2.8$ GeV. *Physics Letters*, 43B:240–244, 1973.

[Eck85]   Volker Eckart. Streamer chamber system. memo VS012, E665, October 1985.

[Ecker]   Uwe Ecker. *Longitudinale und transversale Impulsverteilingen der Hadronen im Endzustand der tiefinelastischen Myon-Nukleon-Streuung*. PhD thesis, Bergische Universität Gasamthochschule Wuppertal, January 1991.

[Edw85]   Helen T. Edwards. The tevatron energy doubler: A superconducting accelerator. *Ann.Rev.Nucl.Part.Sci.*, 35:606–660, 1985.

[Erdmann]   Martin Erdmann. *Lebensdauer des Farbigen Protons in der Myon-Proton-Streuung*. PhD thesis, Albert-Ludwig-Universität Freiburg i.Brsg., March 1990.

[Fra77]   W. R. Francis *et.al.* (Fermilab E98). Diffractive production of ρ mesons by 147-GeV muons. *Physical Review Letters*, 38:633–636, 1977.

[Fen83]   H. Fenker. A standard beam PWC for Fermilab. memo BT005, E665, February 1983.

[FM85]   Y. Fukui, M. Mishina, and *et.al.* Sources for proportional tube gain variation – what to do about it. pages 1–19, 1985.

[GJ64]   K. Gottfried and J. D. Jackson. On the connection between production mechanism and decay of resonances at high energy. *Il Nuovo Cimento*, 33:309, 1964.

[Hei36]   Walter Heitler, editor. *The Quantum Theory of Radiation*. Oxford University Press, London, 1936. QC475.H365 1944.

[Iar83]   E. Iarocci. Plastic streamer tubes and their applications in high energy physics. *Nucl. Inst. Meth.*, 217:30–42, 1983.

[Iwa90]   Sergei Iwata. appendix 2. In *Report of the Tristan ep (e$^+$e$^-$) Working Group*, KEK, Japan, July 1990. KEK.

[Jaf89]   David Jaffe. The 1990 small angle trigger. memo BT087, E665, September 1989.

[Jaf90]   David Jaffe. Preliminary measurements of shadowing at very low x_{Bj}. In *Moriond Conference*, Les Arcs, France, 1990. World Scientific.

[Jansen]   Douglas M. Jansen. *Transverse Momentum and the Energy Flow of Charged Hadrons Produced in 490 GeV/c Deep Inelastic Muon Scattering*. PhD thesis, University of Washington, 1991.

[Joo76]   P. Joos *et.al.* (DESY). Rho production by virtual photons. *Nuclear Physics*, B113:53–92, 1976.

[Kir78]   Tom Kirk. A multihit time encoder system (MUTES). memo FS017, Fermilab, December 1978.

[Kun84]   S. Kunori. Data from fnl test. CAL internal memo CAL052, E665, March 1984.

[Kun89a]   Shuichi Kunori. Plan for LAT filter. software talk ST0156, E665, March 1989.

[Kun89b]   Shuichi Kunori. PTMV output. software talk ST0186, E665, May 1989.

[Lan91]   P. V. Landshoff. The long-range strong interaction at high energy. Technical Report DAMTP 91/20, DAMTP, University of Cambridge, 1991.

[LN87]   P. V. Landshoff and O. Nachtmann. Vacuum structure and diffraction scattering. *Z.Phys.*, C35:405–416, 1987.

[Mag90a]   Stephen Magill. Xe/D_2 cross-section ratio at low x_{Bj} from muon scattering at 490 GeV/c. Technical Report FERMILAB-Conf-90/127-E, Fermilab, June 1990.

[Magill]   Stephen Magill. *XE/D_2 Cross Section Ratio from Muon Scattering at 490 GeV/c*. PhD thesis, University of Illinois at Chicago, 1990.

[Man85a]   Andreas Manz. 2M×2M proportional chambers (PC1-3). memo VS013, E665, October 1985.

[Man85b]   Andreas Manz. The vertex proportional chamber. memo VS012, E665, October 1985.

[Mel86]   Harry Melanson. Drift chamber time sums. memo FS016, E665, July 1986.

[Mel88a]   Harry Melanson. E665 DC calibration, pass 1. report FS027, E665, December 1988.

[Bak89]   Mark Baker. Charged particle trajectories in the "non-bend" view. memo SW109, E665, November 1989.

[Bha86]   Anwar Bhatti. Seattle MWPC system (PCF detector). memo FS011, E665, 1986.

[Bha88]   Anwar Bhatti. Scaler analysis. software talk ST0110, E665, December 1988.

[Bha89]   Anwar Bhatti. LAT filter results. memo ST0171, E665, April 1989.

[Bhatti]   Anwar Ahmad Bhatti. *The Ratio of the Proton and Neutron Structure Functions in 490 GeV/c Deep Inelastic Muon Scattering*. PhD thesis, University of Washington, June 1991.

[BSYP]   T. H. Bauer, R. D. Spital, D. R. Yennie, and F. M. Pipkin. The hadronic properties of the photon in high-energy interactions. *Reviews of Modern Physics*, 50:261–436, 1978.

[BW89]   Anwar Bhatti and Stephen Wolbers. Where is the x axis in E665?—I. memo AN037, E665, February 1989.

[BWJES]   Anwar Bhatti, Steve Wolbers, Doug Jansen, Uwe Ecker, and Michael Schmitt. The DR (Data Reduction) program. report SW113, E665, January 1990.

[CAL]   CAL People. limericks. CAL internal memo CAL100, E665, July 1986.

[Car91]   Timothy Carroll. Hadron contamination. private communication, 1991.

[Clo79]   F. E. Close. *An Introduction to Quarks and Partons*. Academic Press, New York, 1979.

[Cud90]   J. R. Cudell. A QCD-inspired model for exclusive vector meson production in deep inelastic scattering. *Nucl.Phys.*, B336:1–7, 1990.

[Dak73]   J. T. Dakin *et.al.* (SLAC). Measurement of ρ^0 and ϕ-meson electroproduction. *Physical Review*, D8:687–697, 1973.

[Dix79]   R. Dixon *et.al.* (Cornell). Spectrometer study of ϕ-meson electroproduction. *Physical Review*, D19:3185–3196, 1979.

[DL84]   A. Donnachie and P. V. Landshoff. Elastic scattering and diffraction dissociation. *Nucl.Phys.*, B244:322–336, 1984.

[Mel88b]   Harry Melanson. A first look at FILM99 data. report ST0089, E665, October 1988.

[Mel88c]   Harry Melanson. Pattern recognition update. report ST0114, E665, December 1988.

[Mel89a]   Harry Melanson. E665 DC calibration, pass 2. report AN059, E665, December 1989.

[Mel89b]   Harry Melanson. Muon M-C reconstruction efficiency. report ST0192, E665, May 1989.

[Mel89c]   Harry Melanson. PPAM66 muon phase expectations. report ST0183, E665, May 1989.

[Mel91a]   Harry Melanson. Simulating hadron showers in the E665 calorimeter run 87 H2 data. report AN103, E665, April 1991.

[Mel91b]   Harry Melanson. Status report on DC calibration for Run 90. software talk ST0291, E665, January 1991.

[Mel91c]   Harry Melanson. A study of mu-e events from RUN87 data. report AN093, E665, April 1991.

[Mel91d]   Harry Melanson. A study of mu-gamma events from Run 87 data. report AN094, E665, April 1991.

[Mes84]   J. Mester. Pad to pad variation. CAL internal memo CAL034, E665, 1984.

[Mic86]   D. G. Michael. Use of 1885 range bit for TMC EM calorimeter. CAL internal memo CAL103, E665, December 1986.

[Mic87]   D. G. Michael. Options for use of large buffer tank for e665 calorimeter. CAL internal memo CAL114, E665, April 1987.

[Michael]   Douglas Grant Michael. *A Study of Transverse Momentum and Jets Using Forward Hadrons and Photons in Deep Inelastic Muon Scattering at 490 GeV/c*. PhD thesis, Harvard University, April 1990.

[MKW85]   H. Melanson, T. Kirk, and S. Wolbers. Fermilab drift chamber system. memo FS010, E665, October 1985.

[MM86]   A. Melansek, J. Morfin, *et.al.* The Tevatron muon beam: A high intensity beam with well defined polarization, in Tevatron II Facilities Handbook. Technical report, FNAL, 1986.

[Mon84]   H. E. Montgomery. Beam tagging for E665. memo BT007, E665, July 1984.

[Mon86]   H. E. Montgomery. Notes, status of beam tagging for E665 review. memo BT024, E665, October 1986.

[Mor88]   Jorge G. Morfin. The polarized mode of the tevatron muon beam. memo BT063, E665, 1988.

[Nac85]   Otto Nachtmann. Some remarks concerning the vacuum structure in QCD and its manifestations. In S.Brodsky and E.Moniz, editors, *Workshop on Nuclear Chromodynamics*, Santa Barbara, 1985. World Scientific.

[Nic83a]   R. B. Nickerson. Memorandum on use of chambers in e665 e-m calorimeter. CAL internal memo CAL012, E665, August 1983.

[Nic83b]   R. B. Nickerson. Yet more on A/T ratios. CAL internal memo CAL023, E665, October 1983.

[Nic83c]   Richard Nickerson. Collected thoughts concerning electromagnetic calorimeter. calorimeter memo EM001, E665, March 1983.

[Nic84a]   R. B. Nickerson. 600 GeV muon energy deposition. CAL internal memo CAL061, E665, September 1984.

[Nic84b]   R. B. Nickerson. Fake event generator for cal. CAL internal memo CAL063, E665, October 1984.

[Nic84c]   R. B. Nickerson. Offline calorimeter software. CAL internal memo CAL062, E665, September 1984.

[Nic84d]   R. B. Nickerson. Rate dependence test results. CAL internal memo CAL056, E665, August 1984.

[Nic84e]   R. B. Nickerson. Status of analysis of fnl data. CAL internal memo CAL036, E665, January 1984.

[Nic84f]   R. B. Nickerson. Update of analysis of fnl data. CAL internal memo CAL037, E665, February 1984.

[Nic86a]   R. B. Nickerson. Automated capacitance testing. CAL internal memo CAL097, E665, June 1986.

[Nic86b]   R. B. Nickerson. CAMAC and NIM configuration. CAL internal memo CAL090, E665, January 1986.

[Nic87]   R. B. Nickerson. Gas gain stability. CAL internal memo CAL111, E665, November 1987.

[ODa87a]   S. C. O'Day. The e665 gas gain monitor. CAL internal memo CAL115, E665, April 1987.

[ODa87b]   S. C. O'Day. The e665 gas gain monitor pressure transducer calibration. CAL internal memo CAL133, E665, April 1987.

[ODa87c]   S. C. O'Day. GGM data analysis. CAL internal memo CAL110, E665, October 1987.

[ODa88a]   Steve O'Day. LAT filter status. memo ST0010, E665, May 1988.

[ODa88b]   Steve O'Day. Progress on the LAT filter. memo ST0034, E665, July 1988.

[ODa88c]   Steve O'Day. Update on LAT filter. memo ST0060, E665, August 1988.

[O'Day]   Stephen Charles O'Day. *Charged Hadron Multiplicities in 490 GeV Deep Inelastic Muon Scattering.* PhD thesis, University of Maryland, 1990.

[Oli84]   J. Oliver. E665 calorimeter anode wire electronics. CAL internal memo CAL058, E665, August 1984.

[Pap79]   C. del Papa *et.al.* (SLAC). Exclusive vector-meson production in muon-proton scattering. *Physical Review*, D19:1303–1316, 1979.

[PDG]   Particle Data Group. Review of particle properties. *Physics Letters*, B204:1–486, 1988.

[Pip81]   F. M. Pipkin. Photon detector for μ-T experiment. CAL internal memo CAL001, E665, October 1981.

[Qui83]   Chris Quigg. *Gauge Theories of the Strong, Weak, and Electromagnetic Interactions.* Benjamin/Cummings, Reading, Massachusetts, 1983.

[Ram87a]   E. J. Ramberg. Giant physics. CAL internal memo CAL112, E665, December 1987.

[Ram87b]   E. J. Ramberg. If you can't stand the heat, let a computer measure it. CAL internal memo CAL108, E665, April 1987.

[Ram88a]   E. J. Ramberg. Calibration constants fot the pad towers. CAL internal memo CAL120, E665, March 1988.

[Ram88b]   E. J. Ramberg. How to avoid dead spots in CAL. CAL internal memo CAL119, E665, March 1988.

[Ramberg]   Erik J. Ramberg. *Neutral Pion and Eta Production in Deep Inelastic Muon Scattering at 480 GeV*. PhD thesis, University of Maryland, 1989.

[RSB90]   John Ryan, Michael Schmitt, and Anwar Bhatti. Chamber efficiencies. report AN081, E665, Dec,90.

[Rya91]   John Ryan. PRCUTS mistake. private communication, 1991.

[Ryan]   John James Ryan. *Particle Production in Deep Inelastic Muon Scattering*. PhD thesis, Massachusetts Institute of Technology, February 1991.

[SA91a]   Michael Schmitt and Silhacene Aid. Inefficiencies of the muon match, muon projection reconstruction, and LAT filter. report AN090, E665, 21.Mar,91.

[SA91b]   Michael Schmitt and Silhacene Aid. Muon match inefficiency – an update. report AN091, E665, 4.Apr,91.

[Sal86]   Alex Salvarani. Description of track fitting. document SW040, E665, August 1986.

[Salvarani] Alexandro F. Salvarani. *Forward Hadron Production in Muon Deep Inelastic Scattering at 490 GeV from Deuterium and Xenon*. PhD thesis, University of California, San Diego, 1991.

[Sha82]   W. D. Shambroom *et.al.* (Fermilab E98). Diffractive production of vector mesons in muon-proton scattering at 150 and 100 GeV. *Physical Review*, D26:1–22, 1982.

[Sch88a]   M. Schmitt. Second calibration of calorimeter gas gain. CAL memo EM013, E665, March 1988.

[Sch88b]   Michael Schmitt. Event scalers. software talk ST0082, E665, 13.Oct,88.

[Sch89a]   Michael Schmitt. TRNSPT : Routines to transport particles through the spectrometer. memo SW111, E665, December 1989.

[Sch89b]   Michael Schmitt. EM calorimeter based event filter. software talk ST0141, E665, 8.Feb,89.

378

[Sch89c]   Michael Schmitt. Calorimeter high range pedestals. report EM015, E665, 15.Sep,89.

[Sch89d]   Michael Schmitt. Using the calorimeter to remove electromagnetic background. report AN058, E665, 27.Nov,89.

[Sch90a]   Michael Schmitt. Calorimeter pressure and temperature banks. memo SW131, E665, 18.Oct,90.

[Sch90b]   Michael Schmitt. Electron beam 1990 PTMV mini-production. report SW130, E665, 18.Oct,90.

[Sch90c]   Michael Schmitt. Producing calorimeter second level constants. memo SW132, E665, 30.Oct,90.

[Sch90d]   Michael Schmitt. EMEV : Skimming mu-e and mu-gamma events. memo SW156, E665, 15.Feb,90.

[Sch90e]   Michael Schmitt. Drift chamber efficiency model. report AN083, E665, 5.Sep,90.

[Sch90f]   Michael Schmitt. Calorimeter pressure and temperature 1987-88. report AN086, E665, 7.Nov,90.

[Sch91a]   Michael Schmitt. change to nickerson routine (?). memo EM017??, E665, June 1991.

[Sch91b]   Michael Schmitt. Comparison of VTRACK and VCFTRA. memo SW152, E665, February 1991.

[Sch91c]   Michael Schmitt. PCV hit multiplicities in LLIN. report AN085, E665, February 1991.

[Sch91d]   Michael Schmitt. PCV multiplicities in LLIN – an update. report AN089, E665, April 1991.

[Sch91e]   Michael Schmitt. Some beam distributions. memo AN084, E665, January 1991.

[Siegert]   Gabriele Siegert. Identifikation rückwärts gestreuter protonen mit dem E665-Flugzeithodoskop in μD_2- und μXe-Streuung. Master's thesis, Albert-Ludwig-Universität in Freiburg, April 1991.

[SW73]   K. Schilling and G. Wolf. How to analyse vector-meson production in inelastic lepton scattering. *Nuclear Physics*, B61:381–413, 1973.

[Wil83]   R. Wilson. Effect of counting rate on gain. CAL internal memo CAL035, E665, November 1983.

[Wit81a]   Wolfgang Wittek. The convex method. report SW046, E665, 1981.

[Wit81b]   Wolfgang Wittek. Determination of the point(s) of closest approach
            for two charged tracks in an inhomogeneous magnetic field. report
            SW047, E665, 1981.